

Exploration of Microscopic Structure and Dynamics in Halide Perovskite
and Perovskite-Inspired Materials with Solid-State NMR Spectroscopy

by

Abhoy Karmakar

A thesis submitted in partial fulfillment of the requirements for the degree of

Doctor of Philosophy

Department of Chemistry
University of Alberta

© Abhoy Karmakar, 2021

Abstract

The work presented in this thesis describes the synthesis, structure, and optical properties of three different classes of halide-based perovskite materials, namely, metal halide perovskites of ABX_3 type, halide double perovskites of $A_2B'B''X_6$ type, and “vacancy-ordered perovskites” of A_2BX_6 type that have recently been used in various applications, including photovoltaic solar cells, light-emitting diodes, photodetectors, hard radiation detectors, photocatalysis, and many more. The materials were prepared by conventional solvent-based synthesis, and solvent-free mechanochemical and high temperature synthesis routes. A thorough investigation of long- to short-range structural investigation has been undertaken for these materials to understand their complete structural motifs, where, powder X-ray diffraction is used to determine their average long-range structure and crystallinity, and solid-state nuclear magnetic resonance (NMR) spectroscopy is used to study their short ($< 5 \text{ \AA}$) and medium ($5\text{--}10 \text{ \AA}$) structure, dynamics (ion and polyhedral dynamics), degradation kinetics, and mechanisms of these materials. UV-vis-NIR diffuse reflectance spectroscopy has been used to determine the optical absorption properties and bandgap values for these polycrystalline materials, whereas steady-state and time-resolved photoluminescence spectroscopy have been used to understand their optical light emission properties.

Preface

This thesis is an original contribution by Abhoy Karmakar and co-workers. A portion of the research presented in this thesis has been done in collaboration with other national and international researchers, whose contributions are summarized below.

Chapter 2 of this thesis has been published and reprinted with permission from Karmakar, A.; Askar, A. M.; Bernard, G. M.; Terskikh, V. V.; Ha, M.; Patel, S.; Shankar, K.; Michaelis, V. K. Mechanochemical Synthesis of Methylammonium Lead Mixed-Halide Perovskites: Unraveling the Solid-Solution Behavior Using Solid-State NMR. *Chem. Mater.* **2018**, *30*, 2309–2321. Copyright 2018 American Chemical Society. In Chapter 2, my research contribution includes the synthesis, NMR data collection, data analysis, characterization, and preparation of the manuscript. A portion of the synthesis of methylammonium lead mixed-halide perovskites and its powder X-ray diffraction and UV-vis absorption measurements was performed in collaboration with Abdelrahman Askar and Prof. Karthik Shankar at the Department of Electrical and Computer Engineering of the University of Alberta. The solid-state NMR data at 21.14 T and the CASTEP computational results were accomplished in collaboration with Dr. Victor Terskikh from the National Ultrahigh-Field NMR Facility for Solids at the University of Ottawa. Moreover, the DFT computation data to determine ^{207}Pb shielding parameters were supported by Michelle Ha and Dr. Guy Bernard from the Michaelis group at the University of Alberta.

Chapter 3 has been published and reprinted with permission from Karmakar, A.; Bhattacharya, A.; Sarkar, D.; Bernard, G. M.; Mar, A.; Michaelis, V. K. Influence of Hidden Halogen Mobility on Local Structure of $\text{CsSn}(\text{Cl}_{1-x}\text{Br}_x)_3$ Mixed-Halide Perovskites by Solid-State NMR. *Chem. Sci.* **2021**, *12*, 3253–3263. Copyright 2021 Royal Society of Chemistry. In Chapter 3, my research contribution includes the synthesis, NMR data collection, data analysis, characterization, and preparation of the manuscript. A portion of the solid-state high-temperature synthesis to prepare cesium tin(II) mixed-halide perovskites and its unit cell parameter analysis from the powder X-ray diffraction data was carried out in collaboration with Amit Bhattacharya and Prof. Arthur Mar from the Department of Chemistry at the University of Alberta. The X-ray diffraction data were collected by Rebecca Funk from the Department of Earth

and Atmospheric Sciences at the University of Alberta. The variable temperature ^{119}Sn NMR measurements were collected with the help of Dr. Guy Bernard from the Michaelis group at the University of Alberta. The elemental analysis using EDX spectroscopy and the FESEM images were collected with the support of Dr. Guibin Ma from the Department of Earth and Atmospheric Sciences at the University of Alberta.

Chapter 4 of this thesis has been published and reprinted with permission from Karmakar, A.; Dodd, M. S.; Agnihotri, S.; Ravera, E.; Michaelis, V. K. Cu(II)-Doped $\text{Cs}_2\text{SbAgCl}_6$ Double Perovskite: A Lead-Free, Low-Bandgap Material. *Chem. Mater.* **2018**, *30*, 8280–8290. Copyright 2018 American Chemical Society. In Chapter 4, my research contribution includes the synthesis, data collection, data analysis, characterization, and preparation of the manuscript. The solid-state NMR data at 21.14 T were acquired in collaboration with Dr. Victor Terskikh from the National Ultrahigh-Field NMR Facility for Solids at the University of Ottawa. The EPR measurements and their data analysis were performed with the collaboration of Prof. Enrico Ravera of the Department of Chemistry at the University of Florence. The ICP-OES measurements were carried out by Susanna Pucci at the University of Florence. The TGA data were acquired with help from Wayne Moffat and Jennifer Jones from the Analytical and Instrumentation Laboratory, Department of Chemistry at the University of Alberta.

Chapter 5 has been published and reprinted with permission from Karmakar, A.; Bernard, G. M.; Meldrum, A.; Oliynyk, A. O.; Michaelis, V. K. Tailorable Indirect to Direct Band-Gap Double Perovskites with Bright White-Light Emission: Decoding Chemical Structure Using Solid-State NMR. *J. Am. Chem. Soc.* **2020**, *142*, 10780–10793. Copyright 2020 American Chemical Society. In Chapter 5, my research contribution includes the synthesis, data collection, data analysis, characterization, and preparation of the manuscript. The solid-state NMR data at 21.14 T and the CASTEP computational results were accomplished in collaboration with Dr. Victor Terskikh from the National Ultrahigh-Field NMR Facility for Solids at the University of Ottawa. The PL lifetimes were measured in collaboration with Prof. Alkiviathes Meldrum from the Department of Physics at the University of Alberta. The DFT computation calculations were performed in collaboration with Dr. Anton Oliynyk (University of Alberta and Manhattan College). The ICP-OES measurement were performed by Brett

Feland at the Natural Resources Analytical Laboratory, University of Alberta. The TGA data was acquired with the help of Wayne Moffat and Jennifer Jones from the Analytical and Instrumentation Laboratory, Department of Chemistry at the University of Alberta. The elemental analysis using EDX spectroscopy and the FESEM images were collected with a support of Dr. Guibin Ma from the Department of Earth and Atmospheric Sciences at the University of Alberta.

Chapter 6 of this thesis has been published and reprinted with permission from Karmakar, A.; Mukhopadhyay, S.; Gachod, P. G. B.; Mora-Gomez, V. A.; Bernard, G. M.; Brown, A.; Michaelis, V. K. Uncovering Halogen Mixing and Octahedral Dynamics in Cs_2SnX_6 by Multinuclear Magnetic Resonance Spectroscopy. *Chem. Mater.* **2021**, 33, 6078–6090. Copyright 2021 American Chemical Society. In Chapter 6, my research contribution includes the synthesis, data collection, data analysis, characterization, and preparation of the manuscript. The DFT calculations were accomplished in collaboration with Pierre G. B. Gachod, Victor Arturo Mora-Gomez, Prof. Alex Brown at the Department of Chemistry, University of Alberta. The elemental analysis using EDX spectroscopy and the FESEM images were collected with the support of Dr. Guibin Ma from the Department of Earth and Atmospheric Sciences at the University of Alberta.

Please note that minor details such as symbols, figures, and table numbering, etc. have been modified from their original published articles.

I dedicate this thesis to my parents (Joydev and Dipali Karmakar)

“In a day, when you don't come across any problems - you can be sure that you are
travelling in a wrong path”

Swami Vivekananda (1863 – 1902)

Acknowledgements

First, I would like to express my extreme gratefulness to my Ph.D. supervisor, Prof. Vladimir Michaelis for his countless guidance and motivation throughout my Ph.D. degree program. He always encouraged me to think critically and pursue independent research as well as providing research guidance and support when needed. His endless support and advice in my research activities, free-thinking, and writing skills have been invaluable, and I am grateful to be one of his first graduate students. Beyond research activities, his advice towards my career has been vital, and I could not have imagined having a better mentor and advisor during my Ph.D. program.

I would also like to convey my thanks to my supervisory committee members, Prof. Roderick Wasylishen and Prof. Arthur Mar, for their invaluable suggestions and time spent in evaluating my research, thesis, and providing constructive feedback. I also want to thank Prof. Julianne Gibbs, Prof. Jillian Buriak, and Prof. Jonathan Veinot for their participation in my candidacy exam.

It was my great pleasure to work with present and past Michaelis group members, Dr. Guy Bernard, Michelle Ha, Amit Bhattacharya, Riley Hooper, Brittney Klein, Madhu Sudan Chaudhary, Arkadii Pominov, Dylan Tkachuk, Bryce Allen, Katherine Lin, Tony Jin, Enoc Basilio, and many other members that I met during my Ph.D. program and shared valuable research thoughts and ideas. A special thank goes to Dr. Guy Bernard for his continuous support and training in NMR, data analysis, composing manuscripts and thesis, and beyond. I truly appreciate the useful research discussions and assistance from Amit Bhattacharya; a significant amount of work in this thesis may not have been completed without his assistance. I also want to say my heartfelt thanks to nine talented undergraduate students, namely, Satyam Agnihotri, Chuning Shang, Mya Dodd, Xiaoyue Zhang, Srija Mukhopadhyay, Diganta Sarkar, Xiaochuan Ma, Aaron Mitchell, and Brayden Glockzin, who worked alongside me during my Ph.D. program. I express gratitude to members of Prof. Mar's group for sharing ideas and feedback over the years. I also thank Wayne Moffat, Jennifer Jones, and Anita Weiler in the Department of Chemistry, University of Alberta. I am truly grateful to Dr. Anna Jordan for her kind support in editing my Ph.D. thesis.

I really enjoyed working with my first scientific collaborators, Abdelrahman Askar and Prof. Karthik Shankar (University of Alberta) for the first two years of my doctoral program. I also express gratitude to other collaborators, Victor Arturo Mora-Gomez and Prof. Alex Brown (University of Alberta), Meagan Oakley and Prof. Mariusz Klobukowski (University of Alberta), and Dr. Anton Oliynyk (University of Alberta and Manhattan College) for quantum chemical calculations, and Dr. Enrico Ravera (University of Florence) for EPR spectroscopic measurement. I thank Dr. Victor Terskikh at the National Ultrahigh-field NMR Facility for Solids in Ottawa, ON, Canada for acquiring some of the NMR spectra at 21.14 T as well as for CASTEP calculations. I further express thanks to Prof. Alkiviathes Meldrum from the Department of Physics at the University of Alberta for the training and access to his photoluminescence spectroscopic instrumentation.

I am grateful to the Alberta Innovates, FGSR, and the Department of Chemistry (University of Alberta) for financial support with various scholarships, such as the *Alberta Innovates Graduate Student Scholarship*, *Pansy and George Strange Graduate Scholarship*, *Chemistry Alumni International Graduate Scholarship*, and *Graduate Recruitment Scholarship*.

I would like to thank Prof. Anindya Datta and his group members (IIT Bombay) who introduced me to the research for the first time. Finally, I am heartily appreciative of the continuous love, affection, and guidance I received from my parents, sibling, cousins, and other family members. Without their encouragement, I would not be able to complete my studies in higher education. Finally, I would like to take this opportunity to convey my appreciation to all my friends in India and Canada.

Table of Contents

Chapter 1: Introduction: Background of Perovskite Materials and Solid-State NMR Spectroscopy

1.1. Historic Background of Perovskite Materials.....	1
1.2. Halide Perovskites: Structure and Current Interests.....	2
1.2.1. ABX_3 Metal Halide Perovskites.....	2
1.2.2. $A_2B'B''X_6$ Double Perovskites.....	4
1.2.3. A_2BX_6 “Vacancy-Ordered Perovskites”.....	5
1.3. Mechanochemistry: A Solvent-Free Synthesis Approach.....	6
1.4. Investigation of Local Chemical Structure and Dynamics using Solid-State NMR Spectroscopy.....	8
1.4.1. Zeeman Interaction and Boltzmann Distribution of Nuclear Spin States.....	10
1.4.2. Magnetic Shielding and Chemical Shift.....	12
1.4.3. Direct and Indirect Spin-Spin Interactions.....	15
1.4.4. Quadrupolar Interaction.....	17
1.4.5. Magic Angle Spinning.....	21
1.4.6. Nuclear Spin Relaxation – T_1 and T_2	24
1.5. Research Motivation.....	25
1.6. References.....	27

Chapter 2: Mechanochemical Synthesis of Methylammonium Lead Mixed-Halide Perovskites: Unraveling the Solid-Solution Behavior Using Solid-State NMR

2.1. Introduction.....	38
2.2. Experimental Section.....	41
2.2.1. Synthesis of $MAPbX_3$ Using the Inverse Temperature Crystallization (ITC) Technique.....	41
2.2.2. Synthesis of $MAPb(X_xX'_{1-x})_3$ MHPs.....	42
2.2.3. Diffuse Reflectance (DR) Spectroscopy of MHP Perovskites.....	42
2.2.4. Powder X-ray Diffraction (XRD) Measurements.....	42
2.2.5. Solid-State Nuclear Magnetic Resonance Spectroscopy.....	43

2.2.6. NMR Processing, Fitting Procedures, and NMR Considerations.....	44
2.2.7. Quantum Chemical Calculations.....	45
2.2.8. Periodic Calculations.....	45
2.3. Results and Discussion.....	47
2.3.1. MAPb(Cl _x Br _{1-x}) ₃ Hand Ground Mechanochemical Synthesis..	48
2.3.2. MAPb(Cl _x Br _{1-x}) ₃ Ball Milling Mechanochemical Synthesis....	58
2.3.3. MAPb(Br _x I _{1-x}) ₃ Mechanochemical Synthesis.....	62
2.4. Conclusions.....	63
2.5. References.....	64

Chapter 3: Influence of Hidden Halogen Mobility on Local Structure of CsSn(Cl_{1-x}Br_x)₃ Mixed-Halide Perovskites by Solid-State NMR

3.1. Introduction.....	74
3.2. Results and Discussion.....	76
3.2.1 Monoclinic and Cubic Phases of CsSnCl ₃	76
3.2.2 Trapping Cubic CsSnCl ₃ at Room Temperature.....	79
3.2.3 Cubic CsSn(Cl _{1-x} Br _x) ₃ Solid Solution: Synthesis, Long-range Structure and Optical Properties.....	80
3.2.4 Cubic CsSn(Cl _{1-x} Br _x) ₃ Solid Solution: Local Structure using ¹³³ Cs and ¹¹⁹ Sn NMR Spectroscopy.....	82
3.2.5 Local Structure of CsSnBr ₃ Prepared by Solvent, High-Temperature, and Mechanochemical Routes.....	88
3.2.6 Spontaneous Halogen Mobility in CsSnBr ₃	90
3.2.7 Air Stability and Degradation Pathways for CsSnBr ₃	91
3.3. Conclusions.....	93
3.4. References.....	94

Chapter 4: Cu(II)-Doped Cs₂SbAgCl₆ Double Perovskite: A Lead-Free, Low-Bandgap Material

4.1. Introduction.....	103
------------------------	-----

4.2. Results and Discussion.....	106
4.3. Long-Term Stability.....	117
4.4. Conclusions.....	118
4.5. References.....	119

Chapter 5: Tailorable Indirect to Direct Band-Gap Double Perovskites with Bright White-Light Emission: Decoding Chemical Structure Using Solid-State NMR

5.1. Introduction.....	131
5.2. Results and Discussion.....	135
5.2.1. B'-Site Selection Using Goldschmidt Tolerance Factor Directing Bi/In B'(III)-Site Exchange.....	135
5.2.2. Elemental Composition, Morphology, and Thermal Stability.....	135
5.2.3. Optical and Electronic Bandgap Tailoring.....	138
5.2.4. Indirect to Direct Bandgap Transition Using the Calculated Electronic Band Structure.....	139
5.2.5. Steady-State and Time-Resolved PL Spectra.....	141
5.2.6. Insight into HDP Chemical Structure from XRD and NMR Spectroscopy.....	143
5.2.7. Cesium-133 NMR Spectroscopy of the A Site.....	145
5.2.8. Bismuth-209 and Indium-115 NMR Spectroscopy of the B'(III) Sites.....	148
5.2.9. Impact of Medium-Range Structure on ¹¹⁵ In and ²⁰⁹ Bi C _{Qs} Determined Using Quantum Chemical Calculations.....	154
5.3. Conclusions.....	157
5.4. References.....	158

Chapter 6: Uncovering Halogen Mixing and Octahedral Dynamics in Cs₂SnX₆ by Multinuclear Magnetic Resonance Spectroscopy

6.1. Introduction.....	169
6.2. Results and Discussion.....	172
6.2.1. Solvent-Synthesized Cs ₂ SnX ₆ Parents.....	172

6.2.2. Chlorine-35 NMR Spectroscopy in Cs ₂ SnCl ₆	175
6.2.3. SnI ₆ Octahedral Dynamics in Cs ₂ SnI ₆	176
6.2.4. Mechanochemically Synthesized Cs ₂ SnCl _x Br _{6-x} and Cs ₂ SnBr _x I _{6-x} Mixed Halides.....	179
6.2.5. Influence of Synthesis Routes on the Local Structure of Cs ₂ SnI ₆	186
6.3. Conclusions.....	188
6.4. Experimental Section.....	189
6.4.1. Synthesis.....	190
6.4.2. Solid-State NMR Spectroscopy.....	192
6.5. References.....	194
 Chapter 7: Summary and Looking Towards the Future	
7.1. Summary.....	207
7.1.1. ABX ₃ Metal Halide Perovskites.....	207
7.1.2. A ₂ B'B''X ₆ Double Perovskites.....	208
7.1.3. A ₂ BX ₆ "Vacancy-Ordered Perovskites".....	209
7.2. Future Research Priorities Based on my Ph.D. Research.....	210
7.2.1. Stage-I.....	210
7.2.2. Stage-II.....	211
7.2.3. Stage-III.....	212
7.3. References.....	212
 Complete Bibliography.....	 215
 Appendix A: Supplementary Data for Chapter 2.....	 278
Appendix B: Supplementary Data for Chapter 3.....	293
Appendix C: Supplementary Data for Chapter 4.....	309
Appendix D: Supplementary Data for Chapter 5.....	328
Appendix E: Supplementary Data for Chapter 6.....	354

List of Tables

1.1. Properties of NMR active nuclei in halide-based perovskites.....	9
2.1. Assignment of ^{207}Pb NMR peak positions (δ_{cs} , ppm) for parent and MCS-HG mixed-halide perovskites.....	53
5.1. Calculated and experimental bandgap values for $\text{Cs}_2\text{Bi}_{1-x}\text{In}_x\text{AgCl}_6$	140
6.1. Unit cell parameters, direct bandgap, and solid-state ^{133}Cs and ^{119}Sn NMR results for solvent synthesized Cs_2SnX_6 parents.....	172

List of Figures

- 1.1. Crystal structure diagram of (a) ABX_3 metal halide perovskite, (b) $A_2B'B''X_6$ double perovskite, and (c) A_2BX_6 “vacancy-ordered perovskite”3
- 1.2. Schematic diagram of mechanochemical synthesis technique using ball milling or manual hand grinding to prepare perovskite materials from their starting precursors.7
- 1.3. Zeeman interaction of a spin $I = 1/2$ nucleus (e.g., 1H , ^{13}C , etc.) with increasing magnetic field strength.....10
- 1.4. Simulated solid-state NMR spectra under non-spinning condition of ^{13}C nucleus ($I = 1/2$) at 9.4 T ($\omega_0/2\pi = 100$ MHz) with different κ values due to the anisotropic magnetic shielding. Here, $\delta_{iso} = 0$ ppm, $\Omega = 200$ ppm; 250 Hz Gaussian line broadening was applied. Spectra were simulated with the WSolids program.....15
- 1.5. (a) Nuclear charge distributions of spin-1/2 (spherical, $Q = 0$) and quadrupolar nuclei (prolate: $Q > 0$ and oblate: $Q < 0$). (b) Energy level diagram of a spin $I = 3/2$ quadrupolar nucleus showing the Zeeman, first- and second-order perturbation in a strong magnetic field ($B_0 \gg 0$).....17
- 1.6. Simulated full breadth solid-state NMR powder pattern spectra of half-integer quadrupolar nuclei ($I = 3/2, 5/2, 7/2$ and $9/2$) with $\omega_0/2\pi = 100.0$ MHz, $\delta_{iso} = 0$ ppm, $C_Q = 10.0$ MHz, $\eta = 0$, $\Omega = 0$, 250 Hz gaussian line broadening. The x-axis is scaled in units of C_Q . Spectra were simulated with the WSolids program.....19
- 1.7. Simulated solid-state NMR powder pattern spectra of non-spinning sample of a half-integer quadrupolar nucleus (e.g., ^{35}Cl : $I = 3/2$) with $\omega_0/2\pi = 49.0$ MHz, $\delta_{iso} = 0$ ppm, $C_Q = 5.0$ MHz, $\Omega = 0$, 250 Hz Gaussian line broadening. The central transition is shown with different η values due to the second-order perturbation of the Zeeman interaction. Spectra were simulated with the WSolids program.....20
- 1.8. Simulated solid-state NMR spectra of a half-integer quadrupolar nucleus (e.g., ^{35}Cl : $I = 3/2$) with $\omega_0/2\pi = 49.0$ MHz, $\delta_{iso} = 0$ ppm, $C_Q = 5.0$ MHz, Ω

= 0, 250 Hz Gaussian line broadening. The central transition is shown with non-spinning and magic-angle spinning sample conditions. Spectra were simulated with the WSolids program.....	21
1.9. (a) Schematic diagram of magic-angle spinning of sample placed in NMR rotor. (b) Simulated solid-state NMR pattern spectra under non-spinning and magic-angle spinning sample condition of ^{13}C nucleus ($I = 1/2$) at 9.4 T ($\omega_0/2\pi = 100$ MHz) with $\delta_{\text{iso}} = 0$ ppm, $\Omega = 200$ ppm, $\kappa = 0$, and 250 Hz Gaussian line broadening. Spectra were simulated with the WSolids program.....	23
1.10. T_1 and T_2 relaxation decay curves for a nucleus with $T_1 = 4.6$ and $T_2 = 2.0$ arbitrary units.....	25
2.1. ^{207}Pb NMR spectra of nonspinning (a) MCS-BM (blue), (b) MCS-HG (red), and (c) SS (black) samples of $\text{MAPb}(\text{Cl}_{0.5}\text{Br}_{0.5})_3$, acquired at 7.05 T (300 MHz, ^1H), 11.7 T (500 MHz, ^1H), and 21.1 T (900 MHz, ^1H). The gray dotted lines are the best fits for the spectra obtained for the samples prepared with the mechanochemical synthesis methods.....	46
2.2. ^{207}Pb NMR spectra ($B_0 = 11.7$ T) of (a) nonspinning $\text{MAPb}(\text{Cl}_{0.05}\text{Br}_{0.95})_3$ prepared by MCS-HG and (b) nonspinning and (c) MAS ($\omega_r/2\pi = 13.5$ kHz) NMR spectra of $\text{MAPb}(\text{Cl}_{0.95}\text{Br}_{0.05})_3$ prepared by MCS-HG. The δ_{cs} are marked with ‡, and the spinning sideband is identified by an asterisk (*)......	48
2.3. (a) Nonspinning ^{207}Pb NMR spectra (11.7 T) of MCS-HG MHPs and their parent compounds. The assignment of the NMR peaks is shown at the top (the shaded areas are guides to the eye to identify specific NMR sites in the various spectra, and the dashed lines indicate simulated spectra). See the Appendix A for an explanation of how these spectra were fit. (b) Linear relationship of $\delta(^{207}\text{Pb})$ with substitution of Cl with Br (experimental, circles, and $\delta_{\text{iso}}(^{207}\text{Pb})$ quantum chemical calculations (ADF), triangle). (c) Powder X-ray diffraction data. Dotted lines are guides to the eye. (d) A plot of cell parameter ($R^2 = 0.994$) and experimentally determined bandgaps	

extracted from Tauc plots ($R^2 = 0.994$) vs Br mole fraction for the MHP series.....	51
2.4. Anion model quantum chemical calculations (ADF) of $[\text{PbX}_x\text{X}'_{6-x}]^{4-}$ octahedra: (a) calculated shielding vs experimental isotropic chemical shift for the parent perovskites, MAPbX_3 , where $X = \text{Cl, Br, or I}$; (b) calculated isotropic chemical shift with Br substitution for Cl anions (calc. $\delta_{\text{iso}}(^{207}\text{Pb}/\text{ppm}) = 172.25x - 592.57$, where $x = \text{number of Br neighbors}$) and (c) relation between calculated isotropic chemical shift and experimental chemical shift of parent compounds MAPbX_3 , $X = \text{Cl, Br, and I}$ and their respective MHP (Cl/Br or Br/I) (calc. $\delta_{\text{iso}}(^{207}\text{Pb}/\text{ppm}) = 1.03(\text{expt. } \delta_{\text{cs}}(^{207}\text{Pb}/\text{ppm})) + 75.3$).....	55
2.5. Two-dimensional ^{207}Pb EXSY NMR spectra of MAPbCl_3 , MAPbBr_3 , and MCS-HG $\text{MAPb}(\text{Cl}_{0.5}\text{Br}_{0.5})_3$ obtained using (a) 10 μs (red), (b) 50 μs (black), or (c) 2 ms (blue) mixing times. Spectra were acquired at 21.1 T under nonspinning conditions at ambient temperature. Note that the upper spectra are each a superposition of two separate spectra, one for MAPbCl_3 and one for MAPbBr_3	57
2.6. Comparison of data for the $\text{MAPb}(\text{Cl}_{0.5}\text{Br}_{0.5})_3$ MHP prepared using three distinct synthetic approaches: solvent synthesis and mechanochemical synthesis via hand grinding or ball milling. (a) Powder XRD diffraction patterns, (b) nonspinning ^{207}Pb NMR spectra, $B_0 = 21.1 \text{ T}$, and (c) Tauc plots. The straight black lines indicate the bandgap energies at the intersection with the abscissa.....	60
2.7. (a) Nonspinning ^{207}Pb NMR (7.05 T) and (b) powder X-ray diffraction data for MAPbBr_3 (red), MAPbI_3 (blue), and $\text{MAPb}(\text{Br}_{0.5}\text{I}_{0.5})_3$ (green 1 h, black 2 h). The MHP samples were prepared by the MCS-HG method for 1 and 2 h. The black arrows in the NMR spectra (a) indicate incomplete random halide mixing after 1 h (green trace), with small remnants of the parent compounds according to the NMR and XRD data (b, green arrow, 1 h). The black arrow in panel b indicates complete mixing of a single-phase solid solution after 2 h.....	61

3.1. CsSnCl ₃ : (a) monoclinic structure at room temperature, (b) cubic perovskite structure above 379 K, (c) UV-visible absorption spectra collected at room temperature, and (d) Rietveld refinements of powder XRD patterns.....	76
3.2. (a) ¹³³ Cs and (b) ¹¹⁹ Sn NMR spectra collected at room temperature for monoclinic and cubic CsSnCl ₃ . The ¹³³ Cs NMR spectra were acquired at 11.75 T with a magic-angle spinning frequency of 13 kHz. The ¹¹⁹ Sn NMR spectra were acquired at 7.05 T for monoclinic and 11.75 T for cubic CsSnCl ₃ under non-spinning sample conditions at 293 K. In (a), the asterisks (*) indicate spinning side bands.....	77
3.3. (a) Time-dependent ¹³³ Cs NMR spectra ($B_0 = 11.75$ T, $\omega_r/2\pi = 13$ kHz MAS; a short-tip angle and an optimized 300 s recycle delay were used for quantification) of a sample of CsSnCl ₃ prepared by quenching in ice-water. The spectra are normalized to the highest intensity. The asterisks (* _(m)) indicate positions of spinning side bands for the monoclinic phase. (b) Plot of ¹³³ Cs NMR peak area ($\pm 2\%$) as a function of time for the cubic phase.....	79
3.4. (a) Photographs of freshly synthesized CsSn(Cl _{1-x} Br _x) ₃ (top to bottom, $x = 0, 0.10, 0.33, 0.50, 0.67, 0.90, 1$), (b) scanning electron micrograph and elemental maps for CsSn(Cl _{0.50} Br _{0.50}) ₃ , (c) powder XRD patterns, (d) plots of unit cell parameters and band gaps, and (e) UV-visible absorption spectra.....	81
3.5. (a) Local cuboctahedral environment of 12 halogen atoms around the Cs atom. (b) Room temperature ¹³³ Cs NMR spectra for CsSn(Cl _{1-x} Br _x) ₃ , acquired at 11.75 T with a magic-angle spinning frequency of 13 kHz. (c) Plots of $\delta_{\text{iso}}(^{133}\text{Cs})$ and ¹³³ Cs T_1 values as a function of Br content. The δ_{iso} plot was fit to the equation $\delta_{\text{iso}}(^{133}\text{Cs})/\text{ppm} = 64.8 + 40.6x - 41.5x^2$ ($R^2 = 0.999$).....	84
3.6. (a) Local octahedral environment of 6 halogen atoms around the Sn atom. (b) Room-temperature ¹¹⁹ Sn NMR spectra for CsSn(Cl _{1-x} Br _x) ₃ , acquired at	

11.75 T with a magic-angle spinning frequency of 10 kHz. (c) Plots of ^{119}Sn T_1 and ^{119}Sn linewidth values as a function of Br content.....	86
3.7. Room temperature (a) ^{133}Cs NMR spectra with magic-angle spinning (5 kHz) and (b) ^{119}Sn NMR spectra with no magic-angle spinning, acquired at 11.75 T, of CsSnBr_3 samples prepared by solvent synthesis (SS), high-temperature (HT) reactions, and ball-milling (MCS). In (a), the asterisks (*) indicate spinning side bands and the daggers (†) mark peaks attributed to Cs_2SnBr_6	87
3.8. (a) Variable temperature ^{119}Sn NMR non-spinning spectra acquired at 11.75 T and (b) plots of ^{119}Sn T_1 and NMR chemical shift vs. inverse of absolute temperature for solvent synthesized CsSnBr_3	89
3.9. Degraded CsSnBr_3 sample that was exposed to ambient laboratory conditions over 300 days. (a) Powder XRD pattern compared to reference standards shows presence of CsSnBr_3 (p), Cs_2SnBr_6 (⊗), CsBr (◆), and SnBr_4 (#). The blue lines indicate the absence of peaks due to SnO_2 and SnBr_2 . (b) ^{133}Cs NMR spectrum, acquired at 11.75 T with a magic-angle spinning frequency of 5 kHz, shows the presence of CsSnBr_3 , Cs_2SnBr_6 , and CsBr . The asterisks (*) indicate spinning side bands and the dagger (†) indicates an unidentified Cs-containing degradation product. (c) ^{119}Sn NMR spectrum, acquired at 11.75 T with magic-angle spinning frequencies of 0 to 13 kHz.....	92
4.1. (a) Photographs and (b) FESEM images of $\text{Cs}_2\text{SbAgCl}_6$ (i.e., $x = 0.00$) and Cu^{2+} -doped polycrystalline materials. Here, the x values indicate nominal Cu^{2+} loading (see the Appendix C). The scale bar at the lower left of the FESEM images is 2 μm	106
4.2. (a) Powder XRD patterns for $\text{Cs}_2\text{SbAgCl}_6$ ($x = 0.00$) and for Cu^{2+} -doped $\text{Cs}_2\text{SbAgCl}_6$ materials. An expansion of the highly intense (220) peak in the PXRD patterns is shown in (b), illustrating its shift toward higher 2θ values and its broadening as the Cu^{2+} content increases from $x = 0.00$ to 0.10. The dotted line is a guide for the eye. (c) FWHM values of PXRD patterns as a function of Cu^{2+} content ($x = 0.00$ –0.10).....	107

4.3. (a) UV–VIS–NIR DR (solid lines) and normalized absorption (dotted lines) spectrum for Cs₂SbAgCl₆ parent (i.e., $x = 0.00$) and the maximum Cu²⁺-doped ($x = 0.10$) materials. The Tauc plots showing indirect bandgaps of (b) 2.65 eV for Cs₂SbAgCl₆ ($x = 0.00$) and (c) 1.02 eV for the maximum Cu²⁺-doped material ($x = 0.10$). Note that DR spectra are converted to absorbance by using the Kubelka–Munk equation (see the Appendix C).....111

4.4. Solid-state (a) ¹²¹Sb and (b) ¹³³Cs NMR spectra for Cs₂SbAgCl₆ materials with Cu²⁺ doping as indicated; the former spectra were acquired for nonspinning samples at 21.1 T, and the latter were acquired at 11.75 T at a spinning frequency of 13.0 kHz. Contributions of three ¹³³Cs MAS NMR peaks to the total area of the ¹³³Cs NMR spectra are shown in (c). (d) X-band EPR spectra of Cu²⁺-doped Cs₂SbAgCl₆ materials; the arrow indicates the broad and featureless high field g_{II} component of the signal corresponding to isolated Cu²⁺ sites. Note the data presented in (a) were acquired using a selective 90° pulse to emphasize the higher frequency resonance that is subject to a sizable quadrupole coupling constant.....112

4.5. (a) Variable temperature ¹³³Cs MAS NMR spectra of Cu²⁺-doped material ($x = 0.10$) acquired at 11.75 T with a spinning frequency of 13 kHz. Arrows (black and red) are guides to the eye. (b) Temperature dependence of the ¹³³Cs chemical shift of Peak-3; the asterisks (*) and crosses (†) indicate spinning sidebands and Peak-3, respectively. (c) Temperature dependence of the chemical shifts for the three distinct peaks in the ¹³³Cs NMR spectra.....115

4.6. Stability experiments of Cs₂SbAgCl₆ parent (i.e., $x = 0.00$) and the maximum Cu²⁺-doped ($x = 0.10$) materials under the indicated conditions: (a) ¹³³Cs MAS NMR spectra acquired at 11.75 T with a frequency of 13 kHz, and (b) PXRD patterns. (c) TGA analysis data for materials without ($x = 0.00$) and with trace Cu²⁺ doping ($x = 0.01$), showing similar thermal stability.....117

5.1. (a) Photographs of Cs ₂ Bi _{1-x} In _x AgCl ₆ HDPs under visible (upper row) and UV (lower row, $\lambda = 365$ nm) light. (b) FESEM image (2 μ m scale) with corresponding EDS elemental mapping showing a homogeneous distribution of Cs (light green), Bi (dark green), In (orange), Ag (pink), and Cl (violet) for Cs ₂ Bi _{0.085} In _{0.915} AgCl ₆ HDP polycrystals.....	136
5.2. (a) UV-vis absorption spectra (black) and PL spectra (blue), (b) Tauc plots showing indirect ($x \leq 0.5$, gray) and direct ($x > 0.50$, red) bandgaps, and (c) change in bandgap vs indium mole fraction for Cs ₂ Bi _{1-x} In _x AgCl ₆ ($0 \leq x \leq 1$) HDPs.....	137
5.3. (a) HSE06 DFT band structure and density of states for Cs ₂ BiAgCl ₆ . (b) Indirect to direct bandgap transition in the Cs ₂ Bi _{1-x} In _x AgCl ₆ compounds. (c) Electron localization function of the Cs ₂ Bi _{1-x} In _x AgCl ₆ compounds. In c, the 100th slice is shown, with Bi, In, Ag, and Cl atoms located on the plane. Blue, low electron density; red, high electron density.....	137
5.4. (a) PLQY as a function of indium mole fraction (x) for Cs ₂ Bi _{1-x} In _x AgCl ₆ HDPs. (b) PL decay for Cs ₂ Bi _{0.085} In _{0.915} AgCl ₆ with $\lambda_{\text{ex}} = 364$ nm and $\lambda_{\text{em}} = 625$ nm. (c) PXRD patterns, (d) expansion of the (111) peaks in the PXRD patterns, and (e) change in unit cell parameters with indium mole fraction for Cs ₂ Bi _{1-x} In _x AgCl ₆ HDPs. In c, dotted line is a guide for the eye and asterisks (*) denote the positions of background signals for all Cs ₂ Bi _{1-x} In _x AgCl ₆ HDPs (Figure D16).....	142
5.5. Solid-state ¹³³ Cs MAS NMR spectra (solid lines) and its overall best Gaussian fits (blue dotted lines) for Cs ₂ BiAgCl ₆ and Cs ₂ InAgCl ₆ parents and their In ³⁺ - or Bi ³⁺ -doped materials, namely, Cs ₂ Bi _{0.924} In _{0.076} AgCl ₆ and Cs ₂ Bi _{0.085} In _{0.915} AgCl ₆ , respectively. Spectra were acquired at a magnetic field strength of 21.14 T with a spinning frequency of 30 kHz. Gray octahedra represent [AgCl ₆] ⁵⁻ , red octahedra represent [InCl ₆] ³⁻ , and blue octahedra represent [BiCl ₆] ³⁻	145
5.6. Solid-state (a) ²⁰⁹ Bi and (b) ¹¹⁵ In NMR spectra for the Cs ₂ BiAgCl ₆ and Cs ₂ InAgCl ₆ parent materials. NMR spectra were acquired at 21.14 T with and without magic-angle sample spinning as indicated.....	147

5.7. (a) Solid-state ^{209}Bi NMR spectra for the $\text{Cs}_2\text{BiAgCl}_6$ parent, $\text{Cs}_2\text{Bi}_{0.924}\text{In}_{0.076}\text{AgCl}_6$, and $\text{Cs}_2\text{Bi}_{0.085}\text{In}_{0.915}\text{AgCl}_6$ materials. (b) Solid-state ^{115}In NMR spectra for the $\text{Cs}_2\text{InAgCl}_6$ parent, $\text{Cs}_2\text{Bi}_{0.085}\text{In}_{0.915}\text{AgCl}_6$, and $\text{Cs}_2\text{Bi}_{0.924}\text{In}_{0.076}\text{AgCl}_6$ materials. Spectra were acquired at 21.14 T with and without magic-angle spinning as indicated. Asterisks (*) indicate spinning side bands.....	151
5.8. (a) Change in calculated C_Q of the central ^{209}Bi or ^{115}In nuclei with a change in B'(III) site neighbors in the super lattice. Normalized (b) ^{209}Bi and (c) ^{115}In NMR spectra acquired at 21.14 T under nonspinning and magic-angle spinning (18 kHz) conditions, respectively, for the samples as indicated. Normalized intensity in b and c corresponds to vertically scaled spectra with the same amount of Bi or In, respectively, for a sample for a given number of scans. Asterisks (*) in c indicate spinning side bands.....	155
6.1. (a) Crystal structure of Cs_2SnX_6 , local CsX_{12} cuboctahedral environment of 12 halogens around cesium, and local SnX_6 octahedral environment of 6 halogens around tin. (b) Optical absorption spectra (inset—photographs) and (c) powder XRD patterns of solvent-synthesized Cs_2SnX_6 parents.....	170
6.2. Solid-state (a) ^{133}Cs and (b) ^{119}Sn NMR spectra and (c) inversion recovery plot to measure ^{119}Sn spin-lattice (T_1) relaxation values for the solvent-synthesized Cs_2SnX_6 parents. The ^{133}Cs and ^{119}Sn NMR experiments were performed at 11.75 T with MAS frequencies of 5 and 13 kHz, respectively.....	173
6.3. Experimental (lower trace, blue) and simulated (upper trace, red) ^{35}Cl WURST-CPMG solid-state NMR spectrum of the Cs_2SnCl_6 parent ($\nu_r = 0$ kHz, $B_0 = 11.75$ T, sum of 12 frequency steps, 250 kHz/step).....	176
6.4. (a) Schematic diagram of SnI_6 anharmonicity in the Cs_2SnI_6 structure. (b) Variable-temperature ^{119}Sn T_1 data ($\nu_r = 0$ kHz, $B_0 = 11.75$ T) as a function of the inverse of temperature (black text and points), and the ^{119}Sn	

chemical shift as a function of temperature (red text and points) for solvent-synthesized Cs_2SnI_6	177
6.5. (a) Photographs of ball-milled samples: (i) $\text{Cs}_2\text{SnCl}_3\text{Br}_3$, (ii) Cs_2SnBr_6 , (iii) $\text{Cs}_2\text{SnBr}_{4.5}\text{I}_{1.5}$, (iv) $\text{Cs}_2\text{SnBr}_3\text{I}_3$, (v) $\text{Cs}_2\text{SnBr}_{1.5}\text{I}_{4.5}$, and (vi) Cs_2SnI_6 . (b) Scanning electron micrographs and elemental mapping images of $\text{Cs}_2\text{SnBr}_3\text{I}_3$. (c) Powder XRD patterns and (d) normalized optical absorption spectra of ball-milled $\text{Cs}_2\text{SnCl}_x\text{Br}_{6-x}$ and $\text{Cs}_2\text{SnBr}_x\text{I}_{6-x}$ samples (except Cs_2SnCl_6 , solvent synthesized). (e) Plots of unit cell parameters and band gaps of ball-milled $\text{Cs}_2\text{SnBr}_x\text{I}_{6-x}$ series.....	180
6.6. (a) Solid-state ^{133}Cs ($\nu_r = 13$ kHz, $B_0 = 11.75$ T) NMR spectra of ball-milled $\text{Cs}_2\text{SnCl}_x\text{Br}_{6-x}$ and $\text{Cs}_2\text{SnBr}_x\text{I}_{6-x}$ samples (except Cs_2SnCl_6 , solvent synthesized). (b) Experimental and fitted ^{133}Cs NMR spectra, (c) ^{133}Cs chemical shift and ^{133}Cs T_1 values, and (d) population distribution as a function of Br atoms in $\text{CsBr}_m\text{I}_{12-m}$ for $\text{Cs}_2\text{SnBr}_{1.5}\text{I}_{4.5}$	183
6.7. Solid-state ^{119}Sn (non-spinning, $B_0 = 7.05$ T) NMR spectra of (a) ball-milled $\text{Cs}_2\text{SnCl}_x\text{Br}_{6-x}$ and $\text{Cs}_2\text{SnBr}_x\text{I}_{6-x}$ and solvent-synthesized Cs_2SnCl_6 , (b) $\text{Cs}_2\text{SnCl}_3\text{Br}_3$, and (c) $\text{Cs}_2\text{SnBr}_{4.5}\text{I}_{1.5}$. The local $\text{SnCl}_n\text{Br}_{6-n}$ and $\text{SnBr}_n\text{I}_{6-n}$ environments are tentatively assigned in (b,c) from the DFT computations. The blue dotted lines represent the tentative chemical shift ranges for the $\text{SnCl}_n\text{Br}_{6-n}$ octahedra according to the DFT computed results; positional isomers (cis/trans or fac/mer) are not shown for clarity.....	185
6.8. DFT-computed results for $\text{SnCl}_n\text{Br}_{6-n}$: (a) optimized geometries, (b) ^{119}Sn isotropic chemical shift as a function of number of Cl, and (c) simulated ^{119}Sn NMR spectra.....	187
6.9. Solid-state (a) ^{133}Cs ($\nu_r = 5$ kHz, $B_0 = 11.75$ T) and (b) ^{119}Sn (non-spinning, $B_0 = 7.05$ T) NMR spectra of Cs_2SnI_6 samples prepared by solvent-synthesis (SS), hand-grinding (HG), and ball-milling (BM) routes.....	188

List of Schemes

2.1. MCS process for the preparation of MHPs.....	40
4.1. Schematic representation of the (a) $\text{Cs}_2\text{SbAgCl}_6$ double perovskite structure and of possible Cu^{2+} -doped analogues where $[\text{CuCl}_6]^{4-}$ replaces (b) $[\text{AgCl}_6]^{5-}$ or (c) $[\text{SbCl}_6]^{3-}$ or (d) where Cu^{2+} replaces Cs^+ , leading to a formation of a neighboring vacancy.....	108
5.1. Schematic presentation of the crystal structures of the $\text{Cs}_2\text{InAgCl}_6$ and $\text{Cs}_2\text{BiAgCl}_6$ parent materials and of their $\text{Cs}_2\text{Bi}_{1-x}\text{In}_x\text{AgCl}_6$ mixed Bi/In cationic analogues.	134

List of Symbols

0D	Zero-dimensional
2D	Two-dimensional
3D	Three-dimensional
Å	Angstrom
c.a.	Approximately
°C	Degree centigrade
E	Energy
$E(r)$	Electric field at r distance
eV	Electron volt
g	Gram
mg	Milligram
m	Meter
µm	Micrometer
nm	Nanometer
pm	Picometer
s	Second
ms	Millisecond
µs	Microsecond
mL	Microliter
mmol	Millimole
%	Percentage
t	Goldschmidt tolerance factor
µ	Octahedral factor
$V(r)$	Electrostatic potential at r distance
e	Elementary charge
eq	Electric field gradient
h	Planck constant
\hbar	Reduced Planck constant, $h/2\pi$
K	Kelvin
kJ	Kilojoule

Hz	Hertz
kHz	kilohertz
MHz	Megahertz
λ_{ex}	Excitation wavelength
λ_{em}	Emission wavelength
τ	Lifetime
$\tau_{\text{avg.}}$	Average lifetime
r	Distance
T	Absolute temperature
T_1	Spin-lattice relaxation time constant
T_2	Spin-spin relaxation time constant
T_2^*	Effective spin-spin relaxation time constant
t	Time
B_0	Applied static magnetic field strength
I	Nuclear spin
γ	Magnetogyric ratio
ν	Frequency
ν_{ref}	Reference resonance frequency
ν_{sample}	Sample resonance frequency
δ	Chemical shift
δ_{iso}	Isotropic chemical shift
R_{DD}	Direct dipolar coupling constant
R_{eff}	Effective dipolar coupling constant
J	Indirect spin-spin coupling constant
ΔJ	Anisotropy in J
Ω	Span of the magnetic shielding tensor
κ	Skew of the magnetic shielding tensor
λ	Wavelength
Ξ	Frequency ratio
ν_{L}	Larmor frequency
Q	Quadrupolar moment

ν_Q	Quadrupolar frequency
$\Delta\nu_{CT}$	Central transition breadth
$\Delta\nu_{total}$	Total transition breadth
C_Q	Nuclear quadrupolar coupling constant
η	Quadrupolar anisotropy
∞	Infinity
$M_z(t)$	Magnetization along the z -direction at time t
$M_z(\infty)$	Magnetization along the z -direction at time ∞
$M_{xy}(t)$	Net magnetization in the x - y plane at time t
$M_{xy}(\infty)$	Net magnetization in the x - y plane at time ∞
σ	Magnetic shielding tensor
θ	Angle

List of Abbreviations

LHP	Lead halide perovskites
HDP	Halide double perovskites
LED	Light-emitting diode
PCE	Power conversion efficiency
MA	Methyl ammonium
FA	Formamidinium
SS	Solvent synthesis
MCS	Mechanochemical synthesis
HG	Hand grinding
BM	Ball milling
DMF	Dimethyl formamide
DMSO	Dimethyl sulfoxide
HX	Hydrohalic acid
ITC	Inverse temperature crystallization
UV-vis-NIR	Ultraviolet-visible-near infrared spectroscopy
DR	Diffuse reflectance
PL	Photoluminescence
PLQY	Photoluminescence quantum yield
VBM	Valence band maxima
CBM	Conduction band minima
FESEM	Field emission scanning electron microscope
EDX/EDS	Energy-dispersive X-ray spectroscopy
PXRD	Powder X-ray diffraction
ICP-OES	Inductively coupled plasma - optical emission spectrometry
ICP-MS	Inductively coupled plasma - mass spectrometry
TGA	Thermogravimetric analysis
NMR	Nuclear magnetic resonance
N.A.	Natural abundance
RF	Radio frequency

ppm	Part per million
CS	Chemical shift
CG/CGS	Center of gravity shift
CSA	Chemical shift anisotropy
MAS	Magic angle spinning
DFT	Density functional theory
ADF	Amsterdam density functional
CASTEP	Cambridge serial total energy package
EFG	Electric field gradient
CT	Central transition
ST	Satellite transition
GIPAW	Gauge-including projector augmented wave
CPMG	Carr-Purcell-Meiboom-Gill
WURST	Wideband, uniform rate, smooth truncation
vs.	Versus
vide infra	See below
vide supra	See above
et al.	And others

CHAPTER 1

Introduction: Background of Perovskite Materials and Solid-State NMR Spectroscopy

1.1 Historic Background of Perovskite Materials

The journey of perovskite-based material research started in 1839, when a German scientist, Gustav Rose, during his visit to Russia, discovered a new mineral of calcium titanium oxide, CaTiO_3 , in the Ural Mountains.¹ This mineral was named “perovskite” in honor of the Russian mineralogist Lev von Perovski. Nearly five decades later, in 1893, H. L. Wells and his coworkers from the Sheffield Scientific School synthetically prepared a series of cesium lead halide compounds with the similar general formula of CaTiO_3 (ABX_3 type).² Later, in 1926, the crystallographic structure of CaTiO_3 was demonstrated first by Victor Goldschmidt.³ The term “perovskite” has been applied to the entire class of formulations with the perovskite structure. So, what defines a perovskite structure? A perovskite structure is defined as any ABX_3 (or equivalent) stoichiometry with a three-dimensional network of corner-sharing BX_6 octahedra surrounding a larger A-site cation, where the ionic radius of the A-site is larger than the B-site ($r_A > r_B$).⁴⁻⁶ Initially, it was considered as the highest symmetric cubic structure, however, it was found later that a vast majority of ABX_3 compounds have similar corner-sharing BX_6 octahedra but reduced or lower structural symmetry due to distortions of the BX_6 octahedral units. For example, the original CaTiO_3 mineral have a structure that is not truly cubic but rather a slightly deformed modification of the cubic structure (orthorhombic structure) at room temperature.⁷ In 1945, Helen D. Megaw also demonstrated that the structure of BaTiO_3 is, in fact, tetragonal at room temperature, and that the ideal cubic structure is a slight modification of the tetragonal structure, which occurs at a higher temperature (~ 200 °C).⁸ Starting from the 1950s to date, researchers focused on the development of oxide-based perovskites for potential applications as fuel cells, catalysts, gas sensors, glass-ceramics, ferroelectric or superconducting applications, lasers, etc.⁹⁻¹⁵

Though the preparation of cesium lead halide compounds was reported by Wells et al., the structural and physical properties were not investigated until the 1950s. For the first time, in 1958, the “perovskite” structure and photoconductivity properties of colorful cesium lead halides, namely, CsPbX₃ (X = Cl, Br, I), were reported by C. K. Møller.¹⁶ D. Weber first reported the preparation of organic-inorganic hybrid methylammonium lead halide perovskites, MAPbX₃ (methylammonium or MA = CH₃NH₃⁺) in 1978 and their spectroscopic characterizations were started afterwards.¹⁷ Using solid-state NMR spectroscopy, Wasylishen and coworkers reported a rapid reorientation of methylammonium cation inside the cuboctahedral cavity for the first time in these compounds in 1985.¹⁸ Along with solid-state NMR spectroscopy, other spectroscopic techniques such as millimeter-wave and infrared were further used to understand the dynamics and phase transition behaviors in these compounds.^{19–24} The optoelectronic properties of halide perovskites were explored in commercial applications in early 2000.²⁵ The modern era of halide perovskite research began in 2009 when Kojima et al. applied methylammonium lead bromide and iodide perovskites, MAPbBr₃ and MAPbI₃, respectively, in photovoltaic solar cells and reported maximum photoconversion efficiencies (PCEs) of 3.81%.²⁶ Since then, interest in halide perovskites has spiked and led to the introduction of new chemical formulations, enhanced optical and electrical properties, improved device fabrication techniques, and initial steps toward commercialization.^{27–29}

1.2 Halide Perovskites: Structures and Current Interests

1.2.1 ABX₃ Metal Halide Perovskites

The general chemical formula of metal halide perovskites can be written as ABX₃, where A = Cs⁺, CH₃NH₃⁺, CH(NH₂)₂⁺; B = Pb²⁺, Sn²⁺; X = Cl⁻, Br⁻, I⁻. In the ABX₃ perovskite structure, BX₆ octahedra are attached to each other in a corner-sharing manner. The stability of the ABX₃ perovskite structure is elucidated by a semiempirical geometric parameter, known as the Goldschmidt tolerance factor (*t*) (Eq. 1.1), whereas the BX₆ octahedral stability is defined by another semiempirical geometric parameter, known as the octahedral factor (*μ*) (Eq. 1.2).

$$t = \frac{(r_A + r_X)}{\sqrt{2}(r_B + r_X)} \quad (\text{Eq. 1.1})$$

$$\mu = \frac{r_B}{r_X} \quad (\text{Eq. 1.2})$$

where r_A , r_B and r_X are the ionic radii of A, B, and X site ions, respectively.^{30,31} When $t = 0.75 - 1.00$,³² a stable 3D perovskite structure typically forms with corner sharing BX_6 octahedral connectivity. The BX_6 octahedra are usually stable when $\mu = 0.442 - 0.895$.³¹ The values of t and μ provide information on the probability of perovskite structural stability for a given ABX_3 formula.

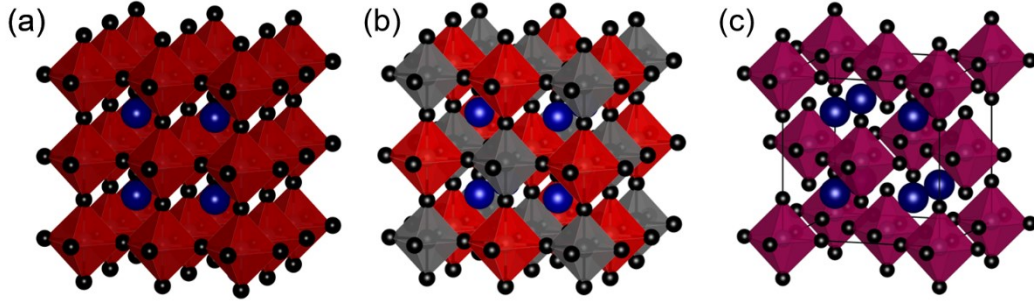


Figure 1.1. Crystal structure diagram of (a) ABX_3 metal halide perovskite, (b) $A_2B'B''X_6$ double perovskite, and (c) A_2BX_6 “vacancy-ordered perovskite”.

In a cubic perovskite structure, as shown in Figure 1.1a, the A-site cation resides in the center of the cuboctahedron, and the B-site is octahedrally coordinated with six X-site halogens. Several structural phases (or polymorphs) of halide perovskites can exist in lower symmetry structures (such as orthorhombic or tetragonal) than that of the highly symmetric cubic structure due to the tilting of the BX_6 octahedral units and deviation of the B–X–B bond angle from 180° . For example, at room temperature, $CH_3NH_3PbCl_3$, $CH_3NH_3PbBr_3$, $CH(NH_2)_2PbX_3$ ($X = Cl, Br, I$), and $CsSnBr_3$ have cubic structures,^{33–36} $CH_3NH_3PbI_3$ is a tetragonal structure,³⁷ while $CsPbX_3$ ($X = Cl, Br$) are orthorhombic structures.^{38–40} Some non-perovskite phases that are stable at room temperature convert to the perovskite phase at higher temperature. For instance, the room temperature non-perovskite phases of $CsSnCl_3$ (monoclinic) and $CsPbI_3$ (orthorhombic or δ -phase) form a perovskite phase above 379 K and 588 K, respectively.^{41,42} On the other hand, perovskite phases also can be obtained by homo- or hetero-valent ion mixing in the A-, B-, and/or X-sites of ABX_3 , which ultimately alter optical properties and can enhance their ambient stability. For example, stable

perovskite phases of A-site mixed $\text{Cs}_x[\text{CH}(\text{NH}_2)_2]_{1-x}\text{PbI}_3$,⁴³ B-site mixed $\text{CH}_3\text{NH}_3\text{Pb}_{1-x}\text{Sn}_x\text{I}_3$,⁴⁴ A- and X-site mixed $(\text{CH}_3\text{NH}_3)_x[\text{CH}(\text{NH}_2)_2]_{1-x}\text{Pb}(\text{Br}_{1-x}\text{I}_x)_3$ (where $0 \leq x \leq 1$)⁴⁵ compositions can be obtained easily under ambient conditions.

Lead halide perovskites (APbX_3) have shown attractive optical and electrical properties for photovoltaic solar cells, light-emitting diodes (LEDs), lasers, UV–vis–NIR photodetectors, X-ray and γ -ray detectors, photocatalysis, and other applications.^{46–52} The perovskite-based solar cells reached a power conversion efficiency (PCE) of 25.5% following a decade of research, whereas the commercialized crystalline-Si based solar cells took nearly five decades to obtain a comparable PCE.⁵³ Despite their attractive optoelectronic properties, the application of lead halide perovskites face significant challenges due to their poor chemical stability and risk of heavy metal lead toxicity.^{54,55} Tin halide perovskites (ASnX_3) are highly promising lead-free alternatives currently showing a PCE of 10–14%;⁵⁶ however, the poor ambient stability of ASnX_3 perovskite drastically reduces their performance within an hour.⁵⁷ Lead-tin mixed $\text{APb}_{1-x}\text{Sn}_x\text{X}_3$ perovskites are more ambient stable alternatives than ASnX_3 perovskites and contain lower lead concentrations than those of the APbX_3 counterparts.⁵⁸ $\text{CH}_3\text{NH}_3\text{Pb}_{1-x}\text{Sn}_x\text{I}_3$ and $\text{CH}(\text{NH}_2)_2\text{Pb}_{1-x}\text{Sn}_x\text{I}_3$ recently have been shown to improve chemical stability in photovoltaic devices, reaching a PCE of 25%.^{44,58}

1.2.2 $\text{A}_2\text{B}'\text{B}''\text{X}_6$ Double Perovskites

Variants of the ABX_3 perovskite structure can be obtained by replacing or partially removing B-site cations to form ordered and vacancy-ordered perovskite structures.⁵⁹ In the ordered perovskites, the two B-site cations are replaced heterovalently by a combination of two cations that are located at specific crystallographic sites.⁵⁹ Because of the double occupancy in the B-site, these perovskites often are called “double perovskites”. The general formula of halide-based double perovskites can be written as $\text{A}_2\text{B}'\text{B}''\text{X}_6$, where $\text{A} = \text{Cs}^+$; $\text{B}' =$ a monovalent cation (e.g., Ag^+ , Na^+); $\text{B}'' =$ a trivalent cation (e.g., Bi^{3+} , Sb^{3+} , In^{3+}), and $\text{X} = \text{Cl}^-$, Br^- , I^- .⁵⁹ The crystallographic structure of $\text{A}_2\text{B}'\text{B}''\text{X}_6$ is shown in Figure 1.1b.

In 2016, Slavney et al. and McClure et al. reported independently for the first time the visible light absorbing capability of lead-free $\text{Cs}_2\text{AgBiX}_6$ ($\text{X} = \text{Cl}$, Br) double

perovskite materials.^{60,61} Unlike ABX₃-type lead and tin halide perovskites, halide double perovskites exhibit a much higher thermal and ambient stability.⁶⁰ The majority of the double perovskite materials are chloride based with larger bandgaps (>2 eV) and exhibit bandgaps that are indirect in nature.⁵⁹ However, a handful of low-bandgap double perovskites have been reported recently in literature. For example, Tl doped Cs₂AgBiBr₆ (*ca.* 1.5 eV), Cs₂AgTlBr₆ (0.95 eV), etc.^{62,63} Double perovskites also have shown excellent photoluminescence (PL) properties both in bulk and nanocrystalline phases.^{59,64,65} The PL properties can be enhanced either in the presence of an activator (e.g., Mn²⁺)⁶⁶ or by changing the chemical compositions on the B' and/or B'' sites.^{65,67} For example, orange light-emitting Mn²⁺ doped Cs₂AgInCl₆ bulk and nanocrystalline materials exhibit an enhanced photoluminescence quantum yield (PLQY),^{68,69} broadband white light emitting Bi-doped Cs₂Ag_xNa_{1-x}InCl₆ (0 ≤ x ≤ 1) double perovskites with stable PLQY of 86% more than 1000 h.⁶⁵

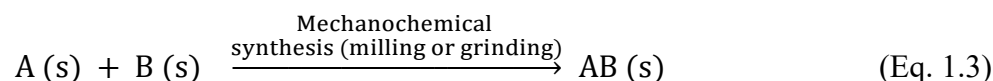
1.2.3 A₂BX₆ “Vacancy-Ordered Perovskites”

Another structurally comparable variant of perovskite-like materials is known as a “vacancy-ordered perovskite” material. The most studied of these is the A₂BX₆ type, where A = monovalent cations (Rb⁺, Cs⁺, CH₃NH₃⁺, CH(NH₂)₂⁺, etc.), B = tetravalent cations (Sn⁴⁺, Te⁴⁺, Pd⁴⁺), X = Cl⁻, Br⁻, I⁻.⁷⁰ The crystallographic structure of A₂BX₆ generally adopts the K₂PtCl₆ structure (space group *Fm* $\bar{3}$ *m*), as shown in Figure 1.1c, which can be compared with the ordered double perovskite structure, where half the B-sites are removed in an ordered fashion and the other half are occupied by a +4 metal ion to form isolated BX₆ octahedral units. Please note that A₂BX₆ materials informally are referred to as “vacancy-ordered perovskite” or “vacancy-ordered double perovskite”, although these materials do not belong to the perovskite family. The isolated BX₆ units in A₂BX₆ provide a degree of dynamic freedom as compared to ABX₃ perovskites.^{71,72} Recently, the rotational disorder of isolated SnI₆ octahedral units has been uncovered by X-ray pair distribution function analysis.⁷¹ Unlike lead- and tin-containing ABX₃ perovskites, vacancy-ordered perovskites of the type A₂BX₆ exhibit a much higher ambient stability. For example, the lower bandgap (1.25–1.62 eV) Cs₂SnI₆ material recently has been used in thin-film photovoltaic devices that

exhibit a much higher air stability and promising optoelectronic properties,⁷³ and Cs₂SnX₆ nanocrystalline materials have shown tailorable light emission properties and photocatalytic activity.^{74–76}

1.3 Mechanochemistry: A Solvent-Free Synthesis Approach

The conventional synthesis methods of advanced functional materials are time consuming and often involve the use of hazardous solvents or heat treatment. Mechanochemical synthesis methods, on the other hand, offer an alternative environmentally friendly material preparation route that may occur under solvent-free or solvent-assisted reaction conditions.^{77–79} Mechanochemical synthesis of materials is enabled by milling or grinding of their starting precursors and the following reaction condition shown in Eq. 1.3:⁷⁸



Mechanochemistry refers to the activation reaction process caused by mechanical energy. An important driving force behind the development of mechanochemical synthesis is the ability to break and form non-covalent bonding interactions quickly, leading to the formation and/or transformation of the desired salt, polymorphs, molecules, etc. at room temperature without the assistance of a bulk solvent.^{77,79} Solvent-free mechanochemical synthesis is highly beneficial to the environment because solvents are usually hazardous for living creatures as well as for the environment. Therefore, mechanochemical synthesis recently has been explored to synthesize a broad variety of organic, inorganic, and organic-inorganic hybrid functional materials, such as organic molecules, metal-organic frameworks, covalent-organic frameworks, graphite, metallic alloys, perovskites, battery materials, etc.^{77–81}

Metal halide perovskite materials can be prepared by various synthetic routes with or without the use of hazardous solvents or costly heat treatments. For example, bulk perovskite materials often are prepared using various solution-based processes, high temperature synthesis, vapor deposition, mechanochemical synthesis, etc.^{82–85} Mechanochemical synthesis is an easy material preparation route by manual hand grinding using a mortar and pestle or by automated ball-milling (Figure 1.2) that

recently has emerged as a promising synthetic route for halide perovskites and other metal halide materials.⁷⁹ Mechanochemical synthesis has many advantages over the more commonly used complementary synthesis routes, such as lower toxicity associated by avoiding the use of organic or inorganic solvents as well as fine control of stoichiometry of the final samples and scalability.⁷⁹ By grinding or milling the binary precursor salts, the desired phase-pure perovskite materials (ABX₃ type) can be obtained by the following equation (Eq. 1.4):⁷⁸

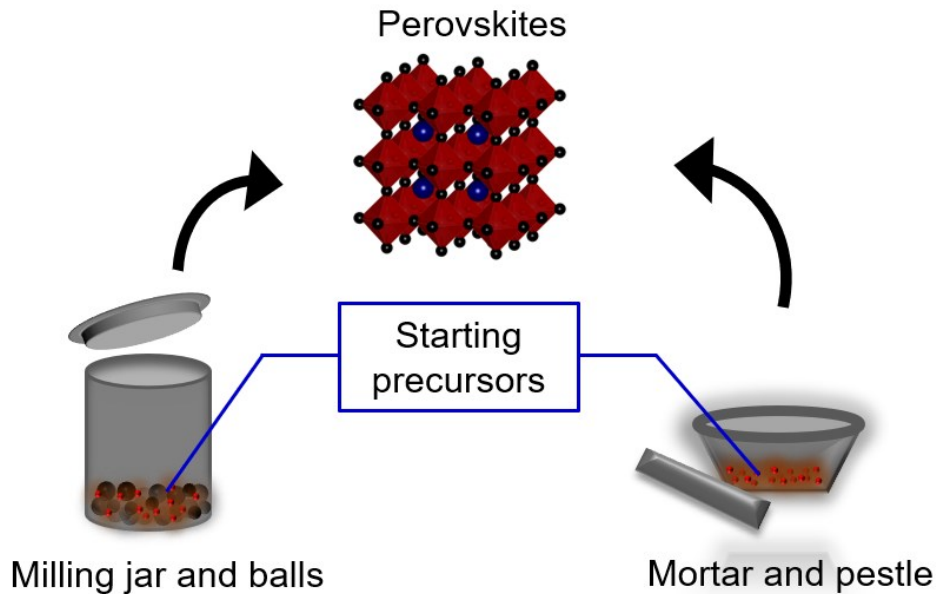
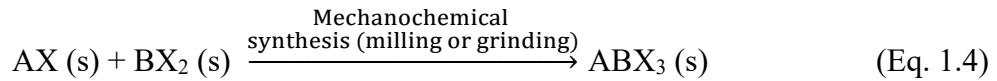


Figure 1.2. Schematic diagram of mechanochemical synthesis technique using ball milling or manual hand grinding to prepare perovskite materials from their starting precursors.

In Eq. 1.4, A is a monovalent organic or inorganic cation (MA⁺, FA⁺, Cs⁺, or their mixture), B is a bivalent cation (Pb²⁺, Sn²⁺, or their mixture), and X is a monovalent halide anion (Cl⁻, Br⁻, I⁻, or their mixture). In 2013, mechanochemical synthesis of lead halide perovskite was demonstrated by Stoumpos et al.; a phase pure product was obtained by hand grinding the starting precursors with a mortar and pestle followed by thermal annealing under vacuum.⁸⁶ In 2015, Prochowicz et al. reported the formation

of a phase-pure product of MAPbI₃ using an automated electric ball milling instrument without the need of any further treatment.⁸⁵

1.4 Investigation of Local Chemical Structure and Dynamics Using Solid-State NMR Spectroscopy

Understanding the structure-property-function relationship is crucial to unravel the working principle of advanced functional materials including halide perovskites.⁸⁷ The structural investigations of new inorganic and hybrid materials usually are undertaken with X-ray, electron, or neutron-based diffraction techniques, as well as vibrational spectroscopy. X-ray diffraction-based techniques are used extensively, providing information about the average long-range structure of the material. On the other hand, solid-state nuclear magnetic resonance (NMR) spectroscopy is a powerful nondestructive analytical technique that provides vital information on the short- and medium-range chemical structure (<10 Å resolution) as well as on the ion dynamics present in materials.^{35,88} As such NMR spectroscopy has been used extensively to explore the local structure and dynamics of a variety of materials, including porous and bulk compounds, nanocrystalline semiconductors, organometallic compounds, and, more recently, they have been applied to study metal halide perovskite materials.^{35,89,90}

NMR spectroscopy is a versatile tool that enables one to understand the nature of chemical environments, polyhedral geometry, ion dynamics, particle size, crystallinity, and degradation kinetics of halide perovskites. A detailed discussion of NMR theory is beyond the scope of this thesis; however, a brief overview of some relevant fundamental NMR concepts and terms are presented below. The readers are referred to several textbooks and articles for further understanding.^{91–97}

Essentially, all elements that form halide perovskites have an NMR-active nucleus, with common ones, such as ¹H, ¹³C, ^{14/15}N, ^{35/37}Cl, ⁷³Ge, ^{79/81}Br, ^{107/109}Ag, ^{113/115}In, ¹¹⁹Sn, ^{121/123}Sb, ¹²⁷I, ¹³³Cs, ²⁰⁷Pb, and ²⁰⁹Bi (Table 1.1). The major magnetic and electromagnetic interactions that couple with the nucleus of interest in NMR spectroscopy are the Zeeman interaction (H_Z), magnetic shielding (H_{MS}), direct and indirect spin-spin interactions (H_D and H_I , respectively), and quadrupolar interactions

(H_Q), as shown in Eq. 1.5.^{98,99} The magnitude of these interactions may vary from less than 1 Hz to several MHz.

$$H_{\text{total}} = H_Z + H_{\text{MS}} + H_D + H_J + H_Q \quad (\text{Eq. 1.5})$$

Table 1.1. Properties of NMR active nuclei in halide-based perovskites.^{100,102}

Isotope	Nuclear spin, I	Natural abundance (%)	Frequency ratio, Ξ (%)	Quadrupolar moment, Q (fm ²)
¹ H	1/2	99.9885	100.000000	N.A.
² H	1	0.0115	15.350609	0.2860
¹³ C	1/2	1.07	25.145020	N.A.
¹⁴ N	1	99.632	7.226317	2.044
¹⁵ N	1/2	0.368	10.136767	N.A.
³⁵ Cl	3/2	75.78	9.797909	-8.165
³⁷ Cl	3/2	24.22	8.155725	-6.435
⁷³ Ge	9/2	7.73	3.488315	-19.6
⁷⁹ Br	3/2	50.69	25.053980	31.3
⁸¹ Br	3/2	49.31	27.006518	26.2
¹⁰⁷ Ag	1/2	51.839	4.047819	N.A.
¹⁰⁹ Ag	1/2	48.161	4.653533	N.A.
¹¹³ In	9/2	4.29	21.865755	79.9
¹¹⁵ In	9/2	95.71	21.912629	81.0
¹¹⁹ Sn	1/2	8.59	37.290632	N.A.
¹²¹ Sb	5/2	57.21	23.930577	-36.0
¹²³ Sb	7/2	42.79	12.959217	-49.0
¹²⁷ I	5/2	100	20.007486	-71.0
¹³³ Cs	7/2	100	13.116142	-0.343
²⁰⁷ Pb	1/2	22.1	20.920599	N.A.
²⁰⁹ Bi	9/2	100	16.069288	-51.6

1.4.1 Zeeman Interaction and Boltzmann Distribution of Nuclear Spin States

In the absence of an external magnetic field ($B_0 = 0$), nuclear spin states of the same absolute values (e.g., $\pm 1/2$, $\pm 3/2$, $\pm 5/2$, etc.) are degenerate in energy. When a nucleus is placed in an external magnetic field ($B_0 > 0$), the nuclear spins interact with the external magnetic field, and the degeneracy of the nuclear spin states is lifted such that they split into distinct energy levels. The energy level diagram for a spin $I = 1/2$ nucleus in the absence and presence of an external magnetic field is shown in Figure 1.3.

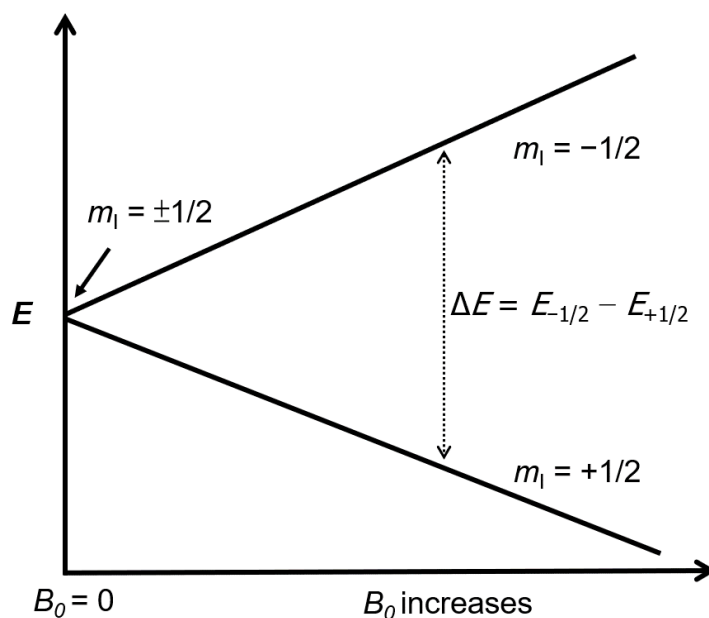


Figure 1.3. Zeeman interaction of a spin $I = 1/2$ nucleus (e.g., ^1H , ^{13}C , etc.) with increasing magnetic field strength.

The Zeeman interaction is expressed by its Hamiltonian as shown in Eq. 1.6,⁹⁸

$$H_Z = -\gamma (\hat{I}_x, \hat{I}_y, \hat{I}_z) \begin{bmatrix} 1 & 0 & 0 \\ 0 & 1 & 0 \\ 0 & 0 & 1 \end{bmatrix} \begin{pmatrix} B_{0,x} \\ B_{0,y} \\ B_{0,z} \end{pmatrix} \quad (\text{Eq. 1.6})$$

where γ is the magnetogyric ratio and \hat{I}_x , \hat{I}_y and \hat{I}_z are the spin angular momentum operators along the x -, y - and z - axes, respectively. As the direction of the external

magnetic field is usually defined along $+z$ axis in the laboratory frame, meaning that $\mathbf{B}_0 = (0, 0, B_{0,z})$, the Hamiltonian in Eq. 1.7. can be simplified as

$$H_z = -\gamma B_0 \hat{I}_z \quad (\text{Eq. 1.7})$$

After a quantum mechanical operation with the Zeeman Hamiltonian, the energy eigen value is obtained as shown in Eq. 1.8:⁹⁹

$$E = -m\gamma\hbar B_0 \quad (\text{Eq. 1.8})$$

The energy difference between these energy levels is proportional to the strength of the applied magnetic field as shown in Eq. 1.9, where a spin $I = 1/2$ nucleus is considered for an example.

$$\Delta E = E_{-1/2} - E_{+1/2} = \gamma\hbar B_0 \quad (\text{Eq. 1.9})$$

$$\nu_L = \frac{\gamma B_0}{2\pi} \quad (\text{Eq. 1.10})$$

Each NMR-active isotope has a specific frequency, defined as the Larmor frequency (ν_L), which corresponds to the Zeeman splitting in the applied magnetic field, as shown by Eq. 1.10. The Larmor frequency typically falls into the radiofrequency (RF) region (i.e., in the order of MHz), and hence it is a low energy spectroscopic method in the electromagnetic spectrum.

The relative populations of two spin states can be determined by the Boltzmann distribution,⁹⁹

$$\frac{n_{\text{upper}}}{n_{\text{lower}}} = e^{-\Delta E/kT} = e^{-\gamma\hbar B_0/kT} \quad (\text{Eq. 1.11})$$

where n_{upper} and n_{lower} are the populations of higher and lower spin states, respectively, ΔE is the energy difference between two spin states, k is the Boltzmann constant, and T is the absolute temperature.

A typical sample used in a solid-state NMR experiment contains about 10^{20} (on the order of mmol) nuclei of interest. For a ^{13}C nucleus at $B_0 = 11.75$ T, $\nu_L = 125$ MHz, and $\Delta E = 0.83 \times 10^{-25}$ J. Then $n_{\text{upper}}/n_{\text{lower}} = 0.99998$ at $T = 298$ K. Thus, only a small proportion of nuclear spins contributes to the NMR signal, and the amplitude of the detected NMR signal is proportional to the difference in the population between the two spin states. The population difference between upper and lower states, n_{diff} , can be obtained from Eq. 1.12 as:

$$n_{\text{diff}} = (n_{\text{upper}} + n_{\text{lower}}) \cdot \frac{1 - e^{-\Delta E/kT}}{1 + e^{-\Delta E/kT}} \quad (\text{Eq. 1.12})$$

Under the high temperature approximation, i.e., $\Delta E/kT \ll 1$, which is appropriate for NMR, one can write:

$$n_{\text{diff}} = (n_{\text{upper}} + n_{\text{lower}}) \cdot (\Delta E/2kT) = (n_{\text{upper}} + n_{\text{lower}}) \cdot (\gamma \hbar B_0/2kT) \quad (\text{Eq. 1.13})$$

From Eq. 1.13, we can conclude that the sensitivity of NMR signal can be enhanced either by increasing the magnetic field strength (i.e., B_0) or by decreasing the experimental temperature (i.e., T). A small proportion of spins contributes to the NMR signal, typically on the order of 1/1000 to 1/10000.

1.4.2 Magnetic Shielding and Chemical Shift

The total magnetic field strength experienced by a nucleus depends on the local electronic environment around that nucleus. In the presence of an external magnetic field (B_0), electrons around a nucleus create a secondary local magnetic field, which may be opposite to or align with B_0 . The magnetic shielding Hamiltonian⁹⁸ can be written as:

$$H_{\text{MS}} = \gamma (\hat{I}_x, \hat{I}_y, \hat{I}_z) \begin{bmatrix} \sigma_{xx} & \sigma_{xy} & \sigma_{xz} \\ \sigma_{yx} & \sigma_{yy} & \sigma_{yz} \\ \sigma_{zx} & \sigma_{zy} & \sigma_{zz} \end{bmatrix} \begin{pmatrix} B_{0,x} \\ B_{0,y} \\ B_{0,z} \end{pmatrix} \quad (\text{Eq. 1.14})$$

Since $\mathbf{B}_0 = (0, 0, B_{0,z})$, the full magnetic shielding Hamiltonian in Eq. 1.15 can be simplified as:

$$H_{\text{MS}} = \gamma [\sigma_{xz} B_0 \hat{I}_x + \sigma_{yz} B_0 \hat{I}_y + \sigma_{zz} B_0 \hat{I}_z] \quad (\text{Eq. 1.15})$$

Considering that the Hamiltonian only interacts with the Zeeman Hamiltonian:

$$H_{\text{MS}} = \gamma \sigma_{zz} B_0 \hat{I}_z \quad (\text{Eq. 1.16})$$

The magnitude of the observed local magnetic field (B_{obs}) at a nucleus can be expressed by Eq. 1.17,

$$B_{\text{obs}} = B_0 (1 - \sigma_{zz}) \quad (\text{Eq. 1.17})$$

where the induced magnetic field is proportional to the applied external magnetic field strength (B_0).

The observed frequency (ν_{obs}) of the nucleus within a sample deviates slightly from ν_L due to the change in the local magnetic environment around the nucleus of interest, as described by Eq. 1.18,

$$\nu_{\text{obs}} = \nu_L(1 - \sigma_{zz}(\theta)) \quad (\text{Eq. 1.18})$$

where the value of $\sigma_{zz}(\theta)$ depends on the orientation of the chemical shift tensor within the external magnetic field, B_0 . For a powder sample, the value of the shielding constant ($\sigma_{zz}(\theta)$) for a given nucleus can be determined as:⁹⁹

$$\sigma_{zz}(\theta) = \frac{1}{3} \text{Tr} \overline{\overline{\sigma}}^{\text{PAS}} + \frac{1}{3} \sum_{j=1}^3 (3 \cos^2 \theta_j - 1) \sigma_{jj} \quad (\text{Eq. 1.19})$$

$$\overline{\overline{\sigma}}^{\text{PAS}} = \begin{bmatrix} \sigma_{11} & 0 & 0 \\ 0 & \sigma_{22} & 0 \\ 0 & 0 & \sigma_{33} \end{bmatrix} \quad (\text{Eq. 1.20})$$

where, $\overline{\overline{\sigma}}^{\text{PAS}}$ is written as shown in Eq. 1.20, $\text{Tr} \overline{\overline{\sigma}}^{\text{PAS}}$ is the trace of the magnetic shielding tensor, and θ_j is the angle between the component σ_{jj} ($j = 1, 2, 3$) and \mathbf{B}_0 . In the principal axis system (PAS), three magnetic shielding tensor components are defined such that $\sigma_{11} \leq \sigma_{22} \leq \sigma_{33}$, i.e., the σ_{11} component is in the direction of minimum shielding and the σ_{33} is the direction of the highest shielding.

Since it is not straightforward to obtain magnetic shielding parameters experimentally, NMR spectroscopists often use the term called chemical shift (δ) to quantify the interaction.¹⁰¹ The chemical shifts are given relative to an agreed reference compound, such as $\delta = 0$ for ^{13}C nucleus in TMS. The experimentally observed chemical shift of a nucleus is expressed by the frequencies of the sample and the reference compound (ν_{ref}) as shown in Eq. 1.21:¹⁰²

$$\delta = \frac{\nu_{\text{obs}} - \nu_{\text{ref}}}{\nu_{\text{ref}}} \quad (\text{Eq. 1.21})$$

$$\delta = \frac{\sigma_{\text{ref}} - \sigma}{1 - \sigma_{\text{ref}}} \approx (\sigma_{\text{ref}} - \sigma) \quad (\text{Eq. 1.22})$$

The chemical shift is usually reported in parts per million (ppm) by multiplying the numerator by 10^6 .

However, the chemical shift also can be expressed by the magnetic shielding parameters, as shown in Eq 1.22, which usually is used to calculate the chemical shift values from the magnetic shielding values obtained from theoretical computations. Note that the approximation in Eq. 1.22 is valid for nuclei with small chemical shift

ranges (e.g., ^1H , ^{13}C , etc.), but a significant error may occur for heavier nuclei with large chemical shift ranges (e.g., ^{119}Sn , ^{195}Pt , ^{207}Pb).

For liquid NMR spectra, the anisotropy of the chemical shift tensor is averaged out because of fast molecular tumbling in the solvents, and a single sharp isotropic chemical shift is observed (assuming no other residual couplings). However, for solid powder samples, the molecules are oriented in all possible orientations with respect to the external magnetic field, and hence the observed NMR powder pattern is the sum of chemical shifts from all crystallites, which ultimately gives a broad NMR signal with a characteristic lineshape. The electronic environment around a nucleus in a solid molecule/material is typically non spherical (i.e., anisotropic), hence, the chemical shift is anisotropic, changing as the orientation of the molecule changes with respect to the applied magnetic field. This is called the orientation dependence of magnetic shielding. The magnetic shielding tensor in Eq. 1.20 can be rewritten in terms of chemical shift as follows:

$$\bar{\delta}^{PAS} = \begin{bmatrix} \delta_{11} & 0 & 0 \\ 0 & \delta_{22} & 0 \\ 0 & 0 & \delta_{33} \end{bmatrix} \quad (\text{Eq. 1.23})$$

The chemical shift tensor can be described by the principal components, where three chemical shift tensor components are defined such as $\delta_{11} \geq \delta_{22} \geq \delta_{33}$, i.e., δ_{11} component is in the direction of the largest chemical shift (least shielded) and δ_{33} component is in the direction of the lowest chemical shift (highest shielding). According to the Maryland convention, the average shift (isotropic chemical shift, δ_{iso}), full breadth of anisotropy (span, Ω) and the shape of the anisotropic peak (skew, κ , where $-1 \leq \kappa \leq 1$) are expressed by Eqs. 1.24, 1.25, and 1.26, respectively.¹⁰³

$$\delta_{\text{iso}} = \frac{\delta_{11} + \delta_{22} + \delta_{33}}{3} \quad (\text{Eq. 1.24})$$

$$\Omega = \delta_{11} - \delta_{33} \quad (\text{Eq. 1.25})$$

$$\kappa = \frac{3(\delta_{22} - \delta_{\text{iso}})}{\Omega} \quad (\text{Eq. 1.26})$$

An isotropic chemical shift is observed for a nucleus which resides in a spherically symmetric chemical environment because in this case $\delta_{11} = \delta_{22} = \delta_{33}$, whereas if $\delta_{11} = \delta_{22} \geq \delta_{33}$ ($\kappa = 1$) or $\delta_{11} \geq \delta_{22} = \delta_{33}$ ($\kappa = -1$) yields an axially symmetric powder pattern under non-spinning sample conditions, as shown in Figure 1.4. The

chemical shift anisotropic interaction typically is found to be on the order of 0 to several 1000 ppm. This interaction increases with increasing magnetic field strength and hence this interaction may be minimized at a lower magnetic field.

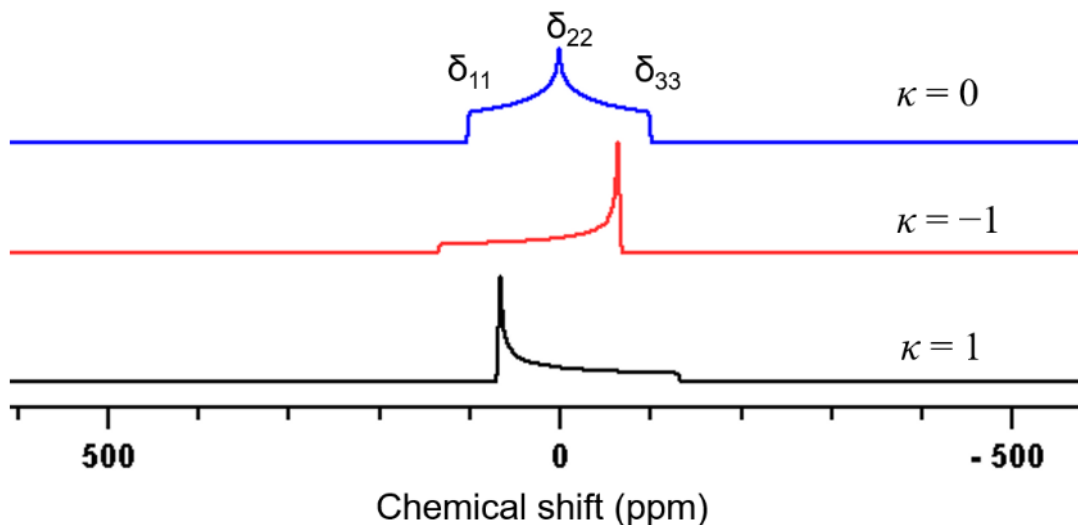


Figure 1.4. Simulated solid-state NMR spectra under non-spinning condition of ^{13}C nucleus ($I = \frac{1}{2}$) at 9.4 T ($\omega_0/2\pi = 100$ MHz) with different κ values due to the anisotropic magnetic shielding. Here, $\delta_{\text{iso}} = 0$ ppm, $\Omega = 200$ ppm; 250 Hz Gaussian line broadening was applied. Spectra were simulated with the WSolids program.¹⁰⁴

1.4.3 Direct and Indirect Spin-Spin Interactions

There are two spin-spin interactions, namely, the direct dipolar and indirect J -coupling interactions.¹⁰⁵ The direct spin-spin interaction, commonly known as dipole-dipole interaction, occurs when the nuclear magnetic moment of a nucleus couples to those of surrounding nuclei. Eq. 1.27 describes the interaction energy (U) between nuclear spins I and S , with a distance of r_{12} and the magnetic dipolar moments of μ_I and μ_S , respectively.

$$U = \frac{\mu_0}{4\pi} \left\{ \frac{\mu_I \cdot \mu_S}{r_{12}^3} - 3 \frac{(\mu_I \cdot r_{12})(\mu_S \cdot r_{12})}{r_{12}^5} \right\} \quad (\text{Eq. 1.27})$$

$$r_{12} = [x^2 + y^2 + z^2]^{1/2} \quad (\text{Eq. 1.28})$$

Here, μ_0 is the permeability constant of free space. The dipolar coupling constant, R_{DD} is inversely proportional to the cube of the internuclear separation between the dipolar coupled nuclei given in Eq. 1.29, providing valuable information about molecular structure,¹⁰³

$$R_{DD} = \frac{\mu_0 \hbar}{8\pi^2} \gamma_I \gamma_S < 1/r_{12}^3 > \quad (\text{Eq. 1.29})$$

where, \hbar is the Planck constant divided by 2π , γ_I and γ_S are the magnetogyric ratios for the dipolar coupled nuclei.

The Hamiltonian for the direct dipolar interaction can be written as:⁹⁸

$$H_D = R_{DD} [\hat{A} + \hat{B} + \hat{C} + \hat{D} + \hat{E} + \hat{F}] \quad (\text{Eq. 1.30})$$

where:

$$\hat{A} = - (3 \cos^2 \theta - 1) \hat{I}_z \hat{S}_z \quad (\text{Eq. 1.31})$$

$$\hat{B} = -\frac{1}{2} (3 \cos^2 \theta - 1) (\hat{I}_z \hat{S}_z - \bar{I} \cdot \bar{S}) \quad (\text{Eq. 1.32})$$

$$\hat{C} = -\frac{3}{2} \sin \theta \cos \theta e^{-i\phi} (\hat{I}_z \hat{S}_+ + \hat{I}_+ \hat{S}_z) \quad (\text{Eq. 1.33})$$

$$\hat{D} = -\frac{3}{2} \sin \theta \cos \theta e^{i\phi} (\hat{I}_z \hat{S}_- + \hat{I}_- \hat{S}_z) \quad (\text{Eq. 1.34})$$

$$\hat{E} = -\frac{3}{4} \sin^2 \theta e^{-2i\phi} \hat{I}_+ \hat{S}_+ \quad (\text{Eq. 1.35})$$

$$\hat{F} = -\frac{3}{4} \sin^2 \theta e^{2i\phi} \hat{I}_- \hat{S}_- \quad (\text{Eq. 1.36})$$

Here, for the nuclear spins I and S , \hat{I}_+ and \hat{S}_+ are the raising operators, and \hat{I}_- and \hat{S}_- are the lowering operators, and θ and ϕ are the polar and azimuthal angles between the dipolar vector and the applied magnetic field along the z -axis, respectively.

The indirect spin-spin coupling, also known as J -coupling, refers to the coupling of two spins through chemical bonds, such as covalent or hydrogen bonding. This indirect interaction arises from the hyperfine interactions between the nuclei and the electrons. The J -coupling provides crucial information about chemical bonding, such as bond angles, which are used extensively in liquid NMR spectroscopy. The anisotropy in the J -coupling (ΔJ) is usually small for the lighter nuclei, however, it may be significant for heavier nuclei. For nuclei subject to noticeable J -coupling, the effective dipolar coupling, R_{eff} , can be measured experimentally from the Eq. 1.37, although please note that this can be quite challenging to measure.

$$R_{\text{eff}} = R_{\text{DD}} - \frac{\Delta J}{3} \quad (\text{Eq. 1.37})$$

In the context of solid materials, such as halide perovskites, the multiplet patterns are much more complex due to the multiple covalently bonded quadrupolar halogen nuclei ($^{35/37}\text{Cl}$ and $^{79/81}\text{Br}$: $I = 3/2$, ^{127}I : $I = 5/2$, total abundance = 100%) to the observed B-site nucleus (e.g., ^{207}Pb , ^{119}Sn , etc.)

1.4.4 Quadrupolar Interaction

The nuclear quadrupolar interaction is an important parameter for solid-state NMR spectroscopy because more than 70% of the NMR-active stable isotopes in the periodic table have a nuclear spin $I > 1/2$.¹⁰⁶ Quadrupolar nuclei have a non-spherical charge distribution and hence possess a nuclear electric quadrupole moment (Q). Quadrupolar nuclei can have a charge distribution that is either prolate or oblate in shape, and have a positive and negative quadrupole moments, respectively (Figure 1.5a).

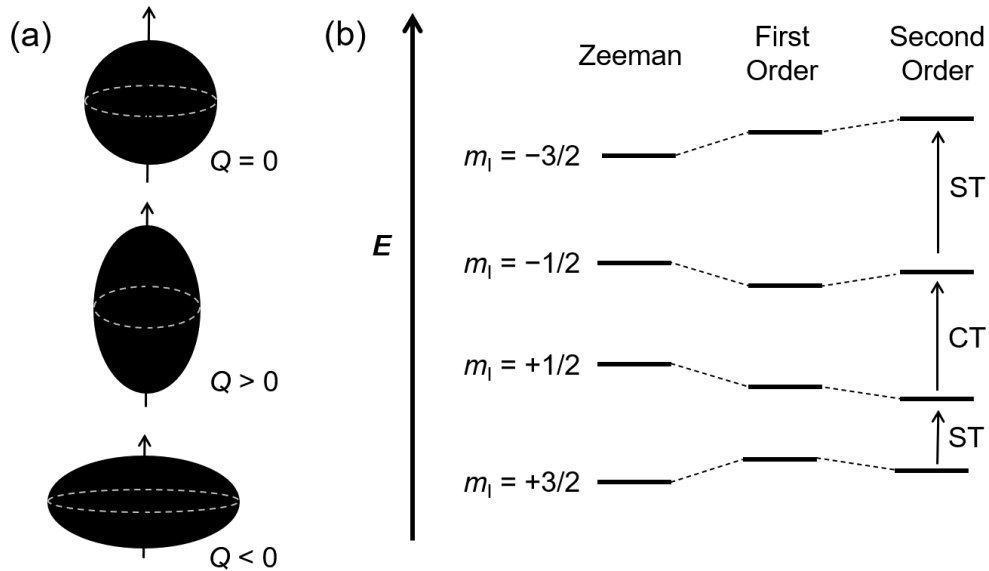


Figure 1.5. (a) Nuclear charge distributions of spin-1/2 (spherical, $Q = 0$) and quadrupolar nuclei (prolate: $Q > 0$ and oblate: $Q < 0$). (b) Energy level diagram of a spin $I = 3/2$ quadrupolar nucleus showing the Zeeman, first- and second-order perturbation in a strong magnetic field ($B_0 \gg 0$).

The magnitude of the quadrupole moment is a measure of the extent of divergence of the nuclear charge distribution from spherical symmetry. Quadrupolar nuclei interact with the surrounding electric field. The electrostatic potential for a point charge can be written by Eq. 1.38,

$$V(r) = \frac{e}{r} \quad (\text{Eq. 1.38})$$

where e and r are the elementary charge and the distance from the point charge, respectively. The electric field is the distance derivative of the electric potential, which can be expressed by Eq. 1.39:

$$E(r) = \frac{-e}{r^2} \quad (\text{Eq. 1.39})$$

The electric field gradient (EFG or eq) is the distance derivative of the electric field, which can be written by Eq. 1.40:

$$\text{EFG} = eq = \frac{2e}{r^3} \quad (\text{Eq. 1.40})$$

The EFG is the sum of contributions from all charge particles in a molecule or in a crystalline solid at a particular nucleus of interest. The EFG at a nucleus is represented by a second-rank symmetrical tensor, where the principal tensor components usually are denoted by V_{XX} , V_{YY} , and V_{ZZ} such that $|V_{XX}| \leq |V_{YY}| \leq |V_{ZZ}|$. NMR spectroscopy provides information on the quadrupolar coupling constant (C_Q ; magnitude) and the asymmetry parameter (η ; shape). C_Q is directly proportional to the largest principal component of the EFG tensor at the nucleus, $V_{ZZ} = eq_{zz}$, and the nuclear quadrupole moment is eQ . C_Q and η are defined by Eqs. 1.41 and 1.42, respectively.

$$C_Q = \frac{e^2 q_{zz}}{h} Q = \frac{eV_{zz}}{h} Q \quad (\text{Eq. 1.41})$$

$$\eta = \frac{V_{XX} - V_{YY}}{V_{ZZ}} \quad (\text{Eq. 1.42})$$

Here, h is Planck's constant and the unit of C_Q is in Hz. Because $|V_{XX}| \leq |V_{YY}| \leq |V_{ZZ}|$, thus $0 \leq \eta \leq 1$. The quadrupolar frequency (ν_Q), which is related to the quadrupolar coupling constant and the nuclear spin number (I), is defined as:

$$\nu_Q = \frac{3C_Q}{2I(2I-1)}. \quad (\text{Eq. 1.43})$$

The quadrupolar Hamiltonian is expressed by the following equation:⁹⁸

$$H_Q = \frac{eQ}{2I(2I-1)\hbar} (\hat{I}_x, \hat{I}_y, \hat{I}_z) \begin{bmatrix} V_{xx} & V_{xy} & V_{xz} \\ V_{yx} & V_{yy} & V_{yz} \\ V_{zx} & V_{zy} & V_{zz} \end{bmatrix} \begin{pmatrix} \hat{I}_x \\ \hat{I}_y \\ \hat{I}_z \end{pmatrix} \quad (\text{Eq. 1.44})$$

Under the high-field approximation, which assumes that the internal NMR interactions are negligible as compared to the Zeeman interaction, the impact of the quadrupolar coupling constant can be described by the first two terms of the quadrupolar Hamiltonian. Hence, the solid-state NMR spectra of the quadrupolar nuclei often are modelled in terms of the first- and second- order quadrupolar interactions to the Zeeman interaction (Figure 1.5b). The powder patterns for the nuclear spin $I = 3/2, 5/2, 7/2,$ and $9/2$ nuclei are shown in Figure 1.6. The total breadth of the powder pattern including the higher order transitions is given by Eq. 1.45:

$$\Delta\nu_{\text{total}} = (2I - 1)\nu_Q \quad (\text{Eq. 1.45})$$

From equations 1.43 and 1.45, one may determine C_Q from the breadth of the spinning sideband manifold of a magic-angle spinning spectrum of a quadrupolar nucleus of interest.

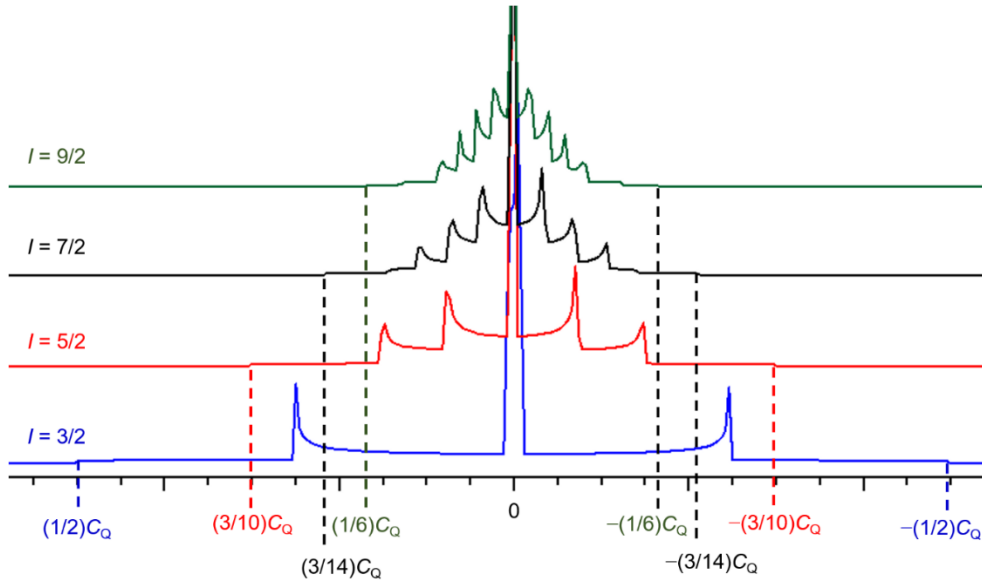


Figure 1.6. Simulated full breadth solid-state NMR powder pattern spectra of half-integer quadrupolar nuclei ($I = 3/2, 5/2, 7/2$ and $9/2$) with $\omega_0/2\pi = 100.0$ MHz, $\delta_{\text{iso}} = 0$ ppm, $C_Q = 10.0$ MHz, $\eta = 0$, $\Omega = 0$, 250 Hz gaussian line broadening. The x-axis is scaled in units of C_Q . Spectra were simulated with the WSolids program.¹⁰⁴

Obtaining NMR spectra of quadrupolar nuclei with all detected transitions may be very challenging and is not always practical since such spectra may span up to several MHz. Thus, NMR spectroscopists usually measure C_Q from the central transition (CT, i.e., $m_I = -1/2 \leftrightarrow m_I = 1/2$) spectra. The CT is impacted by the second-order quadrupolar interaction and often results in broad powder patterns. The shape of the NMR powder pattern is described by the asymmetry parameter as shown in Figure 1.7. Under non-spinning sample conditions, the breadth of the CT ($\Delta\nu_{CT}$) of the powder pattern can be expressed by the following equation:¹⁰⁷

$$\Delta\nu_{CT} = \frac{(25+22\eta+\eta^2)}{144} \frac{\nu_Q^2}{\nu_L} \left[I(I+1) - \frac{3}{4} \right] \quad (\text{Eq. 1.46})$$

while the line width of the CT peak under the magic-angle spinning conditions, $\Delta\nu_{CT}^{MAS}$, is expressed as:

$$\Delta\nu_{CT}^{MAS} = \frac{(\eta+6)^2}{504} \frac{\nu_Q^2}{\nu_L} \left[I(I+1) - \frac{3}{4} \right] \quad (\text{Eq. 1.47})$$

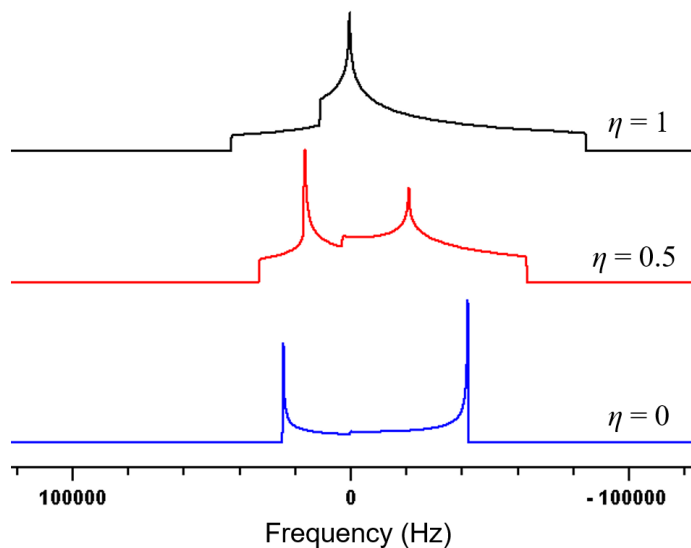


Figure 1.7. Simulated solid-state NMR powder pattern spectra of non-spinning sample of a half-integer quadrupolar nucleus (e.g., ^{35}Cl : $I = 3/2$) with $\omega_0/2\pi = 49.0$ MHz, $\delta_{iso} = 0$ ppm, $C_Q = 5.0$ MHz, $\Omega = 0$, 250 Hz Gaussian line broadening. The central transition is shown with different η values due to the second-order perturbation of the Zeeman interaction. Spectra were simulated with the WSolids program.¹⁰⁴

From equations 1.46 and 1.47, one can demonstrate that the breadth of the CT peak increases with C_Q (i.e., through ν_Q) and decreases with increasing the magnetic field strength, B_0 (i.e., through ν_L). If the magic-angle spinning frequency is greater than the breadth of the CT peak for the sample, then it may be reduced by approximately 60-70 % (Figure 1.8). However, the linewidth and lineshape for the magic-angle spinning NMR spectra is still defined by C_Q and η .

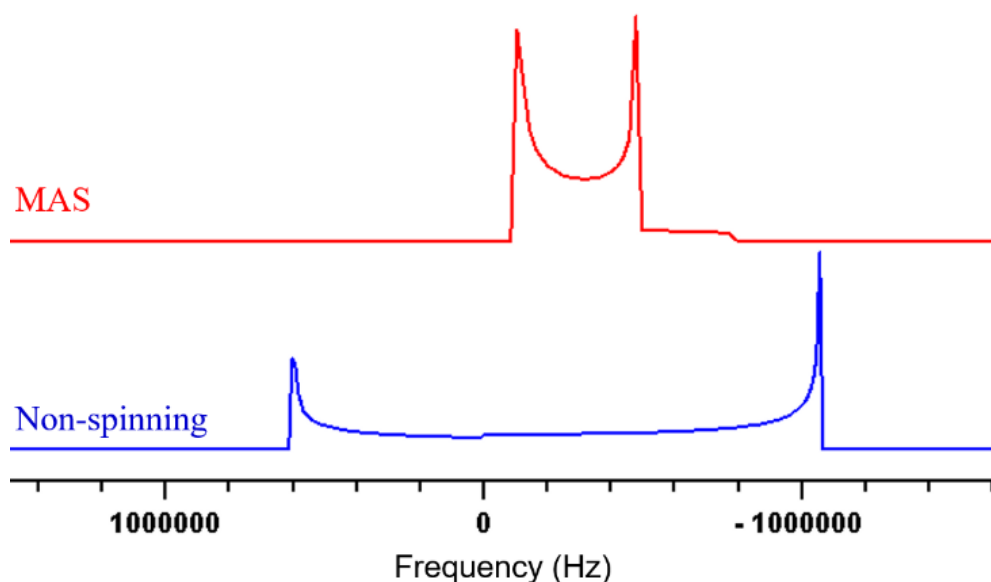


Figure 1.8. Simulated solid-state NMR spectra of a half-integer quadrupolar nucleus (e.g., ^{35}Cl : $I = 3/2$) with $\omega_0/2\pi = 49.0$ MHz, $\delta_{\text{iso}} = 0$ ppm, $C_Q = 5.0$ MHz, $\Omega = 0$, 250 Hz Gaussian line broadening. The central transition is shown with non-spinning and magic-angle spinning sample conditions. Spectra were simulated with the WSolids program.¹⁰⁴

1.4.5 Magic Angle Spinning

NMR spectra of solid samples traditionally were collected under non-spinning sample conditions. The solid-state NMR powder samples consist of millions of tiny crystallites with random orientations in the applied magnetic field, resulting in a characteristic powder pattern, *vide supra*. The powder pattern of the NMR signal contains various

possible information about the anisotropic interactions of the system. Multiple such interactions cause broadening of the NMR signal and create challenges in determining their orientations and magnitudes. Magic angle spinning (MAS)¹⁰⁸ is an experimental process where solid NMR samples are rotated rapidly about an axis 54.74° from the applied external magnetic field to attenuate the orientation dependence of internal NMR interactions (e.g., chemical shielding anisotropy, direct dipole-dipole, etc.) From the Legendre polynomials, some anisotropic interactions contain a common term, $P_2(\cos\theta)$ (Eq. 1.48) when the powder sample is placed in a magnetic field,

$$P_2(\cos\theta) = (3\cos^2\theta - 1)/2 \quad (\text{Eq. 1.48})$$

$$P_4(\cos\theta) = (35\cos^4\theta - 30\cos^2\theta + 3)/8 \quad (\text{Eq. 1.49})$$

where θ can vary between 0° to 90° within the magnetic field. However, at an angle $\theta = 54.74^\circ$ (which is known as “magic-angle”), then, under sample spinning conditions $P_2(\cos\theta) = 0$. If one considers only $I = 1/2$ nuclei, then orientation-dependent anisotropic interactions can be neglected if one can spin solid NMR samples at an “infinite” frequency under the magic-angle orientation. This is the concept of magic-angle spinning (MAS), which frequently is used nowadays by the solid-state NMR community.

In principle, the MAS frequency must be either equal or greater than the magnitude of the anisotropic interactions to remove it completely for $I = 1/2$ nuclei. Hence, MAS of solid samples partially or fully eliminates the effect of these anisotropic interactions, depending on their magnitude. MAS of solid samples not only simplifies the NMR spectra but also improves the signal-to-noise ratio and mimics the NMR spectra of the compounds in solution. If the MAS frequency is significantly less than the breadth of the NMR spectrum obtained in the absence of MAS, then the NMR signal breaks into a series of spinning sidebands, and the spinning sideband manifold can mimic the powder pattern of the non-spinning sample, as shown in Figures 1.9. If the MAS frequency is higher than the breadth of the NMR spectrum, then a sharp NMR peak is observed, which corresponds to the isotropic chemical shift of the nucleus of interest with a nuclear spin $I = 1/2$ or $> 1/2$ with negligible C_Q (Figure 1.9). For example, consider a non-spinning sample containing a ^{13}C nucleus ($I = 1/2$) exhibit a span value of 200 ppm or 20 kHz at a magnetic field of 9.4 T. To obtain a “solution-

like” isotropic ^{13}C peak, one should spin the sample ≥ 20 kHz MAS frequency (Figure 1.9).

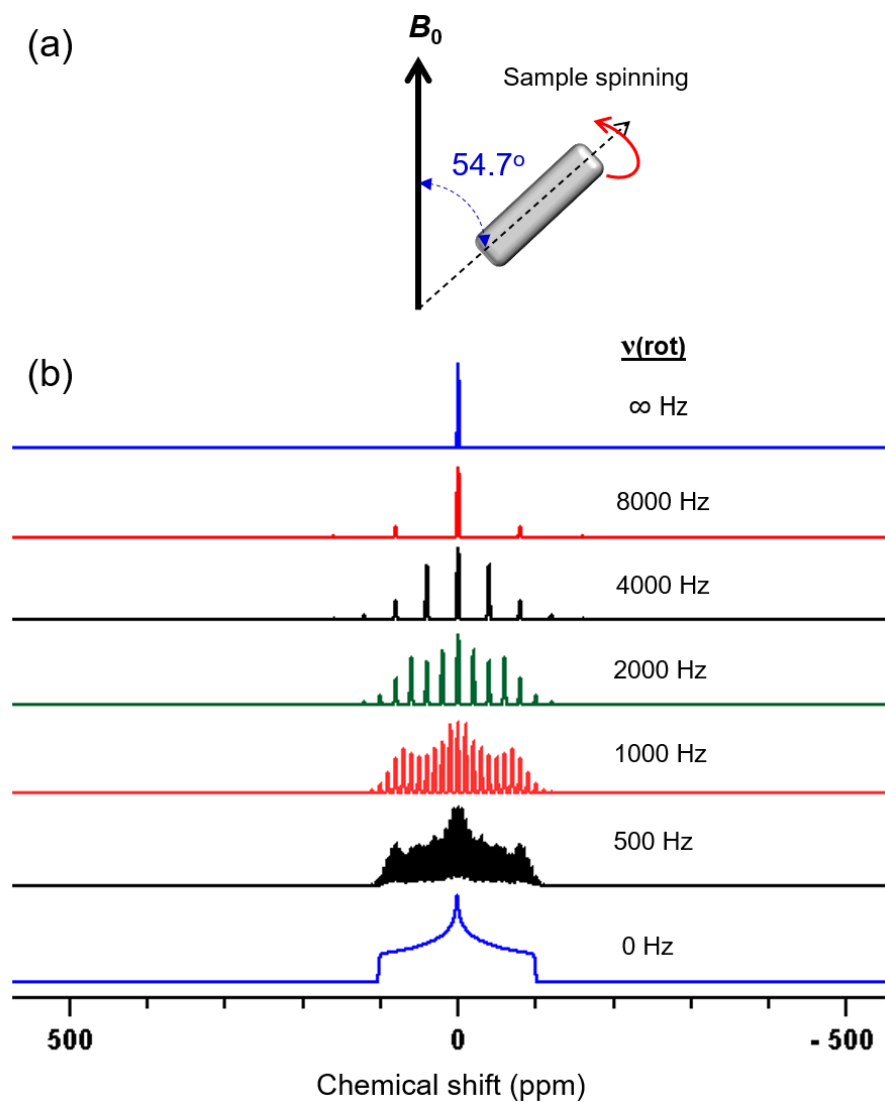


Figure 1.9. (a) Schematic diagram of magic-angle spinning of sample placed in NMR stator. (b) Simulated solid-state NMR spectra under non-spinning and magic-angle spinning sample conditions for a ^{13}C nucleus ($I = 1/2$) at 9.4 T ($\omega_0/2\pi = 100$ MHz) with $\delta_{\text{iso}} = 0$ ppm, $\Omega = 200$ ppm, $\kappa = 0$, and 250 Hz Gaussian line broadening. Spectra were simulated with the WSolids program.¹⁰⁴

The quadrupolar interaction depends on two distinct spatial terms, namely, $P_2(\cos\theta)$ and $P_4(\cos\theta)$, as shown in Eq. 1.48. and 1.49, respectively. A $\theta = 30.6^\circ$ or 70.1° is required to average out the contribution from the $P_4(\cos\theta)$ term. As discussed above, $P_2(\cos\theta)$ can be removed by MAS, whereas the $P_4(\cos\theta)$ is averaged only partially under MAS conditions, and the breadth of the central transition is reduced by a factor of approximately 60–70 % (see above, Figure 1.8).

1.4.6 Nuclear Spin Relaxation – T_1 and T_2

Spin-lattice relaxation (T_1), which is also known as longitudinal relaxation, is a consequence of the energy exchange between the nuclear spin and the surrounding lattice by the emission of phonons. Spin-lattice relaxation times depend on the coupling strength between the spin system and the lattice. Multiple relaxation mechanisms are possible for spin-lattice relaxation in diamagnetic samples. These mechanisms includes: (i) the magnetic dipole-dipole interaction, (ii) the electric quadrupole interaction, (iii) the chemical shift anisotropy interaction, (iv) the scalar coupling interaction, and (v) the spin-phonon Raman scattering interaction.^{97,109,110,111,112}

Following a radiofrequency pulse, the spin-lattice relaxation process helps to restore the magnetization towards the applied external magnetic field (B_0), i.e., along the z -axes, whereas spin-spin relaxation (T_2) describes the magnetization along x - y plane. Both T_1 and T_2 occur simultaneously until the perturbed nuclear spin reestablishes equilibrium. The spin-lattice relaxation for a liquid phase sample, shown in Figure 1.10a, can be described by Eq. 1.50,

$$M_z(t) = M_z(\infty) (1 - e^{-t/T_1}) \quad (\text{Eq. 1.50})$$

where $M_z(t)$ and $M_z(\infty)$ are the magnetization along the z -direction at time t and ∞ , respectively. NMR spectroscopists typically set the relaxation delay to $5 \times T_1$ to obtain quantitative results for the NMR spectra. However, the relaxation processes for nuclei in solids can be complicated and may require multi-exponential terms or stretched exponential terms to model them accurately.^{113,114}

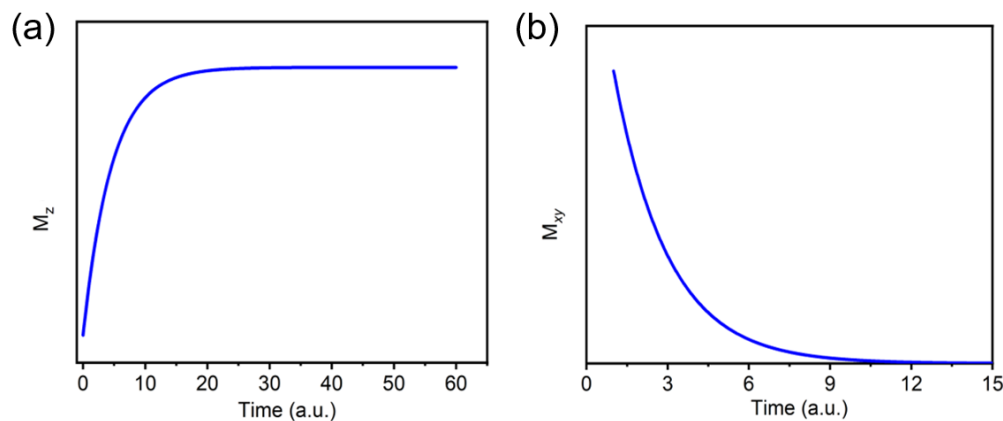


Figure 1.10. T_1 and T_2 relaxation decay curves for a nucleus with $T_1 = 4.6$ and $T_2 = 2.0$ arbitrary units.

Spin-spin relaxation (T_2) determines the decay rate of the free-induction decay (FID). It is shown in Figure 1.10b, and is expressed by Eq. 1.51,

$$M_{xy}(t) = M_{xy}(\infty) e^{-t/T_2} \quad (\text{Eq. 1.51})$$

Here, $M_{xy}(t)$ and $M_{xy}(\infty)$ are the net magnetization in the x - y plane at time t and ∞ , respectively. Note that magnetic field inhomogeneity about the nucleus also contributes to the dephasing of the nuclear spin magnetization in the x - y plane; hence, an effective transverse relaxation time constant, T_2^* , is measured. These types of relaxation measurements can lend aid in further assessing NMR data as well as providing clues into the ion dynamics within perovskite materials.

1.5 Research Motivation

There are three major goals in this thesis. My first aim was to develop a suitable solvent-free synthesis method to prepare ABX_3 ($B = \text{Pb}^{2+}$ and Sn^{2+}) perovskite materials. This will allow for a detailed understanding of how synthesis influences their local chemical structure and halogen dynamics using solid-state NMR spectroscopy, in order to establish a structure-property relationship. My second goal was to find new lead-free compounds such as stable halide double perovskites, $A_2B'B''X_6$, that display suitable optical properties for lighting and solar cell applications. Third, I wanted to prepare mixed-halide compositions of perovskite-

inspired Cs_2SnX_6 “vacancy-ordered perovskite” by a solvent-free mechanochemical synthesis technique as a potentially stable Sn-based material for optoelectronic applications.

The current interests of halide-based perovskite materials are already discussed extensively (see section 1.2). The bulk material of lead(II) and tin(II) containing perovskites are conventionally prepared by solvent phase synthesis routes which involve costly and hazardous solvents. Chapter 2 of this thesis will examine the advantage of using mechanochemical synthesis routes, namely, the automated electric ball-milling and manual hand-grinding techniques in preparing phase-pure products of $\text{MAPb}(\text{Cl}_{1-x}\text{Br}_x)_3$ and $\text{MAPb}(\text{Br}_{1-x}\text{I}_x)_3$ ($0 \leq x \leq 1$) mixed-halide compositions. Chapter 3 of this thesis will explore the superiority of the solid-state high-temperature synthesis method in preparing the complete solid solution of cubic $\text{CsSn}(\text{Cl}_{1-x}\text{Br}_x)_3$ perovskites, which were inaccessible using the traditional solvent phase synthesis route.

Although lead(II) and tin(II) halide perovskites have shown extraordinary optical and electrical properties in photovoltaic and optoelectronic devices, persistent challenges exist. For instance, lead(II) is a toxic element and soluble in water which may create long-term environmental and health risks. Tin(II) containing perovskites exhibit poor ambient stability and rapidly oxidized to tin(IV) in air. In Chapters 4 and 5 I aim to find alternative lead(II) and tin(II) free materials, namely, halide double perovskites which are stable under the ambient atmosphere. My goal was to find new halide double perovskite materials exhibiting promising optical properties such as materials with a lower optical bandgap (1–1.5 eV) and efficient broadband white-light emission from a single material source.

An ambient stable alternative to the ABX_3 ($\text{B} = \text{Pb}^{2+}$ and Sn^{2+}) materials, is A_2BX_6 . These materials exhibit an optical bandgap spanning *ca.* 3 eV upon a change in halogen composition from chloride to bromide to iodide. A_2BX_6 materials are extensively prepared either by solvent phase or by high-temperature synthesis routes. In Chapter 6, I discuss the development of a solvent-free mechanochemical synthesis route to synthesize $\text{Cs}_2\text{Sn}(\text{Cl}_{1-x}\text{Br}_x)_6$ and $\text{Cs}_2\text{Sn}(\text{Br}_{1-x}\text{I}_x)_6$ mixed-halide compositions.

Among many other structural characterization techniques, diffraction-based techniques have been employed to study perovskite and perovskite-inspired materials,

however, they are limited to providing average long-range structural information. Solid-state NMR spectroscopy provides local chemical structure as well as dynamics information related to these materials. It is extremely important to understand how the microscopic structure and ionic dynamics of these materials play a crucial role in their performances ultimately in hopes of establishing a correlation between their structure and optical properties.

1.6 References

- (1) Rose, G. De Perowskite, Fossili Novo. *Novis Quibusdam Foss. Quae Montibus Ural. Inven. AG Schade Berlin* **1839**, pp 3-12.
- (2) Wells, H. L.; Johnston, W. R. Uber Die Ammoniumbleihalogenide. *Anorg. Allg. Chem.* **1893**, *3*, 195–210.
- (3) Golschmidt, V. M. Die Gesetze Der Krystallochemie. *Naturwissenschaften* **1926**, *14*, 477–485.
- (4) Akkerman, Q. A.; Manna, L. What Defines a Halide Perovskite? *ACS Energy Lett.* **2020**, *5*, 604–610.
- (5) Bartel, C. J.; Sutton, C.; Goldsmith, B. R.; Ouyang, R.; Musgrave, C. B.; Ghiringhelli, L. M.; Scheffler, M. New Tolerance Factor to Predict the Stability of Perovskite Oxides and Halides. *Sci. Adv.* **2019**, *5*:eaav0693, 1–9.
- (6) Mitchell, R. H.; Welch, M. D.; Chakhmouradian, A. R. Nomenclature of the Perovskite Supergroup: A Hierarchical System of Classification Based on Crystal Structure and Composition. *Mineral. Mag.* **2017**, *81*, 411–461.
- (7) Kay, H. F.; Bailey, P. C. Structure and Properties of CaTiO₃. *Acta Crystallogr.* **1957**, *10*, 219–226.
- (8) Megaw, H. Crystal Structure of Barium Titanate. *Nature* **1945**, *155*, 484–485.
- (9) Megaw, H. D. Origin of Ferroelectricity in Barium Titanate and Other Perovskite-Type Crystals. *Acta Crystallogr.* **1952**, *5*, 739–749.
- (10) Shannon, R. D.; Bierstedt, P. E. Single-Crystal Growth and Electrical Properties of BaPbO₃. *J. Am. Ceram. Soc.* **1970**, *53*, 635–636.
- (11) Takahashi, T.; Iwahara, H. Ionic Conduction in Perovskite-Type Oxide Solid Solution and Its Application to the Solid Electrolyte Fuel Cell. *Energy Convers.* **1971**,

11, 105–111.

(12) Lawless, W. N. Three Application Areas for SrTiO₃ Glass-Ceramics.

Ferroelectrics **1972**, *3*, 287–293.

(13) Kozuka, H.; Ohbayashi, K.; Koumoto, K. Electronic Conduction in La-Based Perovskite-Type Oxides. *Sci. Technol. Adv. Mater.* **2015**, *16*, 026001.

(14) Labhasetwar, N.; Saravanan, G.; Kumar Megarajan, S.; Manwar, N.; Khobragade, R.; Doggali, P.; Grasset, F. Perovskite-Type Catalytic Materials for Environmental Applications. *Sci. Technol. Adv. Mater.* **2015**, *16*, 036002.

(15) Mazet, L.; Yang, S. M.; Kalinin, S. V.; Schamm-Chardon, S.; Dubourdieu, C. A Review of Molecular Beam Epitaxy of Ferroelectric BaTiO₃ Films on Si, Ge and GaAs Substrates and Their Applications. *Sci. Technol. Adv. Mater.* **2015**, *16*, 036005.

(16) K. C. Møller. Crystal Structure and Photoconductivity of Caesium Plumbahalides. *Nature* **1958**, *182*, 1436.

(17) Weber, D. CH₃NH₃PbX₃, a Pb(II)-System with Cubic Perovskite Structure. *Z. Naturforsch* **1978**, *33*, 1443–1445.

(18) R. E. Wasylishen; Knop, O.; Macdonald, J. B. Cation Rotation in Methylammonium Lead Halides. *Solid State Commun.* **1985**, *56*, 581–582.

(19) Poglitsch, A.; Weber, D. Dynamic Disorder in Methylammoniumtrihalogenoplumbates(II) Observed by Millimeter-Wave Spectroscopy. *J. Chem. Phys.* **1987**, *87*, 6373–6378.

(20) Furukawa, Y.; Nakamura, D. Cationic Dynamics in the Crystalline Phases of (CH₃NH₃)PbX₃ (X: Cl, Br) as Studied by Proton Magnetic Resonance Techniques. *Z. Naturforsch. A Phys. Sci.* **1989**, *44a*, 1122–1126.

(21) Onoda-Yamamuro, N.; Matsuo, T.; Suga, H. Calorimetric and IR Spectroscopic Studies of Phase Transitions in Methylammonium Trihalogenoplumbates (II). *J. Phys. Chem. Solids* **1990**, *51*, 1383–1395.

(22) Knop, O.; Wasylishen, R. E.; White, M. A.; Cameron, T. S.; van Oort, M. J. M. Alkylammonium Lead Halides. Part 2. CH₃NH₃PbX₃ (X = Cl, Br, I) Perovskites: Cuboctahedral Halide Cages with Isotropic Cation Reorientation. *Can. J. Chem.* **1990**, *68*, 412–422.

(23) Xu, Q.; Eguchi, T.; Nakayama, H.; Nakamura, N.; Kishita, M. Molecular

- Motions and Phase Transitions in Solid $\text{CH}_3\text{NH}_3\text{PbX}_3$ ($X = \text{Cl}, \text{Br}, \text{I}$) as Studied by NMR and NQR. *Z. Naturforsch., A Phys. Sci.* **1991**, *46*, 240–246.
- (24) Xu, Q.; Eguchi, T.; Nakayama, H. Molecular Motions in Solid $\text{CD}_3\text{NH}_3\text{PbBr}_3$ as Studied by ^1H NMR. *Bull. Chem. Soc. Jpn.* **1992**, *65*, 2264–2266.
- (25) Mitzi, D. B.; Chondroudis, K.; Kagan, C. R. Organic-Inorganic Electronics. *IBM J. Res. Dev.* **2001**, *45*, 29–45.
- (26) Kojima, A.; Teshima, K.; Shirai, Y.; Miyasaka, T. Organometal Halide Perovskites as Visible-Light Sensitizers for Photovoltaic Cells. *J. Am. Chem. Soc.* **2009**, *131*, 6050–6051.
- (27) Zhao, Y.; Zhu, K. Organic-Inorganic Hybrid Lead Halide Perovskites for Optoelectronic and Electronic Applications. *Chem. Soc. Rev.* **2016**, *45*, 655–689.
- (28) Dunlap-Shohl, W. A.; Zhou, Y.; Padture, N. P.; Mitzi, D. B. Synthetic Approaches for Halide Perovskite Thin Films. *Chem. Rev.* **2019**, *119*, 3193–3295.
- (29) Li, T.; Zhao, X.; Yang, D.; Du, M. H.; Zhang, L. Intrinsic Defect Properties in Halide Double Perovskites for Optoelectronic Applications. *Phys. Rev. Appl.* **2018**, *10*, 041001.
- (30) V. M. Goldschmidt. Die Gesetze Der Krystallochemie. *Naturwissenschaften* **1926**, *14*, 477–485.
- (31) Wei, Y.; Cheng, Z.; Lin, J. An Overview on Enhancing the Stability of Lead Halide Perovskite Quantum Dots and Their Applications in Phosphor-Converted LEDs. *Chem. Soc. Rev.* **2019**, *48*, 310–350.
- (32) Li, C.; Lu, X.; Ding, W.; Feng, L.; Gao, Y.; Guo, Z. Formability of ABX_3 ($X = \text{F}, \text{Cl}, \text{Br}, \text{I}$) Halide Perovskites. *Acta Crystallogr. Sect. B* **2008**, *B64*, 702–707.
- (33) Cheng, X.; Jing, L.; Yuan, Y.; Du, S.; Zhang, J.; Zhan, X.; Ding, J.; Yu, H.; Shi, G. $\text{Fe}^{2+}/\text{Fe}^{3+}$ Doped into MAPbCl_3 Single Crystal: Impact on Crystal Growth and Optical and Photoelectronic Properties. *J. Phys. Chem. C* **2019**, *123*, 1669–1676.
- (34) Fabini, D. H.; Laurita, G.; Bechtel, J. S.; Stoumpos, C. C.; Evans, H. A.; Kontos, A. G.; Raptis, Y. S.; Falaras, P.; Van Der Ven, A.; Kanatzidis, M. G.; et al. Dynamic Stereochemical Activity of the Sn^{2+} Lone Pair in Perovskite CsSnBr_3 . *J. Am. Chem. Soc.* **2016**, *138*, 11820–11832.
- (35) Piveteau, L.; Morad, V.; Kovalenko, M. V. Solid-State NMR and NQR

- Spectroscopy of Lead-Halide Perovskite Materials. *J. Am. Chem. Soc.* **2020**, *142*, 19413–19437.
- (36) Govinda, S.; Kore, B. P.; Swain, D.; Hossain, A.; De, C.; Guru Row, T. N.; Sarma, D. D. Critical Comparison of FAPbX₃ and MAPbX₃ (X = Br and Cl): How Do They Differ? *J. Phys. Chem. C* **2018**, *122*, 13758–13766.
- (37) Gao, W.; Zielinski, K.; Drury, B. N.; Carl, A. D.; Grimm, R. L. Elucidation of Chemical Species and Reactivity at Methylammonium Lead Iodide and Cesium Tin Bromide Perovskite Surfaces via Orthogonal Reaction Chemistry. *J. Phys. Chem. C* **2018**, *122*, 17882–17894.
- (38) Sutton, R. J.; Filip, M. R.; Haghghirad, A. A.; Sakai, N.; Wenger, B.; Giustino, F.; Snaith, H. J. Cubic or Orthorhombic? Revealing the Crystal Structure of Metastable Black-Phase CsPbI₃ by Theory and Experiment. *ACS Energy Lett.* **2018**, *3*, 1787–1794.
- (39) Dirin, D. N.; Cherniukh, I.; Yakunin, S.; Shynkarenko, Y.; Kovalenko, M. V. Solution-Grown CsPbBr₃ Perovskite Single Crystals for Photon Detection. *Chem. Mater.* **2016**, *28*, 8470–8474.
- (40) Linaburg, M. R.; McClure, E. T.; Majher, J. D.; Woodward, P. M. Cs_{1-x}Rb_xPbCl₃ and Cs_{1-x}Rb_xPbBr₃ Solid Solutions: Understanding Octahedral Tilting in Lead Halide Perovskites. *Chem. Mater.* **2017**, *29*, 3507–3514.
- (41) Yamada, K.; Kuranaga, Y.; Ueda, K.; Goto, S.; Okuda, T.; Furukawa, Y. Phase Transition and Electric Conductivity of ASnCl₃ (A = Cs and CH₃NH₃). *Bull. Chem. Soc. Jpn.* **1998**, *71*, 127–134.
- (42) Ke, F.; Wang, C.; Jia, C.; Wolf, N. R.; Yan, J.; Niu, S.; Devereaux, T. P.; Karunadasa, H. I.; Mao, W. L.; Lin, Y. Preserving a Robust CsPbI₃ Perovskite Phase via Pressure-Directed Octahedral Tilt. *Nat. Commun.* **2021**, *12*, 461.
- (43) Li, Z.; Yang, M.; Park, J. S.; Wei, S. H.; Berry, J. J.; Zhu, K. Stabilizing Perovskite Structures by Tuning Tolerance Factor: Formation of Formamidinium and Cesium Lead Iodide Solid-State Alloys. *Chem. Mater.* **2016**, *28*, 284–292.
- (44) Lin, R.; Xiao, K.; Qin, Z.; Han, Q.; Zhang, C.; Wei, M.; Saidaminov, M. I.; Gao, Y.; Xu, J.; Xiao, M.; et al. Monolithic All-Perovskite Tandem Solar Cells with 24.8% Efficiency Exploiting Comproportionation to Suppress Sn(II) Oxidation in Precursor

- Ink. Nat. Energy* **2019**, *4*, 864–873.
- (45) Bag, M.; Kumar, R.; Srivastava, P. Role of A-Site Cation and X-Site Halide Interactions in Mixed-Cation Mixed-Halide Perovskites for Determining Anomalously High Ideality Factor and the Super-Linear Power Law in Ac Ionic Conductivity at Operating Temperature. *ACS Appl. Electron. Mater.* **2020**, *2*, 4087–4098.
- (46) Xu, Q.; Yang, D.; Lv, J.; Sun, Y.-Y.; Zhang, L. Perovskite Solar Absorbers: Materials by Design. *Small Methods* **2018**, *2*, 1700316.
- (47) Sutherland, B. R.; Sargent, E. H. Perovskite Photonic Sources. *Nat. Photonics* **2016**, *10*, 295–302.
- (48) Manser, J. S.; Christians, J. A.; Kamat, P. V. Intriguing Optoelectronic Properties of Metal Halide Perovskites. *Chem. Rev.* **2016**, *116*, 12956–13008.
- (49) Zhao, Y.; Zhu, K. Organic-Inorganic Hybrid Lead Halide Perovskites for Optoelectronic and Electronic Applications. *Chem. Soc. Rev.* **2016**, *45*, 655–689.
- (50) Chen, K.; Deng, X.; Dodekatos, G.; Tüysüz, H. Photocatalytic Polymerization of 3,4-Ethylenedioxythiophene over Cesium Lead Iodide Perovskite Quantum Dots. *J. Am. Chem. Soc.* **2017**, *139*, 12267–12273.
- (51) Yakunin, S.; Sytnyk, M.; Kriegner, D.; Shrestha, S.; Richter, M.; Matt, G. J.; Azimi, H.; Brabec, C. J.; Stangl, J.; Kovalenko, M. V; et al. Detection of X-Ray Photons by Solution-Processed Lead Halide Perovskites. *Nat. Photonics* **2015**, *9*, 444–449.
- (52) Leung, S. F.; Ho, K. T.; Kung, P. K.; Hsiao, V. K. S.; Alshareef, H. N.; Wang, Z. L.; He, J. H. A Self-Powered and Flexible Organometallic Halide Perovskite Photodetector with Very High Detectivity. *Adv. Mater.* **2018**, *30*, 1704611.
- (53) National Renewable Energy Laboratory (NREL). Best Research-Cell Efficiency Chart. <https://www.nrel.gov/pv/assets/pdfs/best-research-cell-efficiencies.20200104.pdf>
- (54) Yang, J.; Siempelkamp, B. D.; Liu, D.; Kelly, T. L. Investigation of CH₃NH₃PbI₃ Degradation Rates and Mechanisms in Controlled Humidity Environments Using in Situ Techniques. *ACS Nano* **2015**, *9*, 1955–1963.
- (55) Li, J.; Cao, H.; Jiao, W.; Wang, Q.; Wei, M.; Cantone, I.; Lü, J.; Abate, A.

Biological Impact of Lead from Halide Perovskites Reveals the Risk of Introducing a Safe Threshold. *Nat. Commun.* **2020**, *11*, 310.

(56) Kamarudin, M. A.; Hirotani, D.; Wang, Z.; Hamada, K.; Nishimura, K.; Shen, Q.; Toyoda, T.; Iikubo, S.; Minemoto, T.; Yoshino, K.; et al. Suppression of Charge Carrier Recombination in Lead-Free Tin Halide Perovskite via Lewis Base Post-Treatment. *J. Phys. Chem. Lett.* **2019**, *10*, 5277–5283.

(57) Song, T. Bin; Yokoyama, T.; Stoumpos, C. C.; Logsdon, J.; Cao, D. H.; Wasielewski, M. R.; Aramaki, S.; Kanatzidis, M. G. Importance of Reducing Vapor Atmosphere in the Fabrication of Tin-Based Perovskite Solar Cells. *J. Am. Chem. Soc.* **2017**, *139*, 836–842.

(58) Zhao, D.; Yu, Y.; Wang, C.; Liao, W.; Shrestha, N.; Grice, C. R.; Cimaroli, A. J.; Guan, L.; Ellingson, R. J.; Zhu, K.; et al. Low-Bandgap Mixed Tin-Lead Iodide Perovskite Absorbers with Long Carrier Lifetimes for All-Perovskite Tandem Solar Cells. *Nat. Energy* **2017**, *2*, 17018.

(59) Luo, J.; Hu, M.; Niu, G.; Tang, J. Lead-Free Halide Perovskites and Perovskite Variants as Phosphors toward Light-Emitting Applications. *ACS Appl. Mater. Interfaces* **2019**, *11*, 31575–31584.

(60) Slavney, A. H.; Hu, T.; Lindenberg, A. M.; Karunadasa, H. I. A Bismuth-Halide Double Perovskite with Long Carrier Recombination Lifetime for Photovoltaic Applications. *J. Am. Chem. Soc.* **2016**, *138*, 2138–2141.

(61) McClure, E. T.; Ball, M. R.; Windl, W.; Woodward, P. M. Cs₂AgBiX₆ (X = Br, Cl): New Visible Light Absorbing, Lead-Free Halide Perovskite Semiconductors. *Chem. Mater.* **2016**, *28*, 1348–1354.

(62) Slavney, A. H.; Leppert, L.; Bartesaghi, D.; Gold-Parker, A.; Toney, M. F.; Savenije, T. J.; Neaton, J. B.; Karunadasa, H. I. Defect-Induced Band-Edge Reconstruction of a Bismuth-Halide Double Perovskite for Visible-Light Absorption. *J. Am. Chem. Soc.* **2017**, *139*, 5015–5018.

(63) Slavney, A. H.; Leppert, L.; Saldivar Valdes, A.; Bartesaghi, D.; Savenije, T. J.; Neaton, J. B.; Karunadasa, H. I. Small-Band-Gap Halide Double Perovskites. *Angew. Chem. Int. Ed.* **2018**, *57*, 12765–12770.

(64) Yang, B.; Mao, X.; Hong, F.; Meng, W.; Tang, Y.; Xia, X.; Yang, S.; Deng, W.;

- Han, K. Lead-Free Direct Bandgap Double Perovskite Nanocrystals with Bright Dual-Color Emission. *J. Am. Chem. Soc.* **2018**, *140*, 17001–17006.
- (65) Luo, J.; Wang, X.; Li, S.; Liu, J.; Guo, Y.; Niu, G.; Yao, L.; Fu, Y.; Gao, L.; Dong, Q.; et al. Efficient and Stable Emission of Warm-White Light from Lead-Free Halide Double Perovskites. *Nature* **2018**, *563*, 541–545.
- (66) Majher, J. D.; Gray, M. B.; Strom, T. A.; Woodward, P. M. Cs₂NaBiCl₆: Mn²⁺- A New Orange-Red Halide Double Perovskite Phosphor. *Chem. Mater.* **2019**, *31*, 1738–1744.
- (67) Manna, D.; Das, T. K.; Yella, A. Tunable and Stable White Light Emission in Bi³⁺ Alloyed Cs₂AgInCl₆ Double Perovskite Nanocrystals. *Chem. Mater.* **2019**, *31*, 10063–10070.
- (68) Nila Nandha, K.; Nag, A. Synthesis and Luminescence of Mn-Doped Cs₂AgInCl₆ Double Perovskites. *Chem. Commun.* **2018**, *54*, 5205–5208.
- (69) Locardi, F.; Cirignano, M.; Baranov, D.; Dang, Z.; Prato, M.; Drago, F.; Ferretti, M.; Pinchetti, V.; Fanciulli, M.; Brovelli, S.; et al. Colloidal Synthesis of Double Perovskite Cs₂AgInCl₆ and Mn-Doped Cs₂AgInCl₆ Nanocrystals. *J. Am. Chem. Soc.* **2018**, *140*, 12989–12995.
- (70) Maughan, A. E.; Ganose, A. M.; Scanlon, D. O.; Neilson, J. R. Perspectives and Design Principles of Vacancy-Ordered Double Perovskite Halide Semiconductors. *Chem. Mater.* **2019**, *31*, 1184–1195.
- (71) Maughan, A. E.; Ganose, A. M.; Candia, A. M.; Granger, J. T.; Scanlon, D. O.; Neilson, J. R. Anharmonicity and Octahedral Tilting in Hybrid Vacancy-Ordered Double Perovskites. *Chem. Mater.* **2018**, *30*, 472–483.
- (72) Maughan, A. E.; Paecklar, A. A.; Neilson, J. R. Bond Valences and Anharmonicity in Vacancy-Ordered Double Perovskite Halides. *J. Mater. Chem. C* **2018**, *6*, 12095–12104.
- (73) Saparov, B.; Sun, J. P.; Meng, W.; Xiao, Z.; Duan, H. S.; Gunawan, O.; Shin, D.; Hill, I. G.; Yan, Y.; Mitzi, D. B. Thin-Film Deposition and Characterization of a Sn-Deficient Perovskite Derivative Cs₂SnI₆. *Chem. Mater.* **2016**, *28*, 2315–2322.
- (74) Wang, A.; Yan, X.; Zhang, M.; Sun, S.; Yang, M.; Shen, W.; Pan, X.; Wang, P.; Deng, Z. Controlled Synthesis of Lead-Free and Stable Perovskite Derivative Cs₂SnI₆

- Nanocrystals via a Facile Hot-Injection Process. *Chem. Mater.* **2016**, *28*, 8132–8140.
- (75) Lim, S. C.; Lin, H. P.; Tsai, W. L.; Lin, H. W.; Hsu, Y. T.; Tuan, H. Y. Binary Halide, Ternary Perovskite-like, and Perovskite-Derivative Nanostructures: Hot Injection Synthesis and Optical and Photocatalytic Properties. *Nanoscale* **2017**, *9*, 3747–3751.
- (76) Veronese, A.; Patrini, M.; Bajoni, D.; Ciarrocchi, C.; Quadrelli, P.; Malavasi, L. Highly Tunable Emission by Halide Engineering in Lead-Free Perovskite-Derivative Nanocrystals: The Cs₂SnX₆ (X = Cl, Br, Br/I, I) System. *Front. Chem.* **2020**, *8*, 1–9.
- (77) James, S. L.; Adams, C. J.; Bolm, C.; Braga, D.; Collier, P.; Friščić, T.; Grepioni, F.; Harris, K. D. M.; Hyett, G.; Jones, W.; et al. Playing with Organic Radicals as Building Blocks for Functional Molecular Materials. *Chem. Soc. Rev.* **2012**, *41*, 413–447.
- (78) Palazon, F.; El Ajjouri, Y.; Bolink, H. J. Making by Grinding: Mechanochemistry Boosts the Development of Halide Perovskites and Other Multinary Metal Halides. *Adv. Energy Mater.* **2020**, *10*, 1902499.
- (79) Tan, D.; García, F. Main Group Mechanochemistry: From Curiosity to Established Protocols. *Chem. Soc. Rev.* **2019**, *48*, 2274–2292.
- (80) Friščić, T. Supramolecular Concepts and New Techniques in Mechanochemistry: Cocrystals, Cages, Rotaxanes, Open Metal–Organic Frameworks. *Chem. Soc. Rev.* **2012**, *41*, 3493–3510.
- (81) Julien, P. A.; Mottillo, C.; Friščić, T. Metal-Organic Frameworks Meet Scalable and Sustainable Synthesis. *Green Chem.* **2017**, *19*, 2729–2747.
- (82) Ju, D.; Dang, Y.; Zhu, Z.; Liu, H.; Chueh, C. C.; Li, X.; Wang, L.; Hu, X.; Jen, A. K. Y.; Tao, X. Tunable Band Gap and Long Carrier Recombination Lifetime of Stable Mixed CH₃NH₃Pb_xSn_{1-x}Br₃ Single Crystals. *Chem. Mater.* **2018**, *30*, 1556–1565.
- (83) Moghe, D.; Wang, L.; Traverse, C. J.; Redoute, A.; Sponseller, M.; Brown, P. R.; Bulović, V.; Lunt, R. R. All Vapor-Deposited Lead-Free Doped CsSnBr₃ Planar Solar Cells. *Nano Energy* **2016**, *28*, 469–474.
- (84) Rosales, B. A.; Men, L.; Cady, S. D.; Hanrahan, M. P.; Rossini, A. J.; Vela, J. Persistent Dopants and Phase Segregation in Organolead Mixed-Halide Perovskites.

- Chem. Mater.* **2016**, *28*, 6848–6859.
- (85) Prochowicz, D.; Franckevicius, M.; Cieslak, A. M.; Zakeeruddin, S. M.; Graetzel, M.; Lewinski, J. Mechano-synthesis of the Hybrid Perovskite CH₃NH₃PbI₃: Characterization and the Corresponding Solar Cell Efficiency. *J. Mater. Chem. A* **2015**, *3*, 20772–20777.
- (86) Stoumpos, C. C.; Malliakas, C. D.; Kanatzidis, M. G. Semiconducting Tin and Lead Iodide Perovskites with Organic Cations: Phase Transitions, High Mobilities, and near-Infrared Photoluminescent Properties. *Inorg. Chem.* **2013**, *52*, 9019–9038.
- (87) Le, T.; Epa, V. C.; Burden, F. R.; Winkler, D. A. Quantitative Structure-Property Relationship Modeling of Diverse Materials Properties. *Chem. Rev.* **2012**, *112*, 2889–2919.
- (88) Franssen, W. M. J.; Kentgens, A. P. M. Solid-State NMR of Hybrid Halide Perovskites. *Solid State Nucl. Magn. Reson.* **2019**, *100*, 36–44.
- (89) Grykałowska, A.; Nowak, B. High-Resolution Solid-State ¹¹⁹Sn and ¹⁹⁵Pt NMR Studies of MPtSn Semiconductors (M = Ti, Zr, Hf, Th). *Solid State Nucl. Magn. Reson.* **2005**, *27*, 223–227.
- (90) Wolf, P.; Valla, M.; Núñez-Zarur, F.; Comas-Vives, A.; Rossini, A. J.; Firth, C.; Kallas, H.; Lesage, A.; Emsley, L.; Copéret, C.; et al. Correlating Synthetic Methods, Morphology, Atomic-Level Structure, and Catalytic Activity of Sn-β Catalysts. *ACS Catal.* **2016**, *6*, 4047–4063.
- (91) *NMR of Quadrupolar Nuclei in Solid Materials*; Wasylshen, R. E., Ashbrook, S. E., Wimperis, S., Eds.; John Wiley & Sons, 2012.
- (92) *Modern Methods in Solid-State NMR: A Practitioner's Guide*; Hodgkinson, P., Ed.; Royal Society of Chemistry, 2018.
- (93) Bakhmutov, V. I. *Solid-State NMR in Materials Science: Principles and Applications*; CRC press, 2016.
- (94) Duer, M. J. *Introduction to Solid-State NMR Spectroscopy*; Oxford, UK, 2004.
- (95) Reif, B.; Ashbrook, S. E.; Emsley, L.; Hong, M. Solid-State NMR Spectroscopy. *Nat. Rev. Methods Prim.* **2021**, *1*, 1–23.
- (96) Bernard, G. M.; Karmakar, A.; Michaelis, V. K. Solid-State NMR Studies of Halide Perovskite Materials with Photoconversion Potential. In *Reference Module in*

- Chemistry, Molecular Sciences and Chemical Engineering*; Elsevier, 2021.
<https://doi.org/https://doi.org/10.1016/B978-0-12-823144-9.00018-2>.
- (97) Moudrakovski, I. L. *Local Dynamics in Hybrid Perovskites by Solid-State NMR*, 1st ed.; Elsevier Ltd., 2021; Vol. 102. <https://doi.org/10.1016/bs.arnmr.2020.10.004>.
- (98) Mehring, M. *Principles of High Resolution NMR in Solids*; Springer-Verlag, 1983.
- (99) Apperley, D. C.; Harris, R. K.; Hodgkinson, P. *Solid-State NMR: Basic Principles and Practice*; Momentum Press, 2012.
- (100) Harris, R. K.; Becker, E. D. NMR Nomenclature: Nuclear Spin Properties and Conventions for Chemical Shifts—IUPAC Recommendations. *J. Magn. Reson.* **2002**, *156*, 323–326.
- (101) Jameson, C. J. Chemical Shift Scales on an Absolute Basis. In *Encyclopedia of Magnetic Resonance*; 2011.
<https://doi.org/10.1002/9780470034590.emrstm0072.pub2>.
- (102) Harris, R. K.; Becker, E. D.; de Menrzes, S. M. C.; Goodfellow, R.; Granger, P. NMR Nomenclature. Nuclear Spin Properties and Conventions for Chemical Shifts. *Pure Appl. Chem.* **2001**, *73*, 1795–1818.
- (103) Mason, J. Conventions for the Reporting of Nuclear Magnetic Shielding (or Shift) Tensors Suggested by Participants in the NATO ARW on NMR Shielding Constants at the University of Maryland, College Park, July 1992. *Solid State Nucl. Magn. Reson.* **1993**, *2*, 285–288.
- (104) Eichele, K. WSolids V. 1.21.3. Universität Tübingen 2015.
- (105) Wasylishen, R. E. Dipolar and Indirect Coupling: Basics. *Encycl. Magn. Reson.* **2009**. <https://doi.org/10.1002/9780470034590.emrstm1023>.
- (106) Bryce, D. L.; Wasylishen, R. E. Quadrupolar Nuclei in Solids: Influence of Different Interactions on Spectra. In *Encyclopedia of Magnetic Resonance*; 2011.
<https://doi.org/10.1002/9780470034590.emrstm1197>.
- (107) Amoureux, J. P.; Fernandez, C.; Granger, P. Multinuclear Magnetic Resonance in Liquids and Solids; Granger, P., Harris, R. K., Eds.; Kluwer Academic Publishers: London, 1990; p 409.
- (108) Hennel, J. W.; Klinowski, J. Magic-Angle Spinning: A Historical Perspective.

- In *New techniques in solid-state NMR. Topics in Current Chemistry*, vol 246; Klinowski, J., Ed.; Springer Berlin Heidelberg: Berlin, Heidelberg, 2005; pp 1–14.
- (109) Farrar, T. C. *Introduction to Pulse NMR Spectroscopy*; Madison: The Farragut, 1997.
- (110) Wasylishen, R. E. NMR relaxation and dynamics. *NMR Spectroscopy Techniques*; Chapt. 3; Bruch, M. D., Ed.; Marcel Dekker, New York, 1996. pp. 105-144.
- (111) Grutzner, J. B.; Stewart, K. W.; Wasylishen, R. E.; Lumsden, M. D.; Dybowski, C.; Beckmann, P. A. A New Mechanism for Spin-Lattice Relaxation of Heavy Nuclei in the Solid State: ^{207}Pb Relaxation in Lead Nitrate. *J. Am. Chem. Soc.* **2001**, *123*, 7094–7100.
- (112) Gryff-Keller, A.; Molchanov, S.; Wodynski, A. Scalar Relaxation of the Second Kind — A Potential Source of Information on the Dynamics of Molecular Movements. 2. Magnetic Dipole Moments and Magnetic Shielding of Bromine Nuclei. *J. Phys. Chem. A* **2014**, *118*, 128–133
- (113) Gordon, M. I.; Hoch, M. J. R. Quadrupolar Spin-Lattice Relaxation in Solids. *J. Phys. C Solid State Phys.* **1978**, *11*, 783–795.
- (114) Kubicki, D. J.; Prochowicz, D.; Pinon, A.; Stevanato, G.; Hofstetter, A.; Zakeeruddin, S. M.; Grätzel, M.; Emsley, L. Doping and Phase Segregation in Mn^{2+} - and Co^{2+} -Doped Lead Halide Perovskites from ^{133}Cs and ^1H NMR Relaxation Enhancement. *J. Mater. Chem. A* **2019**, *7*, 2326–2333.

CHAPTER 2

Mechanochemical Synthesis of Methylammonium Lead Mixed-Halide Perovskites: Unraveling the Solid-Solution Behavior Using Solid-State NMR^{R1}

2.1 Introduction

Hybrid organic–inorganic metal halide perovskites have emerged as promising contenders for next-generation low-cost, high-efficiency solar cells. Fueled by intensive worldwide research efforts, perovskite solar cells (PSCs) surpassed the 22% photoconversion efficiency limit within a few years.¹ This rapid improvement in PSC efficiencies is due to their promising intrinsic properties, such as long-range ambipolar carrier diffusion lengths, high absorption coefficients, and low exciton binding energies.^{2–4} A particularly promising area of research has been on mixed-halide perovskites (MHPs) of the type ABX_3 , where $A = \text{CH}_3\text{NH}_3^+$, $B = \text{Pb}^{2+}$, and $X = \text{Cl}^-$, Br^- , and I^- .⁵ One advantage that MHPs offer is the bandgap tunability made possible through the halide composition, which is important for applications such as tandem solar cells and light emitting diodes (LEDs).⁶ Additionally, MHPs offer enhanced stability against moisture, and thus their use to achieve more stable and higher-performing PSCs is becoming routine.^{7,8}

MHPs possess an intriguing range of properties stemming from the degrees of freedom in their synthesis due to the relatively straight forward reversible-halide exchange both in solution and between gas and solid phases.^{9,10} Nevertheless, challenges with MHPs also have been reported. In particular, the consequences of halide ion mobility on the device performance^{11–13} and of phase segregation due to photoinduced halide ion migration^{14–17} must be considered. Among the many synthesis

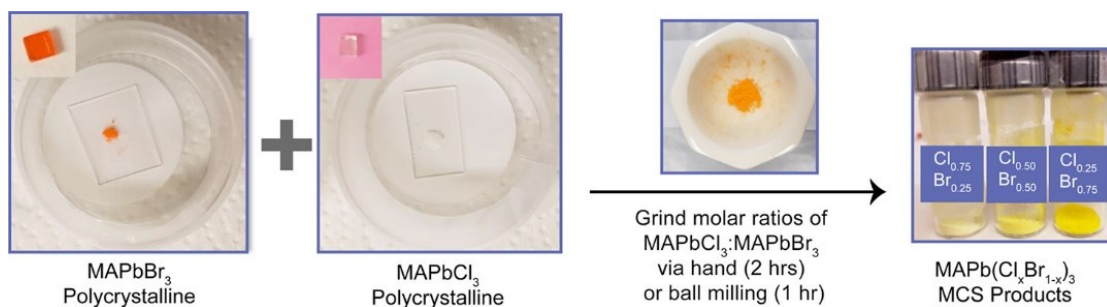
^{R1} The contents of this chapter have been copied and/or adapted from the following publication: Karmakar, A.; Askar, A. M.; Bernard, G. M.; Terskikh, V. V.; Ha, M.; Patel, S.; Shankar, K.; Michaelis, V. K. Mechanochemical Synthesis of Methylammonium Lead Mixed-Halide Perovskites: Unraveling the Solid-Solution Behavior Using Solid-State NMR. *Chem. Mater.* **2018**, *30*, 2309–2321. The supplementary data for this chapter is available in Appendix A: Tables A1–A7 and Figures A1–A17.

techniques for preparing perovskite materials, mechanochemical synthesis (MCS) has gained renewed interest due to the advantages it offers. MCS is a straightforward, green-chemistry method, which is highly efficient, simple, and reproducible. Moreover, it is a solvent-free method that also avoids high-temperature reactions and is capable of mass-yield production. MCS has been applied previously in other systems^{18–21} but recently has shown promise in the preparation of bulk and nanocrystalline perovskites,^{22–26} achieving enhanced material properties and device performance^{27,28} compared to those prepared using traditional solvent synthesis (SS). For instance, preparing $\text{CH}_3\text{NH}_3\text{PbI}_3$ PSCs by MCS leads to a reduction in the interfacial trap density in fabricated PSCs in comparison to the same compound prepared through standard solvent synthesis.²⁹ Recently, MCS was used to prepare complex mixed cation (Cs^+ , Rb^+ , $\text{CH}(\text{NH}_2)_2^+$, in addition to CH_3NH_3^+) lead halide perovskite materials used in the highest performing and most stable PSCs reported to date, revealing similar structural properties to the corresponding perovskite materials prepared by traditional two-step casting techniques.³⁰

The high mobility of halide ions in halide perovskites prompted us to investigate the potential of MCS in the synthesis of $\text{MAPb}(\text{X}_x\text{X}'_{1-x})_3$ ($\text{MA} = \text{CH}_3\text{NH}_3^+$, X and $\text{X}' = \text{Cl}^-$ and Br^- or Br^- and I^-) MHPs for the first time from their parent MAPbX_3 compounds and to examine at the atomic scale the true halide mixing in the products. A suite of techniques, including solid-state nuclear magnetic resonance (NMR) spectroscopy, a powerful tool in probing the local- and medium-range chemical environments of NMR-active nuclides, were used in our investigation. Specifically, in this work ^{207}Pb NMR spectroscopy was used to investigate the change in the Pb chemical environment of these MHPs, complemented by X-ray diffraction (XRD) data and quantum chemical calculations. The challenge is to synthesize stoichiometric and homogeneous mixed-halide variants, avoiding microscopic domains or inhomogeneous phase-separated solid mixtures. X-ray diffraction approaches are excellent for the determination of the long-range crystalline structure, while NMR spectroscopy is one of the few characterization tools capable of measuring atomic-level structure, providing direct information regarding the local chemical environment that is impacted by ion substitutions or rearrangements such as defect sites, solid solutions, or segregated

domains within solids.³¹⁻³⁴ For example, it has been suggested that Cl and Br can substitute for one another in MAPbX_3 , forming a crystalline perovskite with different domains when synthesized using the traditional solvent synthesis as well as high-temperature solid-state synthesis approaches.³⁵

In this report, we demonstrate two mechanochemical stoichiometric synthetic approaches that produce polycrystalline single-phase, ordered or locally disordered MHP solid-solutions with random halide arrangements about the Pb center, avoiding phase-segregated domains. The techniques used for the application of MCS (Scheme 2.1) were manual hand grinding (HG) using a mortar and pestle and a ball milling (BM) method. When appropriate, our MCS results are compared to those obtained from samples prepared by traditional SS protocols.³⁵ MAPbI_3 prepared using the MCS method has been shown to yield a product with superior solar cell performance compared to the corresponding product prepared via SS;^{27,29} thus, we demonstrate that the MCS route described herein for the more commonly used MHPs is a very promising technique as an efficient strategy for commercializing these systems for a wide variety of photovoltaic and optoelectronic applications.



Scheme 2.1. MCS process for the preparation of MHPs.

In the HG method, parent compounds are mixed in the required molar ratio using a mortar and pestle and the HG process continues for 1–2 h to obtain a uniform single-phase product. In MCS-BM, a similar approach is used, but instead of the HG process, an automated BM system is used for 1 h.

2.2 Experimental Section

All starting precursor materials and solvents were obtained from commercial sources and used without further purification: lead(II) iodide (99%), lead(II) bromide (+98%), and lead(II) chloride (99%) from ACROS Organics (Morris Plains, NJ, U.S.A.); methylammonium chloride (MACl), γ -butyrolactone (GBL; >99%), and dimethyl sulfoxide (DMSO) from Sigma-Aldrich (St. Louis, MO, U.S.A.); and methylammonium bromide (MABr) and methylammonium iodide (MAI) from Dyesol LTD (Australia).

2.2.1 Synthesis of MAPbX₃ Using the Inverse Temperature Crystallization (ITC) Technique^{36,37}

MAPbCl₃

A 1 M MAPbCl₃ solution was prepared by adding MACl and PbCl₂ in a 1:1 V/V DMF/DMSO mixture at room temperature. A clear transparent solution formed, which was filtered with 0.2 μ m filters. Then, the solution was distributed into small vials, with 2 mL of solution each. These vials were placed in an oil bath at 60 °C, and the large crystals were allowed to grow for 6 h, then washed thoroughly with DMF, and immediately dried with an N₂ gas flow.

MAPbBr₃

A 1 M MAPbBr₃ solution was prepared at room temperature by adding MABr and PbBr₂ in dimethylformamide (DMF). The resulting mixture formed a clear transparent solution. The solution was filtered using 0.2 μ m filters and then distributed into small vials with 2 mL of solution each. The vials were placed in an oil bath at 80 °C, and crystals were allowed to grow for 3 h, then washed thoroughly with DMF, and immediately dried with a dry N₂ gas flow.

MAPbI₃

A 1 M MAPbI₃ solution was prepared by fully dissolving MAI and PbI₂ in GBL at 60 °C such that it became a bright yellow solution. The solution was filtered using 0.2 μ m filters and then distributed into small vials, with 2 mL of solution each. The vials were placed in an oil bath at 110 °C. Crystals were allowed to grow for 3 h, then

washed thoroughly with GBL, immediately dried with an N₂ gas flow, and then stored under vacuum in the dark.

2.2.2 Synthesis of MAPb(X_xX'_{1-x})₃ MHPs

To synthesize MHPs using the MCS-HG approach, MAPbX₃ and MAPbX'₃ were loaded with molar ratios set to achieve the desired mixed-halide composition. For example, to prepare MAPb(Cl_{0.5}Br_{0.5})₃, 159.66 mg of MAPbBr₃ was loaded in a mortar with 115.21 mg of MAPbCl₃, and hand grinding was applied for 1–2 h. For MCS-BM techniques, the same ratios of precursors as for the MCS-HG approach were loaded into either a planetary (RETSCH Planetary Ball Mill PM 100) or a shaker ball mill (SPEX SamplePrep 8000M Mixer/Mill). We note that, by adjusting the time, ball size, and speed of impacts, one can utilize a planetary mill to obtain similar results to HG within a fraction of the time (i.e., 5–60 min), with good reproducibility. All synthetic procedures were carried out under ambient lab conditions in air. All results presented here for the MCS-BM method were obtained from parent compounds processed by the shaker ball mill for 1 h.

2.2.3 Diffuse Reflectance (DR) Spectroscopy of MHP Perovskites

A Varian Cary 400 UV–visible spectrophotometer, equipped for the analysis of small-quantity fine powdered samples, was used to obtain DR data. Each sample was packed into a black boat (loaded with ~100 mg/sample), with each measurement acquired between wavelengths of 300 and 900 nm.

2.2.4 Powder X-ray Diffraction (XRD) Measurements

Fine powder samples were mounted on a glass slide and analyzed using a Bruker D8 Advance Diffractometer equipped with a Cu K α source and a VANTEC-500 2D detector. All data were acquired at room temperature with a 2 θ range of 10°–60° and 0.005° resolution.

2.2.5 Solid-State Nuclear Magnetic Resonance Spectroscopy

The ^1H NMR spectra were acquired at 7.05 T (^1H , 300.4 MHz) on a Bruker Avance 300 NMR spectrometer with a Bloch pulse using a $4.0\ \mu\text{s}\ \pi/2$ pulse ($\gamma B_1/2\pi = 62.5\ \text{kHz}$) and a recycle delay of 60 s. Samples were packed in 4 mm OD ZrO_2 rotors, and spectra were acquired with a magic-angle spinning (MAS) frequency of 10 kHz. All ^1H spectra were referenced to TMS ($\delta(^1\text{H}) = 0.0\ \text{ppm}$) by setting the ^1H peak of adamantane to 1.85 ppm.

The ^{13}C NMR spectra were acquired at 7.05 T on a Bruker Avance 300 NMR spectrometer equipped with a 4 mm double resonance MAS NMR probe. ^{13}C ($\nu_L = 75.5\ \text{MHz}$) cross-polarization (CP)³⁸ MAS NMR spectra were acquired with a spinning frequency of 10 kHz, a $4.0\ \mu\text{s}\ \pi/2$ pulse ($\gamma B_1/2\pi = 62.5\ \text{kHz}$) for ^1H , a contact time of 3.5 ms, and a recycle delay time of 60 s. All ^{13}C spectra were referenced to TMS ($\delta(^{13}\text{C}) = 0.0\ \text{ppm}$) by setting the high frequency ^{13}C peak of solid adamantane to 38.56 ppm.³⁹ All spectra were acquired with TPPM high-power ^1H decoupling ($\gamma B_1/2\pi = 62.5\ \text{kHz}$).⁴⁰

The ^{207}Pb NMR spectra were acquired at 7.05, 11.7, and 21.1 T on Bruker Avance 300, 500, and Avance II 900 NMR spectrometers, respectively. Nonspinning ^{207}Pb NMR spectra were collected using a 4 mm double resonance H/X Bruker probe using either a Hahn-echo⁴¹ ($(\pi/2)_x-\tau_1-(\pi)_y-\tau_2\text{-ACQ}$, where τ represents the interpulse (τ_1) and refocusing delays (τ_2)) or a modified quadrupolar-echo⁴²⁻⁴⁴ pulse sequence to achieve broader excitation width and minimize line distortions at higher magnetic field strengths. A recycle delay of 5.0 s, a $4.0\ \mu\text{s}\ \pi/2$ pulse ($\gamma B_1/2\pi = 62.5\ \text{kHz}$), and τ_1 values of 20–30 μs were used for all of the measurements to minimize the impact of the echo delay on the quantitative assessment of peak areas. T_2 values were measured using a spin-echo pulse sequence and are summarized in the Appendix A. At 11.7 and 21.1 T, the variable offset cumulative spectra (VOCS)⁴⁵ approach using between 3 and 5 steps with a 50 kHz transmitter stepping frequency across the spectral range was used to ensure acquisition of the complete, undistorted spectrum; the subspectra were added using the skyline projection method. Two-dimensional ^{207}Pb EXSY (exchange spectroscopy)⁴⁶ spectra (21.1 T) were acquired using a series of mixing times between 10 μs and 2 ms. A total of 64 to 128 slices were collected in the indirect dimension

using a 2 μs increment, and between 512 and 3840 coadded transients were acquired per slice, depending on the mixing time. All ^{207}Pb NMR spectra were referenced to PbMe_4 ($\delta(^{207}\text{Pb}) = 0.0$ ppm) by setting the ^{207}Pb peak of nonspinning solid MAPbCl_3 measured at 293 K to -647.5 ppm.⁴⁷

2.2.6 NMR Processing, Fitting Procedures, and NMR Considerations

Spectra were processed using Topspin 3.5 Bruker software with between 250 and 500 Hz exponential apodization, and the data were fit using both OriginPro 8 and WSOLIDS⁴⁸ software. To assess the quantitative nature of the unique $[\text{PbX}_x\text{X}'_{6-x}]^{4-}$ chemical environments observed in the ^{207}Pb NMR spectra, all data were fit using two distinct fitting procedures to assess the distributions of sites. Within Origin, all data were fit using Gaussian lineshapes and up to seven distinct Pb environments. Spectra were also fit using WSOLIDS, with seven distinct Pb environments to incorporate the anisotropic components, as surmised from spectra acquired at multiple magnetic fields and from the results of density functional theory (DFT) calculations. See the Appendix A for a more thorough explanation of the fitting procedure, including errors and statistical analysis. To ensure maximum resolution, these samples initially were assessed using a combination of multiple magnetic field strengths (i.e., 7.05, 11.75, and 21.1 T), nonspinning and magic-angle spinning (MAS) NMR methods, and experiments with and without ^1H decoupling. The benefit of MAS is minimal, (see Appendix A, Table A1) removing a small effect from heteronuclear dipole couplings between Pb and X,^{47,49–53} while high-power proton decoupling did not affect the overall line shape or width significantly compared to those obtained without ^1H decoupling. This is attributed to the fast motion of the MA cation that rotates rapidly within the cuboctahedron, therefore, its ^1H nuclei self-decouple from the Pb. Chemical shift anisotropy was detectable under certain conditions with low mixed-halide doping using a combination of MAS and nonspinning experiments (see below and Appendix A). Overall, site resolution increased at higher magnetic field strengths. To gauge the effect of using an echo pulse sequence to quantify Pb chemical environments, a series of spectra were acquired with varying τ values (10–50 μs); the difference in the relative intensities across all sites (MCS-HG, $\text{MAPb}(\text{Cl}_{0.5}\text{Br}_{0.5})_3$) was negligible (<2%), ensuring

a robust approach. MAS spectra routinely were avoided to limit the impact of unwanted frictional heating on the ^{207}Pb chemical shifts, which are known to be extremely sensitive to temperature.⁴⁷ Hence, most ^{207}Pb NMR spectra were acquired under nonspinning conditions without ^1H decoupling.

2.2.7 Quantum Chemical Calculations

Relativistic Calculations on Model $[\text{PbCl}_x\text{Br}_{6-x}]^{4-}$ Anions

Density functional theory (DFT) calculations of the ^{207}Pb magnetic shielding on a series of 10 $[\text{PbCl}_x\text{Br}_{6-x}]^{4-}$ octahedral model anions were carried out using the Amsterdam Density Functional (ADF) 2017 modeling suite.⁵⁴⁻⁵⁷ The structures were modeled by assuming octahedral coordination about the Pb, with a Pb–Cl bond length of 2.834 Å, derived from XRD data (vide infra), and a Pb–Br bond length of 2.966 Å.⁵⁷ A calculation for $[\text{PbI}_6]^{4-}$ also assumed octahedral symmetry and a bond length of 3.146 Å.⁵⁷ Relativistic effects were calculated using the zeroth order regular approximation (ZORA) method, along with the ZORA/QZ4P basis set, which is optimized for relativistic calculations.^{58,59} All calculated shielding values were converted to chemical shifts using $\delta_{\text{calc}} (\text{ppm}) = -(\sigma_{\text{calc}} - 8858.4 \text{ ppm})$; the relationship was determined from a linear regression between experimental chemical shifts and the calculated magnetic shielding values of the three parent compounds, MAPbCl_3 , MAPbBr_3 , and MAPbI_3 . All principal components of the calculated ^{207}Pb magnetic shielding tensors are available in the Appendix A and are defined using the Maryland Convention.^{60,61} All DFT calculations used the Perdew, Burke, and Ernzerhof (PBE) functional in the generalized gradient approximation (GGA).⁶²⁻⁶⁴

2.2.8 Periodic Calculations

Gauge including projector augmented wave (GIPAW) based DFT calculations, a plane-wave basis set ideal for computing properties in periodic systems,⁶⁵ were undertaken on model $2 \times 2 \times 2$ supercells with primitive symmetry, as implemented in the CASTEP program (version 4.4). In these calculations, ^{207}Pb magnetic shielding values were obtained on a series of structures generated by systematically replacing Cl for Br in MAPbCl_3 . The calculations used the PBE functional in the GGA for the exchange-

correlation energy^{62,63} and ultrasoft pseudopotentials.⁶⁶ All calculations were performed on an HP xw4400 workstation with a single Intel Dual-Core 2.67 GHz processor and 8 GB RAM. No further optimizations were performed regarding the unit cell. An all-atom geometry optimization was performed on the 50:50 fac and mer isomers. However, these did not provide significant changes to the calculated magnetic shielding parameters, and all forces on heavier atoms were below the 0.48 eV/Å threshold. Thus, no further optimization within the computed structures were performed. All calculations were performed with a coarse accuracy basis set and a maximum plane-wave energy of 250.34 eV.

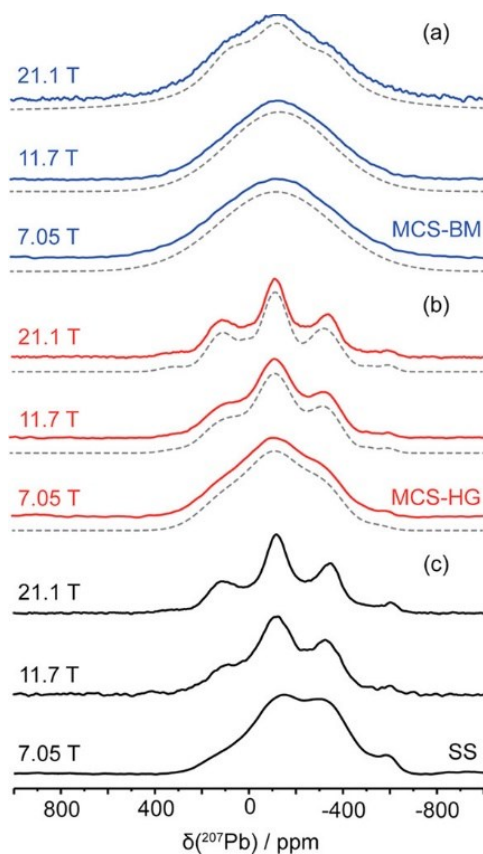


Figure 2.1. ²⁰⁷Pb NMR spectra of nonspinning (a) MCS-BM (blue), (b) MCS-HG (red), and (c) SS (black) samples of MAPb(Cl_{0.5}Br_{0.5})₃, acquired at 7.05 T (300 MHz, ¹H), 11.7 T (500 MHz, ¹H), and 21.1 T (900 MHz, ¹H). The gray dotted lines are the best fits for the spectra obtained for the samples prepared with the mechanochemical synthesis methods.

2.3 Results and Discussion

Figure 2.1 shows ^{207}Pb NMR spectra of $\text{MAPb}(\text{Cl}_{0.5}\text{Br}_{0.5})_3$ prepared using the MCS-BM (Figure 2.1a), MCS-HG (Figure 2.1b), and SS (Figure 2.1c) approaches, acquired at magnetic field strengths ranging from 7.05 to 21.1 T.

The ^{207}Pb NMR spectra exhibit multiple sites, regardless of synthetic approach, illustrating the complex short-range Pb structure present in these otherwise simple primitive cubic crystalline solids ($Pm\bar{3}m$ space group).⁶⁷ The resolution achieved at higher magnetic field strengths suggests distinct local Pb chemical environments, with a potential to assign the various arrangements of halide ions within the MHPs qualitatively and quantitatively. This initial finding suggests that each $[\text{PbX}_x\text{X}'_{6-x}]^{4-}$ unit bears distinct NMR chemical shifts for the various Pb-halide octahedral arrangements, demonstrating a binomial-like distribution characteristic of solid solution random halide mixing behavior.

To date, most of the hybrid perovskite studies have relied extensively on diffraction-based approaches.^{68,69} Solid-state NMR spectroscopy, however, is emerging rapidly as an extremely informative analytical structural tool in characterizing both local structure and dynamics within photovoltaic perovskite materials.^{30,35,47,49,51,70–74} In particular, ^{207}Pb is an information-rich, receptive spin-1/2 nucleus that exhibits a very large chemical shift range; therefore, it is sensitive to even minor changes in local chemical environment. However, unlike solution NMR spectroscopy, solid-state NMR spectra are often subject to broad lines typically arising from various anisotropic interactions. For lead halide perovskites, these can include unfavorable T_2 characteristics, small heteronuclear dipolar coupling contributions (<1 kHz), ^{207}Pb - $^{35/37}\text{Cl}$, ^{207}Pb - $^{79/81}\text{Br}$, or ^{207}Pb - ^{127}I indirect spin–spin (J -coupling) interactions, and the potential of magnetic shielding anisotropy when the nucleus is not at a center of cubic symmetry.^{35,47,49–51,70,72} For the work presented here, line broadening also may result from the presence of isomers such as cis and trans $[\text{PbX}_4\text{X}'_2]^{4-}$ and fac and mer isomers in the $[\text{PbX}_3\text{X}'_3]^{4-}$ mixed-halide octahedron environments or from localized disorder within the lead octahedra similar to the effects often seen in lead-containing glasses.^{75,76} Therefore, the chemical shifts of the peak maxima, δ_{cs} , are reported below instead of conventional isotropic chemical shift, δ_{iso} ,

since at lower magnetic field strengths, J -based splitting⁷² may become apparent, or at higher magnetic fields (e.g., 35 T), magnetic shielding anisotropy⁷⁷ may begin to dominate the spectrum. The observed ^{207}Pb NMR results (i.e., broad peaks and chemical shift distributions) for the BM, HG, and SS samples discussed above warranted further investigation to assess and interpret the local atomic structure.

2.3.1 $\text{MAPb}(\text{Cl}_x\text{Br}_{1-x})_3$ Hand Ground Mechanochemical Synthesis

To unravel the complex nature of anion mixing about the Pb center of the MHPs prepared with the SS and MCS methods, a series of standards of various $\text{MAPbCl}_3/\text{MAPbBr}_3$ molar ratios (100/0, 95/5, 83/17, 75/25, 50/50, 25/75, 5/95, and 0/100) were synthesized using the inverse temperature crystallization (parent compounds)^{36,37} and MCS-HG (MHPs) methods and analyzed by ^{207}Pb NMR spectroscopy to assess the changes in the first coordination sphere about the Pb.

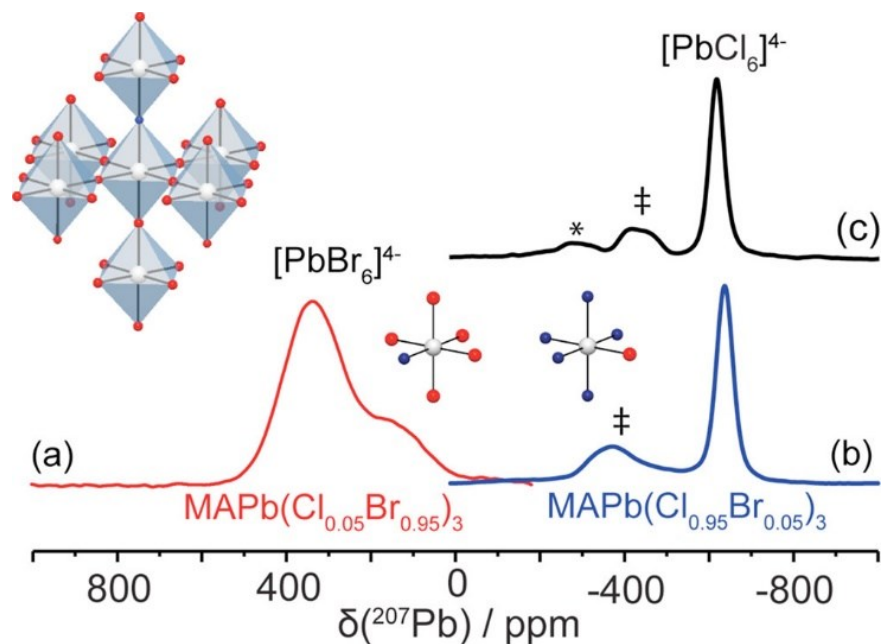


Figure 2.2. ^{207}Pb NMR spectra ($B_0 = 11.7$ T) of (a) nonspinning $\text{MAPb}(\text{Cl}_{0.05}\text{Br}_{0.95})_3$ prepared by MCS-HG and (b) nonspinning and (c) MAS ($\omega_r/2\pi = 13.5$ kHz) NMR spectra of $\text{MAPb}(\text{Cl}_{0.95}\text{Br}_{0.05})_3$ prepared by MCS-HG. The δ_{cs} are marked with ‡, and the spinning sideband is identified by an asterisk (*).

Figure 2.2a shows a nonspinning ^{207}Pb NMR spectrum for $\text{MAPb}(\text{Cl}_{0.05}\text{Br}_{0.95})_3$, with two peaks located at $\delta_{\text{cs}} \approx 340$ and 175 ppm. The pattern seen in Figure 2.2 is consistent with a spectrum expected for a sample with two distinct NMR sites, but is also similar to that expected for a single NMR site experiencing chemical shift anisotropy (CSA).

To investigate, an MAS spectrum of the sample was obtained at 7.05 T at a spinning frequency of 13 kHz. The spectrum, which is slightly asymmetric, can be simulated best with two NMR sites separated by approximately 135 ppm or 8.5 kHz (i.e., less than the spinning frequency and hence a second NMR site rather than a spinning sideband) and with the expected intensity of approximately 30% for the low frequency site (Figure A1). This result is corroborated by DFT calculations (Table A2), which predict that $[\text{PbCl}_1\text{Br}_5]^{4-}$ appears at approximately 50 ppm to lower chemical shift from the peak for $[\text{PbBr}_6]^{4-}$. Likewise, the ^{207}Pb NMR spectrum for $\text{MAPb}(\text{Cl}_{0.95}\text{Br}_{0.05})_3$ (Figure 2.2b) also contains two peaks, at $\delta_{\text{cs}} \approx -641$ and -400 ppm; the corresponding MAS spectrum for the latter (Figure 2.2c) yields similar values, $\delta_{\text{iso}}^{\text{MAS}} \approx -621$ and -450 ppm. The peak at -450 ppm, attributed to $[\text{PbCl}_5\text{Br}_1]^{4-}$ units, appears to be a doublet. However, close examination reveals that the peak is asymmetric, appearing skewed toward its high-frequency edge (see Figure A2 for an expansion of this region and for a comparison with a spectrum obtained at 7.05 T). As seen from this expansion, the peaks do not represent two distinct NMR sites since, in such a case, the chemical shifts of these peaks would be the same regardless of magnetic field strength. A ^{207}Pb nucleus within a $[\text{PbCl}_5\text{Br}_1]^{4-}$ unit under MAS conditions is subject to $^1J(^{207}\text{Pb}, ^{35/37}\text{Cl})$ interactions to the five Cl nuclei and a $^1J(^{207}\text{Pb}, ^{79/81}\text{Br})$ interaction to the Br, but the latter is expected to dominate.⁷² However, the large nuclear quadrupolar coupling expected for $^{79/81}\text{Br}$ (NQR frequencies of 70.451 and 58.842 MHz that have been reported for MAPbBr_3)⁷⁸ will result in an asymmetric splitting pattern⁷⁹ rather than the four equal intensity peaks one may expect in the absence of a large quadrupole interaction. The presence of a spinning sideband for the NMR site at -450 ppm is consistent with the asymmetry of the $[\text{PbCl}_5\text{Br}_1]^{4-}$ unit, and the fact that it is shifted to higher frequency by approximately 170 ppm is qualitatively in agreement with the trend predicted by DFT calculations (vide infra).

At dopant level halide substitutions (i.e., $\leq 5\%$), the halide ion transitions into the lattice replacing a Br for Cl (or Cl for Br) and immediately affects the lattice parameters (vide infra) of the solid-solution and the corresponding $\delta_{\text{cs}}(^{207}\text{Pb})$ chemical shifts of $[\text{PbBr}_6]^{4-}$ or $[\text{PbCl}_6]^{4-}$, reflecting the sensitivity of ^{207}Pb NMR spectroscopy to changes within the material. Thus, it is not surprising that the chemical shift of a slightly Br-doped material is greater than that for the pure parent material (MAPbCl_3) since the ^{207}Pb resonance of the MAPbBr_3 parent complex appears at a higher chemical shift. Accounting for the 5% dopant concentration and for the coordination number of Pb (i.e., 6), 26.5% of the Pb centers are coordinated directly to a Br (or Cl) dopant within their octahedra. Fitting the peak areas of the ^{207}Pb NMR spectra for $\text{MAPb}(\text{Cl}_{0.05}\text{Br}_{0.95})_3$ and for $\text{MAPb}(\text{Cl}_{0.95}\text{Br}_{0.05})_3$, respectively, yielded ratios of 0.72:0.28 (± 0.05) and 0.28:0.72 (± 0.02) for the $[\text{PbBr}_6]^{4-}$ and $[\text{PbCl}_5\text{Br}]^{4-}$ units of the former and for the $[\text{PbCl}_5\text{Br}_1]^{4-}$ and $[\text{PbCl}_6]^{4-}$ units of the latter. Therefore, the lower-frequency resonance in the ^{207}Pb NMR spectrum for $\text{MAPb}(\text{Cl}_{0.05}\text{Br}_{0.95})_3$ is assigned to a $[\text{PbClBr}_5]^{4-}$ local six-coordinate environment; likewise, the higher-frequency resonance observed in $\text{MAPb}(\text{Cl}_{0.95}\text{Br}_{0.05})_3$ is assigned to $[\text{PbCl}_5\text{Br}_1]^{4-}$. A small CSA contribution (span, $\Omega = \delta_1 - \delta_{33} \approx 200 \pm 30$ ppm) was determined for the $\text{MAPb}(\text{Cl}_{0.95}\text{Br}_{0.05})_3$ by using a combination of MAS and nonspinning experiments at 11.7 T; this was only possible for this sample due to the narrow resonance of the $[\text{PbCl}_6]^{4-}$ octahedra (Figure 2.2c). Using this finding and the DFT results (vide infra), we expect only a minor ^{207}Pb CSA contribution from the $[\text{PbClBr}_5]^{4-}$ environment found in the $\text{MAPb}(\text{Cl}_{0.05}\text{Br}_{0.95})_3$ sample; unfortunately the breadth of these two sites and the lack of resolution between them limits our ability to isolate potential anisotropic shielding as well as dipolar and J -coupling contributions or to investigate spin-lattice or spin-spin relaxation mechanisms accurately.

As Cl replaces Br, the ^{207}Pb spectra break into additional resonances due to the formation of new Pb-X bonds, whereby peak maxima shift to lower chemical shifts toward that for the parent compound, MAPbCl_3 (Figure 2.3a). These spectra demonstrate the sensitivity of ^{207}Pb NMR spectroscopy, as exemplified by the extremely large chemical shift range ($\sim 17\,000$ ppm) for this nucleus,⁸⁰ to the halide environment about the Pb center in these samples.^{52,81} See Figure A3 and the

accompanying section in the Appendix A for a discussion of how the spectra for the MHPs illustrated above were deconvoluted.

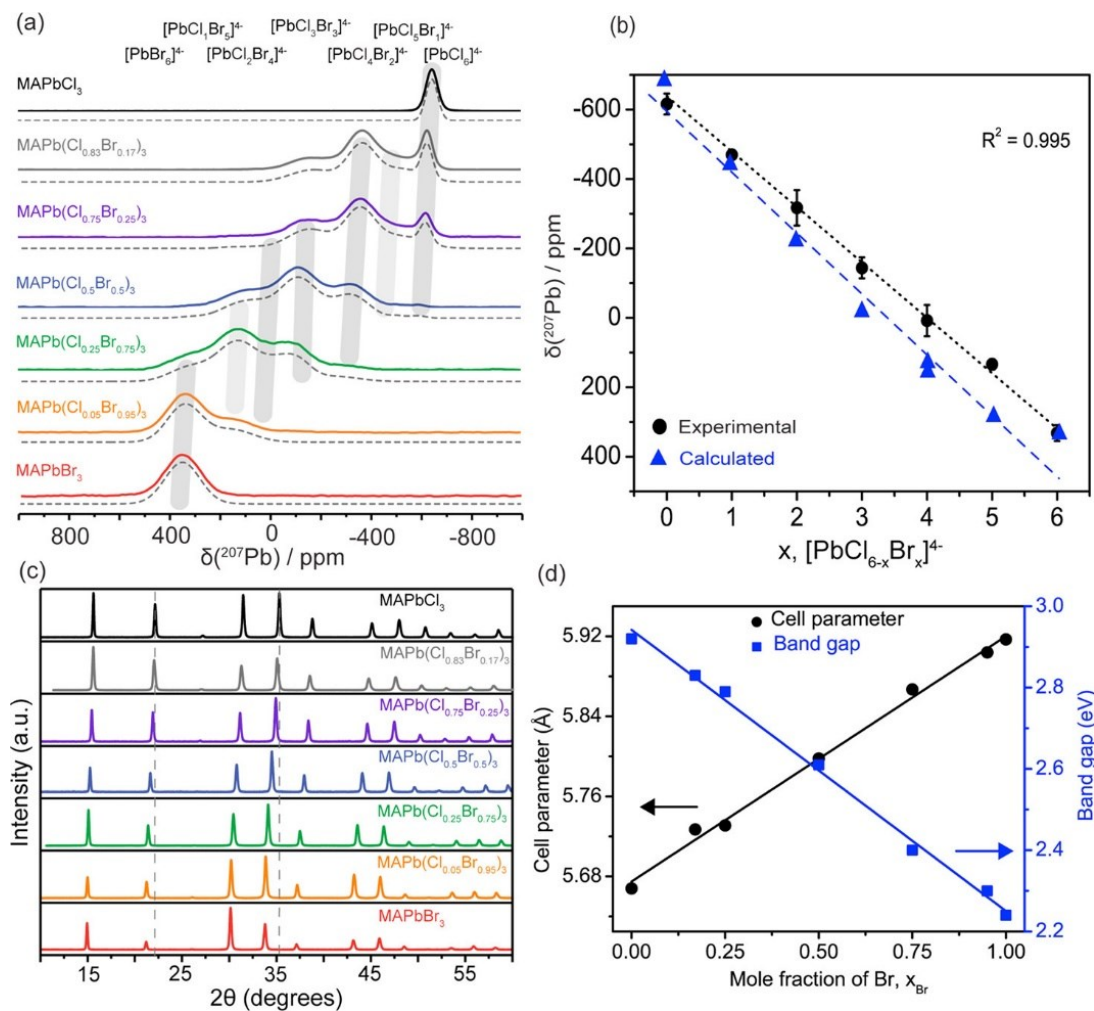


Figure 2.3. (a) Nonspinning ²⁰⁷Pb NMR spectra (11.7 T) of MCS-HG MHPs and their parent compounds. The assignment of the NMR peaks is shown at the top (the shaded areas are guides to the eye to identify specific NMR sites in the various spectra, and the dashed lines indicate simulated spectra). See the Appendix A for an explanation of how these spectra were fit. (b) Linear relationship of $\delta(^{207}\text{Pb})$ with substitution of Cl with Br (experimental, circles, and $\delta_{\text{iso}}(^{207}\text{Pb})$ quantum chemical calculations (ADF), triangle). (c) Powder X-ray diffraction data. Dotted lines are guides to the eye. (d) A plot of cell parameter ($R^2 = 0.994$) and experimentally determined bandgaps extracted from Tauc plots ($R^2 = 0.994$) vs Br mole fraction for the MHP series.

A clear, although smaller, increase in the chemical shift also is observed for the resonance attributed to $[\text{PbCl}_6]^{4-}$ with increasing Br content, as shown in Table 2.1; this is attributed to the change in the unit cell parameters as it expands to allow Br incorporation (Figure A4). Table 2.1 summarizes the distinct ^{207}Pb δ_{cs} values for each $[\text{PbCl}_x\text{Br}_{6-x}]^{4-}$ ($x = 0-6$) octahedron. Using these data, we determined a linear correlation between $\delta_{\text{cs}}(^{207}\text{Pb})$ and the hexa-substituted Pb-X chemical environments (Figure 2.3b) that can be used to identify the distinct $[\text{PbCl}_x\text{Br}_{6-x}]^{4-}$ environments according to $\delta_{\text{cs}}(^{207}\text{Pb}/\text{ppm}) = 160M - 640$, where M is the number of Br atoms in the first coordination sphere of Pb. Moreover, a similar linear relation exists between the electronegativity of the mixed-halide ions and the chemical shift in ^{207}Pb NMR spectra for each of the corresponding $[\text{PbCl}_x\text{Br}_{6-x}]^{4-}$ environments (Figure A5). The ^{207}Pb NMR line widths for MAPbX_3 increase as X is substituted from Cl to Br to I (Table A1); therefore, the ^{207}Pb resonance for a site with more Br neighbors is expected to be broader than that for a site with more Cl neighbors and likewise when I is substituted for Br.^{47,49,70} The ^{207}Pb spin-spin relaxation times (T_2) for the individual $[\text{PbX}_x\text{X}'_{6-x}]^{4-}$ chemical environments present in the MCS-HG $\text{MAPb}(\text{Cl}_{0.5}\text{Br}_{0.5})_3$ sample range from 54 μs for $[\text{PbBr}_6]^{4-}$ to 98 μs for $[\text{PbCl}_6]^{4-}$, with a small systematic increase in T_2 as Cl replaces Br about the Pb center (Table A3). Previous studies on the parent materials indicate the T_2 values to be nearly 1 order of magnitude apart (~ 60 μs for MAPbBr_3 vs ~ 300 μs for MAPbCl_3).^{35,70} These findings further support our conclusion that MCS produces a homogeneous halide mixture.

Table 2.1. Assignment of ^{207}Pb NMR peak positions (δ_{cs} , ppm) for parent and MCS-HG mixed-halide Perovskites.^a

Samples	PbBr ₆	PbClBr ₅	PbCl ₂ Br ₄	PbCl ₃ Br ₃	PbCl ₄ Br ₂	PbCl ₅ Br	PbCl ₆
MAPbBr ₃	355						
MAPb(Cl _{0.05} Br _{0.95}) ₃	340 360 ^b	175 225 ^b					
MAPb(Cl _{0.25} Br _{0.75}) ₃	321	149	-38	-116	-266		
MAPb(Cl _{0.50} Br _{0.50}) ₃	309	119	43	-114	-326	-480	-587
MAPb(Cl _{0.75} Br _{0.25}) ₃		142	53	-160	-360	-500	-622
MAPb(Cl _{0.83} Br _{0.17}) ₃				-174	-368	-520	-627
MAPb(Cl _{0.95} Br _{0.05}) ₃						-400 -450 ^c	-641 -621 ^c
MAPbCl ₃							-646
δ_{cs} (ppm)	332 (30)	134 (40)	8 (45)	-144 (30)	-317 (50)	-473 (50)	-616 (30)

^aUncertainties in peak positions range from 5 to 40 ppm, unless noted data is for nonspinning spectra at 11.7 T.

^bDetermined from a deconvolution of an NMR spectrum obtained under MAS conditions at 7.05 T.

^c δ_{iso} determined from ^{207}Pb MAS NMR spectroscopy

The XRD patterns (Figure 2.3c) for all MCS-HG samples confirm that these consist of a single phase that adopts the cubic $Pm\bar{3}m$ perovskite structure, with diffraction peak positions shifting to higher 2θ values with increasing Cl content.⁸² Substituting the chlorine anion ($r = 167$ pm) with a larger bromine anion ($r = 182$ pm) increases the lattice parameter, linearly obeying Vegard's law describing solid solution behavior, as shown in Figure 2.3d.⁸³ The MCS-HG synthesis method shows a single cutoff energy in the DR spectra (Figure A6), which corresponds systematically to an increase in the bandgap energy from pure MAPbBr₃ to pure MAPbCl₃ (Figure 2.3d).

A series of DFT calculations on model $[\text{PbX}_x\text{X}'_{6-x}]^{4-}$ anions (ADF) and periodic solid (CASTEP) models was performed to assess the sensitivity of the ^{207}Pb chemical shift to halide substitution, and results are presented in Tables A2 and A4. As shown in

Figure 2.4a, the calculated shielding values for the model anions correlate with the experimentally determined chemical shifts. The calculated isotropic chemical shifts also reveal a linear relationship, increasing systematically as Cl anions are replaced by Br anions from $[\text{PbCl}_6]^{4-}$ to $[\text{PbBr}_6]^{4-}$ (Figure 2.4b). The calculated $\delta_{\text{iso}}(^{207}\text{Pb})$ values obtained using the model anions are shown for comparison in Figure 2.3b, revealing a linear trend to lower chemical shift as Cl is substituted for Br, consistent with our qualitative (experimental $\delta_{\text{cs}}(^{207}\text{Pb})$ NMR) assignments of distinct local Pb octahedra found in MHP solid solutions discussed above. Further expanding the model anions to include MAPbI_3 and Br/I MHP reveals excellent agreement between the calculated and experimentally determined (vide infra) $\delta_{\text{cs}}(^{207}\text{Pb})$, demonstrating that the combination of the calculated and experimental NMR parameters can be used to assign the distinct short-range order for six-coordinate (i.e., $[\text{PbX}_x\text{X}'_{6-x}]^{4-}$) chemical environments (Figure 2.4c). This confirms the qualitative nature of the NMR method in assessing the atomic structure of these single-phase solid-solution materials, which is not obtainable using other traditional analytical methods. We note that the same overall trend is seen for the periodic structure models computed using the GIPAW method within CASTEP; however, the range of calculated shielding values appears to be double those computed with ADF or determined experimentally (Tables A2 and A4 and Figure A7). A possible cause for this is the neglect of relativistic effects on the Pb in the CASTEP calculations; better agreement may be achieved by further optimization of the Pb pseudopotential, but this is beyond the scope of the work presented here.

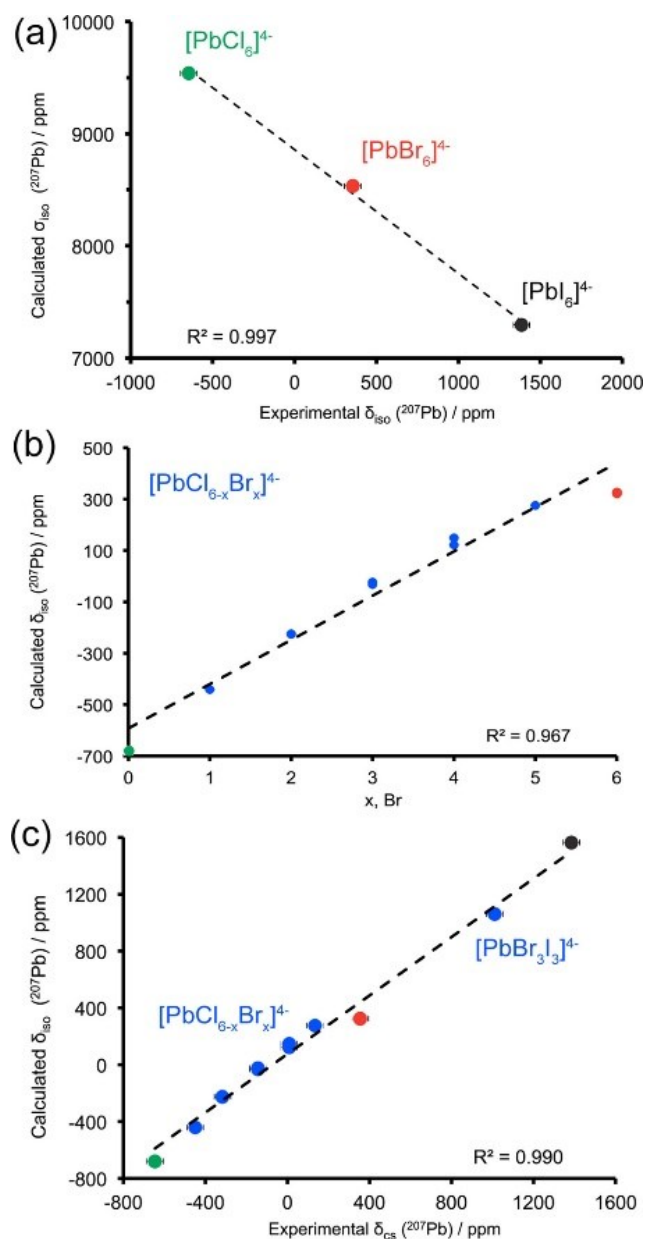


Figure 2.4. Anion model quantum chemical calculations (ADF) of $[PbX_xX'_{6-x}]^{4-}$ octahedra: (a) calculated shielding vs experimental isotropic chemical shift for the parent perovskites, $MAPbX_3$, where $X = Cl, Br, \text{ or } I$; (b) calculated isotropic chemical shift with Br substitution for Cl anions (calc. $\delta_{iso}^{(207Pb)/ppm} = 172.25x - 592.57$, where $x = \text{number of Br neighbors}$) and (c) relation between calculated isotropic chemical shift and experimental chemical shift of parent compounds $MAPbX_3$, $X = Cl, Br, \text{ and } I$ and their respective MHP (Cl/Br or Br/I) (calc. $\delta_{iso}^{(207Pb)/ppm} = 1.03(\text{expt. } \delta_{cs}^{(207Pb)/ppm}) + 75.3$).

The results summarized in Figure 2.3 are those for a material with very fluid properties, whose chemical structure can be adapted readily to accommodate any mixture of halide anions randomly using an MCS method. The diffraction peaks are sharp and of high quality, and the one-dimensional ^{207}Pb NMR spectra suggest a binomial-like distribution of Pb sites, based on the observed δ_{CS} , whose assignment and CSA were estimated through the assistance of DFT calculations (Figure A3). A systematic shift in the bandgap as halide substitution occurs supports the conclusion that these materials exhibit solid-solution behavior, readily adjusting their local ($[\text{PbX}_x\text{X}'_{6-x}]^{4-}$) and long-range (lattice constant) structure as Cl is replaced by Br. To ascertain that these materials are neither phase-separated nor located within micro/nano scale domains, we investigated these materials using a two-dimensional exchange NMR spectroscopy method.

Figure 2.5 shows a series of ^{207}Pb 2D EXSY NMR spectra obtained for MCS sample $\text{MAPb}(\text{Cl}_{0.5}\text{Br}_{0.5})_3$, acquired with mixing times of 10 and 50 μs , and of 2 ms, compared with those for the parent compounds, MAPbCl_3 and MAPbBr_3 . The spectra for the parent samples obtained with a 10 μs mixing time consist of oval-shaped peaks aligned with the diagonal; with increased mixing time, the peak for MAPbBr_3 becomes circular and that for MAPbCl_3 broadens. These observations indicate that self-exchange is occurring for both parent compounds and that the rate of exchange is greater for MAPbBr_3 . In contrast to the spectra for the parent compounds, that for $\text{MAPb}(\text{Cl}_{0.5}\text{Br}_{0.5})_3$ acquired with the shortest mixing time of 10 μs already displays signs of exchange for the individual sites denoted 5, 4, and 3 (i.e., $[\text{PbCl}_2\text{Br}_4]^{4-}$, $[\text{PbCl}_3\text{Br}_3]^{4-}$, and $[\text{PbCl}_4\text{Br}_2]^{4-}$, respectively); increasing the mixing time to 50 μs led to a significant increase in the intensity of the cross peaks. The spectrum obtained with a 2 ms mixing time reveals extensive exchange, with cross-peaks among the seven distinct $[\text{PbX}_x\text{X}'_{6-x}]^{4-}$ chemical environments detected. The observation of exchange for the latter sample confirms that the sample is a solid solution since neither phase-separated materials nor micro/nano domains would yield EXSY spectra susceptible to fast exchange between the NMR sites that may be attributed to various $[\text{PbX}_x\text{X}'_{6-x}]^{4-}$ units. The response to the magnitude of the mixing time in the 2D EXSY⁴⁶ experiment is an indication of the exchange process, which is typically either a chemical exchange

process or a spin diffusion process (i.e., by the direct ^{207}Pb – ^{207}Pb dipolar interaction, R_{DD} , for the samples considered here). R_{DD} scales as the inverse cube of the internuclear separation between the coupled nuclei⁸⁴ and thus, based on the crystal structures for the parent compounds, is expected to be on the order of 25 Hz. Relatively long mixing times would be required to see cross peaks in 2D EXSY spectra induced by spin exchange. In addition, less than 5% of the ^{207}Pb nuclei form ^{207}Pb – ^{207}Pb spin pairs, and thus the EXSY experiment is expected to be relatively insensitive to exchange induced by spin diffusion. Hence, the spectra illustrated here are an indication primarily of a halide chemical exchange process. Note that, regardless of exchange process, correlations are expected only for a domain-free solid-solution material.

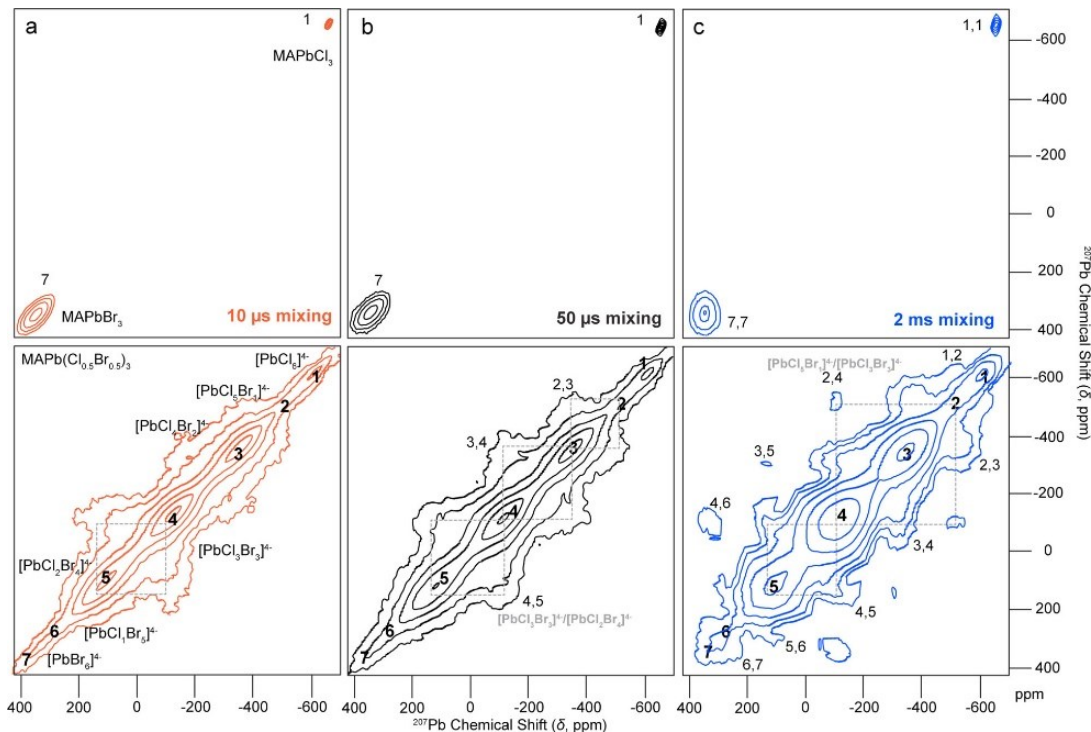


Figure 2.5. Two-dimensional ^{207}Pb EXSY NMR spectra of MAPbCl_3 , MAPbBr_3 , and MCS-HG $\text{MAPb}(\text{Cl}_{0.5}\text{Br}_{0.5})_3$ obtained using (a) 10 μs (red), (b) 50 μs (black), or (c) 2 ms (blue) mixing times. Spectra were acquired at 21.1 T under nonspinning conditions at ambient temperature. Note that the upper spectra are each a superposition of two separate spectra, one for MAPbCl_3 and one for MAPbBr_3 .

Careful analysis of multiple-field NMR spectra (Figure 2.1), as well as XRD, energy dispersive X-ray (EDX) and DR data, indicate that both the MCS-HG and SS methods create a pure, single-phase crystalline solid. The relative populations of $[\text{PbCl}_x\text{Br}_{6-x}]^{4-}$ chemical environments obtained using these methods, while somewhat different, behave similarly as the halide distribution changes from Br- to Cl-rich species. Closer examination of the Cl/Br concentrations in the SS sample, as determined by EDX, reveals that the targeted $\text{MAPb}(\text{Cl}_{0.5}\text{Br}_{0.5})_3$ composition is, in fact, $\text{MAPb}(\text{Cl}_{0.58}\text{Br}_{0.42})_3$. The nonstoichiometric product obtained with the SS approach is, nevertheless, consistent with a binomial-like distribution once accounting for the new composition, with the expected chlorine-rich lead octahedra (i.e., $[\text{PbCl}_6]^{4-}$, $[\text{PbCl}_5\text{Br}_1]^{4-}$, $[\text{PbCl}_4\text{Br}_2]^{4-}$, and $[\text{PbCl}_3\text{Br}_3]^{4-}$) chemical environments (Figure 2.1b,c and Table A5) over other halide mixing combinations, as determined from an analysis of the NMR spectra. Likewise, the sample prepared by the SS method follows Vegard's law, with the lattice constants correlating to the final stoichiometry (see Figure A8 for the XRD pattern of this MHP prepared using the SS method). As for the sample prepared by MCS, there is no indication of phase-separated domains or amorphous structure in the experimental data. In a two-component mixture of MAPbCl_3 and MAPbBr_3 subjected to MCS, the thermodynamics are different from those in the three-component mixture resulting from SS (i.e., MAPbCl_3 , MAPbBr_3 , and the solvent). The former yields a stoichiometric final product, while the latter yields a Cl-rich final product due to the altered driving forces for SS (i.e., nucleation and growth) compared to the high-energy MCS method.^{85–87}

2.3.2 $\text{MAPb}(\text{Cl}_x\text{Br}_{1-x})_3$ Ball Milling Mechanochemical Synthesis

Figure 2.6 shows powder XRD and nonspinning NMR spectra, as well as Tauc plots for the $\text{MAPb}(\text{Cl}_{0.5}\text{Br}_{0.5})_3$ sample prepared using solvent synthesis, hand grinding, and ball milling, illustrating the impact of these synthesis approaches on structural and physical properties. Powder XRD data for the samples indicate that the same crystal structure is obtained in all three cases, but the diffraction line widths indicate that the MCS-BM method yields products that produce broader lines (Figure 2.6a). The SS and HG samples indicate random distributions of halide environments about the octahedral

Pb position $[\text{PbCl}_x\text{Br}_{6-x}]^{4-}$, with the resonance centered at -100 ppm being attributed to the $[\text{PbCl}_3\text{Br}_3]^{4-}$ chemical environment, *vide supra*. At low magnetic fields, the ^{207}Pb NMR spectrum of the BM sample is featureless (Figures 2.1, 2.6b, and A9), appearing Gaussian-like in shape, with evidence of multiple Pb octahedral environments only emerging from higher-field ^{207}Pb NMR data (21.1 T, Figure 2.1a).

As for the SS and HG samples, the solid-solution behavior is preserved for the BM samples. However, the high-energy milling process introduces short-range structural disorder in the otherwise well-ordered cubic environment. This creates a distribution of Pb-X distances and angles and thus leads to local disorder at the Pb sites, as is evident from the observed line widths that indicate a distribution of ^{207}Pb chemical shifts, while XRD data indicate that long-range periodic crystallinity is maintained (Figure 2.6a). The increase in line width of the powder XRD pattern and the amorphization of the well-defined microscopic crystalline solids, as observed in field emission scanning electron microscopy, FESEM (Figures A10 and A11), as well as the impact on the MA cation as indicated by ^1H and ^{13}C MAS NMR spectroscopy (Figures A12 and A13, respectively), further support the conclusion of local structural disorder determined from the ^{207}Pb NMR spectra.

To examine how the local disorder evolved over time, we obtained ^{207}Pb NMR spectra of samples of $\text{MAPb}(\text{Cl}_{0.75}\text{Br}_{0.25})_3$ prepared with 5 min and with 1 h of BM (Figure A14); these spectra confirm that the halide ions quickly begin to mix, already forming a highly ordered random solid solution after 5 min of BM. After 1 h of further high-energy milling, a degradation of the local octahedral structure occurs, and the $[\text{PbCl}_x\text{Br}_{6-x}]^{4-}$ octahedra exhibit short-range local disorder (NMR data) within an otherwise preserved hierarchical periodic crystalline solid framework (XRD data).

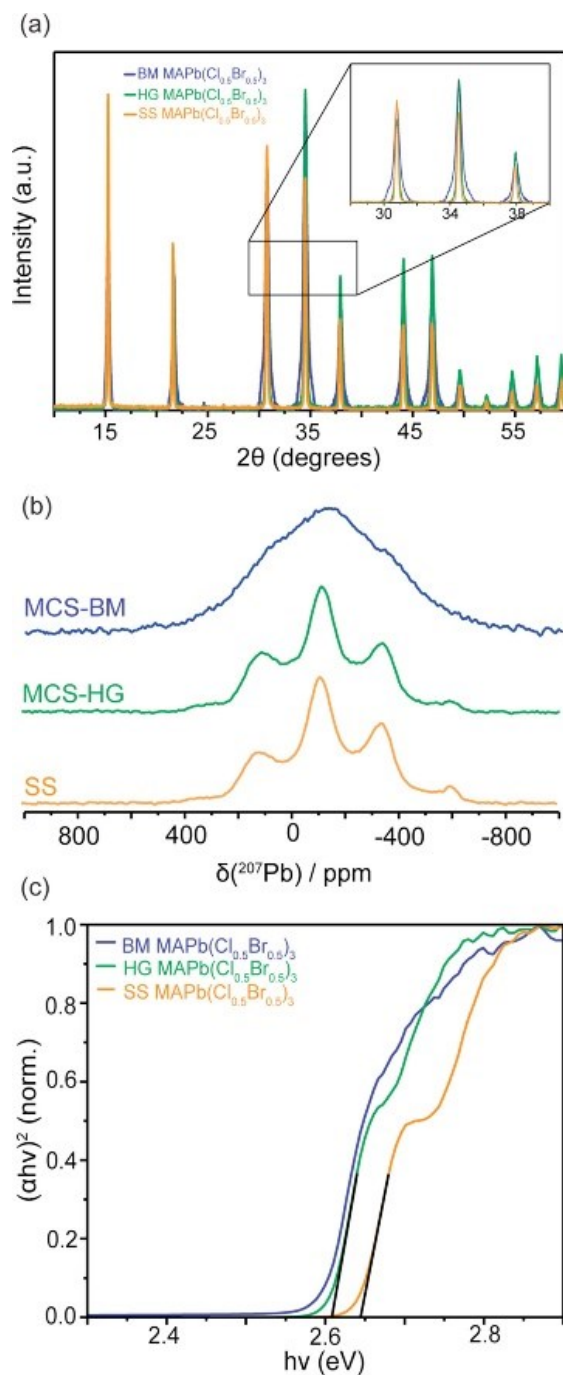


Figure 2.6. Comparison of data for the MAPb(Cl_{0.5}Br_{0.5})₃ MHP prepared using three distinct synthetic approaches: solvent synthesis and mechanochemical synthesis via hand grinding or ball milling. (a) Powder XRD diffraction patterns, (b) nonspinning ²⁰⁷Pb NMR spectra, B₀ = 21.1 T, and (c) Tauc plots. The straight black lines indicate the bandgap energies at the intersection with the abscissa.

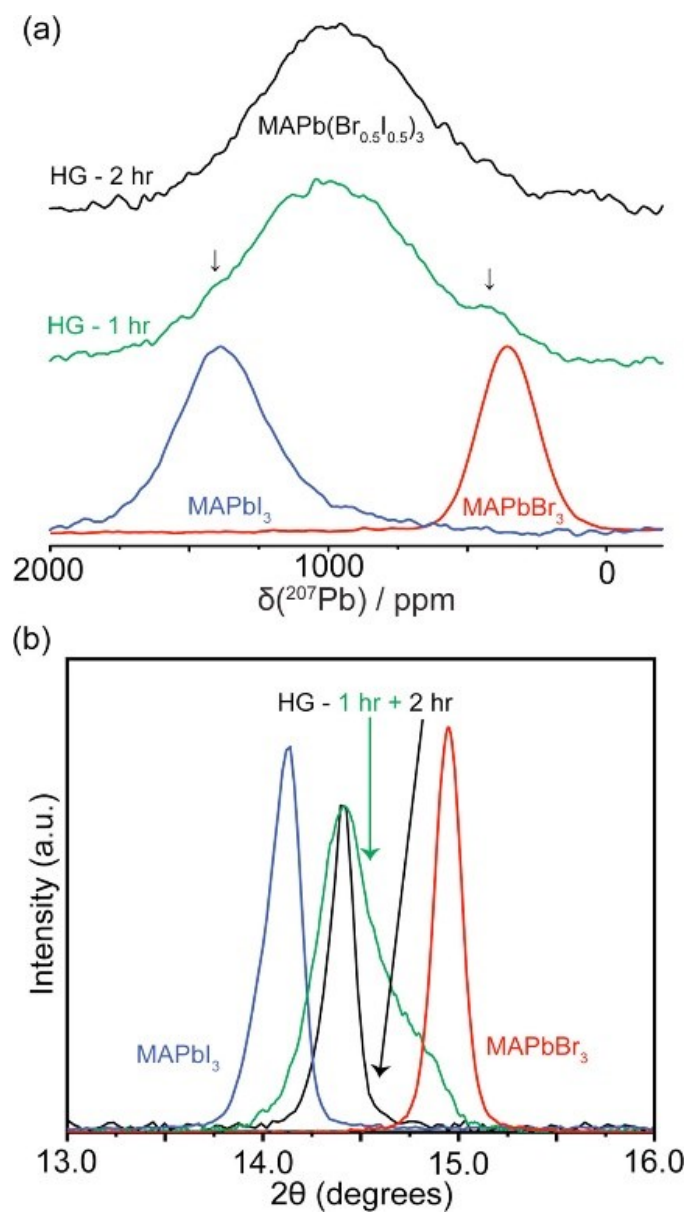


Figure 2.7. (a) Nonspinning ^{207}Pb NMR (7.05 T) and (b) powder X-ray diffraction data for MAPbBr_3 (red), MAPbI_3 (blue), and $\text{MAPb}(\text{Br}_{0.5}\text{I}_{0.5})_3$ (green 1 h, black 2 h). The MHP samples were prepared by the MCS-HG method for 1 and 2 h. The black arrows in the NMR spectra (a) indicate incomplete random halide mixing after 1 h (green trace), with small remnants of the parent compounds according to the NMR and XRD data (b, green arrow, 1 h). The black arrow in panel b indicates complete mixing of a single-phase solid solution after 2 h.

The impact of these synthetic approaches and corresponding structural changes on their optical responses were analyzed using DR⁸⁸ data (Figure A15); these results indicate similar optical bandgaps for all three MAPb(Cl_{0.5}Br_{0.5})₃ samples, but preparing the MHP via the MCS route reduces the bandgap energy by 0.039 eV when compared to the SS technique (2.605 eV for HG vs 2.644 eV for SS). This change is attributed to the fact that the stoichiometry is preserved when using the MCS approach, as determined by the EDX analysis (Table A5), which indicates that a 1.04:1.0 Cl/Br ratio is obtained for the HG samples (1.09:1 Cl/Br for MCS-BM), while a 1.39:1.0 Cl/Br ratio (i.e., a chlorine-rich solid solution) is obtained for the SS sample, despite the 1:1 synthetic molar ratio of the starting reagents for the preparation of all samples. The MCS approach clearly provides superior ease and control of the composition of the solid solution compared to the SS approach, where the final solid product is driven thermodynamically, requiring one to adjust reactant concentrations in order to achieve a 1:1 synthetic molar ratio. Hence, these results demonstrate that this new solvent-free approach allows one to obtain a homogeneous solid solution using low- (HG) or high-energy (BM) mechanical force chemical synthesis.

2.3.3 MAPb(Br_xI_{1-x})₃ Mechanochemical Synthesis

To investigate the application of the MCS synthetic approach further, a 1:1 molar mixture of MAPbBr₃ and MAPbI₃ was prepared. To determine if the transition from phase-separated parent compounds to a randomly mixed solid solution can be visualized, a sample that was manually hand ground over a period of 2 h was characterized by NMR spectroscopy and by XRD, after 1 and 2 h of hand grinding (Figure 2.7). The halide ions begin to exchange, immediately forming a solid solution, and after 1 h of hand grinding, the sample is mixed almost randomly, although XRD and NMR data indicate some of the parent compounds also remain. HG for an additional hour completes the random mixing of the local [PbBr_xI_{6-x}]⁴⁻ octahedra, improving the quality of the solid solution, as seen by the narrow diffraction peaks in the XRD data and by a Gaussian-like resonance in the NMR spectrum. The results indicate that the lower energy MCS-HG approach is effective in creating a single-phase MHP, with a binomial-like distribution similar to that obtained from a sample prepared

by high-temperature solid-state synthesis.³⁵ Contrary to the case for the Cl/Br MHP system, we were unable to resolve multiple resonances for the Br/I system in the corresponding ²⁰⁷Pb NMR spectra, although spectra of the parent compounds indicate that substituting I with Br has the same effect as substituting Br with Cl: a shift to lower frequency. The low resolution is attributed primarily to the Pb–I *J*-couplings for [PbBr_xI_{6-x}]⁴⁻ and the much shorter spin–spin relaxation, such that the FWHM for MAPbI₃ is ~26 kHz,^{35,49,51,72} with further complications arising from the various octahedral arrangements and their respective isomers, as discussed above for the Cl/Br solid solutions.

Figures A16 and A17 show the powder XRD and DR data for the parent compounds and the final 50/50 Br/I MHP solid solution prepared by the MCS-HG technique. These data illustrate the benefit of side-stepping the thermodynamically driven solution process (i.e., avoiding the Br-rich phase)³⁵ with a stoichiometric MCS approach that yields an equal Br/I halide composition, based on XRD and $\delta_{\text{cs}}(^{207}\text{Pb})$ data analysis.

2.4 Conclusions

This work demonstrates the utility of the mechanochemical synthetic approach for the preparation of randomly ordered halides in single crystalline MHP solid solutions with enhanced stoichiometric control, compared to that achieved using traditional solvent synthesis protocols for the Br/Cl MHPs. Increasing the grinding time and introducing a high-energy milling process maintains the long-range crystalline structure, but it can create a highly disordered local [PbX_xX'_{6-x}]⁴⁻ octahedral environment due to rearrangements of bond lengths and angles about the Pb center. Carefully tuning the compositions using the MCS-HG method, monitored by one- and two-dimensional ²⁰⁷Pb NMR spectroscopy and supported by quantum chemical calculations, we identified seven distinct Pb octahedral chemical environments in the Br/Cl MHPs and demonstrated that the synthetic approach can be extended to other Pb-containing mixed-halide perovskites. The ²⁰⁷Pb NMR spectra as well as the XRD results for the Cl/Br MHPs obtained using either solution synthesis or MCS of bulk samples indicate single-phase solid solutions with random halide distributions absent of amorphous or

phase segregated domains. A stoichiometric MAPb(Br_{0.5}I_{0.5})₃ MHP, which has not been achieved previously using traditional room temperature solvent synthesis, was prepared at room temperature using the MCS-HG technique. While ongoing development of perovskite solar cells will require careful characterization, our study has shown that the combination of both X-ray diffraction and solid-state NMR spectroscopy are vital to properly characterize these intrinsically complex materials.

2.5 References

- (1) Shin, S. S.; Yeom, E. J.; Yang, W. S.; Hur, S.; Kim, M. G.; Im, J.; Seo, J.; Noh, J. H.; Seok, S. I., Colloidally Prepared La-Doped BaSnO₃ Electrodes for Efficient, Photostable Perovskite Solar Cells. *Science* **2017**, *356*, 167-171.
- (2) Hsiao, Y.-C.; Wu, T.; Li, M.; Liu, Q.; Qin, W.; Hu, B., Fundamental Physics Behind High-Efficiency Organo-Metal Halide Perovskite Solar Cells. *J. Mater. Chem. A* **2015**, *3* (30), 15372-15385.
- (3) Miyata, A.; Mitioglu, A.; Plochocka, P.; Portugall, O.; Wang, J. T.-W.; Stranks, S. D.; Snaith, H. J.; Nicholas, R. J., Direct Measurement of the Exciton Binding Energy and Effective Masses for Charge Carriers in Organic-Inorganic Tri-Halide Perovskites. *Nat. Phys.* **2015**, *11* (7), 582-587.
- (4) Li, Y.; Yan, W.; Li, Y.; Wang, S.; Wang, W.; Bian, Z.; Xiao, L.; Gong, Q., Direct Observation of Long Electron-Hole Diffusion Distance in CH₃NH₃PbI₃ Perovskite Thin Film. *Sci. Rep.* **2015**, *5*, 14485.
- (5) Stranks, S. D.; Nayak, P. K.; Zhang, W.; Stergiopoulos, T.; Snaith, H. J., Formation of Thin Films of Organic-Inorganic Perovskites for High-Efficiency Solar Cells. *Angew. Chem. Int. Ed.* **2015**, *54* (11), 3240-3248.
- (6) Wong, A. B.; Lai, M.; Eaton, S. W.; Yu, Y.; Lin, E.; Dou, L.; Fu, A.; Yang, P., Growth and Anion Exchange Conversion of CH₃NH₃PbX₃ Nanorod Arrays for Light-Emitting Diodes. *Nano Lett.* **2015**, *15* (8), 5519-5524.
- (7) Tan, H.; Jain, A.; Voznyy, O.; Lan, X.; García de Arquer, F. P.; Fan, J. Z.; Quintero-Bermudez, R.; Yuan, M.; Zhang, B.; Zhao, Y., et al., Efficient and STable Aolution-Processed Planar Perovskite Solar Cells via Contact Passivation. *Science* **2017**, *355*, 722-726.

- (8) Eperon, G. E.; Leijtens, T.; Bush, K. A.; Prasanna, R.; Green, T.; Wang, J. T.-W.; McMeekin, D. P.; Volonakis, G.; Milot, R. L.; May, R., et al., Perovskite-Perovskite Tandem Photovoltaics with Optimized Bandgaps. *Science* **2016**, *354* (6314), 861-865.
- (9) Jang, D. M.; Park, K.; Kim, D. H.; Park, J.; Shojaei, F.; Kang, H. S.; Ahn, J.-P.; Lee, J. W.; Song, J. K., Reversible Halide Exchange Reaction of Organometal Trihalide Perovskite Colloidal Nanocrystals for Full-Range Band Gap Tuning. *Nano Lett.* **2015**, *15* (8), 5191-5199.
- (10) Pellet, N.; Teuscher, J.; Maier, J.; Grätzel, M., Transforming Hybrid Organic Inorganic Perovskites by Rapid Halide Exchange. *Chem. Mater.* **2015**, *27* (6), 2181-2188.
- (11) Colella, S.; Mosconi, E.; Fedeli, P.; Listorti, A.; Gazza, F.; Orlandi, F.; Ferro, P.; Besagni, T.; Rizzo, A.; Calestani, G., et al., MAPbI_{3-x}Cl_x Mixed Halide Perovskite for Hybrid Solar Cells: The Role of Chloride as Dopant on the Transport and Structural Properties. *Chem. Mater.* **2013**, *25* (22), 4613-4618.
- (12) Mosconi, E.; De Angelis, F., Mobile Ions in Organohalide Perovskites: Interplay of Electronic Structure and Dynamics. *ACS Energy Lett.* **2016**, *1* (1), 182-188.
- (13) Brivio, F.; Caetano, C.; Walsh, A., Thermodynamic Origin of Photoinstability in the CH₃NH₃Pb(I_{1-x}Br_x)₃ Hybrid Halide Perovskite Alloy. *J. Phys. Chem. Lett.* **2016**, *7* (6), 1083-1087.
- (14) Hentz, O.; Zhao, Z.; Gradečak, S., Impacts of Ion Segregation on Local Optical Properties in Mixed Halide Perovskite Films. *Nano Lett.* **2016**, *16* (2), 1485-1490.
- (15) Hoke, E. T.; Slotcavage, D. J.; Dohner, E. R.; Bowring, A. R.; Karunadasa, H. I.; McGehee, M. D., Reversible Photo-Induced Trap Formation in Mixed-Halide Hybrid Perovskites for Photovoltaics. *Chem. Sci.* **2015**, *6* (1), 613-617.
- (16) Yoon, S. J.; Draguta, S.; Manser, J. S.; Sharia, O.; Schneider, W. F.; Kuno, M.; Kamat, P. V., Tracking Iodide and Bromide Ion Segregation in Mixed Halide Lead Perovskites During Photoirradiation. *ACS Energy Lett.* **2016**, *1* (1), 290-296.
- (17) Yoon, S. J.; Kuno, M.; Kamat, P. V., Shift Happens. How Halide Ion Defects Influence Photoinduced Segregation in Mixed Halide Perovskites. *ACS Energy Lett.* **2017**, *2* (7), 1507-1514.

- (18) Lewiński, J.; Dutkiewicz, M.; Lesiuk, M.; Śliwiński, W.; Zelga, K.; Justyniak, I.; Lipkowski, J., Solid-State Conversion of the Solvated Dimer [$\{t\text{BuZn}(\mu\text{-OtBu})(\text{thf})\}_2$] into a Long Overlooked Trimeric [$\{t\text{BuZnOtBu}\}_3$] Species. *Angew. Chem. Int. Ed.* **2010**, *49* (44), 8266-8269.
- (19) Prochowicz, D.; Justyniak, I.; Kornowicz, A.; Kaczorowski, T.; Kaszkur, Z.; Lewiński, J., Construction of a Porous Homochiral Coordination Polymer with Two Types of Cu_nI_n Alternating Units Linked by Quinine: A Solvothermal and a Mechanochemical Approach. *Chem. - Eur. J.* **2012**, *18* (24), 7367-7371.
- (20) Prochowicz, D.; Sokołowski, K.; Justyniak, I.; Kornowicz, A.; Fairen-Jimenez, D.; Frišćić, T.; Lewiński, J.; Düren, T.; Hyett, G.; Jones, W., et al., A Mechanochemical Strategy for IRMOF Assembly Based on Pre-Designed Oxo-Zinc Precursors. *Chem. Commun.* **2015**, *51* (19), 4032-4035.
- (21) Lee, J.; Shin, H.; Lee, J.; Chung, H.; Zhang, Q.; Saito, F., Mechanochemical Syntheses of Perovskite $\text{KM}^{\text{II}}\text{F}_3$ with Cubic Structure ($\text{M} = \text{Mg}, \text{Ca}, \text{Mn}, \text{Fe}, \text{Co}, \text{Ni},$ and Zn). *Mater. Trans.* **2003**, *44* (7), 1457-1460.
- (22) Elseman, A. M.; Rashad, M. M.; Hassan, A. M., Easily Attainable, Efficient Solar Cell with Mass Yield of Nanorod Single-Crystalline Organo-Metal Halide Perovskite Based on a Ball Milling Technique. *ACS Sustainable Chem. Eng.* **2016**, *4* (9), 4875-4886.
- (23) Jana, A.; Mittal, M.; Singla, A.; Sapra, S.; Grätzel, M.; Lewiński, J.; Tong, Y.; Polavarapu, L.; Feldmann, J.; Urban, A. S., et al., Solvent-Free, Mechanochemical Syntheses of Bulk Trihalide Perovskites and Their Nanoparticles. *Chem. Commun.* **2017**, *53* (21), 3046-3049.
- (24) Zhu, Z.-Y.; Yang, Q.-Q.; Gao, L.-F.; Zhang, L.; Shi, A.-Y.; Sun, C.-L.; Wang, Q.; Zhang, H.-L., Solvent-Free Mechanochemical Synthesis of Composition-Tunable Cesium Lead Halide Perovskite Quantum Dots. *J. Phys. Chem. Lett.* **2017**, *8* (7), 1610-1614.
- (25) Manukyan, K. V.; Yeghishyan, A. V.; Moskovskikh, D. O.; Kapaldo, J.; Mintairov, A.; Mukasyan, A. S., Mechanochemical Synthesis of Methylammonium Lead Iodide Perovskite. *J. Mater. Sci.* **2016**, *51* (19), 9123-9130.

- (26) Jodlowski, A. D.; Yépez, A.; Luque, R.; Camacho, L.; de Miguel, G., Benign-by-Design Solventless Mechanochemical Synthesis of Three-, Two-, and One-Dimensional Hybrid Perovskites. *Angew. Chem. Int. Ed.* **2016**, *55* (48), 14972-14977.
- (27) Prochowicz, D.; Franckevičius, M.; Cieślak, A. M.; Zakeeruddin, S. M.; Grätzel, M.; Lewiński, J., Mechanochemical Synthesis of the Hybrid Perovskite $\text{CH}_3\text{NH}_3\text{PbI}_3$: Characterization and the Corresponding Solar Cell Efficiency. *J. Mater. Chem. A* **2015**, *3* (41), 20772-20777.
- (28) Prochowicz, D.; Yadav, P.; Saliba, M.; Sasaki, M.; Zakeeruddin, S. M.; Lewiński, J.; Grätzel, M., Mechanochemical Synthesis of Pure Phase Mixed-Cation $\text{MA}_x\text{FA}_{1-x}\text{PbI}_3$ Hybrid Perovskites: Photovoltaic Performance and Electrochemical Properties. *Sustainable Energy Fuels* **2017**, *1* (4), 689-693.
- (29) Prochowicz, D.; Yadav, P.; Saliba, M.; Sasaki, M.; Zakeeruddin, S. M.; Lewiński, J.; Grätzel, M., Reduction in the Interfacial Trap Density of Mechanochemically Synthesized MAPbI_3 . *ACS Appl. Mater. Interfaces* **2017**, *9* (34), 28418-28425.
- (30) Kubicki, D.; Prochowicz, D.; Hofstetter, A.; Zakeeruddin, S. M.; Grätzel, M.; Emsley, L., Phase Segregation in Cs-, Rb- and K-Doped Mixed-Cation $(\text{MA})_x(\text{FA})_{1-x}\text{PbI}_3$ Hybrid Perovskites from Solid-State NMR. *J. Am. Chem. Soc.* **2017**, *139* (40), 14173-14180.
- (31) Hibble, S. J.; Chippindale, A. M.; Marelli, E.; Kroeker, S.; Michaelis, V. K.; Greer, B. J.; Aguiar, P. M.; Bilbé, E. J.; Barney, E. R.; Hannon, A. C., Local and Average Structure in Zinc Cyanide: Toward an Understanding of the Atomistic Origin of Negative Thermal Expansion. *J. Am. Chem. Soc.* **2013**, *135* (44), 16478-16489.
- (32) Aharen, T.; Greedan, J. E.; Ning, F.; Imai, T.; Michaelis, V.; Kroeker, S.; Zhou, H.; Wiebe, C. R.; Cranswick, L. M. D., Magnetic Properties of the $S=3/2$ Geometrically Frustrated Double Perovskites $\text{La}_2\text{LiRuO}_6$ and Ba_2YRuO_6 . *Phys. Rev. B* **2009**, *80* (13), 134423.
- (33) Michaelis, V. K.; Greer, B. J.; Aharen, T.; Greedan, J. E.; Kroeker, S., Determining Electron Spin-Transfer Mechanisms in Paramagnetic Ba_2YMO_6 (M = Mo, Re, Ru) Double Perovskites by ^{89}Y and ^{137}Ba MAS NMR Spectroscopy. *J. Phys. Chem. C* **2012**, *116* (44), 23646-23652.

- (34) Grey, C. P.; Smith, M. E.; Cheetham, A. K.; Dobson, C. M.; Dupree, R., Yttrium-89 Magic Angle Spinning NMR Study of Rare-Earth Pyrochlores: Paramagnetic Shifts in the Solid State. *J. Am. Chem. Soc.* **1990**, *112* (12), 4670-4675.
- (35) Rosales, B. A.; Men, L.; Cady, S. D.; Hanrahan, M. P.; Rossini, A. J.; Vela, J., Persistent Dopants and Phase Segregation in Organolead Mixed-Halide Perovskites. *Chem. Mater.* **2016**, *28* (19), 6848-6859.
- (36) Maculan, G.; Sheikh, A. D.; Abdelhady, A. L.; Saidaminov, M. I.; Haque, M. A.; Murali, B.; Alarousu, E.; Mohammed, O. F.; Wu, T.; Bakr, O. M., CH₃NH₃PbCl₃ Single Crystals: Inverse Temperature Crystallization and Visible-Blind UV-Photodetector. *J. Phys. Chem. Lett.* **2015**, *6* (19), 3781-3786.
- (37) Saidaminov, M. I.; Abdelhady, A. L.; Murali, B.; Alarousu, E.; Burlakov, V. M.; Peng, W.; Dursun, I.; Wang, L.; He, Y.; Maculan, G., et al., High-Quality Bulk Hybrid Perovskite Single Crystals within Minutes by Inverse Temperature Crystallization. *Nat. Commun.* **2015**, *6*, 7586.
- (38) Pines, A.; Gibby, M. G.; Waugh, J. S., Proton-Enhanced Nuclear Induction Spectroscopy. A Method for High Resolution NMR of Dilute Spins in Solids. *J. Chem. Phys.* **1972**, *56* (4), 1776-1777.
- (39) Earl, W. L.; Vanderhart, D. L., Measurement of ¹³C Chemical Shifts in Solids. *J. Magn. Reson. (1969)* **1982**, *48* (1), 35-54.
- (40) Bennett, A. E.; Rienstra, C. M.; Auger, M.; Lakshmi, K. V.; Griffin, R. G., Heteronuclear Decoupling in Rotating Solids. *J. Chem. Phys.* **1995**, *103* (16), 6951-6958.
- (41) Hahn, E. L., Spin Echoes. *Phys. Rev.* **1950**, *80*, 580.
- (42) Mansfield, P., Multiple-Pulse Nuclear Magnetic Resonance Transients in Solids. *Phys. Rev.* **1965**, *137* (3A), A961-A974.
- (43) Bodart, P. R.; Amoureux, J.-P.; Dumazy, Y.; Lefort, R., Theoretical and Experimental Study of Quadrupolar Echoes for Half-Integer Spins in Static Solid-State NMR. *Mol. Phys.* **2000**, *98* (19), 1545-1551.
- (44) Davis, J. H.; Jeffrey, K. R.; Bloom, M.; Valic, M. I.; Higgs, T. P., Quadrupolar Echo Deuteron Magnetic Resonance Spectroscopy in Ordered Hydrocarbon Chains. *Chem. Phys. Lett.* **1976**, *42* (2), 390-394.

- (45) Massiot, D.; Farnan, I.; Gautier, N.; Trumeau, D.; Trokiner, A.; Coutures, J. P., ^{71}Ga and ^{69}Ga Nuclear Magnetic Resonance Study of B-Ga₂O₃: Resolution of Four- and Six-Fold Coordinated Ga Sites in Static Conditions. *Solid State Nucl. Magn. Reson.* **1995**, *4* (4), 241-248.
- (46) Jeener, J.; Meier, B. H.; Bachmann, P.; Ernst, R. R., Investigation of Exchange Processes by Two-Dimensional NMR Spectroscopy. *J. Chem. Phys.* **1979**, *71* (11), 4546-4553.
- (47) Bernard, G. M.; Goyal, A.; Miskolzie, M.; McKay, R.; Wu, Q.; Wasylshen, R. E.; Michaelis, V. K., Methylammonium Lead Chloride: A Sensitive Sample for an Accurate NMR Thermometer. *J. Magn. Reson.* **2017**, *283* (Supplement C), 14-21.
- (48) Eichele, K. *Wsolids NMR Simulation Package*, 1.20.21; Universität Tübingen, 2013.
- (49) Askar, A. M.; Bernard, G. M.; Wiltshire, B.; Shankar, K.; Michaelis, V. K., Multinuclear Magnetic Resonance Tracking of Hydro, Thermal, and Hydrothermal Decomposition of CH₃NH₃PbI₃. *J. Phys. Chem. C* **2017**, *121* (2), 1013-1024.
- (50) Rosales, B. A.; Hanrahan, M. P.; Boote, B. W.; Rossini, A. J.; Smith, E. A.; Vela, J., Lead Halide Perovskites: Challenges and Opportunities in Advanced Synthesis and Spectroscopy. *ACS Energy Lett.* **2017**, *2* (4), 906-914.
- (51) Senocrate, A.; Moudrakovski, I.; Kim, G. Y.; Yang, T.-Y.; Gregori, G.; Grätzel, M.; Maier, J., The Nature of Ion Conduction in Methylammonium Lead Iodide: A Multimethod Approach. *Angew. Chem. Int. Ed.* **2017**, *56* (27), 7755-7759.
- (52) Dybowski, C.; Smith, M. L.; Hepp, M. A.; Gaffney, E. J.; Neue, G.; Perry, D. L., ^{207}Pb NMR Chemical-Shift Tensors of the Lead (II) Halides and the Lead (II) Hydroxyhalides. *Appl. Spectrosc.* **1998**, *52* (3), 426-429.
- (53) Taylor, R. E.; Beckmann, P. A.; Bai, S.; Dybowski, C., ^{127}I and ^{207}Pb Solid-State NMR Spectroscopy and Nuclear Spin Relaxation in PbI₂: A Preliminary Study. *J. Phys. Chem. C* **2014**, *118* (17), 9143-9153.
- (54) ADF2017, SCM; Theoretical Chemistry, Vrije Universiteit, Amsterdam, The Netherlands, <http://www.scm.com>.
- (55) Fonseca Guerra, C.; Snijders, J. G.; Te Velde, G.; Baerends, E. J., Towards an Order-N DFT Method. *Theor. Chem. Acc.* **1998**, *99* (6), 391-403.

- (56) Te Velde, G.; Bickelhaupt, F. M.; Baerends, E. J.; Fonseca Guerra, C.; van Gisbergen, S. J. A.; Snijders, J. G.; Ziegler, T., Chemistry with ADF. *J. Comput. Chem.* **2001**, *22* (9), 931-967.
- (57) Jaffe, A.; Lin, Y.; Beavers, C. M.; Voss, J.; Mao, W. L.; Karunadasa, H. I., High-Pressure Single-Crystal Structures of 3D Lead-Halide Hybrid Perovskites and Pressure Effects on Their Electronic and Optical Properties. *ACS Cent. Sci.* **2016**, *2* (4), 201-209.
- (58) Lenthe, E. V.; Ehlers, A.; Baerends, E.-J., Geometry Optimizations in the Zero Order Regular Approximation for Relativistic Effects. *J. Chem. Phys.* **1999**, *110* (18), 8943-8953.
- (59) Schreckenbach, G.; Ziegler, T., Calculation of NMR Shielding Tensors Using Gauge-Including Atomic Orbitals and Modern Density Functional Theory. *J. Phys. Chem.* **1995**, *99* (2), 606-611.
- (60) Mason, J., Conventions for the Reporting of Nuclear Magnetic Shielding (or Shift) Tensors Suggested by Participants in the Nato Arw on NMR Shielding Constants at the University of Maryland, College Park, July 1992. *Solid State Nucl. Magn. Reson.* **1993**, *2* (5), 285-288.
- (61) Herzfeld, J.; Berger, A. E., Sideband Intensities in NMR-Spectra of Samples Spinning at the Magic Angle. *J. Chem. Phys.* **1980**, *73* (12), 6021-6030.
- (62) Perdew, J. P.; Burke, K.; Ernzerhof, M., Generalized Gradient Approximation Made Simple. *Phys. Rev. Lett.* **1996**, *77*, 3865.
- (63) Perdew, J. P.; Burke, K.; Ernzerhof, M., Perdew, Burke, and Ernzerhof Reply. *Phys. Rev. Lett.* **1998**, *80*, 891.
- (64) Perdew, J. P.; Burke, K.; Ernzerhof, M., Generalized Gradient Approximation Made Simple [Phys. Rev. Lett. *77*, 3865 (1996)]. *Phys. Rev. Lett.* **1997**, *78*, 1396.
- (65) Clark, S. J.; Segall, M. D.; Pickard, C. J.; Hasnip, P. J.; Probert, M. I. J.; Refson, K.; Payne, M. C., First Principles Methods Using Castep. *Z. Kristallogr. - Cryst. Mater.* **2005**, *220*, 567-570.
- (66) Yates, J. R.; Pickard, C. J.; Mauri, F., Calculation of NMR Chemical Shifts for Extended Systems Using Ultrasoft Pseudopotentials. *Phys. Rev. B* **2007**, *76*, 024401.

- (67) Baikie, T.; Barrow, N. S.; Fang, Y.; Keenan, P. J.; Slater, P. R.; Piltz, R. O.; Gutmann, M.; Mhaisalkar, S. G.; White, T. J., A Combined Single Crystal Neutron/X-Ray Diffraction and Solid-State Nuclear Magnetic Resonance Study of the Hybrid Perovskites $\text{CH}_3\text{NH}_3\text{PbX}_3$ ($X = \text{I}, \text{Br}$ and Cl). *J. Mater. Chem. A* **2015**, *3* (17), 9298-9307.
- (68) Misra, R. K.; Ciammaruchi, L.; Aharon, S.; Mogilyansky, D.; Etgar, L.; Visoly-Fisher, I.; Katz, E. A., Effect of Halide Composition on the Photochemical Stability of Perovskite Photovoltaic Materials. *ChemSusChem* **2016**, *9* (18), 2572-2577.
- (69) Rehman, W.; McMeekin, D. P.; Patel, J. B.; Milot, R. L.; Johnston, M. B.; Snaith, H. J.; Herz, L. M., Photovoltaic Mixed-Cation Lead Mixed-Halide Perovskites: Links between Crystallinity, Photo-Stability and Electronic Properties. *Energy Environ. Sci.* **2017**, *10* (1), 361-369.
- (70) Roiland, C.; Trippe-Allard, G.; Jemli, K.; Alonso, B.; Ameline, J.-C.; Gautier, R.; Bataille, T.; Le Polles, L.; Deleporte, E.; Even, J., et al., Multinuclear NMR as a Tool for Studying Local Order and Dynamics in $\text{CH}_3\text{NH}_3\text{PbX}_3$ ($X = \text{Cl}, \text{Br}, \text{I}$) Hybrid Perovskites. *Phys. Chem. Chem. Phys.* **2016**, *18* (39), 27133-27142.
- (71) Wasylishen, R. E.; Knop, O.; Macdonald, J. B., Cation Rotation in Methylammonium Lead Halides. *Solid State Commun.* **1985**, *56* (7), 581-582.
- (72) Bernard, G. M.; Wasylishen, R. E.; Ratcliffe, C. I.; Terskikh, V. V.; Wu, Q.; Buriak, J. M.; Hauger, T., Methylammonium Cation Dynamics in Methylammonium Lead Halide Perovskites—A Solid-State NMR Perspective. *J. Phys. Chem. A* **2018**, *122* (6), 1560-1573.
- (73) Kubicki, D. J.; Prochowicz, D.; Hofstetter, A.; Péchy, P.; Zakeeruddin, S. M.; Grätzel, M.; Emsley, L., Cation Dynamics in Mixed-Cation $(\text{MA})_x(\text{FA})_{1-x}\text{PbI}_3$ Hybrid Perovskites from Solid-State NMR. *J. Am. Chem. Soc.* **2017**, *139* (29), 10055-10061.
- (74) Franssen, W. M. J.; van Es, S. G. D.; Dervişoğlu, R.; de Wijs, G. A.; Kentgens, A. P. M., Symmetry, Dynamics, and Defects in Methylammonium Lead Halide Perovskites. *J. Phys. Chem. Lett.* **2017**, *8* (1), 61-66.
- (75) Fayon, F.; Bessada, C.; Massiot, D.; Farnan, I.; Coutures, J. P., ^{29}Si and ^{207}Pb NMR Study of Local Order in Lead Silicate Glasses. *J. Non-Cryst. Solids* **1998**, *232-234* (Supplement C), 403-408.

- (76) Martin, V.; Wood, B.; Werner-Zwanziger, U.; Zwanziger, J. W., Structural Aspects of the Photoelastic Response in Lead Borate Glasses. *J. Non-Cryst. Solids* **2011**, 357 (10), 2120-2125.
- (77) Keeler, E. G.; Michaelis, V. K.; Colvin, M. T.; Hung, I.; Gor'kov, P. L.; Cross, T. A.; Gan, Z.; Griffin, R. G., ^{17}O MAS NMR Correlation Spectroscopy at High Magnetic Fields. *J. Am. Chem. Soc.* **2017**, 139 (49), 17953-17963.
- (78) Xu, Q.; Eguchi, T.; Nakayama, H.; Nakamura, N.; Kishita, M., Molecular Motions and Phase Transitions in Solid $\text{CH}_3\text{NH}_3\text{PbX}_3$ (X = Cl, Br, I) as Studied by NMR and NQR. *Z. Naturforsch. A* **1991**; 46 (3), 240-246.
- (79) Harris, R. K.; Olivieri, A. C., Quadrupolar Effects Transferred to Spin-1/2 Magic-Angle Spinning Spectra of Solids. *Prog. Nucl. Magn. Reson. Spectrosc.* **1992**, 24 (5), 435-456.
- (80) Wrackmeyer, B., Application of ^{207}Pb NMR Parameters. *Annu. Rep. NMR Spectrosc.* **2002**; 47, 1-37.
- (81) Dybowski, C.; Neue, G., Solid State ^{207}Pb NMR Spectroscopy. *Prog. Nucl. Magn. Reson. Spectrosc.* **2002**, 41, 153-170.
- (82) Dong, X.; Fang, X.; Lv, M.; Lin, B.; Zhang, S.; Ding, J.; Yuan, N., Improvement of the Humidity Stability of Organic-Inorganic Perovskite Solar Cells Using Ultrathin Al_2O_3 Layers Prepared by Atomic Layer Deposition. *J. Mater. Chem. A* **2015**, 3 (10), 5360-5367.
- (83) Vegard, L., Die Konstitution Der Mischkristalle Und Die Raumfüllung Der Atome. *Z. Phys.* **1921**, 5 (1), 17-26.
- (84) Wasylishen, R. E., Indirect Nuclear Spin-Spin Coupling Tensors. *eMagRes*, John Wiley & Sons, Ltd: 2007.
- (85) Liang, P.-W.; Liao, C.-Y.; Chueh, C.-C.; Zuo, F.; Williams, S. T.; Xin, X.-K.; Lin, J.; Jen, A. K. Y., Additive Enhanced Crystallization of Solution-Processed Perovskite for Highly Efficient Planar-Heterojunction Solar Cells. *Adv. Mater.* **2014**, 26 (22), 3748-3754.
- (86) Manser, J. S.; Saidaminov, M. I.; Christians, J. A.; Bakr, O. M.; Kamat, P. V., Making and Breaking of Lead Halide Perovskites. *Acc. Chem. Res.* **2016**, 49 (2), 330-338.

- (87) Tidhar, Y.; Edri, E.; Weissman, H.; Zohar, D.; Hodes, G.; Cahen, D.; Rybtchinski, B.; Kirmayer, S., Crystallization of Methyl Ammonium Lead Halide Perovskites: Implications for Photovoltaic Applications. *J. Am. Chem. Soc.* **2014**, *136* (38), 13249-13256.
- (88) Tauc, J.; Grigorovici, R.; Vancu, A., Optical Properties and Electronic Structure of Amorphous Germanium. *Phys. Status Solidi B* **1966**, *15* (2), 627-637.

CHAPTER 3

Influence of Hidden Halogen Mobility on Local Structure of CsSn(Cl_{1-x}Br_x)₃ Mixed-Halide Perovskites by Solid-State NMR^{R2}

3.1 Introduction

Lead halide perovskites APbX₃ (A = Cs⁺, CH₃NH₃⁺, CH(NH₂)₂⁺; X = Cl⁻, Br⁻, I⁻) show attractive optical and electrical properties for solar cells, lasers, light-emitting diodes, X-ray detectors, and other applications,¹⁻⁶ with power conversion efficiencies now exceeding 25%,⁷ but they face significant challenges for commercialization because of poor chemical stability⁸ and risk of lead toxicity.^{9,10} Among lead-free alternatives, the tin-substituted analogues have been highly promising, showing power conversion efficiencies of up to 10%.¹¹ Most of these compounds are iodides such as CH₃NH₃SnI₃, CH(NH₂)₂SnI₃, and CsSnI₃, which have bandgaps (1.2–1.4 eV) close to the optimum value (1.34 eV) to maximize efficiency.^{12,13} The hybrid organic–inorganic compounds CH₃NH₃SnI₃ and CH(NH₂)₂SnI₃ are more efficient but suffer from poor thermal stability because of the presence of the volatile organic cations; the purely inorganic compound CsSnI₃ is more thermally stable but oxidizes rapidly in air (Sn(+2) → Sn(+4)).^{13,14} Among the bromide analogues, CsSnBr₃ exhibits greater thermal and air stability, imparted by the Cs⁺, than CH₃NH₃SnBr₃, which degrades in air within an hour.^{13,15} Solar devices fabricated with CsSnBr₃ do not have to be encapsulated, lasting for hours with diode characteristics being retained.¹³ The bandgap of CsSnBr₃ (1.75–1.80 eV)^{13,16,17} lies in the optimal region for tandem solar cell technology.¹⁸

Recently, the mixed-halide perovskites CsSn(Cl_{1-x}Br_x)₃ have been prepared in the form of nanocrystals or thin films, in which the bandgap can be adjusted with

^{R2} The contents of this chapter have been copied and/or adapted from the following publication: Karmakar, A.; Bhattacharya, A.; Sarkar, D.; Bernard, G. M.; Mar, A.; Michaelis, V. K. Influence of Hidden Halogen Mobility on Local Structure of CsSn(Cl_{1-x}Br_x)₃ Mixed-Halide Perovskites by Solid-State NMR. *Chem. Sci.* **2021**, *12*, 3253–3263. The supplementary data for this chapter is available in Appendix B: Experimental section, Tables B1–B8 and Figures B1–B14.

composition, making them suitable for optoelectronic applications such as light emitting diodes and lasers.^{19,20} However, some of the structural details of these mixed-halide perovskites are unclear because the end-members are known to exhibit multiple phase transitions: CsSnCl₃ adopts a monoclinic structure at room temperature (own type; space group originally reported as $P2_1/n$, but standardized as $P2_1/c$) and transforms to the cubic perovskite structure (space group $Pm\bar{3}m$) above 379 K,²¹ and CsSnBr₃ undergoes complicated phase transitions at low temperature, but ultimately attains the cubic structure above 292 K.²² Because the physical properties depend sensitively on the structure and stability of these mixed-halide perovskites, it is essential to determine the local and long-range atomic arrangement, to unravel the dynamics of halogen mobility, and to evaluate changes entailed by different synthetic methods and exposure to ambient conditions.

To date, halide perovskites have been extensively characterized by X-ray diffraction (XRD), which gives information about the average long-range structure. However, solid-state nuclear magnetic resonance (NMR) spectroscopy is an invaluable method to investigate local structure (*e.g.*, halide distribution, domain structure) and dynamics in perovskites.^{23–38} In particular, ¹³³Cs ($I = 7/2$, 100% abundance) and ¹¹⁹Sn ($I = 1/2$, 8.59% abundance) are ideal NMR-sensitive nuclei, useful for probing the local structure of the A and B sites in perovskites ABX₃,^{30,37,39–45} as well as of sites in other types of compounds.^{46–49}

Here we target the preparation of CsSn(Cl_{1-x}Br_x)₃ to ascertain if a complete solid solution with the cubic perovskite structure can be attained for the entire range. Powder XRD and NMR spectroscopy were carried out to determine the long-range structure and the local coordination around the Cs and Sn sites by Cl and Br atoms, which could be ordered or disordered. Optical bandgaps were measured by UV-visible absorption spectroscopy and correlated with composition. Given the ambiguity about the nature of CsSnBr₃, we evaluate whether samples prepared by various methods show important structural differences which could influence their optical properties. The activation energy for rapid halogen dynamics in CsSnBr₃ was quantified by variable-temperature ¹¹⁹Sn NMR spectroscopy. Finally, the stability of CsSnBr₃ under ambient conditions was assessed by examining the products and pathways of its degradation.

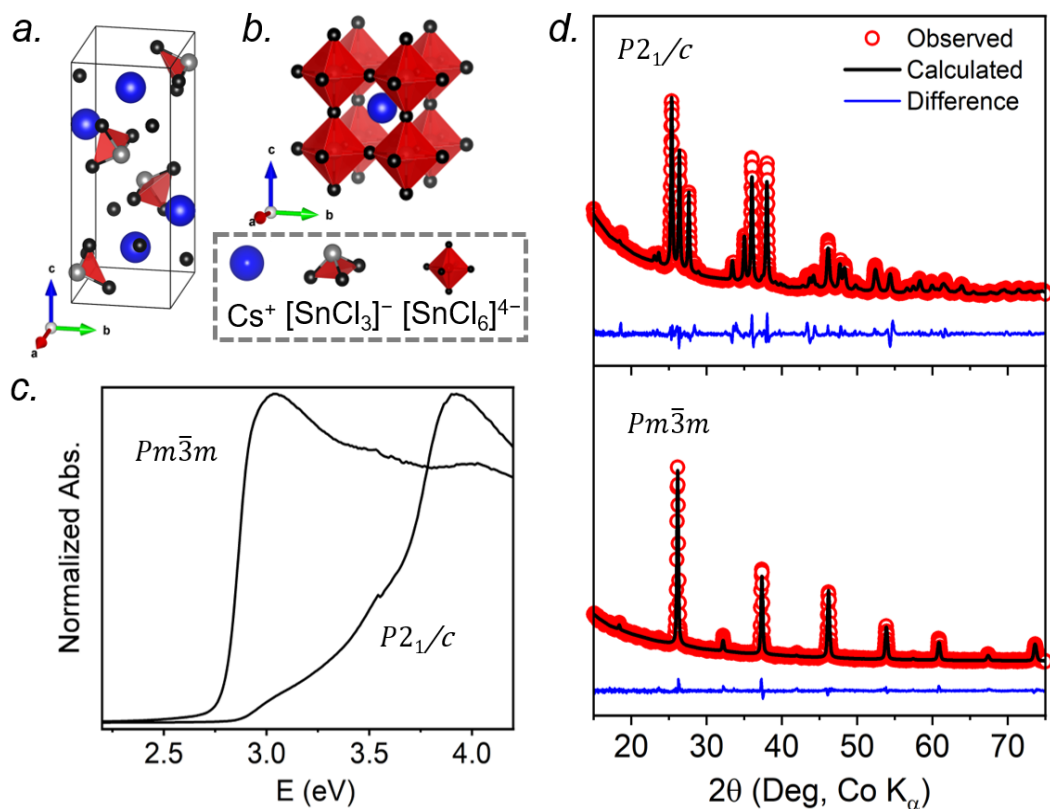


Figure 3.1. CsSnCl₃: (a) monoclinic structure at room temperature, (b) cubic perovskite structure above 379 K, (c) UV-visible absorption spectra collected at room temperature, and (d) Rietveld refinements of powder XRD patterns.

3.2 Results and Discussion

3.2.1 Monoclinic and Cubic Phases of CsSnCl₃

At room temperature, CsSnCl₃ adopts a monoclinic structure (space group $P2_1/c$) containing isolated [SnCl₃]⁻ ions in trigonal pyramidal geometry with Sn–Cl bonds of 2.50–2.55 Å (Figure 3.1a). If three much more distant Cl atoms at 3.21–3.77 Å are included, the coordination geometry around the Sn atoms (coordination number (CN) with 3 shorter and 3 longer bonds, CN3 + 3) could also be described as distorted octahedron.²¹ Above 379 K, CsSnCl₃ transforms to the cubic perovskite structure (space group $Pm\bar{3}m$) containing a network of corner-sharing ideal [SnCl₆]⁴⁻ octahedra with Sn–Cl bonds of 2.78 Å (Figure 3.1b).^{21,50} However, as described later, the cubic

form can be obtained at room temperature as a metastable phase. From le Bail fitting of the powder XRD patterns (Figure 3.1d), the cell parameters were refined to be $a = 5.7286(6)$ Å, $b = 7.6936(11)$ Å, $c = 16.9175(15)$ Å, and $\beta = 106.505(4)^\circ$ for the monoclinic phase and $a = 5.5894(5)$ Å for the room temperature cubic phase, in good agreement with previously reported values.^{50,51} The room temperature UV-visible absorption spectra show that the monoclinic phase has a larger optical bandgap (3.33 eV) than the cubic phase (2.83 eV) (Figure 3.1c), consistent with the less delocalized electronic structure associated with the discrete $[\text{SnCl}_3]^-$ units in the former.

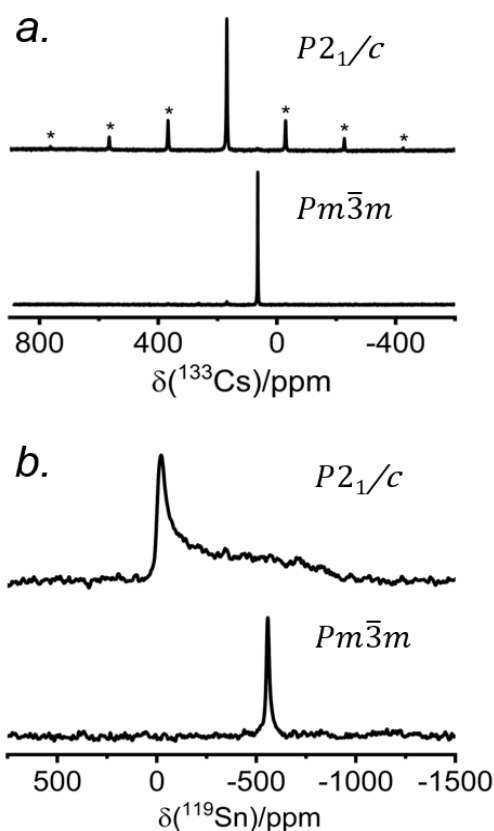


Figure 3.2. (a) ^{133}Cs and (b) ^{119}Sn NMR spectra collected at room temperature for monoclinic and cubic CsSnCl_3 . The ^{133}Cs NMR spectra were acquired at 11.75 T with a magic-angle spinning frequency of 13 kHz. The ^{119}Sn NMR spectra were acquired at 7.05 T for monoclinic and 11.75 T for cubic CsSnCl_3 under non-spinning sample conditions at 293 K. In (a), the asterisks (*) indicate spinning side bands.

The lack of a simple relationship between the monoclinic and cubic structures of CsSnCl_3 implies a reconstructive phase transition involving considerable mobility of atoms, because the process takes place at a relatively low temperature. In preparation for a detailed examination of the dynamics of this process, the local environments around the Cs and Sn atoms within the monoclinic and cubic phases were first probed by solid-state NMR spectroscopy to establish a frame of reference.

The ^{133}Cs NMR characteristics depend strongly on local electronic and chemical environments. The position and widths of the ^{133}Cs resonances, as measured by their isotropic chemical shift (δ_{iso}) and full-width-at-half-maximum (fwhm) values, are quite different within the monoclinic ($\delta_{\text{iso}} = 168.5(1)$ ppm, fwhm = 320 Hz) and cubic structures ($\delta_{\text{iso}} = 64.7(1)$ ppm, fwhm = 138 Hz) (Figure 3.2a). The ^{133}Cs spin-lattice relaxation time decreases significantly from the monoclinic ($T_1 = 252$ s) to the cubic structure ($T_1 = 15$ s), which may be related to greater mobility of Cl atoms in the latter.²¹ The local environment of Cs atoms surrounded by Cl atoms is less symmetrical within the monoclinic structure (CN10, bicapped square prismatic), giving rise to a manifold of spinning sidebands due to a small quadrupole coupling constant (C_Q) of 190 kHz, whereas it is highly symmetrical within the cubic structure (CN12, cuboctahedral) for which C_Q is ~ 0 kHz. At a magic-angle spinning (MAS) frequency of 13 kHz, a single low-intensity spinning side band is observed in cubic CsSnCl_3 (Figure B1), which is most likely due to intrinsic defects (*e.g.*, Cl vacancies).⁵² The distinctly different ^{133}Cs NMR spectra for these two forms of CsSnCl_3 can then be exploited to quantitatively determine their relative amounts in more complex samples obtained by various synthetic procedures.

Similarly, the ^{119}Sn NMR features serve as helpful diagnostics of these forms of CsSnCl_3 (Figure 3.2b). The lower symmetry monoclinic form exhibits a broad pattern characteristic of chemical shift anisotropy ($\delta_{\text{iso}} = -295(2)$ ppm, span $\Omega = 870(5)$ ppm, skew $k = 0.95(2)$), whereas the higher symmetry cubic form exhibits a symmetric resonance ($\delta_{\text{iso}} = -560(1)$ ppm, fwhm = 1.8 kHz) with no evidence for chemical shift anisotropy.

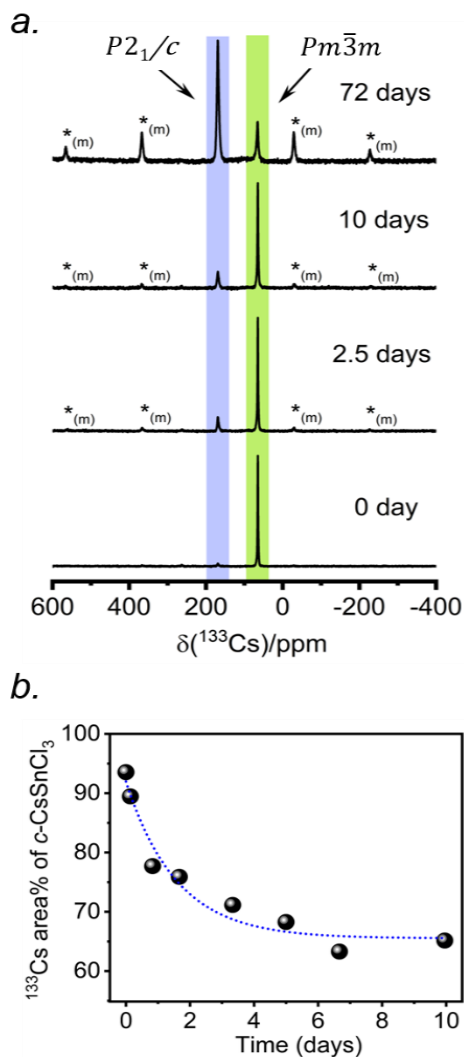


Figure 3.3. (a) Time-dependent ^{133}Cs NMR spectra ($B_0 = 11.75$ T, $\omega_r/2\pi = 13$ kHz MAS; a short-tip angle and an optimized 300 s recycle delay were used for quantification) of a sample of CsSnCl_3 prepared by quenching in ice-water. The spectra are normalized to the highest intensity. The asterisks ($*_{(m)}$) indicate positions of spinning side bands for the monoclinic phase. (b) Plot of ^{133}Cs NMR peak area ($\pm 2\%$) as a function of time for the cubic phase.

3.2.2 Trapping Cubic CsSnCl_3 at Room Temperature

According to recent reports, cubic CsSnCl_3 can be obtained as a metastable phase at room temperature by ball milling,⁵³ or by “briefly heating” the monoclinic form to 380

K.⁴⁴ However, questions still remain about how long this cubic phase persists under ambient conditions, and to our knowledge, there has been no systematic study on its stability upon exposure to air.

Two separate samples of CsSnCl₃ were prepared by reaction of CsCl and SnCl₂, which were loaded into sealed and evacuated fused-silica tubes, and heated at 673(10) K for 15 h in a box furnace (see Experimental section in Appendix B). For the first sample, the tubes were cooled slowly at 5 K min⁻¹ to room temperature. This sample contained a mixture of cubic and monoclinic phases with the latter >50%, as revealed by both powder XRD and ¹³³Cs NMR spectroscopy performed within 24 hours of synthesis (Figure B2). After 6 days at room temperature, the sample transformed to mostly the monoclinic phase, with <10% of the cubic phase remaining. For the second sample, the tubes were cooled at 5 K min⁻¹ to 573 K, followed by quenching in an ice-water bath. Although the powder XRD data suggest a phase-pure sample consisting of only the cubic phase (lower part of Figure 3.1d), the ¹³³Cs NMR spectrum shows a small amount (6%) of the monoclinic phase (Figure 3.3a). Time-dependent ¹³³Cs NMR spectra were collected on the sample, kept at room temperature, at various intervals up to 72 days. The proportion of the cubic phase decreases monotonically in an exponential manner, with 65% remaining after 10 days and 14% after 72 days (Figure 3.3b and B2c). This process is much slower than a similar one that we have recently reported for the transformation of metastable γ -CsPbI₃ perovskite to δ -CsPbI₃ non-perovskite at room temperature, which is complete within 2 hours, as monitored by ¹³³Cs NMR spectroscopy.⁴¹

3.2.3 Cubic CsSn(Cl_{1-x}Br_x)₃ Solid Solution: Synthesis, Long-range Structure and Optical Properties

The multiple phase transitions encountered for both CsSnCl₃ and CsSnBr₃ make it challenging to prepare a complete mixed-halide solid solution CsSn(Cl_{1-x}Br_x)₃ having the cubic perovskite structure over the entire range for x at room temperature. Moreover, the parent end-members only adopt the stable cubic structure above room temperature (>379 K for CsSnCl₃ and >292 K for CsSnBr₃).^{21,22} Samples of CsSn(Cl_{1-x}Br_x)₃ prepared by solution methods were reported

to form monoclinic phases for Cl-rich compositions ($x < 0.50$) and cubic phases for Br-rich compositions ($x > 0.50$) at room temperature.¹⁶ The retention of cubic CsSnCl_3 as a metastable phase at room temperature, presented above, suggests that it may yet be possible to prepare a complete solid solution with the cubic structure through similar high-temperature reactions of CsX and SnX_2 ($\text{X} = \text{Cl}, \text{Br}$). As detailed in the experimental section, the critical step is rapid quenching (see Appendix B).

Freshly synthesized samples of $\text{CsSn}(\text{Cl}_{1-x}\text{Br}_x)_3$ show colors starting from faint yellow (CsSnCl_3) and gradually evolving with increasing Br content to orange, red, and finally black (CsSnBr_3), consistent with a decrease in the bandgap (Figure 3.4a). The samples are polycrystalline with micron-sized particles having uniform distribution of all elements (Cs, Sn, Cl, Br) down to this scale, as seen in elemental mapping images collected on a field-emission scanning electron microscope (Figure 3.4b and B3). The chemical compositions, as determined by energy-dispersive X-ray analysis, agree well with the nominal compositions $\text{CsSn}(\text{Cl}_{1-x}\text{Br}_x)_3$ loaded in the reactions (Table B1).

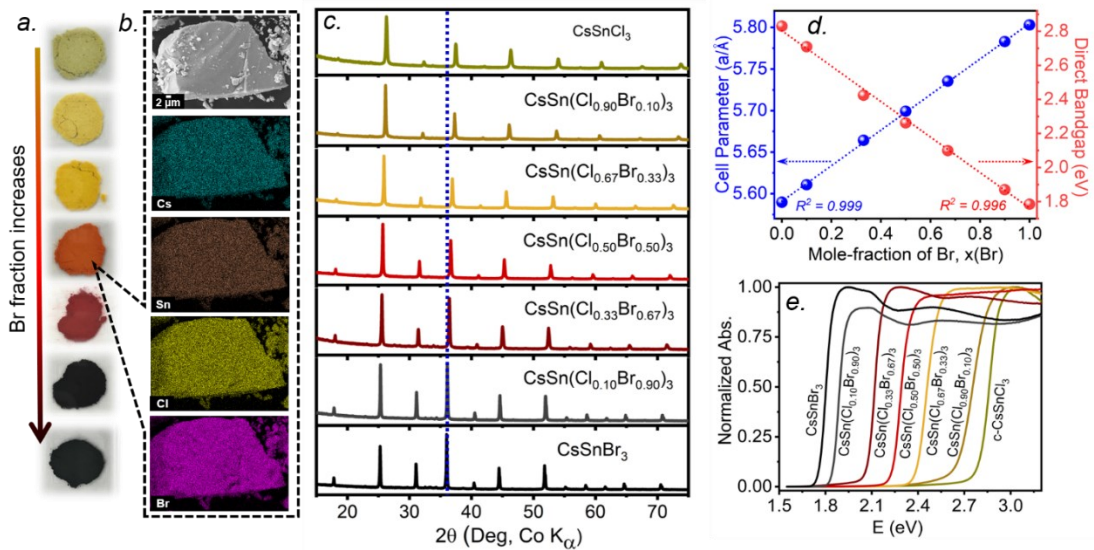


Figure 3.4. (a) Photographs of freshly synthesized $\text{CsSn}(\text{Cl}_{1-x}\text{Br}_x)_3$ (top to bottom, $x = 0, 0.10, 0.33, 0.50, 0.67, 0.90, 1$), (b) scanning electron micrograph and elemental maps for $\text{CsSn}(\text{Cl}_{0.50}\text{Br}_{0.50})_3$, (c) powder XRD patterns, (d) plots of unit cell parameters and bandgaps, and (e) UV-visible absorption spectra.

Powder XRD patterns collected at room temperature confirm the cubic perovskite structure (space group $Pm\bar{3}m$) for all members of the solid solution (Figure 3.4c and B4). The refined unit cell parameter for $\text{CsSn}(\text{Cl}_{1-x}\text{Br}_x)_3$ increases linearly from 5.5894(5) Å for CsSnCl_3 to 5.8031(3) Å for CsSnBr_3 , in accordance with Vegard's law, with no deviations being shown (Figure 3.4d and Table B2). Strict adherence to Vegard's law behavior has also been observed in lead-containing mixed-halide perovskites.^{35,36}

UV-visible absorption spectra, which were converted from diffuse reflectance spectra using the Kubelka–Munk function, show gradual shifts in the absorption edge to lower energy with increasing Br content in $\text{CsSn}(\text{Cl}_{1-x}\text{Br}_x)_3$ (Figure 3.4e). With the assumption of a direct bandgap, the linear regions in the Tauc plots of $(ah\nu)^2$ vs. E were extrapolated to extract optical bandgap values (Figure B5). The bandgap in $\text{CsSn}(\text{Cl}_{1-x}\text{Br}_x)_3$ decreases linearly with increasing Br content from 2.83 eV for CsSnCl_3 to 1.79 eV for CsSnBr_3 (Figure 3.4d), similar to the behavior seen in lead-containing mixed-halide perovskites.^{35,36,41}

3.2.4 Cubic $\text{CsSn}(\text{Cl}_{1-x}\text{Br}_x)_3$ Solid Solution: Local Structure using ^{133}Cs and ^{119}Sn NMR Spectroscopy

The local environments of Cl and Br atoms around the Cs and Sn atoms in $\text{CsSn}(\text{Cl}_{1-x}\text{Br}_x)_3$ were probed by NMR spectroscopy. The Cs atoms reside in a cuboctahedral site surrounded by 12 halogen atoms (Figure 3.5a). For the end-members, the ^{133}Cs chemical shifts are similar but distinguishable: $\delta_{\text{iso}} = 64.7$ ppm for CsSnCl_3 and $\delta_{\text{iso}} = 64.0$ ppm for CsSnBr_3 .⁴⁴ Interestingly, the ^{133}Cs resonances are quite sharp for all members of $\text{CsSn}(\text{Cl}_{1-x}\text{Br}_x)_3$, with fwhm ranging from 70 to 150 Hz (or 1.1 to 2.3 ppm) (Figure 3.5b). This result is in contrast to the lead-containing analogues $\text{CsPb}(\text{Cl}_{0.50}\text{Br}_{0.50})_3$, where much broader ^{133}Cs resonances (fwhm of 2 kHz) were observed and attributed to inhomogeneities caused by the numerous possible arrangements of Cl and Br atoms.⁴¹ The sharper ^{133}Cs NMR spectra for $\text{CsSn}(\text{Cl}_{1-x}\text{Br}_x)_3$ imply that rapid halogen dynamics must be taking place even at room temperature, such that the effects of the 12 surrounding halogen atoms are averaged.⁴⁴

Most surprisingly, the ^{133}Cs chemical shift does not vary monotonically between the end-members; rather, it is displaced to higher frequency relative to the end-members and reaches a maximum of $\delta_{\text{iso}} = 74.7$ ppm in $\text{CsSn}(\text{Cl}_{0.50}\text{Br}_{0.50})_3$. The relationship between the chemical shift δ_{iso} and the Br content x can be fitted to a parabolic curve, following the quadratic function $\delta_{\text{iso}}(^{133}\text{Cs})/\text{ppm} = 64.8 + 40.6x - 41.5x^2$ (Figure 3.5c). A comparable nonlinear change in ^{89}Y and ^{119}Sn NMR chemical shifts has been observed in pyrochlores.^{54,55} A similar nonlinear change in ^{133}Cs NMR chemical shifts was recently reported for mixed-halide double perovskites $\text{Cs}_2\text{AgBi}(\text{Cl}_{1-x}\text{Br}_x)_6$ due to a non-additive effect of nearest and next-nearest neighbours on the chemical shift for ^{133}Cs nuclei and the associated extended halide environment.⁵⁶

A mixture of Cl and Br atoms in the cuboctahedral environment around the Cs atoms would be expected to enhance quadrupolar coupling interactions because of the lowering of symmetry and correspondingly to increase the manifold of ^{133}Cs spinning side bands, as was previously observed in the lead-containing analogues $\text{CsPb}(\text{Cl}_{0.50}\text{Br}_{0.50})_3$.⁴¹ However, at a MAS frequency of 13 kHz, only a single spinning side band of low intensity was observed for all members of $\text{CsSn}(\text{Cl}_{1-x}\text{Br}_x)_3$ (Figure B1), which could occur if the environment contains identical halogen atoms (not possible here) or if the halogen dynamics are sufficiently rapid (*i.e.*, much shorter than the correlation times) such that only average values are measured for the relevant interactions. The ^{133}Cs spin-lattice relaxation times T_1 vary nonlinearly between 10 to 35 s with increasing Br content (Figure 3.5c and Table B3). These short relaxation times, on the order of seconds, are consistent with the absence of significant covalent bonding interactions between Cs and halogen atoms, similar to previous observations for $\text{CsPb}(\text{Cl}_{0.50}\text{Br}_{0.50})_3$.⁴²

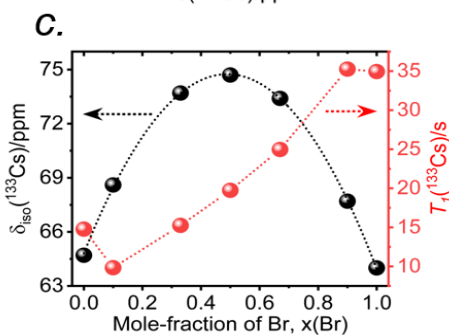
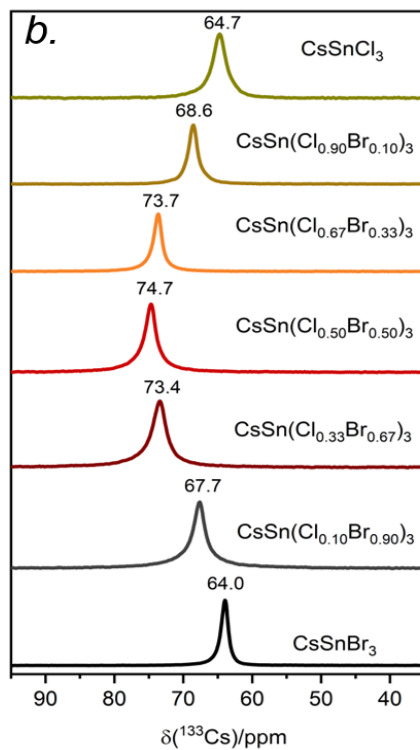
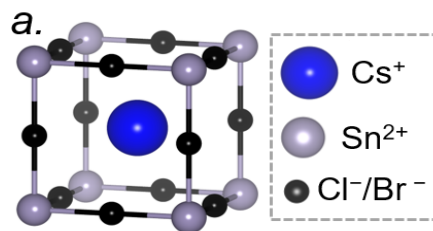


Figure 3.5. (a) Local cuboctahedral environment of 12 halogen atoms around the Cs atom. (b) Room temperature ^{133}Cs NMR spectra for $\text{CsSn}(\text{Cl}_{1-x}\text{Br}_x)_3$, acquired at 11.75 T with a magic-angle spinning frequency of 13 kHz. (c) Plots of $\delta_{\text{iso}}(^{133}\text{Cs})$ and ^{133}Cs T_1 values as a function of Br content. The δ_{iso} plot was fit to the equation $\delta_{\text{iso}}(^{133}\text{Cs})/\text{ppm} = 64.8 + 40.6x - 41.5x^2$ ($R^2 = 0.999$).

The Sn atoms in $\text{CsSn}(\text{Cl}_{1-x}\text{Br}_x)_3$ reside in an octahedral site surrounded by six halogen atoms (Figure 3.6a). For the end-members, the ^{119}Sn NMR spectra show symmetric-like lineshapes with clear differences in isotropic chemical shifts for CsSnCl_3 ($\delta_{\text{iso}} = -562$ ppm) and CsSnBr_3 ($\delta_{\text{iso}} = -289$ ppm) (Figure 3.6b). There is no evidence of spinning side bands, consistent with a highly symmetric chemical environment. As the Br content increases, the ^{119}Sn chemical shift gradually displaces to higher frequency (Figure 3.6b and Table B4) and the linewidth increases from CsSnCl_3 (fwhm = 1.8 kHz) to CsSnBr_3 (fwhm = 19.0 kHz) (Figure 3.6c). For CsSnBr_3 , the ^{119}Sn NMR linewidth and lineshape are unchanged whether the magnetic field (B_0) is 7.05 or 11.75 T (Figure B6). Furthermore, the linewidth (fwhm = 21 kHz) only decreases slightly when magic angle spinning is applied (fwhm = 19 kHz) (Figure B7); the small decrease is attributed to a reduced heteronuclear dipolar coupling between ^{119}Sn and $^{79/81}\text{Br}$. The observed linewidths may also be influenced by indirect spin-spin coupling between ^{119}Sn and six surrounding quadrupolar nuclei ($I = 3/2$ for $^{35/37}\text{Cl}$ and $^{79/81}\text{Br}$) as recently reported in $\text{CH}_3\text{NH}_3\text{PbCl}_3$ and CsPbCl_3 .^{24,28} For the Br-rich samples, the ^{119}Sn signal-to-noise ratio drastically deteriorates upon increasing the echo delays from 24 to 94 μs , due to fast T_2 relaxation (Figure B8).⁴⁴ These results are similar to previous observations on the lead-containing analogues.^{24,28,31,35,36,41}

The occurrence of single symmetric-like ^{119}Sn resonances and the absence of spinning side bands imply that the chemical environment around the Sn atoms is uniform. If a distribution of several types of $\text{SnCl}_{6-n}\text{Br}_n$ ($n = 0-6$) octahedra were present, they would give rise to multiple Sn resonances and possibly spinning side bands due to magnetic shielding anisotropy, but neither of these are observed. As before, the most probable explanation is that rapid halogen dynamics is taking place in $\text{CsSn}(\text{Cl}_{1-x}\text{Br}_x)_3$ on the timescale of the NMR experiment, resulting in averaged chemical environments around the Sn atoms. This situation contrasts with the lead-containing analogues $\text{CsPb}(\text{Cl}_{1-x}\text{Br}_x)_3$, where multiple chemical environments around Pb atoms are observed.⁴¹ The ^{119}Sn NMR chemical shift can be further correlated with the bandgap in $\text{CsSn}(\text{Cl}_{1-x}\text{Br}_x)_3$ (Figure B9). The decrease in bandgap is accompanied by a displacement of the ^{119}Sn NMR chemical shift to higher frequency, suggesting a dominating paramagnetic shielding contribution.

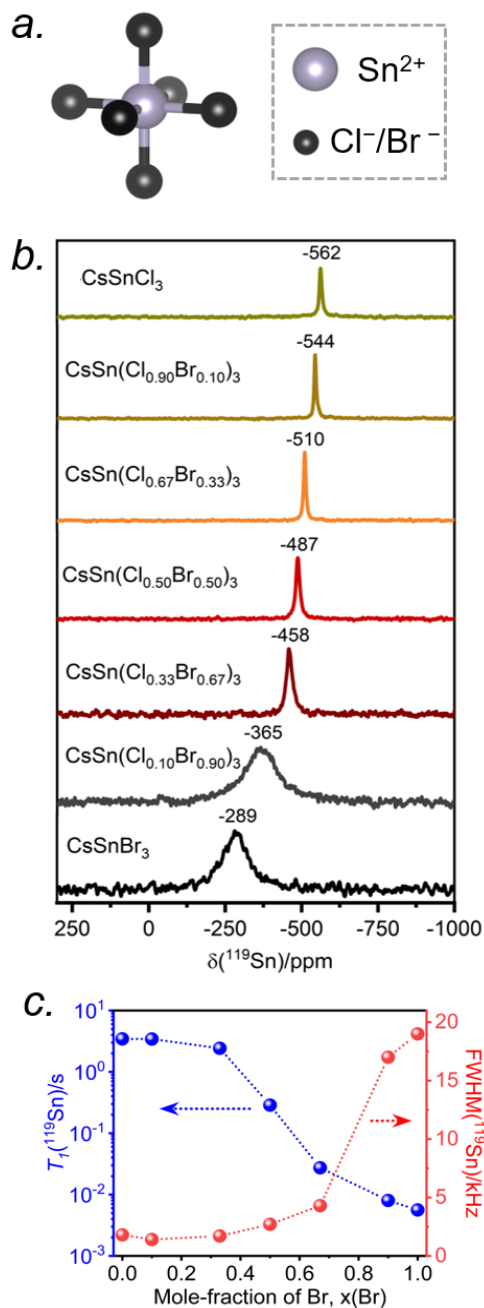


Figure 3.6. (a) Local octahedral environment of 6 halogen atoms around the Sn atom. (b) Room-temperature ^{119}Sn NMR spectra for $\text{CsSn}(\text{Cl}_{1-x}\text{Br}_x)_3$, acquired at 11.75 T with a magic-angle spinning frequency of 10 kHz. (c) Plots of ^{119}Sn T_1 and ^{119}Sn linewidth values as a function of Br content.

The ^{119}Sn spin-lattice relaxation times decrease dramatically from CsSnCl_3 ($T_1 = 3.5$ s) to CsSnBr_3 ($T_1 = 0.006$ s), a difference of three orders of magnitude which is comparable to recent observations on $\text{CH}_3\text{NH}_3\text{SnX}_3$.⁴⁴ The decrease is monotonic with increasing Br content (Figure 3.6c and Table B4). It has been shown previously that the T_1 relaxation mechanism is dominated by the scalar coupling strength $^1J(^{119}\text{Sn}, \text{X})$ ($\text{X} = ^{35/37}\text{Cl}$ or $^{79/81}\text{Br}$) for tin halides.^{44,57,58} The smaller T_1 value for CsSnBr_3 compared to CsSnCl_3 is consistent with $^1J(^{119}\text{Sn}, ^{79/81}\text{Br})$ being larger than $^1J(^{119}\text{Sn}, ^{35/37}\text{Cl})$. In addition to J -coupling, chemical exchange processes due to the rapid halogen dynamics at room temperature may also play a significant role in the ^{119}Sn T_1 values for the Br-rich samples, as discussed later.

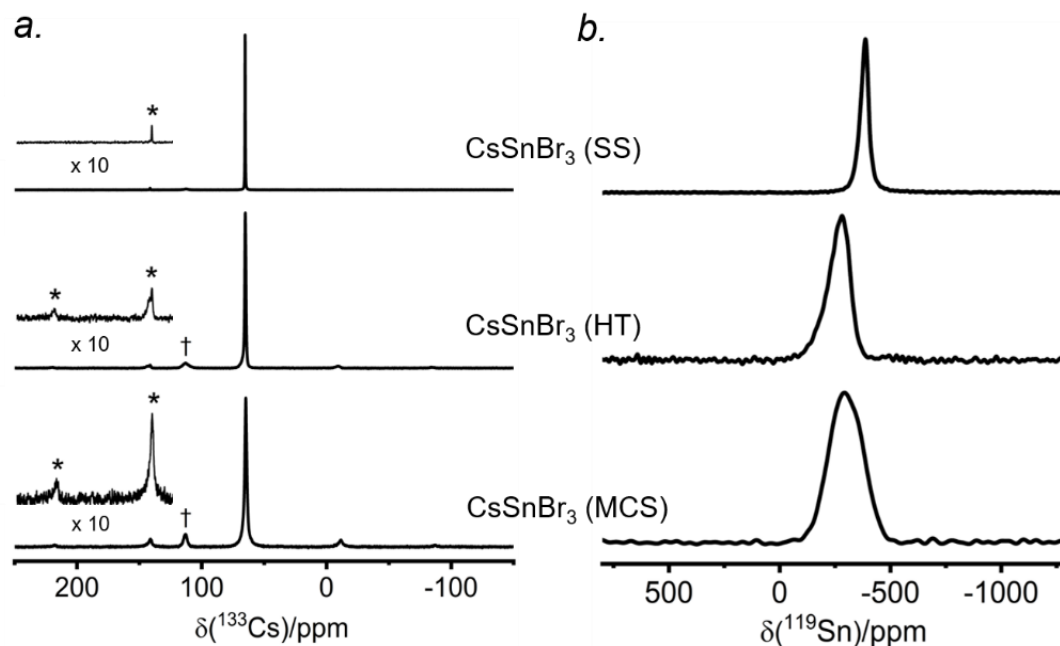


Figure 3.7. Room temperature (a) ^{133}Cs NMR spectra with magic-angle spinning (5 kHz) and (b) ^{119}Sn NMR spectra with no magic-angle spinning, acquired at 11.75 T, of CsSnBr_3 samples prepared by solvent synthesis (SS), high-temperature (HT) reactions, and ball-milling (MCS). In (a), the asterisks (*) indicate spinning side bands and the daggers (†) mark peaks attributed to Cs_2SnBr_6 .

3.2.5 Local Structure of CsSnBr₃ Prepared by Solvent, High-Temperature, and Mechanochemical Routes

There have been many reports of halide perovskites being prepared by nonconventional routes, either in the presence or absence of solvent. For example, solvent-free “mechanochemical synthesis” routes involving ball-milling have been proposed to be advantageous for large-scale production of perovskite photovoltaic materials.^{59,60} However, it is unclear whether samples prepared by these nonconventional routes are really identical to more traditional solution-based methods on a local atomic-level. To understand this, samples of CsSnBr₃ were prepared by three routes (solvent synthesis, high-temperature reaction, and ball-milling) and analyzed by ¹³³Cs and ¹¹⁹Sn NMR spectroscopy.

The ¹³³Cs NMR spectra show resonances appearing in the same position, being sharpest for the sample prepared by solvent-synthesis (fwhm = 15 Hz), and growing increasingly broader for those prepared by high-temperature reaction (fwhm = 70 Hz) and ball-milling (fwhm = 120 Hz) (Figure 3.7a). For these spectra acquired under slow magic-angle spinning (5 kHz), the spinning side band manifold increases along the same order. These observations indicate that the solvent-synthesized sample has the most well-ordered structure containing fewer defects, whereas the ball-milled sample has the most locally disordered structure exhibiting a wide distribution of environments and more defects.^{27,35} The higher defect concentrations in our ball-milled sample are maintained because no further post-grinding annealing treatment was performed. It is worth noting that one may minimize or circumvent the formation of grinding induced defects by performing a subsequent heat treatment after ball milling.^{61,62}

The ¹¹⁹Sn NMR spectra for these samples (Figure 3.7b) show even greater differences in chemical shifts, which span a range of almost 100 ppm, and linewidths: the sharpest at -386 ppm (fwhm = 7.5 kHz) for the solvent-synthesized sample, an intermediate one at -284 ppm (fwhm = 21 kHz) for the sample prepared at high temperature, and the broadest at -295 ppm (fwhm = 34 kHz) for the ball-milled sample. The ¹¹⁹Sn spin-lattice relaxation times depend greatly on the synthetic route: $T_1 = 25$ ms for the solvent-synthesized sample, 7 ms for the high-temperature sample, and 3 ms for the ball-milled sample (Table B5). A faster relaxation process implies greater local

surface disorder/defects in the ball-milled sample, consistent with the conclusions from the ^{133}Cs NMR spectra and the ^{119}Sn NMR linewidths. This greater disorder is also reflected in broader peaks in the powder XRD patterns for the ball-milled sample compared to the other samples (Figure B10); all samples exhibit micron sized crystallites. However, the optical bandgaps extracted from the UV-visible absorption spectra appear to be virtually identical (within experimental error), with values ranging from 1.77 eV for the solution-synthesized sample to 1.81 eV for the ball-milled sample. We note this disorder may also be related to the UV-vis absorption profile being different for the ball-milled sample (Figure B11).

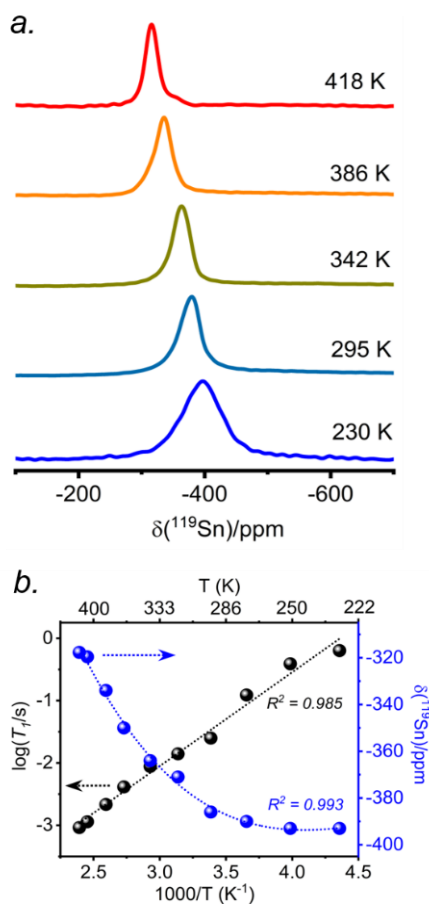


Figure 3.8. (a) Variable temperature ^{119}Sn NMR non-spinning spectra acquired at 11.75 T and (b) plots of ^{119}Sn T_1 and NMR chemical shift vs. inverse of absolute temperature for solvent synthesized CsSnBr_3 .

3.2.6 Spontaneous Halogen Mobility in CsSnBr₃

The presence of point defects or vacancies enables ionic migration within perovskites and plays an important role in photovoltaic efficiency and material stability, while also being responsible for photocurrent hysteresis characteristics.^{63–65} Metal halide perovskites ABX₃ can exhibit a vacancy transport hopping mechanism through A-, B- or X-site migration,⁶⁶ but X-site (halogen) diffusion is most probable as the halogen vacancy formation energy is comparable to the halogen ionic diffusion activation energy barrier (*ca.* 0.30 eV) in organic–inorganic hybrid perovskites.^{52,67,68} The analysis of the ¹³³Cs and ¹¹⁹Sn NMR spectra above suggests that halogen atoms may be highly mobile in CsSn(Cl_{1-x}Br_x)₃ even at room temperature. To deconvolute the halogen dynamics, variable-temperature ¹¹⁹Sn NMR spectroscopy was performed on the parent CsSnBr₃ compound, prepared by solution synthesis. As the temperature increases from 230 to 418 K, the ¹¹⁹Sn resonances shift monotonically to higher frequency by about 75 ppm (Figure 3.8 and Table B6), following the cubic dependence $\delta_{\text{iso}}(^{119}\text{Sn})/\text{ppm} = 364.25 - 497.09 \times \frac{10^3}{T(\text{K})} + 107.16 \times \left\{ \frac{10^3}{T(\text{K})} \right\}^2 - 7.56 \times \left\{ \frac{10^3}{T(\text{K})} \right\}^3$. The ¹¹⁹Sn NMR linewidth narrows from 14.7 to 4.5 kHz, the effective spin–spin relaxation time (*T*₂^{*}) increases from 68 to 222 μs (Figure B12 and Table B6), and most notably, the spin-lattice relaxation time (*T*₁) decreases drastically from 0.635 to 0.0009 s, a difference of three orders of magnitude (Table B6). In accordance with an Arrhenius relationship, a plot of log₁₀[*T*₁(¹¹⁹Sn)/s] vs. [1000/*T* (K)] yields a linear dependence (Figure 3.8b) from which an activation energy of 28.9 ± 1.2 kJ mol⁻¹ (0.30 ± 0.01 eV) for the halogen dynamics was extracted (see Appendix Note B1). Although this result is in contrast to the metallic behavior previously suggested from electrical conductivity measurements,⁶⁷ it is in excellent agreement with those for other Sn- and Pb-based perovskites and metal halide solid ionic conductors including CH₃NH₃SnBr₃ (0.30–0.37 eV),^{44,67,68} CH₃NH₃PbI₃ (0.29 eV),⁶⁹ CsPbCl₃ (0.29 eV),⁷⁰ CsPbBr₃ (0.25 eV),⁷⁰ CsSnCl₃ (0.2 eV, theoretical),⁷¹ α-SnI₂ (0.29 eV),⁷² PbCl₂ (0.20–0.30 eV),^{70,73} and PbBr₂ (0.23–0.25 eV).^{70,74} These observations support the conclusion that CsSnBr₃ behaves like an ionic conductor and Br⁻ mobility is responsible for the fast

relaxation process of ^{119}Sn nuclei in CsSnBr_3 , as observed recently in the organic–inorganic hybrid $\text{CH}_3\text{NH}_3\text{SnBr}_3$ perovskite.⁴⁴

The above NMR results suggest that the replacement of Pb with Sn in perovskite appears to enable faster halogen mobility, which causes an averaging of the relevant interactions through halide dynamics. The faster halogen dynamics alter the electrical properties for tin halide perovskites. For example, cubic CsSnCl_3 was shown to have high ionic conductivity $>10^{-4} \text{ S cm}^{-1}$ at 313 K, fueling its potential as a solid electrolyte candidate for chloride ion batteries.⁷¹ We further note that a higher concentration of B site vacancies (*ca.* 2.9%)⁷¹ was reported in CsSnCl_3 than that for $\text{CH}_3\text{NH}_3\text{PbI}_3$ (*ca.* 0.4%).⁷⁵ The higher B site vacancies in tin halide perovskites is most likely associated with Sn(+2) oxidation ($\text{Sn}(+2) \rightarrow \text{Sn}(+4)$ *vs.* $\text{Pb}(+2)$), which may cause an increase in the rate of halogen dynamics.

3.2.7 Air Stability and Degradation Pathways for CsSnBr_3

CsSnBr_3 shows higher thermal and moisture stability than the organic–inorganic hybrid $\text{CH}_3\text{NH}_3\text{SnBr}_3$. Nevertheless, CsSnBr_3 slowly degrades over time under ambient conditions, becoming partially oxidized to Cs_2SnBr_6 , and the UV-visible absorption spectra change drastically (Figure B13). Powder XRD and solid-state ^{133}Cs and ^{119}Sn NMR spectroscopy were performed to elucidate the decomposition pathways and the nature of the degraded products. A sample of CsSnBr_3 was freshly synthesized by high-temperature reactions and stored in a parafilm-sealed glass vial under ambient laboratory conditions (298 K and 50–70% humidity) over 300 days. The powder XRD pattern of the degraded sample was compared to those for various reference standards (pristine CsSnBr_3 , Cs_2SnBr_6 , CsBr , SnO_2 , SnBr_4 , and SnBr_2) (Figure 3.9a). In addition to CsSnBr_3 , which still constituted about 40% of the sample, significant amounts of Cs_2SnBr_6 and CsBr , and smaller amounts of SnBr_4 were formed, but no SnO_2 or SnBr_2 were present. The powder XRD pattern also shows an increased background, suggestive of amorphous contributions.

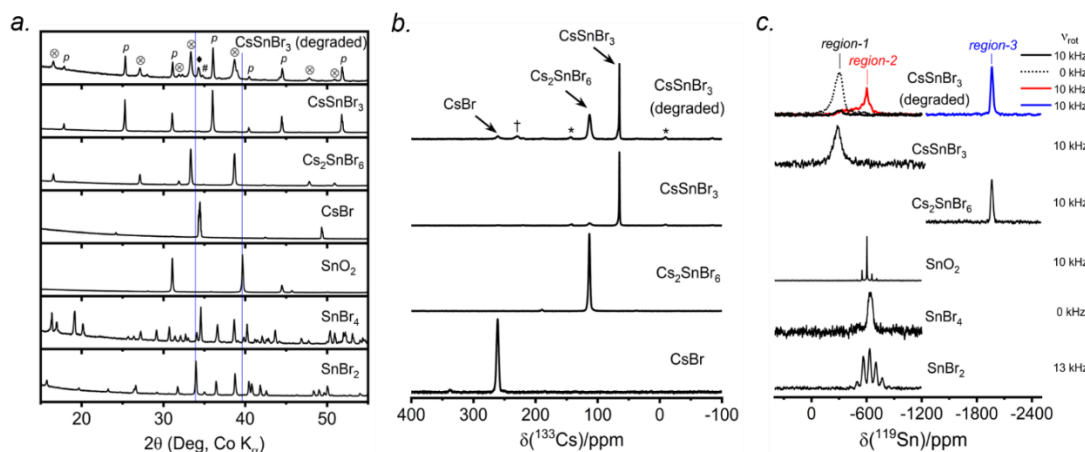


Figure 3.9. Degraded CsSnBr_3 sample that was exposed to ambient laboratory conditions over 300 days. (a) Powder XRD pattern compared to reference standards shows presence of CsSnBr_3 (p), Cs_2SnBr_6 (\otimes), CsBr (\blacklozenge), and SnBr_4 (#). The blue lines indicate the absence of peaks due to SnO_2 and SnBr_2 . (b) ^{133}Cs NMR spectrum, acquired at 11.75 T with a magic-angle spinning frequency of 5 kHz, shows the presence of CsSnBr_3 , Cs_2SnBr_6 , and CsBr . The asterisks (*) indicate spinning side bands and the dagger (\dagger) indicates an unidentified Cs-containing degradation product. (c) ^{119}Sn NMR spectrum, acquired at 11.75 T with magic-angle spinning frequencies of 0 to 13 kHz.

Complementary information about crystalline and amorphous components can be obtained from the solid-state NMR spectra. For quantitative analysis, the NMR parameters were optimized to achieve maximum sensitivity (Tables B7 and B8). The ^{133}Cs NMR spectrum of the degraded sample was compared to those for three reference standards (pristine CsSnBr_3 , Cs_2SnBr_6 , and CsBr) (Figure 3.9b). Based on assignment of the ^{133}Cs NMR resonance areas, the sample consisted of 40% CsSnBr_3 (65 ppm), 45% Cs_2SnBr_6 (113 ppm), 8% CsBr (260 ppm) and 7% of an unidentified Cs-containing phase (230 ppm). The ^{133}Cs resonances are slightly broader for Cs_2SnBr_6 (fwhm of 320 Hz, compared to 170 Hz for the solvent-synthesized standard) and for CsBr (fwhm of 370 Hz, compared to 270 Hz for the standard). This broadening implies that Cs_2SnBr_6 and CsBr formed during the slow degradation

process have smaller crystallite sizes than in the reference standards.⁴⁴ The powder XRD pattern also shows broadening of diffraction peaks for these phases (Figure 3.9a).

In the ^{119}Sn NMR spectrum of the degraded sample, the resonances span about 8800 ppm (1.6 MHz at $B_0 = 11.75$ T, Figure 3.9c and B14), with spin-lattice relaxation times extending over four orders of magnitude (Table B8). Hence, the ^{119}Sn NMR acquisition parameters were optimized within different spectral regions (Table B8). Region 1 shows that a significant amount of CsSnBr_3 is present. The ^{119}Sn resonance intensity for CsSnBr_3 is highly sensitive to the magic-angle spinning frequency; because these spectra were acquired with a spin echo, for which the delay depends on the spinning frequency, the signal is weakened due to the fast T_2 relaxation process when slower MAS frequencies are used. Region 2 shows a ^{119}Sn resonance at -600 ppm, which corresponds to SnO_2 , and a broad underlying component, which most likely corresponds to SnBr_4 , indicating that oxidation from $\text{Sn}(+2)$ to $\text{Sn}(+4)$ has taken place. The ^{119}Sn signal for SnO_2 in the degradation product is much broader (fwhm = 3.7 kHz) than in the bulk SnO_2 standard (fwhm = 0.2 kHz). Although crystalline SnO_2 was not detected in the powder XRD pattern, the broadness of the ^{119}Sn NMR signal suggests that it may either be amorphous or in the form of nanodomains (<10 nm)⁷⁶ embedded within other phases in the sample. Region 3 confirms the presence of Cs_2SnBr_6 , as seen by the ^{119}Sn resonance at -1964 ppm. Region 4 reveals a weak ^{119}Sn signal that is assigned to metallic β -Sn and is Knight-shifted⁷⁷ to higher frequency; however, this signal was detected only after two million scans, implying only a trace amount of β -Sn that likely originated as an impurity in the starting material SnBr_2 used in the synthesis, as shown in Figure B14. Based on the XRD and NMR results, two simultaneous pathways are proposed for the room-temperature oxidation of CsSnBr_3 :

- (1) $2 \text{CsSnBr}_3 + \text{O}_2 (\text{air}) \rightarrow \text{Cs}_2\text{SnBr}_6 (\text{crystalline}) + \text{SnO}_2 (\text{amorphous or nano-sized})$
- (2) $2 \text{CsSnBr}_3 + \text{O}_2 (\text{air}) \rightarrow \text{SnBr}_4 (\text{crystalline}) + 2 \text{CsBr} (\text{crystalline}) + \text{SnO}_2 (\text{amorphous or nano-sized}).$

3.3 Conclusions

The complete solid solution $\text{CsSn}(\text{Cl}_{1-x}\text{Br}_x)_3$ ($0 \leq x \leq 1$) exhibiting the cubic perovskite structure for all members, was prepared by rapid quenching of samples reacted at high

temperature. In particular, this method is able to trap the end-member CsSnCl₃ as a metastable cubic phase (instead of the monoclinic phase) at room temperature. The long-range structure was elucidated by powder XRD and the local structure and dynamics by ¹³³Cs and ¹¹⁹Sn solid-state NMR spectroscopy. In contrast to the lead-containing analogues CsPbX₃, the halogen atoms in CsSn(Cl_{1-x}Br_x)₃ are much more mobile. The rapid halogen dynamics in CsSnBr₃ were analyzed by measuring the ¹¹⁹Sn spin-lattice relaxation times at variable temperatures, giving a low activation energy of 28.9 ± 1.2 kJ mol⁻¹ for the diffusion of Br atoms. Although CsSnBr₃ can be prepared by various synthetic routes that apparently have similar long-range structures, as ascertained by powder XRD and optical properties, the local structure and degree of crystallinity differ, as revealed by NMR spectroscopy; in particular, samples prepared by mechanochemical synthesis tend to show greater local polyhedral disorder and vacancies, resulting in a reduction of the spin-lattice relaxation of ¹¹⁹Sn. In a study of CsSnBr₃ exposed to air, insight into the degradation pathways was sought by NMR spectroscopy, which revealed the formation of amorphous or nano-sized SnO₂, not detected by conventional diffraction methods. The results suggest that although the photophysical properties of Sn-containing perovskites are attractive, and their bandgaps are tunable through halide substitution and not highly affected by synthetic methods despite differences in local structure, challenges remain in ensuring their ambient long-term stability.

3.4 References

- (1) Zhao, Y.; Zhu, K. Organic-Inorganic Hybrid Lead Halide Perovskites for Optoelectronic and Electronic Applications. *Chem. Soc. Rev.* **2016**, *45* (3), 655–689.
- (2) Kovalenko, M. V; Protesescu, L.; Bodnarchuk, M. I. Properties and Potential Optoelectronic Applications of Lead Halide Perovskite Nanocrystals. *Science* **2017**, *750*, 745–750.
- (3) Sutherland, B. R.; Sargent, E. H. Perovskite Photonic Sources. *Nat. Photonics* **2016**, *10*, 295–302.

- (4) Yakunin, S.; Sytnyk, M.; Kriegner, D.; Shrestha, S.; Richter, M.; Matt, G. J.; Azimi, H.; Brabec, C. J.; Stangl, J.; Kovalenko, M. V.; Heiss, W. Detection of X-Ray Photons by Solution-Processed Lead Halide Perovskites. *Nat. Photonics* **2015**, *9*, 444–449.
- (5) Leung, S. F.; Ho, K. T.; Kung, P. K.; Hsiao, V. K. S.; Alshareef, H. N.; Wang, Z. L.; He, J. H. A Self-Powered and Flexible Organometallic Halide Perovskite Photodetector with Very High Detectivity. *Adv. Mater.* **2018**, *30*, 1704611.
- (6) Chen, K.; Deng, X.; Dodekatos, G.; Tüysüz, H. Photocatalytic Polymerization of 3,4-Ethylenedioxythiophene over Cesium Lead Iodide Perovskite Quantum Dots. *J. Am. Chem. Soc.* **2017**, *139* (35), 12267–12273.
- (7) National Renewable Energy Laboratory (NREL). Best Research-Cell Efficiency Chart.
<https://www.nrel.gov/pv/assets/pdfs/best-research-cell-efficiencies.20200104.pdf>
(accessed March 2021).
- (8) Yang, J.; Siempelkamp, B. D.; Liu, D.; Kelly, T. L. Investigation of $\text{CH}_3\text{NH}_3\text{PbI}_3$ degradation Rates and Mechanisms in Controlled Humidity Environments Using in Situ Techniques. *ACS Nano* **2015**, *9*, 1955–1963.
- (9) Babayigit, A.; Ethirajan, A.; Muller, M.; Conings, B. Toxicity of Organometal Halide Perovskite Solar Cells. *Nat. Mater.* **2016**, *15* (3), 247–251.
- (10) Li, J.; Cao, H.; Jiao, W.; Wang, Q.; Wei, M.; Cantone, I.; Lü, J.; Abate, A. Biological Impact of Lead from Halide Perovskites Reveals the Risk of Introducing a Safe Threshold. *Nat. Commun.* **2020**, *11*, 310.
- (11) Kamarudin, M. A.; Hirotsu, D.; Wang, Z.; Hamada, K.; Nishimura, K.; Shen, Q.; Toyoda, T.; Iikubo, S.; Minemoto, T.; Yoshino, K.; Hayase, S. Suppression of Charge Carrier Recombination in Lead-Free Tin Halide Perovskite via Lewis Base Post-Treatment. *J. Phys. Chem. Lett.* **2019**, *10* (17), 5277–5283.
- (12) Stoumpos, C. C.; Malliakas, C. D.; Kanatzidis, M. G. Semiconducting Tin and Lead Iodide Perovskites with Organic Cations: Phase Transitions, High Mobilities, and near-Infrared Photoluminescent Properties. *Inorg. Chem.* **2013**, *52* (15), 9019–9038.
- (13) Song, T. Bin; Yokoyama, T.; Stoumpos, C. C.; Logsdon, J.; Cao, D. H.; Wasielewski, M. R.; Aramaki, S.; Kanatzidis, M. G. Importance of Reducing Vapor

Atmosphere in the Fabrication of Tin-Based Perovskite Solar Cells. *J. Am. Chem. Soc.* **2017**, *139* (2), 836–842.

(14) Konstantakou, M.; Stergiopoulos, T. A Critical Review on Tin Halide Perovskite Solar Cells. *J. Mater. Chem. A* **2017**, *5* (23), 11518–11549.

(15) Li, B.; Long, R.; Xia, Y.; Mi, Q. All-Inorganic Perovskite CsSnBr₃ as a Thermally Stable, Free-Carrier Semiconductor. *Angew. Chemie Int. Ed.* **2018**, *130* (40), 13338–13342.

(16) Peedikakkandy, L.; Bhargava, P. Composition Dependent Optical, Structural and Photoluminescence Characteristics of Cesium Tin Halide Perovskites. *RSC Adv.* **2016**, *6* (24), 19857–19860.

(17) Sabba, D.; Mulmudi, H. K.; Prabhakar, R. R.; Krishnamoorthy, T.; Baikie, T.; Boix, P. P.; Mhaisalkar, S.; Mathews, N. Impact of Anionic Br- Substitution on Open Circuit Voltage in Lead Free Perovskite (CsSnI_{3-x}Br_x) Solar Cells. *J. Phys. Chem. C* **2015**, *119* (4), 1763–1767.

(18) McMeekin, D. P.; Sadoughi, G.; Rehman, W.; Eperon, G. E.; Saliba, M.; Hörlantner, M. T.; Haghighirad, A.; Sakai, N.; Korte, L.; Rech, B.; et al. A Mixed-Cation Lead Mixed-Halide Perovskite Absorber for Tandem Solar Cells. *Science* **2016**, *351* (6269), 151–155.

(19) Jellicoe, T. C.; Richter, J. M.; Glass, H. F. J.; Tabachnyk, M.; Brady, R.; Dutton, S. E.; Rao, A.; Friend, R. H.; Credgington, D.; Greenham, N. C.; et al. Synthesis and Optical Properties of Lead-Free Cesium Tin Halide Perovskite Nanocrystals. *J. Am. Chem. Soc.* **2016**, *138* (9), 2941–2944.

(20) Yuan, F.; Xi, J.; Dong, H.; Xi, K.; Zhang, W.; Ran, C.; Jiao, B.; Hou, X.; Jen, A. K. Y.; Wu, Z. All-Inorganic Hetero-Structured Cesium Tin Halide Perovskite Light-Emitting Diodes With Current Density Over 900 A Cm⁻² and Its Amplified Spontaneous Emission Behaviors. *Phys. Status Solidi - Rapid Res. Lett.* **2018**, *12* (5), 1800090.

(21) Yamada, K.; Kuranaga, Y.; Ueda, K.; Goto, S.; Okuda, T.; Furukawa, Y. Phase Transition and Electric Conductivity of ASnCl₃ (A = Cs and CH₃NH₃). *Bull. Chem. Soc. Jpn.* **1998**, *71* (1), 127–134.

- (22) Mori, M.; Saito, H. An X-Ray Study of Successive Phase Transitions in CsSnBr₃. *J. Phys. C Solid State Phys.* **1986**, *19* (14), 2391–2401.
- (23) R. E. Wasylshen; Knop, O.; Macdonald, J. B. Cation Rotation in Methylammonium Lead Halides. *Solid State Commun.* **1985**, *56*, 581–582.
- (24) Bernard, G. M.; Wasylshen, R. E.; Ratcliffe, C. I.; Terskikh, V.; Wu, Q.; Buriak, J. M.; Hauger, T. Methylammonium Cation Dynamics in Methylammonium Lead Halide Perovskites: A Solid-State NMR Perspective. *J. Phys. Chem. A* **2018**, *122* (6), 1560–1573.
- (25) Rosales, B. A.; Men, L.; Cady, S. D.; Hanrahan, M. P.; Rossini, A. J.; Vela, J. Persistent Dopants and Phase Segregation in Organolead Mixed-Halide Perovskites. *Chem. Mater.* **2016**, *28* (19), 6848–6859.
- (26) Wouter M. J. Franssen; Es, S. G. D. van; Dervişoğlu, R.; Wijs, G. A. de; Kentgens, A. P. M. Symmetry, Dynamics, and Defects in Methylammonium Lead Halide Perovskites. *J. Phys. Chem. Lett.* **2017**, *8*, 61–66.
- (27) Senocrate, A.; Moudrakovski, I.; Kim, G. Y.; Yang, T.; Gregori, G.; Grätzel, M.; Maier, J. The Nature of Ion Conduction in Methylammonium Lead Iodide: A Multimethod Approach. *Angew. Chemie Int. Ed.* **2017**, *56* (27), 7755–7759.
- (28) Senocrate, A.; Moudrakovski, I.; Acartürk, T.; Merkle, R.; Kim, G. Y.; Starke, U.; Grätzel, M.; Maier, J. Slow CH₃NH₃⁺ Diffusion in CH₃NH₃PbI₃ under Light Measured by Solid-State NMR and Tracer Diffusion. *J. Phys. Chem. C* **2018**, *122* (38), 21803–21806.
- (29) Karmakar, A.; Askar, A. M.; Bernard, G. M.; Terskikh, V. V.; Ha, M.; Patel, S.; Shankar, K.; Michaelis, V. K. Mechanochemical Synthesis of Methylammonium Lead Mixed-Halide Perovskites: Unraveling the Solid-Solution Behavior Using Solid-State NMR. *Chem. Mater.* **2018**, *30*, 2309–2321.
- (30) Askar, A. M.; Karmakar, A.; Bernard, G. M.; Ha, M.; Terskikh, V. V.; Wiltshire, B. D.; Patel, S.; Fleet, J.; Shankar, K.; Michaelis, V. K. Composition-Tunable Formamidinium Lead Mixed Halide Perovskites via Solvent-Free Mechanochemical Synthesis: Decoding the Pb Environments Using Solid-State NMR Spectroscopy. *J. Phys. Chem. Lett.* **2018**, *9* (10), 2671–2677.

- (31) Kubicki, D. J.; Prochowicz, D.; Hofstetter, A.; Zakeeruddin, S. M.; Grätzel, M.; Emsley, L. Phase Segregation in Cs-, Rb- and K-Doped Mixed-Cation (MA)_x(FA)_{1-x}PbI₃ Hybrid Perovskites from Solid-State NMR. *J. Am. Chem. Soc.* **2017**, *139* (40), 14173–14180.
- (32) Franssen, W. M. J.; Kentgens, A. P. M. Solid-State NMR of Hybrid Halide Perovskites. *Solid State Nucl. Magn. Reson.* **2019**, *100*, 36–44.
- (33) Kubicki, D. J.; Prochowicz, D.; Hofstetter, A.; Saski, M.; Yadav, P.; Bi, D.; Pellet, N.; Lewiński, J.; Zakeeruddin, S. M.; Grätzel, M.; Emsley, L. Formation of Stable Mixed Guanidinium-Methylammonium Phases with Exceptionally Long Carrier Lifetimes for High-Efficiency Lead Iodide-Based Perovskite Photovoltaics. *J. Am. Chem. Soc.* **2018**, *140*, 3345–3351.
- (34) Karmakar, A.; Dodd, M. S.; Agnihotri, S.; Ravera, E.; Michaelis, V. K. Cu(II)-Doped Cs₂SbAgCl₆ Double Perovskite: A Lead-Free, Low-Bandgap Material. *Chem. Mater.* **2018**, *30*, 8280–8290.
- (35) Karmakar, A.; Bernard, G. M.; Meldrum, A.; Oliynyk, A. O.; Michaelis, V. K. Tailorable Indirect to Direct Bandgap Double Perovskites with Bright White-Light Emission: Decoding Chemical Structure Using Solid-State NMR. *J. Am. Chem. Soc.* **2020**, *142*, 10780–10793.
- (36) Aebli, M.; Piveteau, L.; Nazarenko, O.; Benin, B. M.; Krieg, F.; Verel, R.; Kovalenko, M. V. Lead-Halide Scalar Couplings in ²⁰⁷Pb NMR of APbX₃ Perovskites (A = Cs, Methylammonium, Formamidinium; X = Cl, Br, I). *Sci. Rep.* **2020**, *10*, 8229.
- (37) Piveteau, L.; Aebli, M.; Yazdani, N.; Millen, M.; Korosec, L.; Krieg, F.; Benin, B. M.; Morad, V.; Piveteau, C.; Shiroka, T.; Comas-Vives, A.; Copéret, C.; Lindenberg, A. M.; Wood, V.; Verel, R.; Kovalenko, M. V. Bulk and Nanocrystalline Cesium Lead-Halide Perovskites as Seen by Halide Magnetic Resonance. *ACS Cent. Sci.* **2020**, *6*, 1138–1149.
- (38) Piveteau, L.; Morad, V.; Kovalenko, M. V. Solid-State NMR and NQR Spectroscopy of Lead-Halide Perovskite Materials. *J. Am. Chem. Soc.* **2020**, *142*, 19413–19437.

- (39) Chen, Y.; Smock, S. R.; Flintgruber, A. H.; Perras, F. A.; Brutchey, R. L.; Rossini, A. J. Surface Termination of CsPbBr₃ Perovskite Quantum Dots Determined by Solid-State NMR Spectroscopy. *J. Am. Chem. Soc.* **2020**, *142* (13), 6117–6127.
- (40) Kubicki, D. J.; Prochowicz, D.; Hofstetter, A.; Walder, B. J.; Emsley, L. ¹¹³Cd Solid-State NMR at 21.1 T Reveals the Local Structure and Passivation Mechanism of Cadmium in Hybrid and All-Inorganic Halide Perovskites. *ACS Energy Lett.* **2020**, *5*, 2964–2971.
- (41) Karmakar, A.; Dodd, M. S.; Zhang, X.; Oakley, M. S.; Klobukowski, M.; Michaelis, V. K. Mechanochemical Synthesis of 0D and 3D Cesium Lead Mixed Halide Perovskites. *Chem. Commun.* **2019**, *55*, 5079–5082.
- (42) Prochowicz, D.; Yadav, P.; Saliba, M.; Kubicki, D. J.; Tavakoli, M. M.; Zakeeruddin, S. M.; Lewiński, J.; Emsley, L.; Grätzel, M. One-Step Mechanochemical Incorporation of an Insoluble Cesium Additive for High Performance Planar Heterojunction Solar Cells. *Nano Energy* **2018**, *49*, 523–528.
- (43) Ha, M.; Karmakar, A.; Bernard, G. M.; Basilio, E.; Krishnamurthy, A.; Askar, A. M.; Shankar, K.; Kroeker, S.; Michaelis, V. K. Phase Evolution in Methylammonium Tin Halide Perovskites with Variable Temperature Solid-State ¹¹⁹Sn NMR Spectroscopy. *J. Phys. Chem. C* **2020**, *124*, 15015–15027.
- (44) Kubicki, D. J.; Prochowicz, D.; Salager, E.; Rakhmatullin, A.; Grey, C. P.; Emsley, L.; Stranks, S. D. Local Structure and Dynamics in Methylammonium, Formamidinium and Cesium Tin(II) Mixed-halide Perovskites from ¹¹⁹Sn Solid-state NMR. *J. Am. Chem. Soc.* **2020**, *142*, 7813–7826.
- (45) Yamada, K.; Fujise, K.; Hino, S.; Yamane, Y.; Nakagama, T. Characterization of Sn(II)-Based Perovskites by XRD, DTA, NQR and ¹¹⁹Sn NMR for Photovoltaic Applications. *Chem. Lett.* **2019**, *48* (7), 749–752.
- (46) Wrackmeyer, B. Application of ¹¹⁹Sn NMR Parameters. In *Annu. Rep. NMR Spectrosc.* 1999; Vol. 38, pp 203–264.
- (47) Wolf, P.; Valla, M.; Rossini, A. J.; Comas-Vives, A.; Núñez-Zarur, F.; Malaman, B.; Lesage, A.; Emsley, L.; Copéret, C.; Hermans, I. NMR Signatures of the Active Sites in Sn-β Zeolite. *Angew. Chemie - Int. Ed.* **2014**, *53* (38), 10179–10183.

- (48) Wolf, P.; Valla, M.; Núñez-Zarur, F.; Comas-Vives, A.; Rossini, A. J.; Firth, C.; Kallas, H.; Lesage, A.; Emsley, L.; Copéret, C.; Hermans, I. Correlating Synthetic Methods, Morphology, Atomic-Level Structure, and Catalytic Activity of Sn- β Catalysts. *ACS Catal.* **2016**, *6* (7), 4047–4063.
- (49) Grykałowska, A.; Nowak, B. High-Resolution Solid-State ^{119}Sn and ^{195}Pt NMR Studies of MPtSn Semiconductors (M = Ti, Zr, Hf, Th). *Solid State Nucl. Magn. Reson.* **2005**, *27* (4), 223–227.
- (50) Barrett, J.; Bird, S. R. A.; Donaldson, J. D.; Silver, J. The Mossbauer Effect in Tin(II) Compounds. *J. Chem. Soc. A* **1971**, 3105–3108.
- (51) Poilsen, F. R.; Rasmussen, S. E. Crystal Structure and Phase Transition of Cesium Trichlorostannate(II). *Acta Chem. Scand.* **1970**, *24*, 150–156.
- (52) Oranskaia, A.; Yin, J.; Bakr, O. M.; Brédas, J. L.; Mohammed, O. F. Halogen Migration in Hybrid Perovskites: The Organic Cation Matters. *J. Phys. Chem. Lett.* **2018**, *9*, 5474–5480.
- (53) Hong, Z.; Tan, D.; John, R. A.; Tay, Y. K. E.; Ho, Y. K. T.; Zhao, X.; Sum, T. C.; Mathews, N.; García, F.; Soo, H. Sen. Completely Solvent-Free Protocols to Access Phase-Pure, Metastable Metal Halide Perovskites and Functional Photodetectors from the Precursor Salts. *iScience* **2019**, *16*, 312–325.
- (54) Moran, R. F.; McKay, D.; Tornstrom, P. C.; Aziz, A.; Fernandes, A.; Grau-Crespo, R.; Ashbrook, S. E. Ensemble-Based Modeling of the NMR Spectra of Solid Solutions: Cation Disorder in $\text{Y}_2(\text{Sn},\text{Ti})_2\text{O}_7$. *J. Am. Chem. Soc.* **2019**, *141* (44), 17838–17846.
- (55) Ashbrook, S. E.; Whittle, K. R.; Lumpkin, G. R.; Farnan, I. ^{89}Y Magic-Angle Spinning NMR of $\text{Y}_2\text{Ti}_{2-x}\text{Sn}_x\text{O}_7$ Pyrochlores. *J. Phys. Chem. B* **2006**, *110* (21), 10358–10364.
- (56) Kubicki, D. J.; Sasaki, M.; Macpherson, S.; Gałkowski, K.; Lewiński, J.; Prochowicz, D.; Titman, J. J.; Stranks, S. D. Halide Mixing and Phase Segregation in $\text{Cs}_2\text{AgBiX}_6$ (X = Cl, Br, and I) Double Perovskites from Cesium-133 Solid-State NMR and Optical Spectroscopy. *Chem. Mater.* **2020**, *32* (19), 8129–8138.
- (57) Sharp, R. R. Rotational Diffusion and Magnetic Relaxation of ^{119}Sn in Liquid SnCl_4 and SnI_4 . *J. Chem. Phys.* **1972**, *57* (12), 5321–5330.

- (58) Sharp, R. R. Field Dependence of Nuclear Magnetic Relaxation of ^{119}Sn in SnCl_4 , SnBr_4 , and SnI_4 . *J. Chem. Phys.* **1974**, *60* (3), 1149–1157.
- (59) Prochowicz, D.; Franckevicius, M.; Cieslak, A. M.; Zakeeruddin, S. M.; Graetzel, M.; Lewinski, J. Mechanochemical Synthesis of the Hybrid Perovskite $\text{CH}_3\text{NH}_3\text{PbI}_3$: Characterization and the Corresponding Solar Cell Efficiency. *J. Mater. Chem. A* **2015**, *3*, 20772–20777.
- (60) Prochowicz, D.; Yadav, P.; Saliba, M.; Sasaki, M.; Zakeeruddin, S. M.; Lewiński, J.; Grätzel, M. Mechanochemical Synthesis of Pure Phase Mixed-Cation $\text{MA}_x\text{FA}_{1-x}\text{PbI}_3$ Hybrid Perovskites: Photovoltaic Performance and Electrochemical Properties. *Sustain. Energy Fuels* **2017**, *1* (4), 689–693.
- (61) Friščić, T. Metal-Organic Frameworks: Mechanochemical Synthesis Strategies. In *Encyclopedia of Inorganic and Bioinorganic Chemistry*; Major Reference Works; 2014; p DOI: 10.1002/9781119951438.eibc2202.
- (62) James, S. L.; Adams, C. J.; Bolm, C.; Braga, D.; Collier, P.; Friscic, T.; Grepioni, F.; Harris, K. D. M.; Hyett, G.; Jones, W.; et al. Mechanochemistry: Opportunities for New and Cleaner Synthesis. *Chem. Soc. Rev.* **2012**, *41*, 413–447.
- (63) Chen, B.; Yang, M.; Zheng, X.; Wu, C.; Li, W.; Yan, Y.; Bisquert, J.; Garcia-Belmonte, G.; Zhu, K.; Priya, S. Impact of Capacitive Effect and Ion Migration on the Hysteretic Behavior of Perovskite Solar Cells. *J. Phys. Chem. Lett.* **2015**, *6* (23), 4693–4700.
- (64) Yuan, Y.; Huang, J. Ion Migration in Organometal Trihalide Perovskite and Its Impact on Photovoltaic Efficiency and Stability. *Acc. Chem. Res.* **2016**, *49* (2), 286–293.
- (65) Calado, P.; Telford, A. M.; Bryant, D.; Li, X.; Nelson, J.; O'Regan, B. C.; Barnes, P. R. F. Evidence for Ion Migration in Hybrid Perovskite Solar Cells with Minimal Hysteresis. *Nat. Commun.* **2016**, *7*, 13831.
- (66) Eames, C.; Frost, J. M.; Barnes, P. R. F.; O'Regan, B. C.; Walsh, A.; Islam, M. S. Ionic Transport in Hybrid Lead Iodide Perovskite Solar Cells. *Nat. Commun.* **2015**, *6*, 7497.

- (67) Yamada, K.; Kawaguchi, H.; Matsui, T.; Okuda, T.; Ichiba, S. Structural Phase Transition and Electrical Conductivity of the Perovskite $\text{CH}_3\text{NH}_3\text{Sn}_{1-x}\text{Pb}_x\text{Br}_3$ and CsSnBr_3 . *Bull. Chem. Soc. Jpn.* **1990**, *63*, 2521–2525.
- (68) Onoda-Yamamoto, N.; Matsuo, T.; Suga, H. Thermal, Electric, and Dielectric Properties of $\text{CH}_3\text{NH}_3\text{SnBr}_3$ at Low Temperatures. *J. Chem. Thermodyn.* **1991**, *23* (39), 987–999.
- (69) Futscher, M. H.; Lee, J. M.; McGovern, L.; Muscarella, L. A.; Wang, T.; Haider, M. I.; Fakharuddin, A.; Schmidt-Mende, L.; Ehrler, B. Quantification of Ion Migration in $\text{CH}_3\text{NH}_3\text{PbI}_3$ Perovskite Solar Cells by Transient Capacitance Measurements. *Mater. Horizons* **2019**, *6* (7), 1497–1503.
- (70) Mizusaki, J.; Arai, K.; Fueki, K. Ionic Conduction of the Perovskite-Type Halides. *Solid State Ionics* **1983**, *11*, 203–211.
- (71) Xia, T.; Li, Y.; Huang, L.; Ji, W.; Yang, M.; Zhao, X. Room-Temperature Stable Inorganic Halide Perovskite as Potential Solid Electrolyte for Chloride Ion Batteries. *ACS Appl. Mater. Interfaces* **2020**, *12*, 18634–18641.
- (72) Titilayo A. Kuku. Ionic Conductivity of SnI_2 . *Solid State Ionics* **1986**, *20*, 217–222.
- (73) Hoshino, H.; Yamazaki, M.; Nakamura, Y.; Shimoji, M. Ionic Conductivity of Lead Chloride Crystals. *J. Phys. Soc. Japan* **1969**, *26*, 1422–1426.
- (74) Hoshino, H.; Yokose, S.; Shimoji, M. Ionic Conductivity of Lead Bromide Crystals. *J. Solid State Chem.* **1973**, *7*, 1–6.
- (75) Walsh, A.; Scanlon, D. O.; Chen, S.; Gong, X. G.; Wei, S. H. Self-Regulation Mechanism for Charged Point Defects in Hybrid Halide Perovskites. *Angew. Chemie - Int. Ed.* **2015**, *54* (6), 1791–1794.
- (76) Indris, S.; Scheuermann, M.; Becker, S. M.; Šepelák, V.; Kruk, R.; Suffner, J.; Gyger, F.; Feldmann, C.; Ulrich, A. S.; Hahn, H. Local Structural Disorder and Relaxation in SnO_2 Nanostructures Studied by ^{119}Sn MAS NMR and ^{119}Sn Mössbauer Spectroscopy. *J. Phys. Chem. C* **2011**, *115* (14), 6433–6437.
- (77) Barnes, R. G. Temperature Dependence of the Isotropic and Anisotropic Knight Shift in Polycrystalline Cadmium and β -Tin. *J. Phys. Chem. Solids* **1966**, *27*, 567–573.

CHAPTER 4

Cu(II)-Doped Cs₂SbAgCl₆ Double Perovskite: A Lead-Free, Low-Bandgap Material^{R₃}

4.1 Introduction

With an impressive increase in photoconversion efficiency (PCE) within the past decade,^{1,2} hybrid organic–inorganic lead halide perovskites have prompted global research due to their potential use in high-efficiency solar cell technologies. However, despite their promising electronic properties and low production costs for photovoltaic and optoelectronic applications,^{3–8} commercialization of lead halide perovskites has been hindered by their instability^{9,10} as well as by long-term health and environmental concerns^{11,12} mostly related to the leaching of Pb²⁺ due to their water solubility.^{13–15}

The general formula for perovskites of recent interest in photovoltaic research is ABX₃, where A = Cs⁺, MA⁺, or FA⁺ (MA = methylammonium, FA = formamidinium), B = Pb²⁺ or Sn²⁺, and X = Cl⁻, Br⁻, or I⁻. An important property of these compounds is their bandgap tunability, achieved by modifications of the A, B, and X positions. To improve the photovoltaic efficiency and stability of metal halide perovskites, alternative synthetic design approaches have included the incorporation of A-site mixed cations^{6,16–18} and mixed halides^{19,20} as well as isovalent (Sn²⁺, Co²⁺, Sr²⁺)^{21–23} or heterovalent (Bi³⁺, Au³⁺, In³⁺)²⁴ B-site cations. These modifications influence the photovoltaic performance and optical properties and can lead to enhanced stability.^{25–27} Although MASnI₃ is an attractive less toxic alternative to the isoelectronic Pb²⁺ sister materials, displaying a bandgap of 1.15 eV,²⁸ it is unstable under ambient conditions due to rapid oxidation to Sn⁴⁺ which negatively impacts the photovoltaic properties of the material.²⁹

^{R₃} The contents of this chapter have been copied and/or adapted from the following publication: Karmakar, A.; Dodd, M. S.; Agnihotri, S.; Ravera, E.; Michaelis, V. K. Cu(II)-Doped Cs₂SbAgCl₆ Double Perovskite: A Lead-Free, Low-Bandgap Material. *Chem. Mater.* **2018**, *30*, 8280–8290. The supplementary data for this chapter is available in Appendix C: Experimental section, Tables C1–C6 and Figures C1–C16.

Recent research has shown that replacing the B-site cation with a combination of trivalent (B'), and monovalent (B'') cations results in the formation of $A_2B'B''X_6$ double perovskites that mimic the ABX_3 perovskite structure while displaying enhanced air and moisture stability,^{30–35} as well as bandgap tunability.^{36–38} For example, Cs_2BiAgX_6 ($X = Cl, Br$) shows visible light absorption with indirect bandgaps of 2.77 and 1.95 eV for $X = Cl$ and Br , respectively.^{30,32} Similar bandgap tunability also has been observed by alloying of Sb^{3+} and In^{3+} in $Cs_2BiAgBr_6$.³⁶ In 2017, Deng et al.³⁹ successfully synthesized $Cs_2SbAgCl_6$ double perovskites with an indirect bandgap of 2.6 eV, while Tran et al.³⁷ prepared a series of B'-site mixed-cationic $Cs_2(Sb_xIn_{1-x})AgCl_6$ ($0 \leq x \leq 1$) double perovskites that show an indirect to direct bandgap modification. The structural and photophysical properties of nanocrystals,^{40,41} low-dimensional (i.e., 2D) double perovskites,⁴² hysteresis-free solar cells,⁴³ and highly stable thin films⁴⁴ of $Cs_2BiAgBr_6$ double perovskite have recently been reported. A small bandgap Tl-containing $Cs_2AgTlBr_6$ double perovskite has emerged,⁴⁵ unfortunately, the acute toxicity of thallium makes it ill-suited to replace lead. A new class of layered double perovskite, namely, $Cs_4CuSb_2Cl_{12}$, displays a reduced bandgap, although at the cost of photovoltaic efficiency due to the restriction in structural dimensionality.^{46,47} The search continues for a less-toxic, low-bandgap (ca. 1–1.4 eV) 3D double perovskite material synthesized from inexpensive and highly abundant elements.

Altering the optical and electronic properties for semiconductors is an attractive approach in modern device applications.^{48,49} For example, homo- and heterovalent metal ion doped lead halide perovskites have been reported to enhance the optical and electronic properties of both nanocrystalline^{50–53} and bulk materials.^{24,29,54} Likewise, double perovskites can be modified through a similar metal doping approach. For example, Slavney et al.³⁸ reduced the bandgap of $Cs_2BiAgBr_6$ by successful Tl doping, and Nandha and Nag⁵⁵ enhanced the visible light emission properties of $Cs_2InAgCl_6$ via Mn^{2+} doping.

The ns^2 outer shell electronic configuration of the B-site in the 3D ABX_3 ($B = Pb^{2+}, Sn^{2+}$) perovskite structure is responsible for strong direct bandgap absorption and superior photovoltaic properties. Occupied and unoccupied $6s^2$ and $6p^0$ orbitals,

respectively, of Pb^{2+} contribute to form valence band maximum (VBM) and conduction band minimum (CBM), respectively.⁵⁶ $\text{A}_2\text{B}'\text{B}''\text{X}_6$ double perovskites allow a large diversity of B'- and B''-sites and hence diverse orbital compositions in its band edges. Because double perovskite materials exhibit dominant metal-to-metal charge transfer (MMCT), their electronic band structure relies heavily on the energies of B'- and B''-site metals' frontier orbitals.⁴⁵ For example, it has been shown when Pb^{2+} is replaced with isoelectronic Bi^{3+} and Tl^+ in $\text{MA}_2\text{BiTiBr}_6$, a direct bandgap material is formed, whereas replacing Tl^+ with Ag^+ yields an indirect bandgap material, $\text{Cs}_2\text{BiAgBr}_6$.^{32,38} Similarly, the $\text{Cs}_2\text{SbAgCl}_6$ double perovskite shows an indirect bandgap transition, where the Sb-5s/Ag-4d and Sb-5p orbitals are the main contributors to the VBM and CBM, respectively.³⁷ Vargas et al. have reported a layered 2D double perovskite, $\text{Cs}_4\text{Sb}_2\text{CuCl}_{12}$, that exhibits a direct transition with a narrow bandgap (ca. 1 eV) due to the presence of an unpaired electron in Cu^{2+} ($3d^9$ configuration).⁴⁶ The $[\text{CuCl}_6]^{4-}$ octahedra are inserted between $[\text{SbCl}_6]^{3-}$ layers, corner sharing to each $[\text{SbCl}_6]^{3-}$ neighbor in the extended crystalline structure. These corner-shared octahedra are similar to the 3D perovskite network, which is crucial for their major photovoltaic success in lead-halide perovskites.⁵⁶ The much smaller bandgap of $\text{Cs}_4\text{Sb}_2\text{CuCl}_{12}$ is due to favorable orbital overlap of the Cu-3d orbitals with Cl and Sb orbitals, which broadens the VBM and minimizes the bandgap.⁴⁶ We hypothesized that dilute incorporation of $3d^9$ orbitals near the VBM of $\text{Cs}_2\text{SbAgCl}_6$ may allow us to narrow the bandgap while the 3D double perovskite structural network remains unaltered. A closely related band edge modification has been reported by describing energy- and symmetry-matching of Tl-doped $\text{Cs}_2\text{BiAgBr}_6$ double perovskite.³⁸ These observations inspired us to investigate the possibility of preparing de novo doped 3D double perovskite materials that yield reduced optical bandgaps for photovoltaic applications while maintaining desirable practical properties. Herein, we describe the synthesis of a lead-free, inexpensive, and highly abundant element, heterovalent Cu^{2+} doping analogue of $\text{Cs}_2\text{SbAgCl}_6$ with a bandgap of ca. 1 eV.

Solid-state nuclear magnetic resonance (NMR) spectroscopy is a powerful analytical tool that allows one to characterize atomic-level short- and medium-range structure, as well as dynamics in hybrid perovskites.^{15,57-71} NMR spectroscopy was

used to decode the local atomic structure of the $\text{Cs}_2\text{SbAgCl}_6$ parent and Cu^{2+} -doped $\text{Cs}_2\text{SbAgCl}_6$ double perovskite materials. In addition to NMR spectroscopy, powder X-ray diffraction (PXRD) was used to confirm the crystalline structure and phase purity, while optical properties were obtained using diffuse reflectance (DR). Materials were further characterized using field emission scanning electron microscopy (FESEM), energy dispersive X-ray (EDX), electron paramagnetic resonance (EPR), and thermogravimetric analysis (TGA) techniques. Finally, the long-term stability to environmental thermal and humidity stimuli of the materials was tested to assess their potential for long-term use as photovoltaic materials.

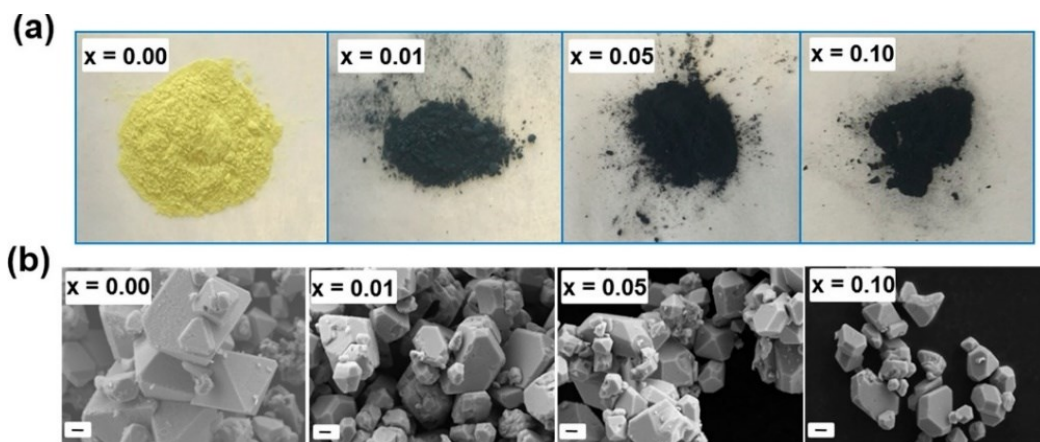


Figure 4.1. (a) Photographs and (b) FESEM images of $\text{Cs}_2\text{SbAgCl}_6$ (i.e., $x = 0.00$) and Cu^{2+} -doped polycrystalline materials. Here, the x values indicate nominal Cu^{2+} loading (see the Appendix C). The scale bar at the lower left of the FESEM images is 2 μm .

4.2 Results and Discussion

The polycrystalline antimony–silver-based double perovskite, $\text{Cs}_2\text{SbAgCl}_6$, was doped with Cu^{2+} by synthetic loading via solvent synthesis to produce $\text{Cs}_2\text{Sb}_{1-a}\text{Ag}_{1-b}\text{Cu}_{2x}\text{Cl}_6$ ($a + b = 2x$, $x = 0.00$ (i.e., parent compound), 0.01, 0.05, and 0.10). The nominal composition is reported due to the low Cu concentrations and associated challenges in elemental analysis of these materials (Table C1). Figure 4.1 shows photographs and the corresponding FESEM images for the $\text{Cs}_2\text{SbAgCl}_6$ parent and the Cu^{2+} -doped materials. The FESEM images confirm that the

materials are composed of multifaced micrometer-sized polycrystals. The PXRD pattern (Figure 4.2a and Figure C1) of $\text{Cs}_2\text{SbAgCl}_6$, which matches earlier reports,³⁹ indicates a face-centered cubic double perovskite structure ($Fm\bar{3}m$ space group) with $a = b = c = 10.699 \text{ \AA}$ unit cell dimensions. The nearly identical PXRD patterns for $\text{Cs}_2\text{SbAgCl}_6$ and the doped materials indicate single-phase crystalline solids.

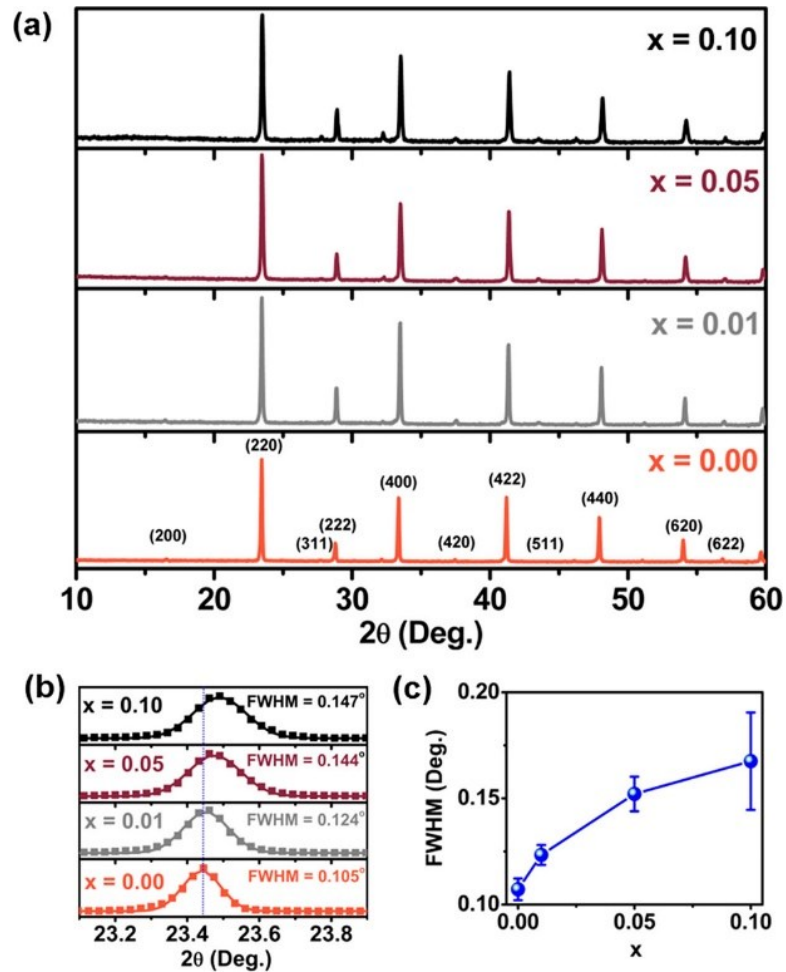
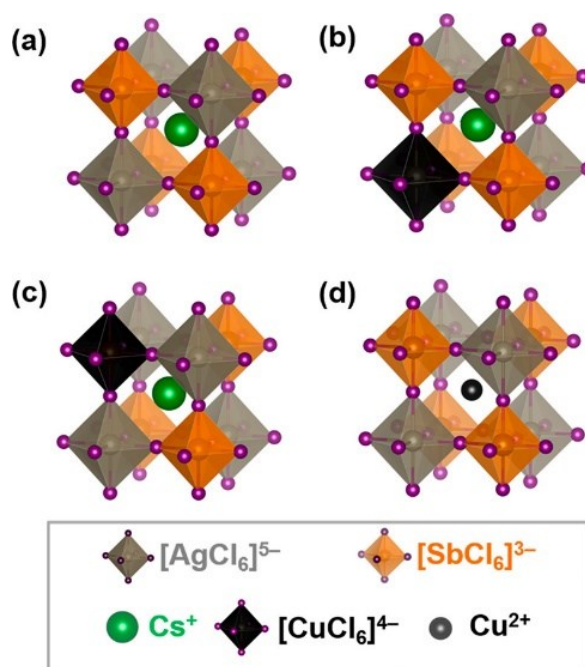


Figure 4.2. (a) Powder XRD patterns for $\text{Cs}_2\text{SbAgCl}_6$ ($x = 0.00$) and for Cu^{2+} -doped $\text{Cs}_2\text{SbAgCl}_6$ materials. An expansion of the highly intense (220) peak in the PXRD patterns is shown in (b), illustrating its shift toward higher 2θ values and its broadening as the Cu^{2+} content increases from $x = 0.00$ to 0.10. The dotted line is a guide for the eye. (c) FWHM values of PXRD patterns as a function of Cu^{2+} content ($x = 0.00$ –0.10).

Closer examination of the PXRD patterns (Figure C2) indicates trace quantities of AgCl in the parent material, with increasing AgCl concentration as Cu is incorporated into the sample. Qualitatively, these findings may suggest that $[\text{AgCl}_6]^{5-}$ octahedra in the $\text{Cs}_2\text{SbAgCl}_6$ double perovskite lattice are being replaced with $[\text{CuCl}_6]^{4-}$ octahedra upon Cu^{2+} doping, forming vacancies to maintain charge balance and causing the formation of insoluble AgCl. The elemental analysis of these materials using EDX spectroscopy (Table C1) provides a clearer interpretation, indicating a decrease in Ag^+ concentration with increasing Cu^{2+} doping, while the concentrations of Cs^+ , Sb^{3+} , and Cl^- are, within experimental uncertainty, unchanged. Note that the initial $\text{Sb}^{3+}:\text{Ag}^+$ loading ratios are kept constant at the beginning of the synthesis for all samples (see the Appendix C).



Scheme 4.1. Schematic representation of the (a) $\text{Cs}_2\text{SbAgCl}_6$ double perovskite structure and of possible Cu^{2+} -doped analogues where $[\text{CuCl}_6]^{4-}$ replaces (b) $[\text{AgCl}_6]^{5-}$ or (c) $[\text{SbCl}_6]^{3-}$ or (d) where Cu^{2+} replaces Cs^+ , leading to a formation of a neighboring vacancy.

Scheme 4.1a displays the crystal structure of the $\text{Cs}_2\text{SbAgCl}_6$ double perovskite, showing that $[\text{SbCl}_6]^{3-}$ and $[\text{AgCl}_6]^{5-}$ octahedra are coordinated to each other in alternating corner-sharing configurations with a Cs^+ ion residing at the center of the cuboctahedra, thus maintaining an extended 3D perovskite crystal structure. There are, in principle, three positions in which Cu^{2+} can be incorporated into a double perovskite crystal lattice: the $[\text{AgCl}_6]^{5-}$ or the $[\text{SbCl}_6]^{3-}$ octahedra may be replaced with $[\text{CuCl}_6]^{4-}$ (Scheme 4.1b or 3.1c, respectively), or Cu^{2+} may occupy an A-site of the lattice (Scheme 4.1d), leading to the formation of a neighboring vacancy. Because of the large difference in the Pauling electronegativity (χ_P) of Cs (0.79) compared to that of Cu (1.90), a structure that includes six covalent Cu–Cl bonds rather than 12 Cu–Cl ionic interactions is favored. Additionally, since χ_P for Ag (1.93) is very close to that for Cu but significantly different from that for Sb (2.05), the $[\text{CuCl}_6]^{4-}$ octahedra in the doped material are expected to primarily replace the $[\text{AgCl}_6]^{5-}$ octahedra, as illustrated in Scheme 4.1b. In summary, we hypothesize that substitution of Ag^+ by Cu^{2+} produces a Ag^+ cationic vacancy to maintain charge balance neutrality of the doped materials. The EPR spectra (vide infra) of the sample at the lowest copper loading are consistent with the presence of tetragonally distorted $[\text{CuCl}_6]^{4-}$ octahedra:^{72–74} the spectrum is substantially axial, with the downfield g_{\parallel} feature, ~ 2.3 , sizably broadened by unresolved hyperfine couplings and with the g_{\perp} component, ~ 2.0 , shifted slightly upfield with respect to literature values. With increased doping, a peak at ~ 2.15 appears, indicating the presence of exchange-coupled copper pairs.⁷⁵ This intriguing observation suggests that copper–copper pairs form with a higher than statistical probability. Exchange coupling is expected to emerge because of the interaction of the electrons on one copper center with electrons on another copper center, through the orbitals of intervening nonmagnetic atoms between them.⁷⁵ This can happen through two bonds, as it would be for a Cu–Cl–Cu arrangement as well as through four bonds, as it would be for a Cu–Cl–M–Cl–Cu arrangement. A tempting explanation for the observed EPR spectrum is the formation of Cu–Cl–Cu pairs in the form of two elongated octahedra that share a vertex and have orthogonal elongation axes. The emergence of such Cu–Cu pairs if the substitution was random would be expected

around 6%, 30%, and 60% for $x = 0.01$, 0.05, and 0.1 Cu^{2+} -doped materials, respectively, including triplets and quartets.

The ionic radius for Cu^{2+} (0.87 Å) is slightly less than that for Sb^{3+} (0.90 Å) and significantly less than that for Ag^+ (1.29 Å);⁷⁶ thus, a decrease in the lattice parameter due to the incorporation of Cu^{2+} into the crystal lattice is expected. For example, Figure 4.2b shows that the highly intense (220) peak in the PXRD pattern shifts slightly toward a higher 2θ value with copper incorporation, suggesting that the average lattice parameters are decreasing for the doped materials and that the Cu^{2+} ion has substituted into the lattice. The full width at half-maximum (FWHM) of the diffraction peaks also increases systematically with increasing dopant concentration. These results imply local nonuniform microstrain structural defects in our doped materials (see below).⁷⁷ Such defects have also been observed in heterovalent Bi^{3+} doping of the MAPbBr_3 perovskite.⁷⁸ We have computed the extent of microstrain by measuring the FWHM values of the PXRD peaks in our materials with and without Cu^{2+} doping. The steadily increasing FWHM values (Figure 4.2c) are consistent with increased Cu^{2+} incorporation into the crystal lattice.

Similar to other halide double perovskites,^{30,38} $\text{Cs}_2\text{SbAgCl}_6$ shows characteristics of a material with an indirect bandgap.^{37,39} Figure 4.3a shows the DR and normalized absorbance spectrum of the $\text{Cs}_2\text{SbAgCl}_6$ parent and of the Cu^{2+} -doped ($x = 0.10$) double perovskites (see Figure C3 for the complete set of the series), which indicate a dramatic shift of the optical band edge upon Cu^{2+} doping. The Tauc plots (Figure 4.3b,c) show that Cu^{2+} doping ($x = 0.10$) reduces the indirect bandgap from 2.65 eV for $\text{Cs}_2\text{SbAgCl}_6$ to 1.02 eV. Assuming a direct allowed transition, Tauc plots give bandgaps of 2.84 eV for $\text{Cs}_2\text{SbAgCl}_6$ and 1.34 eV for the Cu^{2+} -doped material ($x = 0.10$) (Figure C3). This finding is consistent with the pictures shown in Figure 4.1a, where a drastic visual color change from yellow to black occurs upon Cu^{2+} doping, further supporting the conclusion of a reduced bandgap, absorbing in the near-IR range. Similar observations have been reported in other doped double perovskite systems,³⁸ Cu^{2+} alloyed $\text{Cs}_4\text{Sb}_2\text{MnCl}_{12}$ material,⁷⁹ and other Cu^{2+} -containing perovskites.⁸⁰ We note that the band edge is not sharp for the doped materials compared to that for $\text{Cs}_2\text{SbAgCl}_6$. This result suggests lattice disorder/defects in the doped

materials and is consistent with the NMR results, discussed below. Band tailing is also observed in layered halide double perovskites,⁴² thin film hybrid lead mixed-halide (Br, I) perovskite films,⁸¹ and doped lead halide perovskites.^{24,78} Our experimental results agree well with past theoretical calculations by Volonakis et al.,⁸² who showed that the calculated indirect bandgaps are 2.6 and 2.1 eV for $\text{Cs}_2\text{SbAgCl}_6$ and $\text{Cs}_2\text{SbCuCl}_6$, respectively. Our experimental results show a similar decrease in the measured bandgap as copper is introduced into our materials. The stark difference between the experimental determined bandgap of our Cu^{2+} -doped materials (vs calculated $\text{Cs}_2\text{SbCuCl}_6$, diamagnetic $3d^{10}$ Cu(I)) is attributed to the oxidation state; paramagnetic $3d^9$ Cu(II) enters the double perovskite lattice in the materials presented here.

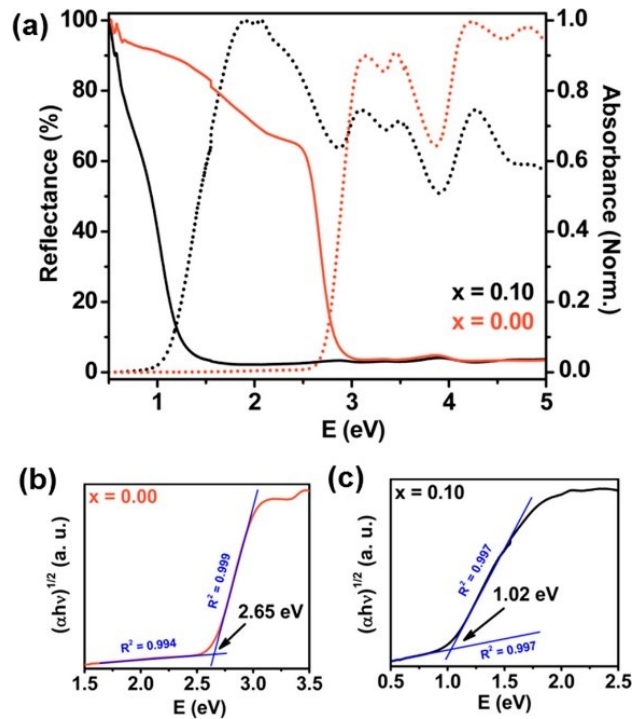


Figure 4.3. (a) UV–VIS–NIR DR (solid lines) and normalized absorption (dotted lines) spectrum for $\text{Cs}_2\text{SbAgCl}_6$ parent (i.e., $x = 0.00$) and the maximum Cu^{2+} -doped ($x = 0.10$) materials. The Tauc plots showing indirect bandgaps of (b) 2.65 eV for $\text{Cs}_2\text{SbAgCl}_6$ ($x = 0.00$) and (c) 1.02 eV for the maximum Cu^{2+} -doped material ($x = 0.10$). Note that DR spectra are converted to absorbance by using the Kubelka–Munk equation (see the Appendix C).

It is worth mentioning that low doping concentrations of Cu^{2+} in $\text{Cs}_2\text{SbAgCl}_6$ double perovskite would cause a localized state near the band edges, which would be responsible for a localized transition. As the dopant Cu^{2+} concentration increases within the lattice, the average Cu–Cu distances between defect sites will decrease dramatically throughout the lattice. These localized impurity states will then form a delocalized state, resulting in an overall narrowing of the bandgap in higher doped materials. Similar effects have been reported in Tl-doped double perovskites and in other semiconducting doped systems.^{38,83,84} Our experimental EPR results (above) show Cu^{2+} – Cu^{2+} coupling at higher Cu^{2+} doping concentrations in $\text{Cs}_2\text{SbAgCl}_6$, supporting the possibility of forming a delocalized state due to suitable Cu–Cu distances.

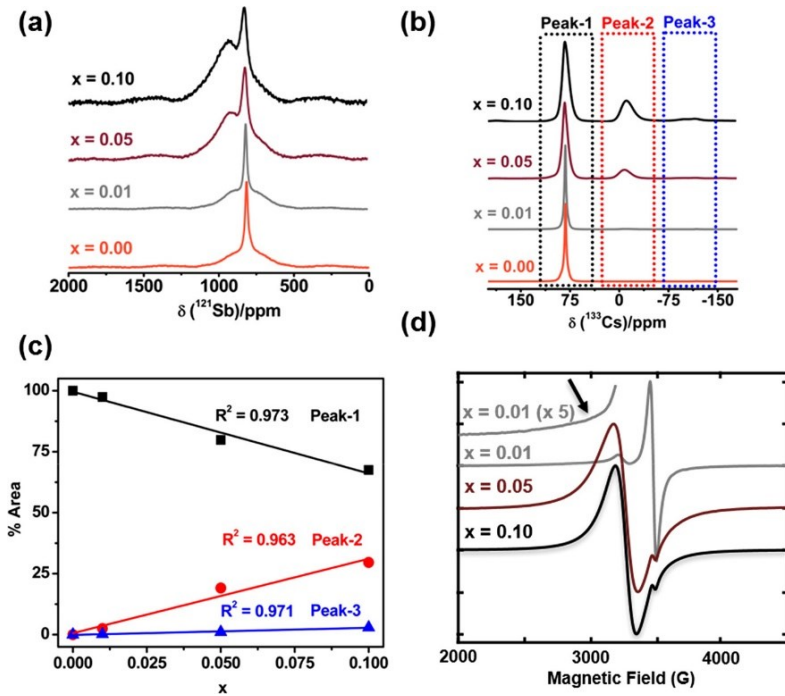


Figure 4.4. Solid-state (a) ^{121}Sb and (b) ^{133}Cs NMR spectra for $\text{Cs}_2\text{SbAgCl}_6$ materials with Cu^{2+} doping as indicated; the former spectra were acquired for nonspinning samples at 21.1 T, and the latter were acquired at 11.75 T at a spinning frequency of 13.0 kHz. Contributions of three ^{133}Cs MAS NMR peaks to the total area of the ^{133}Cs NMR spectra are shown in (c). (d) X-band EPR spectra of Cu^{2+} -doped

Cs₂SbAgCl₆ materials; the arrow indicates the broad and featureless high field g_{\parallel} component of the signal corresponding to isolated Cu²⁺ sites. Note the data presented in (a) were acquired using a selective 90° pulse to emphasize the higher frequency resonance that is subject to a sizable quadrupole coupling constant.

The PXRD and DR results indicate local structural disorder within the doped double perovskites. To further elucidate these finer structural details, NMR spectroscopy, a powerful nondestructive analytical technique, was used to further decode the short- and medium-range structure of the A (¹³³Cs) and B (¹²¹Sb) sites. Figure 4.4a shows the ¹²¹Sb NMR spectrum for nonspinning Cs₂SbAgCl₆ ($x = 0.00$) acquired at 21.1 T, displaying a sharp central transition resonance, centered at 817 ppm. Because Cs₂SbAgCl₆ has cubic symmetry and the Sb chemical environment has octahedral coordination to six Cl⁻ anions and the six next-nearest Ag⁺ cations, second-order quadrupolar broadening is not expected. Nevertheless, a broad underlying component spanning from ~1150 to 500 ppm is detected, which breaks into a series of spinning sidebands when spun at the magic angle; this is attributed to signals from the satellite transitions for crystallites exhibiting slight imperfections/defects. Fitting both nonspinning and magic-angle spinning data obtained at two magnetic field strengths ($B_0 = 11.75$ and 21.1 T) enables the determination of a small ¹²¹Sb quadrupole coupling constant (C_Q) of 1.1 ± 0.3 MHz for the Cs₂SbAgCl₆ parent double perovskite (Figure C4a). This is consistent with other cubic antimony-containing complexes where even slight distortions about the symmetric Sb³⁺ nucleus can give rise to considerable quadrupole coupling constants with visible second-order broadening (e.g., $C_Q = 2\text{--}3$ MHz for K₂SbF₆), a consequence of the sizable ¹²¹Sb quadrupole moment (-36.0 fm²).⁸⁵

Upon Cu²⁺ incorporation, a second broad ¹²¹Sb NMR resonance appears to high frequency of the sharp resonance (Figure 4.4a). The breadth of the peak is attributed to the change in the electric field gradient about the [SbCl₆]³⁻ octahedra that occur when neighboring Ag⁺ cations are replaced with Cu²⁺, that is, [(SbCl₆)Ag₅Cu], resulting in a sizable quadrupole coupling (Figure C4b). Also, a systematic increase in the area of the peak centered at ~900 ppm is observed (Figure C5). Because of the differences in

quadrupole coupling constants between the two sites, we refrain from fitting the two resonances quantitatively, although qualitatively the broad resonance increases with Cu^{2+} doping. Closer examination of the central transition assigned to $[(\text{SbCl}_6)\text{Ag}_6]$ indicates that this NMR site is also impacted by Cu^{2+} incorporation, with the FWHM of the peak at $\delta_{\text{iso}} = 817$ ppm increasing from 2.8 ± 0.3 kHz ($x = 0.00$) to 7.5 ± 0.5 kHz ($x = 0.10$) (Figure C5). The broadening is attributed to a reduction of the medium-range cubic symmetry about Sb^{3+} as Cu^{2+} is incorporated into the cubic lattice, impacting the electric field gradient about Sb, and to the presence of a paramagnetic species (Cu^{2+} , d^9 system), which reduces the spin–lattice relaxation times (T_1) of ^{133}Cs and increases the NMR line widths under magic-angle spinning (T_2^*) for ^{133}Cs and ^{121}Sb NMR (Table C2). The ^{121}Sb Gaussian-like line shape of the $\text{Cs}_2\text{SbAgCl}_6$ parent double perovskite is commonly observed in hybrid perovskites and is attributed to indirect spin–spin coupling (J -coupling) between ^{121}Sb and the six-coordinated $^{35/37}\text{Cl}$ anions (see the Appendix C).⁸⁵

Figure 4.4b shows the ^{133}Cs MAS NMR spectra of $\text{Cs}_2\text{SbAgCl}_6$ with and without Cu^{2+} doping. The small quadrupole moment for ^{133}Cs , $Q = -0.34$ fm², and high nuclear spin, $I = 7/2$, combined with its 100% natural abundance, make it an attractive NMR nucleus that behaves as a pseudo $I = 1/2$ nuclear spin.⁸⁶ Because Cs^+ resides in a cubooctahedral void surrounded by alternating $[\text{SbCl}_6]^{3-}$ and $[\text{AgCl}_6]^{5-}$ octahedra (Scheme 4.1a), it is an ideal method to probe local structural defects within the $\text{Cs}_2\text{SbAgCl}_6$ lattice as there is only one crystallographic position for this nucleus. A peak at $\delta_{\text{iso}} = 82$ ppm in the ^{133}Cs MAS NMR spectra (labeled Peak-1 in Figure 4.4b) is observed for all samples. A new resonance emerges at $\delta_{\text{iso}} = -10$ ppm (Peak-2), as Cu^{2+} is incorporated. Because we expect Cu^{2+} to substitute Ag^+ , this peak is tentatively assigned to a Cs^+ surrounded by four Sb^{3+} , three Ag^+ , and one Cu^{2+} (Scheme 4.1b and Figure C6b). As the Cu^{2+} doping increases further ($x \geq 0.05$), a third resonance begins to emerge at $\delta_{\text{iso}} = -100$ ppm (Peak-3) albeit with very low intensity ($<3\%$ at $x = 0.10$, Table C3), which we tentatively assign to ^{133}Cs nuclei proximate to two Cu^{2+} sites (Figure C6c). Peak-1 also broadens as the Cu^{2+} doping increases (Figures C7 and C8, Tables C4 and C5) due to the incorporation of paramagnetic Cu^{2+} , as discussed above for the ^{121}Sb NMR spectra. In fitting the $\delta_{\text{iso}}(^{133}\text{Cs})$ peaks, we found that the area for

Peak-1 decreases linearly, whereas those for Peak-2 and Peak-3 increase linearly with Cu^{2+} doping (Figure 4.4c and Table C3). The incorporation of Cu^{2+} results in the appearance of new ^{133}Cs resonances, which exhibit a linear relationship with synthetic Cu loading (Figure C9). Using these tentatively assigned ^{133}Cs chemical shifts, and knowledge that each copper center will impact eight cesium centers, we can also obtain an estimate of Cu^{2+} incorporation postsynthesis (Table C1), although this does not account for potential Cu^{2+} clusters and hence is expected to be a lower limit.

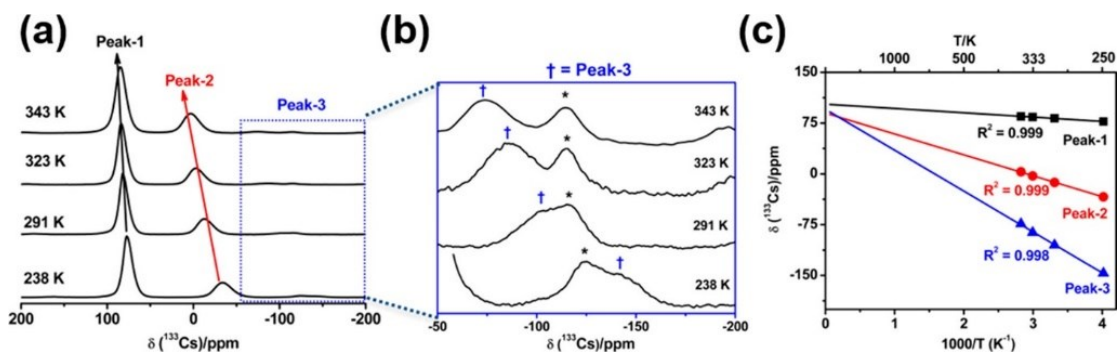


Figure 4.5. (a) Variable temperature ^{133}Cs MAS NMR spectra of Cu^{2+} -doped material ($x = 0.10$) acquired at 11.75 T with a spinning frequency of 13 kHz. Arrows (black and red) are guides to the eye. (b) Temperature dependence of the ^{133}Cs chemical shift of Peak-3; the asterisks (*) and crosses (†) indicate spinning sidebands and Peak-3, respectively. (c) Temperature dependence of the chemical shifts for the three distinct peaks in the ^{133}Cs NMR spectra.

For the samples considered here, the first observation is that Peak-2 and Peak-3 are shifted to lower frequency. There are two mechanisms for paramagnetic shift: the through-space interaction between the nuclear spin and the average magnetic moment of the paramagnetic center (pseudocontact shift), and the interaction between the nuclear spin and the unpaired spin density at the nucleus itself (Fermi contact).⁸⁷ Given that the pseudocontact contribution to the shift, based on the EPR spectrum (Figure 4.4d) and on geometrical arguments,^{87–90} is expected to be positive and smaller than 1 ppm (see the Appendix C), we conclude that the main source of the shift is Fermi contact. The fact that the shift is to lower frequency indicates that contact occurs

through the spin-polarization mechanism.^{91,92} The Fermi contact shift is the interaction of the nucleus with the unpaired spin electron density at the nucleus itself. Therefore, Fermi contact reports on the electronic structure about the nucleus. The observation of Fermi contact indicates that the nature of the interaction of the cesium ions with the lattice is not just ionic but has some degree of covalency (i.e., orbital overlap). Finally, the mechanism of the Fermi contact suggests that the overlap is not with penetrating orbitals such as the 6s, but rather with p- or d-type orbitals.

To further investigate the contributions from the paramagnetic Cu^{2+} center to the three distinct ^{133}Cs NMR chemical shifts discussed above, a series of variable-temperature ^{133}Cs NMR measurements from 238 to 343 K on the $x = 0.10$ Cu^{2+} -doped material were undertaken. The impact of paramagnetic species on the NMR spectra offers a wealth of information, encoded in the changes in chemical shifts and in a reduction of relaxation times as a consequence of the interaction between the nuclei and the unpaired electrons.^{87,93} The observation of paramagnetic effects on the nuclei may provide substantial information about the electronic structure at the paramagnetic centers. The temperature dependence is a revealing feature of the behavior of paramagnetic systems and thus has proven useful in studies of a variety of solids.^{91,94–104} All three ^{133}Cs NMR peaks shift to higher frequency as the temperature is increased (Figure 4.5a,b and Table C6), but each has a distinct temperature dependence.^{74–76,80,81} Peak-1 changes slowly with temperature; the small temperature dependence (0.08 ppm/K) for this peak is attributed to the temperature-induced changes in local structure, such as changes in the unit cell or position within the cuboctahedron (confirmed from variable temperature NMR spectroscopy on the $\text{Cs}_2\text{SbAgCl}_6$ parent material, Figure C10). In contrast, the much larger temperature dependence of the chemical shifts of Peak-2 and Peak-3 (0.35 and 0.70 ppm/K, respectively) are a clear indication of the impact of neighboring Cu^{2+} ions, confirming that the Cs residing in the A site of the double perovskite is in proximity to the induced defect site with increasing incorporation of copper. Extrapolating to “infinite temperature” gives the diamagnetic isotropic chemical shift of $\sim 96 \pm 7$ ppm, which is within the expected chemical shift range for the diamagnetic $\text{Cs}_2\text{SbAgCl}_6$ parent material ($x = 0.00$, $\delta_{\text{iso}}(^{133}\text{Cs}) = 85 \pm 1$ ppm) at 343 K (Figure 4.5c). The fact that the temperature

dependence is Curie-like (i.e., the paramagnetic effect decreases with increasing temperature) and additive indicates either that contact occurs through two uncoupled copper centers or that the coupling between the two copper centers is smaller than the thermal energy (which is consistent with observations reported previously).^{75,87}

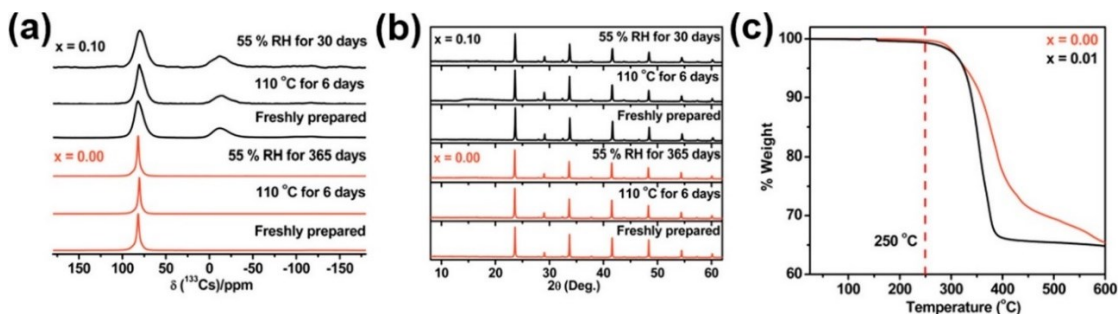


Figure 4.6. Stability experiments of $\text{Cs}_2\text{SbAgCl}_6$ parent (i.e., $x = 0.00$) and the maximum Cu^{2+} -doped ($x = 0.10$) materials under the indicated conditions: (a) ^{133}Cs MAS NMR spectra acquired at 11.75 T with a frequency of 13 kHz, and (b) PXRD patterns. (c) TGA analysis data for materials without ($x = 0.00$) and with trace Cu^{2+} doping ($x = 0.01$), showing similar thermal stability.

Cesium-133 MAS NMR spectra and PXRD patterns for cesium-containing chlorides, including CsCl , $\text{Cs}_3\text{Sb}_2\text{Cl}_9$, $\text{Cs}_4\text{CuSb}_2\text{Cl}_{12}$, and Cs_2CuCl_4 , were acquired (Figure C11).^{46,105} These spectra are distinct from those for $\text{Cs}_2\text{SbAgCl}_6$ parent and Cu^{2+} -doped materials. The distinct chemical shifts for each ^{133}Cs resonance as a function of temperature also correlate well with the EDX, ICP, and PXRD results (vide supra), leading to further confidence that we are observing Cs^+ in a cuboctahedron with one and two Cu^{2+} neighbors; this is consistent with the structure expected for a Cu^{2+} -doped $\text{Cs}_2\text{SbAgCl}_6$ double perovskite and not from Cs-containing impurity phases.

4.3 Long-term Stability

A major concern with lead-containing hybrid perovskites is their low stability upon exposure to light, moisture, and heat.^{10,13–15} Therefore, we examined the moisture and thermal stability of both the $\text{Cs}_2\text{SbAgCl}_6$ parent and of the Cu^{2+} -doped materials.

Polycrystalline materials were placed in a custom-built humidity chamber (Figure C12) with a relative humidity (RH) of $55 \pm 5\%$ under otherwise normal laboratory conditions for 365 days ($x = 0.00$) and 30 days ($x = 0.10$). Based on analyses of the ^{133}Cs MAS NMR spectra (Figure 4.6a), PXRD patterns (Figure 4.6b and C13) and absorption spectra (Figure C14), there are no indications of decomposition from either material, and their bandgaps are retained under humid conditions. TGA indicates that materials with ($x = 0.01$) and without Cu^{2+} doping are stable up to $250\text{ }^\circ\text{C}$ (Figure 4.6c), similar to the thermal stability for the copper–antimony (111) perovskite ($245\text{ }^\circ\text{C}$) reported by Vargas et al.⁴⁶ Long-term thermal stability studies were undertaken by heating these materials at $110\text{ }^\circ\text{C}$ for 6 days under otherwise ambient conditions; ^{133}Cs NMR, PXRD, and absorption spectra analysis (Figures 4.6, Figure C13 and C14, respectively) again indicate high structural and optical stability with no evidence of decomposition.

4.4 Conclusions

In this work, we have investigated $\text{Cs}_2\text{SbAgCl}_6$ and its Cu^{2+} -doped double perovskite materials. The PXRD, EPR, and NMR results indicate a well-ordered double perovskite cubic crystal structure with Cu^{2+} integrated into the lattice, creating local defect sites in multiple local Cs^+ and Sb^{3+} arrangements, whereby Cu^{2+} preferentially substitutes for Ag^+ . These findings are further reinforced by EDX measurements and are consistent with Pauling electronegativity arguments. The optical properties of the material are directly related to the Cu^{2+} doping, which leads to a reduction of the optical indirect bandgap, from 2.65 eV for the parent material to 1.02 eV for the $x = 0.10$ Cu^{2+} -doped material. The material's feasibility for photovoltaic applications was further examined through thermal and moisture exposure, demonstrating long-term structural and photophysical stability up to 365 days. Previously it has been shown that heterovalent doping in lead halide perovskites leads to an increase in conductivity and the formation of an n-type semiconductor.⁵⁴ Likewise, a series of DFT calculations for double perovskites including the parent compound studied here ($\text{Cs}_2\text{SbAgCl}_6$) indicate these materials exhibit small carrier effective masses ($<0.4m_e$), which are comparable to those calculated for MAPbI_3 .^{82,106} Although further study is needed, based on the observations discussed above, we propose that Cu^{2+} doping creates a cation defect,

which could lead to an increase in conductivity. In summary, the antimony–silver based double perovskites presented here exhibit several desirable properties in comparison to lead halide perovskites including the potential for greater bandgap tunability and superior stability, as well as being composed of inexpensive and highly abundant elements.

4.5 References

- (1) Kojima, A.; Teshima, K.; Shirai, Y.; Miyasaka, T. Organometal Halide Perovskites as Visible-Light Sensitizers for Photovoltaic Cells. *J. Am. Chem. Soc.* **2009**, *131*, 6050–6051.
- (2) Green, M. A.; Hishikawa, Y.; Warta, W.; Dunlop, E. D.; Levi, D. H.; Hohl-Ebinger, J.; Ho-Baillie, A. W. H. Solar Cell Efficiency Tables (version 50). *Prog. Photovoltaics Res. Appl.* **2017**, *25*, 668–676.
- (3) Tan, Z.-K.; Moghaddam, R. S.; Lai, M. L.; Docampo, P.; Higler, R.; Deschler, F.; Price, M.; Sadhanala, A.; Pazos, L. M.; Credgington, D.; et al. Bright Light-Emitting Diodes Based on Organometal Halide Perovskite. *Nat. Nanotechnol.* **2014**, *9*, 687–692.
- (4) Zhu, H.; Fu, Y.; Meng, F.; Wu, X.; Gong, Z.; Ding, Q.; Gustafsson, M. V.; Trinh, M. T.; Jin, S.; Zhu, X. Y. Lead Halide Perovskite Nanowire Lasers with Low Lasing Thresholds and High Quality Factors. *Nat. Mater.* **2015**, *14*, 636–642.
- (5) Xing, G.; Mathews, N.; Lim, S. S.; Yantara, N.; Liu, X.; Sabba, D.; Grätzel, M.; Mhaisalkar, S.; Sum, T. C. Low-Temperature Solution-Processed Wavelength-Tunable Perovskites for Lasing. *Nat. Mater.* **2014**, *13*, 476–480.
- (6) Jeon, N. J.; Noh, J. H.; Yang, W. S.; Kim, Y. C.; Ryu, S.; Seo, J.; Seok, S. I. Compositional Engineering of Perovskite Materials for High-Performance Solar Cells. *Nature* **2015**, *517*, 476–480.
- (7) Liu, M.; Johnston, M. B.; Snaith, H. J. Efficient Planar Heterojunction Perovskite Solar Cells by Vapour Deposition. *Nature* **2013**, *501*, 395–398.
- (8) Shi, D.; Adinolfi, V.; Comin, R.; Yuan, M.; Alarousu, E.; Buin, A.; Chen, Y.; Hoogland, S.; Rothenberger, A.; Katsiev, K.; et al. Low Trap-State Density and Long Carrier Diffusion in Organolead Trihalide Perovskite Single Crystals. *Science* **2015**,

347, 519–522.

(9) Yang, J.; Siempelkamp, B. D.; Mosconi, E.; De Angelis, F.; Kelly, T. L. Origin of the Thermal Instability in $\text{CH}_3\text{NH}_3\text{PbI}_3$ Thin Films Deposited on ZnO. *Chem. Mater.* **2015**, *27*, 4229–4236.

(10) Berhe, T. A.; Su, W.-N.; Chen, C.-H.; Pan, C.-J.; Cheng, J.-H.; Chen, H.-M.; Tsai, M.-C.; Chen, L.-Y.; Dubale, A. A.; Hwang, B.-J. Organometal Halide Perovskite Solar Cells: Degradation and Stability. *Energy Environ. Sci.* **2016**, *9*, 323–356.

(11) Needleman, H. Lead Poisoning. *Annu. Rev. Med.* **2004**, *55*, 209–222.

(12) Babayigit, A.; Ethirajan, A.; Muller, M.; Conings, B. Toxicity of Organometal Halide Perovskite Solar Cells. *Nat. Mater.* **2016**, *15*, 247–251.

(13) Herrera, P. A. M.; Kamat, P. V. Transformation of the Excited State and Photovoltaic Efficiency of $\text{CH}_3\text{NH}_3\text{PbI}_3$ Perovskite upon Controlled Exposure to Humidified Air. *J. Am. Chem. Soc.* **2015**, *137*, 1530–1538.

(14) Leguy, M. A.; Hu, Y.; Campoy-quiles, M.; Alonso, M. I.; Weber, O. J.; Azarhoosh, P.; Schilfgaarde, M. Van; Weller, M. T.; Bein, T.; Nelson, J.; et al. Reversible Hydration of $\text{CH}_3\text{NH}_3\text{PbI}_3$ in Films, Single Crystals, and Solar Cells. *Chem. Mater.* **2015**, *27*, 3397–3407.

(15) Askar, A. M.; Bernard, G. M.; Wiltshire, B.; Shankar, K.; Michaelis, V. K. Multinuclear Magnetic Resonance Tracking of Hydro, Thermal, and Hydrothermal Decomposition of $\text{CH}_3\text{NH}_3\text{PbI}_3$. *J. Phys. Chem. C* **2017**, *121*, 1013–1024.

(16) Saliba, M.; Matsui, T.; Seo, J. Y.; Domanski, K.; Correa-Baena, J. P.; Nazeeruddin, M. K.; Zakeeruddin, S. M.; Tress, W.; Abate, A.; Hagfeldt, A.; et al. Cesium-Containing Triple Cation Perovskite Solar Cells: Improved Stability, Reproducibility and High Efficiency. *Energy Environ. Sci.* **2016**, *9*, 1989–1997.

(17) Li, Z.; Yang, M.; Park, J. S.; Wei, S. H.; Berry, J. J.; Zhu, K. Stabilizing Perovskite Structures by Tuning Tolerance Factor: Formation of Formamidinium and Cesium Lead Iodide Solid-State Alloys. *Chem. Mater.* **2016**, *28*, 284–292.

(18) Zhang, M.; Yun, J. S.; Ma, Q.; Zheng, J.; Lau, C. F. J.; Deng, X.; Kim, J.; Kim, D.; Seidel, J.; Green, M. A.; et al. High-Efficiency Rubidium-Incorporated Perovskite Solar Cells by Gas Quenching. *ACS Energy Lett.* **2017**, *2*, 438–444.

- (19) Eperon, G. E.; Leijtens, T.; Bush, K. A.; Green, T.; Wang, J. T.-W.; McMeekin, D. P.; Volonakis, G.; Milot, R. L.; Slotcavage, D. J.; Belisle, R.; et al. Perovskite-Perovskite Tandem Photovoltaics with Ideal Bandgaps. *Science* **2016**, *354*, 861–865.
- (20) Tan, H.; Jain, A.; Voznyy, O.; Lan, X.; Arquer, F. P. G. de; Fan, J. Z.; Quintero-Bermudez, R.; Yuan, M.; Zhang, B.; Zhao, Y.; et al. Efficient and Stable Solution Processed Planar Perovskite Solar Cell via Contact Passivation. *Science* **2017**, *355*, 722–726.
- (21) Lau, C. F. J.; Zhang, M.; Deng, X.; Zheng, J.; Bing, J.; Ma, Q.; Kim, J.; Hu, L.; Green, M. A.; Huang, S.; et al. Strontium-Doped Low-Temperature-Processed CsPbI₂Br Perovskite Solar Cells. *ACS Energy Lett.* **2017**, *2*, 2319–2325.
- (22) Zuo, F.; Williams, S. T.; Liang, P. W.; Chueh, C. C.; Liao, C. Y.; Jen, A. K. Y. Binary-Metal Perovskites Toward High-Performance Planar-Heterojunction Hybrid Solar Cells. *Adv. Mater.* **2014**, *26*, 6454–6460.
- (23) Klug, M. T.; Osherov, A.; Haghghirad, A. A.; Stranks, S. D.; Brown, P. R.; Bai, S.; Wang, J. T. W.; Dang, X.; Bulović, V.; Snaith, H. J.; et al. Tailoring Metal Halide Perovskites through Metal Substitution: Influence on Photovoltaic and Material Properties. *Energy Environ. Sci.* **2017**, *10*, 236–246.
- (24) Abdelhady, A. L.; Saidaminov, M. I.; Murali, B.; Adinolfi, V.; Voznyy, O.; Katsiev, K.; Alarousu, E.; Comin, R.; Dursun, I.; Sinatra, L.; et al. Heterovalent Dopant Incorporation for Bandgap and Type Engineering of Perovskite Crystals. *J. Phys. Chem. Lett.* **2016**, *7*, 295–301.
- (25) Levchuk, I.; Osvet, A.; Tang, X.; Brandl, M.; Perea, J. D.; Hoegl, F.; Matt, G. J.; Hock, R.; Batentschuk, M.; Brabec, C. J. Brightly Luminescent and Color-Tunable Formamidinium Lead Halide Perovskite FAPbX₃ (X = Cl, Br, I) Colloidal Nanocrystals. *Nano Lett.* **2017**, *17*, 2765–2770.
- (26) Hu, Y.; Bai, F.; Liu, X.; Ji, Q.; Miao, X.; Qiu, T.; Zhang, S. Bismuth Incorporation Stabilized α -CsPbI₃ for Fully Inorganic Perovskite Solar Cells. *ACS Energy Lett.* **2017**, *2*, 2219–2227.
- (27) Lee, J.-W., Kim, D.-H., Kim, H.-S., Seo, S.-W., Cho, S.M., Park, N.-G. Formamidinium and Cesium Hybridization for Photo- and Moisture-Stable Perovskite Solar Cell. *Adv. Energy Mater.* **2015**, *5*, 1501310.

- (28) Dang, Y.; Zhou, Y.; Liu, X.; Ju, D.; Xia, S.; Xia, H.; Tao, X. Formation of Hybrid Perovskite Tin Iodide Single Crystals by Top-Seeded Solution Growth. *Angew. Chem. Int. Ed.* **2016**, *55*, 3447–3450.
- (29) Babu, R.; Giribabu, L.; Singh, S. P. Recent Advances in Halide-Based Perovskite Crystals and their Optoelectronic Applications. *Cryst. Growth Des.* **2018**, *18*, 2645–2664.
- (30) Slavney, A. H.; Hu, T.; Lindenberg, A. M.; Karunadasa, H. I. A Bismuth-Halide Double Perovskite with Long Carrier Recombination Lifetime for Photovoltaic Applications. *J. Am. Chem. Soc.* **2016**, *138*, 2138–2141.
- (31) Volonakis, G.; Haghighirad, A. A.; Milot, R. L.; Sio, W. H.; Filip, M. R.; Wenger, B.; Johnston, M. B.; Herz, L. M.; Snaith, H. J.; Giustino, F. Cs₂InAgCl₆: A New Lead-Free Halide Double Perovskite with Direct Band Gap. *J. Phys. Chem. Lett.* **2017**, *8*, 772–778.
- (32) McClure, E. T.; Ball, M. R.; Windl, W.; Woodward, P. M. Cs₂AgBiX₆ (X = Br, Cl): New Visible Light Absorbing, Lead-Free Halide Perovskite Semiconductors. *Chem. Mater.* **2016**, *28*, 1348–1354.
- (33) Filip, M. R.; Liu, X.; Miglio, A.; Hautier, G.; Giustino, F. Phase Diagrams and Stability of Lead-Free Halide Double Perovskites Cs₂BB'X₆: B = Sb and Bi, B' = Cu, Ag, and Au, and X = Cl, Br, and I. *J. Phys. Chem. C* **2018**, *122*, 158–170.
- (34) Jain, A.; Voznyy, O.; Sargent, E. H. High-Throughput Screening of Lead-Free Perovskite-like Materials for Optoelectronic Applications. *J. Phys. Chem. C* **2017**, *121*, 7183–7187.
- (35) Wei, F.; Deng, Z.; Sun, S.; Zhang, F.; Evans, D. M.; Kieslich, G.; Tominaka, S.; Carpenter, M. A.; Zhang, J.; Bristowe, P. D.; Cheetham, A. K. Synthesis and Properties of a Lead-Free Hybrid Double Perovskite: (CH₃NH₃)₂AgBiBr₆. *Chem. Mater.* **2017**, *29*, 1089–1094.
- (36) Du, K. Z.; Meng, W.; Wang, X.; Yan, Y.; Mitzi, D. B. Bandgap Engineering of Lead-Free Double Perovskite Cs₂AgBiBr₆ through Trivalent Metal Alloying. *Angew. Chem. Int. Ed.* **2017**, *56*, 8158–8162.
- (37) Tran, T. T.; Panella, J. R.; Chamorro, J. R.; Morey, J. R.; McQueen, T. M. Designing Indirect-Direct Bandgap Transitions in Double Perovskites. *Mater.*

Horizons **2017**, *4*, 688–693.

(38) Slavney, A. H.; Leppert, L.; Bartesaghi, D.; Gold-Parker, A.; Toney, M. F.; Savenije, T. J.; Neaton, J. B.; Karunadasa, H. I. Defect-Induced Band-Edge Reconstruction of a Bismuth-Halide Double Perovskite for Visible-Light Absorption. *J. Am. Chem. Soc.* **2017**, *139*, 5015–5018.

(39) Deng, W.; Deng, Z.; He, J.; Wang, M.; Chen, Z.; Wei, S.; Feng, H.-J. Synthesis of Cs₂AgSbCl₆ and Improved Optoelectronic Properties of Cs₂AgSbCl₆/TiO₂ Heterostructure Driven by the Interface Effect for Lead-Free Double Perovskites Solar Cells. *Appl. Phys. Lett.* **2017**, *111*, 151602.

(40) Bekenstein, Y.; Dahl, J. C.; Huang, J.; Osowiecki, W. T.; Swabeck, J. K.; Chan, E. M.; Yang, P.; Alivisatos, A. P. The Making and Breaking of Lead-Free Double Perovskite Nanocrystals of Cesium Silver-Bismuth Halide Compositions. *Nano Lett.* **2018**, *18*, 3502-3508.

(41) Creutz, S. E.; Crites, E. N.; De Siena, M. C.; Gamelin, D. R. Colloidal Nanocrystals of Lead-Free Double-Perovskite (Elpasolite) Semiconductors: Synthesis and Anion Exchange to Access New Materials. *Nano Lett.* **2018**, *18*, 1118–1123.

(42) Connor, B. A.; Leppert, L.; Smith, M. D.; Neaton, J. B.; Karunadasa, H. I. Layered Halide Double Perovskites: Dimensional Reduction of Cs₂AgBiBr₆. *J. Am. Chem. Soc.* **2018**, *140*, 5235–5240.

(43) Pantaler, M.; Cho, K. T.; Queloz, V.; Garcia Benito, I.; Fettkenhauer, C.; Anusca, I.; Nazeeruddin, M. K.; Lupascu, D. C.; Grancini, G. Hysteresis-Free Lead-Free Double Perovskite Solar Cells by Interface Engineering. *ACS Energy Lett.* **2018**, *3*, 1781–1786.

(44) Greul, E.; Petrus, M. L.; Binek, A.; Docampo, P.; Bein, T. Highly Stable, Phase Pure Cs₂AgBiBr₆ Double Perovskite Thin Films for Optoelectronic Applications. *J. Mater. Chem. A* **2017**, *5*, 19972–19981.

(45) Slavney, A. H.; Leppert, L.; Saldivar Valdes, A.; Bartesaghi, D.; Savenije, T. J.; Neaton, J. B.; Karunadasa, H. Small-Bandgap Halide Double Perovskites. *Angew. Chem. Int. Ed.* **2018**, *57*, 12765 –12770.

(46) Vargas, B.; Ramos, E.; Pérez-Gutiérrez, E.; Alonso, J. C.; Solis-Ibarra, D. A Direct Bandgap Copper-Antimony Halide Perovskite. *J. Am. Chem. Soc.* **2017**, *139*,

9116–9119.

- (47) Singhal, N.; Chakraborty, R.; Ghosh, P.; Nag, A. Low-Bandgap Cs₄CuSb₂Cl₁₂ Layered Double Perovskite: Synthesis, Reversible Thermal Changes, and Magnetic Interaction. *Chem. Asian J.* **2018**, *13*, 2085–2092.
- (48) Abram, R. A.; Rees, G. J.; Wilson, B. L. H. Heavily Doped Semiconductors and Devices. *Adv. Phys.* **1978**, *27*, 799–892.
- (49) Piao, Y.; Meany, B.; Powell, L. R.; Valley, N.; Kwon, H.; Schatz, G. C.; Wang, Y. Brightening of Carbon Nanotube Photoluminescence through the Incorporation of sp³ Defects. *Nat. Chem.* **2013**, *5*, 840–845.
- (50) Misra, R. K.; Aharon, S.; Li, B.; Mogilyansky, D.; Visoly-Fisher, I.; Etgar, L.; Katz, E. A. Temperature- and Component-Dependent Degradation of Perovskite Photovoltaic Materials under Concentrated Sunlight. *J. Phys. Chem. Lett.* **2015**, *6*, 326–330.
- (51) Shao, H.; Bai, X.; Cui, H.; Pan, G.; Jing, P.; Qu, S.; Zhu, J.; Zhai, Y.; Dong, B.; Song, H. White Light Emission in Bi³⁺/Mn²⁺ Ion Co-Doped CsPbCl₃ Perovskite Nanocrystals. *Nanoscale* **2018**, *10*, 1023–1029.
- (52) Das Adhikari, S.; Dutta, A.; Dutta, S. K.; Pradhan, N. Layered Perovskites L₂(Pb_{1-x}Mn_x)Cl₄ to Mn-Doped CsPbCl₃ Perovskite Platelets. *ACS Energy Lett.* **2018**, *3*, 1247–1253.
- (53) Meinardi, F.; Akkerman, Q. A.; Bruni, F.; Park, S.; Mauri, M.; Dang, Z.; Manna, L.; Brovelli, S. Doped Halide Perovskite Nanocrystals for Reabsorption-Free Luminescent Solar Concentrators. *ACS Energy Lett.* **2017**, *2*, 2368–2377.
- (54) Zhou, Y.; Chen, J.; Bakr, O. M.; Sun, H. Metal-Doped Lead Halide Perovskites: Synthesis, Properties, and Optoelectronic Applications. *Chem. Mater.* **2018**, *30*, 6589–6613.
- (55) K., N. N.; Nag, A. Synthesis and Luminescence of Mn-Doped Cs₂AgInCl₆ Double Perovskites. *Chem. Commun.* **2018**, *54*, 5205–5208.
- (56) Yin, W.; Shi, T.; Yan, Y. Superior Photovoltaic Properties of Lead Halide Perovskites: Insights from First-Principles Theory. *J. Phys. Chem. C* **2015**, *119*, 5253–5264.
- (57) Knop, O.; Wasylishen, R. E.; White, M. A.; Cameron, T. S.; Van Oort, M. J. M.

- Alkylammonium Lead Halides. Part 2. $\text{CH}_3\text{NH}_3\text{PbX}_3$ (X=Cl, Br, I) Perovskites: Cuboctahedral Halide Cages with Isotropic Cation Reorientation. *Can. J. Chem.* **1990**, *68*, 412–422.
- (58) Kubicki, D. J.; Prochowicz, D.; Hofstetter, A.; Zakeeruddin, S. M.; Grätzel, M.; Emsley, L. Phase Segregation in Potassium-Doped Lead Halide Perovskites from ^{39}K Solid-State NMR at 21.1 T. *J. Am. Chem. Soc.* **2018**, *140*, 7232–7238.
- (59) Senocrate, A.; Moudrakovski, I.; Kim, G. Y.; Yang, T.; Gregori, G.; Grätzel, M.; Maier, J. The Nature of Ion Conduction in Methylammonium Lead Iodide: A Multimethod Approach. *Angew. Chem. Int. Ed.* **2017**, *56*, 7755–7759.
- (60) Fabini, D. H.; Siaw, T. A.; Stoumpos, C. C.; Laurita, G.; Olds, D.; Page, K.; Hu, J. G.; Kanatzidis, M. G.; Han, S.; Seshadri, R. Universal Dynamics of Molecular Reorientation in Hybrid Lead Iodide Perovskites. *J. Am. Chem. Soc.* **2017**, *139*, 16875–16884.
- (61) Rosales, B. A.; Men, L.; Cady, S. D.; Hanrahan, M. P.; Rossini, A. J.; Vela, J. Persistent Dopants and Phase Segregation in Organolead Mixed-Halide Perovskites. *Chem. Mater.* **2016**, *28*, 6848–6859.
- (62) Franssen, W. M. J.; Van Es, S. G. D.; Dervişolu, R.; De Wijs, G. A.; Kentgens, A. P. M. Symmetry, Dynamics, and Defects in Methylammonium Lead Halide Perovskites. *J. Phys. Chem. Lett.* **2017**, *8*, 61–66.
- (63) Prochowicz, D.; Yadav, P.; Saliba, M.; Kubicki, D. J.; Tavakoli, M. M.; Zakeeruddin, S. M.; Lewiński, J.; Emsley, L.; Grätzel, M. One-Step Mechanochemical Incorporation of an Insoluble Cesium Additive for High Performance Planar Heterojunction Solar Cells. *Nano Energy* **2018**, *49*, 523–528.
- (64) Wasylshen, R. E.; Knop, O.; Macdonald, J. B. Cation Rotation in Methylammonium Lead Halides. *Solid State Commun.* **1985**, *56*, 581–582.
- (65) Karmakar, A.; Askar, A. M.; Bernard, G. M.; Terskikh, V. V.; Ha, M.; Patel, S.; Shankar, K.; Michaelis, V. K. Mechanochemical Synthesis of Methylammonium Lead Mixed-Halide Perovskites: Unraveling the Solid-Solution Behavior Using Solid-State NMR. *Chem. Mater.* **2018**, *30*, 2309–2321.
- (66) Askar, A. M.; Karmakar, A.; Bernard, G. M.; Ha, M.; Terskikh, V. V.; Wiltshire, B. D.; Patel, S.; Fleet, J.; Shankar, K.; Michaelis, V. K. Composition-Tunable

Formamidinium Lead Mixed Halide Perovskites via Solvent-Free Mechanochemical Synthesis: Decoding the Pb Environments Using Solid-State NMR Spectroscopy. *J. Phys. Chem. Lett.* **2018**, *9*, 2671–2677.

(67) Bernard, G. M.; Goyal, A.; Miskolzie, M.; McKay, R.; Wu, Q.; Wasylshen, R. E.; Michaelis, V. K. Methylammonium Lead Chloride: A Sensitive Sample for an Accurate NMR Thermometer. *J. Magn. Reson.* **2017**, *283*, 14–21.

(68) Bernard, G. M.; Wasylshen, R. E.; Ratcliffe, C. I.; Terskikh, V.; Wu, Q.; Buriak, J. M.; Hauger, T. Methylammonium Cation Dynamics in Methylammonium Lead Halide Perovskites: A Solid-State NMR Perspective. *J. Phys. Chem. A* **2018**, *122*, 1560–1573.

(69) Kubicki, D. J.; Prochowicz, D.; Hofstetter, A.; Saski, M.; Yadav, P.; Bi, D.; Pellet, N.; Lewiński, J.; Zakeeruddin, S. M.; Grätzel, M.; et al. Formation of Stable Mixed Guanidinium-Methylammonium Phases with Exceptionally Long Carrier Lifetimes for High-Efficiency Lead Iodide-Based Perovskite Photovoltaics. *J. Am. Chem. Soc.* **2018**, *140*, 3345–3351.

(70) Kubicki, D. J.; Prochowicz, D.; Hofstetter, A.; Zakeeruddin, S. M.; Grätzel, M.; Emsley, L. Phase Segregation in Cs-, Rb- and K-Doped Mixed-Cation (MA)_x(FA)_{1-x}PbI₃ Hybrid Perovskites from Solid-State NMR. *J. Am. Chem. Soc.* **2017**, *139*, 14173–14180.

(71) Kubicki, D. J.; Prochowicz, D.; Hofstetter, A.; Péchy, P.; Zakeeruddin, S. M.; Grätzel, M.; Emsley, L. Cation Dynamics in Mixed-Cation (MA)_x(FA)_{1-x}PbI₃ Hybrid Perovskites from Solid-State NMR. *J. Am. Chem. Soc.* **2017**, *139*, 10055–10061.

(72) Yang, M.; Wen-chen, Z.; Lv, H. Defect Structure and Spin-Hamiltonian Parameters for the CuCl₆⁴⁻ Cluster in the Tetragonal RbCdCl₃:Cu²⁺ crystal. *Spectrochim. Acta Part A Mol. Biomol. Spectrosc.* **2009**, *72*, 515–517.

(73) Wei, M.; Willett, R. D.; Hipps, K. W. EPR, Electronic, and Vibrational Spectra of the CuCl₆⁴⁻ Anion in [tris(2-aminoethyl)amineH₄]₂ [CuCl₆]Cl₄ · 2H₂O and Crystal Structure of the Complex. *Inorg. Chem.* **1996**, *35*, 5300–5303.

(74) McDonald, R. G.; Hitchman, M. A. Electronic, EPR and Vibrational Spectra of the Hexachlorocuprate(4-) Ion. *Inorg. Chem.* **1989**, *28*, 3996–4001.

(75) Stratemeier, H.; Wagner, B.; Krausz, E. R.; Linder, R.; Schmidtke, H.; Pebler, J.;

- Hatfield, W. E.; ter Haar, L.; Reinen, D.; Hitchman, M. A. EPR and Electronic Spectra of (3-chloroanilinium)₈[CuCl₆]Cl₄: Evidence for Tetragonally Elongated CuCl₆⁴⁻ Ions with the Long Axis Disordered in 2-Dimensions. *Inorg. Chem.* **1994**, *33*, 2320–2329.
- (76) Shannon, R. D.; H, M.; Baur, N. H.; Gibbs, O. H.; Eu, M.; Cu, V. Revised Effective Ionic Radii and Systematic Studies of Interatomic Distances in Halides and Chalcogenides. *Acta Cryst.* **1976**, *A32*, 751–767.
- (77) Pramanick, A.; Wang, X. P.; Hoffmann, C.; Diallo, S. O.; Jørgensen, M. R. V.; Wang, X. Microdomain Dynamics in Single-Crystal BaTiO₃ during Paraelectric-Ferroelectric Phase Transition Measured with Time-of-Flight Neutron Scattering. *Phys. Rev. B* **2015**, *92*, 174103.
- (78) Nayak, P.; Sendner, M.; Wenger, B.; Wang, Z.; Sharma, K.; Ramadan, A. J.; Lovrincic, R.; Pucci, A.; Madhu, P. K.; Snaith, H. J. The Impact of Bi³⁺ Heterovalent Doping in Organic-Inorganic Metal Halide Perovskite Crystals. *J. Am. Chem. Soc.* **2018**, *140*, 574–577.
- (79) Vargas, B., Torres-Cadena, R., Rodriguez-Hernández, J. Gembicky, M., Xie, H., Jiménez-Mier, J., Liu, Y.; Menéndez-Proupin, E.; Dunbar, K. R.; Lopez, N., et al. Optical, Electronic, and Magnetic Engineering of (111) Layered Halide Perovskites. *Chem. Mater.* **2018**, *30*, 5315-5321.
- (80) Cortecchia, D.; Dewi, H. A.; Yin, J.; Bruno, A.; Chen, S.; Baikie, T.; Boix, P. P.; Grätzel, M.; Mhaisalkar, S.; Soci, C.; et al. Lead-Free MA₂CuCl_xBr_{4-x} Hybrid Perovskites. *Inorg. Chem.* **2016**, *55*, 1044–1052.
- (81) Fedeli, P.; Gazza, F.; Calestani, D.; Ferro, P.; Besagni, T.; Zappettini, A.; Calestani, G.; Marchi, E.; Ceroni, P.; Mosca, R. Influence of the Synthetic Procedures on the Structural and Optical Properties of Mixed-Halide (Br, I) Perovskite Films. *J. Phys. Chem. C* **2015**, *119*, 21304–21313.
- (82) Volonakis, G.; Filip, M. R.; Haghighirad, A. A.; Sakai, N.; Wenger, B.; Snaith, H. J.; Giustino, F. Lead-Free Halide Double Perovskites via Heterovalent Substitution of Noble Metals. *J. Phys. Chem. Lett.* **2016**, *7*, 1254–1259.
- (83) Sunkara, S.; Vendra, V. K.; Jasinski, J. B.; Deutsch, T.; Andriotis, A. N.; Rajan, K.; Menon, M.; Sunkara, M. New Visible Light Absorbing Materials for Solar Fuels,

- Ga(Sb_x)N_{1-x}. *Adv. Mater.* **2014**, *26*, 2878–2882.
- (84) Weyers, M.; Sato, M.; Ando, H. Red Shift of Photoluminescence and Absorption in Dilute GaAsN Alloy Layers. *Jpn. J. Appl. Phys.* **1992**, *31*, L853-L855.
- (85) Faucher, A.; Terskikh, V. V.; Wasylishen, R. E. Assessing Distortion of the AF₆(A=As, Sb) Octahedra in Solid Hexafluorometallates (V) via NMR Spectroscopy. *Can. J. Chem.* **2015**, *93*, 938–944.
- (86) Harris, R. K.; Becker, E. D.; de Menrzes, S. M. C.; Goodfellow, R.; Granger, P. Commission on Molecular Structure and Spectroscopy. *Pure Appl. Chem.* **2001**, *73*, 1795–1818.
- (87) Bertini, I.; Luchinat, C.; Parigi, G.; Ravera, E. *NMR of Paramagnetic Molecules*; Elsevier; 2016.
- (88) Van Vleck, J. H. The Theory of Electric and Magnetic Susceptibilities. *Oxford University Press*; 1932; p 226.
- (89) Kurland, R. J.; Mcgarvey, B. R. Isotropic NMR Shifts in Transition Metal Complexes: The Calculation of the Fermi Contact and Pseudocontact Terms. *J. Magn. Reson.* **1970**, *2*, 286–301.
- (90) Walder, B. J.; Patterson, A. M.; Baltisberger, J. H.; Grandinetti, P. J. Hydrogen Motional Disorder in Crystalline Iron Group Chloride Dihydrates. *J. Chem. Phys.* **2018**, *149*, 084503.
- (91) Michaelis, V. K.; Greer, B. J.; Aharen, T.; Greedan, J. E.; Kroeker, S. Determining Electron Spin-Transfer Mechanisms in Paramagnetic Ba₂YMO₆ (M = Mo, Re, Ru) Double Perovskites by ⁸⁹Y and ¹³⁷Ba MAS NMR Spectroscopy. *J. Phys. Chem. C* **2012**, *116*, 23646–23652.
- (92) Ceder, D.; Menetrier, M.; P, G. C.; Delmas, C.; Ceder, G. Understanding the NMR Shifts in Paramagnetic Transition Metal Oxides Using Density Functional Theory Calculations. *Phys. Rev. B* **2003**, *67*, 174103.
- (93) La Mar, G. N.; Horrocks, W. E.; Holm, R. H. *NMR of Paramagnetic Molecules*; Academic Press Inc., 1973.
- (94) Wickramasinghe, N. P.; Ishii, Y. Sensitivity Enhancement, Assignment, and Distance Measurement in ¹³C Solid-State NMR Spectroscopy for Paramagnetic Systems under Fast Magic Angle Spinning. *J. Magn. Reson.* **2006**, *181*, 233–243.

- (95) Ooms, K.; Polenova, T.; Shough, A.; Doren, D. J.; Nash, M. J.; Lobo, R. F. Identification of Mixed Valence Vanadium in ETS-10 Using Electron Paramagnetic Resonance, ^{51}V Solid-State Nuclear Magnetic Resonance, and Density Functional Theory Studies. *J. Phys. Chem. C* **2009**, *113*, 10477–10484.
- (96) Kermarrec, E.; Marjerrison, C. A.; Thompson, C. M.; Maharaj, D. D.; Levin, K.; Kroeker, S.; Granroth, G. E.; Flacau, R.; Yamani, Z.; Greedan, J. E.; et al. Frustrated FCC Antiferromagnet Ba_2YOsO_6 : Structural Characterization, Magnetic Properties, and Neutron Scattering Studies. *Phys. Rev. B* **2015**, *075133*, 1–9.
- (97) Grey, C. P.; Dupre, N. NMR Studies of Cathode Materials for Lithium-Ion Rechargeable Batteries. *Chem. Rev.* **2004**, *104*, 4493–4512.
- (98) Ishii, Y.; Wickramasinghe, N. P.; Chimon, S. A New Approach in 1D and 2D ^{13}C High-Resolution Solid-State NMR Spectroscopy of Paramagnetic Organometallic Complexes by Very Fast Magic-Angle Spinning. *J. Am. Chem. Soc.* **2003**, *125*, 3438–3439.
- (99) Aguiar, P. M.; Katz, M. J.; Leznof, D. B.; Kroeker, S. Natural Abundance ^{13}C and ^{15}N Solid-state NMR Analysis of Paramagnetic Transition-metal Cyanide Coordination Polymers. *Phys. Chem. Chem. Phys.* **2009**, *11*, 6925–6934.
- (100) Grey, C. P.; Smith, M. E.; Cheetham, A. K.; Dobson, C. M.; Dupree, R. MAS NMR Study of Rare-Earth Pyrochlores: Paramagnetic Shifts in the Solid State. *J. Am. Chem. Soc.* **1990**, *112*, 4670–4675.
- (101) Brough, A. R.; Grey, C. P.; Dobson, C. M. Paramagnetic Ions as Structural Probes in Solid-State NMR: Distance Measurements in Crystalline Lanthanide Acetates. *J. Am. Chem. Soc.* **1993**, *115*, 7318–7327.
- (102) Bertarello, A.; Schubeis, T.; Fuccio, C.; Ravera, E.; Fragai, M.; Parigi, G.; Emsley, L.; Pintacuda, G.; Luchinat, C. Paramagnetic Properties of a Crystalline Iron-Sulfur Protein by Magic-Angle Spinning NMR Spectroscopy. *Inorg. Chem.* **2017**, *56*, 6624–6629.
- (103) Pell, A. J.; Middlemiss, D. S.; Strobridge, F. C.; Miller, J. K.; Cle, J.; Whittingham, M. S.; Emsley, L.; Grey, C. P.; Pintacuda, G. Spin-Transfer Pathways in Paramagnetic Lithium Transition-Metal Phosphates from Combined Broadband Isotropic Solid-State MAS NMR Spectroscopy and DFT Calculations. *J. Am. Chem.*

Soc. **2012**, *134*, 17178–17185.

(104) Liu, K.; Ryan, D.; Nakanishi, K.; Mcdermott, A. Solid State NMR Studies of Paramagnetic Coordination Complexes: A Comparison of Protons and Deuterons in Detection and Decoupling. *J. Am. Chem. Soc.* **1995**, *117*, 6897–6906.

(105) Helmholz, B. L.; Kruh, R. F. The Crystal Structure of Cesium Chlorocuprate, Cs_2CuCl_4 , and the Spectrum of the Chlorocuprate Ion. *J. Am. Chem. Soc.* **1952**, *74*, 1176–1181.

(106) Filip, M. R.; Verdi, C.; Giustino, F. G.W. Band Structures and Carrier Effective Masses of $\text{CH}_3\text{NH}_3\text{PbI}_3$ and Hypothetical Perovskites of the Type APbI_3 : $\text{A}=\text{NH}_4$, PH_4 , AsH_4 , and SbH_4 . *J. Phys. Chem. C* **2015**, *119*, 25209–25219.

CHAPTER 5

Tailorable Indirect to Direct Bandgap Double Perovskites with Bright White-Light Emission: Decoding Chemical Structure Using Solid-State NMR^{R4}

5.1 Introduction

Lead halide perovskite (LHP) materials, with a generic formula ABX_3 (where $A = Cs^+$, $CH_3NH_3^+$, $CH(NH_2)_2^+$; $B = Pb^{2+}$; $X = Cl^-$, Br^- , and I^-) have emerged as a potential disruptive technology due to their remarkable photoconversion efficiencies of 25.2% (single-junction) or 28% when combined with silicon tandem solar cells.¹ Beyond their exciting photovoltaic properties, perovskites have been used in a variety of cost-efficient optoelectronic and electronic applications including light-emitting devices, photodetectors, lasers, water splitting, and X-ray imaging.²⁻⁷ Lighting consumes approximately 20% of the electricity produced globally with growing demand from both developed and developing countries. Identifying sustainable energy solutions, such as highly efficient and low-cost materials for light-emitting diode (LED) applications, is essential. For example, LEDs are expected to produce energy savings of billions of dollars annually in the United States alone.⁸

Recently, halide perovskites have emerged as an attractive light-emitting material due to their near unity photoluminescent quantum yield (PLQY), widely tailorable narrow-band visible-light emission, and cost-efficient solution processability.^{2,4,9} Building beyond their photoluminescent properties, structural modifications in LHPs to form two-dimensional (2D) LHPs has yielded materials that

^{R4} The contents of this chapter have been copied and/or adapted from the following publication: Karmakar, A.; Bernard, G. M.; Meldrum, A.; Oliynyk, A. O.; Michaelis, V. K. Tailorable Indirect to Direct Band-Gap Double Perovskites with Bright White-Light Emission: Decoding Chemical Structure Using Solid-State NMR. *J. Am. Chem. Soc.* **2020**, *142*, 10780–10793. The supplementary data for this chapter is available in Appendix D: Experimental section, Tables D1–D6 and Figures D1–D27.

show broad-band emission in the visible-light range. For example, the intrinsic broad-band white-light emission which is observed upon ultraviolet excitation is attributed to self-trapped excitons in these 2D LHP materials.¹⁰⁻¹² One such attractive broad-band white-light emitting 2D LHP material is (EDBE)PbBr₄ (EDBE = 2,2'-(ethylenedioxy)bis(ethylammonium)) with a PLQY of 9%.¹² White-light emission from a single-material source is an attractive avenue for lighting and display applications, since a single-source emitter simplifies device structure and fabrication, avoiding color instability due to the different degradation rates and self-absorption issues encountered with mixed and multiple emitters.^{13,14}

Though LHPs have excellent potential for optoelectronic and photovoltaic applications, they suffer from commercialization concerns due to their poor chemical stability^{15,16} and have long-term environmental and societal concerns associated with prolonged use of Pb-containing materials.^{17,18} For example, bulk LHP materials as well as thin films or LHP solar-cell devices have been shown to undergo chemical decomposition while exposed to ambient light, humid environments, or elevated temperatures.^{16,19,20} Moreover, these lead salts are highly soluble in water, which over time has lasting environmental and toxicological implications.^{21,22} One avenue being explored to circumvent the lead toxicity of LHPs involves partial (or full) substitution of isoelectronic and low-toxicity elements (i.e., Sn²⁺, Ge²⁺) into these materials. Unfortunately, tin(II) and germanium(II) halide perovskite materials are prone to oxidation, creating additional challenges associated with their long-term chemical stability.²³

As a result of the vast structural and elemental diversity present in the perovskite family, a series of lead-free, chemically stable halide double perovskite (HDP) materials are now being explored as sustainable alternatives to LHPs due to their attractive optical properties both in bulk and in nanocrystals (NCs).²⁴⁻³⁴ The general formula of a HDP is A₂B'(III)B''(I)X₆, where A is a monovalent cation, B'(III) and B''(I) are trivalent and monovalent cations, respectively, and X is a halide anion. A further benefit of HDP materials compared to LHPs is that they exhibit much higher thermal and moisture resistance.³⁵⁻³⁸

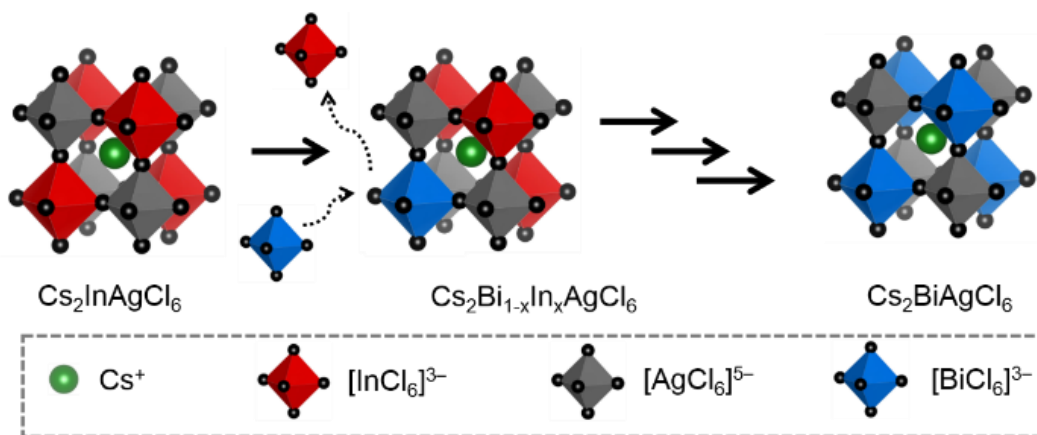
The vast majority of HDPs reported are chloride based with wide bandgaps ranging above 2 eV, limiting their ability as solar-absorbing materials. However, these materials have exhibited good photoluminescent (PL) properties with promising quantum yields.^{24,32} For example, PL properties for HDPs can be achieved either in the presence of an activator (such as Mn^{2+})^{25,27,29,31,39,40} or by a chemical modification on the B'(III) and/or B''(I) site(s).^{24,30,41} Orange-light emission of Mn^{2+} -doped $\text{Cs}_2\text{InAgCl}_6$ NCs has been demonstrated with PLQYs enhanced by an order of magnitude (i.e., ca. 1.6–16%) upon Mn^{2+} doping in $\text{Cs}_2\text{InAgCl}_6$ NCs.²⁹ Bi-doped $\text{Cs}_2\text{InAg}_x\text{Na}_{1-x}\text{Cl}_6$ HDP provided stable (>1000 h) warm white-light emission with a maximum PLQY of 86%,²⁴ whereas Bi-doped $\text{Cs}_2\text{InAg}_x\text{Na}_{1-x}\text{Cl}_6$ NC was found to have a maximum PLQY of ca. 22%.⁴² A broad orange-light emission has been reported from Bi-doped $\text{Cs}_2\text{InAgCl}_6$ NCs with a PLQY of 11.4%.³⁴

Altering the magnitude of the bandgap for perovskite materials upon metal alloying is one attractive avenue often reported in the literature.^{43–46} Converting materials from an indirect to a direct band-gap semiconductor is less common in semiconducting materials,^{47–49} although this offers one stream that could further enable fine tailoring of their optical properties. As most reported HDP materials are either indirect or direct band-gap semiconductors, this class of compounds can support this type of band-gap transformation. For instance, $\text{Cs}_2\text{BiAgCl}_6$ HDPs exhibit an indirect bandgap due to the presence of a lone pair on Bi^{3+} ($6s^2$).^{36,50} In contrast, $\text{Cs}_2\text{InAgCl}_6$ HDPs are direct band-gap semiconductors due to the absence of a lone pair on In(III) .⁵¹

To date, diffraction-based techniques have been used extensively to evaluate the structural properties of HDP materials. These techniques provide long-range structural information but are devoid of detail pertaining to atomic-level structural properties. As a result, atomic-level structural insight of these currently developing HDP materials are not well discussed in the literature. It is essential to characterize the long-range crystalline nature of these materials as well as the complex evolution of short-range structure as $\text{Bi}^{3+}/\text{In}^{3+}$ cations are mixed in $\text{Cs}_2\text{Bi}_{1-x}\text{In}_x\text{AgCl}_6$ HDPs. Solid-state nuclear magnetic resonance (NMR) spectroscopy is one of the most powerful,

nondestructive analytical methods able to decode this complex structural evolution and provide insights for the dynamics of these perovskite-based materials.^{16,52–72}

These observations motivated us to prepare a series of bulk $\text{Cs}_2\text{Bi}_{1-x}\text{In}_x\text{AgCl}_6$ HDP solid solutions where changes in $\text{Bi}^{3+}/\text{In}^{3+}$ cationic ratios can be associated with an indirect (Bi rich) to direct (In rich) bandgap. This collection of HDPs demonstrates how tunable white-light PLQY behavior can be attained. We investigate the unique electronic structures from a first-principles point of view and the photophysical properties using UV-vis and PL techniques for these HDP semiconductors. We further explore the interplay of these materials using robust NMR and XRD measurements as well as density functional theory (DFT) calculations to reveal atomic-level chemical structural insights into the seemingly random $\text{Bi}^{3+}/\text{In}^{3+}$ cationic mixing (i.e., solid solution in $\text{Cs}_2\text{Bi}_{1-x}\text{In}_x\text{AgCl}_6$ HDP materials along with a high degree of B'(III)/B''(I) site ordering). Moreover, antisite defects (i.e., the disorder on B'(III) and B''(I) sites which have similar octahedral environments)⁷³ and phase segregation upon $\text{Bi}^{3+}/\text{In}^{3+}$ mixing are also investigated for the complete HDP series.



Scheme 5.1. Schematic presentation of the crystal structures of the $\text{Cs}_2\text{InAgCl}_6$ and $\text{Cs}_2\text{BiAgCl}_6$ parent materials and of their $\text{Cs}_2\text{Bi}_{1-x}\text{In}_x\text{AgCl}_6$ mixed Bi/In cationic analogues.

5.2 Results and Discussion

5.2.1 B'-Site Selection Using Goldschmidt Tolerance Factor Directing Bi/In B'(III)-Site Exchange

A semiempirical geometric parameter known as the Goldschmidt tolerance factor (t) is often applied to elucidate the structural stability of ABX_3 perovskite materials. It is defined as:

$$t = \frac{(r_A + r_X)}{\sqrt{2}(r_B + r_X)} \quad (\text{Eq. 5.1})$$

where r_A , r_B , and r_X are the ionic radii of the A, B, and X sites, respectively.⁷⁴ Stable perovskite systems are typically formed with 3D octahedral connectivity when $t = 0.75$ – 1.00 .⁷⁵ Another semiempirical geometric parameter is used to define the octahedral stability, known as the octahedral factor (μ), defined as:

$$\mu = \frac{r_B}{r_X} \quad (\text{Eq. 5.2})$$

Usually, BX_6 octahedra are stable when $0.442 \leq \mu \leq 0.895$.² The combination of t and μ provides insight into the probability of the formation of a stable perovskite phase. As double perovskites have two different B sites (B' and B'') and thus r_B is taken as an arithmetic mean of B' and B'' radii ($r_{B'}$, $r_{B''}$), one can increase the elemental dimensionality (i.e., cation and valency options increase). Applying Shannon's ionic radii,⁷⁶ one can obtain (t , μ) values for $Cs_2InAgCl_6$ and $Cs_2BiAgCl_6$ of (0.937, 0.539) and (0.900, 0.602), respectively. For mixed Bi/In cationic $Cs_2Bi_{1-x}In_xAgCl_6$ solid solutions, t and μ values span between $0.900 \leq t \leq 0.937$ and $0.539 \leq \mu \leq 0.602$, respectively, suggesting that it is possible to form the desired stable perovskite phase for $Cs_2Bi_{1-x}In_xAgCl_6$ ($0 \leq x \leq 1$) solid solutions (Scheme 5.1).

5.2.2 Elemental Composition, Morphology, and Thermal Stability

The $Cs_2BiAgCl_6$ and $Cs_2InAgCl_6$ parent HDPs were synthesized via a solvent-phase synthesis approach starting from their chloride salts, namely, CsCl, BiCl₃, InCl₃, and AgCl, in concentrated hydrochloric acid media. The mixed Bi³⁺/In³⁺ cationic analogues, i.e., $Cs_2Bi_{1-x}In_xAgCl_6$ (nominal; $x = 0$ to 1, Table D1), were synthesized similarly using stoichiometric BiCl₃:InCl₃ nominal molar ratios. Further synthesis details are discussed in the Appendix D. Figure 5.1a illustrates photographs of

$\text{Cs}_2\text{Bi}_{1-x}\text{In}_x\text{AgCl}_6$ HDPs. The solvent synthesis approach leads to multifaceted micrometer-sized crystals confirmed through field-emission scanning electron microscopy (FESEM) as shown in Figures 5.1b and D1. Elemental analysis by energy-dispersive X-ray spectroscopy (EDS) indicates that the molar ratio $\text{Cs}^+:\text{B}'^{3+}:\text{Ag}^+:\text{Cl}^-$, where $\text{B}' = \text{In}, \text{Bi}$, or both, $\approx 2:1:1:6$ (Table D1), which is the desired elemental composition for the HDP materials. Elemental mapping using EDS analysis shows a homogeneous distribution of all elements (Cs, Bi, In, Ag, and Cl) throughout the powdered solids (Figures 5.1b and D2). The accuracy of the $\text{Bi}^{3+}:\text{In}^{3+}$ compositional ratios in the final products were further confirmed using the inductively coupled plasma optical emission spectrometry (ICP-OES) technique (Table D1), which yielded results similar to the nominal $\text{Bi}^{3+}:\text{In}^{3+}$ batch compositional ratios (Table D2).

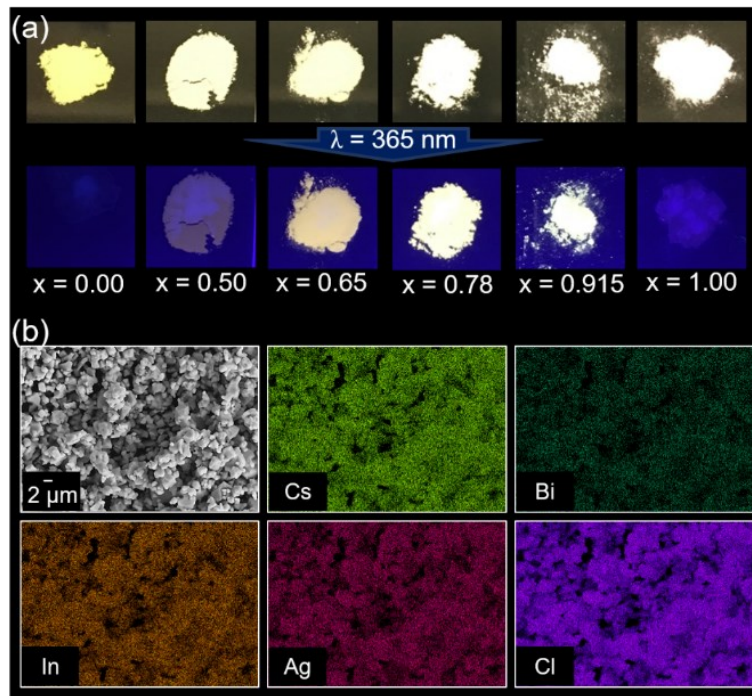


Figure 5.1. (a) Photographs of $\text{Cs}_2\text{Bi}_{1-x}\text{In}_x\text{AgCl}_6$ HDPs under visible (upper row) and UV (lower row, $\lambda = 365 \text{ nm}$) light. (b) FESEM image ($2 \mu\text{m}$ scale) with corresponding EDS elemental mapping showing a homogeneous distribution of Cs (light green), Bi (dark green), In (orange), Ag (pink), and Cl (violet) for $\text{Cs}_2\text{Bi}_{0.085}\text{In}_{0.915}\text{AgCl}_6$ HDP polycrystals.

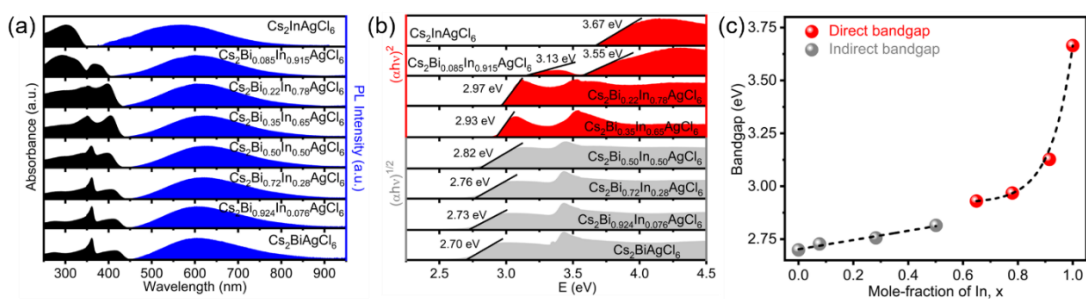


Figure 5.2. (a) UV-vis absorption spectra (black) and PL spectra (blue), (b) Tauc plots showing indirect ($x \leq 0.5$, gray) and direct ($x > 0.50$, red) bandgaps, and (c) change in bandgap vs indium mole fraction for $\text{Cs}_2\text{Bi}_{1-x}\text{In}_x\text{AgCl}_6$ ($0 \leq x \leq 1$) HDPs.

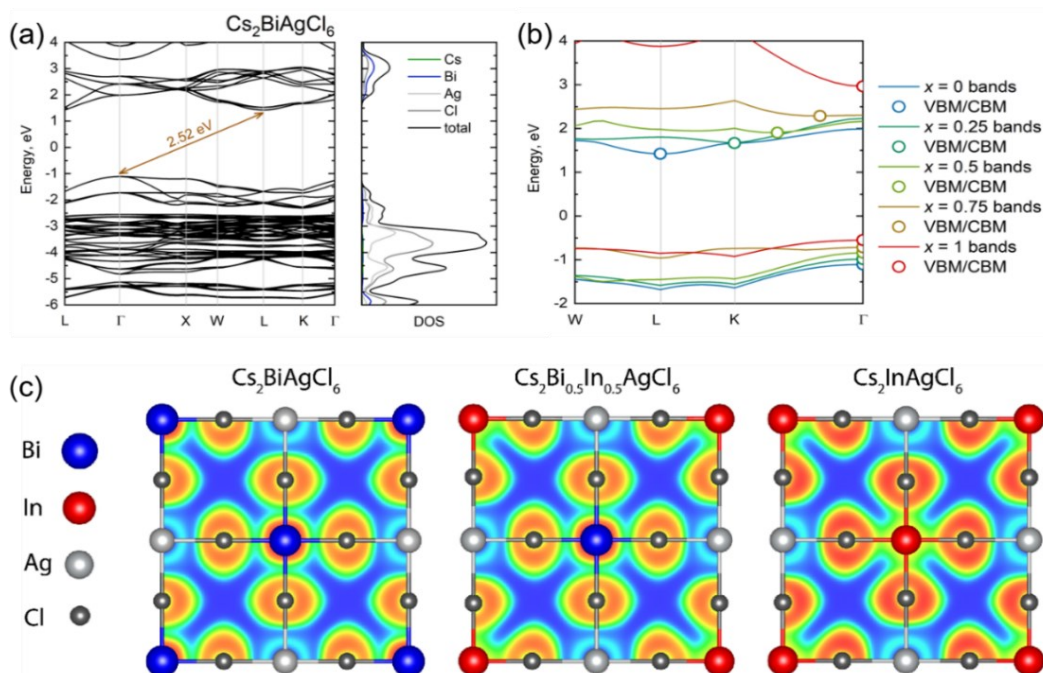


Figure 5.3. (a) HSE06 DFT band structure and density of states for $\text{Cs}_2\text{BiAgCl}_6$. (b) Indirect to direct bandgap transition in the $\text{Cs}_2\text{Bi}_{1-x}\text{In}_x\text{AgCl}_6$ compounds. (c) Electron localization function of the $\text{Cs}_2\text{Bi}_{1-x}\text{In}_x\text{AgCl}_6$ compounds. In c, the 100th slice is shown, with Bi, In, Ag, and Cl atoms located on the plane. Blue, low electron density; red, high electron density.

Thermal stability measurements using thermogravimetric analysis (TGA) for $\text{Cs}_2\text{BiAgCl}_6$ and $\text{Cs}_2\text{InAgCl}_6$ parents and for one $\text{Bi}^{3+}/\text{In}^{3+}$ mixed-cationic material, specifically $\text{Cs}_2\text{Bi}_{0.085}\text{In}_{0.915}\text{AgCl}_6$, are shown in Figure D3. TGA data indicate that the materials are all thermally stable up to 500 °C and that $\text{Bi}^{3+}/\text{In}^{3+}$ cationic mixing has a negligible effect on the thermal stability.

5.2.3 Optical and Electronic Bandgap Tailoring

The optical band-gap properties of $\text{Cs}_2\text{Bi}_{1-x}\text{In}_x\text{AgCl}_6$ HDPs were measured by UV–vis diffuse reflectance (DR) spectroscopy. Figure 5.2a shows the absorbance spectra for the $\text{Cs}_2\text{Bi}_{1-x}\text{In}_x\text{AgCl}_6$ HDPs. These absorbance data were obtained from DR measurements and analyzed using the Kubelka–Munk transformation method⁷⁷ (see Materials and Methods in the Appendix D). The experimentally obtained indirect and direct bandgaps for the $\text{Cs}_2\text{Bi}_{1-x}\text{In}_x\text{AgCl}_6$ HDPs are shown in Figure 5.2b. $\text{Cs}_2\text{BiAgCl}_6$ is reminiscent of an indirect band-gap semiconductor due to the mixing between frontier orbitals of Bi and Ag in the valence and conduction band extrema. This has been identified as the origin of the indirect bandgaps of Bi–Ag-based HDPs in past studies.^{36,78} As substitution of Bi^{3+} with In^{3+} proceeds in a migratory fashion to form $\text{Cs}_2\text{InAgCl}_6$, a direct band-gap material emerges, where valence-band maxima and conduction band minima originate from In-4d/Ag-4d and In-5s/Ag-5s states, respectively.⁵¹ On the basis of Tauc plots, $(\alpha h\nu)^{1/2}$ vs energy, $\text{Cs}_2\text{BiAgCl}_6$ exhibits an indirect bandgap of 2.70 eV (Figure 5.2b), agreeing well with an earlier calculated bandgap of 2.62 eV using a hybrid functional.³⁶ A Tauc plot of $(\alpha h\nu)^2$ vs energy indicates that $\text{Cs}_2\text{InAgCl}_6$ has an experimental direct bandgap of 3.67 eV ($\Delta E_g \approx 1$ eV). However, the experimental bandgap of $\text{Cs}_2\text{InAgCl}_6$ is much higher than the calculated fundamental bandgap of 2.5 eV because the associated direct band transition is parity forbidden.⁷⁹

This unique behavior for HDP materials, whereby they are either indirect or parity-forbidden direct band-gap materials, leads to inferior absorption behavior around the bandgap, rendering them unfavorable candidates for optoelectronic applications such as LEDs.^{37,79} These observations motivated us to investigate the optical properties of bulk polycrystalline mixed $\text{Bi}^{3+}/\text{In}^{3+}$ $\text{Cs}_2\text{Bi}_{1-x}\text{In}_x\text{AgCl}_6$ double perovskites. A band

structure calculation using DFT with the Heyd–Scuseria–Ernzerhof (HSE06) functional shows that $\text{Cs}_2\text{Bi}_{1-x}\text{In}_x\text{AgCl}_6$ materials with $x \leq 0.50$ have an indirect bandgap, whereas materials with $x > 0.50$ possess a direct bandgap (vide infra). The indirect bandgap for $\text{Cs}_2\text{Bi}_{1-x}\text{In}_x\text{AgCl}_6$ increases linearly from 2.70 to 2.82 eV as x increases from 0 to 0.50. In contrast, the direct bandgap increases from 2.93 to 3.67 eV in an exponential-like fashion for x values ranging from 0.65 to 1 (Figure 5.2c). The change in the bandgap of $\text{Cs}_2\text{Bi}_{1-x}\text{In}_x\text{AgCl}_6$ agrees well with the visual color of these materials (Figure 5.1a); for example, $\text{Cs}_2\text{BiAgCl}_6$ ($x = 0$) is pale yellow (2.70 eV), but as In^{3+} is incorporated, the material becomes increasingly white, with $\text{Cs}_2\text{InAgCl}_6$ (3.67 eV) appearing as a microcrystalline pristine white solid.

5.2.4 Indirect to Direct Bandgap Transition Using the Calculated Electronic Band Structure

A transition from an indirect to a direct bandgap occurs with Bi to In substitution in the $\text{Cs}_2\text{Bi}_{1-x}\text{In}_x\text{AgCl}_6$ ($0 \leq x \leq 1$) HDP series. This case is similar to previously reported isoelectronic Sb to In substitution in $\text{Cs}_2\text{Sb}_{1-x}\text{In}_x\text{AgCl}_6$ compounds.⁵⁰ The HSE06 DFT functional was applied to correct for the underestimated PBE bandgap (Figure 5.3a), which resulted in good agreement with the band-gap estimation (i.e., 2.52 (DFT) vs 2.70 eV (expt.)). Similar HSE06 DFT bandgap and density of states (DOS) plots are available for the rest of the $\text{Cs}_2\text{Bi}_{1-x}\text{In}_x\text{AgCl}_6$ series ($x = 0.25, 0.5, 0.75, \text{ and } 1$) in the Appendix D (Figures D4–D7).

The transition from an indirect to a direct bandgap was observed in the $\text{Cs}_2\text{Bi}_{1-x}\text{In}_x\text{AgCl}_6$ ($0 \leq x \leq 1$) HDP series (Figure 5.3b). The valence band maximum (VBM) is indicated (Figure 5.3b), and for each sample it is located at the Γ point. The conduction band maximum (CBM), also indicated in Figure 5.3b, is different for each sample. For $\text{Cs}_2\text{BiAgCl}_6$, the CBM is at the L symmetry point, composing an indirect Γ –L bandgap. With 25% substitution of Bi with In atoms, the bandgap still remains indirect (Γ –K). The rest of the solid solution results indicate that the CBM lies between the K and Γ points: with the sample 50% substituted with In, the CBM is closer to K, while for the 75% Bi-substituted sample, the CBM is closer to the Γ point, and as a result, it is measured as a direct Γ – Γ bandgap, in good agreement with the experimental

values. The end-point compound, Cs₂InAgCl₆, has a direct Γ – Γ bandgap, with a HSE06 DFT value of 3.51 eV, which agrees well with the experimental value of 3.67 eV. More information is listed in Table 5.1.

Table 5.1. Calculated and experimental bandgap values for Cs₂Bi_{1-x}In_xAgCl₆.

x	0	0.25	0.5	0.75	1
CBM, eV	1.42 (L)	1.67 (K)	1.91	2.29	2.96 (Γ)
VBM, eV	-1.10 (Γ)	-0.98 (Γ)	-0.83 (Γ)	-0.72 (Γ)	-0.55 (Γ)
HSE06 gap, eV	2.52	2.65	2.74	3.01	3.51
Experimental gap, eV	2.70	2.76 ^a	2.82	2.97 ^b	3.67

^a The ICP-OES-detected composition is $x = 0.28$. ^b The ICP-OES-detected composition is $x = 0.78$.

To further utilize DFT tools, electronic properties were investigated with electron localization function (ELF) and Bader charge analyses. Substitution of Bi for In gradually localizes more electron density on the Cl atoms (more intense red cloud about the Cl, Figure 5.3c); however, the Bader charge values indicate that there is only a dramatic charge change in the end member of the solid solution series (Table D3, Figure D8). In the systems with Bi/In substitution, Ag atom charge differences are negligible and are essentially close to the average Ag charge, regardless of the second-neighbor atom, but the Cl atoms have a 2–3% charge difference, depending on whether Bi or In atoms are in the coordination environment, with the In atom giving a more negative charge on the bonded Cl atoms.

Crystal orbital overlap population (COOP) analyses were undertaken on Cs–Cl, Ag–Cl, Bi–Cl, and In–Cl bonds (Figures D9–D12). These analyses indicate that mostly bonding states are present, resulting in a positive overall contribution in the bonds, with the overall population scaled to the amount of Bi and In in each individual compound. A strong antibonding character is observed near the Fermi level in the Ag–Cl interaction but with the overall bonding states prevailing. Substitution of Bi with In affects the Ag d-band splitting, which is more pronounced in the Bi-containing analogs, broadening the antibonding contributions.

5.2.5 Steady-State and Time-Resolved PL Spectra

All $\text{Cs}_2\text{Bi}_{1-x}\text{In}_x\text{AgCl}_6$ samples exhibit broad PL emission ranging from 400 to 850 nm (Figures 5.2a and D13a) with a nearly constant spectral width of ~ 200 nm full width at half-maximum (fwhm) (Figure D13b). The broad PL spectra at ambient temperatures have been attributed to strong electron–phonon Fröhlich interactions in HDP materials.⁸⁰ In addition, the emission and excitation wavelengths do not affect the shape of PL excitation or emission spectra, as shown in Figure D14. This result indicates that the white-light emission originates from recombination of the same excitonic state for these HDPs.

$\text{Cs}_2\text{InAgCl}_6$ shows a PL maximum at 570 nm (2.18 eV), whereas the PL maximum for $\text{Cs}_2\text{BiAgCl}_6$ is comparatively red shifted and centered at 605 nm (2.05 eV) (Figure D13). The PL maxima extend to a wavelength of 626 nm (1.98 eV) for $\text{Cs}_2\text{Bi}_{0.50}\text{In}_{0.50}\text{AgCl}_6$, which is the reddest PL spectrum among the materials (Figure D13c). As a result, the PL emission for all of the materials appeared to be yellowish/orange in color.

The luminescence of the indirect band-gap perovskite materials ($\text{Cs}_2\text{Bi}_{1-x}\text{In}_x\text{AgCl}_6$ with $x \leq 0.50$) appeared visibly dim under a UV light, while the perovskites with direct bandgaps ($\text{Cs}_2\text{Bi}_{1-x}\text{In}_x\text{AgCl}_6$ with $x > 0.50$) revealed bright PL (Figure 5.1a). $\text{Cs}_2\text{InAgCl}_6$ in particular did not fit this general trend, however, as it has a direct bandgap but displayed faint emission due to the parity-forbidden band transition at the fundamental bandgap. The PLQY for $\text{Cs}_2\text{Bi}_{1-x}\text{In}_x\text{AgCl}_6$ increased gradually as a function of In concentration, reaching a maximum when $x = 0.915$ (PLQY = $34 \pm 4\%$); this is followed by a stark decrease in PLQY upon reaching the pure endmember $\text{Cs}_2\text{InAgCl}_6$, Figure 5.4a. Although $\text{Cs}_2\text{InAgCl}_6$ exhibits a direct bandgap, it too suffers from a low PLQY ($< 1\%$) due to the In-5s orbital beginning to dominate in the conduction band, which is in good agreement with DFT calculations (Figures D4–D7).⁷⁹ As a result, the parity-forbidden transition from the valence band to the conduction band becomes quite long and is no longer competitive with the nonradiative (faster) recombination causing a lower PLQY.

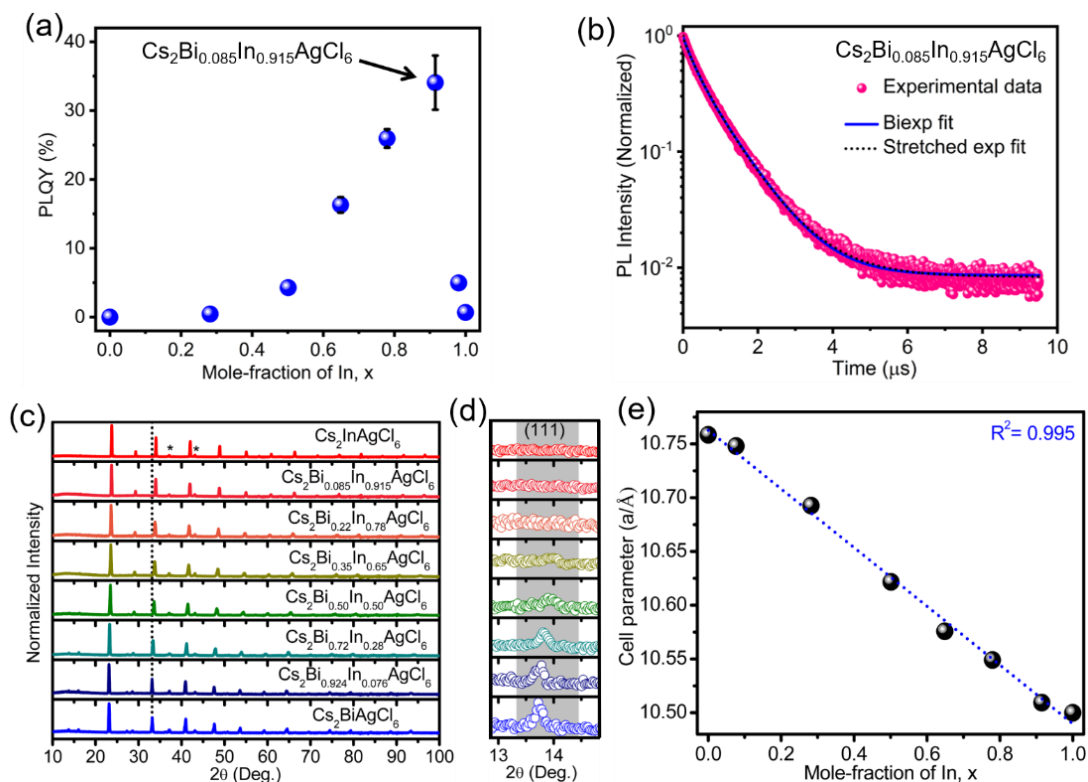


Figure 5.4. (a) PLQY as a function of indium mole fraction (x) for $\text{Cs}_2\text{Bi}_{1-x}\text{In}_x\text{AgCl}_6$ HDPs. (b) PL decay for $\text{Cs}_2\text{Bi}_{0.085}\text{In}_{0.915}\text{AgCl}_6$ with $\lambda_{\text{ex}} = 364$ nm and $\lambda_{\text{em}} = 625$ nm. (c) PXR D patterns, (d) expansion of the (111) peaks in the PXR D patterns, and (e) change in unit cell parameters with indium mole fraction for $\text{Cs}_2\text{Bi}_{1-x}\text{In}_x\text{AgCl}_6$ HDPs. In c, dotted line is a guide for the eye and asterisks (*) denote the positions of background signals for all $\text{Cs}_2\text{Bi}_{1-x}\text{In}_x\text{AgCl}_6$ HDPs (Figure D16).

The time-resolved PL spectrum for $\text{Cs}_2\text{Bi}_{0.085}\text{In}_{0.915}\text{AgCl}_6$ (with maximum PLQY) is shown in Figure 5.4b. Several decay models were fit using a nonlinear least-squares fitting algorithm, including a single exponential, a biexponential, and a stretched exponential (Figure D15). While the correct model is difficult to determine unambiguously from these data, the biexponential and stretched exponential gave the lowest sum of squares of the residuals and showed comparatively little bias in the residuals, Table D4. The biexponential model results yielded a fast component with a time constant of 279 ns (36%) and a slow component of 865 ns (64%). From these two components, a weighted mean time constant of 774 ns can be extracted for comparative

purposes. The stretched exponential yielded similar although slightly longer mean time constants calculated according to $\tau = \tau_{SE}[\Gamma(2/\beta)/\Gamma(1/\beta)]$,⁸¹ where τ_{SE} is the time constant obtained from the stretched exponential model fit and β is the stretching parameter. A comparable behavior is observed for $\text{Cs}_2\text{Bi}_{0.22}\text{In}_{0.78}\text{AgCl}_6$, which gave a weighted mean biexponential lifetime of 978 ns. The PL decay traces and average lifetimes were nearly the same upon changing the wavelength from 550 to 700 nm (using a monochromator with an 8 nm band pass) for both materials (Figure D15 and Table D5). This result suggests that the broad-band emission is unlikely to arise from different mechanisms in these HDP materials. A similar observation has been noted in 2D LHP material.⁸² In contrast, $\text{Cs}_2\text{InAgCl}_6$ shows two different transition mechanisms with short (<10 ns) and long (tens to hundreds of nanoseconds) PL lifetime components, where the longer lifetime component is attributed to the parity-forbidden transitions from CBM to VBM.⁸³ We further note that the PL lifetime of $\text{Cs}_2\text{InAgCl}_6$ HDP is insensitive to the intensity of the pump laser,⁵¹ whereas different excitation flux may explain some of the differences in the reported dynamics in LHP materials.^{84,85}

5.2.6 Insight into HDP Chemical Structure from XRD and NMR Spectroscopy

The $\text{Cs}_2\text{BiAgCl}_6$ and $\text{Cs}_2\text{InAgCl}_6$ parent materials are phase pure and adopt a face-centered cubic double perovskite lattice (space group $Fm\bar{3}m$) with unit cell constants of 10.7584(14) and 10.5000(12) Å, respectively. The small difference (<3%) in the unit cell parameters between $\text{Cs}_2\text{BiAgCl}_6$ and $\text{Cs}_2\text{InAgCl}_6$ allows formation of mixed-cationic, $\text{Cs}_2\text{Bi}_{1-x}\text{In}_x\text{AgCl}_6$ HDP solid solutions that adopt the same $Fm\bar{3}m$ space group. Since the ionic radii of In^{3+} ($r(\text{In}^{3+}) = 80$ pm) are less than those of Bi^{3+} ($r(\text{Bi}^{3+}) = 103$ pm),⁷⁶ the diffraction peak is sequentially shifted to a higher 2θ value with increasing In^{3+} content in $\text{Cs}_2\text{Bi}_{1-x}\text{In}_x\text{AgCl}_6$ (Figure 5.4c) as the unit cell decreases in volume. It has been shown that the appearance of a (111) diffraction peak is fundamentally related to the B'(III) and B''(I) site ordering in $\text{Cs}_2\text{InAg}_x\text{Na}_{1-x}\text{Cl}_6$ HDPs.²⁴ The appearance of (111) diffraction peaks in

$\text{Cs}_2\text{Bi}_{1-x}\text{In}_x\text{AgCl}_6$ HDPs also indicates a high degree B'(Bi³⁺, In³⁺) and B''(Ag⁺) site ordering (Figure 5.4d).

The presence of an intense (111) diffraction peak for the $\text{Cs}_2\text{BiAgCl}_6$ parent indicates extremely well-ordered Bi³⁺ and Ag⁺ cationic sites, further supported by the NMR, *vide infra*. The peak intensity decreases with increasing In³⁺ concentration (i.e., $\text{Cs}_2\text{Bi}_{1-x}\text{In}_x\text{AgCl}_6$ HDPs) and becomes undetectable for the $\text{Cs}_2\text{InAgCl}_6$ parent material. The isoelectronic nature of In³⁺ and Ag⁺ cations limits the sensitivity of the (111) diffraction peak, and it becomes uninformative for B'(III) and B''(I) site cation ordering for the $\text{Cs}_2\text{InAgCl}_6$ parent and In³⁺-rich $\text{Cs}_2\text{Bi}_{1-x}\text{In}_x\text{AgCl}_6$ HDP materials. We therefore applied NMR spectroscopy to understand the atomic-level ordering of these materials. The cell parameters for the mixed-cation $\text{Cs}_2\text{Bi}_{1-x}\text{In}_x\text{AgCl}_6$ compounds extracted from the PXRD patterns show a linear relationship as a function of In concentration as shown in Figure 5.4e. This result is consistent with Vegard's law,⁸⁶ whereby the mixed B'(III) site HDP, $\text{Cs}_2\text{Bi}_{1-x}\text{In}_x\text{AgCl}_6$, demonstrates solid solution behavior.

Diffraction approaches provide insight into the long-range structure of these $\text{Cs}_2\text{Bi}_{1-x}\text{In}_x\text{AgCl}_6$ perovskite materials. Most of the HDP parent materials rely on structural elucidation using these techniques. However, it has been shown that solid-state NMR spectroscopy yields a deeper understanding of local (<5 Å)- and medium (5–10 Å)-range structure when cation and anion doping (or mixing) is present in perovskite-based materials.^{52,53,63,66–72} Previously, we used ¹³³Cs and ¹²¹Sb NMR spectroscopy to unravel unique structural motifs for paramagnetic Cu(II)-doped $\text{Cs}_2\text{SbAgCl}_6$ HDPs.⁷⁰ Here, we performed ¹¹⁵In, ¹³³Cs, and ²⁰⁹Bi NMR spectroscopy to improve our structural understanding of the A(¹³³Cs) and B'(²⁰⁹Bi and ¹¹⁵In) sites for $\text{Cs}_2\text{Bi}_{1-x}\text{In}_x\text{AgCl}_6$ solid solutions.

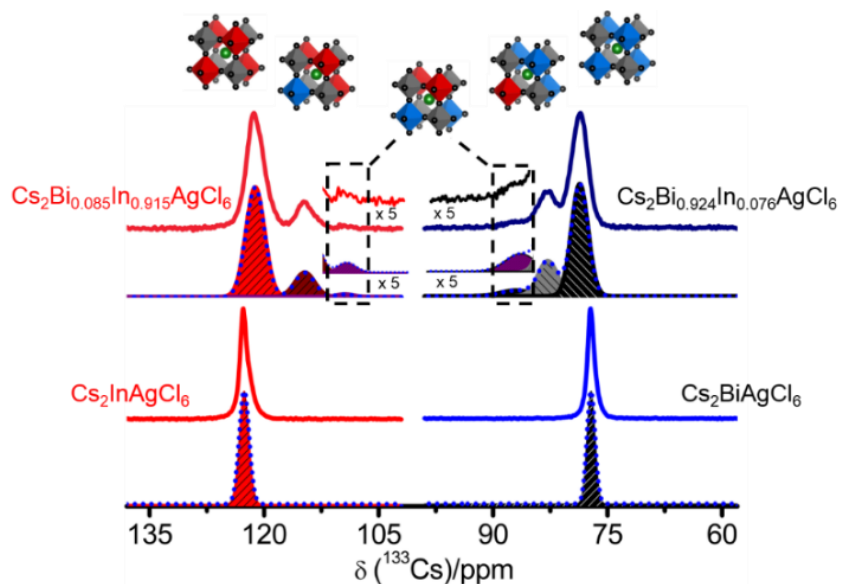


Figure 5.5. Solid-state ^{133}Cs MAS NMR spectra (solid lines) and its overall best Gaussian fits (blue dotted lines) for $\text{Cs}_2\text{BiAgCl}_6$ and $\text{Cs}_2\text{InAgCl}_6$ parents and their In^{3+} - or Bi^{3+} -doped materials, namely, $\text{Cs}_2\text{Bi}_{0.924}\text{In}_{0.076}\text{AgCl}_6$ and $\text{Cs}_2\text{Bi}_{0.085}\text{In}_{0.915}\text{AgCl}_6$, respectively. Spectra were acquired at a magnetic field strength of 21.14 T with a spinning frequency of 30 kHz. Gray octahedra represent $[\text{AgCl}_6]^{5-}$, red octahedra represent $[\text{InCl}_6]^{3-}$, and blue octahedra represent $[\text{BiCl}_6]^{3-}$.

5.2.7 Cesium-133 NMR Spectroscopy of the A Site

The cesium ion in $\text{Cs}_2\text{InAgCl}_6$ or $\text{Cs}_2\text{BiAgCl}_6$ resides in a cuboctahedral void surrounded by either four $[\text{InCl}_6]^{3-}$ or four $[\text{BiCl}_6]^{3-}$ octahedra alternating with four $[\text{AgCl}_6]^{5-}$ octahedra, as shown in Scheme 5.1. Their proximity to B'(III) sites of the $\text{Cs}_2\text{Bi}_{1-x}\text{In}_x\text{AgCl}_6$ materials makes ^{133}Cs an ideal NMR nucleus to study changes occurring in the crystalline system. Quadrupolar ^{133}Cs (nuclear spin, $I = 7/2$, $Q_m = -0.34 \text{ fm}^2$, 100% natural abundance) is a highly sensitive NMR nucleus with excellent resolution, as it behaves as a pseudo-spin-1/2 nucleus, rendering it ideal to investigate small changes in its local coordination environment.⁸⁷⁻⁹⁰ Crystallographically, there is only one cesium site in the parent materials, $\text{Cs}_2\text{InAgCl}_6$ and $\text{Cs}_2\text{BiAgCl}_6$, giving sharp peaks (fwhm = 1 ppm) with distinguishable ^{133}Cs NMR isotropic chemical shifts, $\delta_{\text{iso}}(^{133}\text{Cs})$, of 122(1) and 77(1) ppm, respectively (Figure 5.5). The parent phases are highly symmetric with a high degree of B'(III)/B''(I) cation ordering and both B'(III) or

B''(I) sites giving tetrahedral symmetry at the Cs site; in other words, cesium cations reside at the center of a perfect cuboctahedra, surrounded by 12 chlorides with equal Cs–Cl distances for the parent materials ($\text{Cs}_2\text{BiAgCl}_6$ and $\text{Cs}_2\text{InAgCl}_6$). Hence, the vanishing C_Q suggests a very low level of defects.

To further understand the $\text{In}^{3+}/\text{Bi}^{3+}$ mixed-cationic $\text{Cs}_2\text{Bi}_{1-x}\text{In}_x\text{AgCl}_6$ system, we performed ^{133}Cs MAS NMR spectroscopy on the complete series (Figure D17). Figure 5.5 shows ^{133}Cs MAS NMR spectra for Bi^{3+} -doped $\text{Cs}_2\text{Bi}_{0.085}\text{In}_{0.915}\text{AgCl}_6$ with three resolved ^{133}Cs NMR resonances centered at 121, 115, and 109 ppm and with a ratio of 78:20:2 (fitted peak area; $\pm 2\%$), which follow a binominal-like distribution (Figure D18 and Appendix Note D1). This statistical distribution suggests atomic-level solid solution behavior upon $\text{Bi}^{3+}/\text{In}^{3+}$ mixing that would be consistent with the associated Vegard's analysis, *vide supra*. The peak at $\delta_{\text{iso}}(^{133}\text{Cs}) = 121$ ppm is assigned to the parent $\text{Cs}_2\text{InAgCl}_6$, where Cs^+ is surrounded alternatively by four $[\text{InCl}_6]^{3-}$ and four $[\text{AgCl}_6]^{5-}$ octahedra, whereas the other two peaks to lower frequencies at 115 and 109 ppm correspond to one $[\text{InCl}_6]^{3-}$ and two $[\text{InCl}_6]^{3-}$ octahedra substituted by one $[\text{BiCl}_6]^{3-}$ and two $[\text{BiCl}_6]^{3-}$ octahedra, respectively.

Similarly, Figure 5.5 shows ^{133}Cs NMR spectra for the In^{3+} -doped component, *i.e.*, $\text{Cs}_2\text{Bi}_{0.924}\text{In}_{0.076}\text{AgCl}_6$, which show three resolved $\delta_{\text{iso}}(^{133}\text{Cs})$ peaks at 79, 83, and 87 ppm with a fitted peak area ratio of 70:25:5 ($\pm 2\%$) that also follow a binomial-like distribution (Figure D18); these peaks are attributed to the bismuth parent ($\text{Cs}_2\text{BiAgCl}_6$), one and two $[\text{InCl}_6]^{3-}$ substitutions at a $[\text{BiCl}_6]^{3-}$ site, respectively. Though the local Cs environment for the third low-intensity ^{133}Cs NMR resonances for both $\text{Cs}_2\text{Bi}_{0.085}\text{In}_{0.915}\text{AgCl}_6$ (109 ppm) and $\text{Cs}_2\text{Bi}_{0.924}\text{In}_{0.076}\text{AgCl}_6$ (87 ppm) are similar (*i.e.*, Cs is surrounded by two $[\text{InCl}_6]^{3-}$ and two $[\text{BiCl}_6]^{3-}$ octahedra), the chemical shift is significantly different due to the composition and the long-range crystal structure. Beyond dopant quantities (*i.e.*, $<10\%$) of Bi^{3+} or In^{3+} , the ^{133}Cs NMR resonances broaden and shift to lower and higher frequencies between the two parent phases, further limiting resolution. For example, $\text{Cs}_2\text{InAgCl}_6$ has a $\delta_{\text{iso}}(^{133}\text{Cs})$ of 122 ppm and a fwhm of ca. 130 Hz vs $\delta_{\text{iso}}(^{133}\text{Cs})$ of 117 ppm and fwhm ca. 650 Hz for $\text{Cs}_2\text{Bi}_{0.22}\text{In}_{0.78}\text{AgCl}_6$, although both resonances correspond to Cs^+ surrounded by four

$[\text{InCl}_6]^{3-}$ and four $[\text{AgCl}_6]^{5-}$ (Figure D17b). Gradual changes in isotropic chemical shifts as the unit cell volume changes have previously been observed for NMR spectroscopy of other halide perovskite systems, such as ^{133}Cs (Cu^{2+} -doped $\text{Cs}_2\text{SbAgCl}_6$) and ^{207}Pb ($\text{APb}(\text{Cl}/\text{Br})_3$, where $\text{A} = \text{Cs}^+$, CH_3NH_3^+ , or $\text{CH}(\text{NH}_2)_2^+$).^{52,63,66,70} For higher $\text{In}^{3+}/\text{Bi}^{3+}$ mixed $\text{Cs}_2\text{Bi}_{1-x}\text{In}_x\text{AgCl}_6$ materials with $0.10 < x < 0.90$, ^{133}Cs NMR resonances are inhomogeneously broadened due to the possible substitution patterns of Bi and In of the next-nearest neighboring octahedra and beyond, further limiting resolution. The Cs environments span a chemical shift range of 44 ppm, inhibiting baseline resolution and thus limiting our ability to deconvolute the multiple ^{133}Cs NMR sites (Figure D17). Nonetheless, ^{133}Cs NMR chemical shift maxima for $\text{CsIn}_{0.50}\text{Bi}_{0.50}\text{AgCl}_6$, corresponding to two $[\text{InCl}_6]^{3-}$ and two $[\text{BiCl}_6]^{3-}$ within its cuboctahedron site, is exactly the average of the two parent resonances with $\delta_{\text{max}}(^{133}\text{Cs}) = 99$ ppm (Figure D17c).

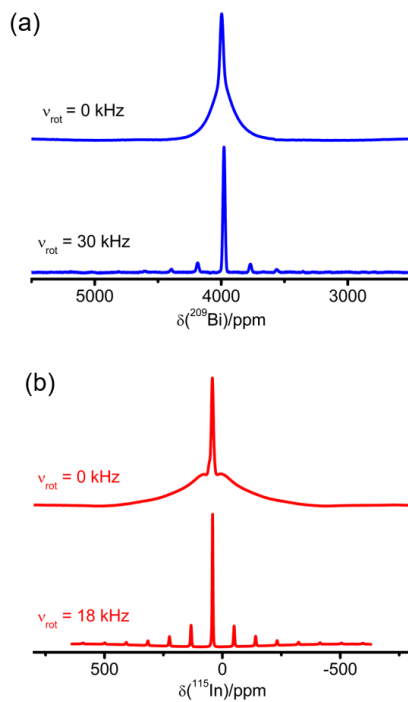


Figure 5.6. Solid-state (a) ^{209}Bi and (b) ^{115}In NMR spectra for the $\text{Cs}_2\text{BiAgCl}_6$ and $\text{Cs}_2\text{InAgCl}_6$ parent materials. NMR spectra were acquired at 21.14 T with and without magic-angle sample spinning as indicated.

5.2.8 Bismuth-209 and Indium-115 NMR Spectroscopy of the B'(III) Sites

Both B'(III) site cations, ^{209}Bi (N.A. = 100%) and ^{115}In (N.A. = 95.7%), are quadrupolar nuclei ($I = 9/2$) with quadrupole moments ($Q_m(^{209}\text{Bi}) = -51.6 \text{ fm}^2$ and $Q_m(^{115}\text{In}) = 81 \text{ fm}^2$) that are more than two orders of magnitude greater than that for ^{133}Cs . These intrinsic NMR properties can potentially lead to significant second-order quadrupolar broadening of the central transition.^{87,91–93} Figure 5.6a shows the nonspinning ^{209}Bi NMR spectrum for the $\text{Cs}_2\text{BiAgCl}_6$ parent material acquired at 21.14 T. Bismuth-209 NMR spectroscopy for $\text{Cs}_2\text{BiAgCl}_6$ gives a sharp resonance at ca. 4000 ppm with no evidence of second-order quadrupolar broadening as expected from its high local octahedral symmetry. A broad underlying component was observed, spanning between ca. 3600 and 4400 ppm, which breaks into a series of first-order spinning side bands upon magic-angle spinning (Figure 5.6a), corresponding to the satellite transition manifold. Comparing ^{209}Bi NMR spectra at multiple magnetic field strengths, i.e., $\mathbf{B}_0 = 7.05, 11.75, \text{ and } 21.14 \text{ T}$ (Figure D19), a small ^{209}Bi C_Q of $0.80 \pm 0.20 \text{ MHz}$ is obtained for $\text{Cs}_2\text{BiAgCl}_6$, which leads to no significant second-order broadening (ca. 20 Hz) of the central transition, unlike the typically significant second-order quadrupolar broadening (order of MHz) that is observed in cases where there is a lower symmetry chemical environment about Bi; for example, $\text{Bi}(\text{CH}_3\text{CO}_2)_3$ results in a very large C_Q of 256 MHz.⁹³ Therefore, broadening of the central transition peak (fwhm = 2.8 kHz) under MAS conditions is not due to the second-order quadrupolar interaction. This line width is decreased from the 7.5 kHz observed in the absence of spinning, suggesting that heteronuclear dipolar coupling is also a factor but not the sole source of the observed broadening. A previous study on lead halide perovskite systems^{67,94} demonstrated that indirect spin–spin (J) coupling between the halide atoms and ^{207}Pb is a significant factor in the observed ^{207}Pb line widths in those systems.⁹⁵ Thus, the broadening of the ^{209}Bi central transition is attributed to both direct and indirect spin–spin interactions between ^{209}Bi and the six directly coordinated $^{35/37}\text{Cl}$ nuclei. The lack of resolution for these fine couplings is attributed to spin–spin (i.e., T_2) relaxation.

The $[\text{BiCl}_6]^{3-}$ (or $[\text{InCl}_6]^{3-}$) and $[\text{AgCl}_6]^{5-}$ octahedra are alternately arranged in the HDP crystal structure to form the $\text{Cs}_2\text{BiAgCl}_6$ (or $\text{Cs}_2\text{InAgCl}_6$) parent material. The central Bi atom is surrounded by six $[\text{AgCl}_6]^{5-}$ followed by a set of $[\text{BiCl}_6]^{3-}$ octahedra, which repeats (i.e., along one dimension the atoms are arranged as follows, Bi–Cl–Ag–Cl–Bi). As such, the central $[\text{BiCl}_6]^{3-}$ octahedron is surrounded by a total of 12 $[\text{BiCl}_6]^{3-}$ octahedra in the first B'(III) coordination sphere ($\sim 8 \text{ \AA}$) within the structure (Figure D20a). As the EFG is sensitive to the minute B'(III) site mixing, as the medium-range symmetry begins to break down, distinct NMR line shapes and breadths for each possible combination can occur. The system becomes increasingly complex once significant Bi/In substitution is considered due to the multiple distinct Bi chemical environments. A second B'(III) coordination sphere ($< 12 \text{ \AA}$) may further exacerbate this, where an additional six sites could also contribute to changes in the EFG for these large quadrupole-moment nuclei (Figure D20b). Therefore, the resulting ^{209}Bi NMR spectra of these materials may appear broad and be spectrally unresolved due to the overlap of multiple chemical shifts and quadrupolar coupling parameters when solid solutions are formed. In light of the complex situation, assigning the source for any impacts at a given NMR site must be tentative. In the ensuing, we assume that a given center is only impacted by substitutions in the first B'(III) coordination sphere, because of the much greater distance of octahedra in the second B'(III) coordination sphere and lower probability of substitution at these sites (6 sites compared to 12 in the first B'(III) coordination sphere), but another possibility is that EFGs resulting from substitutions in the first B'(III) coordination sphere are such that their impact is not detected (vide infra) and that we are in fact detecting the impact from substitutions at the greater distance.

Nevertheless, to extract some further structural insight, a strategic low-doping approach was performed and is shown in Figure 5.7a (^{209}Bi NMR) and 7b (^{115}In NMR) for $\text{Cs}_2\text{Bi}_{0.085}\text{In}_{0.915}\text{AgCl}_6$ and $\text{Cs}_2\text{Bi}_{0.924}\text{In}_{0.076}\text{AgCl}_6$. The low In^{3+} -doping concentration in $\text{Cs}_2\text{Bi}_{0.924}\text{In}_{0.076}\text{AgCl}_6$ renders statistically improbable multiple substitutions (i.e., substitution of only one $[\text{InCl}_6]^{3-}$ octahedron out of 13 $[\text{BiCl}_6]^{3-}$ octahedra, $(\frac{x(\text{In})}{x(\text{In})+x(\text{Bi})} \sim \frac{1}{13})$). Therefore, the Bi center will recognize one $[\text{InCl}_6]^{3-}$ octahedron on average within the medium-range structure. Unfortunately, the

substitution during crystal growth will be random across the 12 possible B'(III) positions that are surrounding the Bi center. The same explanation is applicable for the In system ($\text{Cs}_2\text{Bi}_{0.085}\text{In}_{0.915}\text{AgCl}_6$) as well. The labels in Figure 5.7 represent new ^{209}Bi and ^{115}In NMR resonances for a single or double B'(III) site substitution(s) in our doped HDP system, as discussed below.

Upon doping with In^{3+} to form $\text{Cs}_2\text{Bi}_{0.924}\text{In}_{0.076}\text{AgCl}_6$, a second broad low-intensity ^{209}Bi resonance appears to lower frequency (Figure 5.7a). The high-frequency resonance is assigned to $(\text{BiCl}_6)^{3-}$ surrounded by six $\{\text{AgCl}_6\}^{5-}$ octahedra and then by 12 $[\text{BiCl}_6]^{3-}$ octahedra in the first B'(III) coordination sphere, noted as *site-i* (i.e., $(\text{BiCl}_6)\{\text{AgCl}_6\}_6[\text{BiCl}_6]_{12}$), with a center-of-gravity shift, $\delta_{\text{cgs}} \approx 3980$ ppm. The low-intensity resonance to lower frequency with $\delta_{\text{cgs}} \approx 3920$ ppm (*site-ii*) is tentatively assigned to ^{209}Bi nuclei where one of the $[\text{BiCl}_6]^{3-}$ positions in the first B'(III) coordination sphere has been replaced by a single $[\text{InCl}_6]^{3-}$ octahedron (i.e., $(\text{BiCl}_6)\{\text{AgCl}_6\}_6[\text{BiCl}_6]_{11}[\text{InCl}_6]_1$).

Likewise, the ^{209}Bi MAS NMR data for the same sample appears to have a low-intensity third resonance at $\delta_{\text{cgs}} = \sim 3860$ ppm, which is tentatively assigned as the signal due to sites where two $[\text{BiCl}_6]^{3-}$ octahedra in the first B'(III) octahedral coordination environment are replaced by two $[\text{InCl}_6]^{3-}$, i.e., *site-ii'*, $(\text{BiCl}_6)\{\text{AgCl}_6\}_6[\text{BiCl}_6]_{10}[\text{InCl}_6]_2$ (Figures 5.7a and D21). A slight broadening of the high-frequency resonance is also observed (ca. 2.8 kHz $\text{Cs}_2\text{BiAgCl}_6$ vs ca. 3.2 kHz for $\text{Cs}_2\text{Bi}_{0.924}\text{In}_{0.076}\text{AgCl}_6$) which is attributed to a reduction in medium-range symmetry about the central $(\text{BiCl}_6)^{3-}$ octahedron.

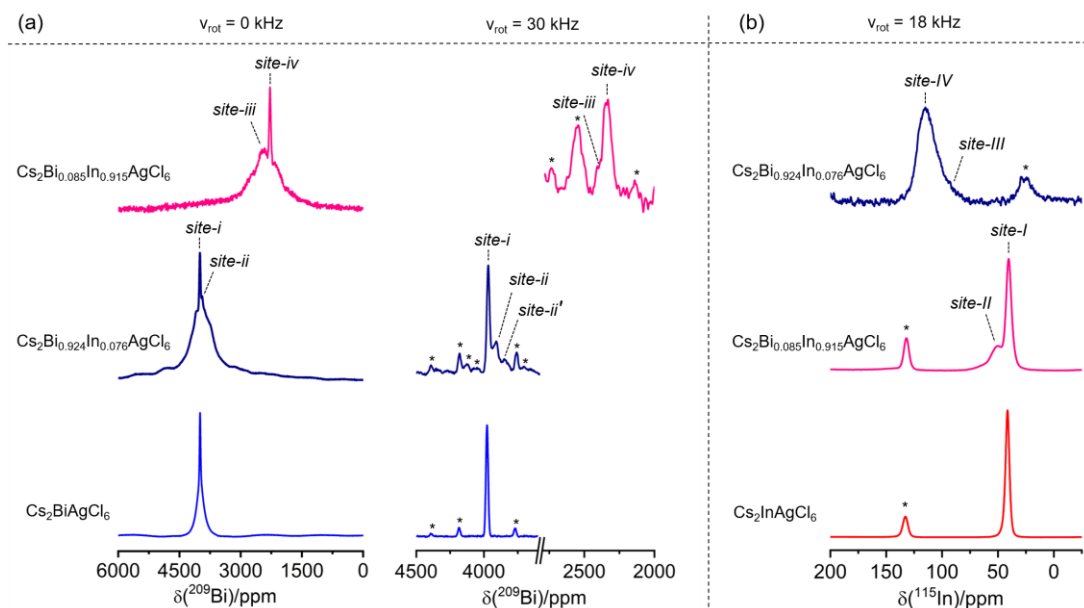


Figure 5.7. (a) Solid-state ^{209}Bi NMR spectra for the $\text{Cs}_2\text{BiAgCl}_6$ parent, $\text{Cs}_2\text{Bi}_{0.924}\text{In}_{0.076}\text{AgCl}_6$, and $\text{Cs}_2\text{Bi}_{0.085}\text{In}_{0.915}\text{AgCl}_6$ materials. (b) Solid-state ^{115}In NMR spectra for the $\text{Cs}_2\text{InAgCl}_6$ parent, $\text{Cs}_2\text{Bi}_{0.085}\text{In}_{0.915}\text{AgCl}_6$, and $\text{Cs}_2\text{Bi}_{0.924}\text{In}_{0.076}\text{AgCl}_6$ materials. Spectra were acquired at 21.14 T with and without magic-angle spinning as indicated. Asterisks (*) indicate spinning side bands.

For $\text{Cs}_2\text{Bi}_{1-x}\text{In}_x\text{AgCl}_6$ samples with higher indium mole fractions (i.e., $\text{Cs}_2\text{In}_{0.28}\text{Bi}_{0.72}\text{AgCl}_6$, $\text{Cs}_2\text{In}_{0.50}\text{Bi}_{0.50}\text{AgCl}_6$, $\text{Cs}_2\text{In}_{0.78}\text{Bi}_{0.22}\text{AgCl}_6$), multiple resonances are observed to low frequency in the ^{209}Bi NMR spectra compared to that for $\text{Cs}_2\text{BiAgCl}_6$ (Figure D22). These multiple sites correspond to distinct ^{209}Bi chemical environments which arise from the variation of $[\text{InCl}_6]^{3-}$ and $[\text{BiCl}_6]^{3-}$ substitutions in the medium-range chemical environment with respect to the central $(\text{BiCl}_6)^{3-}$ unit. Interestingly, for the very low bismuth-containing material, $\text{Cs}_2\text{Bi}_{0.085}\text{In}_{0.915}\text{AgCl}_6$, two distinguishable ^{209}Bi NMR sites centered at $\delta_{\text{cgs}} = \sim 2280$ and $\delta_{\text{cgs}} = \sim 2450$ ppm are observed (Figure 5.7a). The low-frequency Gaussian-like sharp ^{209}Bi peak at 2280 ppm (*site-iv*) corresponds to a very symmetric $(\text{BiCl}_6)^{3-}$ octahedral site surrounded by $[\text{InCl}_6]^{3-}$ octahedra in the first B'(III) octahedral environment, i.e., $(\text{BiCl}_6)\{\text{AgCl}_6\}_6[\text{InCl}_6]_{12}$. The broad peak at the higher frequency region ($\delta_{\text{cgs}} = \sim 2450$ ppm, *site-iii*) corresponds to a $(\text{BiCl}_6)\{\text{AgCl}_6\}_6[\text{BiCl}_6]_1[\text{InCl}_6]_{11}$ site. This composition

is also where the maximum PLQYs are observed, consistent with the importance of the doping of Bi in Cs₂InAgCl₆ as noted above.

Indium-115 NMR spectra were acquired at 21.14 T for the complete series of Cs₂Bi_{1-x}In_xAgCl₆ solid solutions. Figure 5.6b shows the ¹¹⁵In nonspinning and MAS NMR spectra for the Cs₂InAgCl₆ parent material. Similar to the ²⁰⁹Bi NMR data discussed above, the ¹¹⁵In NMR spectrum shows a sharp central transition resonance, $\delta_{\text{cgs}} = \sim 42$ ppm. The absence of a second-order quadrupolar interaction is due to the octahedral symmetry of the In³⁺ environment formed by six coordinating Cl⁻, (InCl₆)³⁻, and by the overall high symmetry of the medium-range structure (i.e., each In octahedron is surrounded by six {AgCl₆}⁵⁻ and 12 [InCl₆]³⁻ octahedra in the first B'(III) coordination environment, (InCl₆){AgCl₆}₆[InCl₆]₁₂, *site-I*). The line shape is Gaussian-like with the bulk of the broadening attributed to both direct and indirect spin-spin coupling between ¹¹⁵In and six directly attached ^{35/37}Cl to form InCl₆³⁻ octahedra, as observed for the ²⁰⁹Bi NMR spectrum for Cs₂BiAgCl₆. Along with the central transition, a broad underlying component, spanning between ca. 500 and -400 ppm, corresponds to the ¹¹⁵In satellite transitions.^{96,97} Using the field dependence of the quadrupole coupling interaction, a small C_Q(¹¹⁵In) of 1.10 ± 0.25 MHz was calculated for Cs₂InAgCl₆ (Figure D23). As bismuth is incorporated at low concentrations to form Cs₂Bi_{0.085}In_{0.915}AgCl₆, a second broad ¹¹⁵In MAS NMR resonance appears at higher frequency at $\delta_{\text{cgs}} = \sim 50$ ppm (*site-II*), along with the sharp resonance observed for the parent material (Figure 5.7b). The broadening in the new resonance is due to an increase in the EFG about the indium center as one [InCl₆]³⁻ octahedron is replaced by a [BiCl₆]³⁻ octahedron, breaking the medium-range symmetry, i.e., *site-II*, (InCl₆){AgCl₆}₆[InCl₆]₁₁[BiCl₆]₁. Likewise, examination of the central transition peaks for the ¹¹⁵In MAS NMR spectra indicates a broadening with the fwhm increasing 160% from ca. 0.7 (Cs₂InAgCl₆) to ca. 1.1 kHz (Cs₂Bi_{0.085}In_{0.915}AgCl₆), similar to what was discussed above for the ²⁰⁹Bi spectra. Figure D24 shows ¹¹⁵In NMR spectra for the full Cs₂Bi_{1-x}In_xAgCl₆ HDP series. As the bismuth mole fraction increases, multiple ¹¹⁵In NMR resonances are observed in the higher frequency region (e.g., Cs₂Bi_{0.22}In_{0.78}AgCl₆), along with the central transition peak for the parent compound. However, for samples with much

higher bismuth mole fractions, i.e., for $\text{Cs}_2\text{Bi}_{0.50}\text{In}_{0.50}\text{AgCl}_6$ and for $\text{Cs}_2\text{Bi}_{0.72}\text{In}_{0.28}\text{AgCl}_6$, nearly Gaussian-like ^{115}In NMR line shapes centered between ca. 85 and 105 ppm, respectively, are observed. For materials with low indium, $\text{Cs}_2\text{Bi}_{0.924}\text{In}_{0.076}\text{AgCl}_6$, an asymmetric narrow line shape ($\delta_{\text{cgs}} = \sim 115$ ppm, *site-IV*) is observed. *Site-IV* corresponds to $(\text{InCl}_6)^{3-}$ octahedra surrounded by 12 $[\text{BiCl}_6]^{3-}$ octahedra in the first B'(III) octahedral coordination environment (i.e., $(\text{InCl}_6)\{\text{AgCl}_6\}_6[\text{BiCl}_6]_{12}$).

Turning our attention back to the cubic parent compounds, the observation of spinning side bands and nonzero C_{QS} for ^{209}Bi and ^{115}In is direct evidence of the presence of defects. The exact concentration of defects cannot be determined precisely; however, some qualitative insight can be gained from examination of the ^{133}Cs , ^{209}Bi , and ^{115}In NMR spectra of the parent compounds. The ^{133}Cs MAS NMR spectra of the parent materials are dominated by a sharp single isotropic resonance with only a single low-intensity (<1%) spinning side band upon slow (5 kHz) magic-angle spinning conditions (Figure D17a). On the basis of past studies, the small spinning side band may be attributed to chloride vacancies (V_{Cl}) as halogen vacancies are one of the dominant and stable point defects in HDP due to their low formation energy.^{73,98} It has also been shown to be energetically favored to have alternating AgCl_6 and BiCl_6 site arrangements for $\text{Cs}_2\text{BiAgCl}_6$; the electronic configuration of B'(III) site cations plays an important role in the halogen vacancies, where $\text{Cs}_2\text{InAgCl}_6$ has a lower V_{Cl} formation energy than that for $\text{Cs}_2\text{BiAgCl}_6$ due to the absence of an s orbital in In^{3+} ion.⁹⁹ The ^{133}Cs quadrupole moment is ~ 240 times smaller than that for ^{115}In (or ~ 150 times smaller than that for ^{209}Bi); therefore these small V_{Cl} defects would manifest more readily as a series of spinning side bands for both ^{115}In and ^{209}Bi spectra, which are shown in Figures D24a and D21a, respectively. Low alloying of Bi (or In), whereby we purposefully introduce new B'(III) sites (<10% loading), causes new resonances to appear in the ^{133}Cs NMR spectra as well as increases the presence of spinning side bands across all three NMR-active nuclei (^{115}In , ^{133}Cs , and ^{209}Bi) studied here, consistent with an increase in the quadrupole coupling interaction. With the sensitivity of the ^{133}Cs chemical shift and its receptivity, a change in the surrounding eight B''(Ag)/B'(In or Bi) neighbors in the parent materials (i.e., an antisite defect)

should induce a new resonance as the alloying discussed above shows. Considering that a spinning side band at <1% intensity is detectable, we predict a new Cs chemical environment induced by an antisite defect would be observed in the parent ^{133}Cs NMR spectra if present at $\sim 0.15\%$ as each B site substitution would impact eight neighboring Cs sites in the extended unit cell.⁷¹ This is further supported by the very small quadrupole coupling constants for the ^{209}Bi and ^{115}In parent compounds where only a few first-order spinning side bands are observed from the satellite transitions and the PXRD (above), suggesting minimal intrinsic defects in these materials. Taking these factors into consideration, we estimate that intrinsic defects in the parent phases are less than 0.1%. This is in contrast to oxide-based perovskites where antisite defects are commonly observed.^{100–102}

5.2.9 Impact of Medium-Range Structure on ^{115}In and ^{209}Bi C_{QS} Determined Using Quantum Chemical Calculations

The medium-range structure discussed above was used to describe the appearance of additional ^{115}In and ^{209}Bi NMR resonances upon formation of the various $\text{Cs}_2\text{Bi}_{1-x}\text{In}_x\text{AgCl}_6$ solid solutions. As noted, when the extended symmetry begins to break down, the large ^{209}Bi and ^{115}In quadrupole moments result in sizable quadrupole coupling constants for ^{209}Bi and ^{115}In nuclei and their NMR line shapes are then dominated by second-order quadrupolar broadening (i.e., the peaks broaden drastically). For example, previous studies have shown that C_{QS} can reach up to 256 ± 10 MHz for ^{209}Bi ⁹³ and 200 ± 4 MHz for ^{115}In ;⁹¹ this translates into resonances that span MHz (or 1000s of ppm) at moderate magnetic field strengths.

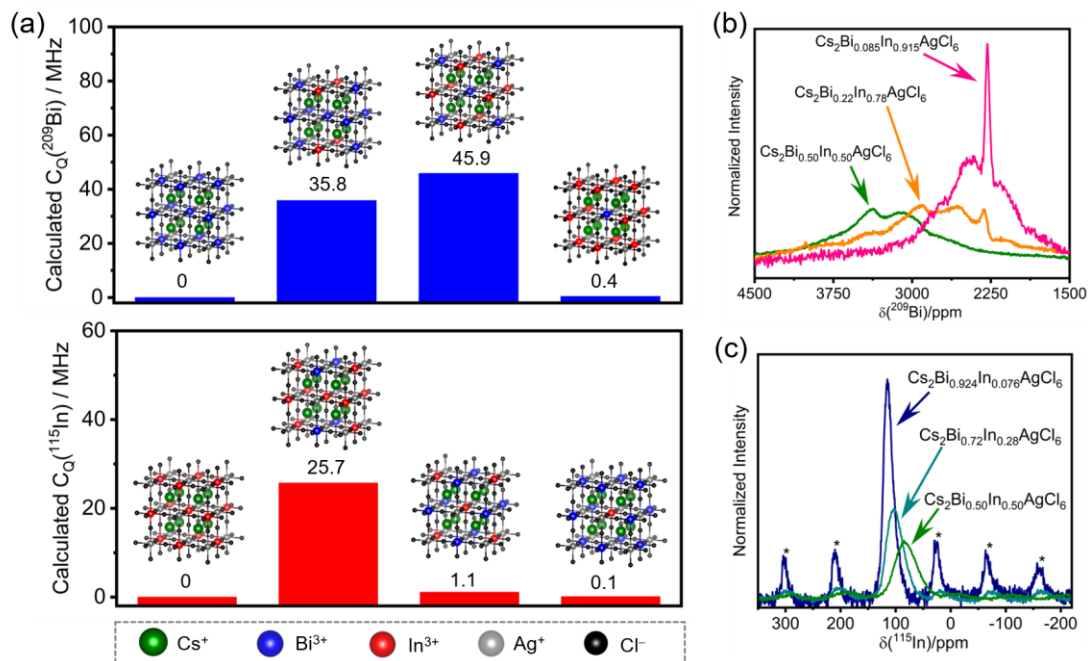


Figure 5.8. (a) Change in calculated C_Q of the central ^{209}Bi or ^{115}In nuclei with a change in B'(III) site neighbors in the super lattice. Normalized (b) ^{209}Bi and (c) ^{115}In NMR spectra acquired at 21.14 T under nonspinning and magic-angle spinning (18 kHz) conditions, respectively, for the samples as indicated. Normalized intensity in b and c corresponds to vertically scaled spectra with the same amount of Bi or In, respectively, for a sample for a given number of scans. Asterisks (*) in c indicate spinning side bands.

To assess the range of possible C_Q s when Bi/In substitutions occur, DFT calculations were undertaken on a series of medium-range structural models shown in Figure 5.8a. The heavy atoms considered in this study as well as the size of the crystal lattice required to properly model the medium-range structure precluded calculation of EFGs for all possible combinations of substitution sites. However, calculations were undertaken with substitutions at a few symmetric positions to provide insight into the possible impact of these substitutions on the EFGs. Calculated ^{209}Bi and ^{115}In C_Q values range from 0 MHz for the $\text{Cs}_2\text{BiAgCl}_6$ and $\text{Cs}_2\text{InAgCl}_6$ parent crystal structures to a maximum of 45.9 MHz (^{209}Bi) or 25.7 MHz (^{115}In) for nearly equal Bi/In populations (Figure 5.8a). The moderately sized quadrupole coupling

constants for these symmetrically substituted chemical environments hint that the couplings could increase further when nonsymmetric Bi/In substitutions within the multiple possible environments occur (Figure D20). For example, for $\text{Cs}_2\text{Bi}_{0.50}\text{In}_{0.50}\text{AgCl}_6$, only 5 of 12 possible B'(III) substitutions have populations > 10%. If we now consider that each of these substitutions can have multiple arrangements across the first and second B'(III) coordination spheres, a daunting scenario develops where the probability for a particular unique arrangement is considerably less than 10%. Taking these factors into consideration and combining the changes in chemical shifts with the distribution of quadrupole coupling constants yields ^{115}In and ^{209}Bi NMR spectra that are unresolvable. Furthermore, if the C_Q 's for any arrangement are larger than those predicted by the symmetrically substituted DFT calculations, it could render the site undetectable (vide infra) under the experimental conditions used here. We observed a significant loss in both ^{209}Bi and ^{115}In NMR signal intensities upon increments in In or Bi concentrations to form $\text{Cs}_2\text{Bi}_{1-x}\text{In}_x\text{AgCl}_6$ solid solutions. Interestingly, further increasing In or Bi concentrations, i.e., toward Bi-doped $\text{Cs}_2\text{InAgCl}_6$ or In-doped $\text{Cs}_2\text{BiAgCl}_6$ materials, caused both ^{209}Bi and ^{115}In NMR intensities to increase (Figure 5.8b and 5.8c, respectively) due to an increase in medium-range coordination environment. The experimental ^{209}Bi and ^{115}In NMR results for the $\text{Cs}_2\text{Bi}_{1-x}\text{In}_x\text{AgCl}_6$ series are shown in Figures D25 and D26, respectively.

Figures D27a and D27b show ^{209}Bi and ^{115}In NMR spectra one may expect for a two-site system, one with $C_Q = 0$ and with 90% of the NMR sites and the other with $C_Q = 45$ and 25 MHz, respectively, for ^{209}Bi and ^{115}In (i.e., the maximum values calculated via DFT). Clearly, sites with these magnitudes of C_Q and such a low level of incorporation (i.e., very low doping levels) are beyond the detection limits of current instruments. Note also that these are “best-case” scenarios, in that other factors that may further negatively impact detectability, such as magnetic shielding anisotropy or T_2 relaxation, were not considered in these simulations. Figures D27c and D27d illustrate the impact of C_Q on the intensity of a given NMR site. These demonstrate that one may hope to observe ^{115}In and ^{209}Bi NMR sites impacted by substitution if the probability of that site is a significant percentage of the total. Figures D27e and D27f illustrate overlays of simulated NMR spectra expected for a system

with two sites with equal probability, one $C_Q = 0$ and the other with significant C_Q values. These simulated spectra illustrate that there may very well be undetectable ^{209}Bi and ^{115}In NMR sites in our NMR spectra. These simulations also demonstrate that considering that the NMR sites vary only in the nature of the substitutions at the first or second B'(III) coordination spheres (i.e., $>7 \text{ \AA}$) they will not vary greatly in isotropic chemical shifts, and thus, we cannot hope to resolve distinct sites even at the high field (21.14 T) used here. As noted above, for most of these systems, one needs to consider a minimum of 12 unique Bi/In positions, and thus, observed NMR sites are probably contributions from multiple distinct sites. As such, we refrain from fitting these data due to the lack of resolution and confidence in observing all Bi (or In) resonances. Widelin approaches^{103,104} such as WURST, CPMG, or VOCS, which have been successful to detect broad quadrupolar line shapes, would not provide the resolution that is needed here and thus probably would not help decipher these complex spectra.

5.3 Conclusions

We presented an analysis of a lead-free and environmentally stable $\text{Cs}_2\text{Bi}_{1-x}\text{In}_x\text{AgCl}_6$ double perovskite series in which indium composition (x) can be tuned from 0 to 1. The Bi/In alloying allows exquisite tailoring of the band-gap properties with an indirect to direct band-gap crossover occurring at $x > 0.5$. These HDP materials are capable of broad-band white-light PL emission upon ultraviolet excitation, and the emission efficiency highly depends on Bi/In compositional ratios. The Bi-rich materials with an indirect bandgap show lower PLQY as compared to In-rich materials with a direct bandgap which has a maximum PLQY of $34 \pm 4\%$. PL spectroscopy reveals white-light production from a unique source for these HDPs with an average PL carrier lifetime of approximately $1 \mu\text{s}$.

The PXRD information elucidates comprehensive long-range structural behavior, indicating solid solutions through a Vegard's analysis for these $\text{Cs}_2\text{Bi}_{1-x}\text{In}_x\text{AgCl}_6$ HDPs. Building beyond these findings a unique short- and medium-range structural evolution can be uncovered using a combination of solid-state NMR spectroscopy of exotic quadrupolar nuclei. Specifically, we have shown that there is a

high degree of B'(III)/B''(I) site ordering; complementary XRD and NMR results reveal complete Bi³⁺/In³⁺ mixing with no evidence of phase segregation or antisite defects (<0.1%) in these HDPs. Furthermore, a maximum PLQY is observed when Bi is surrounded by 12 In neighbors about its medium-range structure. This work demonstrates the intricate atomic-level chemical structural information afforded by NMR spectroscopy of these newly developed solid-state optoelectronic-based HDP materials, especially when cationic mixing is present.

5.4 References

- (1) National Renewable Energy Laboratory (NREL). Best Research-Cell Efficiency Chart.
<https://www.nrel.gov/pv/assets/pdfs/best-research-cell-efficiencies.20190923.pdf>
- (2) Wei, Y.; Cheng, Z.; Lin, J. An Overview on Enhancing the Stability of Lead Halide Perovskite Quantum Dots and Their Applications in Phosphor-Converted LEDs. *Chem. Soc. Rev.* **2019**, *48*, 310–350.
- (3) Zhao, Y.; Zhu, K. Organic-Inorganic Hybrid Lead Halide Perovskites for Optoelectronic and Electronic Applications. *Chem. Soc. Rev.* **2016**, *45*, 655–689.
- (4) Kovalenko, M. V; Protesescu, L.; Bodnarchuk, M. I. Properties and Potential Optoelectronic Applications of Lead Halide Perovskite Nanocrystals. *Science* **2017**, *750*, 745–750.
- (5) Sutherland, B. R.; Sargent, E. H. Perovskite Photonic Sources. *Nat. Photonics* **2016**, *10*, 295–302.
- (6) Luo, J.; Im, J. H.; Mayer, M. T.; Schreier, M.; Nazeeruddin, M. K.; Park, N. G.; Tilley, S. D.; Fan, H. J.; Grätzel, M. Water Photolysis at 12.3% Efficiency via Perovskite Photovoltaics and Earth-Abundant Catalysts. *Science* **2014**, *345*, 1593–1596.
- (7) Yakunin, S.; Sytnyk, M.; Kriegner, D.; Shrestha, S.; Richter, M.; Matt, G. J.; Azimi, H.; Brabec, C. J.; Stangl, J.; Kovalenko, M. V; Heiss, W. Detection of X-Ray Photons by Solution-Processed Lead Halide Perovskites. *Nat. Photonics* **2015**, *9*, 444–449.
- (8) LED Lighting, U.S. Department of Energy.

<https://www.energy.gov/energysaver/save-electricity-and-fuel/lighting-choices-save-you-money/led-lighting> (Accessed Dec 2019).

- (9) Manser, J. S.; Christians, J. A.; Kamat, P. V. Intriguing Optoelectronic Properties of Metal Halide Perovskites. *Chem. Rev.* **2016**, *116*, 12956–13008.
- (10) Dohner, E. R.; Hoke, E. T.; Karunadasa, H. I. Self-Assembly of Broadband White-Light Emitters. *J. Am. Chem. Soc.* **2014**, *136*, 1718–1721.
- (11) Smith, M. D.; Connor, B. A.; Karunadasa, H. I. Tuning the Luminescence of Layered Halide Perovskites. *Chem. Rev.* **2019**, *119*, 3104–3139.
- (12) Smith, M. D.; Karunadasa, H. I. White-Light Emission from Layered Halide Perovskites. *Acc. Chem. Res.* **2018**, *51*, 619–627.
- (13) Wang, M.; Guo, G.-C. Inorganic–Organic Hybrid White Light Phosphors. *Chem. Commun.* **2016**, *52*, 13194–13204.
- (14) Shang, M.; Li, C.; Lin, J. How to Produce White Light in a Single-Phase Host? *Chem. Soc. Rev.* **2014**, *43*, 1372–1386.
- (15) Yang, J.; Siempelkamp, B. D.; Mosconi, E.; De Angelis, F.; Kelly, T. L. Origin of the Thermal Instability in $\text{CH}_3\text{NH}_3\text{PbI}_3$ Thin Films Deposited on ZnO. *Chem. Mater.* **2015**, *27*, 4229–4236.
- (16) Askar, A. M.; Bernard, G. M.; Wiltshire, B.; Shankar, K.; Michaelis, V. K. Multinuclear Magnetic Resonance Tracking of Hydro, Thermal, and Hydrothermal Decomposition of $\text{CH}_3\text{NH}_3\text{PbI}_3$. *J. Phys. Chem. C* **2017**, *121*, 1013–1024.
- (17) Needleman, H. Lead Poisoning. *Annu. Rev. Med.* **2004**, *55*, 209–222.
- (18) Babayigit, A.; Ethirajan, A.; Muller, M.; Conings, B. Toxicity of Organometal Halide Perovskite Solar Cells. *Nat. Mater.* **2016**, *15*, 247–251.
- (19) Yang, J.; Siempelkamp, B. D.; Liu, D.; Kelly, T. L. Investigation of $\text{CH}_3\text{NH}_3\text{PbI}_3$ Degradation Rates and Mechanisms in Controlled Humidity Environments Using In Situ Techniques. *ACS Nano* **2015**, *9*, 1955–1963.
- (20) Domanski, K.; Alharbi, E. A.; Hagfeldt, A.; Grätzel, M.; Tress, W. Systematic Investigation of the Impact of Operation Conditions on the Degradation Behaviour of Perovskite Solar Cells. *Nat. Energy* **2018**, *3*, 61–67.

- (21) Li, J.; Cao, H.; Jiao, W.; Wang, Q.; Wei, M.; Cantone, I.; Lü, J.; Abate, A. Biological Impact of Lead from Halide Perovskites Reveals the Risk of Introducing a Safe Threshold. *Nat. Commun.* **2020**, *11*, 310.
- (22) Abate, A. Perovskite Solar Cells Go Lead Free. *Joule* **2017**, *1*, 659–664.
- (23) Shi, Z.; Guo, J.; Chen, Y.; Li, Q.; Pan, Y.; Zhang, H.; Xia, Y.; Huang, W. Lead-Free Organic–Inorganic Hybrid Perovskites for Photovoltaic Applications: Recent Advances and Perspectives. *Adv. Mater.* **2017**, *29*, 1605005.
- (24) Luo, J.; Wang, X.; Li, S.; Liu, J.; Guo, Y.; Niu, G.; Yao, L.; Fu, Y.; Gao, L.; Dong, Q.; Zhao, C.; Leng, M.; Ma, F.; Liang, W.; Wang, L.; Jin, S.; Han, J.; Zhang, L.; Etheridge, J.; Wang, J.; Yan, Y.; Sargent, E. H.; Tang, J. Efficient and Stable Emission of Warm-White Light from Lead-Free Halide Double Perovskites. *Nature* **2018**, *563*, 541–545.
- (25) Gray, M. B.; Majher, J. D.; Strom, T. A.; Woodward, P. M. Broadband White Emission in $\text{Cs}_2\text{AgIn}_{1-x}\text{Bi}_x\text{Cl}_6$ Phosphors. *Inorg. Chem.* **2019**, *58*, 13403–13410.
- (26) Yang, B.; Mao, X.; Hong, F.; Meng, W.; Tang, Y.; Xia, X.; Yang, S.; Deng, W.; Han, K. Lead-Free Direct Bandgap Double Perovskite Nanocrystals with Bright Dual-Color Emission. *J. Am. Chem. Soc.* **2018**, *140*, 17001–17006.
- (27) Majher, J. D.; Gray, M. B.; Strom, T. A.; Woodward, P. M. $\text{Cs}_2\text{NaBiCl}_6$: Mn^{2+} - A New Orange-Red Halide Double Perovskite Phosphor. *Chem. Mater.* **2019**, *31*, 1738–1744.
- (28) Hu, Q.; Niu, G.; Zheng, Z.; Li, S.; Zhang, Y.; Song, H.; Zhai, T.; Tang, J. Tunable Color Temperatures and Efficient White Emission from $\text{Cs}_2\text{Ag}_{1-x}\text{Na}_x\text{In}_{1-y}\text{Bi}_y\text{Cl}_6$ Double Perovskite Nanocrystals. *Small* **2019**, 1903496.
- (29) Locardi, F.; Cirignano, M.; Baranov, D.; Dang, Z.; Prato, M.; Drago, F.; Ferretti, M.; Pinchetti, V.; Fanciulli, M.; Brovelli, S.; Trizio, T. D.; Manna, L. Colloidal Synthesis of Double Perovskite $\text{Cs}_2\text{AgInCl}_6$ and Mn-Doped $\text{Cs}_2\text{AgInCl}_6$ Nanocrystals. *J. Am. Chem. Soc.* **2018**, *140*, 12989–12995.
- (30) Lee, W.; Hong, S.; Kim, S. Colloidal Synthesis of Lead-Free Silver–Indium Double-Perovskite $\text{Cs}_2\text{AgInCl}_6$ Nanocrystals and Their Doping with Lanthanide Ions. *J. Phys. Chem. C* **2019**, *123*, 2665–2672.

- (31) Zhou, J.; Rong, X.; Zhang, P.; Molokeev, M. S.; Wei, P.; Liu, Q. Manipulation of Bi³⁺/In³⁺ Transmutation and Mn²⁺ -Doping Effect on the Structure and Optical Properties of Double Perovskite Cs₂NaBi_{1-x}In_xCl₆. *Adv. Opt. Mater.* **2019**, *7*, 1801435.
- (32) Luo, J.; Hu, M.; Niu, G.; Tang, J. Lead-Free Halide Perovskites and Perovskite Variants as Phosphors toward Light-Emitting Applications. *ACS Appl. Mater. Interfaces* **2019**, *11*, 31575–31584.
- (33) Lamba, R. S.; Basera, P.; Bhattacharya, S.; Sapra, S. Band Gap Engineering in Cs₂(Na_xAg_{1-x})BiCl₆ Double Perovskite Nanocrystals. *J. Phys. Chem. Lett.* **2019**, *10*, 5173-5181.
- (34) Liu, Y.; Jing, Y.; Zhao, J.; Liu, Q.; Xia, Z. Design Optimization of Lead-Free Perovskite Cs₂AgInCl₆:Bi Nanocrystals with 11.4% Photoluminescence Quantum Yield. *Chem. Mater.* **2019**, *31*, 3333–3339.
- (35) Slavney, A. H.; Hu, T.; Lindenberg, A. M.; Karunadasa, H. I. A Bismuth-Halide Double Perovskite with Long Carrier Recombination Lifetime for Photovoltaic Applications. *J. Am. Chem. Soc.* **2016**, *138*, 2138–2141.
- (36) McClure, E. T.; Ball, M. R.; Windl, W.; Woodward, P. M. Cs₂AgBiX₆ (X = Br, Cl): New Visible Light Absorbing, Lead-Free Halide Perovskite Semiconductors. *Chem. Mater.* **2016**, *28*, 1348–1354.
- (37) Volonakis, G.; Filip, M. R.; Haghighirad, A. A.; Sakai, N.; Wenger, B.; Snaith, H. J.; Giustino, F. Lead-Free Halide Double Perovskites via Heterovalent Substitution of Noble Metals. *J. Phys. Chem. Lett.* **2016**, *7*, 1254–1259.
- (38) Filip, M. R.; Liu, X.; Miglio, A.; Hautier, G.; Giustino, F. Phase Diagrams and Stability of Lead-Free Halide Double Perovskites Cs₂BB'X₆: B = Sb and Bi, B' = Cu, Ag, and Au, and X = Cl, Br, and I. *J. Phys. Chem. C* **2018**, *122*, 158–170.
- (39) K., N. N.; Nag, A. Synthesis and Luminescence of Mn-Doped Cs₂AgInCl₆ Double Perovskites. *Chem. Commun.* **2018**, *54*, 5205--5208.
- (40) Lawson, K. E. Optical Studies of Electronic Transitions in Hexa- and Tetracoordinated Mn²⁺ Crystals. *J. Chem. Phys.* **1967**, *47*, 3627–3633.
- (41) Zeng, R.; Zhang, L.; Xue, Y.; Ke, B.; Zhao, Z.; Huang, D.; Wei, Q.; Zhou, W.; Zou, B. Highly Efficient Blue Emission from Self-Trapped Excitons in Stable Db³⁺-Doped Cs₂NaInCl₆ Double Perovskites. *J. Phys. Chem. Lett.* **2020**, *11*, 2053–2061.

- (42) Locardi, F.; Sartori, E.; Buha, J.; Zito, J.; Prato, M.; Pinchetti, V.; Zaffalon, M. L.; Ferretti, M.; Brovelli, S.; Infante, I.; Trizio, L. D.; Manna, L. Emissive Bi-Doped Double Perovskite $\text{Cs}_2\text{Ag}_{1-x}\text{Na}_x\text{InCl}_6$ Nanocrystals. *ACS Energy Lett.* **2019**, *4*, 1976–1982.
- (43) Hu, Z.; Lin, Z.; Su, J.; Zhang, J.; Chang, J.; Hao, Y. A Review on Energy Band-Gap Engineering for Perovskite Photovoltaics. *Sol. RRL* **2019**, *3*, 1900304.
- (44) Xiao, Z.; Zhou, Y.; Hosono, H.; Kamiya, T.; Padture, N. P. Bandgap Optimization of Perovskite Semiconductors for Photovoltaic Applications. *Chem. - A Eur. J.* **2018**, *24*, 2305–2316.
- (45) Du, K. Z.; Meng, W.; Wang, X.; Yan, Y.; Mitzi, D. B. Bandgap Engineering of Lead-Free Double Perovskite $\text{Cs}_2\text{AgBiBr}_6$ through Trivalent Metal Alloying. *Angew. Chem. Int. Ed.* **2017**, *56*, 8158–8162.
- (46) Gray, M. B.; McClure, E. T.; Woodward, P. M. $\text{Cs}_2\text{AgBiBr}_{6-x}\text{Cl}_x$ Solid Solutions-Band Gap Engineering with Halide Double Perovskites. *J. Mater. Chem. C* **2019**, *7*, 9686–9689.
- (47) Jiang, J. T.; Xiu, S. L.; Zheng, M. M.; Jia, T. T.; Liu, H. Y.; Zhang, Y.; Chen, G. Indirect–Direct Bandgap Transition and Gap Width Tuning in Bilayer MoS_2 Superlattices. *Chem. Phys. Lett.* **2014**, *613*, 74–79.
- (48) Wang, Y. J.; Zhou, K. G.; Yu, G.; Zhong, X.; Zhang, H. L. Partial Oxidized Arsenene: Emerging Tunable Direct Bandgap Semiconductor. *Sci. Rep.* **2016**, *6*, 24981.
- (49) Chen, X.; Yang, Q.; Meng, R.; Jiang, J.; Liang, Q.; Tan, C.; Sun, X. The Electronic and Optical Properties of Novel Germanene and Antimonene Heterostructures. *J. Mater. Chem. C* **2016**, *4*, 5434–5441.
- (50) Tran, T. T.; Panella, J. R.; Chamorro, J. R.; Morey, J. R.; McQueen, T. M. Designing Indirect-Direct Bandgap Transitions in Double Perovskites. *Mater. Horizons* **2017**, *4*, 688–693.
- (51) Volonakis, G.; Haghighirad, A. A.; Milot, R. L.; Sio, W. H.; Filip, M. R.; Wenger, B.; Johnston, M. B.; Herz, L. M.; Snaith, H. J.; Giustino, F. $\text{Cs}_2\text{InAgCl}_6$: A New Lead-Free Halide Double Perovskite with Direct Band Gap. *J. Phys. Chem. Lett.* **2017**, *8*, 772–778.

- (52) Askar, A. M.; Karmakar, A.; Bernard, G. M.; Ha, M.; Terskikh, V. V.; Wiltshire, B. D.; Patel, S.; Fleet, J.; Shankar, K.; Michaelis, V. K. Composition-Tunable Formamidinium Lead Mixed Halide Perovskites via Solvent-Free Mechanochemical Synthesis: Decoding the Pb Environments Using Solid-State NMR Spectroscopy. *J. Phys. Chem. Lett.* **2018**, *9*, 2671–2677.
- (53) Pan, C.; Lee, Y. J.; Amundsen, B.; Grey, C. P. ⁶Li MAS NMR Studies of the Local Structure and Electrochemical Properties of Cr-Doped Lithium Manganese and Lithium Cobalt Oxide Cathode Materials for Lithium-Ion Batteries. *Chem. Mater.* **2002**, *14*, 2289–2299.
- (54) Wasylshen, R. E.; Knop, O.; Macdonald, J. B. Cation Rotation in Methylammonium Lead Halides. *Solid State Commun.* **1985**, *56*, 581–582.
- (55) Senocrate, A.; Moudrakovski, I.; Kim, G. Y.; Yang, T.; Gregori, G.; Grätzel, M.; Maier, J. The Nature of Ion Conduction in Methylammonium Lead Iodide: A Multimethod Approach. *Angew. Chem. Int. Ed.* **2017**, *56*, 7755–7759.
- (56) Senocrate, A.; Moudrakovski, I.; Maier, J. Short-Range Ion Dynamics in Methylammonium Lead Iodide by Multinuclear Solid State NMR and ¹²⁷I NQR. *Phys. Chem. Chem. Phys.* **2018**, *20*, 20043–20055.
- (57) Kubicki, D. J.; Prochowicz, D.; Hofstetter, A.; Péchy, P.; Zakeeruddin, S. M.; Grätzel, M.; Emsley, L. Cation Dynamics in Mixed-Cation (MA)_x(FA)_{1-x}PbI₃ Hybrid Perovskites from Solid-State NMR. *J. Am. Chem. Soc.* **2017**, *139*, 10055–10061.
- (58) Kubicki, D. J.; Prochowicz, D.; Hofstetter, A.; Sasaki, M.; Yadav, P.; Bi, D.; Pellet, N.; Lewiński, J.; Zakeeruddin, S. M.; Grätzel, M.; Emsley, L. Formation of Stable Mixed Guanidinium-Methylammonium Phases with Exceptionally Long Carrier Lifetimes for High-Efficiency Lead Iodide-Based Perovskite Photovoltaics. *J. Am. Chem. Soc.* **2018**, *140*, 3345–3351.
- (59) Hanrahan, M. P.; Men, L.; Rosales, B. A.; Vela, J.; Rossini, A. J. Sensitivity-Enhanced ²⁰⁷Pb Solid-State NMR Spectroscopy for the Rapid, Non-Destructive Characterization of Organolead Halide Perovskites. *Chem. Mater.* **2018**, *30*, 7005–7015.
- (60) Kubicki, D. J.; Prochowicz, D.; Pinon, A.; Stevanato, G.; Hofstetter, A.; Zakeeruddin, S. M.; Grätzel, M.; Emsley, L. Doping and Phase Segregation in Mn²⁺ -

and Co²⁺-Doped Lead Halide Perovskites from ¹³³Cs and ¹H NMR Relaxation Enhancement. *J. Mater. Chem. A* **2019**, *7*, 2326–2333.

(61) Franssen, W. M. J.; Kentgens, A. P. M. Solid-State NMR of Hybrid Halide Perovskites. *Solid State Nucl. Magn. Reson.* **2019**, *100*, 36–44.

(62) Franssen, W. M. J.; Van Es, S. G. D.; Dervişoğlu, R.; De Wijs, G. A.; Kentgens, A. P. M. Symmetry, Dynamics, and Defects in Methylammonium Lead Halide Perovskites. *J. Phys. Chem. Lett.* **2017**, *8*, 61–66.

(63) Karmakar, A.; Dodd, M. S.; Zhang, X.; Oakley, M. S.; Klobukowski, M.; Michaelis, V. K. Mechanochemical Synthesis of 0D and 3D Cesium Lead Mixed Halide Perovskites. *Chem. Commun.* **2019**, *55*, 5079–5082.

(64) Chen, Y.; Smock, S. R.; Flintgruber, A. H.; Perras, F. A.; Brutchey, R. L.; Rossini, A. J. Surface Termination of CsPbBr₃ Perovskite Quantum Dots Determined by Solid-State NMR Spectroscopy. *J. Am. Chem. Soc.* **2020**, *142*, 6117–6127.

(65) Kubicki, D. J.; Prochowicz, D.; Salager, E.; Rakhmatullin, A.; Grey, C. P.; Emsley, L.; Stranks, S. D. Local Structure and Dynamics in Methylammonium, Formamidinium and Cesium Tin(II) Mixed-halide Perovskites from ¹¹⁹Sn Solid-state NMR. *J. Am. Chem. Soc.* **2020**, *142*, 7813–7826.

(66) Karmakar, A.; Askar, A. M.; Bernard, G. M.; Terskikh, V. V.; Ha, M.; Patel, S.; Shankar, K.; Michaelis, V. K. Mechanochemical Synthesis of Methylammonium Lead Mixed-Halide Perovskites: Unraveling the Solid-Solution Behavior Using Solid-State NMR. *Chem. Mater.* **2018**, *30*, 2309–2321.

(67) Rosales, B. A.; Men, L.; Cady, S. D.; Hanrahan, M. P.; Rossini, A. J.; Vela, J. Persistent Dopants and Phase Segregation in Organolead Mixed-Halide Perovskites. *Chem. Mater.* **2016**, *28*, 6848–6859.

(68) Kubicki, D. J.; Prochowicz, D.; Hofstetter, A.; Zakeeruddin, S. M.; Grätzel, M.; Emsley, L. Phase Segregation in Potassium-Doped Lead Halide Perovskites from ³⁹K Solid-State NMR at 21.1 T. *J. Am. Chem. Soc.* **2018**, *140*, 7232–7238.

(69) Kubicki, D. J.; Prochowicz, D.; Hofstetter, A.; Zakeeruddin, S. M.; Grätzel, M.; Emsley, L. Phase Segregation in Cs-, Rb- and K-Doped Mixed-Cation (MA)_x(FA)_{1-x}PbI₃ Hybrid Perovskites from Solid-State NMR. *J. Am. Chem. Soc.* **2017**, *139*, 14173–14180.

- (70) Karmakar, A.; Dodd, M. S.; Agnihotri, S.; Ravera, E.; Michaelis, V. K. Cu(II)-Doped Cs₂SbAgCl₆ Double Perovskite: A Lead-Free, Low-Bandgap Material. *Chem. Mater.* **2018**, *30*, 8280–8290.
- (71) Michaelis, V. K.; Greer, B. J.; Aharen, T.; Greedan, J. E.; Kroeker, S. Determining Electron Spin-Transfer Mechanisms in Paramagnetic. *J. Phys. Chem. C* **2012**, *116*, 23646–23652.
- (72) Aharen, T.; Greedan, J. E.; Bridges, C. A.; Aczel, A. A.; Rodriguez, J.; Macdougall, G.; Luke, G. M.; Imai, T.; Michaelis, V. K.; Kroeker, S.; Zhou, H.; Wiebe, C. R.; Cranswick, L. M. D. Magnetic Properties of the Geometrically Frustrated S=1/2 Antiferromagnets, La₂LiMoO₆ and Ba₂YMoO₆, with the B-Site Ordered Double Perovskite Structure: Evidence for a Collective Spin-Singlet Ground State. *Phys. Rev.* **2010**, *81*, 224409.
- (73) Li, T.; Zhao, X.; Yang, D.; Du, M. H.; Zhang, L. Intrinsic Defect Properties in Halide Double Perovskites for Optoelectronic Applications. *Phys. Rev. Appl.* **2018**, *10*, 041001.
- (74) V. M. Goldschmidt. Die Gesetze Der Krystallochemie. *Naturwissenschaften* **1926**, *14*, 477–485.
- (75) Li, C.; Lu, X.; Ding, W.; Feng, L.; Gao, Y.; Guo, Z. Formability of ABX₃ (X = F, Cl, Br, I) Halide Perovskites. *Acta Crystallogr. Sect. B* **2008**, *B64*, 702–707.
- (76) Shannon, R. D. Revised Effective Ionic Radii and Systematic Studies of Interatomic Distances in Halides and Chalcogenides. *Acta Cryst.* **1976**, *A32*, 751–767.
- (77) Kubelka, P.; Munk, F. Ein Beitrag Zur Optik Der Farbanstriche. *Z. Tech. Phys. (Leipzig)* **1931**, *12*, 593–601.
- (78) Slavney, A. H.; Leppert, L.; Bartesaghi, D.; Gold-Parker, A.; Toney, M. F.; Savenije, T. J.; Neaton, J. B.; Karunadasa, H. I. Defect-Induced Band-Edge Reconstruction of a Bismuth-Halide Double Perovskite for Visible-Light Absorption. *J. Am. Chem. Soc.* **2017**, *139* (14), 5015–5018.
- (79) Meng, W.; Wang, X.; Xiao, Z.; Wang, J.; Mitzi, D. B.; Yan, Y. Parity-Forbidden Transitions and Their Impact on the Optical Absorption Properties of Lead-Free Metal Halide Perovskites and Double Perovskites. *J. Phys. Chem. Lett.* **2017**, *8*, 2999–3007.

- (80) Steele, J. A.; Puech, P.; Keshavarz, M.; Yang, R.; Banerjee, S.; Debroye, E.; Kim, C. W.; Yuan, H.; Heo, N. H.; Vanacken, J.; Walsh, A.; Hofkens, J.; Roeffaers, M. B. J. Giant Electron–Phonon Coupling and Deep Conduction Band Resonance in Metal Halide Double Perovskite. *ACS Nano* **2018**, *12*, 8081–8090.
- (81) Jakob, M.; Aissiou, A.; Morrish, W.; Marsiglio, F.; Islam, M.; Kartouzian, A.; Meldrum, A. Reappraising the Luminescence Lifetime Distributions in Silicon Nanocrystals. *Nanoscale Res. Lett.* **2018**, *13*, 383.
- (82) Thirumal, K.; Chong, W. K.; Xie, W.; Ganguly, R.; Muduli, S. K.; Sherburne, M.; Asta, M.; Mhaisalkar, S.; Sum, T. C.; Soo, H. S.; Mathews, N. Morphology-Independent Stable White-Light Emission from Self-Assembled Two-Dimensional Perovskites Driven by Strong Exciton-Phonon Coupling to the Organic Framework. *Chem. Mater.* **2017**, *29*, 3947–3953.
- (83) Luo, J.; Li, S.; Wu, H.; Zhou, Y.; Li, Y.; Liu, J.; Li, J.; Li, K.; Yi, F.; Niu, G.; Tang, J. Cs₂AgInCl₆ Double Perovskite Single Crystals: Parity Forbidden Transitions and Their Application for Sensitive and Fast UV Photodetectors. *ACS Photonics* **2018**, *5*, 398–405.
- (84) Johnston, M. B.; Herz, L. M. Hybrid Perovskites for Photovoltaics: Charge-Carrier Recombination, Diffusion, and Radiative Efficiencies. *Acc. Chem. Res.* **2016**, *49*, 146–154.
- (85) Dequillettes, D. W.; Frohna, K.; Emin, D.; Kirchartz, T.; Bulovic, V.; Ginger, D. S.; Stranks, S. D. Charge-Carrier Recombination in Halide Perovskites. *Chem. Rev.* **2019**, *119*, 11007–11019.
- (86) Vegard, L. Die Konstitution Der Mischkristalle Und Die Raumffillung Der Atome. *Zeitschrift für Phys.* **1921**, *5*, 17–26.
- (87) Harris, R. K.; Becker, E. D.; de Menrzes, S. M. C.; Goodfellow, R.; Granger, P. NMR Nomenclature. Nuclear Spin Properties and Conventions for Chemical Shifts. *Pure Appl. Chem.* **2001**, *73*, 1795–1818.
- (88) Michaelis, V. K.; Aguiar, P. M.; Kroeker, S. Probing Alkali Coordination Environments in Alkali Borate Glasses by Multinuclear Magnetic Resonance. *J. Non. Cryst. Solids* **2007**, *353*, 2582–2590.

- (89) Kroeker, S.; Eichele, K.; Wasylshen, R. E.; Britten, J. F. Cesium-133 NMR Study of CsCd(SCN)₃: Relative Orientation of the Chemical Shift and Electric Field Gradient Tensors. *J. Phys. Chem. B* **1997**, *101*, 3727–3733.
- (90) MacKenzie, K. J.; Smith, M. E. *Multinuclear Solid-State Nuclear Magnetic Resonance of Inorganic Materials*; Elsevier. 2002.
- (91) Chen, F.; Ma, G.; Cavell, R. G.; Terskikh, V.; Wasylshen, R. E. Solid-State ¹¹⁵In NMR Study of Indium Coordination Complexes. *Chem. Commun.* **2008**, 5933–5935.
- (92) Chen, F.; Ma, G.; Bernard, G. M.; Cavell, R. G.; McDonald, R.; Ferguson, M. J.; Wasylshen, R. E. Solid-State ¹¹⁵In and ³¹P NMR Studies of Triarylphosphine Indium Trihalide Adducts. *J. Am. Chem. Soc.* **2010**, *132*, 5479–5493.
- (93) Hamaed, H.; Laschuk, M. W.; Terskikh, V. V.; Schurko, R. W. Application of Solid-State ²⁰⁹Bi NMR to the Structural Characterization of Bismuth-Containing Materials. *J. Am. Chem. Soc.* **2009**, *131*, 8271–8279.
- (94) Bernard, G. M.; Wasylshen, R. E.; Ratcliffe, C. I.; Terskikh, V.; Wu, Q.; Buriak, J. M.; Hauger, T. Methylammonium Cation Dynamics in Methylammonium Lead Halide Perovskites: A Solid-State NMR Perspective. *J. Phys. Chem. A* **2018**, *122*, 1560–1573.
- (95) Taylor, R. E.; Beckmann, P. A.; Bai, S.; Dybowski, C. ¹²⁷I and ²⁰⁷Pb Solid-State NMR Spectroscopy and Nuclear Spin Relaxation in PbI₂: A Preliminary Study. *J. Phys. Chem. C* **2014**, *118*, 9143–9153.
- (96) Greer, B. J.; Michaelis, V. K.; Terskikh, V. V.; Kroeker, S. Reconnaissance of Diverse Structural and Electronic Environments in Germanium Halides by Solid-State ⁷³Ge NMR and Quantum Chemical Calculations. *Can. J. Chem.* **2011**, *89*, 1118–1129.
- (97) Hamaed, H.; Johnston, K. E.; Cooper, B. F. T.; Terskikh, V. V.; Ye, E.; Charles L. B. Macdonald, D. C. A.; Schurko, R. W. A ¹¹⁵In Solid-State NMR Study of Low Oxidation-State Indium Complexes. *Chem. Sci.* **2014**, *5*, 982–995.
- (98) Lan, C.; Zhao, S.; Luo, J.; Fan, P. First-Principles Study of Anion Diffusion in Lead-Free Halide Double Perovskites. *Phys. Chem. Chem. Phys.* **2018**, *20*, 24339–24344.

- (99) Zhao, X. G.; Yang, J. H.; Fu, Y.; Yang, D.; Xu, Q.; Yu, L.; Wei, S. H.; Zhang, L. Design of Lead-Free Inorganic Halide Perovskites for Solar Cells via Cation-Transmutation. *J. Am. Chem. Soc.* **2017**, *139*, 2630–2638.
- (100) Muñoz-García, A. B.; Pavone, M.; Carter, E. A. Effect of Antisite Defects on the Formation of Oxygen Vacancies in $\text{Sr}_2\text{FeMoO}_6$: Implications for Ion and Electron Transport. *Chem. Mater.* **2011**, *23*, 4525–4536.
- (101) Colis, S.; Stoeffler, D.; Mny, C.; Fix, T.; Leuvrey, C.; Pourroy, G.; Dinia, A.; Panissod, P. Structural Defects in $\text{Sr}_2\text{FeMoO}_6$ Double Perovskite: Experimental versus Theoretical Approach. *J. Appl. Phys.* **2005**, *98*, 033905.
- (102) Greneche, J. M.; Venkatesan, M.; Suryanarayanan, R.; Coey, J. M. D. Mössbauer Spectrometry of A_2FeMoO_6 (A = Ca, Sr, Ba): Search for Antiphase Domains. *Phys. Rev. B* **2001**, *63*, 174403.
- (103) O'Dell, L. A. Ultra-Wideline Solid-State NMR: Developments and Applications of the WCPMG Experiment. In: Webb G. (Eds). *Mod. Magn. Reson. Springer, Cham* **2017**.
- (104) O'Dell, L. A.; Schurko, R. W. QCPMG Using Adiabatic Pulses for Faster Acquisition of Ultra-Wideline NMR Spectra. *Chem. Phys. Lett.* **2008**, *464*, 97–102.

CHAPTER 6

Uncovering Halogen Mixing and Octahedral Dynamics in Cs₂SnX₆ by Multinuclear Magnetic Resonance Spectroscopy^{R5}

6.1 Introduction

Lead halide perovskites (APbX₃; A = Cs⁺, CH₃NH₃⁺, or CH(NH₂)₂⁺; X = Cl⁻, Br⁻, or I⁻) have gained tremendous attention as semiconducting materials due to their desirable optical and electrical properties including photovoltaic solar cells,¹ light-emitting diodes,² hard-radiation detectors,³ photocatalytic reactions,⁴ and so forth.^{5,6} Although lead-containing perovskites have a high power conversion efficiency (PCE) of 25.5% in photovoltaic solar cells,⁷ they unfortunately suffer from mediocre chemical stability⁸⁻¹¹ and the potential risk of lead toxicity.^{12,13} The tin(II) halide perovskites ASnX₃ are possible alternatives with lower toxicity, but they exhibit a lower PCE of up to 10% and rapidly oxidize in air (Sn²⁺ to Sn⁴⁺).¹⁴⁻¹⁷

A₂BX₆ (A = Cs⁺, CH₃NH₃⁺, and CH(NH₂)₂⁺; B = Sn⁴⁺; X = Cl⁻, Br⁻, and I⁻) materials, generally adopt the K₂PtCl₆ structure type (space group *Fm* $\bar{3}$ *m*) and demonstrate much higher ambient stability and lower toxicity.¹⁸ The structure of A₂BX₆ can be described as an ABX₃ perovskite, with half of the B-sites removed in an ordered fashion,¹⁹ with 12 halogens surrounding the A-site to form a CsX₁₂ cuboctahedron, whereas the B-site is octahedrally coordinated with six halogens to form BX₆ octahedra (Figure 6.1a). The iodide analogue, Cs₂SnI₆, has a bandgap (1.25–1.62 eV) close to the optimum value (1.34 eV) to maximize the thin-film solar cell efficiency.^{18,20,21} Recently, Cs₂SnI₆ has shown promising optoelectronic properties to develop air-stable and lead-free perovskite photovoltaics.²² The mixed-halide

^{R5} The contents of this chapter have been copied and/or adapted from the following publication: Karmakar, A.; Mukhopadhyay, S.; Gachod, P. G. B.; Mora-Gomez, V. A.; Bernard, G. M.; Brown, A.; Michaelis, V. K. Uncovering Halogen Mixing and Octahedral Dynamics in Cs₂SnX₆ by Multinuclear Magnetic Resonance Spectroscopy. *Chem. Mater.* **2021**, *33*, 6078–6090. The supplementary data for this chapter is available in Appendix E: Tables E1–E12 and Figures E1–E23.

analogues $\text{Cs}_2\text{SnBr}_x\text{I}_{6-x}$ reveal bandgap tailorability with the halogen composition,²³ making them suitable as hole-transporting materials in solid-state dye-sensitized solar cells.²⁴ On the other hand, Cs_2SnX_6 nanocrystals have demonstrated tunable light emission and photocatalytic activity.^{25–27} Recently, doped (Bi^{3+} and Sb^{3+}) Cs_2SnCl_6 has been shown to produce efficient blue and orange-red light emissions; this development brings about de novo opportunities for these materials as solid-state lighting candidates.^{28–30}

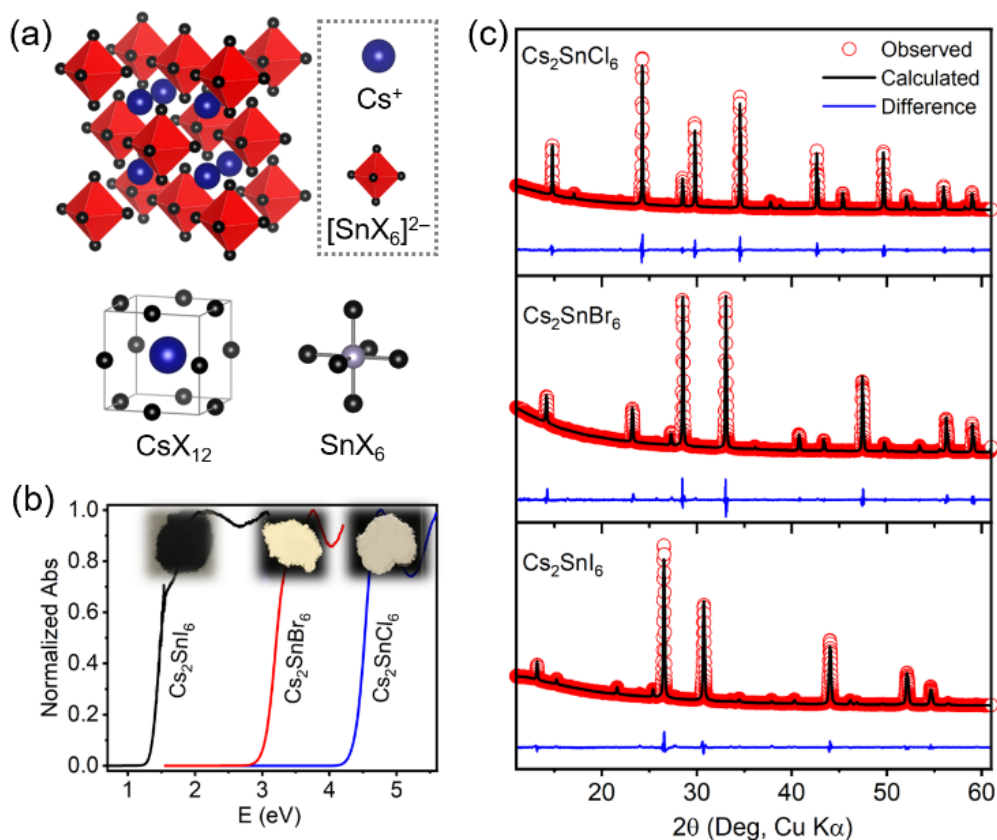


Figure 6.1. (a) Crystal structure of Cs_2SnX_6 , local CsX_{12} cuboctahedral environment of 12 halogens around cesium, and local SnX_6 octahedral environment of 6 halogens around tin. (b) Optical absorption spectra (inset—photographs) and (c) powder XRD patterns of solvent-synthesized Cs_2SnX_6 parents.

To date, A_2BX_6 materials have been extensively characterized by X-ray diffraction (XRD) techniques, which provide information about the average long-range

structure but not about the local chemical environments. Fundamentally, it is essential to correlate the bulk photophysical properties with the microstructural characteristics for perovskites. Solid-state nuclear magnetic resonance (NMR) spectroscopy is a robust analytical characterization tool to determine short-range (<5 Å) and medium-range (5–10 Å) structures as well as ion dynamics in perovskites.^{16,31–47} More specifically, ¹³³Cs ($I = 7/2$, $Q_m = -0.34 \text{ fm}^2$, 100% abundance)⁴⁸ is an ideal NMR-active nucleus to identify the chemical environments around the A-site in perovskites.^{36,42,47,49–52} ¹¹⁹Sn ($I = 1/2$, 8.6% abundance), the most receptive nucleus among three NMR-active tin isotopes (¹¹⁵Sn, ¹¹⁷Sn, and ¹¹⁹Sn) (Table E1),⁴⁸ has been used to resolve the local B-site structural environments and halogen dynamics in ABX₃ perovskites and other tin-containing compounds.^{16,17,53–59} Furthermore, the ¹¹⁹Sn NMR spectra display an extensive chemical shift range for diamagnetic Sn-containing compounds, shown to span nearly 6000 ppm.^{16,60–62} Earlier variable-temperature ³⁵Cl nuclear quadrupolar resonance (NQR) experiments have been used to examine phase transitions of K₂BCl₆ (B = Pt, Pd, and Ir) compounds.^{63,64}

The present study shows an impressive ability to tailor the optical bandgap over a 3 eV range using a high-energy mechanochemical synthetic design of Cs₂SnCl_xBr_{6-x} and Cs₂SnBr_xI_{6-x} mixed-halide materials. Powder XRD and NMR spectroscopy allow the identification of the long-, medium-, and short-range chemical and coordination environments around Cs and Sn sites upon interhalogen substitutions in mixed-halide analogues. The experimentally observed broad (>100 kHz) and multiple resonances in the ¹¹⁹Sn NMR spectra for the mixed-halide analogues are correlated with ¹¹⁹Sn magnetic shielding parameters obtained from density functional theory (DFT) computations and reveal the importance of the spin-orbit shielding term. Variable-temperature ¹¹⁹Sn NMR measurements allowed a tentative estimate of the activation energy for SnI₆ octahedral anharmonic dynamics in Cs₂SnI₆. Finally, Cs₂SnI₆ materials prepared by the solvent or solvent-free synthesis routes are discussed to examine how the synthetic approach influences the local chemical structure and bulk optical properties. The comparison is important as mechanochemistry continues to be shown as an effective greener approach for synthesizing solids.

6.2 Results and Discussion

6.2.1 Solvent-Synthesized Cs₂SnX₆ Parents

Cs₂SnX₆ (X = Cl⁻, Br⁻, and I⁻) parents were prepared by solvent-assisted synthetic routes starting with CsX and SnX₄ precursors (see the Experimental Section). As determined by energy-dispersive X-ray spectroscopy (EDS), the chemical compositions agree well with the expected Cs₂SnX₆ chemical formulation formed by solvent synthesis (Table E2 and Figure E1). Cs₂SnX₆ samples are polycrystalline with micron-sized particles as determined by field-emission scanning electron microscopy (FESEM) (Figure E2). The color of Cs₂SnX₆ changes from white (Cs₂SnCl₆) to faint yellow (Cs₂SnBr₆) to black (Cs₂SnI₆), consistent with a decrease in their optical absorption edge (Figure 6.1b). The powder XRD patterns are consistent with a cubic structure (K₂PtCl₆-type, space group *Fm* $\bar{3}$ *m*) for all three Cs₂SnX₆ parents at room temperature (Figure 6.1c). The cell parameters, as refined by Le Bail fitting of the powder XRD patterns, systematically increase for the Cs₂SnX₆ parents as the ionic radius of the associated halogen anion increases from 1.81 Å $r(\text{Cl}^-) < 1.96$ Å $r(\text{Br}^-) < 2.20$ Å $r(\text{I}^-)$ (Table 6.1).⁶⁵

Table 6.1. Unit cell parameters, direct bandgap, and solid-state ¹³³Cs and ¹¹⁹Sn NMR results for solvent-synthesized Cs₂SnX₆ parents.

Samples	Cell parameter (Å)	Bandgap (eV)	¹³³ Cs NMR ($\nu_r = 5$ kHz, $B_0 = 11.75$ T)		¹¹⁹ Sn NMR ($\nu_r = 13$ kHz, $B_0 = 11.75$ T)		
			δ (ppm)	fwhm (Hz)	δ (ppm)	fwhm (kHz)	T_1 (s)
Cs ₂ SnCl ₆	10.3826(1)	4.48	125.8 ± 0.1	62 ± 2	-708 ± 1	1.5 ± 0.1	146 ± 6
Cs ₂ SnBr ₆	10.8377(2)	3.13	112.3 ± 0.2	175 ± 5	-1964 ± 2	5.2 ± 0.2	5.4 ± 0.2
Cs ₂ SnI ₆	11.6342(2)	1.42	-46.1 ± 0.1	66 ± 2	-4540 ± 5	11.5 ± 0.5	0.170 ± 0.007

The optical absorption spectra, which are extracted from the diffuse reflectance spectra by the Kubelka–Munk function, exhibit a gradual shift of the absorption edge to lower energy as Cl is replaced by Br and followed by I in Cs₂SnX₆ parents (Figure 6.1b). Considering a direct bandgap property for these semiconducting

materials,⁶⁶ the optical bandgap values are extracted from the linear region in the Tauc plot of $(\alpha h\nu)^2$ against energy (Figure E3). The bandgaps for the Cs_2SnX_6 parents exhibit a dramatic decrease from 4.48 eV for Cs_2SnCl_6 to 1.42 eV for Cs_2SnI_6 , spanning across 3 eV (Table 6.1).

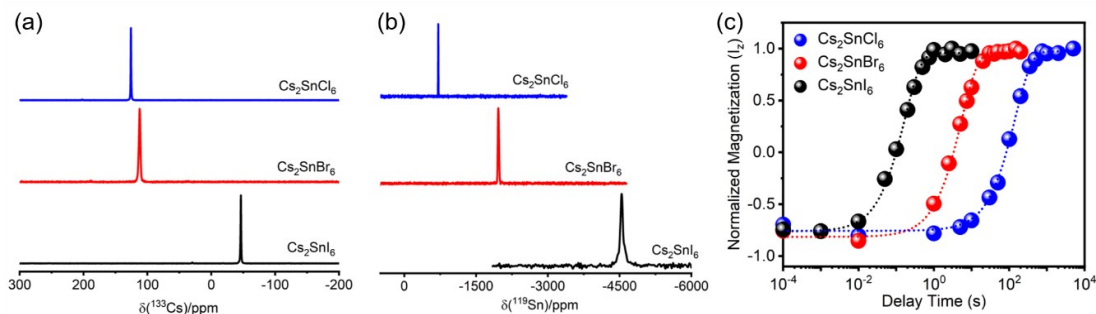


Figure 6.2. Solid-state (a) ^{133}Cs and (b) ^{119}Sn NMR spectra and (c) inversion recovery plot to measure ^{119}Sn spin-lattice (T_1) relaxation values for the solvent-synthesized Cs_2SnX_6 parents. The ^{133}Cs and ^{119}Sn NMR experiments were performed at 11.75 T with MAS frequencies of 5 and 13 kHz, respectively.

Solid-state ^{133}Cs and ^{119}Sn NMR spectroscopy was used to investigate the local halogen environments around cesium and tin. The Cs atoms occupy a crystallographic site with a $\bar{4}3m$ symmetry in Cs_2SnX_6 . Twelve nearest neighbor halogen atoms surround each Cs atom to form a local CsX_{12} cuboctahedral environment (Figure 6.1a). Accordingly, the ^{133}Cs magic-angle spinning (MAS) NMR spectra exhibit a single sharp resonance with chemical shifts of 125.8 ppm (full width at half maximum, fwhm = 62 Hz) for Cs_2SnCl_6 , 114.6 ppm (fwhm = 175 Hz) for Cs_2SnBr_6 , and -41.4 ppm (fwhm = 66 Hz) for Cs_2SnI_6 , indicating one unique crystallographic Cs site (Figure 6.2a and Table 6.1). A gradual change in the ^{133}Cs NMR chemical shift toward lower frequency is in agreement with a recent observation on CsSnX_3 perovskites,¹⁶ but in contrast to CsPbX_3 perovskites,³⁶ where an opposite trend in the chemical shift was observed. Due to Cs residing in the center of a perfect CsX_{12} cuboctahedral environment in the Cs_2SnX_6 parents, a vanishing ^{133}Cs quadrupole coupling constant ($C_Q = 0$ kHz) is expected with no spinning sidebands (SSBs) under MAS conditions.

However, a low-intensity (<1%) SSB was observed under slow MAS ($\nu_r = 5$ kHz) for all three Cs_2SnX_6 parents (Figure E4), which is associated with intrinsic defects such as halogen vacancies.^{49,67}

The Sn atoms in the Cs_2SnX_6 structure occupy sites with a $m\bar{3}m$ symmetry with six nearest neighbor halogen atoms surrounding Sn to form local SnX_6 octahedral units (Figure 6.1a). The Cs_2SnX_6 parents exhibit symmetric ^{119}Sn NMR resonances with no evidence of SSBs under MAS conditions (Figure 6.2b), consistent with the highly symmetric local SnX_6 octahedral environment. The ^{119}Sn NMR peaks for Cs_2SnX_6 shift toward a lower frequency with a chemical shift of -708 ppm for Cs_2SnCl_6 , -1964 ppm for Cs_2SnBr_6 and -4540 ppm for Cs_2SnI_6 , which represents a large change spanning over 3800 ppm for these diamagnetic tin-containing compounds. The trend of increased Sn shielding (to a lower frequency) with increased halogen atomic number observed here, a normal halogen dependence, is opposite to previous studies on Sn(II)-based perovskites (ASnX_3), where an inverse halogen dependence was observed with a smaller chemical shift range (<1300 ppm).^{16,56,68} The unprecedented change in ^{119}Sn chemical shifts was further studied using theoretical calculations, which revealed that the diamagnetic and paramagnetic shielding terms are nearly unchanged. Hence, the changes in the chemical shift originate from considerable spin-orbit effects, whereby this term changes ca. 4500 ppm as the halide anions increase in size (Table E3), demonstrating the importance of including the spin-orbit term in relativistic DFT calculations for these materials which contain heavy elements.⁶⁹ The ^{119}Sn NMR linewidths depend on the halogen in Cs_2SnX_6 , increasing monotonically from 1.5 (Cs_2SnCl_6) to 5.2 (Cs_2SnBr_6) to 11.5 kHz (Cs_2SnI_6). For Cs_2SnBr_6 , the ^{119}Sn NMR linewidth and lineshape are independent of the magnetic field strength ($B_0 = 7.05$ to 11.75 T, Figure E5), with no indication of shielding anisotropy. Furthermore, the ^{119}Sn NMR linewidth decreases slightly (ca. 0.8 kHz) once MAS is applied (Figure E6), confirming a small contribution from heteronuclear dipolar coupling (through space) between Sn and Br nuclei ($^{79/81}\text{Br}$: $I = 3/2$, total abundance = 100%). These findings suggest that a dominant $^1J(^{119}\text{Sn}, ^{79/81}\text{Br})$ scalar coupling between ^{119}Sn and the six directly bonded $^{79/81}\text{Br}$ nuclei in SnBr_6 octahedra is responsible for the ^{119}Sn NMR linewidth.^{35,36,38,70} The ^{119}Sn spin-lattice relaxation time

(T_1) decreases from Cs_2SnCl_6 ($T_1 = 146$ s) to Cs_2SnBr_6 ($T_1 = 5.4$ s) to Cs_2SnI_6 ($T_1 = 0.170$ s), a difference of 3 orders of magnitude (Figure 6.2c and Table 6.1), which is comparable to recent observations on ASnX_3 perovskites.^{16,17} The trend in ^{119}Sn T_1 values where the relaxation decreases dramatically with increasing halogen atomic number (Figure 6.2c) is the inverse of the trend in the scalar coupling strength, where $^1J(^{127}\text{I}, ^{119}\text{Sn}) > ^1J(^{119}\text{Sn}, ^{79/81}\text{Br}) > ^1J(^{119}\text{Sn}, ^{35/37}\text{Cl})$. Similar results have been observed in other tin halide perovskite compounds.^{16,71,72}

6.2.2 Chlorine-35 NMR Spectroscopy in Cs_2SnCl_6

The stable halogen elements are NMR active; but unlike ^{19}F ($I = 1/2$), the heavier group 17 elements are quadrupolar [nuclear spin, $I = 3/2$ ($^{35/37}\text{Cl}$, $^{79/81}\text{Br}$) or $I = 5/2$ (^{127}I)] with significant quadrupole moments (Table E1). ^{35}Cl NMR spectroscopy has been used to investigate the local structural environments in pharmaceuticals, amino acids, lead halide perovskites, and organic and organometallic compounds, due to its overall NMR sensitivity as well as the insight into the structure that it provides.^{73–78} Crystallographically, the halogen atoms in Cs_2SnX_6 occupy a single site with symmetry $4mm$, where each halogen is bonded to a single Sn atom (Figure 6.1a). Hence, this lower site symmetry of the X site in Cs_2SnX_6 is expected to impart a sizable electric field gradient (EFG) that will cause substantial spectral broadening. Figure 6.3 shows the frequency-stepped wide-band, uniform, and smooth truncation Carr–Purcell–Meiboom–Gill (WURST-CPMG)^{79,80} ^{35}Cl NMR spectrum of Cs_2SnCl_6 . The ultrawideline NMR spectrum that spans ca. 2.7 MHz at 11.75 T was obtained in 12 steps using the variable offset cumulative spectrum (VOCS) technique (Figure E7). Fitting the central transition reveals that $\delta_{\text{iso}} = 560 \pm 20$ ppm, $C_Q = 32.0 \pm 0.3$ MHz, and the quadrupolar asymmetry parameter, $\eta = 0.00$. The spectral lineshape is consistent with the presence of a terminal Cl atom in Cs_2SnCl_6 , as the terminal Cl atoms are in a higher axial symmetric environment, which results in a large C_Q and a low η . Moreover, the large ^{35}Cl C_Q values are consistent with chloride ions coordinated to a Sn(IV) ion in a local SnCl_6 octahedral environment.⁷⁸ In contrast, Cl atoms attached to Sn(II) ions show smaller C_Q values of <30 MHz, as recently reported in metal tin chlorides.⁷⁸ We note that the bulk and nanocrystalline forms of

CsPbCl₃ perovskites exhibit smaller ³⁵Cl C_Q values of ca. 15.5 MHz ($\eta = 0$).⁷⁶ The magnitude of the observed ³⁵Cl quadrupolar interaction may, in principle, yield information on the dynamics of the SnCl₆ octahedra. An early NQR study⁸¹ showed a modest temperature dependence to ³⁵Cl NQR frequencies for K₂PtCl₆ of $-940 \text{ Hz}\cdot\text{K}^{-1}$ in the 50–350 K range but the temperature dependence is significantly lower ($-560 \text{ Hz}\cdot\text{K}^{-1}$) for K₂IrCl₆; the temperature dependence was attributed to oscillations of the BCl₆ units. Hence, any temperature dependence of the ³⁵Cl C_Q values due to the dynamics of the SnCl₆ octahedra are anticipated to be relatively small (100–200 kHz, within our experimental error of 300 kHz) due to hardware limitations.

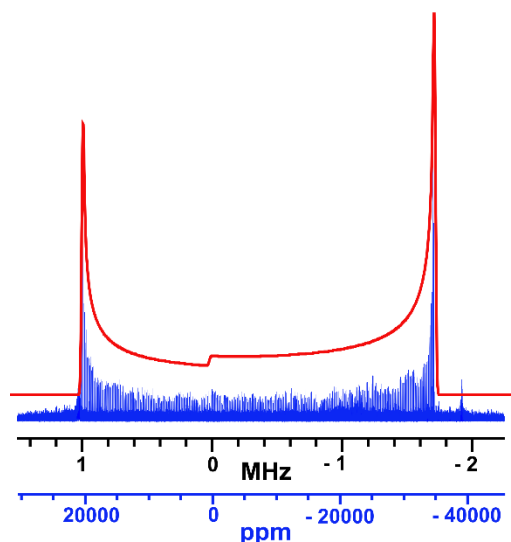


Figure 6.3. Experimental (lower trace, blue) and simulated (upper trace, red) ³⁵Cl WURST-CPMG solid-state NMR spectrum of the Cs₂SnCl₆ parent ($\nu_r = 0 \text{ kHz}$, $B_0 = 11.75 \text{ T}$, sum of 12 frequency steps, 250 kHz/step).

6.2.3 SnI₆ Octahedral Dynamics in Cs₂SnI₆

Anharmonic lattice dynamics of BX₆ octahedra in halide perovskites play a vital role in optical and electrical properties of these materials.^{82–84} The isolated BX₆ octahedral units in A₂BX₆ extend the degree of dynamical freedom compared to that for their sister materials, ABX₃ perovskites (Figure 6.4a). Recently, X-ray pair distribution function

analysis on Cs_2SnI_6 has revealed asymmetry in the interoctahedral I–I distance, which can be correlated with the rotational disorder for the isolated SnI_6 octahedral units.^{85,86} To further investigate this behavior, variable-temperature ^{119}Sn NMR measurements were carried out on a solvent-synthesized Cs_2SnI_6 sample.

As the sample temperature increases from 208 to 380 K, the ^{119}Sn NMR resonance shifts linearly toward lower frequencies from -4522 to -4547 ppm (Table E4, Figures 6.4b and E8), attributed to a change in the interatomic distance as the temperature changes. The linewidth of the ^{119}Sn NMR resonance is unaltered (fwhm = 18 ± 1 kHz) across the temperature range studied, indicating that the ^{119}Sn NMR linewidth in Cs_2SnI_6 is primarily driven by indirect (J) and direct (dipolar) spin–spin couplings between ^{119}Sn and ^{127}I nuclei. Most interestingly, the ^{119}Sn NMR spin-lattice relaxation time (T_1) changes drastically from 4.6 s (208 K) to 0.12 s (380 K); nearly a 40-fold change in the T_1 value over a 170 K temperature range.

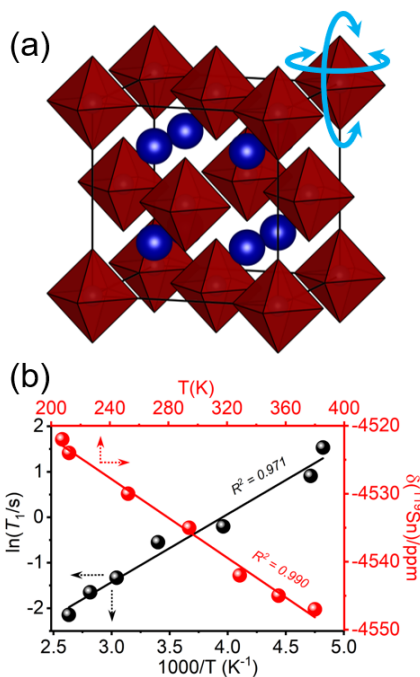


Figure 6.4. (a) Schematic diagram of SnI_6 anharmonicity in the Cs_2SnI_6 structure. (b) Variable-temperature ^{119}Sn T_1 data ($\nu_r = 0$ kHz, $B_0 = 11.75$ T) as a function of the inverse of temperature (black text and points), and the ^{119}Sn chemical shift as a function of temperature (red text and points) for solvent-synthesized Cs_2SnI_6 .

Several interactions may contribute to the ^{119}Sn spin-lattice (i.e., T_1) relaxation for Cs_2SnI_6 , such as chemical shift anisotropy (CSA), scalar relaxation, spin-phonon Raman scattering processes, magic-angle spinning-induced heteronuclear polarization changes, and dipole–dipole interactions (see Appendix E, Appendix Note E1 for a detailed discussion). It is possible to ascertain experimentally whether some of these interactions make significant contributions to $T_1(^{119}\text{Sn})$. For example, a comparison of ^{119}Sn NMR spectra for non-spinning samples acquired at 7.05 and 11.75 T demonstrate that CSA is negligible for this nucleus in Cs_2SnI_6 and hence cannot make a significant contribution to $T_1(^{119}\text{Sn})$. As shown in Figure 6.4b, in the 208–380 K temperature range, a plot of $\ln(T_1)$ versus $1000 T^{-1}$ yields a linear Arrhenius relationship. If other relaxation mechanisms contributing to $T_1(^{119}\text{Sn})$ can either be quantified or discounted, the apparent Arrhenius relationship permits the determination of the activation energy (E_a) for SnI_6 octahedral lattice dynamics. Such an approach has been used to investigate methylammonium (MA) cation dynamics in MAPbX_3 perovskites,^{35,87} and a comparable temperature-dependent change in ^{119}Sn T_1 has been reported for the ionic conductors, $\text{CH}_3\text{NH}_3\text{SnBr}_3$ and CsSnBr_3 perovskites, where much higher activation energies (0.3–0.4 eV) were observed, in this case attributed to halogen migration.^{16,17} If one were to assume that the dipole–dipole relaxation mechanism is the primary relaxation process, a plot of $\ln[T_1/\text{s}]$ against $[1000/T(\text{K})]$ is linear, allowing the determination of an activation energy of 12.45 ± 0.87 kJ/mol (0.129 ± 0.009 eV), in accordance with the Arrhenius relationship (see Table E4, Figure 6.4b, Appendix Note E2), suggesting a low energy barrier for the SnI_6 octahedral lattice dynamics. Unfortunately, we are not able to discount contributions to relaxation from spin-phonon Raman scattering. A proper investigation of this mechanism requires that one obtain data over a much wider temperature range than our hardware permits. Hence, the activation energy for anharmonic SnI_6 rotation discussed above must be considered tentative.

6.2.4 Mechanochemically Synthesized $\text{Cs}_2\text{SnCl}_x\text{Br}_{6-x}$ and $\text{Cs}_2\text{SnBr}_x\text{I}_{6-x}$ Mixed Halides

Halide perovskites are predominately prepared by solvent, high-temperature, or vapor deposition techniques.^{1,88,89} Mechanochemical synthesis is an entrenched “greener” synthetic route to prepare a broad range of advanced functional materials^{90–92} and has recently been applied successfully in the large-scale production of perovskite photovoltaic materials.^{36,38,93–96} Moreover, certain compositions of APbX_3 mixed-halide perovskites were achieved only by mechanochemical synthesis but not via solvent-synthesized routes.^{37,38,97}

Both manual hand-grinding using a mortar and pestle and automated electric ball milling have been used as solvent-free mechanochemical synthesis routes to prepare bulk halide perovskites.^{16,36–38,94,95} Recently, we have shown that, using a hand-grinding approach, one can obtain phase-pure APbX_3 perovskites within hours.^{36–38} We found that the hand-grinding preparation of Cs_2SnI_6 requires a substantially longer mixing time (6 h) compared to APbX_3 perovskites. In comparison, electric ball milling is more efficient (1.5 h) over the labor-intensive manual route (Figure E9). The phase-pure $\text{Cs}_2\text{SnCl}_x\text{Br}_{6-x}$ ($x = 3$) and $\text{Cs}_2\text{SnBr}_x\text{I}_{6-x}$ ($x = 0, 1.5, 3, 4.5,$ and 6) samples were prepared by mechanochemical ball milling under ambient conditions (detailed synthesis is discussed in the Experimental Section, Table E5 and Figures E10 and E11).

Figure 6.5a shows photographs of the ball-milled $\text{Cs}_2\text{SnCl}_x\text{Br}_{6-x}$ and $\text{Cs}_2\text{SnBr}_x\text{I}_{6-x}$ samples; their colors are consistent with the optical bandgaps. The samples are micron-sized particles having uniform distributions of the constituent elements (Cs, Sn, Cl, Br, and I), as determined from elemental mapping images collected using FESEM (Figures 6.5b and E12). The elemental compositions of mixed-halide analogues, as determined by EDS analysis, agree well with the nominal compositions (Table E2 and Figure E13).

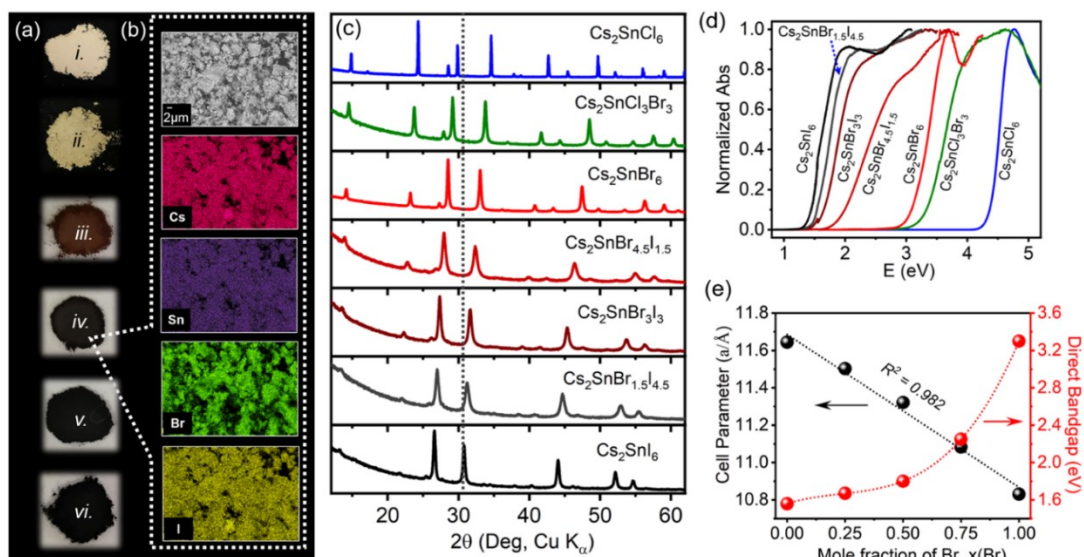


Figure 6.5. (a) Photographs of ball-milled samples: (i) Cs₂SnCl₃Br₃, (ii) Cs₂SnBr₆, (iii) Cs₂SnBr_{4.5}I_{1.5}, (iv) Cs₂SnBr₃I₃, (v) Cs₂SnBr_{1.5}I_{4.5}, and (vi) Cs₂SnI₆. (b) Scanning electron micrographs and elemental mapping images of Cs₂SnBr₃I₃. (c) Powder XRD patterns and (d) normalized optical absorption spectra of ball-milled Cs₂SnCl_xBr_{6-x} and Cs₂SnBr_xI_{6-x} samples (except Cs₂SnCl₆, solvent synthesized). (e) Plots of unit cell parameters and bandgaps of ball-milled Cs₂SnBr_xI_{6-x} series.

The powder XRD patterns collected at room temperature are consistent with the cubic structure (space group $Fm\bar{3}m$) for Cs₂SnCl_xBr_{6-x} and Cs₂SnBr_xI_{6-x} (Figures 6.5c and E14). The powder XRD peaks are shifted toward a higher diffraction angle (Figure 6.5c), and the refined unit cell parameter increases as smaller halogens are replaced with larger variants (Table E6). The unit cell parameters in Cs₂SnBr_xI_{6-x} against Br content shows no significant deviation from linearity, in agreement with Vegard's law (Figure 6.5e). This finding suggests that Br and I atoms are randomly mixed in Cs₂SnBr_xI_{6-x}, consistent with our previous observations in lead-based mixed-halide perovskites.^{37,38}

The optical absorption spectra show that the absorption edge shifts to lower energy with greater Br content in Cs₂SnCl_xBr_{6-x} and I content in Cs₂SnBr_xI_{6-x} (Figure 6.5d). As extracted from the Tauc plot of the direct bandgap, the optical bandgap values span about 3 eV for these samples (Table E6 and Figure E15),

which agrees well with previous observations.^{66,98} The bandgap in the $\text{Cs}_2\text{SnBr}_x\text{I}_{6-x}$ mixed-halide series decreases nonlinearly from 3.30 eV for Cs_2SnBr_6 to 1.54 eV for Cs_2SnI_6 (Figure 5e). The nonlinearity of the direct bandgap in Cs_2SnX_6 mixed-halide samples was recently examined by DFT computations which suggested that the dipolar-disallowed fundamental bandgap becomes optically active once the local symmetry breaks.⁹⁸ This behavior is different from the linear bandgap trend observed in lead-containing mixed-halide perovskites^{36–38} but is similar to the observed anomalous nonlinear trend in the mixed tin–lead perovskites.⁹⁹

A more complete local structural model for the mixed-halide samples can be obtained by solid-state ^{133}Cs and ^{119}Sn NMR spectroscopy to interrogate the A- and B-sites, respectively. Figure 6.6a shows the ^{133}Cs MAS NMR spectra for $\text{Cs}_2\text{SnCl}_x\text{Br}_{6-x}$ and $\text{Cs}_2\text{SnBr}_x\text{I}_{6-x}$. $\text{Cs}_2\text{SnCl}_3\text{Br}_3$ exhibits an inhomogeneously broadened ^{133}Cs NMR resonance (fwhm = 1.1 kHz) due to the spectral overlap of multiple local $\text{CsCl}_m\text{Br}_{12-m}$ ($m = 0–12$) environments according to the random distribution (Table E7 and Figure E16a).³⁶ The asymmetric tailing in the ^{133}Cs NMR spectrum toward a lower frequency is due to the broader linewidth associated with Br-rich compounds (Table 6.1). The ^{133}Cs SSB manifold is related to the local CsX_{12} cuboctahedral symmetry,⁴⁹ an increase in the ^{133}Cs SSBs in $\text{Cs}_2\text{SnCl}_3\text{Br}_3$ indicates a perturbation of the EFG due to the lowering in the local cuboctahedral symmetry upon Cl and Br mixing and hence, an increase in the quadrupolar coupling constant (Figure E17). For the $\text{Cs}_2\text{SnBr}_x\text{I}_{6-x}$ series, the ^{133}Cs NMR resonances span across 160 ppm between 115 and –45 ppm. The resonances are either spectrally unresolved for Br-rich or resolved for I-rich samples (Figure 6.6a). The Br-rich sample $\text{Cs}_2\text{SnBr}_{4.5}\text{I}_{1.5}$ shows an inhomogeneously broadened ^{133}Cs NMR peak due to the spectral overlap of multiple local $\text{CsBr}_m\text{I}_{12-m}$ environments according to the random population distribution (Table E7 and Figure E16b), thereby limiting the spectral resolution. $\text{Cs}_2\text{SnBr}_3\text{I}_3$, which contains equal proportions of Br and I atoms, exhibits a partial spectrally resolved ^{133}Cs NMR resonance. Remarkably, I-rich $\text{Cs}_2\text{SnBr}_{1.5}\text{I}_{4.5}$ shows spectrally resolved ^{133}Cs NMR resonances, which correspond to six distinguishably local $\text{CsBr}_m\text{I}_{12-m}$ ($m = 0, 1, 2, 3, 4, \text{ and } 5$) environments (Figure 6.6b). The lowest chemical shift at –38.4 ppm (fwhm = 500 Hz) is assigned to

the CsI₁₂ environment, which is comparable to the local chemical environment at -41.5 ppm (fwhm = 110 Hz) for the Cs₂SnI₆ parent (Figure 6.6a). The observed broadening and shift of the resonance to a higher frequency is associated with the lower than cubic site symmetry as the next-nearest neighbors in the medium-range structure (>5 Å) consist of a mixture of Br and I atoms.⁴⁹ The remaining peaks within the sets of ¹³³Cs resonances in Cs₂SnBr_{1.5}I_{4.5} shift toward a higher frequency as I is substituted by Br (Figure 6.6c and Table E8), following a strict linear dependence (Eq. 6.1) with *m* in CsBr_{*m*}I_{12-*m*}.

$$\delta(^{133}\text{Cs})/\text{ppm} = 17.0 \cdot m - 36.78 \quad (\text{Eq. 6.1})$$

Furthermore, the observation of increased ¹³³Cs linewidths for CsBr_{*m*}I_{12-*m*} peaks with an increased Br content (Table E8) is due to the broader linewidth attributed to Cs₂SnBr₆, which is three times larger than Cs₂SnI₆ (Table 6.1). The ¹³³Cs spin-lattice relaxation times decrease linearly from 40 to 14 s with an increasing number of Br attached in CsBr_{*m*}I_{12-*m*} (Figure 6.6c). Acquiring the ¹³³Cs NMR spectra with a quantitative recycle delay for Cs₂SnBr_{1.5}I_{4.5} (Figure E18), the fitted ¹³³Cs peak areas for each CsBr_{*m*}I_{12-*m*} environment closely follows a binomial population distribution (Figure 6.6d and Table E8). This observation is consistent with random Br and I mixing at the local structure, forming an atomic-level mixed-halide solid-solution without evidence of phase segregation or domains. Our findings are consistent for these types of materials, where the Cs₂Sn_{1-*y*}Te_{*y*}I₆ (0 ≤ *y* ≤ 1) mixed B-site series, recently investigated using X-ray pair distribution function analysis, showed an asymmetry in the Cs-I-I pair correlation that was dependent on tellurium content.⁸⁶ Similarly, a near-random halogen distribution has been found in a local SnX₆ octahedral environment of Cs₂SnCl_{*x*}Br_{6-*x*} and Cs₂SnBr_{*x*}I_{6-*x*} samples, studied by Raman spectroscopy.⁹⁸

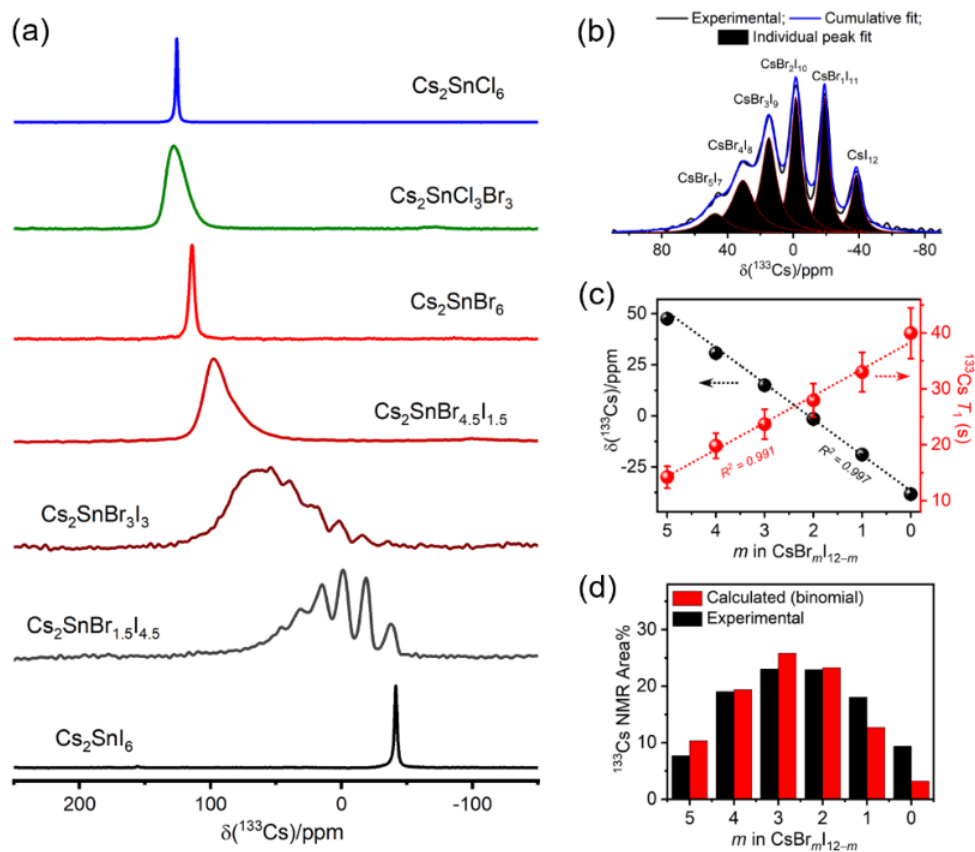


Figure 6.6. (a) Solid-state ^{133}Cs ($\nu_r = 13$ kHz, $B_0 = 11.75$ T) NMR spectra of ball-milled $\text{Cs}_2\text{SnCl}_x\text{Br}_{6-x}$ and $\text{Cs}_2\text{SnBr}_x\text{I}_{6-x}$ samples (except Cs_2SnCl_6 , solvent synthesized). (b) Experimental and fitted ^{133}Cs NMR spectra, (c) ^{133}Cs chemical shift and $^{133}\text{Cs } T_1$ values, and (d) population distribution as a function of Br atoms in $\text{CsBr}_m\text{I}_{12-m}$ for $\text{Cs}_2\text{SnBr}_{1.5}\text{I}_{4.5}$.

The ^{119}Sn NMR spectra for the $\text{Cs}_2\text{SnCl}_x\text{Br}_{6-x}$ and $\text{Cs}_2\text{SnBr}_x\text{I}_{6-x}$ series exhibit broad (hundreds of kHz) and partially spectrally resolved multiple ^{119}Sn resonances (Figure 6.7). To achieve maximum ^{119}Sn NMR sensitivity, optimized ^{119}Sn recycle delays and VOCS (if required) were used due to their drastic differences in $^{119}\text{Sn } T_1$ and large chemical shift spans (Table E9d). This observation contrasts with the recent observations on ASnX_3 mixed-halide perovskites, where single ^{119}Sn resonances are reported due to rapid halogen dynamics.^{16,17} However, the broadening and

multiresonance spectral behavior agrees well with ^{207}Pb NMR spectra for APbX_3 mixed-halide perovskites.^{36–38}

To understand the observed ^{119}Sn NMR spectra for the mixed-halide analogues, the ^{119}Sn magnetic shielding parameters of isolated octahedral clusters, that is, $\text{SnCl}_n\text{Br}_{6-n}$ ($n = 0–6$) for $\text{Cs}_2\text{SnCl}_x\text{Br}_{6-x}$ and $\text{SnBr}_n\text{I}_{6-n}$ for $\text{Cs}_2\text{SnBr}_x\text{I}_{6-x}$, were computed using DFT, and the computational details are provided in the Experimental Section and Tables E10 and E11. The computed ^{119}Sn isotropic chemical shifts are linearly shifted to a lower frequency as Cl is substituted by Br in $\text{SnCl}_n\text{Br}_{6-n}$ (Figure 6.8a) and Br is substituted by I in $\text{SnBr}_n\text{I}_{6-n}$ (Figure E19). The computed magnetic shielding anisotropy parameters (span and skew) exhibit a wide range of values that depend on n values and on their positional isomers (cis/trans or fac/mer) in $\text{SnCl}_n\text{Br}_{6-n}$ and $\text{SnBr}_n\text{I}_{6-n}$; this is responsible for the increased NMR linewidths (Figures 6.7, 6.8 and E20). For example, the computed ^{119}Sn span is 1058 ppm for *trans*- SnCl_2Br_4 in $\text{Cs}_2\text{SnCl}_x\text{Br}_{6-x}$ and up to 4702 ppm for *trans*- SnI_4Br_2 in $\text{Cs}_2\text{SnBr}_x\text{I}_{6-x}$. The experimentally observed ^{119}Sn NMR spectra in $\text{Cs}_2\text{SnCl}_x\text{Br}_{6-x}$ and $\text{Cs}_2\text{SnBr}_x\text{I}_{6-x}$ are a combination of individual resonances of all possible $\text{SnCl}_n\text{Br}_{6-n}$ or $\text{SnBr}_n\text{I}_{6-n}$ species according to their populations, following a random distribution (Table E12 and Figure E21). Along with magnetic shielding anisotropy, the experimental NMR spectra are further broadened by both indirect and direct spin–spin coupling between ^{119}Sn and six quadrupolar halogens ($^{35/37}\text{Cl}$, $^{79/81}\text{Br}$, or ^{127}I) in $\text{SnCl}_n\text{Br}_{6-n}$ or $\text{SnBr}_n\text{I}_{6-n}$, vide supra. Due to the complex nature of these parameters, inability to acquire ultrafast MAS, sensitivity, and less spectral resolution among the ten possible unique halogen arrangements including the isomers in $\text{SnCl}_n\text{Br}_{6-n}$ or $\text{SnBr}_n\text{I}_{6-n}$, we refrain from quantitatively deconvoluting the experimental ^{119}Sn NMR spectra for $\text{Cs}_2\text{SnCl}_x\text{Br}_{6-x}$ and $\text{Cs}_2\text{SnBr}_x\text{I}_{6-x}$, but these are discussed qualitatively below.

The multiple ^{119}Sn NMR peaks in mixed-halide samples correspond to several distinct local Sn octahedral environments. Guided by the DFT computations, the five spectrally distinguishable ^{119}Sn NMR resonances in $\text{Cs}_2\text{SnCl}_3\text{Br}_3$ are tentatively assigned by peak maxima and by a spectral region (Figure 6.7b, blue dotted lines): SnCl_6 (–707 ppm), SnCl_5Br_1 (–966 ppm), $\text{SnCl}_4\text{Br}_2/\text{SnCl}_3\text{Br}_3/\text{SnCl}_2\text{Br}_4$ (–1291 ppm), SnCl_1Br_5 (–1610 ppm), and SnBr_6 (–1962 ppm). The ^{119}Sn NMR peaks for

$\text{Cs}_2\text{SnBr}_x\text{I}_{6-x}$ are much broader due to the stronger $^1J(^{119}\text{Sn}, ^{79/81}\text{Br})$ and $^1J(^{127}\text{I}, ^{119}\text{Sn})$ in $\text{SnBr}_n\text{I}_{6-n}$ along with their higher magnetic shielding anisotropy (thousands of ppm) predicted by DFT (Table E10) and thus are unresolved. Nevertheless, using the DFT results as a guide, four spectrally resolved ^{119}Sn NMR resonances can be tentatively assigned (peak maxima) for Br-rich $\text{Cs}_2\text{SnBr}_{4.5}\text{I}_{1.5}$ as follows: SnBr_6 (−1962 ppm), SnBr_5I (−2434 ppm), SnBr_4I_2 (−2842 ppm), and $\text{SnBr}_4\text{I}_2/\text{SnBr}_3\text{I}_3$ (−3378 ppm) (Figure 6.7c).

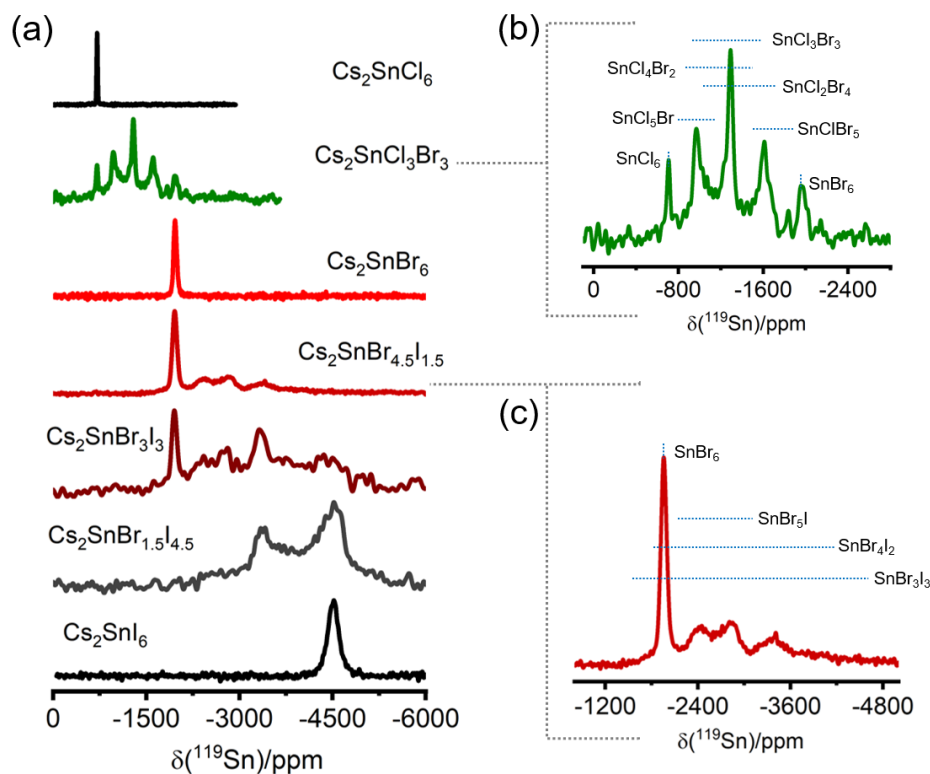


Figure 6.7. Solid-state ^{119}Sn (non-spinning, $B_0 = 7.05$ T) NMR spectra of (a) ball-milled $\text{Cs}_2\text{SnCl}_x\text{Br}_{6-x}$ and $\text{Cs}_2\text{SnBr}_x\text{I}_{6-x}$ and solvent-synthesized Cs_2SnCl_6 , (b) $\text{Cs}_2\text{SnCl}_3\text{Br}_3$, and (c) $\text{Cs}_2\text{SnBr}_{4.5}\text{I}_{1.5}$. The local $\text{SnCl}_n\text{Br}_{6-n}$ and $\text{SnBr}_n\text{I}_{6-n}$ environments are tentatively assigned in (b,c) from the DFT computations. The blue dotted lines represent the tentative chemical shift ranges for the $\text{SnCl}_n\text{Br}_{6-n}$ octahedra according to the DFT computed results; positional isomers (cis/trans or fac/mer) are not shown for clarity.

6.2.5 Influence of Synthesis Routes on the Local Structure of Cs₂SnI₆

A feature of photovoltaic perovskites is that they can be synthesized by various avenues, with or without solvents; however, the local chemical structure resulting from these approaches is poorly understood. Thus, to elucidate the structure, solid-state ¹³³Cs and ¹¹⁹Sn NMR spectroscopy was performed for three Cs₂SnI₆ samples prepared by three different preparation techniques, namely, the solvent-free ball-milling and hand-grinding routes and solvent-based synthesis.

The ¹³³Cs NMR spectra of these three Cs₂SnI₆ samples show resonances in the same spectral positions with nearly identical linewidths (Figure 6.9a). However, the slight asymmetry of the underlying ¹³³Cs resonance for the ball-milled sample corresponds to a higher local structural disorder as compared to solvent-synthesized and hand-ground samples. The ¹¹⁹Sn NMR spectra for all three Cs₂SnI₆ samples show symmetric resonances with different chemical shifts and linewidths (Figure 6.9b). The solvent-synthesized and hand-ground samples exhibit sharper resonances at -4535 ppm (fwhm = 17 kHz) and -4527 ppm (fwhm = 17 kHz), respectively, whereas, the ball-milled sample shows a broad resonance at -4505 ppm (fwhm = 20 kHz). The sharper ¹¹⁹Sn resonance indicates that the solvent-synthesized sample has a more ordered structure with minimum defects, whereas the broader ¹¹⁹Sn resonance indicates the presence of the higher defect concentration in the ball-milled sample. Ball-milling is a high-energy grinding technique that causes grinding-induced defects as compared to the low-energy manual hand-grinding route. The ¹¹⁹Sn spin-lattice relaxation depends significantly on the synthesis routes with $T_1 = 0.01$ s for the ball-milled sample, which is an order of magnitude less than that of the solvent-synthesized counterpart. The faster relaxation process for the ball-milled sample suggests higher local structural disorder and defects, which is consistent with the conclusion based on ¹¹⁹Sn NMR linewidths.^{17,100,101}

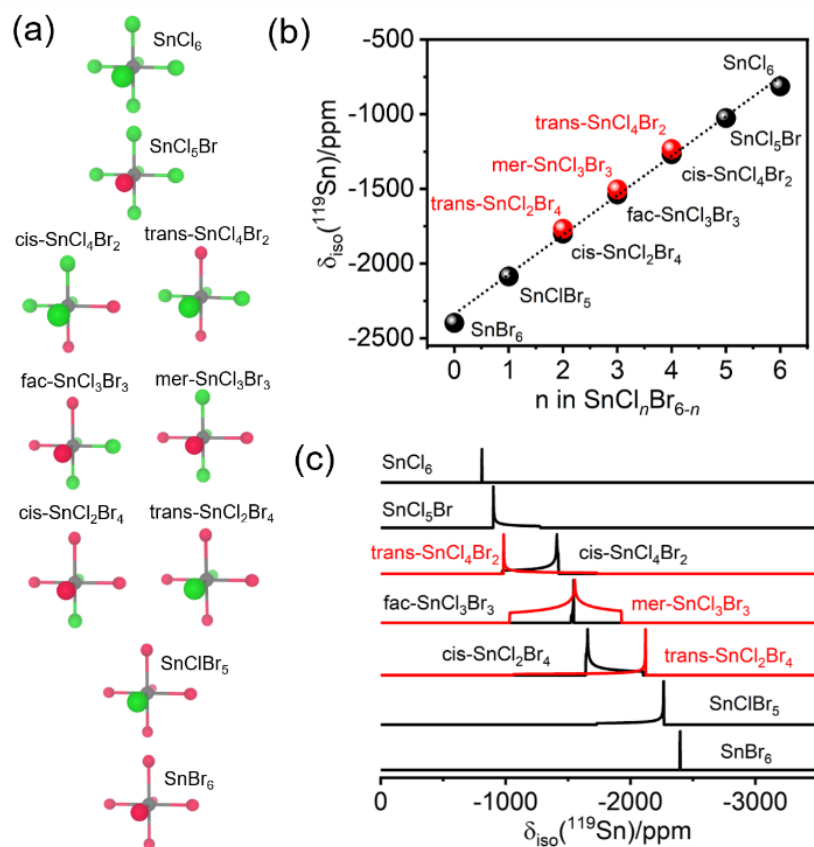


Figure 6.8. DFT-computed results for $\text{SnCl}_n\text{Br}_{6-n}$: (a) optimized geometries, (b) ^{119}Sn isotropic chemical shift as a function of number of Cl, and (c) simulated ^{119}Sn NMR spectra.

The higher structural disorder is also reflected in broader peaks in powder XRD patterns for the ball-milled sample as compared to the structurally well-ordered solvent-synthesized sample (Figure E22). The different degrees of crystallinity in Cs_2SnI_6 samples are also reflected in the optical absorption properties, where a tailing is observed in the optical absorption edge for the mechanochemically prepared Cs_2SnI_6 samples as compared to that for the solvent-synthesized counterpart (Figure E23). The optical absorption edge tailing in mechanochemically synthesized Cs_2SnI_6 samples suggest the presence of a higher structural disorder or defect concentration consistent with the observation of broader linewidths in the solid-state ^{119}Sn and ^{133}Cs NMR results.

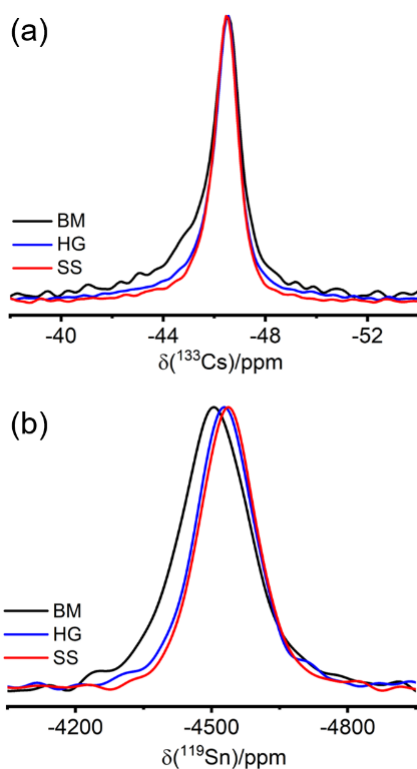


Figure 6.9. Solid-state (a) ^{133}Cs ($\nu_r = 5$ kHz, $B_0 = 11.75$ T) and (b) ^{119}Sn (non-spinning, $B_0 = 7.05$ T) NMR spectra of Cs_2SnI_6 samples prepared by solvent-synthesis (SS), hand-grinding (HG), and ball-milling (BM) routes.

6.3 Conclusions

The macro- to microscopic structures and bulk photophysical properties of Cs_2SnX_6 ($X = \text{Cl}, \text{Br}, \text{and I}$) parent perovskites prepared by the solvent synthesis route were evaluated using powder XRD and multinuclear magnetic resonance spectroscopy. Sn-119 NMR spectroscopy revealed a massive chemical shift range spanning ca. 4000 ppm that, according to DFT computations, is dominated by a large spin-orbit component. Likewise, the ^{119}Sn spin-lattice relaxation times change by 3 orders of magnitude for these materials as the halide anion increases in size. The ^{35}Cl quadrupole coupling constant for Cs_2SnCl_6 is nearly double that for the hybrid and non-hybrid lead(II) chloride perovskites, APbCl_3 , consistent with Cl bound to Sn in a +4 oxidation

state. The rapid octahedral dynamics of SnI₆ units in Cs₂SnI₆ are remarkable for the polyhedral motion in these stable “static” solids.

The complete Cs₂SnCl_xBr_{6-x} and Cs₂SnBr_xI_{6-x} ($0 \leq x \leq 6$) solid-solution mixed-halide series exhibit attractive optical bandgaps spanning approximately 3 eV, which were successfully prepared by a solvent-free ball-milling synthesis route at room temperature. According to solid-state ¹³³Cs and ¹¹⁹Sn NMR spectroscopy, the mixed-halide analogues undergo a complete random distribution of Cl/Br or Br/I halogens at the atomic level, with no evidence of the halogen-rich phase segregation or domains under dark conditions. Furthermore, the broad ¹¹⁹Sn NMR resonances observed in mixed-halide samples, supported by magnetic shielding parameters obtained by DFT, assisted in assigning the unique Sn chemical environments, reinforcing the complex nature one must contend with due to considerable shielding anisotropy.

The bulk optical bandgap properties for the Cs₂SnI₆ samples prepared by solvent-free and solvent-based synthesis routes are sensitive to local structural changes, as confirmed by NMR. For example, materials prepared by high-energy ball-milling tend to show a lower degree of crystallinity (i.e., higher local structural disorder), resulting in faster ¹¹⁹Sn relaxation and a slight increase in the bandgap (0.14 eV) compared to those for the solvent-synthesized counterpart. Overall, solid-state NMR spectroscopy, alongside powder XRD and DFT, bestows an unprecedented ability to unravel the complex chemical structure and dynamics present within A₂BX₆ materials, whereby random halogen arrangements and defects govern the optical bandgaps.

In conclusion, these results have shown a unique optical bandgap tailorability of a lead-free alternative for perovskite-based materials used for photovoltaic and optoelectronic applications. This work has also demonstrated multiple synthesis routes to prepare the low bandgap Cs₂SnI₆ material with and without the use of solvents; however, their optical properties rely heavily on the nature of the local chemical structure (concentration of defects) in the final synthesized products.

6.4 Experimental Section

All starting precursors and solvents were purchased from commercial sources and used directly without further purification: CsCl (Terochem Laboratories Ltd., 99.7%), CsBr

(Sigma, 99%), CsI (Sigma, 99.9%), anhydrous SnCl₄ (Sigma, 98%), SnBr₄ (Alfa Aesar, 99%), SnI₄ (Alfa Aesar, 95%), HCl (Caledon Laboratory Chemicals), HBr (Anachemia, 48%), and acetonitrile (Sigma, 99.5%).

6.4.1 Synthesis

Solvent Synthesis of Cs₂SnX₆ (X = Cl, Br, and I): Cs₂SnCl₆ and Cs₂SnBr₆

The starting materials, SnX₄ (1 mmol) and CsX (2 mmol) (X = Cl, Br) were weighed, taken in a clean vial, and 5 mL of concentrated HX (aq) was added to the mixture. The solution mixture was heated using a hot plate set to 120 °C and stirred at 300 rpm continuously for 1 h using a magnetic stir bar. The solution was cooled to room temperature over a period of 2 h. The precipitates were filtered by vacuum filtration using a Buchner funnel, followed by washing with 95% ethanol, and allowed to dry overnight. The samples were stored in clean sealed vials under ambient conditions for further use. Cs₂SnI₆ was synthesized following a previous report with some modification.¹⁰² SnI₄ (0.25 mmol) and CsI (0.5 mmol) starting precursors were weighed and taken in a molar ratio of 1:2 in a clean vial and 2 mL of the acetonitrile solvent was added to the mixture. The solution mixture was stirred using a magnetic stir bar for 3 h until a homogeneous mixture was obtained. Then, the solvent was boiled off by heating the vial over a hotplate set to 80 °C. The remaining black powder was stored in a sealed vial under ambient conditions until needed.

Mechanochemical Synthesis of Cs₂SnX_xX_{6-x}' (X, X' = Cl/Br, Br, and Br/I, I): Ball-Mill Synthesis

The starting materials to prepare the Cs₂SnCl_xBr_{6-x} ($x = 3$) and Cs₂SnBr_xI_{6-x} ($x = 0, 1.5, 3, 4.5, \text{ and } 6$) samples were first ground using an agate mortar and pestle for 5–10 min. The mixture was then transferred to a 50 mL zirconia grinding vessel, containing ca. 50 g of zirconia balls (3–8 mm diameter) and sealed under ambient conditions. The sample was ground in an electric planetary ball-mill instrument (Changsha Deco-PBM-V-0.4L) at a rotation frequency of 550 rpm for 0.5 h. The inner wall of the vessel was scraped by using a clean spatula and sealed again. This process was repeated to achieve a total 1.5 or 3 h of grinding time.

The Cs_2SnBr_6 and Cs_2SnI_6 parents were prepared by ball-milling from solid CsX and SnX_4 ($X = \text{Br}$ and I) binary precursor salts; however, Cs_2SnCl_6 was prepared only by the solvent-assisted synthesis route to avoid the handling of SnCl_4 , which is a hygroscopic liquid. We note that an excess SnBr_4 may be required for the ball-milling preparation to obtain phase-pure Cs_2SnBr_6 (Figure E10) due to the compound's physical properties, a low melting point (31 °C) and a hygroscopic nature, whereas phase-pure Cs_2SnI_6 can easily be obtained by ball-milling with proper starting precursor compositions ($\text{CsI}/\text{SnI}_4 = 2:1$) due to SnI_4 's considerably higher melting point of 144 °C. Therefore, to avoid the direct use of SnCl_4 and SnBr_4 as starting precursors under our ambient condition ball-milling preparations, $\text{Cs}_2\text{SnCl}_3\text{Br}_3$ ($x = 3$) mixed halides were synthesized from the Cs_2SnCl_6 and Cs_2SnBr_6 parents, while $\text{Cs}_2\text{SnBr}_x\text{I}_{6-x}$ ($x = 1.5, 3.0, \text{ and } 4.5$) mixed halides were obtained from the appropriate molar ratios of Cs_2SnBr_6 , CsI , and SnI_4 (Table E2). On the other hand, the grinding time is a crucial parameter in the ball-milling process. The phase-pure product of the Cs_2SnBr_6 and Cs_2SnI_6 parents was obtained in 1.5 h, whereas the $\text{Cs}_2\text{SnCl}_x\text{Br}_{6-x}$ and $\text{Cs}_2\text{SnBr}_x\text{I}_{6-x}$ mixed-halide analogues required grinding times of 3 h under the same experimental conditions (Figure E11). The quantities of the starting materials and grinding times are summarized in Table E5. Hand-ground synthesis of Cs_2SnI_6 : a mixture of 2 mmol of CsI and 1 mmol of SnI_4 were hand ground using an agate mortar and pestle for up to 6 h until phase-pure Cs_2SnI_6 was obtained. We note that the targeted phase-pure Cs_2SnI_6 sample was not obtained after 4 h of grinding time as confirmed by powder XRD (Figure E9).

Powder XRD

Powder XRD patterns were collected on a Rigaku Ultima IV powder diffractometer equipped with a Co K_α ($K_{\alpha 1} = 1.78900 \text{ \AA}$ and $K_{\alpha 2} = 1.79283 \text{ \AA}$) radiation source at 38 kV and 38 mA, and a D/Tex Ultra detector with an Fe filter to eliminate the K_β (= 1.62083 Å) radiation. All the samples were loaded on zero background plates, and the data were collected in the continuous scan mode between 5 and 90° in a 2θ angle with a step size of 0.0200°. All the data presented in the main text were converted to a Cu K_α ($K_{\alpha 1} = 1.54056 \text{ \AA}$ and $K_{\alpha 2} = 1.54439 \text{ \AA}$) source. The profile fitting of the powder

XRD data was performed using FullProf suite software, and the unit cell parameters were refined.

Some complementary powder XRD patterns (Figure E9) were collected on an Inel multipurpose diffractometer equipped with a Cu K_{α} (= 1.540596 Å) radiation source at 40 kV and 50 mA, and a CPS 120 detector.

EDS and FESEM

The samples were examined on a Zeiss Sigma 300 VP field-emission scanning electron microscope instrument equipped with dual silicon drift detectors for EDS to determine chemical compositions.

Diffuse Reflectance Spectroscopy

The diffuse reflectance spectra for all the samples were collected using a Cary 5000 UV–vis–NIR spectrophotometer in the 2000–200 nm wavelength range and calibrated using a Spectralon (>99%) reflectance standard. The diffuse reflectance data were converted to pseudo-absorbance spectra using the Kubelka–Munk transformation¹⁰³ through: $\alpha \sim (1 - R)^2/(2R)$, where R = absolute reflectance and α = pseudo-absorbance. Direct bandgaps were determined from the Tauc plot upon the extrapolation of the intercept value in a $(ah\nu)^2$ versus $E(\text{eV})$ plot.

6.4.2 Solid-State NMR Spectroscopy

Cesium-133 NMR Spectroscopy

Solid-state ^{133}Cs NMR spectroscopy was performed at 295 K on a Bruker AVANCE NEO 500 spectrometer ($B_0 = 11.75$ T) under MAS conditions using a 4 mm H/X MAS Bruker probe ($\omega_0/2\pi(^{133}\text{Cs}) = 65.6$ MHz). The samples were packed into 4 mm (outer diameter) zirconia rotors with Kel-F caps. All ^{133}Cs NMR data were acquired using a 1.38 μs short tip angle ($\pi/8$) Bloch decay pulse sequence with an optimized recycle delay. Detailed experimental parameters for ^{133}Cs NMR measurements are shown in Table E9a,c,e. All the ^{133}Cs NMR spectra were referenced with a 0.1 M CsNO_3 (aq) solution at $\delta(^{133}\text{Cs}) = 0.00$ ppm.

Tin-119 NMR Spectroscopy

Solid-state ^{119}Sn NMR measurements were performed at $B_0 = 7.05$ and 11.75 T on Bruker AVANCE NEO 300 and 500 NMR spectrometers, respectively, under both

MAS and non-spinning sample conditions using 4 mm H/X MAS Bruker probes. All the samples were packed into 4 mm (outer diameter) zirconia rotors with Kel-F caps. The ^{119}Sn NMR spectra were acquired using either a $4.0\ \mu\text{s}\ \pi/2$ ($\gamma B_1/2\pi = 62.5\ \text{kHz}$) or a $1.7\ \mu\text{s}\ \pi/2$ ($\gamma B_1/2\pi = 147.1\ \text{kHz}$) Hahn-echo pulse sequence $[(\pi/2)_x - \tau_1 - (\pi)_y - \tau_2 - \text{ACQ}]$, where τ represents the inter-pulse and refocusing delays], with an optimized recycle delay. The detailed experimental parameters for ^{119}Sn NMR measurements are presented in Table E9b,d,f.

Variable-temperature ($200 < T(\text{K}) < 400$) ^{119}Sn NMR measurements were performed on a Bruker AVANCE NEO 500 NMR spectrometer ($B_0 = 11.75\ \text{T}$) using a 4 mm H/X MAS double resonance probe under non-spinning sample conditions. The sample was packed into a 4 mm (outer diameter) zirconia rotor with a Vespel cap. Temperatures were controlled using a Bruker VT unit. The sample temperature was calibrated using the ^{207}Pb chemical shifts of the $\text{CH}_3\text{NH}_3\text{PbCl}_3$ powder.¹⁰⁴

The ^{119}Sn spin-lattice relaxation time (T_1) was measured using an inversion recovery pulse sequence $(\pi - \tau_D - \pi/2 - \text{ACQ}$ or $\pi - \tau_D - \pi/2 - \tau - \pi/2 - \text{ACQ}$, where τ_D and τ are the variable delay and echo delay, respectively). All the ^{119}Sn T_1 values were calculated by fitting the peak intensity values using a mono-exponential decay function: $I_t = I_\infty + Ae^{-t/T_1}$, where I_t and I_∞ are the NMR signal intensities measured at time t and at infinity, respectively, and A is the pre-exponential constant.

All ^{119}Sn NMR spectra were referenced by setting the isotropic peak of tetracyclohexyl-tin(IV) powder to $\delta(^{119}\text{Sn}) = -97.35\ \text{ppm}$, a secondary reference with respect to $\text{Sn}(\text{CH}_3)_4$ at $\delta(^{119}\text{Sn}) = 0.00\ \text{ppm}$.

Chlorine-35 NMR Spectroscopy

Solid-state ^{35}Cl NMR measurements for Cs_2SnCl_6 were performed at 295 K on a Bruker AVANCE NEO 500 spectrometer ($B_0 = 11.75\ \text{T}$) under non-spinning sample conditions using a 4 mm H/X MAS Bruker probe ($\omega_0/2\pi(^{35}\text{Cl}) = 47\text{--}50\ \text{MHz}$). A powdered sample was packed into a 4 mm (outer diameter) zirconia rotor fitted with a Kel-F cap. The ^{35}Cl NMR spectra were acquired using a frequency-stepped WURST-CPMG pulse sequence^{79,80} ($50\ \mu\text{s}$ pulse width, 512 scans, 50 echoes, and 5 kHz spikelet spacing), and the overall spectra were constructed by taking the skyline projection of

12 sub-spectra (Figure E7). ^{35}Cl NMR spectra were referenced by setting the peak for 0.1 M NaCl (aq) to $\delta(^{35}\text{Cl}) = 0.00$ ppm.

DFT Computations

The structures and properties of the $\text{SnCl}_n\text{Br}_{6-n}$ and $\text{SnBr}_n\text{I}_{6-n}$ ($n = 0-6$) environments were obtained using DFT and carried out using ADF.¹⁰⁵⁻¹⁰⁷ The geometries were optimized using the PBE0 exchange–correlation functional¹⁰⁸ with the TZ2P basis sets,¹⁰⁹ chosen to avoid the convergence issues and the computational cost of larger basis sets. The gradient convergence criterion for the geometry optimizations was set to 1.0×10^{-7} . Optimizations were done at the relativistic scalar ZORA level of theory.^{110,111} Sn shielding tensor components were obtained using the PBE0 functional and TZ2P basis set. Shielding tensors for Sn in $\text{SnCl}_n\text{Br}_{6-n}$ and $\text{SnBr}_n\text{I}_{6-n}$ ($n = 0-6$) octahedral clusters were calculated using the FXC parameter¹¹² (unless otherwise specified) at the relativistic spin-orbit ZORA level of theory.¹¹³ The ^{119}Sn NMR spectra were simulated using the WSolids1 NMR simulation package (WSolids1, Version: 1.21.3, 2015, K. Eichele, Universität Tübingen).

6.5 References

- (1) Zhao, Y.; Zhu, K. Organic-Inorganic Hybrid Lead Halide Perovskites for Optoelectronic and Electronic Applications. *Chem. Soc. Rev.* **2016**, *45*, 655–689.
- (2) Miao, Y.; Ke, Y.; Wang, N.; Zou, W.; Xu, M.; Cao, Y.; Sun, Y.; Yang, R.; Wang, Y.; Tong, Y.; Xu, W.; Zhang, L.; Li, R.; Li, J.; He, H.; Jin, Y.; Gao, F.; Huang, W.; Wang, J. Stable and Bright Formamidinium-Based Perovskite Light-Emitting Diodes with High Energy Conversion Efficiency. *Nat. Commun.* **2019**, *10*, 3624.
- (3) Wei, H.; Huang, J. Halide Lead Perovskites for Ionizing Radiation Detection. *Nat. Commun.* **2019**, *10*, 1066.
- (4) Chen, K.; Deng, X.; Dodekatos, G.; Tüysüz, H. Photocatalytic Polymerization of 3,4-Ethylenedioxythiophene over Cesium Lead Iodide Perovskite Quantum Dots. *J. Am. Chem. Soc.* **2017**, *139*, 12267–12273.
- (5) Babu, R.; Giribabu, L.; Singh, S. P. Recent Advances in Halide-Based Perovskite Crystals and Their Optoelectronic Applications. *Cryst. Growth Des.* **2018**, *18*, 2645–2664.

- (6) Kovalenko, M. V.; Protesescu, L.; Bodnarchuk, M. I. Properties and Potential Optoelectronic Applications of Lead Halide Perovskite Nanocrystals. *Science* **2017**, *750*, 745–750.
- (7) National Renewable Energy Laboratory (NREL). Best Research-Cell Efficiency Chart.
<https://www.nrel.gov/pv/assets/pdfs/best-research-cell-efficiencies.20200104.pdf>
(accessed March 2021).
- (8) Berhe, T. A.; Su, W. N.; Chen, C. H.; Pan, C. J.; Cheng, J. H.; Chen, H. M.; Tsai, M. C.; Chen, L. Y.; Dubale, A. A.; Hwang, B. J. Organometal Halide Perovskite Solar Cells: Degradation and Stability. *Energy Environ. Sci.* **2016**, *9*, 323–356.
- (9) Yang, J.; Siempelkamp, B. D.; Liu, D.; Kelly, T. L. Investigation of CH₃NH₃PbI₃ degradation Rates and Mechanisms in Controlled Humidity Environments Using in Situ Techniques. *ACS Nano* **2015**, *9*, 1955–1963.
- (10) Domanski, K.; Alharbi, E. A.; Hagfeldt, A.; Grätzel, M.; Tress, W. Systematic Investigation of the Impact of Operation Conditions on the Degradation Behaviour of Perovskite Solar Cells. *Nat. Energy* **2018**, *3*, 61–67.
- (11) Askar, A. M.; Bernard, G. M.; Wiltshire, B.; Shankar, K.; Michaelis, V. K. Multinuclear Magnetic Resonance Tracking of Hydro, Thermal, and Hydrothermal Decomposition of CH₃NH₃PbI₃. *J. Phys. Chem. C* **2017**, *121*, 1013–1024.
- (12) Li, J.; Cao, H.; Jiao, W.; Wang, Q.; Wei, M.; Cantone, I.; Lü, J.; Abate, A. Biological Impact of Lead from Halide Perovskites Reveals the Risk of Introducing a Safe Threshold. *Nat. Commun.* **2020**, *11*, 310.
- (13) Babayigit, A.; Ethirajan, A.; Muller, M.; Conings, B. Toxicity of Organometal Halide Perovskite Solar Cells. *Nat. Mater.* **2016**, *15*, 247–251.
- (14) Kamarudin, M. A.; Hirotani, D.; Wang, Z.; Hamada, K.; Nishimura, K.; Shen, Q.; Toyoda, T.; Iikubo, S.; Minemoto, T.; Yoshino, K.; Hayase, S. Suppression of Charge Carrier Recombination in Lead-Free Tin Halide Perovskite via Lewis Base Post-Treatment. *J. Phys. Chem. Lett.* **2019**, *10*, 5277–5283.
- (15) Song, T. Bin; Yokoyama, T.; Stoumpos, C. C.; Logsdon, J.; Cao, D. H.; Wasielewski, M. R.; Aramaki, S.; Kanatzidis, M. G. Importance of Reducing Vapor

Atmosphere in the Fabrication of Tin-Based Perovskite Solar Cells. *J. Am. Chem. Soc.* **2017**, *139*, 836–842.

(16) Kubicki, D. J.; Prochowicz, D.; Salager, E.; Rakhmatullin, A.; Grey, C. P.; Emsley, L.; Stranks, S. D. Local Structure and Dynamics in Methylammonium, Formamidinium and Cesium Tin(II) Mixed-halide Perovskites from ^{119}Sn Solid-state NMR. *J. Am. Chem. Soc.* **2020**, *142*, 7813–7826.

(17) Karmakar, A.; Bhattacharya, A.; Sarkar, D.; Bernard, G. M.; Mar, A.; Michaelis, V. K. Influence of Hidden Halogen Mobility on Local Structure of $\text{CsSn}(\text{Cl}_{1-x}\text{Br}_x)_3$ Mixed-Halide Perovskites by Solid-State NMR. *Chem. Sci.* **2021**, *12*, 3253–3263.

(18) Maughan, A. E.; Ganose, A. M.; Scanlon, D. O.; Neilson, J. R. Perspectives and Design Principles of Vacancy-Ordered Double Perovskite Halide Semiconductors. *Chem. Mater.* **2019**, *31*, 1184–1195.

(19) Brik, M. G.; Kityk, I. V. Modeling of Lattice Constant and Their Relations with Ionic Radii and Electronegativity of Constituting Ions of A_2XY_6 Cubic Crystals ($\text{A} = \text{K}, \text{Cs}, \text{Rb}, \text{Tl}$; $\text{X} = \text{tetraivalent Cation}$, $\text{Y} = \text{F}, \text{Cl}, \text{Br}, \text{I}$). *J. Phys. Chem. Solids* **2011**, *72*, 1256–1260.

(20) Saparov, B.; Sun, J. P.; Meng, W.; Xiao, Z.; Duan, H. S.; Gunawan, O.; Shin, D.; Hill, I. G.; Yan, Y.; Mitzi, D. B. Thin-Film Deposition and Characterization of a Sn-Deficient Perovskite Derivative Cs_2SnI_6 . *Chem. Mater.* **2016**, *28*, 2315–2322.

(21) Maughan, A. E.; Ganose, A. M.; Bordelon, M. M.; Miller, E. M.; Scanlon, D. O.; Neilson, J. R. Defect Tolerance to Intolerance in the Vacancy-Ordered Double Perovskite Semiconductors Cs_2SnI_6 and Cs_2TeI_6 . *J. Am. Chem. Soc.* **2016**, *138*, 8453–8464.

(22) Lee, B.; Stoumpos, C. C.; Zhou, N.; Hao, F.; Malliakas, C.; Yeh, C. Y.; Marks, T. J.; Kanatzidis, M. G.; Chang, R. P. H. Air-Stable Molecular Semiconducting Iodosalts for Solar Cell Applications: Cs_2SnI_6 as a Hole Conductor. *J. Am. Chem. Soc.* **2014**, *136*, 15379–15385.

(23) Lee, B.; Krenselewski, A.; Baik, S. Il; Seidman, D. N.; Chang, R. P. H. Solution Processing of Air-Stable Molecular Semiconducting Iodosalts, $\text{Cs}_2\text{SnI}_{6-x}\text{Br}_x$, for Potential Solar Cell Applications. *Sustain. Energy Fuels* **2017**, *1*, 710–724.

- (24) Kaltzoglou, A.; Antoniadou, M.; Perganti, D.; Siranidi, E.; Raptis, V.; Trohidou, K.; Psycharis, V.; Kontos, A. G.; Falaras, P. Mixed-Halide Cs₂SnI₃Br₃ Perovskite as Low Resistance Hole-Transporting Material in Dye-Sensitized Solar Cells. *Electrochim. Acta* **2015**, *184*, 466–474.
- (25) Wang, A.; Yan, X.; Zhang, M.; Sun, S.; Yang, M.; Shen, W.; Pan, X.; Wang, P.; Deng, Z. Controlled Synthesis of Lead-Free and Stable Perovskite Derivative Cs₂SnI₆ Nanocrystals via a Facile Hot-Injection Process. *Chem. Mater.* **2016**, *28*, 8132–8140.
- (26) Lim, S. C.; Lin, H. P.; Tsai, W. L.; Lin, H. W.; Hsu, Y. T.; Tuan, H. Y. Binary Halide, Ternary Perovskite-like, and Perovskite-Derivative Nanostructures: Hot Injection Synthesis and Optical and Photocatalytic Properties. *Nanoscale* **2017**, *9*, 3747–3751.
- (27) Veronese, A.; Patrini, M.; Bajoni, D.; Ciarrocchi, C.; Quadrelli, P.; Malavasi, L. Highly Tunable Emission by Halide Engineering in Lead-Free Perovskite-Derivative Nanocrystals: The Cs₂SnX₆ (X = Cl, Br, Br/I, I) System. *Front. Chem.* **2020**, *8*, 1–9.
- (28) Tan, Z.; Li, J.; Zhang, C.; Li, Z.; Hu, Q.; Xiao, Z.; Kamiya, T.; Hosono, H.; Niu, G.; Lifshitz, E.; Cheng, Y.; Tang, J. Highly Efficient Blue-Emitting Bi-Doped Cs₂SnCl₆ Perovskite Variant: Photoluminescence Induced by Impurity Doping. *Adv. Funct. Mater.* **2018**, *28*, 1801131.
- (29) Jing, Y.; Liu, Y.; Zhao, J.; Xia, Z. Sb³⁺ Doping-Induced Triplet Self-Trapped Excitons Emission in Lead-Free Cs₂SnCl₆ Nanocrystals. *J. Phys. Chem. Lett.* **2019**, *10*, 7439–7444.
- (30) Arfin, H.; Kshirsagar, A. S.; Kaur, J.; Mondal, B.; Xia, Z.; Chakraborty, S.; Nag, A. ns² Electron (Bi³⁺ and Sb³⁺) Doping in Lead-Free Metal Halide Perovskite Derivatives. *Chem. Mater.* **2020**, *32*, 10255–10267.
- (31) Wasylshen, R. E.; Knop, O.; Macdonald, J. B. Cation Rotation in Methylammonium Lead Halides. *Solid State Commun.* **1985**, *56*, 581–582.
- (32) Kubicki, D. J.; Prochowicz, D.; Hofstetter, A.; Zakeeruddin, S. M.; Grätzel, M.; Emsley, L. Phase Segregation in Potassium-Doped Lead Halide Perovskites from ³⁹K Solid-State NMR at 21.1 T. *J. Am. Chem. Soc.* **2018**, *140*, 7232–7238.

- (33) Kubicki, D. J.; Prochowicz, D.; Hofstetter, A.; Péchy, P.; Zakeeruddin, S. M.; Grätzel, M.; Emsley, L. Cation Dynamics in Mixed-Cation (MA)_x(FA)_{1-x}PbI₃ Hybrid Perovskites from Solid-State NMR. *J. Am. Chem. Soc.* **2017**, *139*, 10055–10061.
- (34) Kubicki, D. J.; Prochowicz, D.; Hofstetter, A.; Sasaki, M.; Yadav, P.; Bi, D.; Pellet, N.; Lewiński, J.; Zakeeruddin, S. M.; Grätzel, M.; Emsley, L. Formation of Stable Mixed Guanidinium-Methylammonium Phases with Exceptionally Long Carrier Lifetimes for High-Efficiency Lead Iodide-Based Perovskite Photovoltaics. *J. Am. Chem. Soc.* **2018**, *140*, 3345–3351.
- (35) Bernard, G. M.; Wasylshen, R. E.; Ratcliffe, C. I.; Terskikh, V.; Wu, Q.; Buriak, J. M.; Hauger, T. Methylammonium Cation Dynamics in Methylammonium Lead Halide Perovskites: A Solid-State NMR Perspective. *J. Phys. Chem. A* **2018**, *122*, 1560–1573.
- (36) Karmakar, A.; Dodd, M. S.; Zhang, X.; Oakley, M. S.; Klobukowski, M.; Michaelis, V. K. Mechanochemical Synthesis of 0D and 3D Cesium Lead Mixed Halide Perovskites. *Chem. Commun.* **2019**, *55*, 5079–5082.
- (37) Askar, A. M.; Karmakar, A.; Bernard, G. M.; Ha, M.; Terskikh, V. V.; Wiltshire, B. D.; Patel, S.; Fleet, J.; Shankar, K.; Michaelis, V. K. Composition-Tunable Formamidinium Lead Mixed Halide Perovskites via Solvent-Free Mechanochemical Synthesis: Decoding the Pb Environments Using Solid-State NMR Spectroscopy. *J. Phys. Chem. Lett.* **2018**, *9*, 2671–2677.
- (38) Karmakar, A.; Askar, A. M.; Bernard, G. M.; Terskikh, V. V.; Ha, M.; Patel, S.; Shankar, K.; Michaelis, V. K. Mechanochemical Synthesis of Methylammonium Lead Mixed-Halide Perovskites: Unraveling the Solid-Solution Behavior Using Solid-State NMR. *Chem. Mater.* **2018**, *30*, 2309–2321.
- (39) Kubicki, D. J.; Prochowicz, D.; Hofstetter, A.; Walder, B. J.; Emsley, L. ¹¹³Cd Solid-State NMR at 21.1 T Reveals the Local Structure and Passivation Mechanism of Cadmium in Hybrid and All-Inorganic Halide Perovskites. *ACS Energy Lett.* **2020**, *5*, 2964–2971.
- (40) Rosales, B. A.; Men, L.; Cady, S. D.; Hanrahan, M. P.; Rossini, A. J.; Vela, J. Persistent Dopants and Phase Segregation in Organolead Mixed-Halide Perovskites. *Chem. Mater.* **2016**, *28*, 6848–6859.

- (41) Rosales, B. A.; Hanrahan, M. P.; Boote, B. W.; Rossini, A. J.; Smith, E. A.; Vela, J. Lead Halide Perovskites: Challenges and Opportunities in Advanced Synthesis and Spectroscopy. *ACS Energy Lett.* **2017**, *2*, 906–914.
- (42) Chen, Y.; Smock, S. R.; Flintgruber, A. H.; Perras, F. A.; Brutchey, R. L.; Rossini, A. J. Surface Termination of CsPbBr₃ Perovskite Quantum Dots Determined by Solid-State NMR Spectroscopy. *J. Am. Chem. Soc.* **2020**, *142*, 6117–6127.
- (43) Franssen, W. M. J.; Kentgens, A. P. M. Solid-State NMR of Hybrid Halide Perovskites. *Solid State Nucl. Magn. Reson.* **2019**, *100*, 36–44.
- (44) Wouter M. J. Franssen; Es, S. G. D. van; Dervişoğlu, R.; Wijs, G. A. de; Kentgens, A. P. M. Symmetry, Dynamics, and Defects in Methylammonium Lead Halide Perovskites. *J. Phys. Chem. Lett.* **2017**, *8*, 61–66.
- (45) Senocrate, A.; Moudrakovski, I.; Kim, G. Y.; Yang, T.; Gregori, G.; Grätzel, M.; Maier, J. The Nature of Ion Conduction in Methylammonium Lead Iodide: A Multimethod Approach. *Angew. Chem. Int. Ed.* **2017**, *56*, 7755–7759.
- (46) Senocrate, A.; Moudrakovski, I.; Acartuerk, T.; Merkle, R.; Kim, G. Y.; Starke, U.; Grätzel, M.; Maier, J. Slow CH₃NH₃⁺ Diffusion in CH₃NH₃PbI₃ Under Light Measured by Solid-State NMR and Tracer Diffusion. *J. Phys. Chem. C* **2018**, *122*, 21803–21806.
- (47) Prochowicz, D.; Yadav, P.; Saliba, M.; Kubicki, D. J.; Tavakoli, M. M.; Zakeeruddin, S. M.; Lewiński, J.; Emsley, L.; Grätzel, M. One-Step Mechanochemical Incorporation of an Insoluble Cesium Additive for High Performance Planar Heterojunction Solar Cells. *Nano Energy* **2018**, *49*, 523–528.
- (48) Harris, R. K.; Becker, E. D. NMR Nomenclature: Nuclear Spin Properties and Conventions for Chemical Shifts—IUPAC Recommendations. *J. Magn. Reson.* **2002**, *156*, 323–326.
- (49) Karmakar, A.; Bernard, G. M.; Meldrum, A.; Oliynyk, A. O.; Michaelis, V. K. Tailorable Indirect to Direct Bandgap Double Perovskites with Bright White-Light Emission: Decoding Chemical Structure Using Solid-State NMR. *J. Am. Chem. Soc.* **2020**, *142*, 10780–10793.

- (50) Karmakar, A.; Dodd, M. S.; Agnihotri, S.; Ravera, E.; Michaelis, V. K. Cu(II)-Doped Cs₂SbAgCl₆ Double Perovskite: A Lead-Free, Low-Bandgap Material. *Chem. Mater.* **2018**, *30*, 8280–8290.
- (51) Kubicki, D. J.; Prochowicz, D.; Pinon, A.; Stevanato, G.; Hofstetter, A.; Zakeeruddin, S. M.; Grätzel, M.; Emsley, L. Doping and Phase Segregation in Mn²⁺ - and Co²⁺ -Doped Lead Halide Perovskites from ¹³³Cs and ¹H NMR Relaxation Enhancement. *J. Mater. Chem. A* **2019**, *7*, 2326–2333.
- (52) Kubicki, D. J.; Prochowicz, D.; Hofstetter, A.; Zakeeruddin, S. M.; Grätzel, M.; Emsley, L. Phase Segregation in Cs-, Rb- and K-Doped Mixed-Cation (MA)_x(FA)_{1-x}PbI₃ Hybrid Perovskites from Solid-State NMR. *J. Am. Chem. Soc.* **2017**, *139*, 14173–14180.
- (53) Wolf, P.; Valla, M.; Núñez-Zarur, F.; Comas-Vives, A.; Rossini, A. J.; Firth, C.; Kallas, H.; Lesage, A.; Emsley, L.; Copéret, C.; Hermans, I. Correlating Synthetic Methods, Morphology, Atomic-Level Structure, and Catalytic Activity of Sn-β Catalysts. *ACS Catal.* **2016**, *6*, 4047–4063.
- (54) Grykałowska, A.; Nowak, B. High-Resolution Solid-State ¹¹⁹Sn and ¹⁹⁵Pt NMR Studies of MPtSn Semiconductors (M = Ti, Zr, Hf, Th). *Solid State Nucl. Magn. Reson.* **2005**, *27*, 223–227.
- (55) Wrackmeyer, B. Application of ¹¹⁹Sn NMR Parameters. Editor: G. A. Webb, *Annu. Rep. NMR Spectrosc., Academic Press*, **1999**; Vol. 38, pp 203–264.
- (56) Ha, M.; Karmakar, A.; Bernard, G. M.; Basilio, E.; Krishnamurthy, A.; Askar, A. M.; Shankar, K.; Kroeker, S.; Michaelis, V. K. Phase Evolution in Methylammonium Tin Halide Perovskites with Variable Temperature Solid-State ¹¹⁹Sn NMR Spectroscopy. *J. Phys. Chem. C* **2020**, *124*, 15015–15027.
- (57) Jastrzebski, J. T. B. H.; Grove, D. M.; Boersma, J.; van Koten, G.; Ernsting, J. - M. ¹¹⁹Sn NMR Study of Organotin Compounds Having Intramolecular Sn—N Coordination. *Magn. Reson. Chem.* **1991**, *29*, S25–S30.
- (58) Gunther, W. R.; Michaelis, V. K.; Caporini, M. A.; Griffin, R. G.; Román-Leshkov, Y. Dynamic Nuclear Polarization NMR Enables the Analysis of Sn-Beta Zeolite Prepared with Natural Abundance ¹¹⁹Sn Precursors. *J. Am. Chem. Soc.* **2014**, *136*, 6219–6222.

- (59) Karmakar, A.; Bhattacharya, A.; Bernard, G. M.; Mar, A.; Michaelis, V. K. Revealing the Local Sn and Pb Arrangements in $\text{CsSn}_x\text{Pb}_{1-x}\text{Br}_3$ Perovskites with Solid-State NMR Spectroscopy. *ACS Mater. Lett.* **2021**, *3*, 261–267.
- (60) Yeh, H. M. M.; Geanangel, R. A. ^{119}Sn NMR Spectra of Tin(II) Halides. *Inorganica Chim. Acta* **1981**, *52*, 113–118.
- (61) Amornsakchai, P.; Apperley, D. C.; Harris, R. K.; Hodgkinson, P.; Waterfield, P. C. Solid-State NMR Studies of Some Tin(II) Compounds. *Solid State Nucl. Magn. Reson.* **2004**, *26*, 160–171.
- (62) Hunter, B. K.; Reeves, L. W. Chemical Shifts for Compounds of the Group IV Elements Silicon and Tin. *Can. J. Chem.* **1968**, *46*, 1399–1414.
- (63) Armstrong, R. L.; van Driel, H. M. The Observation of Incipient Phase Transitions in K_2PtCl_6 , K_2PdCl_6 , and K_2IrCl_6 . *Can. J. Phys.* **1972**, *50*, 2048–2053.
- (64) Dimitropoulos, C.; Van Der Klink, J. J.; Pelzl, J.; Regelsberger, M.; Rossler, K. Nuclear Quadrupole Resonance and Nuclear Magnetic Resonance Studies of K_2PtCl_6 Type Mixed Crystals. *Faraday Symp. Chem. Soc.* **1978**, *13*, 124–132.
- (65) Shannon, R. D. Revised Effective Ionic Radii and Systematic Studies of Interatomic Distances in Halides and Chalcogenides. *Acta Cryst.* **1976**, *A32*, 751–767.
- (66) Kaltzoglou, A.; Antoniadou, M.; Kontos, A. G.; Stoumpos, C. C.; Perganti, D.; Siranidi, E.; Raptis, V.; Trohidou, K.; Psycharis, V.; Kanatzidis, M. G.; Falaras, P. Optical-Vibrational Properties of the Cs_2SnX_6 ($X = \text{Cl}, \text{Br}, \text{I}$) Defect Perovskites and Hole-Transport Efficiency in Dye-Sensitized Solar Cells. *J. Phys. Chem. C* **2016**, *120*, 11777–11785.
- (67) Xiao, Z.; Zhou, Y.; Hosono, H.; Kamiya, T. Intrinsic Defects in a Photovoltaic Perovskite Variant Cs_2SnI_6 . *Phys. Chem. Chem. Phys.* **2015**, *17*, 18900–18903.
- (68) Dmitrenko, O.; Bai, S.; Dybowski, C. Prediction of ^{207}Pb NMR Parameters for the Solid Ionic Lead(II) Halides Using the Relativistic ZORA-DFT Formalism: Comparison with the Lead-Containing Molecular Systems. *Solid State Nucl. Magn. Reson.* **2008**, *34*, 186–190.
- (69) Bagno, A.; Casella, G.; Saielli, G. Relativistic DFT Calculation of ^{119}Sn Chemical Shifts and Coupling Constants in Tin Compounds. *J. Chem. Theory Comput.* **2006**, *2*, 37–46.

- (70) Aebli, M.; Piveteau, L.; Nazarenko, O.; Benin, B. M.; Krieg, F.; Verel, R.; Kovalenko, M. V. Lead-Halide Scalar Couplings in ^{207}Pb NMR of APbX_3 Perovskites (A = Cs, Methylammonium, Formamidinium; X = Cl, Br, I). *Sci. Rep.* **2020**, *10*, 8229.
- (71) Sharp, R. R. Rotational Diffusion and Magnetic Relaxation of ^{119}Sn in Liquid SnCl_4 and SnI_4 . *J. Chem. Phys.* **1972**, *57*, 5321–5330.
- (72) Sharp, R. R. Field Dependence of Nuclear Magnetic Relaxation of ^{119}Sn in SnCl_4 , SnBr_4 , and SnI_4 . *J. Chem. Phys.* **1974**, *60*, 1149–1157.
- (73) Hamaed, H.; Pawlowski, J. M.; Cooper, B. F. T.; Fu, R.; Eichhorn, S. H.; Schurko, R. W. Application of Solid-State ^{35}Cl NMR to the Structural Characterization of Hydrochloride Pharmaceuticals and Their Polymorphs. *J. Am. Chem. Soc.* **2008**, *130*, 11056–11065.
- (74) Widdifield, C. M.; Chapman, R. P.; Bryce, D. L. Chapter 5 Chlorine, Bromine, and Iodine Solid-State NMR Spectroscopy, *Annu. Rep. NMR Spectrosc.* **2009**, *66*, 195–326.
- (75) Chapman, R. P.; Widdifield, C. M.; Bryce, D. L. Solid-State NMR of Quadrupolar Halogen Nuclei. *Prog. Nucl. Magn. Reson. Spectrosc.* **2009**, *55*, 215–237.
- (76) Piveteau, L.; Aebli, M.; Yazdani, N.; Millen, M.; Korosec, L.; Krieg, F.; Benin, B. M.; Morad, V.; Piveteau, C.; Shiroka, T.; Comas-Vives, A.; Copéret, C.; Lindenberg, A. M.; Wood, V.; Verel, R.; Kovalenko, M. Bulk and Nanocrystalline Cesium Lead-Halide Perovskites as Seen by Halide Magnetic Resonance. *ACS Cent. Sci.* **2020**, *6*, 1138–1149.
- (77) Greer, B. J.; Michaelis, V. K.; Terskikh, V. V.; Kroeker, S. Reconnaissance of Diverse Structural and Electronic Environments in Germanium Halides by Solid-State ^{73}Ge NMR and Quantum Chemical Calculations. *Can. J. Chem.* **2011**, *89*, 1118–1129.
- (78) Lucier, B. E. G.; Terskikh, V. V.; Guo, J.; Bourque, J. L.; Mconie, S. L.; Ripmeester, J. A.; Huang, Y.; Baines, K. M. Chlorine-35 Solid-State Nuclear Magnetic Resonance Spectroscopy as an Indirect Probe of the Oxidation Number of Tin in Tin Chlorides. *Inorg. Chem.* **2020**, *59*, 13651–13670.
- (79) O'Dell, L. A.; Schurko, R. W. QCPMG Using Adiabatic Pulses for Faster Acquisition of Ultra-Wideline NMR Spectra. *Chem. Phys. Lett.* **2008**, *464*, 97–102.

- (80) Dell, L. A. O. The WURST Kind of Pulses in Solid-State NMR. *Solid State Nucl. Magn. Reson.* **2013**, *55–56*, 28–41.
- (81) Armstrong, R. L.; Baker, G. L. Temperature and Pressure Variation of the ^{35}Cl Nuclear Quadrupole Resonance Frequency in K_2IrCl_6 . *Can. J. Phys.* **1970**, *48*, 1649–1656.
- (82) Patrick, C. E.; Jacobsen, K. W.; Thygesen, K. S. Anharmonic Stabilization and Band Gap Renormalization in the Perovskite CsSnI_3 . *Phys. Rev. B* **2015**, *92*, 201205.
- (83) Yaffe, O.; Guo, Y.; Tan, L. Z.; Egger, D. A.; Hull, T.; Stoumpos, C. C.; Zheng, F.; Heinz, T. F.; Kronik, L.; Kanatzidis, M. G.; Owen, J. S.; Rappe, A. M.; Pimenta, M. A.; Brus, L. E. Local Polar Fluctuations in Lead Halide Perovskite Crystals. *Phys. Rev. Lett.* **2017**, *118*, 136001.
- (84) Yang, R. X.; Skelton, J. M.; Da Silva, E. L.; Frost, J. M.; Walsh, A. Spontaneous Octahedral Tilting in the Cubic Inorganic Cesium Halide Perovskites CsSnX_3 and CsPbX_3 ($X = \text{F}, \text{Cl}, \text{Br}, \text{I}$). *J. Phys. Chem. Lett.* **2017**, *8*, 4720–4726.
- (85) Maughan, A. E.; Ganose, A. M.; Candia, A. M.; Granger, J. T.; Scanlon, D. O.; Neilson, J. R. Anharmonicity and Octahedral Tilting in Hybrid Vacancy-Ordered Double Perovskites. *Chem. Mater.* **2018**, *30*, 472–483.
- (86) Maughan, A. E.; Paecklar, A. A.; Neilson, J. R. Bond Valences and Anharmonicity in Vacancy-Ordered Double Perovskite Halides. *J. Mater. Chem. C* **2018**, *6*, 12095–12104.
- (87) Senocrate, A.; Moudrakovski, I.; Maier, J. Short-Range Ion Dynamics in Methylammonium Lead Iodide by Multinuclear Solid State NMR and ^{127}I NQR. *Phys. Chem. Chem. Phys.* **2018**, *20*, 20043–20055.
- (88) Dunlap-Shohl, W. A.; Zhou, Y.; Padture, N. P.; Mitzi, D. B. Synthetic Approaches for Halide Perovskite Thin Films. *Chem. Rev.* **2019**, *119*, 3193–3295.
- (89) Liu, M.; Johnston, M. B.; Snaith, H. J. Efficient Planar Heterojunction Perovskite Solar Cells by Vapour Deposition. *Nature* **2013**, *501*, 395–398.
- (90) James, S. L.; Adams, C. J.; Bolm, C.; Braga, D.; Collier, P.; Friscic, T.; Grepioni, F.; Harris, K. D. M.; Hyett, G.; Jones, W.; Krebs, A.; Mack, J.; Maini, L.; Orpen, A. G.; Parkin, I. P.; Shearouse, W. C.; Steed, J. W.; Waddell, D. C. Mechanochemistry: Opportunities for New and Cleaner Synthesis. *Chem. Soc. Rev.* **2012**, *41*, 413–447.

- (91) Chizhik, S.; Panda, M. K.; Nath, N. K.; Boldyreva, E. Mechanically Responsive Molecular Crystals. *Chem. Rev.* **2015**, *115*, 12440–12490.
- (92) Stock, N.; Biswas, S. Synthesis of Metal-Organic Frameworks (MOFs): Routes to Various MOF Topologies, Morphologies, and Composites. *Chem. Rev.* **2012**, *112*, 933–969.
- (93) Prochowicz, D.; Franckevicius, M.; Cieslak, A. M.; Zakeeruddin, S. M.; Graetzel, M.; Lewinski, J. Mechano-synthesis of the Hybrid Perovskite $\text{CH}_3\text{NH}_3\text{PbI}_3$: Characterization and the Corresponding Solar Cell Efficiency. *J. Mater. Chem. A* **2015**, *3*, 20772–20777.
- (94) Rosales, B. A.; Wei, L.; Vela, J. Synthesis and Mixing of Complex Halide Perovskites by Solvent-Free Solid-State Methods. *J. Solid State Chem.* **2019**, *271*, 206–215.
- (95) Hong, Z.; Tan, D.; John, R. A.; Tay, Y. K. E.; Ho, Y. K. T.; Zhao, X.; Sum, T. C.; Mathews, N.; García, F.; Soo, H. Sen. Completely Solvent-Free Protocols to Access Phase-Pure, Metastable Metal Halide Perovskites and Functional Photodetectors from the Precursor Salts. *iScience* **2019**, *16*, 312–325.
- (96) Protesescu, L.; Yakunin, S.; Nazarenko, O.; Dirin, D. N.; Kovalenko, M. V. Low-Cost Synthesis of Highly Luminescent Colloidal Lead Halide Perovskite Nanocrystals by Wet Ball Milling. *ACS Appl. Nano Mater.* **2018**, *1*, 1300–1308.
- (97) Prochowicz, D.; Franckevičius, M.; Cieślak, A. M.; Zakeeruddin, S. M.; Grätzel, M.; Lewiński, J. Mechano-synthesis of the Hybrid Perovskite $\text{CH}_3\text{NH}_3\text{PbI}_3$: Characterization and the Corresponding Solar Cell Efficiency. *J. Mater. Chem. A* **2015**, *3*, 20772–20777.
- (98) Zarick, H. F.; Soetan, N.; Erwin, W. R.; Bardhan, R. Mixed Halide Hybrid Perovskites: A Paradigm Shift in Photovoltaics. *J. Mater. Chem. A* **2018**, *6*, 5507–5537.
- (99) Karim, M. M. S.; Ganose, A. M.; Pieters, L.; Winnie Leung, W. W.; Wade, J.; Zhang, L.; Scanlon, D. O.; Palgrave, R. G. Anion Distribution, Structural Distortion, and Symmetry-Driven Optical Band Gap Bowing in Mixed Halide Cs_2SnX_6 Vacancy Ordered Double Perovskites. *Chem. Mater.* **2019**, *31*, 9430–9444.
- (100) Im, J.; Stoumpos, C. C.; Jin, H.; Freeman, A. J.; Kanatzidis, M. G. Antagonism between Spin-Orbit Coupling and Steric Effects Causes Anomalous Band Gap

Evolution in the Perovskite Photovoltaic Materials $\text{CH}_3\text{NH}_3\text{Sn}_{1-x}\text{Pb}_x\text{I}_3$. *J. Phys. Chem. Lett.* **2015**, *6*, 3503–3509.

(101) Rabbani, S. R.; Edmonds, D. T. Nuclear Spin-Lattice Relaxation-Time Reduction in Small Particles. *Phys. Rev. B* **1994**, *50*, 6184–6188.

(102) Dempah, K. E.; Lubach, J. W.; Munson, E. J. Characterization of the Particle Size and Polydispersity of Dicumarol Using Solid-State NMR Spectroscopy. *Mol. Pharm.* **2017**, *14*, 856–865.

(103) Nairui, X.; Yehua, T.; Yali, Q.; Duoduo, L.; Ke-Fan, W. One-Step Solution Synthesis and Stability Study of Inorganic Perovskite Semiconductor Cs_2SnI_6 . *Sol. Energy* **2020**, *204*, 429–439.

(104) Kubelka, P.; Munk, F. Ein Beitrag Zur Optik Der Farbanstriche. *Z. Tech. Phys. (Leipzig)* **1931**, *12*, 593–601.

(105) Bernard, G. M.; Goyal, A.; Miskolzie, M.; McKay, R.; Wu, Q.; Wasylshen, R. E.; Michaelis, V. K. Methylammonium Lead Chloride: A Sensitive Sample for an Accurate NMR Thermometer. *J. Magn. Reson.* **2017**, *283*, 14–21.

(106) te Velde, G.; Bickelhaupt, F. M.; Baerends, E. J.; Fonseca Guerra, C.; van Gisbergen, S. J. A.; Snijders, J. G.; Ziegler, T. Chemistry with ADF. *J. Comput. Chem.* **2001**, *22*, 931–967.

(107) Guerra, C. F.; Snijders, J. G.; te Velde, G.; Baerends, E. J. Towards an Order-N DFT Method. *Theor. Chem. Acc.* **1998**, *99*, 391–403.

(108) Baerends, E. J.; Ziegler, T.; Atkins, A. J.; Autschbach, J.; Baseggio, O.; Bashford, D.; Bérces, A.; Bickelhaupt, F. M.; Bo, C.; Boerrigter, P.M.; et al. ADF2018, SCM, Theoretical Chemistry, Vrije Universiteit, Amsterdam, The Netherlands, <https://www.scm.com>.

(109) Adamo, C.; Barone, V. Toward Reliable Density Functional Methods without Adjustable Parameters: The PBE0 Model. *J. Chem. Phys.* **1999**, *110*, 6158–6170.

(110) Lenthe, E. van; Baerends, E. J. Optimized Slater-Type Basis Sets for the Elements 1-118. *J. Comput. Chem.* **2003**, *24*, 1142–1156.

(111) Wolff, S. K.; Ziegler, T.; Lenthe, E. van; Baerends, E. J. Density Functional Calculations of Nuclear Magnetic Shieldings Using the Zeroth-Order Regular

Approximation (ZORA) for Relativistic Effects: ZORA Nuclear Magnetic Resonance. *J. Chem. Phys.* **1999**, *110*, 7689–7698.

(112) Lenthe, E. van; Baerends, E. J.; Snijders, J. G. Relativistic Regular Two-component Hamiltonians. *J. Chem. Phys.* **1993**, *99*, 4597–4610.

(113) Autschbach, J. The Role of the Exchange-Correlation Response Kernel and Scaling Corrections in Relativistic Density Functional Nuclear Magnetic Shielding Calculations with the Zeroth-Order Regular Approximation. *Mol. Phys.* **2013**, *111*, 2544–2554.

(114) Wolff, S. K.; Ziegler, T. Calculation of DFT-GIAO NMR Shifts with the Inclusion of Spin-Orbit Coupling. *J. Chem. Phys.* **1998**, *109*, 895–905.

CHAPTER 7

Summary and Looking Towards the Future

7.1 Summary

7.1.1 ABX₃ Metal Halide Perovskites

In the last decade, metal halide perovskites, ABX₃, have gained tremendous attention in the photovoltaic and optoelectronic community for their applications in solar cells, laser, light-emitting diodes, photocatalysis, X-ray detectors, and many more.^{1,2} In Chapters 2 and 3, synthetic development, along with a thorough structure-property investigation of Pb²⁺- and Sn²⁺-containing metal halide perovskites, respectively, were discussed.

Chapter 2 described the advantage of using a mechanochemical approach versus the conventional solvent phase synthesis in preparing phase-pure products of methylammonium lead mixed-halide perovskites, namely, MAPb(Cl_{1-x}Br_x)₃ and MAPb(Br_{1-x}I_x)₃ (0 ≤ x ≤ 1) materials. The careful selection of Cl/Br and Br/I mixed-halide compositions ultimately allowed for fine tailoring of their optical bandgap properties using solvent-free mechanochemical synthesis. For example, a stoichiometric MAPb(Br_{0.5}I_{0.5})₃ mixed-halide perovskite composition, previously impossible to prepare using a traditional solvent-based synthesis approach, was synthesized successfully using the mechanochemical synthesis route described herein. The average and local structure of these materials were understood using powder X-ray diffraction and solid-state NMR spectroscopy, respectively. One- and two-dimensional ²⁰⁷Pb NMR spectroscopy enabled the identification, for the first time, of seven chemically distinct [PbX_xX'_{6-x}]⁴⁻ octahedral environments in MAPb(Cl_{1-x}Br_x)₃ mixed halide perovskites. Chemical assignments were supported further by quantum chemical calculations. Furthermore, ²⁰⁷Pb–²⁰⁷Pb 2D EXSY data provided crucial information identifying atomic-level halide mixing and halogen mobility within these compounds.

Chapter 3 described the complete solid solution of $\text{CsSn}(\text{Cl}_{1-x}\text{Br}_x)_3$, exhibiting the cubic perovskite structure for all compounds prepared by the high-temperature solid-state synthesis method. The average long-range structure was determined by powder X-ray diffraction, while the local chemical structure and rapid halogen mobility were identified by ^{133}Cs and ^{119}Sn solid-state NMR spectroscopy. This work provided one of the first pieces of evidence contrasting with lead halide perovskite analogues (APbX_3), where halogen anions within tin(II) halide perovskites, $\text{CsSn}(\text{Cl}_{1-x}\text{Br}_x)_3$, exhibit faster anion mobility. The rapid halogen mobility in CsSnBr_3 was studied by variable temperature ^{119}Sn T_1 measurements, where a low activation energy of $28.9 \pm 1.2 \text{ kJ}\cdot\text{mol}^{-1}$ for the bromine ion diffusion was determined. Furthermore, the degradation mechanism of CsSnBr_3 perovskite under ambient laboratory conditions was monitored by powder X-ray diffraction ^{133}Cs and ^{119}Sn NMR spectroscopy.

7.1.2 $\text{A}_2\text{B}'\text{B}''\text{X}_6$ Double Perovskites

Although lead halide perovskites (APbX_3) have gained tremendous attention in the photovoltaic and optoelectronic community, their application faces remarkable challenges for commercialization because of a lack of ambient stability and the risk of lead toxicity.³⁻⁵ On the other hand, tin(II) halide perovskites ASnX_3 are low toxic alternatives, but they also are subject to poor ambient stability and rapidly oxidize ($\text{Sn}^{2+} \rightarrow \text{Sn}^{4+}$) in air.³ Among lead-free and chemically stable alternatives, halide double perovskites $\text{A}_2\text{B}'\text{B}''\text{X}_6$ have proven highly promising because of their attractive optical properties.⁶ However, the absorption profiles of most reported halide double perovskites exhibit larger optical bandgaps ($>2 \text{ eV}$) that are aligned poorly with the solar spectrum, as the optimum bandgap value to maximize the thin-film solar cell efficiency is 1.34 eV .⁶ In Chapter 4, a new lead-free and low bandgap halide double perovskite was discussed, and Chapter 5 described another halide double perovskite composition, which emits bright broadband white-light upon ultraviolet light excitation.

Chapter 4 described the solvent-phase synthesis of a Cu(II)-doped $\text{Cs}_2\text{SbAgCl}_6$ double perovskite material, exhibiting a low bandgap of ca. 1 eV . This material exhibited much higher thermal and moisture stability than the well-known Pb(II)- and

Sn(II)-based ABX_3 perovskite materials. Powder X-ray diffraction, solid-state NMR, and EPR spectroscopy were performed to determine the incorporation of paramagnetic Cu(II) ions into the $Cs_2SbAgCl_6$ parent structure. Variable temperature ^{133}Cs NMR spectroscopy confirmed that Cu(II) ions impact ^{133}Cs NMR spectra through a Fermi contact interaction.

Chapter 5 depicted the synthesis of a single-material broadband white-light-emitting $Cs_2Bi_{1-x}In_xAgCl_6$ double perovskite materials. Density functional theory (DFT) calculations indicated an indirect–direct bandgap transition occurring when $x > 0.50$. All the materials emit in the entire visible light spectrum upon ultraviolet light excitation, and a maximum photoluminescence quantum yield of ca. 34% was recorded for In-rich materials (92% In). The long- to short-range structures of these materials were studied extensively by powder X-ray diffraction and solid-state NMR spectroscopy of quadrupolar nuclei (^{115}In , ^{133}Cs , and ^{209}Bi), respectively, to elucidate the key role of Bi incorporation and its optical performances.

7.1.3 A_2BX_6 “Vacancy-Ordered Perovskites”

A developing class of lead-free and ambient stable alternative to the ABX_3 type (B = Pb^{2+} and/or Sn^{2+}) materials is A_2BX_6 , a “vacancy-ordered perovskite”.^{6,7} These compounds are made of low toxic elements and exhibit much higher ambient stability than the ABX_3 perovskite materials which were discussed in Chapters 2 and 3.⁶ For example, Sn(IV)-containing Cs_2SnX_6 materials recently have shown attractive optical and electrical properties in thin-film solar cells, photocatalysis, and light emitting applications.^{8–11}

In Chapter 6, the solvent-free mechanochemical synthesis of Cs_2SnX_6 mixed-halide materials was discussed. The solvent-free mechanochemical synthesis using the ball-milling route yielded a series of mixed-halide compositions of $Cs_2SnCl_xBr_{6-x}$ and $Cs_2SnBr_xI_{6-x}$ ($0 \leq x \leq 6$), which exhibited attractive optical bandgaps spanning ca. 3 eV throughout the halogen compositions. An atomic-level analysis by solid-state ^{119}Sn and ^{133}Cs NMR spectroscopy and quantum chemical calculations confirmed the solid-solution behavior of $Cs_2SnCl_xBr_{6-x}$ and $Cs_2SnBr_xI_{6-x}$ materials. Finally, the octahedral

dynamics of SnX_6 unit in Cs_2SnX_6 was uncovered by variable temperature ^{119}Sn NMR measurements.

In summary, I believe that the most significant research contributions resulting from my Ph.D. research are: (i) an investigation of rapid X-site dynamics in ABX_3 type perovskite materials, (ii) development of lead-free low bandgap as well as broadband white-light emitting halide double perovskite materials, and (iii) uncovering local structure and octahedral dynamics of SnX_6 unit in Cs_2SnX_6 materials.

7.2 Future Research Priorities Based on my Ph.D. Research

7.2.1 Stage-I

The next stage for metal(II)-based perovskites will involve the solvent-free mechanochemical synthesis of two-dimensional (2D) layered Ruddlesden–Popper and Dion–Jacobson halide perovskite-like materials. Organic-inorganic hybrid 2D layered perovskite materials show enhanced ambient stability compared to their 3D counterparts. The 2D layered perovskite materials have gained tremendous interest as candidates for next-generation optoelectronic devices due to their high degree of modification via inorganic ions and organic linking ligands.¹² The general formula of 2D layered metal halide perovskites can be written as $\text{A}'_2\text{A}_{n-1}\text{B}_n\text{X}_{3n+1}$, where A' represents R-NH_3^+ or $\text{NH}_3^+-\text{R-NH}_3^+$ (R = large aliphatic alkyl chain or an aromatic group), A represents small organic or inorganic cations (CH_3NH_3^+ , $\text{CH}(\text{NH}_2)_2^+$ and Cs^+), B is a divalent metal ion (Pb^{2+} and/or Sn^{2+}), X is a halide anion (Cl^- , Br^- , I^-), and n is the number of metal halide monolayer sheets between organic layers. A strict 2D structure is formed when $n = 1$, a quasi-2D structure is formed once $n = 2-5$, and $n = \infty$ for a conventional 3D structure. The atomic-level structure and bonding between large organic cations and the inorganic metal halide framework still are understood poorly. Solid-state NMR spectroscopy of multiple NMR-active nuclei (e.g., ^1H , ^{13}C , ^{19}F , $^{14/15}\text{N}$, ^{119}Sn , ^{133}Cs , ^{207}Pb , etc.) is emerging in this field just now. It will be vital to inform on the ordered/disordered structures present in these materials. Furthermore, halide perovskite materials exhibit dynamic processes, such as reorientation modes of organic cations, cation diffusion and halogen migration, which are challenging to capture using diffraction methods. Two-dimensional homo- and hetero-nuclear

correlation NMR spectra of these solid materials is a natural evolution in identifying and deconvoluting the unique chemical environments, distances for intermolecular distances and ion diffusion. Dipolar-based 2D homonuclear correlation experiments such as DQ-SQ (^1H - ^1H , ^{13}C - ^{13}C , ^{19}F - ^{19}F), and EXSY (^{207}Pb - ^{207}Pb), and heteronuclear HETCOR (^{13}C - ^1H , ^{133}Cs - ^1H , ^{207}Pb - ^1H , ^{207}Pb - ^{19}F , etc.), are promising, with further accessibility using emerging fast MAS methods, strategic isotopic labeling, or even high-field dynamic nuclear polarization. Interestingly, nuclear quadrupole resonance (NQR) spectroscopy of the halide ions in the X-site ($^{35/37}\text{Cl}$, $^{79/81}\text{Br}$, ^{127}I ; Table 1.1), is gaining traction to be used in understanding medium-range effects such as dopants, vacancies, and influence on local chemical environments. Although Br and I have sizeable quadrupolar interactions, limiting rapid studies indicate that $^{35/37}\text{Cl}$ NMR appears attractive. To predict the NQR/NMR spectra, quantum chemical calculations will play an increasingly important role in predicting where these resonances may appear and assembling larger structural models to assist in interpreting the experimental results.

7.2.2 Stage-II

Further developments in halide double perovskite, $\text{A}_2\text{B}'\text{B}''\text{X}_6$, materials will continue to advance to fill requirements for optoelectronic applications, such as low energy LED technologies. The targeted materials which I would like to suggest are Na/Ag alloyed $\text{Cs}_2\text{BiNa}_x\text{Ag}_{1-x}\text{Cl}_6$ ($0 \leq x \leq 1$) as these materials exhibit a broadband orange-light emission upon ultraviolet excitation.¹³ The influence of Na^+ and Ag^+ mixing on its chemical structure is understood poorly. Considering the advances of solid-state NMR spectroscopy that I have outlined in this thesis, it is anticipated that ^{23}Na , ^{133}Cs , and ^{209}Bi NMR spectroscopy will have favor in determining the Na^+/Ag^+ ionic distributions within the B'(I) site of $\text{Cs}_2\text{Na}_x\text{Ag}_{1-x}\text{BiCl}_6$. Further exploration through variable temperature ^{23}Na NMR spectroscopy may be worthwhile in assessing whether or not these materials behave as a Na-ion conductor, a growing area of interest for sodium-based energy storage materials.

7.2.3 Stage-III

Interest in the "vacancy-ordered perovskites" A_2BX_6 is growing rapidly due to their increased stability and ease in accommodating both distinct A-, B- and X-sites. One area meriting further research is mixed A-site cationic materials. Organic–inorganic hybrid materials, namely, methylammonium and rubidium alloyed $[(CH_3NH_3)_xRb_{1-x}]_2SnI_6$ ($0 \leq x \leq 1$) compounds would be targeted directly. The $(CH_3NH_3)_2SnI_6$ parent material exhibits a cubic structure at room temperature, whereas Rb_2SnI_6 exhibits a tetragonal structure.^{14,15} A cubic to tetragonal structural change upon incorporating Rb^+ into $[(CH_3NH_3)_xRb_{1-x}]_2SnI_6$ materials is expected, although the exact moment at this switch occurs is unknown to date. The concept of this project is inspired by one of the recent works from our group on kesterite /stannite-based solar-cell materials.¹⁶ Since the short- versus long-range arrangements have not been characterized well for these materials, it is not known how the physical properties are related to structural changes entailed by A-site $CH_3NH_3^+$ and Rb^+ mixing. Solid-state NMR spectroscopy of multiple NMR-active nuclei (^{14}N , ^{87}Rb , ^{119}Sn) will provide crucial information about the local structure which can be correlated with their optical properties.

7.3 References

- (1) Dunlap-Shohl, W. A.; Zhou, Y.; Padture, N. P.; Mitzi, D. B. Synthetic Approaches for Halide Perovskite Thin Films. *Chem. Rev.* **2019**, *119*, 3193–3295.
- (2) Kim, H.; Han, J. S.; Choi, J.; Kim, S. Y.; Jang, H. W. Halide Perovskites for Applications beyond Photovoltaics. *Small Methods* **2018**, *2*, 1700310.
- (3) Song, T. Bin; Yokoyama, T.; Stoumpos, C. C.; Logsdon, J.; Cao, D. H.; Wasielewski, M. R.; Aramaki, S.; Kanatzidis, M. G. Importance of Reducing Vapor Atmosphere in the Fabrication of Tin-Based Perovskite Solar Cells. *J. Am. Chem. Soc.* **2017**, *139*, 836–842.
- (4) Li, J.; Cao, H.; Jiao, W.; Wang, Q.; Wei, M.; Cantone, I.; Lü, J.; Abate, A. Biological Impact of Lead from Halide Perovskites Reveals the Risk of Introducing a Safe Threshold. *Nat. Commun.* **2020**, *11*, 310.
- (5) Yang, J.; Siempelkamp, B. D.; Liu, D.; Kelly, T. L. Investigation of $CH_3NH_3PbI_3$

Degradation Rates and Mechanisms in Controlled Humidity Environments Using in Situ Techniques. *ACS Nano* **2015**, *9*, 1955–1963.

(6) Luo, J.; Hu, M.; Niu, G.; Tang, J. Lead-Free Halide Perovskites and Perovskite Variants as Phosphors toward Light-Emitting Applications. *ACS Appl. Mater. Interfaces* **2019**, *11*, 31575–31584.

(7) Maughan, A. E.; Ganose, A. M.; Scanlon, D. O.; Neilson, J. R. Perspectives and Design Principles of Vacancy-Ordered Double Perovskite Halide Semiconductors. *Chem. Mater.* **2019**, *31*, 1184–1195.

(8) Saparov, B.; Sun, J. P.; Meng, W.; Xiao, Z.; Duan, H. S.; Gunawan, O.; Shin, D.; Hill, I. G.; Yan, Y.; Mitzi, D. B. Thin-Film Deposition and Characterization of a Sn-Deficient Perovskite Derivative Cs₂SnI₆. *Chem. Mater.* **2016**, *28*, 2315–2322.

(9) Wang, A.; Yan, X.; Zhang, M.; Sun, S.; Yang, M.; Shen, W.; Pan, X.; Wang, P.; Deng, Z. Controlled Synthesis of Lead-Free and Stable Perovskite Derivative Cs₂SnI₆ Nanocrystals via a Facile Hot-Injection Process. *Chem. Mater.* **2016**, *28*, 8132–8140.

(10) Lim, S. C.; Lin, H. P.; Tsai, W. L.; Lin, H. W.; Hsu, Y. T.; Tuan, H. Y. Binary Halide, Ternary Perovskite-like, and Perovskite-Derivative Nanostructures: Hot Injection Synthesis and Optical and Photocatalytic Properties. *Nanoscale* **2017**, *9*, 3747–3751.

(11) Veronese, A.; Patrini, M.; Bajoni, D.; Ciarrocchi, C.; Quadrelli, P.; Malavasi, L. Highly Tunable Emission by Halide Engineering in Lead-Free Perovskite-Derivative Nanocrystals: The Cs₂SnX₆ (X = Cl, Br, Br/I, I) System. *Front. Chem.* **2020**, *8*, 1–9.

(12) Gao, X.; Zhang, X.; Yin, W.; Wang, H.; Hu, Y.; Zhang, Q.; Shi, Z.; Colvin, V. L.; Yu, W. W.; Zhang, Y. Ruddlesden–Popper Perovskites: Synthesis and Optical Properties for Optoelectronic Applications. *Adv. Sci.* **2019**, *6*, 1900941.

(13) Lamba, R. S.; Basera, P.; Bhattacharya, S.; Sapra, S. Band Gap Engineering in Cs₂(Na_xAg_{1-x})BiCl₆ Double Perovskite Nanocrystals. *J. Phys. Chem. Lett.* **2019**, *10*, 5173–5181.

(14) Funabiki, F.; Toda, Y.; Hosono, H. Optical and Electrical Properties of Perovskite Variant (CH₃NH₃)₂SnI₆. *J. Phys. Chem. C* **2018**, *122*, 10749–10754.

(15) Maughan, A. E.; Ganose, A. M.; Almaker, M. A.; Scanlon, D. O.; Neilson, J. R. Tolerance Factor and Cooperative Tilting Effects in Vacancy-Ordered Double

Perovskite Halides. *Chem. Mater.* **2018**, *30*, 3909–3919.

(16) Bhattacharya, A.; Tkachuk, D. G.; Mar, A.; Michaelis, V. K. Mere Anarchy Is Loosed: Structural Disorder in $\text{Cu}_2\text{Zn}_{1-x}\text{Cd}_x\text{SnS}_4$. *Chem. Mater.* **2021**, *33*, 4709–4722.

Complete Bibliography

Chapter 1

- (1) Rose, G. De Perowskite, Fossili Novo. *Novis Quibusdam Foss. Quae Montibus Ural. Inven. AG Schade Berlin* **1839**, pp 3-12.
- (2) Wells, H. L.; Johnston, W. R. Uber Die Ammoniumbleihalogenide. *Anorg. Allg. Chem.* **1893**, 3, 195–210.
- (3) Golschmidt, V. M. Die Gesetze Der Krystallochemie. *Naturwissenschaften* **1926**, 14, 477–485.
- (4) Akkerman, Q. A.; Manna, L. What Defines a Halide Perovskite? *ACS Energy Lett.* **2020**, 5, 604–610.
- (5) Bartel, C. J.; Sutton, C.; Goldsmith, B. R.; Ouyang, R.; Musgrave, C. B.; Ghiringhelli, L. M.; Scheffler, M. New Tolerance Factor to Predict the Stability of Perovskite Oxides and Halides. *Sci. Adv.* **2019**, 5:eaav0693, 1–9.
- (6) Mitchell, R. H.; Welch, M. D.; Chakhmouradian, A. R. Nomenclature of the Perovskite Supergroup: A Hierarchical System of Classification Based on Crystal Structure and Composition. *Mineral. Mag.* **2017**, 81, 411–461.
- (7) Kay, H. F.; Bailey, P. C. Structure and Properties of CaTiO₃. *Acta Crystallogr.* **1957**, 10, 219–226.
- (8) Megaw, H. Crystal Structure of Barium Titanate. *Nature* **1945**, 155, 484–485.
- (9) Megaw, H. D. Origin of Ferroelectricity in Barium Titanate and Other Perovskite-Type Crystals. *Acta Crystallogr.* **1952**, 5, 739–749.
- (10) Shannon, R. D.; Bierstedt, P. E. Single-Crystal Growth and Electrical Properties of BaPbO₃. *J. Am. Ceram. Soc.* **1970**, 53, 635–636.
- (11) Takahashi, T.; Iwahara, H. Ionic Conduction in Perovskite-Type Oxide Solid Solution and Its Application to the Solid Electrolyte Fuel Cell. *Energy Convers.* **1971**, 11, 105–111.
- (12) Lawless, W. N. Three Application Areas for SrTiO₃ Glass-Ceramics. *Ferroelectrics* **1972**, 3, 287–293.
- (13) Kozuka, H.; Ohbayashi, K.; Koumoto, K. Electronic Conduction in La-Based Perovskite-Type Oxides. *Sci. Technol. Adv. Mater.* **2015**, 16, 026001.

- (14) Labhasetwar, N.; Saravanan, G.; Kumar Megarajan, S.; Manwar, N.; Khobragade, R.; Doggali, P.; Grasset, F. Perovskite-Type Catalytic Materials for Environmental Applications. *Sci. Technol. Adv. Mater.* **2015**, *16*, 036002.
- (15) Mazet, L.; Yang, S. M.; Kalinin, S. V.; Schamm-Chardon, S.; Dubourdieu, C. A Review of Molecular Beam Epitaxy of Ferroelectric BaTiO₃ Films on Si, Ge and GaAs Substrates and Their Applications. *Sci. Technol. Adv. Mater.* **2015**, *16*, 036005.
- (16) K. C. Møller. Crystal Structure and Photoconductivity of Caesium Plumbohalides. *Nature* **1958**, *182*, 1436.
- (17) Weber, D. CH₃NH₃PbX₃, a Pb(II)-System with Cubic Perovskite Structure. *Z. Naturforsch* **1978**, *33*, 1443–1445.
- (18) R. E. Wasylshen; Knop, O.; Macdonald, J. B. Cation Rotation in Methylammonium Lead Halides. *Solid State Commun.* **1985**, *56*, 581–582.
- (19) Poglitsch, A.; Weber, D. Dynamic Disorder in Methylammoniumtrihalogenoplumbates(II) Observed by Millimeter-Wave Spectroscopy. *J. Chem. Phys.* **1987**, *87*, 6373–6378.
- (20) Furukawa, Y.; Nakamura, D. Cationic Dynamics in the Crystalline Phases of (CH₃NH₃)PbX₃ (X: Cl, Br) as Studied by Proton Magnetic Resonance Techniques. *Z. Naturforsch. A Phys. Sci.* **1989**, *44a*, 1122–1126.
- (21) Onoda-Yamamuro, N.; Matsuo, T.; Suga, H. Calorimetric and IR Spectroscopic Studies of Phase Transitions in Methylammonium Trihalogenoplumbates (II). *J. Phys. Chem. Solids* **1990**, *51*, 1383–1395.
- (22) Knop, O.; Wasylshen, R. E.; White, M. A.; Cameron, T. S.; van Oort, M. J. M. Alkylammonium Lead Halides. Part 2. CH₃NH₃PbX₃ (X = Cl, Br, I) Perovskites: Cuboctahedral Halide Cages with Isotropic Cation Reorientation. *Can. J. Chem.* **1990**, *68*, 412–422.
- (23) Xu, Q.; Eguchi, T.; Nakayama, H.; Nakamura, N.; Kishita, M. Molecular Motions and Phase Transitions in Solid CH₃NH₃PbX₃ (X = Cl, Br, I) as Studied by NMR and NQR. *Z. Naturforsch., A Phys. Sci.* **1991**, *46*, 240–246.
- (24) Xu, Q.; Eguchi, T.; Nakayama, H. Molecular Motions in Solid CD₃NH₃PbBr₃ as Studied by ¹H NMR. *Bull. Chem. Soc. Jpn.* **1992**, *65*, 2264–2266.
- (25) Mitzi, D. B.; Chondroudis, K.; Kagan, C. R. Organic-Inorganic Electronics. *IBM*

- J. Res. Dev.* **2001**, *45*, 29–45.
- (26) Kojima, A.; Teshima, K.; Shirai, Y.; Miyasaka, T. Organometal Halide Perovskites as Visible-Light Sensitizers for Photovoltaic Cells. *J. Am. Chem. Soc.* **2009**, *131*, 6050–6051.
- (27) Zhao, Y.; Zhu, K. Organic-Inorganic Hybrid Lead Halide Perovskites for Optoelectronic and Electronic Applications. *Chem. Soc. Rev.* **2016**, *45*, 655–689.
- (28) Dunlap-Shohl, W. A.; Zhou, Y.; Padture, N. P.; Mitzi, D. B. Synthetic Approaches for Halide Perovskite Thin Films. *Chem. Rev.* **2019**, *119*, 3193–3295.
- (29) Li, T.; Zhao, X.; Yang, D.; Du, M. H.; Zhang, L. Intrinsic Defect Properties in Halide Double Perovskites for Optoelectronic Applications. *Phys. Rev. Appl.* **2018**, *10*, 041001.
- (30) V. M. Goldschmidt. Die Gesetze Der Krystallochemie. *Naturwissenschaften* **1926**, *14*, 477–485.
- (31) Wei, Y.; Cheng, Z.; Lin, J. An Overview on Enhancing the Stability of Lead Halide Perovskite Quantum Dots and Their Applications in Phosphor-Converted LEDs. *Chem. Soc. Rev.* **2019**, *48*, 310–350.
- (32) Li, C.; Lu, X.; Ding, W.; Feng, L.; Gao, Y.; Guo, Z. Formability of ABX₃ (X = F, Cl, Br, I) Halide Perovskites. *Acta Crystallogr. Sect. B* **2008**, *B64*, 702–707.
- (33) Cheng, X.; Jing, L.; Yuan, Y.; Du, S.; Zhang, J.; Zhan, X.; Ding, J.; Yu, H.; Shi, G. Fe²⁺/Fe³⁺ Doped into MAPbCl₃ Single Crystal: Impact on Crystal Growth and Optical and Photoelectronic Properties. *J. Phys. Chem. C* **2019**, *123*, 1669–1676.
- (34) Fabini, D. H.; Laurita, G.; Bechtel, J. S.; Stoumpos, C. C.; Evans, H. A.; Kontos, A. G.; Raptis, Y. S.; Falaras, P.; Van Der Ven, A.; Kanatzidis, M. G.; et al. Dynamic Stereochemical Activity of the Sn²⁺ Lone Pair in Perovskite CsSnBr₃. *J. Am. Chem. Soc.* **2016**, *138*, 11820–11832.
- (35) Piveteau, L.; Morad, V.; Kovalenko, M. V. Solid-State NMR and NQR Spectroscopy of Lead-Halide Perovskite Materials. *J. Am. Chem. Soc.* **2020**, *142*, 19413–19437.
- (36) Govinda, S.; Kore, B. P.; Swain, D.; Hossain, A.; De, C.; Guru Row, T. N.; Sarma, D. D. Critical Comparison of FAPbX₃ and MAPbX₃ (X = Br and Cl): How Do They Differ? *J. Phys. Chem. C* **2018**, *122*, 13758–13766.

- (37) Gao, W.; Zielinski, K.; Drury, B. N.; Carl, A. D.; Grimm, R. L. Elucidation of Chemical Species and Reactivity at Methylammonium Lead Iodide and Cesium Tin Bromide Perovskite Surfaces via Orthogonal Reaction Chemistry. *J. Phys. Chem. C* **2018**, *122*, 17882–17894.
- (38) Sutton, R. J.; Filip, M. R.; Haghighirad, A. A.; Sakai, N.; Wenger, B.; Giustino, F.; Snaith, H. J. Cubic or Orthorhombic? Revealing the Crystal Structure of Metastable Black-Phase CsPbI₃ by Theory and Experiment. *ACS Energy Lett.* **2018**, *3*, 1787–1794.
- (39) Dirin, D. N.; Cherniukh, I.; Yakunin, S.; Shynkarenko, Y.; Kovalenko, M. V. Solution-Grown CsPbBr₃ Perovskite Single Crystals for Photon Detection. *Chem. Mater.* **2016**, *28*, 8470–8474.
- (40) Linaburg, M. R.; McClure, E. T.; Majher, J. D.; Woodward, P. M. Cs_{1-x}Rb_xPbCl₃ and Cs_{1-x}Rb_xPbBr₃ Solid Solutions: Understanding Octahedral Tilting in Lead Halide Perovskites. *Chem. Mater.* **2017**, *29*, 3507–3514.
- (41) Yamada, K.; Kuranaga, Y.; Ueda, K.; Goto, S.; Okuda, T.; Furukawa, Y. Phase Transition and Electric Conductivity of ASnCl₃ (A = Cs and CH₃NH₃). *Bull. Chem. Soc. Jpn.* **1998**, *71*, 127–134.
- (42) Ke, F.; Wang, C.; Jia, C.; Wolf, N. R.; Yan, J.; Niu, S.; Devereaux, T. P.; Karunadasa, H. I.; Mao, W. L.; Lin, Y. Preserving a Robust CsPbI₃ Perovskite Phase via Pressure-Directed Octahedral Tilt. *Nat. Commun.* **2021**, *12*, 461.
- (43) Li, Z.; Yang, M.; Park, J. S.; Wei, S. H.; Berry, J. J.; Zhu, K. Stabilizing Perovskite Structures by Tuning Tolerance Factor: Formation of Formamidinium and Cesium Lead Iodide Solid-State Alloys. *Chem. Mater.* **2016**, *28*, 284–292.
- (44) Lin, R.; Xiao, K.; Qin, Z.; Han, Q.; Zhang, C.; Wei, M.; Saidaminov, M. I.; Gao, Y.; Xu, J.; Xiao, M.; et al. Monolithic All-Perovskite Tandem Solar Cells with 24.8% Efficiency Exploiting Comproportionation to Suppress Sn(II) Oxidation in Precursor Ink. *Nat. Energy* **2019**, *4*, 864–873.
- (45) Bag, M.; Kumar, R.; Srivastava, P. Role of A-Site Cation and X-Site Halide Interactions in Mixed-Cation Mixed-Halide Perovskites for Determining Anomalously High Ideality Factor and the Super-Linear Power Law in Ac Ionic Conductivity at Operating Temperature. *ACS Appl. Electron. Mater.* **2020**, *2*, 4087–

4098.

(46) Xu, Q.; Yang, D.; Lv, J.; Sun, Y.-Y.; Zhang, L. Perovskite Solar Absorbers: Materials by Design. *Small Methods* **2018**, *2*, 1700316.

(47) Sutherland, B. R.; Sargent, E. H. Perovskite Photonic Sources. *Nat. Photonics* **2016**, *10*, 295–302.

(48) Manser, J. S.; Christians, J. A.; Kamat, P. V. Intriguing Optoelectronic Properties of Metal Halide Perovskites. *Chem. Rev.* **2016**, *116*, 12956–13008.

(49) Zhao, Y.; Zhu, K. Organic-Inorganic Hybrid Lead Halide Perovskites for Optoelectronic and Electronic Applications. *Chem. Soc. Rev.* **2016**, *45*, 655–689.

(50) Chen, K.; Deng, X.; Dodekatos, G.; Tüysüz, H. Photocatalytic Polymerization of 3,4-Ethylenedioxythiophene over Cesium Lead Iodide Perovskite Quantum Dots. *J. Am. Chem. Soc.* **2017**, *139*, 12267–12273.

(51) Yakunin, S.; Sytnyk, M.; Kriegner, D.; Shrestha, S.; Richter, M.; Matt, G. J.; Azimi, H.; Brabec, C. J.; Stangl, J.; Kovalenko, M. V; et al. Detection of X-Ray Photons by Solution-Processed Lead Halide Perovskites. *Nat. Photonics* **2015**, *9*, 444–449.

(52) Leung, S. F.; Ho, K. T.; Kung, P. K.; Hsiao, V. K. S.; Alshareef, H. N.; Wang, Z. L.; He, J. H. A Self-Powered and Flexible Organometallic Halide Perovskite Photodetector with Very High Detectivity. *Adv. Mater.* **2018**, *30*, 1704611.

(53) National Renewable Energy Laboratory (NREL). Best Research-Cell Efficiency Chart. <https://www.nrel.gov/pv/assets/pdfs/best-research-cell-efficiencies.20200104.pdf>

(54) Yang, J.; Siempelkamp, B. D.; Liu, D.; Kelly, T. L. Investigation of CH₃NH₃PbI₃ Degradation Rates and Mechanisms in Controlled Humidity Environments Using in Situ Techniques. *ACS Nano* **2015**, *9*, 1955–1963.

(55) Li, J.; Cao, H.; Jiao, W.; Wang, Q.; Wei, M.; Cantone, I.; Lü, J.; Abate, A. Biological Impact of Lead from Halide Perovskites Reveals the Risk of Introducing a Safe Threshold. *Nat. Commun.* **2020**, *11*, 310.

(56) Kamarudin, M. A.; Hirotsu, D.; Wang, Z.; Hamada, K.; Nishimura, K.; Shen, Q.; Toyoda, T.; Iikubo, S.; Minemoto, T.; Yoshino, K.; et al. Suppression of Charge Carrier Recombination in Lead-Free Tin Halide Perovskite via Lewis Base Post-

- Treatment. *J. Phys. Chem. Lett.* **2019**, *10*, 5277–5283.
- (57) Song, T. Bin; Yokoyama, T.; Stoumpos, C. C.; Logsdon, J.; Cao, D. H.; Wasielewski, M. R.; Aramaki, S.; Kanatzidis, M. G. Importance of Reducing Vapor Atmosphere in the Fabrication of Tin-Based Perovskite Solar Cells. *J. Am. Chem. Soc.* **2017**, *139*, 836–842.
- (58) Zhao, D.; Yu, Y.; Wang, C.; Liao, W.; Shrestha, N.; Grice, C. R.; Cimaroli, A. J.; Guan, L.; Ellingson, R. J.; Zhu, K.; et al. Low-Bandgap Mixed Tin-Lead Iodide Perovskite Absorbers with Long Carrier Lifetimes for All-Perovskite Tandem Solar Cells. *Nat. Energy* **2017**, *2*, 17018.
- (59) Luo, J.; Hu, M.; Niu, G.; Tang, J. Lead-Free Halide Perovskites and Perovskite Variants as Phosphors toward Light-Emitting Applications. *ACS Appl. Mater. Interfaces* **2019**, *11*, 31575–31584.
- (60) Slavney, A. H.; Hu, T.; Lindenberg, A. M.; Karunadasa, H. I. A Bismuth-Halide Double Perovskite with Long Carrier Recombination Lifetime for Photovoltaic Applications. *J. Am. Chem. Soc.* **2016**, *138*, 2138–2141.
- (61) McClure, E. T.; Ball, M. R.; Windl, W.; Woodward, P. M. Cs₂AgBiX₆ (X = Br, Cl): New Visible Light Absorbing, Lead-Free Halide Perovskite Semiconductors. *Chem. Mater.* **2016**, *28*, 1348–1354.
- (62) Slavney, A. H.; Leppert, L.; Bartesaghi, D.; Gold-Parker, A.; Toney, M. F.; Savenije, T. J.; Neaton, J. B.; Karunadasa, H. I. Defect-Induced Band-Edge Reconstruction of a Bismuth-Halide Double Perovskite for Visible-Light Absorption. *J. Am. Chem. Soc.* **2017**, *139*, 5015–5018.
- (63) Slavney, A. H.; Leppert, L.; Saldivar Valdes, A.; Bartesaghi, D.; Savenije, T. J.; Neaton, J. B.; Karunadasa, H. I. Small-Band-Gap Halide Double Perovskites. *Angew. Chem. Int. Ed.* **2018**, *57*, 12765–12770.
- (64) Yang, B.; Mao, X.; Hong, F.; Meng, W.; Tang, Y.; Xia, X.; Yang, S.; Deng, W.; Han, K. Lead-Free Direct Bandgap Double Perovskite Nanocrystals with Bright Dual-Color Emission. *J. Am. Chem. Soc.* **2018**, *140*, 17001–17006.
- (65) Luo, J.; Wang, X.; Li, S.; Liu, J.; Guo, Y.; Niu, G.; Yao, L.; Fu, Y.; Gao, L.; Dong, Q.; et al. Efficient and Stable Emission of Warm-White Light from Lead-Free Halide Double Perovskites. *Nature* **2018**, *563*, 541–545.

- (66) Majher, J. D.; Gray, M. B.; Strom, T. A.; Woodward, P. M. Cs₂NaBiCl₆: Mn²⁺-A New Orange-Red Halide Double Perovskite Phosphor. *Chem. Mater.* **2019**, *31*, 1738–1744.
- (67) Manna, D.; Das, T. K.; Yella, A. Tunable and Stable White Light Emission in Bi³⁺ Alloyed Cs₂AgInCl₆ Double Perovskite Nanocrystals. *Chem. Mater.* **2019**, *31*, 10063–10070.
- (68) Nila Nandha, K.; Nag, A. Synthesis and Luminescence of Mn-Doped Cs₂AgInCl₆ Double Perovskites. *Chem. Commun.* **2018**, *54*, 5205–5208.
- (69) Locardi, F.; Cirignano, M.; Baranov, D.; Dang, Z.; Prato, M.; Drago, F.; Ferretti, M.; Pinchetti, V.; Fanciulli, M.; Brovelli, S.; et al. Colloidal Synthesis of Double Perovskite Cs₂AgInCl₆ and Mn-Doped Cs₂AgInCl₆ Nanocrystals. *J. Am. Chem. Soc.* **2018**, *140*, 12989–12995.
- (70) Maughan, A. E.; Ganose, A. M.; Scanlon, D. O.; Neilson, J. R. Perspectives and Design Principles of Vacancy-Ordered Double Perovskite Halide Semiconductors. *Chem. Mater.* **2019**, *31*, 1184–1195.
- (71) Maughan, A. E.; Ganose, A. M.; Candia, A. M.; Granger, J. T.; Scanlon, D. O.; Neilson, J. R. Anharmonicity and Octahedral Tilting in Hybrid Vacancy-Ordered Double Perovskites. *Chem. Mater.* **2018**, *30*, 472–483.
- (72) Maughan, A. E.; Paecklar, A. A.; Neilson, J. R. Bond Valences and Anharmonicity in Vacancy-Ordered Double Perovskite Halides. *J. Mater. Chem. C* **2018**, *6*, 12095–12104.
- (73) Saparov, B.; Sun, J. P.; Meng, W.; Xiao, Z.; Duan, H. S.; Gunawan, O.; Shin, D.; Hill, I. G.; Yan, Y.; Mitzi, D. B. Thin-Film Deposition and Characterization of a Sn-Deficient Perovskite Derivative Cs₂SnI₆. *Chem. Mater.* **2016**, *28*, 2315–2322.
- (74) Wang, A.; Yan, X.; Zhang, M.; Sun, S.; Yang, M.; Shen, W.; Pan, X.; Wang, P.; Deng, Z. Controlled Synthesis of Lead-Free and Stable Perovskite Derivative Cs₂SnI₆ Nanocrystals via a Facile Hot-Injection Process. *Chem. Mater.* **2016**, *28*, 8132–8140.
- (75) Lim, S. C.; Lin, H. P.; Tsai, W. L.; Lin, H. W.; Hsu, Y. T.; Tuan, H. Y. Binary Halide, Ternary Perovskite-like, and Perovskite-Derivative Nanostructures: Hot Injection Synthesis and Optical and Photocatalytic Properties. *Nanoscale* **2017**, *9*, 3747–3751.

- (76) Veronese, A.; Patrini, M.; Bajoni, D.; Ciarrocchi, C.; Quadrelli, P.; Malavasi, L. Highly Tunable Emission by Halide Engineering in Lead-Free Perovskite-Derivative Nanocrystals: The Cs_2SnX_6 ($\text{X} = \text{Cl}, \text{Br}, \text{Br/I}, \text{I}$) System. *Front. Chem.* **2020**, *8*, 1–9.
- (77) James, S. L.; Adams, C. J.; Bolm, C.; Braga, D.; Collier, P.; Friščić, T.; Grepioni, F.; Harris, K. D. M.; Hyett, G.; Jones, W.; et al. Playing with Organic Radicals as Building Blocks for Functional Molecular Materials. *Chem. Soc. Rev.* **2012**, *41*, 413–447.
- (78) Palazon, F.; El Ajjouri, Y.; Bolink, H. J. Making by Grinding: Mechanochemistry Boosts the Development of Halide Perovskites and Other Multinary Metal Halides. *Adv. Energy Mater.* **2020**, *10*, 1902499.
- (79) Tan, D.; García, F. Main Group Mechanochemistry: From Curiosity to Established Protocols. *Chem. Soc. Rev.* **2019**, *48*, 2274–2292.
- (80) Friščić, T. Supramolecular Concepts and New Techniques in Mechanochemistry: Cocrystals, Cages, Rotaxanes, Open Metal–Organic Frameworks. *Chem. Soc. Rev.* **2012**, *41*, 3493–3510.
- (81) Julien, P. A.; Mottillo, C.; Friščić, T. Metal–Organic Frameworks Meet Scalable and Sustainable Synthesis. *Green Chem.* **2017**, *19*, 2729–2747.
- (82) Ju, D.; Dang, Y.; Zhu, Z.; Liu, H.; Chueh, C. C.; Li, X.; Wang, L.; Hu, X.; Jen, A. K. Y.; Tao, X. Tunable Band Gap and Long Carrier Recombination Lifetime of Stable Mixed $\text{CH}_3\text{NH}_3\text{Pb}_x\text{Sn}_{1-x}\text{Br}_3$ Single Crystals. *Chem. Mater.* **2018**, *30*, 1556–1565.
- (83) Moghe, D.; Wang, L.; Traverse, C. J.; Redoute, A.; Sponseller, M.; Brown, P. R.; Bulović, V.; Lunt, R. R. All Vapor-Deposited Lead-Free Doped CsSnBr_3 Planar Solar Cells. *Nano Energy* **2016**, *28*, 469–474.
- (84) Rosales, B. A.; Men, L.; Cady, S. D.; Hanrahan, M. P.; Rossini, A. J.; Vela, J. Persistent Dopants and Phase Segregation in Organolead Mixed-Halide Perovskites. *Chem. Mater.* **2016**, *28*, 6848–6859.
- (85) Prochowicz, D.; Franckevicius, M.; Cieslak, A. M.; Zakeeruddin, S. M.; Graetzel, M.; Lewinski, J. Mechanochemistry of the Hybrid Perovskite $\text{CH}_3\text{NH}_3\text{PbI}_3$: Characterization and the Corresponding Solar Cell Efficiency. *J. Mater. Chem. A* **2015**, *3*, 20772–20777.

- (86) Stoumpos, C. C.; Malliakas, C. D.; Kanatzidis, M. G. Semiconducting Tin and Lead Iodide Perovskites with Organic Cations: Phase Transitions, High Mobilities, and near-Infrared Photoluminescent Properties. *Inorg. Chem.* **2013**, *52*, 9019–9038.
- (87) Le, T.; Epa, V. C.; Burden, F. R.; Winkler, D. A. Quantitative Structure-Property Relationship Modeling of Diverse Materials Properties. *Chem. Rev.* **2012**, *112*, 2889–2919.
- (88) Franssen, W. M. J.; Kentgens, A. P. M. Solid-State NMR of Hybrid Halide Perovskites. *Solid State Nucl. Magn. Reson.* **2019**, *100*, 36–44.
- (89) Grykałowska, A.; Nowak, B. High-Resolution Solid-State ^{119}Sn and ^{195}Pt NMR Studies of MPtSn Semiconductors (M = Ti, Zr, Hf, Th). *Solid State Nucl. Magn. Reson.* **2005**, *27*, 223–227.
- (90) Wolf, P.; Valla, M.; Núñez-Zarur, F.; Comas-Vives, A.; Rossini, A. J.; Firth, C.; Kallas, H.; Lesage, A.; Emsley, L.; Copéret, C.; et al. Correlating Synthetic Methods, Morphology, Atomic-Level Structure, and Catalytic Activity of Sn- β Catalysts. *ACS Catal.* **2016**, *6*, 4047–4063.
- (91) *NMR of Quadrupolar Nuclei in Solid Materials*; Wasylshen, R. E., Ashbrook, S. E., Wimperis, S., Eds.; John Wiley & Sons, 2012.
- (92) *Modern Methods in Solid-State NMR: A Practitioner's Guide*; Hodgkinson, P., Ed.; Royal Society of Chemistry, 2018.
- (93) Bakmutov, V. I. *Solid-State NMR in Materials Science: Principles and Applications*; CRC press, 2016.
- (94) Duer, M. J. *Introduction to Solid-State NMR Spectroscopy*; Oxford, UK, 2004.
- (95) Reif, B.; Ashbrook, S. E.; Emsley, L.; Hong, M. Solid-State NMR Spectroscopy. *Nat. Rev. Methods Prim.* **2021**, *1*, 1–23.
- (96) Bernard, G. M.; Karmakar, A.; Michaelis, V. K. Solid-State NMR Studies of Halide Perovskite Materials with Photoconversion Potential. In *Reference Module in Chemistry, Molecular Sciences and Chemical Engineering*; Elsevier, 2021. <https://doi.org/https://doi.org/10.1016/B978-0-12-823144-9.00018-2>.
- (97) Moudrakovski, I. L. *Local Dynamics in Hybrid Perovskites by Solid-State NMR*, 1st ed.; Elsevier Ltd., 2021; Vol. 102. <https://doi.org/10.1016/bs.arnmr.2020.10.004>.
- (98) Mehring, M. *Principles of High Resolution NMR in Solids*; Springer-Verlag,

1983.

(99) Apperley, D. C.; Harris, R. K.; Hodgkinson, P. *Solid-State NMR: Basic Principles and Practice*; Momentum Press, 2012.

(100) Harris, R. K.; Becker, E. D. NMR Nomenclature: Nuclear Spin Properties and Conventions for Chemical Shifts—IUPAC Recommendations. *J. Magn. Reson.* **2002**, *156*, 323–326.

(101) Jameson, C. J. Chemical Shift Scales on an Absolute Basis. In *Encyclopedia of Magnetic Resonance*; 2011.

<https://doi.org/10.1002/9780470034590.emrstm0072.pub2>.

(102) Harris, R. K.; Becker, E. D.; de Menrzes, S. M. C.; Goodfellow, R.; Granger, P. NMR Nomenclature. Nuclear Spin Properties and Conventions for Chemical Shifts. *Pure Appl. Chem.* **2001**, *73*, 1795–1818.

(103) Mason, J. Conventions for the Reporting of Nuclear Magnetic Shielding (or Shift) Tensors Suggested by Participants in the NATO ARW on NMR Shielding Constants at the University of Maryland, College Park, July 1992. *Solid State Nucl. Magn. Reson.* **1993**, *2*, 285–288.

(104) Eichele, K. WSolids V. 1.21.3. Universität Tübingen 2015.

(105) Wasylishen, R. E. Dipolar and Indirect Coupling: Basics. *Encycl. Magn. Reson.* **2009**. <https://doi.org/10.1002/9780470034590.emrstm1023>.

(106) Bryce, D. L.; Wasylishen, R. E. Quadrupolar Nuclei in Solids: Influence of Different Interactions on Spectra. In *Encyclopedia of Magnetic Resonance*; 2011. <https://doi.org/10.1002/9780470034590.emrstm1197>.

(107) Amoureux, J. P.; Fernandez, C.; Granger, P. Multinuclear Magnetic Resonance in Liquids and Solids; Granger, P., Harris, R. K., Eds.; Kluwer Academic Publishers: London, 1990; p 409.

(108) Hennel, J. W.; Klinowski, J. Magic-Angle Spinning: A Historical Perspective. In *New techniques in solid-state NMR. Topics in Current Chemistry, vol 246*; Klinowski, J., Ed.; Springer Berlin Heidelberg: Berlin, Heidelberg, 2005; pp 1–14.

(109) Farrar, T. C. *Introduction to Pulse NMR Spectroscopy*; Madison: The Farragut, 1997.

(110) Wasylishen, R. E. NMR relaxation and dynamics. *NMR Spectroscopy*

Techniques; Chapt. 3; Bruch, M. D., Ed.; Marcel Dekker, New York, 1996. pp. 105-144.

(111) Grutzner, J. B.; Stewart, K. W.; Wasylishen, R. E.; Lumsden, M. D.; Dybowski, C.; Beckmann, P. A. A New Mechanism for Spin-Lattice Relaxation of Heavy Nuclei in the Solid State: ^{207}Pb Relaxation in Lead Nitrate. *J. Am. Chem. Soc.* **2001**, *123*, 7094–7100.

(112) Gryff-Keller, A.; Molchanov, S.; Wodynski, A. Scalar Relaxation of the Second Kind — A Potential Source of Information on the Dynamics of Molecular Movements. 2. Magnetic Dipole Moments and Magnetic Shielding of Bromine Nuclei. *J. Phys. Chem. A* **2014**, *118*, 128–133

(113) Gordon, M. I.; Hoch, M. J. R. Quadrupolar Spin-Lattice Relaxation in Solids. *J. Phys. C Solid State Phys.* **1978**, *11*, 783–795.

(114) Kubicki, D. J.; Prochowicz, D.; Pinon, A.; Stevanato, G.; Hofstetter, A.; Zakeeruddin, S. M.; Grätzel, M.; Emsley, L. Doping and Phase Segregation in Mn^{2+} - and Co^{2+} -Doped Lead Halide Perovskites from ^{133}Cs and ^1H NMR Relaxation Enhancement. *J. Mater. Chem. A* **2019**, *7*, 2326–2333.

Chapter 2

(1) Shin, S. S.; Yeom, E. J.; Yang, W. S.; Hur, S.; Kim, M. G.; Im, J.; Seo, J.; Noh, J. H.; Seok, S. I., Colloidally Prepared La-Doped BaSnO_3 Electrodes for Efficient, Photostable Perovskite Solar Cells. *Science* **2017**, *356*, 167-171.

(2) Hsiao, Y.-C.; Wu, T.; Li, M.; Liu, Q.; Qin, W.; Hu, B., Fundamental Physics Behind High-Efficiency Organo-Metal Halide Perovskite Solar Cells. *J. Mater. Chem. A* **2015**, *3* (30), 15372-15385.

(3) Miyata, A.; Mitioglu, A.; Plochocka, P.; Portugall, O.; Wang, J. T.-W.; Stranks, S. D.; Snaith, H. J.; Nicholas, R. J., Direct Measurement of the Exciton Binding Energy and Effective Masses for Charge Carriers in Organic-Inorganic Tri-Halide Perovskites. *Nat. Phys.* **2015**, *11* (7), 582-587.

(4) Li, Y.; Yan, W.; Li, Y.; Wang, S.; Wang, W.; Bian, Z.; Xiao, L.; Gong, Q., Direct Observation of Long Electron-Hole Diffusion Distance in $\text{CH}_3\text{NH}_3\text{PbI}_3$ Perovskite Thin Film. *Sci. Rep.* **2015**, *5*, 14485.

- (5) Stranks, S. D.; Nayak, P. K.; Zhang, W.; Stergiopoulos, T.; Snaith, H. J., Formation of Thin Films of Organic–Inorganic Perovskites for High-Efficiency Solar Cells. *Angew. Chem. Int. Ed.* **2015**, *54* (11), 3240-3248.
- (6) Wong, A. B.; Lai, M.; Eaton, S. W.; Yu, Y.; Lin, E.; Dou, L.; Fu, A.; Yang, P., Growth and Anion Exchange Conversion of $\text{CH}_3\text{NH}_3\text{PbX}_3$ Nanorod Arrays for Light-Emitting Diodes. *Nano Lett.* **2015**, *15* (8), 5519-5524.
- (7) Tan, H.; Jain, A.; Voznyy, O.; Lan, X.; García de Arquer, F. P.; Fan, J. Z.; Quintero-Bermudez, R.; Yuan, M.; Zhang, B.; Zhao, Y., et al., Efficient and Stable Solution-Processed Planar Perovskite Solar Cells via Contact Passivation. *Science* **2017**, *355*, 722-726.
- (8) Eperon, G. E.; Leijtens, T.; Bush, K. A.; Prasanna, R.; Green, T.; Wang, J. T.-W.; McMeekin, D. P.; Volonakis, G.; Milot, R. L.; May, R., et al., Perovskite-Perovskite Tandem Photovoltaics with Optimized Bandgaps. *Science* **2016**, *354* (6314), 861-865.
- (9) Jang, D. M.; Park, K.; Kim, D. H.; Park, J.; Shojaei, F.; Kang, H. S.; Ahn, J.-P.; Lee, J. W.; Song, J. K., Reversible Halide Exchange Reaction of Organometal Trihalide Perovskite Colloidal Nanocrystals for Full-Range Band Gap Tuning. *Nano Lett.* **2015**, *15* (8), 5191-5199.
- (10) Pellet, N.; Teuscher, J.; Maier, J.; Grätzel, M., Transforming Hybrid Organic Inorganic Perovskites by Rapid Halide Exchange. *Chem. Mater.* **2015**, *27* (6), 2181-2188.
- (11) Colella, S.; Mosconi, E.; Fedeli, P.; Listorti, A.; Gazza, F.; Orlandi, F.; Ferro, P.; Besagni, T.; Rizzo, A.; Calestani, G., et al., $\text{MAPbI}_{3-x}\text{Cl}_x$ Mixed Halide Perovskite for Hybrid Solar Cells: The Role of Chloride as Dopant on the Transport and Structural Properties. *Chem. Mater.* **2013**, *25* (22), 4613-4618.
- (12) Mosconi, E.; De Angelis, F., Mobile Ions in Organohalide Perovskites: Interplay of Electronic Structure and Dynamics. *ACS Energy Lett.* **2016**, *1* (1), 182-188.
- (13) Brivio, F.; Caetano, C.; Walsh, A., Thermodynamic Origin of Photoinstability in the $\text{CH}_3\text{NH}_3\text{Pb}(\text{I}_{1-x}\text{Br}_x)_3$ Hybrid Halide Perovskite Alloy. *J. Phys. Chem. Lett.* **2016**, *7* (6), 1083-1087.
- (14) Hentz, O.; Zhao, Z.; Gradečak, S., Impacts of Ion Segregation on Local Optical Properties in Mixed Halide Perovskite Films. *Nano Lett.* **2016**, *16* (2), 1485-1490.

- (15) Hoke, E. T.; Slotcavage, D. J.; Dohner, E. R.; Bowring, A. R.; Karunadasa, H. I.; McGehee, M. D., Reversible Photo-Induced Trap Formation in Mixed-Halide Hybrid Perovskites for Photovoltaics. *Chem. Sci.* **2015**, *6* (1), 613-617.
- (16) Yoon, S. J.; Draguta, S.; Manser, J. S.; Sharia, O.; Schneider, W. F.; Kuno, M.; Kamat, P. V., Tracking Iodide and Bromide Ion Segregation in Mixed Halide Lead Perovskites During Photoirradiation. *ACS Energy Lett.* **2016**, *1* (1), 290-296.
- (17) Yoon, S. J.; Kuno, M.; Kamat, P. V., Shift Happens. How Halide Ion Defects Influence Photoinduced Segregation in Mixed Halide Perovskites. *ACS Energy Lett.* **2017**, *2* (7), 1507-1514.
- (18) Lewiński, J.; Dutkiewicz, M.; Lesiuk, M.; Śliwiński, W.; Zelga, K.; Justyniak, I.; Lipkowski, J., Solid-State Conversion of the Solvated Dimer [$\{t\text{BuZn}(\mu\text{-OtBu})(\text{thf})_2\}_2$] into a Long Overlooked Trimeric [$\{t\text{BuZnOtBu}\}_3$] Species. *Angew. Chem. Int. Ed.* **2010**, *49* (44), 8266-8269.
- (19) Prochowicz, D.; Justyniak, I.; Kornowicz, A.; Kaczorowski, T.; Kaszkur, Z.; Lewiński, J., Construction of a Porous Homochiral Coordination Polymer with Two Types of Cu_nI_n Alternating Units Linked by Quinine: A Solvothermal and a Mechanochemical Approach. *Chem. - Eur. J.* **2012**, *18* (24), 7367-7371.
- (20) Prochowicz, D.; Sokołowski, K.; Justyniak, I.; Kornowicz, A.; Fairen-Jimenez, D.; Frišćić, T.; Lewiński, J.; Düren, T.; Hyett, G.; Jones, W., et al., A Mechanochemical Strategy for IRMOF Assembly Based on Pre-Designed Oxo-Zinc Precursors. *Chem. Commun.* **2015**, *51* (19), 4032-4035.
- (21) Lee, J.; Shin, H.; Lee, J.; Chung, H.; Zhang, Q.; Saito, F., Mechanochemical Syntheses of Perovskite $\text{KM}^{\text{II}}\text{F}_3$ with Cubic Structure (M = Mg, Ca, Mn, Fe, Co, Ni, and Zn). *Mater. Trans.* **2003**, *44* (7), 1457-1460.
- (22) Elseman, A. M.; Rashad, M. M.; Hassan, A. M., Easily Attainable, Efficient Solar Cell with Mass Yield of Nanorod Single-Crystalline Organo-Metal Halide Perovskite Based on a Ball Milling Technique. *ACS Sustainable Chem. Eng.* **2016**, *4* (9), 4875-4886.
- (23) Jana, A.; Mittal, M.; Singla, A.; Sapra, S.; Grätzel, M.; Lewiński, J.; Tong, Y.; Polavarapu, L.; Feldmann, J.; Urban, A. S., et al., Solvent-Free, Mechanochemical

- Syntheses of Bulk Trihalide Perovskites and Their Nanoparticles. *Chem. Commun.* **2017**, 53 (21), 3046-3049.
- (24) Zhu, Z.-Y.; Yang, Q.-Q.; Gao, L.-F.; Zhang, L.; Shi, A.-Y.; Sun, C.-L.; Wang, Q.; Zhang, H.-L., Solvent-Free Mechanochemical Synthesis of Composition-Tunable Cesium Lead Halide Perovskite Quantum Dots. *J. Phys. Chem. Lett.* **2017**, 8 (7), 1610-1614.
- (25) Manukyan, K. V.; Yeghishyan, A. V.; Moskovskikh, D. O.; Kapaldo, J.; Mintairov, A.; Mukasyan, A. S., Mechanochemical Synthesis of Methylammonium Lead Iodide Perovskite. *J. Mater. Sci.* **2016**, 51 (19), 9123-9130.
- (26) Jodlowski, A. D.; Yépez, A.; Luque, R.; Camacho, L.; de Miguel, G., Benign-by-Design Solventless Mechanochemical Synthesis of Three-, Two-, and One-Dimensional Hybrid Perovskites. *Angew. Chem. Int. Ed.* **2016**, 55 (48), 14972-14977.
- (27) Prochowicz, D.; Franckevičius, M.; Cieślak, A. M.; Zakeeruddin, S. M.; Grätzel, M.; Lewiński, J., Mechanochemical Synthesis of the Hybrid Perovskite $\text{CH}_3\text{NH}_3\text{PbI}_3$: Characterization and the Corresponding Solar Cell Efficiency. *J. Mater. Chem. A* **2015**, 3 (41), 20772-20777.
- (28) Prochowicz, D.; Yadav, P.; Saliba, M.; Sasaki, M.; Zakeeruddin, S. M.; Lewiński, J.; Grätzel, M., Mechanochemical Synthesis of Pure Phase Mixed-Cation $\text{MA}_x\text{FA}_{1-x}\text{PbI}_3$ Hybrid Perovskites: Photovoltaic Performance and Electrochemical Properties. *Sustainable Energy Fuels* **2017**, 1 (4), 689-693.
- (29) Prochowicz, D.; Yadav, P.; Saliba, M.; Sasaki, M.; Zakeeruddin, S. M.; Lewiński, J.; Grätzel, M., Reduction in the Interfacial Trap Density of Mechanochemically Synthesized MAPbI_3 . *ACS Appl. Mater. Interfaces* **2017**, 9 (34), 28418-28425.
- (30) Kubicki, D.; Prochowicz, D.; Hofstetter, A.; Zakeeruddin, S. M.; Grätzel, M.; Emsley, L., Phase Segregation in Cs-, Rb- and K-Doped Mixed-Cation $(\text{MA})_x(\text{FA})_{1-x}\text{PbI}_3$ Hybrid Perovskites from Solid-State NMR. *J. Am. Chem. Soc.* **2017**, 139 (40), 14173-14180.
- (31) Hibble, S. J.; Chippindale, A. M.; Marelli, E.; Kroeker, S.; Michaelis, V. K.; Greer, B. J.; Aguiar, P. M.; Bilbé, E. J.; Barney, E. R.; Hannon, A. C., Local and Average Structure in Zinc Cyanide: Toward an Understanding of the Atomistic Origin of Negative Thermal Expansion. *J. Am. Chem. Soc.* **2013**, 135 (44), 16478-16489.

- (32) Aharen, T.; Greedan, J. E.; Ning, F.; Imai, T.; Michaelis, V.; Kroeker, S.; Zhou, H.; Wiebe, C. R.; Cranswick, L. M. D., Magnetic Properties of the $S=3/2$ Geometrically Frustrated Double Perovskites $\text{La}_2\text{LiRuO}_6$ and Ba_2YRuO_6 . *Phys. Rev. B* **2009**, *80* (13), 134423.
- (33) Michaelis, V. K.; Greer, B. J.; Aharen, T.; Greedan, J. E.; Kroeker, S., Determining Electron Spin-Transfer Mechanisms in Paramagnetic Ba_2YMO_6 (M = Mo, Re, Ru) Double Perovskites by ^{89}Y and ^{137}Ba MAS NMR Spectroscopy. *J. Phys. Chem. C* **2012**, *116* (44), 23646-23652.
- (34) Grey, C. P.; Smith, M. E.; Cheetham, A. K.; Dobson, C. M.; Dupree, R., Yttrium-89 Magic Angle Spinning NMR Study of Rare-Earth Pyrochlores: Paramagnetic Shifts in the Solid State. *J. Am. Chem. Soc.* **1990**, *112* (12), 4670-4675.
- (35) Rosales, B. A.; Men, L.; Cady, S. D.; Hanrahan, M. P.; Rossini, A. J.; Vela, J., Persistent Dopants and Phase Segregation in Organolead Mixed-Halide Perovskites. *Chem. Mater.* **2016**, *28* (19), 6848-6859.
- (36) Maculan, G.; Sheikh, A. D.; Abdelhady, A. L.; Saidaminov, M. I.; Haque, M. A.; Murali, B.; Alarousu, E.; Mohammed, O. F.; Wu, T.; Bakr, O. M., $\text{CH}_3\text{NH}_3\text{PbCl}_3$ Single Crystals: Inverse Temperature Crystallization and Visible-Blind UV-Photodetector. *J. Phys. Chem. Lett.* **2015**, *6* (19), 3781-3786.
- (37) Saidaminov, M. I.; Abdelhady, A. L.; Murali, B.; Alarousu, E.; Burlakov, V. M.; Peng, W.; Dursun, I.; Wang, L.; He, Y.; Maculan, G., et al., High-Quality Bulk Hybrid Perovskite Single Crystals within Minutes by Inverse Temperature Crystallization. *Nat. Commun.* **2015**, *6*, 7586.
- (38) Pines, A.; Gibby, M. G.; Waugh, J. S., Proton-Enhanced Nuclear Induction Spectroscopy. A Method for High Resolution NMR of Dilute Spins in Solids. *J. Chem. Phys.* **1972**, *56* (4), 1776-1777.
- (39) Earl, W. L.; Vanderhart, D. L., Measurement of ^{13}C Chemical Shifts in Solids. *J. Magn. Reson. (1969)* **1982**, *48* (1), 35-54.
- (40) Bennett, A. E.; Rienstra, C. M.; Auger, M.; Lakshmi, K. V.; Griffin, R. G., Heteronuclear Decoupling in Rotating Solids. *J. Chem. Phys.* **1995**, *103* (16), 6951-6958.
- (41) Hahn, E. L., Spin Echoes. *Phys. Rev.* **1950**, *80*, 580.

- (42) Mansfield, P., Multiple-Pulse Nuclear Magnetic Resonance Transients in Solids. *Phys. Rev.* **1965**, *137* (3A), A961-A974.
- (43) Bodart, P. R.; Amoureux, J.-P.; Dumazy, Y.; Lefort, R., Theoretical and Experimental Study of Quadrupolar Echoes for Half-Integer Spins in Static Solid-State NMR. *Mol. Phys.* **2000**, *98* (19), 1545-1551.
- (44) Davis, J. H.; Jeffrey, K. R.; Bloom, M.; Valic, M. I.; Higgs, T. P., Quadrupolar Echo Deuteron Magnetic Resonance Spectroscopy in Ordered Hydrocarbon Chains. *Chem. Phys. Lett.* **1976**, *42* (2), 390-394.
- (45) Massiot, D.; Farnan, I.; Gautier, N.; Trumeau, D.; Trokner, A.; Coutures, J. P., ⁷¹Ga and ⁶⁹Ga Nuclear Magnetic Resonance Study of B-Ga₂O₃: Resolution of Four- and Six-Fold Coordinated Ga Sites in Static Conditions. *Solid State Nucl. Magn. Reson.* **1995**, *4* (4), 241-248.
- (46) Jeener, J.; Meier, B. H.; Bachmann, P.; Ernst, R. R., Investigation of Exchange Processes by Two-Dimensional NMR Spectroscopy. *J. Chem. Phys.* **1979**, *71* (11), 4546-4553.
- (47) Bernard, G. M.; Goyal, A.; Miskolzie, M.; McKay, R.; Wu, Q.; Wasylshen, R. E.; Michaelis, V. K., Methylammonium Lead Chloride: A Sensitive Sample for an Accurate NMR Thermometer. *J. Magn. Reson.* **2017**, *283* (Supplement C), 14-21.
- (48) Eichele, K. *Wsolids NMR Simulation Package*, 1.20.21; Universität Tübingen, 2013.
- (49) Askar, A. M.; Bernard, G. M.; Wiltshire, B.; Shankar, K.; Michaelis, V. K., Multinuclear Magnetic Resonance Tracking of Hydro, Thermal, and Hydrothermal Decomposition of CH₃NH₃PbI₃. *J. Phys. Chem. C* **2017**, *121* (2), 1013-1024.
- (50) Rosales, B. A.; Hanrahan, M. P.; Boote, B. W.; Rossini, A. J.; Smith, E. A.; Vela, J., Lead Halide Perovskites: Challenges and Opportunities in Advanced Synthesis and Spectroscopy. *ACS Energy Lett.* **2017**, *2* (4), 906-914.
- (51) Senocrate, A.; Moudrakovski, I.; Kim, G. Y.; Yang, T.-Y.; Gregori, G.; Grätzel, M.; Maier, J., The Nature of Ion Conduction in Methylammonium Lead Iodide: A Multimethod Approach. *Angew. Chem. Int. Ed.* **2017**, *56* (27), 7755-7759.

- (52) Dybowski, C.; Smith, M. L.; Hepp, M. A.; Gaffney, E. J.; Neue, G.; Perry, D. L., ^{207}Pb NMR Chemical-Shift Tensors of the Lead (II) Halides and the Lead (II) Hydroxyhalides. *Appl. Spectrosc.* **1998**, *52* (3), 426-429.
- (53) Taylor, R. E.; Beckmann, P. A.; Bai, S.; Dybowski, C., ^{127}I and ^{207}Pb Solid-State NMR Spectroscopy and Nuclear Spin Relaxation in PbI_2 : A Preliminary Study. *J. Phys. Chem. C* **2014**, *118* (17), 9143-9153.
- (54) ADF2017, SCM; Theoretical Chemistry, Vrije Universiteit, Amsterdam, The Netherlands, <http://www.scm.com>.
- (55) Fonseca Guerra, C.; Snijders, J. G.; Te Velde, G.; Baerends, E. J., Towards an Order-N DFT Method. *Theor. Chem. Acc.* **1998**, *99* (6), 391-403.
- (56) Te Velde, G.; Bickelhaupt, F. M.; Baerends, E. J.; Fonseca Guerra, C.; van Gisbergen, S. J. A.; Snijders, J. G.; Ziegler, T., Chemistry with ADF. *J. Comput. Chem.* **2001**, *22* (9), 931-967.
- (57) Jaffe, A.; Lin, Y.; Beavers, C. M.; Voss, J.; Mao, W. L.; Karunadasa, H. I., High-Pressure Single-Crystal Structures of 3D Lead-Halide Hybrid Perovskites and Pressure Effects on Their Electronic and Optical Properties. *ACS Cent. Sci.* **2016**, *2* (4), 201-209.
- (58) Lenthe, E. V.; Ehlers, A.; Baerends, E.-J., Geometry Optimizations in the Zero Order Regular Approximation for Relativistic Effects. *J. Chem. Phys.* **1999**, *110* (18), 8943-8953.
- (59) Schreckenbach, G.; Ziegler, T., Calculation of NMR Shielding Tensors Using Gauge-Including Atomic Orbitals and Modern Density Functional Theory. *J. Phys. Chem.* **1995**, *99* (2), 606-611.
- (60) Mason, J., Conventions for the Reporting of Nuclear Magnetic Shielding (or Shift) Tensors Suggested by Participants in the Nato Arw on NMR Shielding Constants at the University of Maryland, College Park, July 1992. *Solid State Nucl. Magn. Reson.* **1993**, *2* (5), 285-288.
- (61) Herzfeld, J.; Berger, A. E., Sideband Intensities in NMR-Spectra of Samples Spinning at the Magic Angle. *J. Chem. Phys.* **1980**, *73* (12), 6021-6030.
- (62) Perdew, J. P.; Burke, K.; Ernzerhof, M., Generalized Gradient Approximation Made Simple. *Phys. Rev. Lett.* **1996**, *77*, 3865.

- (63) Perdew, J. P.; Burke, K.; Ernzerhof, M., Perdew, Burke, and Ernzerhof Reply. *Phys. Rev. Lett.* **1998**, *80*, 891.
- (64) Perdew, J. P.; Burke, K.; Ernzerhof, M., Generalized Gradient Approximation Made Simple [Phys. Rev. Lett. *77*, 3865 (1996)]. *Phys. Rev. Lett.* **1997**, *78*, 1396.
- (65) Clark, S. J.; Segall, M. D.; Pickard, C. J.; Hasnip, P. J.; Probert, M. I. J.; Refson, K.; Payne, M. C., First Principles Methods Using Castep. *Z. Kristallogr. - Cryst. Mater.* **2005**, *220*, 567–570.
- (66) Yates, J. R.; Pickard, C. J.; Mauri, F., Calculation of NMR Chemical Shifts for Extended Systems Using Ultrasoft Pseudopotentials. *Phys. Rev. B* **2007**, *76*, 024401.
- (67) Baikie, T.; Barrow, N. S.; Fang, Y.; Keenan, P. J.; Slater, P. R.; Piltz, R. O.; Gutmann, M.; Mhaisalkar, S. G.; White, T. J., A Combined Single Crystal Neutron/X-Ray Diffraction and Solid-State Nuclear Magnetic Resonance Study of the Hybrid Perovskites $\text{CH}_3\text{NH}_3\text{PbX}_3$ ($X = \text{I, Br and Cl}$). *J. Mater. Chem. A* **2015**, *3* (17), 9298-9307.
- (68) Misra, R. K.; Ciammaruchi, L.; Aharon, S.; Mogilyansky, D.; Etgar, L.; Visoly-Fisher, I.; Katz, E. A., Effect of Halide Composition on the Photochemical Stability of Perovskite Photovoltaic Materials. *ChemSusChem* **2016**, *9* (18), 2572-2577.
- (69) Rehman, W.; McMeekin, D. P.; Patel, J. B.; Milot, R. L.; Johnston, M. B.; Snaith, H. J.; Herz, L. M., Photovoltaic Mixed-Cation Lead Mixed-Halide Perovskites: Links between Crystallinity, Photo-Stability and Electronic Properties. *Energy Environ. Sci.* **2017**, *10* (1), 361-369.
- (70) Roiland, C.; Trippe-Allard, G.; Jemli, K.; Alonso, B.; Ameline, J.-C.; Gautier, R.; Bataille, T.; Le Polles, L.; Deleporte, E.; Even, J., et al., Multinuclear NMR as a Tool for Studying Local Order and Dynamics in $\text{CH}_3\text{NH}_3\text{PbX}_3$ ($X = \text{Cl, Br, I}$) Hybrid Perovskites. *Phys. Chem. Chem. Phys.* **2016**, *18* (39), 27133-27142.
- (71) Wasylishen, R. E.; Knop, O.; Macdonald, J. B., Cation Rotation in Methylammonium Lead Halides. *Solid State Commun.* **1985**, *56* (7), 581-582.
- (72) Bernard, G. M.; Wasylishen, R. E.; Ratcliffe, C. I.; Terskikh, V. V.; Wu, Q.; Buriak, J. M.; Hauger, T., Methylammonium Cation Dynamics in Methylammonium Lead Halide Perovskites—A Solid-State NMR Perspective. *J. Phys. Chem. A* **2018**, *122* (6), 1560-1573.

- (73) Kubicki, D. J.; Prochowicz, D.; Hofstetter, A.; Péchy, P.; Zakeeruddin, S. M.; Grätzel, M.; Emsley, L., Cation Dynamics in Mixed-Cation (MA)_x(FA)_{1-x}PbI₃ Hybrid Perovskites from Solid-State NMR. *J. Am. Chem. Soc.* **2017**, *139* (29), 10055-10061.
- (74) Franssen, W. M. J.; van Es, S. G. D.; Dervişoğlu, R.; de Wijs, G. A.; Kentgens, A. P. M., Symmetry, Dynamics, and Defects in Methylammonium Lead Halide Perovskites. *J. Phys. Chem. Lett.* **2017**, *8* (1), 61-66.
- (75) Fayon, F.; Bessada, C.; Massiot, D.; Farnan, I.; Coutures, J. P., ²⁹Si and ²⁰⁷Pb NMR Study of Local Order in Lead Silicate Glasses. *J. Non-Cryst. Solids* **1998**, *232-234* (Supplement C), 403-408.
- (76) Martin, V.; Wood, B.; Werner-Zwanziger, U.; Zwanziger, J. W., Structural Aspects of the Photoelastic Response in Lead Borate Glasses. *J. Non-Cryst. Solids* **2011**, *357* (10), 2120-2125.
- (77) Keeler, E. G.; Michaelis, V. K.; Colvin, M. T.; Hung, I.; Gor'kov, P. L.; Cross, T. A.; Gan, Z.; Griffin, R. G., ¹⁷O MAS NMR Correlation Spectroscopy at High Magnetic Fields. *J. Am. Chem. Soc.* **2017**, *139* (49), 17953-17963.
- (78) Xu, Q.; Eguchi, T.; Nakayama, H.; Nakamura, N.; Kishita, M., Molecular Motions and Phase Transitions in Solid CH₃NH₃PbX₃ (X = Cl, Br, I) as Studied by NMR and NQR. *Z. Naturforsch. A* **1991**; *46* (3), 240-246.
- (79) Harris, R. K.; Olivieri, A. C., Quadrupolar Effects Transferred to Spin-1/2 Magic-Angle Spinning Spectra of Solids. *Prog. Nucl. Magn. Reson. Spectrosc.* **1992**, *24* (5), 435-456.
- (80) Wrackmeyer, B., Application of ²⁰⁷Pb NMR Parameters. *Annu. Rep. NMR Spectrosc.* **2002**; *47*, 1-37.
- (81) Dybowski, C.; Neue, G., Solid State ²⁰⁷Pb NMR Spectroscopy. *Prog. Nucl. Magn. Reson. Spectrosc.* **2002**, *41*, 153-170.
- (82) Dong, X.; Fang, X.; Lv, M.; Lin, B.; Zhang, S.; Ding, J.; Yuan, N., Improvement of the Humidity Stability of Organic-Inorganic Perovskite Solar Cells Using Ultrathin Al₂O₃ Layers Prepared by Atomic Layer Deposition. *J. Mater. Chem. A* **2015**, *3* (10), 5360-5367.
- (83) Vegard, L., Die Konstitution Der Mischkristalle Und Die Raumfüllung Der Atome. *Z. Phys.* **1921**, *5* (1), 17-26.

- (84) Wasylishen, R. E., Indirect Nuclear Spin-Spin Coupling Tensors. *eMagRes*, John Wiley & Sons, Ltd: 2007.
- (85) Liang, P.-W.; Liao, C.-Y.; Chueh, C.-C.; Zuo, F.; Williams, S. T.; Xin, X.-K.; Lin, J.; Jen, A. K. Y., Additive Enhanced Crystallization of Solution-Processed Perovskite for Highly Efficient Planar-Heterojunction Solar Cells. *Adv. Mater.* **2014**, *26* (22), 3748-3754.
- (86) Manser, J. S.; Saidaminov, M. I.; Christians, J. A.; Bakr, O. M.; Kamat, P. V., Making and Breaking of Lead Halide Perovskites. *Acc. Chem. Res.* **2016**, *49* (2), 330-338.
- (87) Tidhar, Y.; Edri, E.; Weissman, H.; Zohar, D.; Hodes, G.; Cahen, D.; Rytchinski, B.; Kirmayer, S., Crystallization of Methyl Ammonium Lead Halide Perovskites: Implications for Photovoltaic Applications. *J. Am. Chem. Soc.* **2014**, *136* (38), 13249-13256.
- (88) Tauc, J.; Grigorovici, R.; Vancu, A., Optical Properties and Electronic Structure of Amorphous Germanium. *Phys. Status Solidi B* **1966**, *15* (2), 627-637.

Chapter 3

- (1) Zhao, Y.; Zhu, K. Organic-Inorganic Hybrid Lead Halide Perovskites for Optoelectronic and Electronic Applications. *Chem. Soc. Rev.* **2016**, *45* (3), 655–689.
- (2) Kovalenko, M. V; Protesescu, L.; Bodnarchuk, M. I. Properties and Potential Optoelectronic Applications of Lead Halide Perovskite Nanocrystals. *Science* **2017**, *750*, 745–750.
- (3) Sutherland, B. R.; Sargent, E. H. Perovskite Photonic Sources. *Nat. Photonics* **2016**, *10*, 295–302.
- (4) Yakunin, S.; Sytnyk, M.; Kriegner, D.; Shrestha, S.; Richter, M.; Matt, G. J.; Azimi, H.; Brabec, C. J.; Stangl, J.; Kovalenko, M. V; Heiss, W. Detection of X-Ray Photons by Solution-Processed Lead Halide Perovskites. *Nat. Photonics* **2015**, *9*, 444–449.
- (5) Leung, S. F.; Ho, K. T.; Kung, P. K.; Hsiao, V. K. S.; Alshareef, H. N.; Wang, Z. L.; He, J. H. A Self-Powered and Flexible Organometallic Halide Perovskite Photodetector with Very High Detectivity. *Adv. Mater.* **2018**, *30*, 1704611.

- (6) Chen, K.; Deng, X.; Dodekatos, G.; Tüysüz, H. Photocatalytic Polymerization of 3,4-Ethylenedioxythiophene over Cesium Lead Iodide Perovskite Quantum Dots. *J. Am. Chem. Soc.* **2017**, *139* (35), 12267–12273.
- (7) National Renewable Energy Laboratory (NREL). Best Research-Cell Efficiency Chart.
<https://www.nrel.gov/pv/assets/pdfs/best-research-cell-efficiencies.20200104.pdf>
(accessed March 2021).
- (8) Yang, J.; Siempelkamp, B. D.; Liu, D.; Kelly, T. L. Investigation of CH₃NH₃PbI₃ degradation Rates and Mechanisms in Controlled Humidity Environments Using in Situ Techniques. *ACS Nano* **2015**, *9*, 1955–1963.
- (9) Babayigit, A.; Ethirajan, A.; Muller, M.; Conings, B. Toxicity of Organometal Halide Perovskite Solar Cells. *Nat. Mater.* **2016**, *15* (3), 247–251.
- (10) Li, J.; Cao, H.; Jiao, W.; Wang, Q.; Wei, M.; Cantone, I.; Lü, J.; Abate, A. Biological Impact of Lead from Halide Perovskites Reveals the Risk of Introducing a Safe Threshold. *Nat. Commun.* **2020**, *11*, 310.
- (11) Kamarudin, M. A.; Hirotani, D.; Wang, Z.; Hamada, K.; Nishimura, K.; Shen, Q.; Toyoda, T.; Iikubo, S.; Minemoto, T.; Yoshino, K.; Hayase, S. Suppression of Charge Carrier Recombination in Lead-Free Tin Halide Perovskite via Lewis Base Post-Treatment. *J. Phys. Chem. Lett.* **2019**, *10* (17), 5277–5283.
- (12) Stoumpos, C. C.; Malliakas, C. D.; Kanatzidis, M. G. Semiconducting Tin and Lead Iodide Perovskites with Organic Cations: Phase Transitions, High Mobilities, and near-Infrared Photoluminescent Properties. *Inorg. Chem.* **2013**, *52* (15), 9019–9038.
- (13) Song, T. Bin; Yokoyama, T.; Stoumpos, C. C.; Logsdon, J.; Cao, D. H.; Wasielewski, M. R.; Aramaki, S.; Kanatzidis, M. G. Importance of Reducing Vapor Atmosphere in the Fabrication of Tin-Based Perovskite Solar Cells. *J. Am. Chem. Soc.* **2017**, *139* (2), 836–842.
- (14) Konstantakou, M.; Stergiopoulos, T. A Critical Review on Tin Halide Perovskite Solar Cells. *J. Mater. Chem. A* **2017**, *5* (23), 11518–11549.
- (15) Li, B.; Long, R.; Xia, Y.; Mi, Q. All-Inorganic Perovskite CsSnBr₃ as a Thermally Stable, Free-Carrier Semiconductor. *Angew. Chemie Int. Ed.* **2018**, *130* (40), 13338–13342.

- (16) Peedikakkandy, L.; Bhargava, P. Composition Dependent Optical, Structural and Photoluminescence Characteristics of Cesium Tin Halide Perovskites. *RSC Adv.* **2016**, *6* (24), 19857–19860.
- (17) Sabba, D.; Mulmudi, H. K.; Prabhakar, R. R.; Krishnamoorthy, T.; Baikie, T.; Boix, P. P.; Mhaisalkar, S.; Mathews, N. Impact of Anionic Br- Substitution on Open Circuit Voltage in Lead Free Perovskite ($\text{CsSnI}_{3-x}\text{Br}_x$) Solar Cells. *J. Phys. Chem. C* **2015**, *119* (4), 1763–1767.
- (18) McMeekin, D. P.; Sadoughi, G.; Rehman, W.; Eperon, G. E.; Saliba, M.; Hörlantner, M. T.; Haghighirad, A.; Sakai, N.; Korte, L.; Rech, B.; et al. A Mixed-Cation Lead Mixed-Halide Perovskite Absorber for Tandem Solar Cells. *Science* **2016**, *351* (6269), 151–155.
- (19) Jellicoe, T. C.; Richter, J. M.; Glass, H. F. J.; Tabachnyk, M.; Brady, R.; Dutton, S. E.; Rao, A.; Friend, R. H.; Credgington, D.; Greenham, N. C.; et al. Synthesis and Optical Properties of Lead-Free Cesium Tin Halide Perovskite Nanocrystals. *J. Am. Chem. Soc.* **2016**, *138* (9), 2941–2944.
- (20) Yuan, F.; Xi, J.; Dong, H.; Xi, K.; Zhang, W.; Ran, C.; Jiao, B.; Hou, X.; Jen, A. K. Y.; Wu, Z. All-Inorganic Hetero-Structured Cesium Tin Halide Perovskite Light-Emitting Diodes With Current Density Over 900 A cm^{-2} and Its Amplified Spontaneous Emission Behaviors. *Phys. Status Solidi - Rapid Res. Lett.* **2018**, *12* (5), 1800090.
- (21) Yamada, K.; Kuranaga, Y.; Ueda, K.; Goto, S.; Okuda, T.; Furukawa, Y. Phase Transition and Electric Conductivity of ASnCl_3 ($A = \text{Cs}$ and CH_3NH_3). *Bull. Chem. Soc. Jpn.* **1998**, *71* (1), 127–134.
- (22) Mori, M.; Saito, H. An X-Ray Study of Successive Phase Transitions in CsSnBr_3 . *J. Phys. C Solid State Phys.* **1986**, *19* (14), 2391–2401.
- (23) R. E. Wasylshen; Knop, O.; Macdonald, J. B. Cation Rotation in Methylammonium Lead Halides. *Solid State Commun.* **1985**, *56*, 581–582.
- (24) Bernard, G. M.; Wasylshen, R. E.; Ratcliffe, C. I.; Terskikh, V.; Wu, Q.; Buriak, J. M.; Hauger, T. Methylammonium Cation Dynamics in Methylammonium Lead Halide Perovskites: A Solid-State NMR Perspective. *J. Phys. Chem. A* **2018**, *122* (6), 1560–1573.

- (25) Rosales, B. A.; Men, L.; Cady, S. D.; Hanrahan, M. P.; Rossini, A. J.; Vela, J. Persistent Dopants and Phase Segregation in Organolead Mixed-Halide Perovskites. *Chem. Mater.* **2016**, *28* (19), 6848–6859.
- (26) Wouter M. J. Franssen; Es, S. G. D. van; Dervişoğlu, R.; Wijs, G. A. de; Kentgens, A. P. M. Symmetry, Dynamics, and Defects in Methylammonium Lead Halide Perovskites. *J. Phys. Chem. Lett.* **2017**, *8*, 61–66.
- (27) Senocrate, A.; Moudrakovski, I.; Kim, G. Y.; Yang, T.; Gregori, G.; Grätzel, M.; Maier, J. The Nature of Ion Conduction in Methylammonium Lead Iodide: A Multimethod Approach. *Angew. Chemie Int. Ed.* **2017**, *56* (27), 7755–7759.
- (28) Senocrate, A.; Moudrakovski, I.; Acartürk, T.; Merkle, R.; Kim, G. Y.; Starke, U.; Grätzel, M.; Maier, J. Slow CH_3NH_3^+ Diffusion in $\text{CH}_3\text{NH}_3\text{PbI}_3$ under Light Measured by Solid-State NMR and Tracer Diffusion. *J. Phys. Chem. C* **2018**, *122* (38), 21803–21806.
- (29) Karmakar, A.; Askar, A. M.; Bernard, G. M.; Terskikh, V. V.; Ha, M.; Patel, S.; Shankar, K.; Michaelis, V. K. Mechanochemical Synthesis of Methylammonium Lead Mixed-Halide Perovskites: Unraveling the Solid-Solution Behavior Using Solid-State NMR. *Chem. Mater.* **2018**, *30*, 2309–2321.
- (30) Askar, A. M.; Karmakar, A.; Bernard, G. M.; Ha, M.; Terskikh, V. V.; Wiltshire, B. D.; Patel, S.; Fleet, J.; Shankar, K.; Michaelis, V. K. Composition-Tunable Formamidinium Lead Mixed Halide Perovskites via Solvent-Free Mechanochemical Synthesis: Decoding the Pb Environments Using Solid-State NMR Spectroscopy. *J. Phys. Chem. Lett.* **2018**, *9* (10), 2671–2677.
- (31) Kubicki, D. J.; Prochowicz, D.; Hofstetter, A.; Zakeeruddin, S. M.; Grätzel, M.; Emsley, L. Phase Segregation in Cs-, Rb- and K-Doped Mixed-Cation $(\text{MA})_x(\text{FA})_{1-x}\text{PbI}_3$ Hybrid Perovskites from Solid-State NMR. *J. Am. Chem. Soc.* **2017**, *139* (40), 14173–14180.
- (32) Franssen, W. M. J.; Kentgens, A. P. M. Solid-State NMR of Hybrid Halide Perovskites. *Solid State Nucl. Magn. Reson.* **2019**, *100*, 36–44.
- (33) Kubicki, D. J.; Prochowicz, D.; Hofstetter, A.; Sasaki, M.; Yadav, P.; Bi, D.; Pellet, N.; Lewiński, J.; Zakeeruddin, S. M.; Grätzel, M.; Emsley, L. Formation of Stable Mixed Guanidinium-Methylammonium Phases with Exceptionally Long Carrier

Lifetimes for High-Efficiency Lead Iodide-Based Perovskite Photovoltaics. *J. Am. Chem. Soc.* **2018**, *140*, 3345–3351.

(34) Karmakar, A.; Dodd, M. S.; Agnihotri, S.; Ravera, E.; Michaelis, V. K. Cu(II)-Doped Cs₂SbAgCl₆ Double Perovskite: A Lead-Free, Low-Bandgap Material. *Chem. Mater.* **2018**, *30*, 8280–8290.

(35) Karmakar, A.; Bernard, G. M.; Meldrum, A.; Oliynyk, A. O.; Michaelis, V. K. Tailorable Indirect to Direct Bandgap Double Perovskites with Bright White-Light Emission: Decoding Chemical Structure Using Solid-State NMR. *J. Am. Chem. Soc.* **2020**, *142*, 10780–10793.

(36) Aebli, M.; Piveteau, L.; Nazarenko, O.; Benin, B. M.; Krieg, F.; Verel, R.; Kovalenko, M. V. Lead-Halide Scalar Couplings in ²⁰⁷Pb NMR of APbX₃ Perovskites (A = Cs, Methylammonium, Formamidinium; X = Cl, Br, I). *Sci. Rep.* **2020**, *10*, 8229.

(37) Piveteau, L.; Aebli, M.; Yazdani, N.; Millen, M.; Korosec, L.; Krieg, F.; Benin, B. M.; Morad, V.; Piveteau, C.; Shiroka, T.; Comas-Vives, A.; Copéret, C.; Lindenberg, A. M.; Wood, V.; Verel, R.; Kovalenko, M. V. Bulk and Nanocrystalline Cesium Lead-Halide Perovskites as Seen by Halide Magnetic Resonance. *ACS Cent. Sci.* **2020**, *6*, 1138–1149.

(38) Piveteau, L.; Morad, V.; Kovalenko, M. V. Solid-State NMR and NQR Spectroscopy of Lead-Halide Perovskite Materials. *J. Am. Chem. Soc.* **2020**, *142*, 19413–19437.

(39) Chen, Y.; Smock, S. R.; Flintgruber, A. H.; Perras, F. A.; Brutchey, R. L.; Rossini, A. J. Surface Termination of CsPbBr₃ Perovskite Quantum Dots Determined by Solid-State NMR Spectroscopy. *J. Am. Chem. Soc.* **2020**, *142* (13), 6117–6127.

(40) Kubicki, D. J.; Prochowicz, D.; Hofstetter, A.; Walder, B. J.; Emsley, L. ¹¹³Cd Solid-State NMR at 21.1 T Reveals the Local Structure and Passivation Mechanism of Cadmium in Hybrid and All-Inorganic Halide Perovskites. *ACS Energy Lett.* **2020**, *5*, 2964–2971.

(41) Karmakar, A.; Dodd, M. S.; Zhang, X.; Oakley, M. S.; Klobukowski, M.; Michaelis, V. K. Mechanochemical Synthesis of 0D and 3D Cesium Lead Mixed Halide Perovskites. *Chem. Commun.* **2019**, *55*, 5079–5082.

- (42) Prochowicz, D.; Yadav, P.; Saliba, M.; Kubicki, D. J.; Tavakoli, M. M.; Zakeeruddin, S. M.; Lewiński, J.; Emsley, L.; Grätzel, M. One-Step Mechanochemical Incorporation of an Insoluble Cesium Additive for High Performance Planar Heterojunction Solar Cells. *Nano Energy* **2018**, *49*, 523–528.
- (43) Ha, M.; Karmakar, A.; Bernard, G. M.; Basilio, E.; Krishnamurthy, A.; Askar, A. M.; Shankar, K.; Kroeker, S.; Michaelis, V. K. Phase Evolution in Methylammonium Tin Halide Perovskites with Variable Temperature Solid-State ^{119}Sn NMR Spectroscopy. *J. Phys. Chem. C* **2020**, *124*, 15015–15027.
- (44) Kubicki, D. J.; Prochowicz, D.; Salager, E.; Rakhmatullin, A.; Grey, C. P.; Emsley, L.; Stranks, S. D. Local Structure and Dynamics in Methylammonium, Formamidinium and Cesium Tin(II) Mixed-halide Perovskites from ^{119}Sn Solid-state NMR. *J. Am. Chem. Soc.* **2020**, *142*, 7813–7826.
- (45) Yamada, K.; Fujise, K.; Hino, S.; Yamane, Y.; Nakagama, T. Characterization of Sn(II)-Based Perovskites by XRD, DTA, NQR and ^{119}Sn NMR for Photovoltaic Applications. *Chem. Lett.* **2019**, *48* (7), 749–752.
- (46) Wrackmeyer, B. Application of ^{119}Sn NMR Parameters. In *Annu. Rep. NMR Spectrosc.* 1999; Vol. 38, pp 203–264.
- (47) Wolf, P.; Valla, M.; Rossini, A. J.; Comas-Vives, A.; Núñez-Zarur, F.; Malaman, B.; Lesage, A.; Emsley, L.; Copéret, C.; Hermans, I. NMR Signatures of the Active Sites in Sn- β Zeolite. *Angew. Chemie - Int. Ed.* **2014**, *53* (38), 10179–10183.
- (48) Wolf, P.; Valla, M.; Núñez-Zarur, F.; Comas-Vives, A.; Rossini, A. J.; Firth, C.; Kallas, H.; Lesage, A.; Emsley, L.; Copéret, C.; Hermans, I. Correlating Synthetic Methods, Morphology, Atomic-Level Structure, and Catalytic Activity of Sn- β Catalysts. *ACS Catal.* **2016**, *6* (7), 4047–4063.
- (49) Grykałowska, A.; Nowak, B. High-Resolution Solid-State ^{119}Sn and ^{195}Pt NMR Studies of MPtSn Semiconductors (M = Ti, Zr, Hf, Th). *Solid State Nucl. Magn. Reson.* **2005**, *27* (4), 223–227.
- (50) Barrett, J.; Bird, S. R. A.; Donaldson, J. D.; Silver, J. The Mossbauer Effect in Tin(II) Compounds. *J. Chem. Soc. A* **1971**, 3105–3108.
- (51) Poilsen, F. R.; Rasmussen, S. E. Crystal Structure and Phase Transition of Cesium Trichlorostannate(II). *Acta Chem. Scand.* **1970**, *24*, 150–156.

- (52) Oranskaia, A.; Yin, J.; Bakr, O. M.; Brédas, J. L.; Mohammed, O. F. Halogen Migration in Hybrid Perovskites: The Organic Cation Matters. *J. Phys. Chem. Lett.* **2018**, *9*, 5474–5480.
- (53) Hong, Z.; Tan, D.; John, R. A.; Tay, Y. K. E.; Ho, Y. K. T.; Zhao, X.; Sum, T. C.; Mathews, N.; García, F.; Soo, H. Sen. Completely Solvent-Free Protocols to Access Phase-Pure, Metastable Metal Halide Perovskites and Functional Photodetectors from the Precursor Salts. *iScience* **2019**, *16*, 312–325.
- (54) Moran, R. F.; McKay, D.; Tornstrom, P. C.; Aziz, A.; Fernandes, A.; Grau-Crespo, R.; Ashbrook, S. E. Ensemble-Based Modeling of the NMR Spectra of Solid Solutions: Cation Disorder in $Y_2(Sn,Ti)_2O_7$. *J. Am. Chem. Soc.* **2019**, *141* (44), 17838–17846.
- (55) Ashbrook, S. E.; Whittle, K. R.; Lumpkin, G. R.; Farnan, I. ^{89}Y Magic-Angle Spinning NMR of $Y_2Ti_{2-x}Sn_xO_7$ Pyrochlores. *J. Phys. Chem. B* **2006**, *110* (21), 10358–10364.
- (56) Kubicki, D. J.; Saski, M.; Macpherson, S.; Gałkowski, K.; Lewiński, J.; Prochowicz, D.; Titman, J. J.; Stranks, S. D. Halide Mixing and Phase Segregation in Cs_2AgBiX_6 ($X = Cl, Br, \text{ and } I$) Double Perovskites from Cesium-133 Solid-State NMR and Optical Spectroscopy. *Chem. Mater.* **2020**, *32* (19), 8129–8138.
- (57) Sharp, R. R. Rotational Diffusion and Magnetic Relaxation of ^{119}Sn in Liquid $SnCl_4$ and SnI_4 . *J. Chem. Phys.* **1972**, *57* (12), 5321–5330.
- (58) Sharp, R. R. Field Dependence of Nuclear Magnetic Relaxation of ^{119}Sn in $SnCl_4$, $SnBr_4$, and SnI_4 . *J. Chem. Phys.* **1974**, *60* (3), 1149–1157.
- (59) Prochowicz, D.; Franckevicius, M.; Cieslak, A. M.; Zakeeruddin, S. M.; Graetzel, M.; Lewinski, J. Mechano-synthesis of the Hybrid Perovskite $CH_3NH_3PbI_3$: Characterization and the Corresponding Solar Cell Efficiency. *J. Mater. Chem. A* **2015**, *3*, 20772–20777.
- (60) Prochowicz, D.; Yadav, P.; Saliba, M.; Saski, M.; Zakeeruddin, S. M.; Lewiński, J.; Grätzel, M. Mechano-synthesis of Pure Phase Mixed-Cation $MA_xFA_{1-x}PbI_3$ Hybrid Perovskites: Photovoltaic Performance and Electrochemical Properties. *Sustain. Energy Fuels* **2017**, *1* (4), 689–693.

- (61) Friščić, T. Metal-Organic Frameworks: Mechanochemical Synthesis Strategies. In *Encyclopedia of Inorganic and Bioinorganic Chemistry*; Major Reference Works; 2014; p DOI: 10.1002/9781119951438.eibc2202.
- (62) James, S. L.; Adams, C. J.; Bolm, C.; Braga, D.; Collier, P.; Friscic, T.; Grepioni, F.; Harris, K. D. M.; Hyett, G.; Jones, W.; et al. Mechanochemistry: Opportunities for New and Cleaner Synthesis. *Chem. Soc. Rev.* **2012**, *41*, 413–447.
- (63) Chen, B.; Yang, M.; Zheng, X.; Wu, C.; Li, W.; Yan, Y.; Bisquert, J.; Garcia-Belmonte, G.; Zhu, K.; Priya, S. Impact of Capacitive Effect and Ion Migration on the Hysteretic Behavior of Perovskite Solar Cells. *J. Phys. Chem. Lett.* **2015**, *6* (23), 4693–4700.
- (64) Yuan, Y.; Huang, J. Ion Migration in Organometal Trihalide Perovskite and Its Impact on Photovoltaic Efficiency and Stability. *Acc. Chem. Res.* **2016**, *49* (2), 286–293.
- (65) Calado, P.; Telford, A. M.; Bryant, D.; Li, X.; Nelson, J.; O'Regan, B. C.; Barnes, P. R. F. Evidence for Ion Migration in Hybrid Perovskite Solar Cells with Minimal Hysteresis. *Nat. Commun.* **2016**, *7*, 13831.
- (66) Eames, C.; Frost, J. M.; Barnes, P. R. F.; O'Regan, B. C.; Walsh, A.; Islam, M. S. Ionic Transport in Hybrid Lead Iodide Perovskite Solar Cells. *Nat. Commun.* **2015**, *6*, 7497.
- (67) Yamada, K.; Kawaguchi, H.; Matsui, T.; Okuda, T.; Ichiba, S. Structural Phase Transition and Electrical Conductivity of the Perovskite $\text{CH}_3\text{NH}_3\text{Sn}_{1-x}\text{Pb}_x\text{Br}_3$ and CsSnBr_3 . *Bull. Chem. Soc. Jpn.* **1990**, *63*, 2521–2525.
- (68) Onoda-Yamamoto, N.; Matsuo, T.; Suga, H. Thermal, Electric, and Dielectric Properties of $\text{CH}_3\text{NH}_3\text{SnBr}_3$ at Low Temperatures. *J. Chem. Thermodyn.* **1991**, *23* (39), 987–999.
- (69) Futscher, M. H.; Lee, J. M.; McGovern, L.; Muscarella, L. A.; Wang, T.; Haider, M. I.; Fakharuddin, A.; Schmidt-Mende, L.; Ehrler, B. Quantification of Ion Migration in $\text{CH}_3\text{NH}_3\text{PbI}_3$ Perovskite Solar Cells by Transient Capacitance Measurements. *Mater. Horizons* **2019**, *6* (7), 1497–1503.
- (70) Mizusaki, J.; Arai, K.; Fueki, K. Ionic Conduction of the Perovskite-Type Halides. *Solid State Ionics* **1983**, *11*, 203–211.

- (71) Xia, T.; Li, Y.; Huang, L.; Ji, W.; Yang, M.; Zhao, X. Room-Temperature Stable Inorganic Halide Perovskite as Potential Solid Electrolyte for Chloride Ion Batteries. *ACS Appl. Mater. Interfaces* **2020**, *12*, 18634–18641.
- (72) Titilayo A. Kuku. Ionic Conductivity of SnI₂. *Solid State Ionics* **1986**, *20*, 217–222.
- (73) Hoshino, H.; Yamazaki, M.; Nakamura, Y.; Shimoji, M. Ionic Conductivity of Lead Chloride Crystals. *J. Phys. Soc. Japan* **1969**, *26*, 1422–1426.
- (74) Hoshino, H.; Yokose, S.; Shimoji, M. Ionic Conductivity of Lead Bromide Crystals. *J. Solid State Chem.* **1973**, *7*, 1–6.
- (75) Walsh, A.; Scanlon, D. O.; Chen, S.; Gong, X. G.; Wei, S. H. Self-Regulation Mechanism for Charged Point Defects in Hybrid Halide Perovskites. *Angew. Chemie - Int. Ed.* **2015**, *54* (6), 1791–1794.
- (76) Indris, S.; Scheuermann, M.; Becker, S. M.; Šepelák, V.; Kruk, R.; Suffner, J.; Gyger, F.; Feldmann, C.; Ulrich, A. S.; Hahn, H. Local Structural Disorder and Relaxation in SnO₂ Nanostructures Studied by ¹¹⁹Sn MAS NMR and ¹¹⁹Sn Mössbauer Spectroscopy. *J. Phys. Chem. C* **2011**, *115* (14), 6433–6437.
- (77) Barnes, R. G. Temperature Dependence of the Isotropic and Anisotropic Knight Shift in Polycrystalline Cadmium and β-Tin. *J. Phys. Chem. Solids* **1966**, *27*, 567–573.

Chapter 4

- (1) Kojima, A.; Teshima, K.; Shirai, Y.; Miyasaka, T. Organometal Halide Perovskites as Visible-Light Sensitizers for Photovoltaic Cells. *J. Am. Chem. Soc.* **2009**, *131*, 6050–6051.
- (2) Green, M. A.; Hishikawa, Y.; Warta, W.; Dunlop, E. D.; Levi, D. H.; Hohl-Ebinger, J.; Ho-Baillie, A. W. H. Solar Cell Efficiency Tables (version 50). *Prog. Photovoltaics Res. Appl.* **2017**, *25*, 668–676.
- (3) Tan, Z.-K.; Moghaddam, R. S.; Lai, M. L.; Docampo, P.; Higler, R.; Deschler, F.; Price, M.; Sadhanala, A.; Pazos, L. M.; Credgington, D.; et al. Bright Light-Emitting Diodes Based on Organometal Halide Perovskite. *Nat. Nanotechnol.* **2014**, *9*, 687–692.
- (4) Zhu, H.; Fu, Y.; Meng, F.; Wu, X.; Gong, Z.; Ding, Q.; Gustafsson, M. V.; Trinh,

- M. T.; Jin, S.; Zhu, X. Y. Lead Halide Perovskite Nanowire Lasers with Low Lasing Thresholds and High Quality Factors. *Nat. Mater.* **2015**, *14*, 636–642.
- (5) Xing, G.; Mathews, N.; Lim, S. S.; Yantara, N.; Liu, X.; Sabba, D.; Grätzel, M.; Mhaisalkar, S.; Sum, T. C. Low-Temperature Solution-Processed Wavelength-Tunable Perovskites for Lasing. *Nat. Mater.* **2014**, *13*, 476–480.
- (6) Jeon, N. J.; Noh, J. H.; Yang, W. S.; Kim, Y. C.; Ryu, S.; Seo, J.; Seok, S. I. Compositional Engineering of Perovskite Materials for High-Performance Solar Cells. *Nature* **2015**, *517*, 476–480.
- (7) Liu, M.; Johnston, M. B.; Snaith, H. J. Efficient Planar Heterojunction Perovskite Solar Cells by Vapour Deposition. *Nature* **2013**, *501*, 395–398.
- (8) Shi, D.; Adinolfi, V.; Comin, R.; Yuan, M.; Alarousu, E.; Buin, A.; Chen, Y.; Hoogland, S.; Rothenberger, A.; Katsiev, K.; et al. Low Trap-State Density and Long Carrier Diffusion in Organolead Trihalide Perovskite Single Crystals. *Science* **2015**, *347*, 519–522.
- (9) Yang, J.; Siempelkamp, B. D.; Mosconi, E.; De Angelis, F.; Kelly, T. L. Origin of the Thermal Instability in $\text{CH}_3\text{NH}_3\text{PbI}_3$ Thin Films Deposited on ZnO. *Chem. Mater.* **2015**, *27*, 4229–4236.
- (10) Berhe, T. A.; Su, W.-N.; Chen, C.-H.; Pan, C.-J.; Cheng, J.-H.; Chen, H.-M.; Tsai, M.-C.; Chen, L.-Y.; Dubale, A. A.; Hwang, B.-J. Organometal Halide Perovskite Solar Cells: Degradation and Stability. *Energy Environ. Sci.* **2016**, *9*, 323–356.
- (11) Needleman, H. Lead Poisoning. *Annu. Rev. Med.* **2004**, *55*, 209–222.
- (12) Babayigit, A.; Ethirajan, A.; Muller, M.; Conings, B. Toxicity of Organometal Halide Perovskite Solar Cells. *Nat. Mater.* **2016**, *15*, 247–251.
- (13) Herrera, P. A. M.; Kamat, P. V. Transformation of the Excited State and Photovoltaic Efficiency of $\text{CH}_3\text{NH}_3\text{PbI}_3$ Perovskite upon Controlled Exposure to Humidified Air. *J. Am. Chem. Soc.* **2015**, *137*, 1530–1538.
- (14) Leguy, M. A.; Hu, Y.; Campoy-quiles, M.; Alonso, M. I.; Weber, O. J.; Azarhoosh, P.; Schilfgaarde, M. Van; Weller, M. T.; Bein, T.; Nelson, J.; et al. Reversible Hydration of $\text{CH}_3\text{NH}_3\text{PbI}_3$ in Films, Single Crystals, and Solar Cells. *Chem. Mater.* **2015**, *27*, 3397–3407.

- (15) Askar, A. M.; Bernard, G. M.; Wiltshire, B.; Shankar, K.; Michaelis, V. K. Multinuclear Magnetic Resonance Tracking of Hydro, Thermal, and Hydrothermal Decomposition of $\text{CH}_3\text{NH}_3\text{PbI}_3$. *J. Phys. Chem. C* **2017**, *121*, 1013–1024.
- (16) Saliba, M.; Matsui, T.; Seo, J. Y.; Domanski, K.; Correa-Baena, J. P.; Nazeeruddin, M. K.; Zakeeruddin, S. M.; Tress, W.; Abate, A.; Hagfeldt, A.; et al. Cesium-Containing Triple Cation Perovskite Solar Cells: Improved Stability, Reproducibility and High Efficiency. *Energy Environ. Sci.* **2016**, *9*, 1989–1997.
- (17) Li, Z.; Yang, M.; Park, J. S.; Wei, S. H.; Berry, J. J.; Zhu, K. Stabilizing Perovskite Structures by Tuning Tolerance Factor: Formation of Formamidinium and Cesium Lead Iodide Solid-State Alloys. *Chem. Mater.* **2016**, *28*, 284–292.
- (18) Zhang, M.; Yun, J. S.; Ma, Q.; Zheng, J.; Lau, C. F. J.; Deng, X.; Kim, J.; Kim, D.; Seidel, J.; Green, M. A.; et al. High-Efficiency Rubidium-Incorporated Perovskite Solar Cells by Gas Quenching. *ACS Energy Lett.* **2017**, *2*, 438–444.
- (19) Eperon, G. E.; Leijtens, T.; Bush, K. A.; Green, T.; Wang, J. T.-W.; McMeekin, D. P.; Volonakis, G.; Milot, R. L.; Slotcavage, D. J.; Belisle, R.; et al. Perovskite-Perovskite Tandem Photovoltaics with Ideal Bandgaps. *Science* **2016**, *354*, 861–865.
- (20) Tan, H.; Jain, A.; Voznyy, O.; Lan, X.; Arquer, F. P. G. de; Fan, J. Z.; Quintero-Bermudez, R.; Yuan, M.; Zhang, B.; Zhao, Y.; et al. Efficient and Stable Solution Processed Planar Perovskite Solar Cell via Contact Passivation. *Science* **2017**, *355*, 722–726.
- (21) Lau, C. F. J.; Zhang, M.; Deng, X.; Zheng, J.; Bing, J.; Ma, Q.; Kim, J.; Hu, L.; Green, M. A.; Huang, S.; et al. Strontium-Doped Low-Temperature-Processed CsPbI_2Br Perovskite Solar Cells. *ACS Energy Lett.* **2017**, *2*, 2319–2325.
- (22) Zuo, F.; Williams, S. T.; Liang, P. W.; Chueh, C. C.; Liao, C. Y.; Jen, A. K. Y. Binary-Metal Perovskites Toward High-Performance Planar-Heterojunction Hybrid Solar Cells. *Adv. Mater.* **2014**, *26*, 6454–6460.
- (23) Klug, M. T.; Osherov, A.; Haghghirad, A. A.; Stranks, S. D.; Brown, P. R.; Bai, S.; Wang, J. T. W.; Dang, X.; Bulović, V.; Snaith, H. J.; et al. Tailoring Metal Halide Perovskites through Metal Substitution: Influence on Photovoltaic and Material Properties. *Energy Environ. Sci.* **2017**, *10*, 236–246.
- (24) Abdelhady, A. L.; Saidaminov, M. I.; Murali, B.; Adinolfi, V.; Voznyy, O.;

- Katsiev, K.; Alarousu, E.; Comin, R.; Dursun, I.; Sinatra, L.; et al. Heterovalent Dopant Incorporation for Bandgap and Type Engineering of Perovskite Crystals. *J. Phys. Chem. Lett.* **2016**, *7*, 295–301.
- (25) Levchuk, I.; Osvet, A.; Tang, X.; Brandl, M.; Perea, J. D.; Hoegl, F.; Matt, G. J.; Hock, R.; Batentschuk, M.; Brabec, C. J. Brightly Luminescent and Color-Tunable Formamidinium Lead Halide Perovskite $FAPbX_3$ ($X = Cl, Br, I$) Colloidal Nanocrystals. *Nano Lett.* **2017**, *17*, 2765–2770.
- (26) Hu, Y.; Bai, F.; Liu, X.; Ji, Q.; Miao, X.; Qiu, T.; Zhang, S. Bismuth Incorporation Stabilized α - $CsPbI_3$ for Fully Inorganic Perovskite Solar Cells. *ACS Energy Lett.* **2017**, *2*, 2219–2227.
- (27) Lee, J.-W., Kim, D.-H., Kim, H.-S., Seo, S.-W., Cho, S.M., Park, N.-G. Formamidinium and Cesium Hybridization for Photo- and Moisture-Stable Perovskite Solar Cell. *Adv. Energy Mater.* **2015**, *5*, 1501310.
- (28) Dang, Y.; Zhou, Y.; Liu, X.; Ju, D.; Xia, S.; Xia, H.; Tao, X. Formation of Hybrid Perovskite Tin Iodide Single Crystals by Top-Seeded Solution Growth. *Angew. Chem. Int. Ed.* **2016**, *55*, 3447–3450.
- (29) Babu, R.; Giribabu, L.; Singh, S. P. Recent Advances in Halide-Based Perovskite Crystals and their Optoelectronic Applications. *Cryst. Growth Des.* **2018**, *18*, 2645–2664.
- (30) Slavney, A. H.; Hu, T.; Lindenberg, A. M.; Karunadasa, H. I. A Bismuth-Halide Double Perovskite with Long Carrier Recombination Lifetime for Photovoltaic Applications. *J. Am. Chem. Soc.* **2016**, *138*, 2138–2141.
- (31) Volonakis, G.; Haghighirad, A. A.; Milot, R. L.; Sio, W. H.; Filip, M. R.; Wenger, B.; Johnston, M. B.; Herz, L. M.; Snaith, H. J.; Giustino, F. $Cs_2InAgCl_6$: A New Lead-Free Halide Double Perovskite with Direct Band Gap. *J. Phys. Chem. Lett.* **2017**, *8*, 772–778.
- (32) McClure, E. T.; Ball, M. R.; Windl, W.; Woodward, P. M. Cs_2AgBiX_6 ($X = Br, Cl$): New Visible Light Absorbing, Lead-Free Halide Perovskite Semiconductors. *Chem. Mater.* **2016**, *28*, 1348–1354.
- (33) Filip, M. R.; Liu, X.; Miglio, A.; Hautier, G.; Giustino, F. Phase Diagrams and Stability of Lead-Free Halide Double Perovskites $Cs_2BB'X_6$: $B = Sb$ and Bi , $B' = Cu$,

- Ag, and Au, and X = Cl, Br, and I. *J. Phys. Chem. C* **2018**, *122*, 158–170.
- (34) Jain, A.; Voznyy, O.; Sargent, E. H. High-Throughput Screening of Lead-Free Perovskite-like Materials for Optoelectronic Applications. *J. Phys. Chem. C* **2017**, *121*, 7183–7187.
- (35) Wei, F.; Deng, Z.; Sun, S.; Zhang, F.; Evans, D. M.; Kieslich, G.; Tominaka, S.; Carpenter, M. A.; Zhang, J.; Bristowe, P. D.; Cheetham, A. K. Synthesis and Properties of a Lead-Free Hybrid Double Perovskite: $(\text{CH}_3\text{NH}_3)_2\text{AgBiBr}_6$. *Chem. Mater.* **2017**, *29*, 1089–1094.
- (36) Du, K. Z.; Meng, W.; Wang, X.; Yan, Y.; Mitzi, D. B. Bandgap Engineering of Lead-Free Double Perovskite $\text{Cs}_2\text{AgBiBr}_6$ through Trivalent Metal Alloying. *Angew. Chem. Int. Ed.* **2017**, *56*, 8158–8162.
- (37) Tran, T. T.; Panella, J. R.; Chamorro, J. R.; Morey, J. R.; McQueen, T. M. Designing Indirect-Direct Bandgap Transitions in Double Perovskites. *Mater. Horizons* **2017**, *4*, 688–693.
- (38) Slavney, A. H.; Leppert, L.; Bartesaghi, D.; Gold-Parker, A.; Toney, M. F.; Savenije, T. J.; Neaton, J. B.; Karunadasa, H. I. Defect-Induced Band-Edge Reconstruction of a Bismuth-Halide Double Perovskite for Visible-Light Absorption. *J. Am. Chem. Soc.* **2017**, *139*, 5015–5018.
- (39) Deng, W.; Deng, Z.; He, J.; Wang, M.; Chen, Z.; Wei, S.; Feng, H.-J. Synthesis of $\text{Cs}_2\text{AgSbCl}_6$ and Improved Optoelectronic Properties of $\text{Cs}_2\text{AgSbCl}_6/\text{TiO}_2$ Heterostructure Driven by the Interface Effect for Lead-Free Double Perovskites Solar Cells. *Appl. Phys. Lett.* **2017**, *111*, 151602.
- (40) Bekenstein, Y.; Dahl, J. C.; Huang, J.; Osowiecki, W. T.; Swabeck, J. K.; Chan, E. M.; Yang, P.; Alivisatos, A. P. The Making and Breaking of Lead-Free Double Perovskite Nanocrystals of Cesium Silver-Bismuth Halide Compositions. *Nano Lett.* **2018**, *18*, 3502–3508.
- (41) Creutz, S. E.; Crites, E. N.; De Siena, M. C.; Gamelin, D. R. Colloidal Nanocrystals of Lead-Free Double-Perovskite (Elpasolite) Semiconductors: Synthesis and Anion Exchange to Access New Materials. *Nano Lett.* **2018**, *18*, 1118–1123.
- (42) Connor, B. A.; Leppert, L.; Smith, M. D.; Neaton, J. B.; Karunadasa, H. I. Layered Halide Double Perovskites: Dimensional Reduction of $\text{Cs}_2\text{AgBiBr}_6$. *J. Am.*

Chem. Soc. **2018**, *140*, 5235–5240.

(43) Pantaler, M.; Cho, K. T.; Queloz, V.; Garcia Benito, I.; Fettkenhauer, C.; Anusca, I.; Nazeeruddin, M. K.; Lupascu, D. C.; Grancini, G. Hysteresis-Free Lead-Free Double Perovskite Solar Cells by Interface Engineering. *ACS Energy Lett.* **2018**, *3*, 1781–1786.

(44) Greul, E.; Petrus, M. L.; Binek, A.; Docampo, P.; Bein, T. Highly Stable, Phase Pure Cs₂AgBiBr₆ Double Perovskite Thin Films for Optoelectronic Applications. *J. Mater. Chem. A* **2017**, *5*, 19972–19981.

(45) Slavney, A. H.; Leppert, L.; Saldivar Valdes, A.; Bartesaghi, D.; Savenije, T. J.; Neaton, J. B.; Karunadasa, H. Small-Bandgap Halide Double Perovskites. *Angew. Chem. Int. Ed.* **2018**, *57*, 12765–12770.

(46) Vargas, B.; Ramos, E.; Pérez-Gutiérrez, E.; Alonso, J. C.; Solis-Ibarra, D. A Direct Bandgap Copper-Antimony Halide Perovskite. *J. Am. Chem. Soc.* **2017**, *139*, 9116–9119.

(47) Singhal, N.; Chakraborty, R.; Ghosh, P.; Nag, A. Low-Bandgap Cs₄CuSb₂Cl₁₂ Layered Double Perovskite: Synthesis, Reversible Thermal Changes, and Magnetic Interaction. *Chem. Asian J.* **2018**, *13*, 2085–2092.

(48) Abram, R. A.; Rees, G. J.; Wilson, B. L. H. Heavily Doped Semiconductors and Devices. *Adv. Phys.* **1978**, *27*, 799–892.

(49) Piao, Y.; Meany, B.; Powell, L. R.; Valley, N.; Kwon, H.; Schatz, G. C.; Wang, Y. Brightening of Carbon Nanotube Photoluminescence through the Incorporation of sp³ Defects. *Nat. Chem.* **2013**, *5*, 840–845.

(50) Misra, R. K.; Aharon, S.; Li, B.; Mogilyansky, D.; Visoly-Fisher, I.; Etgar, L.; Katz, E. A. Temperature- and Component-Dependent Degradation of Perovskite Photovoltaic Materials under Concentrated Sunlight. *J. Phys. Chem. Lett.* **2015**, *6*, 326–330.

(51) Shao, H.; Bai, X.; Cui, H.; Pan, G.; Jing, P.; Qu, S.; Zhu, J.; Zhai, Y.; Dong, B.; Song, H. White Light Emission in Bi³⁺/Mn²⁺ Ion Co-Doped CsPbCl₃ Perovskite Nanocrystals. *Nanoscale* **2018**, *10*, 1023–1029.

(52) Das Adhikari, S.; Dutta, A.; Dutta, S. K.; Pradhan, N. Layered Perovskites L₂(Pb_{1-x}Mn_x)Cl₄ to Mn-Doped CsPbCl₃ Perovskite Platelets. *ACS Energy Lett.* **2018**,

3, 1247–1253.

(53) Meinardi, F.; Akkerman, Q. A.; Bruni, F.; Park, S.; Mauri, M.; Dang, Z.; Manna, L.; Brovelli, S. Doped Halide Perovskite Nanocrystals for Reabsorption-Free Luminescent Solar Concentrators. *ACS Energy Lett.* **2017**, *2*, 2368–2377.

(54) Zhou, Y.; Chen, J.; Bakr, O. M.; Sun, H. Metal-Doped Lead Halide Perovskites: Synthesis, Properties, and Optoelectronic Applications. *Chem. Mater.* **2018**, *30*, 6589–6613.

(55) K., N. N.; Nag, A. Synthesis and Luminescence of Mn-Doped Cs₂AgInCl₆ Double Perovskites. *Chem. Commun.* **2018**, *54*, 5205–5208.

(56) Yin, W.; Shi, T.; Yan, Y. Superior Photovoltaic Properties of Lead Halide Perovskites: Insights from First-Principles Theory. *J. Phys. Chem. C* **2015**, *119*, 5253–5264.

(57) Knop, O.; Wasylshen, R. E.; White, M. A.; Cameron, T. S.; Van Oort, M. J. M. Alkylammonium Lead Halides. Part 2. CH₃NH₃PbX₃ (X=Cl, Br, I) Perovskites: Cuboctahedral Halide Cages with Isotropic Cation Reorientation. *Can. J. Chem.* **1990**, *68*, 412–422.

(58) Kubicki, D. J.; Prochowicz, D.; Hofstetter, A.; Zakeeruddin, S. M.; Grätzel, M.; Emsley, L. Phase Segregation in Potassium-Doped Lead Halide Perovskites from ³⁹K Solid-State NMR at 21.1 T. *J. Am. Chem. Soc.* **2018**, *140*, 7232–7238.

(59) Senocrate, A.; Moudrakovski, I.; Kim, G. Y.; Yang, T.; Gregori, G.; Grätzel, M.; Maier, J. The Nature of Ion Conduction in Methylammonium Lead Iodide: A Multimethod Approach. *Angew. Chem. Int. Ed.* **2017**, *56*, 7755–7759.

(60) Fabini, D. H.; Siaw, T. A.; Stoumpos, C. C.; Laurita, G.; Olds, D.; Page, K.; Hu, J. G.; Kanatzidis, M. G.; Han, S.; Seshadri, R. Universal Dynamics of Molecular Reorientation in Hybrid Lead Iodide Perovskites. *J. Am. Chem. Soc.* **2017**, *139*, 16875–16884.

(61) Rosales, B. A.; Men, L.; Cady, S. D.; Hanrahan, M. P.; Rossini, A. J.; Vela, J. Persistent Dopants and Phase Segregation in Organolead Mixed-Halide Perovskites. *Chem. Mater.* **2016**, *28*, 6848–6859.

(62) Franssen, W. M. J.; Van Es, S. G. D.; Dervişolu, R.; De Wijs, G. A.; Kentgens, A. P. M. Symmetry, Dynamics, and Defects in Methylammonium Lead Halide

- Perovskites. *J. Phys. Chem. Lett.* **2017**, *8*, 61–66.
- (63) Prochowicz, D.; Yadav, P.; Saliba, M.; Kubicki, D. J.; Tavakoli, M. M.; Zakeeruddin, S. M.; Lewiński, J.; Emsley, L.; Grätzel, M. One-Step Mechanochemical Incorporation of an Insoluble Cesium Additive for High Performance Planar Heterojunction Solar Cells. *Nano Energy* **2018**, *49*, 523–528.
- (64) Wasylishen, R. E.; Knop, O.; Macdonald, J. B. Cation Rotation in Methylammonium Lead Halides. *Solid State Commun.* **1985**, *56*, 581–582.
- (65) Karmakar, A.; Askar, A. M.; Bernard, G. M.; Terskikh, V. V.; Ha, M.; Patel, S.; Shankar, K.; Michaelis, V. K. Mechanochemical Synthesis of Methylammonium Lead Mixed-Halide Perovskites: Unraveling the Solid-Solution Behavior Using Solid-State NMR. *Chem. Mater.* **2018**, *30*, 2309–2321.
- (66) Askar, A. M.; Karmakar, A.; Bernard, G. M.; Ha, M.; Terskikh, V. V.; Wiltshire, B. D.; Patel, S.; Fleet, J.; Shankar, K.; Michaelis, V. K. Composition-Tunable Formamidinium Lead Mixed Halide Perovskites via Solvent-Free Mechanochemical Synthesis: Decoding the Pb Environments Using Solid-State NMR Spectroscopy. *J. Phys. Chem. Lett.* **2018**, *9*, 2671–2677.
- (67) Bernard, G. M.; Goyal, A.; Miskolzie, M.; McKay, R.; Wu, Q.; Wasylishen, R. E.; Michaelis, V. K. Methylammonium Lead Chloride: A Sensitive Sample for an Accurate NMR Thermometer. *J. Magn. Reson.* **2017**, *283*, 14–21.
- (68) Bernard, G. M.; Wasylishen, R. E.; Ratcliffe, C. I.; Terskikh, V.; Wu, Q.; Buriak, J. M.; Hauger, T. Methylammonium Cation Dynamics in Methylammonium Lead Halide Perovskites: A Solid-State NMR Perspective. *J. Phys. Chem. A* **2018**, *122*, 1560–1573.
- (69) Kubicki, D. J.; Prochowicz, D.; Hofstetter, A.; Sasaki, M.; Yadav, P.; Bi, D.; Pellet, N.; Lewiński, J.; Zakeeruddin, S. M.; Grätzel, M.; et al. Formation of Stable Mixed Guanidinium-Methylammonium Phases with Exceptionally Long Carrier Lifetimes for High-Efficiency Lead Iodide-Based Perovskite Photovoltaics. *J. Am. Chem. Soc.* **2018**, *140*, 3345–3351.
- (70) Kubicki, D. J.; Prochowicz, D.; Hofstetter, A.; Zakeeruddin, S. M.; Grätzel, M.; Emsley, L. Phase Segregation in Cs-, Rb- and K-Doped Mixed-Cation (MA)_x(FA)_{1-x}PbI₃ Hybrid Perovskites from Solid-State NMR. *J. Am. Chem. Soc.*

2017, *139*, 14173–14180.

(71) Kubicki, D. J.; Prochowicz, D.; Hofstetter, A.; Péchy, P.; Zakeeruddin, S. M.; Grätzel, M.; Emsley, L. Cation Dynamics in Mixed-Cation (MA)_x(FA)_{1-x}PbI₃ Hybrid Perovskites from Solid-State NMR. *J. Am. Chem. Soc.* **2017**, *139*, 10055–10061.

(72) Yang, M.; Wen-chen, Z.; Lv, H. Defect Structure and Spin-Hamiltonian Parameters for the CuCl₆⁴⁻ Cluster in the Tetragonal RbCdCl₃:Cu²⁺ crystal. *Spectrochim. Acta Part A Mol. Biomol. Spectrosc.* **2009**, *72*, 515–517.

(73) Wei, M.; Willett, R. D.; Hipps, K. W. EPR, Electronic, and Vibrational Spectra of the CuCl₆⁴⁻ Anion in [tris(2-aminoethyl)amineH₄]₂ [CuCl₆]Cl₄ · 2H₂O and Crystal Structure of the Complex. *Inorg. Chem.* **1996**, *35*, 5300–5303.

(74) McDonald, R. G.; Hitchman, M. A. Electronic, EPR and Vibrational Spectra of the Hexachlorocuprate(4-) Ion. *Inorg. Chem.* **1989**, *28*, 3996–4001.

(75) Stratemeier, H.; Wagner, B.; Krausz, E. R.; Linder, R.; Schmidtke, H.; Pebler, J.; Hatfield, W. E.; ter Haar, L.; Reinen, D.; Hitchman, M. A. EPR and Electronic Spectra of (3-chloroanilinium)₈[CuCl₆]Cl₄: Evidence for Tetragonally Elongated CuCl₆⁴⁻ Ions with the Long Axis Disordered in 2-Dimensions. *Inorg. Chem.* **1994**, *33*, 2320–2329.

(76) Shannon, B. Y. R. D.; H, M.; Baur, N. H.; Gibbs, O. H.; Eu, M.; Cu, V. Revised Effective Ionic Radii and Systematic Studies of Interatomic Distances in Halides and Chalcogenides. *Acta Cryst.* **1976**, *A32*, 751–767.

(77) Pramanick, A.; Wang, X. P.; Hoffmann, C.; Diallo, S. O.; Jørgensen, M. R. V.; Wang, X. Microdomain Dynamics in Single-Crystal BaTiO₃ during Paraelectric-Ferroelectric Phase Transition Measured with Time-of-Flight Neutron Scattering. *Phys. Rev. B* **2015**, *92*, 174103.

(78) Nayak, P.; Sendner, M.; Wenger, B.; Wang, Z.; Sharma, K.; Ramadan, A. J.; Lovrincic, R.; Pucci, A.; Madhu, P. K.; Snaith, H. J. The Impact of Bi³⁺ Heterovalent Doping in Organic-Inorganic Metal Halide Perovskite Crystals. *J. Am. Chem. Soc.* **2018**, *140*, 574–577.

(79) Vargas, B., Torres-Cadena, R., Rodriguez-Hernández, J. Gembicky, M., Xie, H., Jiménez-Mier, J., Liu, Y.; Menéndez-Proupin, E.; Dunbar, K. R.; Lopez, N., et al. Optical, Electronic, and Magnetic Engineering of (111) Layered Halide Perovskites.

- Chem. Mater.* **2018**, *30*, 5315-5321.
- (80) Cortecchia, D.; Dewi, H. A.; Yin, J.; Bruno, A.; Chen, S.; Baikie, T.; Boix, P. P.; Grätzel, M.; Mhaisalkar, S.; Soci, C.; et al. Lead-Free MA₂CuCl_xBr_{4-x} Hybrid Perovskites. *Inorg. Chem.* **2016**, *55*, 1044–1052.
- (81) Fedeli, P.; Gazza, F.; Calestani, D.; Ferro, P.; Besagni, T.; Zappettini, A.; Calestani, G.; Marchi, E.; Ceroni, P.; Mosca, R. Influence of the Synthetic Procedures on the Structural and Optical Properties of Mixed-Halide (Br, I) Perovskite Films. *J. Phys. Chem. C* **2015**, *119*, 21304–21313.
- (82) Volonakis, G.; Filip, M. R.; Haghighirad, A. A.; Sakai, N.; Wenger, B.; Snaith, H. J.; Giustino, F. Lead-Free Halide Double Perovskites via Heterovalent Substitution of Noble Metals. *J. Phys. Chem. Lett.* **2016**, *7*, 1254–1259.
- (83) Sunkara, S.; Vendra, V. K.; Jasinski, J. B.; Deutsch, T.; Andriotis, A. N.; Rajan, K.; Menon, M.; Sunkara, M. New Visible Light Absorbing Materials for Solar Fuels, Ga(Sb_x)N_{1-x}. *Adv. Mater.* **2014**, *26*, 2878–2882.
- (84) Weyers, M.; Sato, M.; Ando, H. Red Shift of Photoluminescence and Absorption in Dilute GaAsN Alloy Layers. *Jpn. J. Appl. Phys.* **1992**, *31*, L853-L855.
- (85) Faucher, A.; Terskikh, V. V.; Wasylishen, R. E. Assessing Distortion of the AF₆(A=As, Sb) Octahedra in Solid Hexafluorometallates (V) via NMR Spectroscopy. *Can. J. Chem.* **2015**, *93*, 938–944.
- (86) Harris, R. K.; Becker, E. D.; de Menrzes, S. M. C.; Goodfellow, R.; Granger, P. Commission on Molecular Structure and Spectroscopy. *Pure Appl. Chem.* **2001**, *73*, 1795–1818.
- (87) Bertini, I.; Luchinat, C.; Parigi, G.; Ravera, E. *NMR of Paramagnetic Molecules*; Elsevier; 2016.
- (88) Van Vleck, J. H. The Theory of Electric and Magnetic Susceptibilities. *Oxford University Press*; 1932; p 226.
- (89) Kurland, R. J.; Mcgarvey, B. R. Isotropic NMR Shifts in Transition Metal Complexes: The Calculation of the Fermi Contact and Pseudocontact Terms. *J. Magn. Reson.* **1970**, *2*, 286–301.
- (90) Walder, B. J.; Patterson, A. M.; Baltisberger, J. H.; Grandinetti, P. J. Hydrogen Motional Disorder in Crystalline Iron Group Chloride Dihydrates. *J. Chem. Phys.*

2018, *149*, 084503.

- (91) Michaelis, V. K.; Greer, B. J.; Aharen, T.; Greedan, J. E.; Kroeker, S. Determining Electron Spin-Transfer Mechanisms in Paramagnetic Ba₂YMO₆ (M = Mo, Re, Ru) Double Perovskites by ⁸⁹Y and ¹³⁷Ba MAS NMR Spectroscopy. *J. Phys. Chem. C* **2012**, *116*, 23646–23652.
- (92) Ceder, D.; Menetrier, M.; P, G. C.; Delmas, C.; Ceder, G. Understanding the NMR Shifts in Paramagnetic Transition Metal Oxides Using Density Functional Theory Calculations. *Phys. Rev. B* **2003**, *67*, 174103.
- (93) La Mar, G. N.; Horrocks, W. E.; Holm, R. H. *NMR of Paramagnetic Molecules*; Academic Press Inc., 1973.
- (94) Wickramasinghe, N. P.; Ishii, Y. Sensitivity Enhancement, Assignment, and Distance Measurement in ¹³C Solid-State NMR Spectroscopy for Paramagnetic Systems under Fast Magic Angle Spinning. *J. Magn. Reson.* **2006**, *181*, 233–243.
- (95) Ooms, K.; Polenova, T.; Shough, A.; Doren, D. J.; Nash, M. J.; Lobo, R. F. Identification of Mixed Valence Vanadium in ETS-10 Using Electron Paramagnetic Resonance, ⁵¹V Solid-State Nuclear Magnetic Resonance, and Density Functional Theory Studies. *J. Phys. Chem. C* **2009**, *113*, 10477–10484.
- (96) Kermarrec, E.; Marjerrison, C. A.; Thompson, C. M.; Maharaj, D. D.; Levin, K.; Kroeker, S.; Granroth, G. E.; Flacau, R.; Yamani, Z.; Greedan, J. E.; et al. Frustrated FCC Antiferromagnet Ba₂YO₆: Structural Characterization, Magnetic Properties, and Neutron Scattering Studies. *Phys. Rev. B* **2015**, *075133*, 1–9.
- (97) Grey, C. P.; Dupre, N. NMR Studies of Cathode Materials for Lithium-Ion Rechargeable Batteries. *Chem. Rev.* **2004**, *104*, 4493–4512.
- (98) Ishii, Y.; Wickramasinghe, N. P.; Chimon, S. A New Approach in 1D and 2D ¹³C High-Resolution Solid-State NMR Spectroscopy of Paramagnetic Organometallic Complexes by Very Fast Magic-Angle Spinning. *J. Am. Chem. Soc.* **2003**, *125*, 3438–3439.
- (99) Aguiar, P. M.; Katz, M. J.; Leznof, D. B.; Kroeker, S. Natural Abundance ¹³C and ¹⁵N Solid-state NMR Analysis of Paramagnetic Transition-metal Cyanide Coordination Polymers. *Phys. Chem. Chem. Phys.* **2009**, *11*, 6925–6934.
- (100) Grey, C. P.; Smith, M. E.; Cheetham, A. K.; Dobson, C. M.; Dupree, R. MAS

NMR Study of Rare-Earth Pyrochlores: Paramagnetic Shifts in the Solid State. *J. Am. Chem. Soc.* **1990**, *112*, 4670–4675.

(101) Brough, A. R.; Grey, C. P.; Dobson, C. M. Paramagnetic Ions as Structural Probes in Solid-State NMR: Distance Measurements in Crystalline Lanthanide Acetates. *J. Am. Chem. Soc.* **1993**, *115*, 7318–7327.

(102) Bertarello, A.; Schubeis, T.; Fuccio, C.; Ravera, E.; Fragai, M.; Parigi, G.; Emsley, L.; Pintacuda, G.; Luchinat, C. Paramagnetic Properties of a Crystalline Iron-Sulfur Protein by Magic-Angle Spinning NMR Spectroscopy. *Inorg. Chem.* **2017**, *56*, 6624–6629.

(103) Pell, A. J.; Middlemiss, D. S.; Strobridge, F. C.; Miller, J. K.; Cle, J.; Whittingham, M. S.; Emsley, L.; Grey, C. P.; Pintacuda, G. Spin-Transfer Pathways in Paramagnetic Lithium Transition-Metal Phosphates from Combined Broadband Isotropic Solid-State MAS NMR Spectroscopy and DFT Calculations. *J. Am. Chem. Soc.* **2012**, *134*, 17178–17185.

(104) Liu, K.; Ryan, D.; Nakanishi, K.; Mcdermott, A. Solid State NMR Studies of Paramagnetic Coordination Complexes: A Comparison of Protons and Deuterons in Detection and Decoupling. *J. Am. Chem. Soc.* **1995**, *117*, 6897–6906.

(105) Helmholz, B. L.; Kruh, R. F. The Crystal Structure of Cesium Chlorocuprate, Cs_2CuCl_4 , and the Spectrum of the Chlorocuprate Ion. *J. Am. Chem. Soc.* **1952**, *74*, 1176–1181.

(106) Filip, M. R.; Verdi, C.; Giustino, F. G.W. Band Structures and Carrier Effective Masses of $\text{CH}_3\text{NH}_3\text{PbI}_3$ and Hypothetical Perovskites of the Type APbI_3 : $\text{A}=\text{NH}_4$, PH_4 , AsH_4 , and SbH_4 . *J. Phys. Chem. C* **2015**, *119*, 25209–25219.

Chapter 5

(1) National Renewable Energy Laboratory (NREL). Best Research-Cell Efficiency Chart.

<https://www.nrel.gov/pv/assets/pdfs/best-research-cell-efficiencies.20190923.pdf>

(2) Wei, Y.; Cheng, Z.; Lin, J. An Overview on Enhancing the Stability of Lead Halide Perovskite Quantum Dots and Their Applications in Phosphor-Converted LEDs. *Chem. Soc. Rev.* **2019**, *48*, 310–350.

- (3) Zhao, Y.; Zhu, K. Organic-Inorganic Hybrid Lead Halide Perovskites for Optoelectronic and Electronic Applications. *Chem. Soc. Rev.* **2016**, *45*, 655–689.
- (4) Kovalenko, M. V.; Protesescu, L.; Bodnarchuk, M. I. Properties and Potential Optoelectronic Applications of Lead Halide Perovskite Nanocrystals. *Science* **2017**, *750*, 745–750.
- (5) Sutherland, B. R.; Sargent, E. H. Perovskite Photonic Sources. *Nat. Photonics* **2016**, *10*, 295–302.
- (6) Luo, J.; Im, J. H.; Mayer, M. T.; Schreier, M.; Nazeeruddin, M. K.; Park, N. G.; Tilley, S. D.; Fan, H. J.; Grätzel, M. Water Photolysis at 12.3% Efficiency via Perovskite Photovoltaics and Earth-Abundant Catalysts. *Science* **2014**, *345*, 1593–1596.
- (7) Yakunin, S.; Sytnyk, M.; Kriegner, D.; Shrestha, S.; Richter, M.; Matt, G. J.; Azimi, H.; Brabec, C. J.; Stangl, J.; Kovalenko, M. V.; Heiss, W. Detection of X-Ray Photons by Solution-Processed Lead Halide Perovskites. *Nat. Photonics* **2015**, *9*, 444–449.
- (8) LED Lighting, U.S. Department of Energy.
<https://www.energy.gov/energysaver/save-electricity-and-fuel/lighting-choices-save-you-money/led-lighting> (Accessed Dec 2019).
- (9) Manser, J. S.; Christians, J. A.; Kamat, P. V. Intriguing Optoelectronic Properties of Metal Halide Perovskites. *Chem. Rev.* **2016**, *116*, 12956–13008.
- (10) Dohner, E. R.; Hoke, E. T.; Karunadasa, H. I. Self-Assembly of Broadband White-Light Emitters. *J. Am. Chem. Soc.* **2014**, *136*, 1718–1721.
- (11) Smith, M. D.; Connor, B. A.; Karunadasa, H. I. Tuning the Luminescence of Layered Halide Perovskites. *Chem. Rev.* **2019**, *119*, 3104–3139.
- (12) Smith, M. D.; Karunadasa, H. I. White-Light Emission from Layered Halide Perovskites. *Acc. Chem. Res.* **2018**, *51*, 619–627.
- (13) Wang, M.; Guo, G.-C. Inorganic–Organic Hybrid White Light Phosphors. *Chem. Commun.* **2016**, *52*, 13194–13204.
- (14) Shang, M.; Li, C.; Lin, J. How to Produce White Light in a Single-Phase Host? *Chem. Soc. Rev.* **2014**, *43*, 1372–1386.

- (15) Yang, J.; Siempelkamp, B. D.; Mosconi, E.; De Angelis, F.; Kelly, T. L. Origin of the Thermal Instability in $\text{CH}_3\text{NH}_3\text{PbI}_3$ Thin Films Deposited on ZnO. *Chem. Mater.* **2015**, *27*, 4229–4236.
- (16) Askar, A. M.; Bernard, G. M.; Wiltshire, B.; Shankar, K.; Michaelis, V. K. Multinuclear Magnetic Resonance Tracking of Hydro, Thermal, and Hydrothermal Decomposition of $\text{CH}_3\text{NH}_3\text{PbI}_3$. *J. Phys. Chem. C* **2017**, *121*, 1013–1024.
- (17) Needleman, H. Lead Poisoning. *Annu. Rev. Med.* **2004**, *55*, 209–222.
- (18) Babayigit, A.; Ethirajan, A.; Muller, M.; Conings, B. Toxicity of Organometal Halide Perovskite Solar Cells. *Nat. Mater.* **2016**, *15*, 247–251.
- (19) Yang, J.; Siempelkamp, B. D.; Liu, D.; Kelly, T. L. Investigation of $\text{CH}_3\text{NH}_3\text{PbI}_3$ Degradation Rates and Mechanisms in Controlled Humidity Environments Using In Situ Techniques. *ACS Nano* **2015**, *9*, 1955–1963.
- (20) Domanski, K.; Alharbi, E. A.; Hagfeldt, A.; Grätzel, M.; Tress, W. Systematic Investigation of the Impact of Operation Conditions on the Degradation Behaviour of Perovskite Solar Cells. *Nat. Energy* **2018**, *3*, 61–67.
- (21) Li, J.; Cao, H.; Jiao, W.; Wang, Q.; Wei, M.; Cantone, I.; Lü, J.; Abate, A. Biological Impact of Lead from Halide Perovskites Reveals the Risk of Introducing a Safe Threshold. *Nat. Commun.* **2020**, *11*, 310.
- (22) Abate, A. Perovskite Solar Cells Go Lead Free. *Joule* **2017**, *1*, 659–664.
- (23) Shi, Z.; Guo, J.; Chen, Y.; Li, Q.; Pan, Y.; Zhang, H.; Xia, Y.; Huang, W. Lead-Free Organic–Inorganic Hybrid Perovskites for Photovoltaic Applications: Recent Advances and Perspectives. *Adv. Mater.* **2017**, *29*, 1605005.
- (24) Luo, J.; Wang, X.; Li, S.; Liu, J.; Guo, Y.; Niu, G.; Yao, L.; Fu, Y.; Gao, L.; Dong, Q.; Zhao, C.; Leng, M.; Ma, F.; Liang, W.; Wang, L.; Jin, S.; Han, J.; Zhang, L.; Etheridge, J.; Wang, J.; Yan, Y.; Sargent, E. H.; Tang, J. Efficient and Stable Emission of Warm-White Light from Lead-Free Halide Double Perovskites. *Nature* **2018**, *563*, 541–545.
- (25) Gray, M. B.; Majher, J. D.; Strom, T. A.; Woodward, P. M. Broadband White Emission in $\text{Cs}_2\text{AgIn}_{1-x}\text{Bi}_x\text{Cl}_6$ Phosphors. *Inorg. Chem.* **2019**, *58*, 13403–13410.

- (26) Yang, B.; Mao, X.; Hong, F.; Meng, W.; Tang, Y.; Xia, X.; Yang, S.; Deng, W.; Han, K. Lead-Free Direct Bandgap Double Perovskite Nanocrystals with Bright Dual-Color Emission. *J. Am. Chem. Soc.* **2018**, *140*, 17001–17006.
- (27) Majher, J. D.; Gray, M. B.; Strom, T. A.; Woodward, P. M. Cs₂NaBiCl₆: Mn²⁺- A New Orange-Red Halide Double Perovskite Phosphor. *Chem. Mater.* **2019**, *31*, 1738–1744.
- (28) Hu, Q.; Niu, G.; Zheng, Z.; Li, S.; Zhang, Y.; Song, H.; Zhai, T.; Tang, J. Tunable Color Temperatures and Efficient White Emission from Cs₂Ag_{1-x}Na_xIn_{1-y}Bi_yCl₆ Double Perovskite Nanocrystals. *Small* **2019**, 1903496.
- (29) Locardi, F.; Cirignano, M.; Baranov, D.; Dang, Z.; Prato, M.; Drago, F.; Ferretti, M.; Pinchetti, V.; Fanciulli, M.; Brovelli, S.; Trizio, T. D.; Manna, L. Colloidal Synthesis of Double Perovskite Cs₂AgInCl₆ and Mn-Doped Cs₂AgInCl₆ Nanocrystals. *J. Am. Chem. Soc.* **2018**, *140*, 12989–12995.
- (30) Lee, W.; Hong, S.; Kim, S. Colloidal Synthesis of Lead-Free Silver–Indium Double-Perovskite Cs₂AgInCl₆ Nanocrystals and Their Doping with Lanthanide Ions. *J. Phys. Chem. C* **2019**, *123*, 2665–2672.
- (31) Zhou, J.; Rong, X.; Zhang, P.; Molokeev, M. S.; Wei, P.; Liu, Q. Manipulation of Bi³⁺/In³⁺ Transmutation and Mn²⁺ -Doping Effect on the Structure and Optical Properties of Double Perovskite Cs₂NaBi_{1-x}In_xCl₆. *Adv. Opt. Mater.* **2019**, *7*, 1801435.
- (32) Luo, J.; Hu, M.; Niu, G.; Tang, J. Lead-Free Halide Perovskites and Perovskite Variants as Phosphors toward Light-Emitting Applications. *ACS Appl. Mater. Interfaces* **2019**, *11*, 31575–31584.
- (33) Lamba, R. S.; Basera, P.; Bhattacharya, S.; Sapra, S. Band Gap Engineering in Cs₂(Na_xAg_{1-x})BiCl₆ Double Perovskite Nanocrystals. *J. Phys. Chem. Lett.* **2019**, *10*, 5173-5181.
- (34) Liu, Y.; Jing, Y.; Zhao, J.; Liu, Q.; Xia, Z. Design Optimization of Lead-Free Perovskite Cs₂AgInCl₆:Bi Nanocrystals with 11.4% Photoluminescence Quantum Yield. *Chem. Mater.* **2019**, *31*, 3333–3339.
- (35) Slavney, A. H.; Hu, T.; Lindenberg, A. M.; Karunadasa, H. I. A Bismuth-Halide Double Perovskite with Long Carrier Recombination Lifetime for Photovoltaic Applications. *J. Am. Chem. Soc.* **2016**, *138*, 2138–2141.

- (36) McClure, E. T.; Ball, M. R.; Windl, W.; Woodward, P. M. Cs₂AgBiX₆ (X = Br, Cl): New Visible Light Absorbing, Lead-Free Halide Perovskite Semiconductors. *Chem. Mater.* **2016**, *28*, 1348–1354.
- (37) Volonakis, G.; Filip, M. R.; Haghighirad, A. A.; Sakai, N.; Wenger, B.; Snaith, H. J.; Giustino, F. Lead-Free Halide Double Perovskites via Heterovalent Substitution of Noble Metals. *J. Phys. Chem. Lett.* **2016**, *7*, 1254–1259.
- (38) Filip, M. R.; Liu, X.; Miglio, A.; Hautier, G.; Giustino, F. Phase Diagrams and Stability of Lead-Free Halide Double Perovskites Cs₂BB'X₆: B = Sb and Bi, B' = Cu, Ag, and Au, and X = Cl, Br, and I. *J. Phys. Chem. C* **2018**, *122*, 158–170.
- (39) K., N. N.; Nag, A. Synthesis and Luminescence of Mn-Doped Cs₂AgInCl₆ Double Perovskites. *Chem. Commun.* **2018**, *54*, 5205--5208.
- (40) Lawson, K. E. Optical Studies of Electronic Transitions in Hexa- and Tetracoordinated Mn²⁺ Crystals. *J. Chem. Phys.* **1967**, *47*, 3627–3633.
- (41) Zeng, R.; Zhang, L.; Xue, Y.; Ke, B.; Zhao, Z.; Huang, D.; Wei, Q.; Zhou, W.; Zou, B. Highly Efficient Blue Emission from Self-Trapped Excitons in Stable Db³⁺-Doped Cs₂NaInCl₆ Double Perovskites. *J. Phys. Chem. Lett.* **2020**, *11*, 2053–2061.
- (42) Locardi, F.; Sartori, E.; Buha, J.; Zito, J.; Prato, M.; Pinchetti, V.; Zaffalon, M. L.; Ferretti, M.; Brovelli, S.; Infante, I.; Trizio, L. D.; Manna, L. Emissive Bi-Doped Double Perovskite Cs₂Ag_{1-x}Na_xInCl₆ Nanocrystals. *ACS Energy Lett.* **2019**, *4*, 1976–1982.
- (43) Hu, Z.; Lin, Z.; Su, J.; Zhang, J.; Chang, J.; Hao, Y. A Review on Energy Band-Gap Engineering for Perovskite Photovoltaics. *Sol. RRL* **2019**, *3*, 1900304.
- (44) Xiao, Z.; Zhou, Y.; Hosono, H.; Kamiya, T.; Padture, N. P. Bandgap Optimization of Perovskite Semiconductors for Photovoltaic Applications. *Chem. - A Eur. J.* **2018**, *24*, 2305–2316.
- (45) Du, K. Z.; Meng, W.; Wang, X.; Yan, Y.; Mitzi, D. B. Bandgap Engineering of Lead-Free Double Perovskite Cs₂AgBiBr₆ through Trivalent Metal Alloying. *Angew. Chem. Int. Ed.* **2017**, *56*, 8158–8162.
- (46) Gray, M. B.; McClure, E. T.; Woodward, P. M. Cs₂AgBiBr_{6-x}Cl_x Solid Solutions-Band Gap Engineering with Halide Double Perovskites. *J. Mater. Chem. C* **2019**, *7*, 9686–9689.

- (47) Jiang, J. T.; Xiu, S. L.; Zheng, M. M.; Jia, T. T.; Liu, H. Y.; Zhang, Y.; Chen, G. Indirect–Direct Bandgap Transition and Gap Width Tuning in Bilayer MoS₂ Superlattices. *Chem. Phys. Lett.* **2014**, *613*, 74–79.
- (48) Wang, Y. J.; Zhou, K. G.; Yu, G.; Zhong, X.; Zhang, H. L. Partial Oxidized Arsenene: Emerging Tunable Direct Bandgap Semiconductor. *Sci. Rep.* **2016**, *6*, 24981.
- (49) Chen, X.; Yang, Q.; Meng, R.; Jiang, J.; Liang, Q.; Tan, C.; Sun, X. The Electronic and Optical Properties of Novel Germanene and Antimonene Heterostructures. *J. Mater. Chem. C* **2016**, *4*, 5434–5441.
- (50) Tran, T. T.; Panella, J. R.; Chamorro, J. R.; Morey, J. R.; McQueen, T. M. Designing Indirect-Direct Bandgap Transitions in Double Perovskites. *Mater. Horizons* **2017**, *4*, 688–693.
- (51) Volonakis, G.; Haghighirad, A. A.; Milot, R. L.; Sio, W. H.; Filip, M. R.; Wenger, B.; Johnston, M. B.; Herz, L. M.; Snaith, H. J.; Giustino, F. Cs₂InAgCl₆: A New Lead-Free Halide Double Perovskite with Direct Band Gap. *J. Phys. Chem. Lett.* **2017**, *8*, 772–778.
- (52) Askar, A. M.; Karmakar, A.; Bernard, G. M.; Ha, M.; Terskikh, V. V.; Wiltshire, B. D.; Patel, S.; Fleet, J.; Shankar, K.; Michaelis, V. K. Composition-Tunable Formamidinium Lead Mixed Halide Perovskites via Solvent-Free Mechanochemical Synthesis: Decoding the Pb Environments Using Solid-State NMR Spectroscopy. *J. Phys. Chem. Lett.* **2018**, *9*, 2671–2677.
- (53) Pan, C.; Lee, Y. J.; Amundsen, B.; Grey, C. P. ⁶Li MAS NMR Studies of the Local Structure and Electrochemical Properties of Cr-Doped Lithium Manganese and Lithium Cobalt Oxide Cathode Materials for Lithium-Ion Batteries. *Chem. Mater.* **2002**, *14*, 2289–2299.
- (54) Wasylshen, R. E.; Knop, O.; Macdonald, J. B. Cation Rotation in Methylammonium Lead Halides. *Solid State Commun.* **1985**, *56*, 581–582.
- (55) Senocrate, A.; Moudrakovski, I.; Kim, G. Y.; Yang, T.; Gregori, G.; Grätzel, M.; Maier, J. The Nature of Ion Conduction in Methylammonium Lead Iodide: A Multimethod Approach. *Angew. Chem. Int. Ed.* **2017**, *56*, 7755–7759.

- (56) Senocrate, A.; Moudrakovski, I.; Maier, J. Short-Range Ion Dynamics in Methylammonium Lead Iodide by Multinuclear Solid State NMR and ^{127}I NQR. *Phys. Chem. Chem. Phys.* **2018**, *20*, 20043–20055.
- (57) Kubicki, D. J.; Prochowicz, D.; Hofstetter, A.; Péchy, P.; Zakeeruddin, S. M.; Grätzel, M.; Emsley, L. Cation Dynamics in Mixed-Cation $(\text{MA})_x(\text{FA})_{1-x}\text{PbI}_3$ Hybrid Perovskites from Solid-State NMR. *J. Am. Chem. Soc.* **2017**, *139*, 10055–10061.
- (58) Kubicki, D. J.; Prochowicz, D.; Hofstetter, A.; Sasaki, M.; Yadav, P.; Bi, D.; Pellet, N.; Lewiński, J.; Zakeeruddin, S. M.; Grätzel, M.; Emsley, L. Formation of Stable Mixed Guanidinium-Methylammonium Phases with Exceptionally Long Carrier Lifetimes for High-Efficiency Lead Iodide-Based Perovskite Photovoltaics. *J. Am. Chem. Soc.* **2018**, *140*, 3345–3351.
- (59) Hanrahan, M. P.; Men, L.; Rosales, B. A.; Vela, J.; Rossini, A. J. Sensitivity-Enhanced ^{207}Pb Solid-State NMR Spectroscopy for the Rapid, Non-Destructive Characterization of Organolead Halide Perovskites. *Chem. Mater.* **2018**, *30*, 7005–7015.
- (60) Kubicki, D. J.; Prochowicz, D.; Pinon, A.; Stevanato, G.; Hofstetter, A.; Zakeeruddin, S. M.; Grätzel, M.; Emsley, L. Doping and Phase Segregation in Mn^{2+} - and Co^{2+} -Doped Lead Halide Perovskites from ^{133}Cs and ^1H NMR Relaxation Enhancement. *J. Mater. Chem. A* **2019**, *7*, 2326–2333.
- (61) Franssen, W. M. J.; Kentgens, A. P. M. Solid-State NMR of Hybrid Halide Perovskites. *Solid State Nucl. Magn. Reson.* **2019**, *100*, 36–44.
- (62) Franssen, W. M. J.; Van Es, S. G. D.; Dervişoğlu, R.; De Wijs, G. A.; Kentgens, A. P. M. Symmetry, Dynamics, and Defects in Methylammonium Lead Halide Perovskites. *J. Phys. Chem. Lett.* **2017**, *8*, 61–66.
- (63) Karmakar, A.; Dodd, M. S.; Zhang, X.; Oakley, M. S.; Klobukowski, M.; Michaelis, V. K. Mechanochemical Synthesis of 0D and 3D Cesium Lead Mixed Halide Perovskites. *Chem. Commun.* **2019**, *55*, 5079–5082.
- (64) Chen, Y.; Smock, S. R.; Flintgruber, A. H.; Perras, F. A.; Brutchey, R. L.; Rossini, A. J. Surface Termination of CsPbBr_3 Perovskite Quantum Dots Determined by Solid-State NMR Spectroscopy. *J. Am. Chem. Soc.* **2020**, *142*, 6117–6127.

- (65) Kubicki, D. J.; Prochowicz, D.; Salager, E.; Rakhmatullin, A.; Grey, C. P.; Emsley, L.; Stranks, S. D. Local Structure and Dynamics in Methylammonium, Formamidinium and Cesium Tin(II) Mixed-halide Perovskites from ^{119}Sn Solid-state NMR. *J. Am. Chem. Soc.* **2020**, *142*, 7813–7826.
- (66) Karmakar, A.; Askar, A. M.; Bernard, G. M.; Terskikh, V. V.; Ha, M.; Patel, S.; Shankar, K.; Michaelis, V. K. Mechanochemical Synthesis of Methylammonium Lead Mixed-Halide Perovskites: Unraveling the Solid-Solution Behavior Using Solid-State NMR. *Chem. Mater.* **2018**, *30*, 2309–2321.
- (67) Rosales, B. A.; Men, L.; Cady, S. D.; Hanrahan, M. P.; Rossini, A. J.; Vela, J. Persistent Dopants and Phase Segregation in Organolead Mixed-Halide Perovskites. *Chem. Mater.* **2016**, *28*, 6848–6859.
- (68) Kubicki, D. J.; Prochowicz, D.; Hofstetter, A.; Zakeeruddin, S. M.; Grätzel, M.; Emsley, L. Phase Segregation in Potassium-Doped Lead Halide Perovskites from ^{39}K Solid-State NMR at 21.1 T. *J. Am. Chem. Soc.* **2018**, *140*, 7232–7238.
- (69) Kubicki, D. J.; Prochowicz, D.; Hofstetter, A.; Zakeeruddin, S. M.; Grätzel, M.; Emsley, L. Phase Segregation in Cs-, Rb- and K-Doped Mixed-Cation $(\text{MA})_x(\text{FA})_{1-x}\text{PbI}_3$ Hybrid Perovskites from Solid-State NMR. *J. Am. Chem. Soc.* **2017**, *139*, 14173–14180.
- (70) Karmakar, A.; Dodd, M. S.; Agnihotri, S.; Ravera, E.; Michaelis, V. K. Cu(II)-Doped $\text{Cs}_2\text{SbAgCl}_6$ Double Perovskite: A Lead-Free, Low-Bandgap Material. *Chem. Mater.* **2018**, *30*, 8280–8290.
- (71) Michaelis, V. K.; Greer, B. J.; Aharen, T.; Greedan, J. E.; Kroeker, S. Determining Electron Spin-Transfer Mechanisms in Paramagnetic. *J. Phys. Chem. C* **2012**, *116*, 23646–23652.
- (72) Aharen, T.; Greedan, J. E.; Bridges, C. A.; Aczel, A. A.; Rodriguez, J.; Macdougall, G.; Luke, G. M.; Imai, T.; Michaelis, V. K.; Kroeker, S.; Zhou, H.; Wiebe, C. R.; Cranswick, L. M. D. Magnetic Properties of the Geometrically Frustrated $S=1/2$ Antiferromagnets, $\text{La}_2\text{LiMoO}_6$ and Ba_2YMoO_6 , with the B-Site Ordered Double Perovskite Structure: Evidence for a Collective Spin-Singlet Ground State. *Phys. Rev.* **2010**, *81*, 224409.

- (73) Li, T.; Zhao, X.; Yang, D.; Du, M. H.; Zhang, L. Intrinsic Defect Properties in Halide Double Perovskites for Optoelectronic Applications. *Phys. Rev. Appl.* **2018**, *10*, 041001.
- (74) V. M. Goldschmidt. Die Gesetze Der Krystallochemie. *Naturwissenschaften* **1926**, *14*, 477–485.
- (75) Li, C.; Lu, X.; Ding, W.; Feng, L.; Gao, Y.; Guo, Z. Formability of ABX₃ (X = F, Cl, Br, I) Halide Perovskites. *Acta Crystallogr. Sect. B* **2008**, *B64*, 702–707.
- (76) Shannon, R. D. Revised Effective Ionic Radii and Systematic Studies of Interatomic Distances in Halides and Chalcogenides. *Acta Cryst.* **1976**, *A32*, 751–767.
- (77) Kubelka, P.; Munk, F. Ein Beitrag Zur Optik Der Farbanstriche. *Z.Tech. Phys. (Leipzig)* **1931**, *12*, 593–601.
- (78) Slavney, A. H.; Leppert, L.; Bartesaghi, D.; Gold-Parker, A.; Toney, M. F.; Savenije, T. J.; Neaton, J. B.; Karunadasa, H. I. Defect-Induced Band-Edge Reconstruction of a Bismuth-Halide Double Perovskite for Visible-Light Absorption. *J. Am. Chem. Soc.* **2017**, *139* (14), 5015–5018.
- (79) Meng, W.; Wang, X.; Xiao, Z.; Wang, J.; Mitzi, D. B.; Yan, Y. Parity-Forbidden Transitions and Their Impact on the Optical Absorption Properties of Lead-Free Metal Halide Perovskites and Double Perovskites. *J. Phys. Chem. Lett.* **2017**, *8*, 2999–3007.
- (80) Steele, J. A.; Puech, P.; Keshavarz, M.; Yang, R.; Banerjee, S.; Debroye, E.; Kim, C. W.; Yuan, H.; Heo, N. H.; Vanacken, J.; Walsh, A.; Hofkens, J.; Roeffaers, M. B. J. Giant Electron–Phonon Coupling and Deep Conduction Band Resonance in Metal Halide Double Perovskite. *ACS Nano* **2018**, *12*, 8081–8090.
- (81) Jakob, M.; Aissiou, A.; Morrish, W.; Marsiglio, F.; Islam, M.; Kartouzian, A.; Meldrum, A. Reappraising the Luminescence Lifetime Distributions in Silicon Nanocrystals. *Nanoscale Res. Lett.* **2018**, *13*, 383.
- (82) Thirumal, K.; Chong, W. K.; Xie, W.; Ganguly, R.; Muduli, S. K.; Sherburne, M.; Asta, M.; Mhaisalkar, S.; Sum, T. C.; Soo, H. S.; Mathews, N. Morphology-Independent Stable White-Light Emission from Self-Assembled Two-Dimensional Perovskites Driven by Strong Exciton-Phonon Coupling to the Organic Framework. *Chem. Mater.* **2017**, *29*, 3947–3953.

- (83) Luo, J.; Li, S.; Wu, H.; Zhou, Y.; Li, Y.; Liu, J.; Li, J.; Li, K.; Yi, F.; Niu, G.; Tang, J. Cs₂AgInCl₆ Double Perovskite Single Crystals: Parity Forbidden Transitions and Their Application for Sensitive and Fast UV Photodetectors. *ACS Photonics* **2018**, *5*, 398–405.
- (84) Johnston, M. B.; Herz, L. M. Hybrid Perovskites for Photovoltaics: Charge-Carrier Recombination, Diffusion, and Radiative Efficiencies. *Acc. Chem. Res.* **2016**, *49*, 146–154.
- (85) Dequilettes, D. W.; Frohna, K.; Emin, D.; Kirchartz, T.; Bulovic, V.; Ginger, D. S.; Stranks, S. D. Charge-Carrier Recombination in Halide Perovskites. *Chem. Rev.* **2019**, *119*, 11007–11019.
- (86) Vegard, L. Die Konstitution Der Mischkristalle Und Die Raumffüllung Der Atome. *Zeitschrift für Phys.* **1921**, *5*, 17–26.
- (87) Harris, R. K.; Becker, E. D.; de Menrzes, S. M. C.; Goodfellow, R.; Granger, P. NMR Nomenclature. Nuclear Spin Properties and Conventions for Chemical Shifts. *Pure Appl. Chem.* **2001**, *73*, 1795–1818.
- (88) Michaelis, V. K.; Aguiar, P. M.; Kroeker, S. Probing Alkali Coordination Environments in Alkali Borate Glasses by Multinuclear Magnetic Resonance. *J. Non. Cryst. Solids* **2007**, *353*, 2582–2590.
- (89) Kroeker, S.; Eichele, K.; Wasylishen, R. E.; Britten, J. F. Cesium-133 NMR Study of CsCd(SCN)₃: Relative Orientation of the Chemical Shift and Electric Field Gradient Tensors. *J. Phys. Chem. B* **1997**, *101*, 3727–3733.
- (90) MacKenzie, K. J.; Smith, M. E. Multinuclear Solid-State Nuclear Magnetic Resonance of Inorganic Materials; Elsevier. 2002.
- (91) Chen, F.; Ma, G.; Cavell, R. G.; Terskikh, V.; Wasylishen, R. E. Solid-State ¹¹⁵In NMR Study of Indium Coordination Complexes. *Chem. Commun.* **2008**, 5933–5935.
- (92) Chen, F.; Ma, G.; Bernard, G. M.; Cavell, R. G.; Mcdonald, R.; Ferguson, M. J.; Wasylishen, R. E. Solid-State ¹¹⁵In and ³¹P NMR Studies of Triarylphosphine Indium Trihalide Adducts. *J. Am. Chem. Soc.* **2010**, *132*, 5479–5493.
- (93) Hamaed, H.; Laschuk, M. W.; Terskikh, V. V.; Schurko, R. W. Application of Solid-State ²⁰⁹Bi NMR to the Structural Characterization of Bismuth-Containing Materials. *J. Am. Chem. Soc.* **2009**, *131*, 8271–8279.

- (94) Bernard, G. M.; Wasylshen, R. E.; Ratcliffe, C. I.; Terskikh, V.; Wu, Q.; Buriak, J. M.; Hauger, T. Methylammonium Cation Dynamics in Methylammonium Lead Halide Perovskites: A Solid-State NMR Perspective. *J. Phys. Chem. A* **2018**, *122*, 1560–1573.
- (95) Taylor, R. E.; Beckmann, P. A.; Bai, S.; Dybowski, C. ^{127}I and ^{207}Pb Solid-State NMR Spectroscopy and Nuclear Spin Relaxation in PbI_2 : A Preliminary Study. *J. Phys. Chem. C* **2014**, *118*, 9143–9153.
- (96) Greer, B. J.; Michaelis, V. K.; Terskikh, V. V.; Kroeker, S. Reconnaissance of Diverse Structural and Electronic Environments in Germanium Halides by Solid-State ^{73}Ge NMR and Quantum Chemical Calculations. *Can. J. Chem.* **2011**, *89*, 1118–1129.
- (97) Hamaed, H.; Johnston, K. E.; Cooper, B. F. T.; Terskikh, V. V.; Ye, E.; Charles L. B. Macdonald, D. C. A.; Schurko, R. W. A ^{115}In Solid-State NMR Study of Low Oxidation-State Indium Complexes. *Chem. Sci.* **2014**, *5*, 982–995.
- (98) Lan, C.; Zhao, S.; Luo, J.; Fan, P. First-Principles Study of Anion Diffusion in Lead-Free Halide Double Perovskites. *Phys. Chem. Chem. Phys.* **2018**, *20*, 24339–24344.
- (99) Zhao, X. G.; Yang, J. H.; Fu, Y.; Yang, D.; Xu, Q.; Yu, L.; Wei, S. H.; Zhang, L. Design of Lead-Free Inorganic Halide Perovskites for Solar Cells via Cation-Transmutation. *J. Am. Chem. Soc.* **2017**, *139*, 2630–2638.
- (100) Muñoz-García, A. B.; Pavone, M.; Carter, E. A. Effect of Antisite Defects on the Formation of Oxygen Vacancies in $\text{Sr}_2\text{FeMoO}_6$: Implications for Ion and Electron Transport. *Chem. Mater.* **2011**, *23*, 4525–4536.
- (101) Colis, S.; Stoeffler, D.; Mny, C.; Fix, T.; Leuvrey, C.; Pourroy, G.; Dinia, A.; Panissod, P. Structural Defects in $\text{Sr}_2\text{FeMoO}_6$ Double Perovskite: Experimental versus Theoretical Approach. *J. Appl. Phys.* **2005**, *98*, 033905.
- (102) Greneche, J. M.; Venkatesan, M.; Suryanarayanan, R.; Coey, J. M. D. Mössbauer Spectrometry of A_2FeMoO_6 (A = Ca, Sr, Ba): Search for Antiphase Domains. *Phys. Rev. B* **2001**, *63*, 174403.
- (103) O'Dell, L. A. Ultra-Wideline Solid-State NMR: Developments and Applications of the WCPMG Experiment. In: Webb G. (Eds). *Mod. Magn. Reson. Springer, Cham* **2017**.

(104) O'Dell, L. A.; Schurko, R. W. QCPMG Using Adiabatic Pulses for Faster Acquisition of Ultra-Wideline NMR Spectra. *Chem. Phys. Lett.* **2008**, *464*, 97–102.

Chapter 6

(1) Zhao, Y.; Zhu, K. Organic-Inorganic Hybrid Lead Halide Perovskites for Optoelectronic and Electronic Applications. *Chem. Soc. Rev.* **2016**, *45*, 655–689.

(2) Miao, Y.; Ke, Y.; Wang, N.; Zou, W.; Xu, M.; Cao, Y.; Sun, Y.; Yang, R.; Wang, Y.; Tong, Y.; Xu, W.; Zhang, L.; Li, R.; Li, J.; He, H.; Jin, Y.; Gao, F.; Huang, W.; Wang, J. Stable and Bright Formamidinium-Based Perovskite Light-Emitting Diodes with High Energy Conversion Efficiency. *Nat. Commun.* **2019**, *10*, 3624.

(3) Wei, H.; Huang, J. Halide Lead Perovskites for Ionizing Radiation Detection. *Nat. Commun.* **2019**, *10*, 1066.

(4) Chen, K.; Deng, X.; Dodekatos, G.; Tüysüz, H. Photocatalytic Polymerization of 3,4-Ethylenedioxythiophene over Cesium Lead Iodide Perovskite Quantum Dots. *J. Am. Chem. Soc.* **2017**, *139*, 12267–12273.

(5) Babu, R.; Giribabu, L.; Singh, S. P. Recent Advances in Halide-Based Perovskite Crystals and Their Optoelectronic Applications. *Cryst. Growth Des.* **2018**, *18*, 2645–2664.

(6) Kovalenko, M. V; Protesescu, L.; Bodnarchuk, M. I. Properties and Potential Optoelectronic Applications of Lead Halide Perovskite Nanocrystals. *Science* **2017**, *750*, 745–750.

(7) National Renewable Energy Laboratory (NREL). Best Research-Cell Efficiency Chart.

<https://www.nrel.gov/pv/assets/pdfs/best-research-cell-efficiencies.20200104.pdf>
(accessed March 2021).

(8) Berhe, T. A.; Su, W. N.; Chen, C. H.; Pan, C. J.; Cheng, J. H.; Chen, H. M.; Tsai, M. C.; Chen, L. Y.; Dubale, A. A.; Hwang, B. J. Organometal Halide Perovskite Solar Cells: Degradation and Stability. *Energy Environ. Sci.* **2016**, *9*, 323–356.

(9) Yang, J.; Siempelkamp, B. D.; Liu, D.; Kelly, T. L. Investigation of CH₃NH₃PbI₃ degradation Rates and Mechanisms in Controlled Humidity Environments Using in Situ Techniques. *ACS Nano* **2015**, *9*, 1955–1963.

- (10) Domanski, K.; Alharbi, E. A.; Hagfeldt, A.; Grätzel, M.; Tress, W. Systematic Investigation of the Impact of Operation Conditions on the Degradation Behaviour of Perovskite Solar Cells. *Nat. Energy* **2018**, *3*, 61–67.
- (11) Askar, A. M.; Bernard, G. M.; Wiltshire, B.; Shankar, K.; Michaelis, V. K. Multinuclear Magnetic Resonance Tracking of Hydro, Thermal, and Hydrothermal Decomposition of $\text{CH}_3\text{NH}_3\text{PbI}_3$. *J. Phys. Chem. C* **2017**, *121*, 1013–1024.
- (12) Li, J.; Cao, H.; Jiao, W.; Wang, Q.; Wei, M.; Cantone, I.; Lü, J.; Abate, A. Biological Impact of Lead from Halide Perovskites Reveals the Risk of Introducing a Safe Threshold. *Nat. Commun.* **2020**, *11*, 310.
- (13) Babayigit, A.; Ethirajan, A.; Muller, M.; Conings, B. Toxicity of Organometal Halide Perovskite Solar Cells. *Nat. Mater.* **2016**, *15*, 247–251.
- (14) Kamarudin, M. A.; Hirotsu, D.; Wang, Z.; Hamada, K.; Nishimura, K.; Shen, Q.; Toyoda, T.; Iikubo, S.; Minemoto, T.; Yoshino, K.; Hayase, S. Suppression of Charge Carrier Recombination in Lead-Free Tin Halide Perovskite via Lewis Base Post-Treatment. *J. Phys. Chem. Lett.* **2019**, *10*, 5277–5283.
- (15) Song, T. Bin; Yokoyama, T.; Stoumpos, C. C.; Logsdon, J.; Cao, D. H.; Wasielewski, M. R.; Aramaki, S.; Kanatzidis, M. G. Importance of Reducing Vapor Atmosphere in the Fabrication of Tin-Based Perovskite Solar Cells. *J. Am. Chem. Soc.* **2017**, *139*, 836–842.
- (16) Kubicki, D. J.; Prochowicz, D.; Salager, E.; Rakhmatullin, A.; Grey, C. P.; Emsley, L.; Stranks, S. D. Local Structure and Dynamics in Methylammonium, Formamidinium and Cesium Tin(II) Mixed-halide Perovskites from ^{119}Sn Solid-state NMR. *J. Am. Chem. Soc.* **2020**, *142*, 7813–7826.
- (17) Karmakar, A.; Bhattacharya, A.; Sarkar, D.; Bernard, G. M.; Mar, A.; Michaelis, V. K. Influence of Hidden Halogen Mobility on Local Structure of $\text{CsSn}(\text{Cl}_{1-x}\text{Br}_x)_3$ Mixed-Halide Perovskites by Solid-State NMR. *Chem. Sci.* **2021**, *12*, 3253–3263.
- (18) Maughan, A. E.; Ganose, A. M.; Scanlon, D. O.; Neilson, J. R. Perspectives and Design Principles of Vacancy-Ordered Double Perovskite Halide Semiconductors. *Chem. Mater.* **2019**, *31*, 1184–1195.
- (19) Brik, M. G.; Kityk, I. V. Modeling of Lattice Constant and Their Relations with Ionic Radii and Electronegativity of Constituting Ions of A_2XY_6 Cubic Crystals (A =

- K, Cs, Rb, Tl; X = tetravalent Cation, Y = F, Cl, Br, I). *J. Phys. Chem. Solids* **2011**, *72*, 1256–1260.
- (20) Saparov, B.; Sun, J. P.; Meng, W.; Xiao, Z.; Duan, H. S.; Gunawan, O.; Shin, D.; Hill, I. G.; Yan, Y.; Mitzi, D. B. Thin-Film Deposition and Characterization of a Sn-Deficient Perovskite Derivative Cs₂SnI₆. *Chem. Mater.* **2016**, *28*, 2315–2322.
- (21) Maughan, A. E.; Ganose, A. M.; Bordelon, M. M.; Miller, E. M.; Scanlon, D. O.; Neilson, J. R. Defect Tolerance to Intolerance in the Vacancy-Ordered Double Perovskite Semiconductors Cs₂SnI₆ and Cs₂TeI₆. *J. Am. Chem. Soc.* **2016**, *138*, 8453–8464.
- (22) Lee, B.; Stoumpos, C. C.; Zhou, N.; Hao, F.; Malliakas, C.; Yeh, C. Y.; Marks, T. J.; Kanatzidis, M. G.; Chang, R. P. H. Air-Stable Molecular Semiconducting Iodosalts for Solar Cell Applications: Cs₂SnI₆ as a Hole Conductor. *J. Am. Chem. Soc.* **2014**, *136*, 15379–15385.
- (23) Lee, B.; Krenselewski, A.; Baik, S. Il; Seidman, D. N.; Chang, R. P. H. Solution Processing of Air-Stable Molecular Semiconducting Iodosalts, Cs₂SnI_{6-x}Br_x, for Potential Solar Cell Applications. *Sustain. Energy Fuels* **2017**, *1*, 710–724.
- (24) Kaltzoglou, A.; Antoniadou, M.; Perganti, D.; Siranidi, E.; Raptis, V.; Trohidou, K.; Psycharis, V.; Kontos, A. G.; Falaras, P. Mixed-Halide Cs₂SnI₃Br₃ Perovskite as Low Resistance Hole-Transporting Material in Dye-Sensitized Solar Cells. *Electrochim. Acta* **2015**, *184*, 466–474.
- (25) Wang, A.; Yan, X.; Zhang, M.; Sun, S.; Yang, M.; Shen, W.; Pan, X.; Wang, P.; Deng, Z. Controlled Synthesis of Lead-Free and Stable Perovskite Derivative Cs₂SnI₆ Nanocrystals via a Facile Hot-Injection Process. *Chem. Mater.* **2016**, *28*, 8132–8140.
- (26) Lim, S. C.; Lin, H. P.; Tsai, W. L.; Lin, H. W.; Hsu, Y. T.; Tuan, H. Y. Binary Halide, Ternary Perovskite-like, and Perovskite-Derivative Nanostructures: Hot Injection Synthesis and Optical and Photocatalytic Properties. *Nanoscale* **2017**, *9*, 3747–3751.
- (27) Veronese, A.; Patrini, M.; Bajoni, D.; Ciarrocchi, C.; Quadrelli, P.; Malavasi, L. Highly Tunable Emission by Halide Engineering in Lead-Free Perovskite-Derivative Nanocrystals: The Cs₂SnX₆ (X = Cl, Br, Br/I, I) System. *Front. Chem.* **2020**, *8*, 1–9.

- (28) Tan, Z.; Li, J.; Zhang, C.; Li, Z.; Hu, Q.; Xiao, Z.; Kamiya, T.; Hosono, H.; Niu, G.; Lifshitz, E.; Cheng, Y.; Tang, J. Highly Efficient Blue-Emitting Bi-Doped Cs₂SnCl₆ Perovskite Variant: Photoluminescence Induced by Impurity Doping. *Adv. Funct. Mater.* **2018**, *28*, 1801131.
- (29) Jing, Y.; Liu, Y.; Zhao, J.; Xia, Z. Sb³⁺ Doping-Induced Triplet Self-Trapped Excitons Emission in Lead-Free Cs₂SnCl₆ Nanocrystals. *J. Phys. Chem. Lett.* **2019**, *10*, 7439–7444.
- (30) Arfin, H.; Kshirsagar, A. S.; Kaur, J.; Mondal, B.; Xia, Z.; Chakraborty, S.; Nag, A. ns² Electron (Bi³⁺ and Sb³⁺) Doping in Lead-Free Metal Halide Perovskite Derivatives. *Chem. Mater.* **2020**, *32*, 10255–10267.
- (31) Wasylshen, R. E.; Knop, O.; Macdonald, J. B. Cation Rotation in Methylammonium Lead Halides. *Solid State Commun.* **1985**, *56*, 581–582.
- (32) Kubicki, D. J.; Prochowicz, D.; Hofstetter, A.; Zakeeruddin, S. M.; Grätzel, M.; Emsley, L. Phase Segregation in Potassium-Doped Lead Halide Perovskites from ³⁹K Solid-State NMR at 21.1 T. *J. Am. Chem. Soc.* **2018**, *140*, 7232–7238.
- (33) Kubicki, D. J.; Prochowicz, D.; Hofstetter, A.; Péchy, P.; Zakeeruddin, S. M.; Grätzel, M.; Emsley, L. Cation Dynamics in Mixed-Cation (MA)_x(FA)_{1-x}PbI₃ Hybrid Perovskites from Solid-State NMR. *J. Am. Chem. Soc.* **2017**, *139*, 10055–10061.
- (34) Kubicki, D. J.; Prochowicz, D.; Hofstetter, A.; Saski, M.; Yadav, P.; Bi, D.; Pellet, N.; Lewiński, J.; Zakeeruddin, S. M.; Grätzel, M.; Emsley, L. Formation of Stable Mixed Guanidinium-Methylammonium Phases with Exceptionally Long Carrier Lifetimes for High-Efficiency Lead Iodide-Based Perovskite Photovoltaics. *J. Am. Chem. Soc.* **2018**, *140*, 3345–3351.
- (35) Bernard, G. M.; Wasylshen, R. E.; Ratcliffe, C. I.; Terskikh, V.; Wu, Q.; Buriak, J. M.; Hauger, T. Methylammonium Cation Dynamics in Methylammonium Lead Halide Perovskites: A Solid-State NMR Perspective. *J. Phys. Chem. A* **2018**, *122*, 1560–1573.
- (36) Karmakar, A.; Dodd, M. S.; Zhang, X.; Oakley, M. S.; Klobukowski, M.; Michaelis, V. K. Mechanochemical Synthesis of 0D and 3D Cesium Lead Mixed Halide Perovskites. *Chem. Commun.* **2019**, *55*, 5079–5082.

- (37) Askar, A. M.; Karmakar, A.; Bernard, G. M.; Ha, M.; Terskikh, V. V.; Wiltshire, B. D.; Patel, S.; Fleet, J.; Shankar, K.; Michaelis, V. K. Composition-Tunable Formamidinium Lead Mixed Halide Perovskites via Solvent-Free Mechanochemical Synthesis: Decoding the Pb Environments Using Solid-State NMR Spectroscopy. *J. Phys. Chem. Lett.* **2018**, *9*, 2671–2677.
- (38) Karmakar, A.; Askar, A. M.; Bernard, G. M.; Terskikh, V. V.; Ha, M.; Patel, S.; Shankar, K.; Michaelis, V. K. Mechanochemical Synthesis of Methylammonium Lead Mixed-Halide Perovskites: Unraveling the Solid-Solution Behavior Using Solid-State NMR. *Chem. Mater.* **2018**, *30*, 2309–2321.
- (39) Kubicki, D. J.; Prochowicz, D.; Hofstetter, A.; Walder, B. J.; Emsley, L. ^{113}Cd Solid-State NMR at 21.1 T Reveals the Local Structure and Passivation Mechanism of Cadmium in Hybrid and All-Inorganic Halide Perovskites. *ACS Energy Lett.* **2020**, *5*, 2964–2971.
- (40) Rosales, B. A.; Men, L.; Cady, S. D.; Hanrahan, M. P.; Rossini, A. J.; Vela, J. Persistent Dopants and Phase Segregation in Organolead Mixed-Halide Perovskites. *Chem. Mater.* **2016**, *28*, 6848–6859.
- (41) Rosales, B. A.; Hanrahan, M. P.; Boote, B. W.; Rossini, A. J.; Smith, E. A.; Vela, J. Lead Halide Perovskites: Challenges and Opportunities in Advanced Synthesis and Spectroscopy. *ACS Energy Lett.* **2017**, *2*, 906–914.
- (42) Chen, Y.; Smock, S. R.; Flintgruber, A. H.; Perras, F. A.; Brutchey, R. L.; Rossini, A. J. Surface Termination of CsPbBr₃ Perovskite Quantum Dots Determined by Solid-State NMR Spectroscopy. *J. Am. Chem. Soc.* **2020**, *142*, 6117–6127.
- (43) Franssen, W. M. J.; Kentgens, A. P. M. Solid-State NMR of Hybrid Halide Perovskites. *Solid State Nucl. Magn. Reson.* **2019**, *100*, 36–44.
- (44) Wouter M. J. Franssen; Es, S. G. D. van; Dervişoğlu, R.; Wijs, G. A. de; Kentgens, A. P. M. Symmetry, Dynamics, and Defects in Methylammonium Lead Halide Perovskites. *J. Phys. Chem. Lett.* **2017**, *8*, 61–66.
- (45) Senocrate, A.; Moudrakovski, I.; Kim, G. Y.; Yang, T.; Gregori, G.; Grätzel, M.; Maier, J. The Nature of Ion Conduction in Methylammonium Lead Iodide: A Multimethod Approach. *Angew. Chem. Int. Ed.* **2017**, *56*, 7755–7759.

- (46) Senocrate, A.; Moudrakovski, I.; Acartuerk, T.; Merkle, R.; Kim, G. Y.; Starke, U.; Grätzel, M.; Maier, J. Slow CH_3NH_3^+ Diffusion in $\text{CH}_3\text{NH}_3\text{PbI}_3$ Under Light Measured by Solid-State NMR and Tracer Diffusion. *J. Phys. Chem. C* **2018**, *122*, 21803–21806.
- (47) Prochowicz, D.; Yadav, P.; Saliba, M.; Kubicki, D. J.; Tavakoli, M. M.; Zakeeruddin, S. M.; Lewiński, J.; Emsley, L.; Grätzel, M. One-Step Mechanochemical Incorporation of an Insoluble Cesium Additive for High Performance Planar Heterojunction Solar Cells. *Nano Energy* **2018**, *49*, 523–528.
- (48) Harris, R. K.; Becker, E. D. NMR Nomenclature: Nuclear Spin Properties and Conventions for Chemical Shifts—IUPAC Recommendations. *J. Magn. Reson.* **2002**, *156*, 323–326.
- (49) Karmakar, A.; Bernard, G. M.; Meldrum, A.; Oliynyk, A. O.; Michaelis, V. K. Tailorable Indirect to Direct Bandgap Double Perovskites with Bright White-Light Emission: Decoding Chemical Structure Using Solid-State NMR. *J. Am. Chem. Soc.* **2020**, *142*, 10780–10793.
- (50) Karmakar, A.; Dodd, M. S.; Agnihotri, S.; Ravera, E.; Michaelis, V. K. Cu(II)-Doped $\text{Cs}_2\text{SbAgCl}_6$ Double Perovskite: A Lead-Free, Low-Bandgap Material. *Chem. Mater.* **2018**, *30*, 8280–8290.
- (51) Kubicki, D. J.; Prochowicz, D.; Pinon, A.; Stevanato, G.; Hofstetter, A.; Zakeeruddin, S. M.; Grätzel, M.; Emsley, L. Doping and Phase Segregation in Mn^{2+} - and Co^{2+} -Doped Lead Halide Perovskites from ^{133}Cs and ^1H NMR Relaxation Enhancement. *J. Mater. Chem. A* **2019**, *7*, 2326–2333.
- (52) Kubicki, D. J.; Prochowicz, D.; Hofstetter, A.; Zakeeruddin, S. M.; Grätzel, M.; Emsley, L. Phase Segregation in Cs-, Rb- and K-Doped Mixed-Cation $(\text{MA})_x(\text{FA})_{1-x}\text{PbI}_3$ Hybrid Perovskites from Solid-State NMR. *J. Am. Chem. Soc.* **2017**, *139*, 14173–14180.
- (53) Wolf, P.; Valla, M.; Núñez-Zarur, F.; Comas-Vives, A.; Rossini, A. J.; Firth, C.; Kallas, H.; Lesage, A.; Emsley, L.; Copéret, C.; Hermans, I. Correlating Synthetic Methods, Morphology, Atomic-Level Structure, and Catalytic Activity of Sn- β Catalysts. *ACS Catal.* **2016**, *6*, 4047–4063.

- (54) Grykałowska, A.; Nowak, B. High-Resolution Solid-State ^{119}Sn and ^{195}Pt NMR Studies of MPtSn Semiconductors (M = Ti, Zr, Hf, Th). *Solid State Nucl. Magn. Reson.* **2005**, *27*, 223–227.
- (55) Wrackmeyer, B. Application of ^{119}Sn NMR Parameters. Editor: G. A. Webb, *Annu. Rep. NMR Spectrosc., Academic Press*, **1999**; Vol. 38, pp 203–264.
- (56) Ha, M.; Karmakar, A.; Bernard, G. M.; Basilio, E.; Krishnamurthy, A.; Askar, A. M.; Shankar, K.; Kroeker, S.; Michaelis, V. K. Phase Evolution in Methylammonium Tin Halide Perovskites with Variable Temperature Solid-State ^{119}Sn NMR Spectroscopy. *J. Phys. Chem. C* **2020**, *124*, 15015–15027.
- (57) Jastrzebski, J. T. B. H.; Grove, D. M.; Boersma, J.; van Koten, G.; Ernsting, J. - M. ^{119}Sn NMR Study of Organotin Compounds Having Intramolecular Sn—N Coordination. *Magn. Reson. Chem.* **1991**, *29*, S25–S30.
- (58) Gunther, W. R.; Michaelis, V. K.; Caporini, M. A.; Griffin, R. G.; Román-Leshkov, Y. Dynamic Nuclear Polarization NMR Enables the Analysis of Sn-Beta Zeolite Prepared with Natural Abundance ^{119}Sn Precursors. *J. Am. Chem. Soc.* **2014**, *136*, 6219–6222.
- (59) Karmakar, A.; Bhattacharya, A.; Bernard, G. M.; Mar, A.; Michaelis, V. K. Revealing the Local Sn and Pb Arrangements in $\text{CsSn}_x\text{Pb}_{1-x}\text{Br}_3$ Perovskites with Solid-State NMR Spectroscopy. *ACS Mater. Lett.* **2021**, *3*, 261–267.
- (60) Yeh, H. M. M.; Geanangel, R. A. ^{119}Sn NMR Spectra of Tin(II) Halides. *Inorganica Chim. Acta* **1981**, *52*, 113–118.
- (61) Amornsakchai, P.; Apperley, D. C.; Harris, R. K.; Hodgkinson, P.; Waterfield, P. C. Solid-State NMR Studies of Some Tin(II) Compounds. *Solid State Nucl. Magn. Reson.* **2004**, *26*, 160–171.
- (62) Hunter, B. K.; Reeves, L. W. Chemical Shifts for Compounds of the Group IV Elements Silicon and Tin. *Can. J. Chem.* **1968**, *46*, 1399–1414.
- (63) Armstrong, R. L.; van Driel, H. M. The Observation of Incipient Phase Transitions in K_2PtCl_6 , K_2PdCl_6 , and K_2IrCl_6 . *Can. J. Phys.* **1972**, *50*, 2048–2053.
- (64) Dimitropoulos, C.; Van Der Klink, J. J.; Pelzl, J.; Regelsberger, M.; Rossler, K. Nuclear Quadrupole Resonance and Nuclear Magnetic Resonance Studies of K_2PtCl_6 Type Mixed Crystals. *Faraday Symp. Chem. Soc.* **1978**, *13*, 124–132.

- (65) Shannon, R. D. Revised Effective Ionic Radii and Systematic Studies of Interatomic Distances in Halides and Chalcogenides. *Acta Cryst.* **1976**, *A32*, 751–767.
- (66) Kaltzoglou, A.; Antoniadou, M.; Kontos, A. G.; Stoumpos, C. C.; Perganti, D.; Siranidi, E.; Raptis, V.; Trohidou, K.; Psycharis, V.; Kanatzidis, M. G.; Falaras, P. Optical-Vibrational Properties of the Cs₂SnX₆ (X = Cl, Br, I) Defect Perovskites and Hole-Transport Efficiency in Dye-Sensitized Solar Cells. *J. Phys. Chem. C* **2016**, *120*, 11777–11785.
- (67) Xiao, Z.; Zhou, Y.; Hosono, H.; Kamiya, T. Intrinsic Defects in a Photovoltaic Perovskite Variant Cs₂SnI₆. *Phys. Chem. Chem. Phys.* **2015**, *17*, 18900–18903.
- (68) Dmitrenko, O.; Bai, S.; Dybowski, C. Prediction of ²⁰⁷Pb NMR Parameters for the Solid Ionic Lead(II) Halides Using the Relativistic ZORA-DFT Formalism: Comparison with the Lead-Containing Molecular Systems. *Solid State Nucl. Magn. Reson.* **2008**, *34*, 186–190.
- (69) Bagno, A.; Casella, G.; Saielli, G. Relativistic DFT Calculation of ¹¹⁹Sn Chemical Shifts and Coupling Constants in Tin Compounds. *J. Chem. Theory Comput.* **2006**, *2*, 37–46.
- (70) Aebli, M.; Piveteau, L.; Nazarenko, O.; Benin, B. M.; Krieg, F.; Verel, R.; Kovalenko, M. V. Lead-Halide Scalar Couplings in ²⁰⁷Pb NMR of APbX₃ Perovskites (A = Cs, Methylammonium, Formamidinium; X = Cl, Br, I). *Sci. Rep.* **2020**, *10*, 8229.
- (71) Sharp, R. R. Rotational Diffusion and Magnetic Relaxation of ¹¹⁹Sn in Liquid SnCl₄ and SnI₄. *J. Chem. Phys.* **1972**, *57*, 5321–5330.
- (72) Sharp, R. R. Field Dependence of Nuclear Magnetic Relaxation of ¹¹⁹Sn in SnCl₄, SnBr₄, and SnI₄. *J. Chem. Phys.* **1974**, *60*, 1149–1157.
- (73) Hamaed, H.; Pawlowski, J. M.; Cooper, B. F. T.; Fu, R.; Eichhorn, S. H.; Schurko, R. W. Application of Solid-State ³⁵Cl NMR to the Structural Characterization of Hydrochloride Pharmaceuticals and Their Polymorphs. *J. Am. Chem. Soc.* **2008**, *130*, 11056–11065.
- (74) Widdifield, C. M.; Chapman, R. P.; Bryce, D. L. Chapter 5 Chlorine, Bromine, and Iodine Solid-State NMR Spectroscopy, *Annu. Rep. NMR Spectrosc.* **2009**, *66*, 195–326.

- (75) Chapman, R. P.; Widdifield, C. M.; Bryce, D. L. Solid-State NMR of Quadrupolar Halogen Nuclei. *Prog. Nucl. Magn. Reson. Spectrosc.* **2009**, *55*, 215–237.
- (76) Piveteau, L.; Aebli, M.; Yazdani, N.; Millen, M.; Korosec, L.; Krieg, F.; Benin, B. M.; Morad, V.; Piveteau, C.; Shiroka, T.; Comas-Vives, A.; Copéret, C.; Lindenberg, A. M.; Wood, V.; Verel, R.; Kovalenko, M. Bulk and Nanocrystalline Cesium Lead-Halide Perovskites as Seen by Halide Magnetic Resonance. *ACS Cent. Sci.* **2020**, *6*, 1138–1149.
- (77) Greer, B. J.; Michaelis, V. K.; Terskikh, V. V.; Kroeker, S. Reconnaissance of Diverse Structural and Electronic Environments in Germanium Halides by Solid-State ^{73}Ge NMR and Quantum Chemical Calculations. *Can. J. Chem.* **2011**, *89*, 1118–1129.
- (78) Lucier, B. E. G.; Terskikh, V. V.; Guo, J.; Bourque, J. L.; Mconie, S. L.; Ripmeester, J. A.; Huang, Y.; Baines, K. M. Chlorine-35 Solid-State Nuclear Magnetic Resonance Spectroscopy as an Indirect Probe of the Oxidation Number of Tin in Tin Chlorides. *Inorg. Chem.* **2020**, *59*, 13651–13670.
- (79) O'Dell, L. A.; Schurko, R. W. QCPMG Using Adiabatic Pulses for Faster Acquisition of Ultra-Wideline NMR Spectra. *Chem. Phys. Lett.* **2008**, *464*, 97–102.
- (80) Dell, L. A. O. The WURST Kind of Pulses in Solid-State NMR. *Solid State Nucl. Magn. Reson.* **2013**, *55–56*, 28–41.
- (81) Armstrong, R. L.; Baker, G. L. Temperature and Pressure Variation of the ^{35}Cl Nuclear Quadrupole Resonance Frequency in K_2IrCl_6 . *Can. J. Phys.* **1970**, *48*, 1649–1656.
- (82) Patrick, C. E.; Jacobsen, K. W.; Thygesen, K. S. Anharmonic Stabilization and Band Gap Renormalization in the Perovskite CsSnI_3 . *Phys. Rev. B* **2015**, *92*, 201205.
- (83) Yaffe, O.; Guo, Y.; Tan, L. Z.; Egger, D. A.; Hull, T.; Stoumpos, C. C.; Zheng, F.; Heinz, T. F.; Kronik, L.; Kanatzidis, M. G.; Owen, J. S.; Rappe, A. M.; Pimenta, M. A.; Brus, L. E. Local Polar Fluctuations in Lead Halide Perovskite Crystals. *Phys. Rev. Lett.* **2017**, *118*, 136001.
- (84) Yang, R. X.; Skelton, J. M.; Da Silva, E. L.; Frost, J. M.; Walsh, A. Spontaneous Octahedral Tilting in the Cubic Inorganic Cesium Halide Perovskites CsSnX_3 and CsPbX_3 ($X = \text{F}, \text{Cl}, \text{Br}, \text{I}$). *J. Phys. Chem. Lett.* **2017**, *8*, 4720–4726.

- (85) Maughan, A. E.; Ganose, A. M.; Candia, A. M.; Granger, J. T.; Scanlon, D. O.; Neilson, J. R. Anharmonicity and Octahedral Tilting in Hybrid Vacancy-Ordered Double Perovskites. *Chem. Mater.* **2018**, *30*, 472–483.
- (86) Maughan, A. E.; Paecklar, A. A.; Neilson, J. R. Bond Valences and Anharmonicity in Vacancy-Ordered Double Perovskite Halides. *J. Mater. Chem. C* **2018**, *6*, 12095–12104.
- (87) Senocrate, A.; Moudrakovski, I.; Maier, J. Short-Range Ion Dynamics in Methylammonium Lead Iodide by Multinuclear Solid State NMR and ^{127}I NQR. *Phys. Chem. Chem. Phys.* **2018**, *20*, 20043–20055.
- (88) Dunlap-Shohl, W. A.; Zhou, Y.; Padture, N. P.; Mitzi, D. B. Synthetic Approaches for Halide Perovskite Thin Films. *Chem. Rev.* **2019**, *119*, 3193–3295.
- (89) Liu, M.; Johnston, M. B.; Snaith, H. J. Efficient Planar Heterojunction Perovskite Solar Cells by Vapour Deposition. *Nature* **2013**, *501*, 395–398.
- (90) James, S. L.; Adams, C. J.; Bolm, C.; Braga, D.; Collier, P.; Friscic, T.; Grepioni, F.; Harris, K. D. M.; Hyett, G.; Jones, W.; Krebs, A.; Mack, J.; Maini, L.; Orpen, A. G.; Parkin, I. P.; Shearouse, W. C.; Steed, J. W.; Waddell, D. C. Mechanochemistry: Opportunities for New and Cleaner Synthesis. *Chem. Soc. Rev.* **2012**, *41*, 413–447.
- (91) Chizhik, S.; Panda, M. K.; Nath, N. K.; Boldyreva, E. Mechanically Responsive Molecular Crystals. *Chem. Rev.* **2015**, *115*, 12440–12490.
- (92) Stock, N.; Biswas, S. Synthesis of Metal-Organic Frameworks (MOFs): Routes to Various MOF Topologies, Morphologies, and Composites. *Chem. Rev.* **2012**, *112*, 933–969.
- (93) Prochowicz, D.; Franckevicius, M.; Cieslak, A. M.; Zakeeruddin, S. M.; Graetzel, M.; Lewinski, J. Mechanochemistry of the Hybrid Perovskite $\text{CH}_3\text{NH}_3\text{PbI}_3$: Characterization and the Corresponding Solar Cell Efficiency. *J. Mater. Chem. A* **2015**, *3*, 20772–20777.
- (94) Rosales, B. A.; Wei, L.; Vela, J. Synthesis and Mixing of Complex Halide Perovskites by Solvent-Free Solid-State Methods. *J. Solid State Chem.* **2019**, *271*, 206–215.
- (95) Hong, Z.; Tan, D.; John, R. A.; Tay, Y. K. E.; Ho, Y. K. T.; Zhao, X.; Sum, T. C.; Mathews, N.; García, F.; Soo, H. Sen. Completely Solvent-Free Protocols to Access

Phase-Pure, Metastable Metal Halide Perovskites and Functional Photodetectors from the Precursor Salts. *iScience* **2019**, *16*, 312–325.

(96) Protesescu, L.; Yakunin, S.; Nazarenko, O.; Dirin, D. N.; Kovalenko, M. V. Low-Cost Synthesis of Highly Luminescent Colloidal Lead Halide Perovskite Nanocrystals by Wet Ball Milling. *ACS Appl. Nano Mater.* **2018**, *1*, 1300–1308.

(97) Prochowicz, D.; Franckevičius, M.; Cieślak, A. M.; Zakeeruddin, S. M.; Grätzel, M.; Lewiński, J. Mechanochemical Synthesis of the Hybrid Perovskite $\text{CH}_3\text{NH}_3\text{PbI}_3$: Characterization and the Corresponding Solar Cell Efficiency. *J. Mater. Chem. A* **2015**, *3*, 20772–20777.

(98) Zarick, H. F.; Soetan, N.; Erwin, W. R.; Bardhan, R. Mixed Halide Hybrid Perovskites: A Paradigm Shift in Photovoltaics. *J. Mater. Chem. A* **2018**, *6*, 5507–5537.

(99) Karim, M. M. S.; Ganose, A. M.; Pieters, L.; Winnie Leung, W. W.; Wade, J.; Zhang, L.; Scanlon, D. O.; Palgrave, R. G. Anion Distribution, Structural Distortion, and Symmetry-Driven Optical Band Gap Bowing in Mixed Halide Cs_2SnX_6 Vacancy Ordered Double Perovskites. *Chem. Mater.* **2019**, *31*, 9430–9444.

(100) Im, J.; Stoumpos, C. C.; Jin, H.; Freeman, A. J.; Kanatzidis, M. G. Antagonism between Spin-Orbit Coupling and Steric Effects Causes Anomalous Band Gap Evolution in the Perovskite Photovoltaic Materials $\text{CH}_3\text{NH}_3\text{Sn}_{1-x}\text{Pb}_x\text{I}_3$. *J. Phys. Chem. Lett.* **2015**, *6*, 3503–3509.

(101) Rabbani, S. R.; Edmonds, D. T. Nuclear Spin-Lattice Relaxation-Time Reduction in Small Particles. *Phys. Rev. B* **1994**, *50*, 6184–6188.

(102) Dempah, K. E.; Lubach, J. W.; Munson, E. J. Characterization of the Particle Size and Polydispersity of Dicumarol Using Solid-State NMR Spectroscopy. *Mol. Pharm.* **2017**, *14*, 856–865.

(103) Nairui, X.; Yehua, T.; Yali, Q.; Duoduo, L.; Ke-Fan, W. One-Step Solution Synthesis and Stability Study of Inorganic Perovskite Semiconductor Cs_2SnI_6 . *Sol. Energy* **2020**, *204*, 429–439.

(104) Kubelka, P.; Munk, F. Ein Beitrag Zur Optik Der Farbanstriche. *Z. Tech. Phys. (Leipzig)* **1931**, *12*, 593–601.

- (105) Bernard, G. M.; Goyal, A.; Miskolzie, M.; McKay, R.; Wu, Q.; Wasylshen, R. E.; Michaelis, V. K. Methylammonium Lead Chloride: A Sensitive Sample for an Accurate NMR Thermometer. *J. Magn. Reson.* **2017**, *283*, 14–21.
- (106) te Velde, G.; Bickelhaupt, F. M.; Baerends, E. J.; Fonseca Guerra, C.; van Gisbergen, S. J. A.; Snijders, J. G.; Ziegler, T. Chemistry with ADF. *J. Comput. Chem.* **2001**, *22*, 931–967.
- (107) Guerra, C. F.; Snijders, J. G.; te Velde, G.; Baerends, E. J. Towards an Order-N DFT Method. *Theor. Chem. Acc.* **1998**, *99*, 391–403.
- (108) Baerends, E. J.; Ziegler, T.; Atkins, A. J.; Autschbach, J.; Baseggio, O.; Bashford, D.; Bérces, A.; Bickelhaupt, F. M.; Bo, C.; Boerrigter, P.M.; et al. ADF2018, SCM, Theoretical Chemistry, Vrije Universiteit, Amsterdam, The Netherlands, <https://www.scm.com>.
- (109) Adamo, C.; Barone, V. Toward Reliable Density Functional Methods without Adjustable Parameters: The PBE0 Model. *J. Chem. Phys.* **1999**, *110*, 6158–6170.
- (110) Lenthe, E. van; Baerends, E. J. Optimized Slater-Type Basis Sets for the Elements 1-118. *J. Comput. Chem.* **2003**, *24*, 1142–1156.
- (111) Wolff, S. K.; Ziegler, T.; Lenthe, E. van; Baerends, E. J. Density Functional Calculations of Nuclear Magnetic Shieldings Using the Zeroth-Order Regular Approximation (ZORA) for Relativistic Effects: ZORA Nuclear Magnetic Resonance. *J. Chem. Phys.* **1999**, *110*, 7689–7698.
- (112) Lenthe, E. van; Baerends, E. J.; Snijders, J. G. Relativistic Regular Two-component Hamiltonians. *J. Chem. Phys.* **1993**, *99*, 4597–4610.
- (113) Autschbach, J. The Role of the Exchange-Correlation Response Kernel and Scaling Corrections in Relativistic Density Functional Nuclear Magnetic Shielding Calculations with the Zeroth-Order Regular Approximation. *Mol. Phys.* **2013**, *111*, 2544–2554.
- (114) Wolff, S. K.; Ziegler, T. Calculation of DFT-GIAO NMR Shifts with the Inclusion of Spin-Orbit Coupling. *J. Chem. Phys.* **1998**, *109*, 895–905.

Chapter 7

- (1) Dunlap-Shohl, W. A.; Zhou, Y.; Padture, N. P.; Mitzi, D. B. Synthetic

- Approaches for Halide Perovskite Thin Films. *Chem. Rev.* **2019**, *119*, 3193–3295.
- (2) Kim, H.; Han, J. S.; Choi, J.; Kim, S. Y.; Jang, H. W. Halide Perovskites for Applications beyond Photovoltaics. *Small Methods* **2018**, *2*, 1700310.
- (3) Song, T. Bin; Yokoyama, T.; Stoumpos, C. C.; Logsdon, J.; Cao, D. H.; Wasielewski, M. R.; Aramaki, S.; Kanatzidis, M. G. Importance of Reducing Vapor Atmosphere in the Fabrication of Tin-Based Perovskite Solar Cells. *J. Am. Chem. Soc.* **2017**, *139*, 836–842.
- (4) Li, J.; Cao, H.; Jiao, W.; Wang, Q.; Wei, M.; Cantone, I.; Lü, J.; Abate, A. Biological Impact of Lead from Halide Perovskites Reveals the Risk of Introducing a Safe Threshold. *Nat. Commun.* **2020**, *11*, 310.
- (5) Yang, J.; Siempelkamp, B. D.; Liu, D.; Kelly, T. L. Investigation of $\text{CH}_3\text{NH}_3\text{PbI}_3$ Degradation Rates and Mechanisms in Controlled Humidity Environments Using in Situ Techniques. *ACS Nano* **2015**, *9*, 1955–1963.
- (6) Luo, J.; Hu, M.; Niu, G.; Tang, J. Lead-Free Halide Perovskites and Perovskite Variants as Phosphors toward Light-Emitting Applications. *ACS Appl. Mater. Interfaces* **2019**, *11*, 31575–31584.
- (7) Maughan, A. E.; Ganose, A. M.; Scanlon, D. O.; Neilson, J. R. Perspectives and Design Principles of Vacancy-Ordered Double Perovskite Halide Semiconductors. *Chem. Mater.* **2019**, *31*, 1184–1195.
- (8) Saparov, B.; Sun, J. P.; Meng, W.; Xiao, Z.; Duan, H. S.; Gunawan, O.; Shin, D.; Hill, I. G.; Yan, Y.; Mitzi, D. B. Thin-Film Deposition and Characterization of a Sn-Deficient Perovskite Derivative Cs_2SnI_6 . *Chem. Mater.* **2016**, *28*, 2315–2322.
- (9) Wang, A.; Yan, X.; Zhang, M.; Sun, S.; Yang, M.; Shen, W.; Pan, X.; Wang, P.; Deng, Z. Controlled Synthesis of Lead-Free and Stable Perovskite Derivative Cs_2SnI_6 Nanocrystals via a Facile Hot-Injection Process. *Chem. Mater.* **2016**, *28*, 8132–8140.
- (10) Lim, S. C.; Lin, H. P.; Tsai, W. L.; Lin, H. W.; Hsu, Y. T.; Tuan, H. Y. Binary Halide, Ternary Perovskite-like, and Perovskite-Derivative Nanostructures: Hot Injection Synthesis and Optical and Photocatalytic Properties. *Nanoscale* **2017**, *9*, 3747–3751.
- (11) Veronese, A.; Patrini, M.; Bajoni, D.; Ciarrocchi, C.; Quadrelli, P.; Malavasi, L. Highly Tunable Emission by Halide Engineering in Lead-Free Perovskite-Derivative

- Nanocrystals: The Cs_2SnX_6 ($\text{X} = \text{Cl}, \text{Br}, \text{Br/I}, \text{I}$) System. *Front. Chem.* **2020**, *8*, 1–9.
- (12) Gao, X.; Zhang, X.; Yin, W.; Wang, H.; Hu, Y.; Zhang, Q.; Shi, Z.; Colvin, V. L.; Yu, W. W.; Zhang, Y. Ruddlesden–Popper Perovskites: Synthesis and Optical Properties for Optoelectronic Applications. *Adv. Sci.* **2019**, *6*, 1900941.
- (13) Lamba, R. S.; Basera, P.; Bhattacharya, S.; Sapra, S. Band Gap Engineering in $\text{Cs}_2(\text{Na}_x\text{Ag}_{1-x})\text{BiCl}_6$ Double Perovskite Nanocrystals. *J. Phys. Chem. Lett.* **2019**, *10*, 5173–5181.
- (14) Funabiki, F.; Toda, Y.; Hosono, H. Optical and Electrical Properties of Perovskite Variant $(\text{CH}_3\text{NH}_3)_2\text{SnI}_6$. *J. Phys. Chem. C* **2018**, *122*, 10749–10754.
- (15) Maughan, A. E.; Ganose, A. M.; Almaker, M. A.; Scanlon, D. O.; Neilson, J. R. Tolerance Factor and Cooperative Tilting Effects in Vacancy-Ordered Double Perovskite Halides. *Chem. Mater.* **2018**, *30*, 3909–3919.
- (16) Bhattacharya, A.; Tkachuk, D. G.; Mar, A.; Michaelis, V. K. Mere Anarchy Is Loosed: Structural Disorder in $\text{Cu}_2\text{Zn}_{1-x}\text{Cd}_x\text{SnS}_4$. *Chem. Mater.* **2021**, *33*, 4709–4722.

Appendix A: Supplementary Data for Chapter 2

Mechanochemical Synthesis of Methylammonium Lead Mixed-Halide Perovskites: Unraveling the Solid-Solution Behavior Using Solid-State NMR

Table A1. ^{207}Pb NMR linewidth (FWHM) of MAPbX_3 .

MAPbX_3	FWHM (Hz) non-spinning, 21.1 T	FWHM (Hz) non-spinning, 7.05 T (ref. ¹)	FWHM (Hz) MAS, 14.1 T (ref. ¹)	FWHM (Hz) MAS, 14.1 T (ref. ²)
X = Cl	3,700	3,700	3,000	3,000
X = Br	15,000	15,300	17,000	15,900
X = I	25,500	19,800	30,500	21,100

Table A2. DFT quantum chemical calculations (ADF) on $[\text{PbCl}_x\text{Br}_{6-x}]^{4-}$ anions.

Environment	σ_{iso} (ppm)	δ_{iso} (ppm) ^a	Ω (ppm)	κ
$[\text{PbCl}_6]^{4-}$	9538	-914	0.0	0.00
$[\text{PbCl}_5\text{Br}]^{4-}$	9300	-675	282	1.00
<i>trans</i> - $[\text{PbCl}_4\text{Br}_2]^{4-}$	9084	-460	537	1.00
<i>cis</i> - $[\text{PbCl}_4\text{Br}_2]^{4-}$	9082	-458	283	-0.57
<i>mer</i> - $[\text{PbCl}_3\text{Br}_3]^{4-}$	8890	-266	470	0.09
<i>fac</i> - $[\text{PbCl}_3\text{Br}_3]^{4-}$	8881	-257	92	-1.00
<i>trans</i> - $[\text{PbCl}_2\text{Br}_4]^{4-}$	8736	-112	354	-1.00
<i>cis</i> - $[\text{PbCl}_2\text{Br}_4]^{4-}$	8709	-85	252	0.51

$[\text{PbClBr}_5]^{4-}$	8584	41	149	-1.00
$[\text{PbBr}_6]^{4-}$	8534	90	0.0	0.00

$${}^a\delta_{\text{iso,calc}} \text{ (ppm)} = -(\sigma_{\text{iso,calc}} - 8858.4 \text{ ppm})$$

Table A3. Spin-spin relaxation time (T_2 , μs) of parent and 50/50 MCS MHP.

Sample	$[\text{PbBr}_6]^{4-}$	$[\text{PbClBr}_5]^{4-}/$ $[\text{PbCl}_2\text{Br}_4]^{4-}$	$[\text{PbCl}_3\text{Br}_3]^{4-}$	$[\text{PbCl}_4\text{Br}_2]^{4-}/$ $[\text{PbCl}_5\text{Br}]^{4-}$	$[\text{PbCl}_6]^{4-}$
$\text{MAPb}(\text{Cl}_{0.5}\text{Br}_{0.5})_3$	54 ^a	57 ^a	66 ^a	93 ^a	98 ^a
MAPbCl_3	-	-	-	-	150 ^b ,
MAPbBr_3	70 ^c , 63 ^d	-	-	-	-

^a21.1 T, (T_2 , spin-echo, non-spinning)

^b11.75 T, (T_2 , spin-echo, non-spinning)

^cRef.¹ (T_2^* , MAS, 14.1 T)

^dRef.² (T_2 , spin-echo, non-spinning, 9.4 T)

Table A4. DFT GIPAW periodic-based quantum chemical calculations (CASTEP).

Environment	σ_{iso} (ppm)	Ω (ppm)	κ
$[\text{PbCl}_6]^{4-}$	5799	0.1	-0.68
$[\text{PbCl}_5\text{Br}]^{4-}$	5514	428	-1.00
$[\text{PbCl}_4\text{Br}_2]^{4-}$	5217	44	1.00
$[\text{PbCl}_4\text{Br}_2]^{4-}$	5195	894	-1.00
$[\text{PbCl}_3\text{Br}_3]^{4-}$	4886	924	-0.01
$[\text{PbCl}_3\text{Br}_3]^{4-}$	4909	1.4	-0.98
$[\text{PbCl}_2\text{Br}_4]^{4-}$	4564	480	-0.99
$[\text{PbCl}_2\text{Br}_4]^{4-}$	4545	946	1.00
$[\text{PbClBr}_5]^{4-}$	4209	483	1.00
$[\text{PbBr}_6]^{4-}$	3842	0.04	0.15

Table A5. Elemental atomic ratios for the MHP samples determined using the EDX technique.

Sample	Cl (at. %)	Br (at. %)	Ratio	Cl+Br (X) (at. %)	Pb (at. %)	X : Pb
MAPb(Cl _{0.25} Br _{0.75}) ₃ -HG	5.8	19.2	1:3.3	25	8.8	2.8:1
MAPb(Cl _{0.50} Br _{0.50}) ₃ -HG	10.8	10.4	1.03:1	21.2	7.7	2.8:1
MAPb(Cl _{0.75} Br _{0.25}) ₃ -HG	5.9	1.9	3.01:1	7.8	2.7	2.8:1
MAPb(Cl _{0.50} Br _{0.50}) ₃ -BM	7.3	8.0	1:1.09	15.3	5.5	2.8:1
MAPb(Cl _{0.50} Br _{0.50}) ₃ -SS	6.94	5.0	1.38:1	11.9	5.12	2.3:1

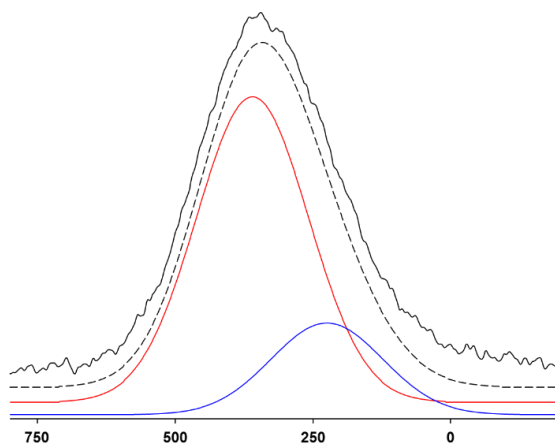


Figure A1. ²⁰⁷Pb NMR spectrum of an MAS sample of MAPb(Cl_{0.05}Br_{0.95})₃ acquired at 7.05 T with a spinning frequency of 13 kHz (upper trace). The dashed line is the simulated spectrum and is the sum of a site at $\delta_{CS} = 360$ ppm (red trace) and at $\delta_{CS} = 225$ ppm (blue trace). The latter has 30 % the intensity of the former.

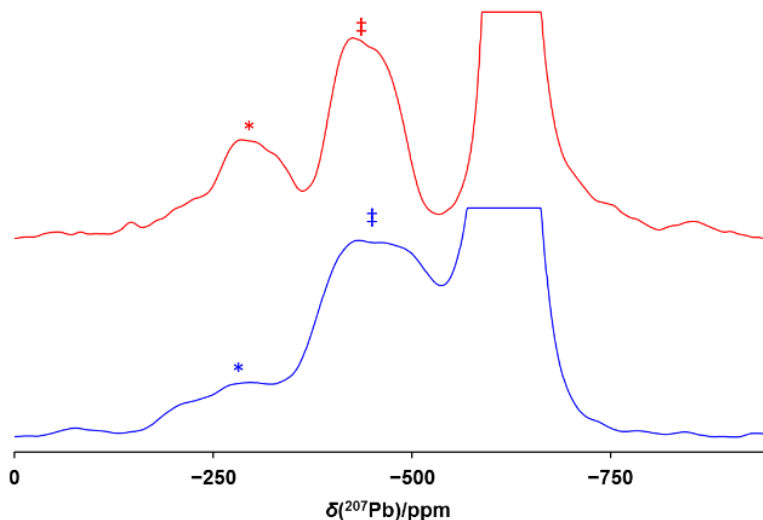


Figure A2. ^{207}Pb NMR spectra of an MAS sample of $\text{MAPb}(\text{Cl}_{0.95}\text{Br}_{0.05})_3$ acquired at 11.7 T at 13.5 kHz (upper red trace) and at 7.05 T with a spinning frequency of 13 kHz (lower, blue trace). The truncated peak is attributed to $[\text{PbCl}_6]^{4-}$ units—see Figure 2.2 of the manuscript for a full spectrum of the sample acquired at 11.7 T. The peaks marked with ‡ are attributed to $[\text{PbCl}_5\text{Br}]^{4-}$ units. The asterisks indicate spinning side bands.

Deconvolution of ^{207}Pb NMR Spectra

In principle, a ^{207}Pb NMR spectrum for a MHP of the type $[\text{PbX}_x\text{X}'_{6-x}]^{4-}$ ($0 < x < 6$) may consist of 10 distinct sites arising from the isomers summarized in Table A6. In fact, as discussed in the manuscript, only seven distinct peak maxima were identified. These have been attributed to one each of the seven possible $[\text{PbCl}_x\text{Br}_{6-x}]^{4-}$ octahedra, with the assumption that the chemical shift difference between each pair of geometric isomers (e.g., *cis*- and *trans*- $[\text{PbCl}_4\text{Br}_2]^{4-}$) is not resolved because of the moderate field strength used here and because there is significant overlap for these sites. Our calculations support this conclusion, with differences between geometric isomers ≤ 27 ppm (see Table A2) compared to an average chemical shift difference between distinct anion units of greater than 160 ppm. Experimental data for the $[\text{PbCl}_x\text{Br}_{6-x}]^{4-}$ anions are not available, but studies on a series of $[\text{PtCl}_x\text{Br}_{6-x}]^{2-}$ anions are instructive.^{3,4} As for ^{207}Pb , the coordination about the ^{195}Pt is octahedral, and the ^{195}Pt chemical shift is

even more sensitive to its environment than that for ^{207}Pb . For example, the chemical shift difference between $[\text{PtCl}_6]^{2-}$ and $[\text{PtBr}_6]^{2-}$ is almost 1900 ppm,^{3,4} compared to approximately 1000 ppm for the corresponding ^{207}Pb anions. Nevertheless, these groups both report chemical shift differences of 3 ppm or less between each of the three pairs of geometric isomers.

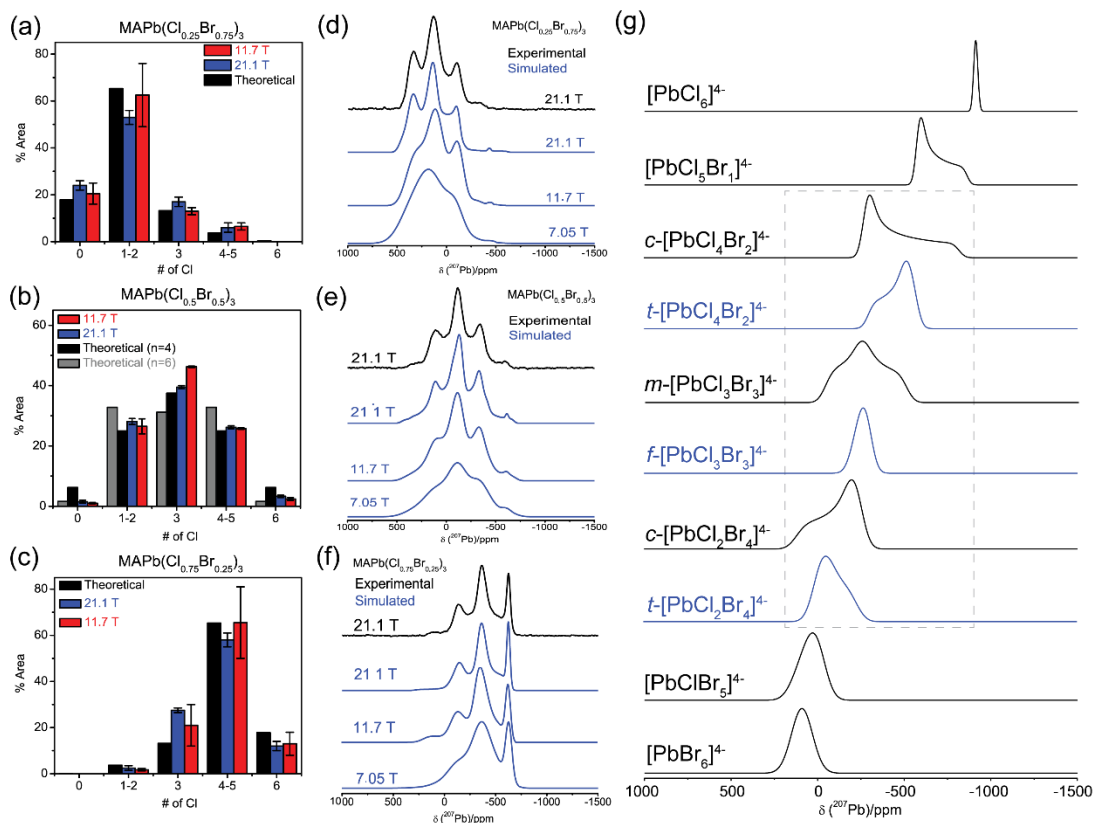


Figure A3. Simulated ^{207}Pb NMR spectra for (a) $\text{MAPb}(\text{Cl}_{0.25}\text{Br}_{0.75})_3$ (b) $\text{MAPb}(\text{Cl}_{0.5}\text{Br}_{0.5})_3$ and for (c) $\text{MAPb}(\text{Cl}_{0.75}\text{Br}_{0.25})_3$ acquired at the indicated fields fit according to the population distributions indicated by the bar charts, following a binomial-like distribution based on Gaussians. Data were further fit (d-f) using insight from the DFT calculated shielding parameters (g) determined using ADF on model anions, whereby the site distribution of seven unique Pb environments were fixed at a binomial distribution and slight changes to the CSA parameters were implemented to obtain best overall fits. Errors were assessed using the Gaussian fitting procedure at multiple field strengths. NB: c = cis; t = trans; f = fac & m = mer.

Table A6. Probabilities for the $[\text{PbCl}_x\text{Br}_{6-x}]^{4-}$ anions.^a

Isomer	Probability/% ^a
$[\text{PbCl}_6]^{4-}$	100
$[\text{PbCl}_5\text{Br}_1]^{4-}$	100
<i>t</i> - $[\text{PbCl}_4\text{Br}_2]^{4-}$	50
<i>c</i> - $[\text{PbCl}_4\text{Br}_2]^{4-}$	50
<i>m</i> - $[\text{PbCl}_3\text{Br}_3]^{4-}$	50
<i>f</i> - $[\text{PbCl}_3\text{Br}_3]^{4-}$	50
<i>t</i> - $[\text{PbCl}_2\text{Br}_4]^{4-}$	50
<i>c</i> - $[\text{PbCl}_2\text{Br}_4]^{4-}$	50
$[\text{PbCl}_1\text{Br}_5]^{4-}$	100
$[\text{PbBr}_6]^{4-}$	100

^aProbabilities listed here are those expected in the absence of thermodynamic or other governing factors.

^b*c* = *cis*; *t* = *trans*; *f* = *fac* & *m* = *mer*

Although seven distinct peak maxima were identified (Table 1.1), the anions, apart from $[\text{PbCl}_6]^{4-}$ and $[\text{PbBr}_6]^{4-}$, are subject to CSA. Thus, a further complication is that the geometric isomers are predicted to have different lineshapes, Figure A3g (but similar chemical shifts, as discussed above). Since the spans of these sites are greater than the chemical shift differences between neighboring sites, there is significant overlap, rendering it impossible to isolate the contributions from separate sites. For the simulations, initial populations were based on the theoretical values obtained from the assumption of a binomial distribution, and initial lineshapes were based on the calculated values (Table A2). These were adjusted to obtain simulated spectra that best fit experimental spectra, as illustrated in Figure A3d-f. To compare the agreement between the fits of the experimental data and those expected on the basis of computational results, the areas under five regions were determined; these are summarized in Table A7.

Table A7. Percent contribution to the total area of the ^{207}Pb NMR spectra for MHPs from a given $[\text{PbCl}_x\text{Br}_{6-x}]^{4-}$ unit. Spectra acquired at 11.75 T

Samples		$[\text{PbBr}_6]^{4-}$	$[\text{PbClBr}_5]^{4-}$ + $[\text{PbCl}_2\text{Br}_4]^{4-}$	$[\text{PbCl}_3\text{Br}_3]^{4-}$	$[\text{PbCl}_4\text{Br}_2]^{4-}$ + $[\text{PbCl}_5\text{Br}]^{4-}$	$[\text{PbCl}_6]^{4-}$
MAPbBr ₃	(%) ^a	100	0	0	0	0
	(%) ^b	100	0	0	0	0
MAPb(Cl _{0.05} Br _{0.95}) ₃	(%) ^a	73.5	26.3	0.2	0	0
	(%) ^b	72 (5)	28 (5)	0	0	0
MAPb(Cl _{0.25} Br _{0.75}) ₃ ⁴	(%) ^a	17.8	65.3	13.2	3.7	0
	(%) ^b	20.5 (5)	61.5 (14)	13 (3)	6.5 (2)	0
MAPb(Cl _{0.50} Br _{0.50}) ₃ ⁴	(%) ^a	1.6	32.8	31.2	32.8	1.6
	(%) ^b	1.5 (1)	21 (5)	50 (10)	27 (5)	1 (1)
MAPb(Cl _{0.75} Br _{0.25}) ₃ ⁴	(%) ^a	0	3.7	13.3	65.3	17.8
	(%) ^b	0	1.75 (1)	21 (9)	65.5 (17)	13 (5)
MAPb(Cl _{0.95} Br _{0.05}) ₃	(%) ^a	0	0	0.2	26.3	73.5
	(%) ^b	0	0	0	28 (2) ^c	72 (2) ^c
MAPbCl ₃	(%) ^a	0	0	0	0	100
	(%) ^b	0	0	0	0	100

^aTheoretical binomial distribution for seven sites ($n = 6$), using Gaussians as a first approximation.

^bExperimental results based on 11.75 T.

^cAssessed from MAS NMR experiments at 7.05 and 11.75 T.

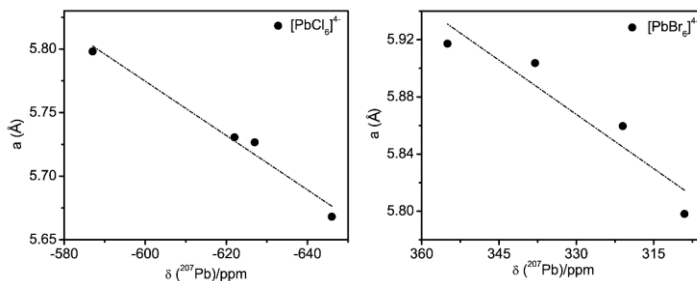


Figure A4. Sensitivity of experimental $\delta_{\text{cs}}(^{207}\text{Pb})$ for $[\text{PbCl}_6]^{4-}$ (left) and $[\text{PbBr}_6]^{4-}$ (right) as the unit cell changes ($a = b = c$) to accommodate halide mixing.

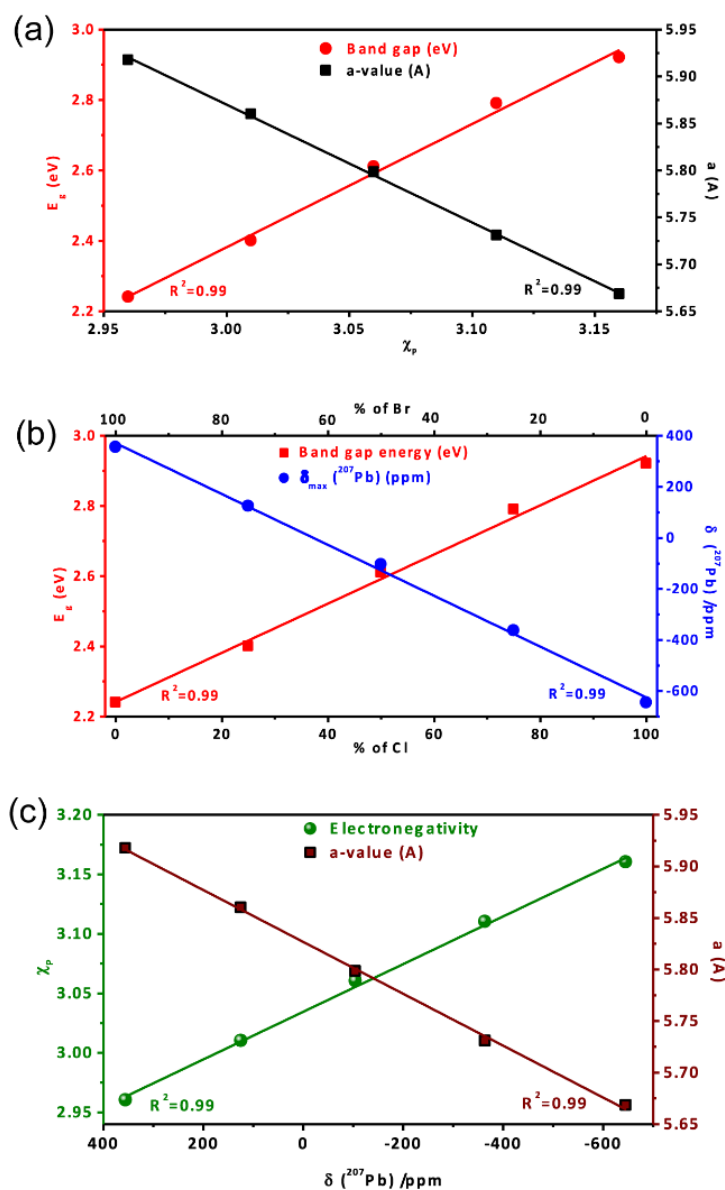


Figure A4. Relationship between MHP physical properties (Bandgap (E_g)) and electronegativity (χ_p ; $\chi_p = \sum_i a(i)\chi(i)$, where, $a(i)$ = fraction of halide ‘i’ (Cl or Br) and $\chi(i)$ = Pauling electronegativity of halide ‘i’ ($\chi(\text{Cl})$ or $\chi(\text{Br})$) with atomic structure from X-ray diffraction (unit cell parameter, a (Å)) and NMR spectroscopy (chemical shift, $\delta^{(207\text{Pb})}$ /ppm).

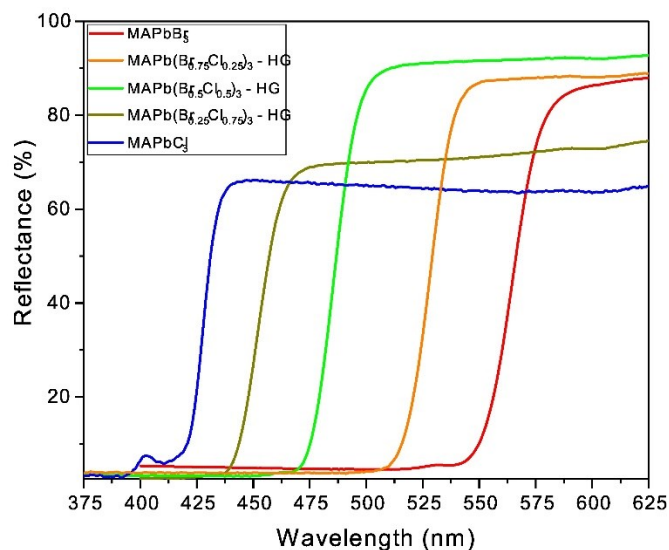


Figure A6. Diffuse reflectance spectra for MCS-HG $\text{MAPb}(\text{Cl}_x\text{Br}_{1-x})_3$, with $x = 0.75$, 0.50 , and 0.25 , along with those for their parent compounds, MAPbBr_3 and MAPbCl_3 .

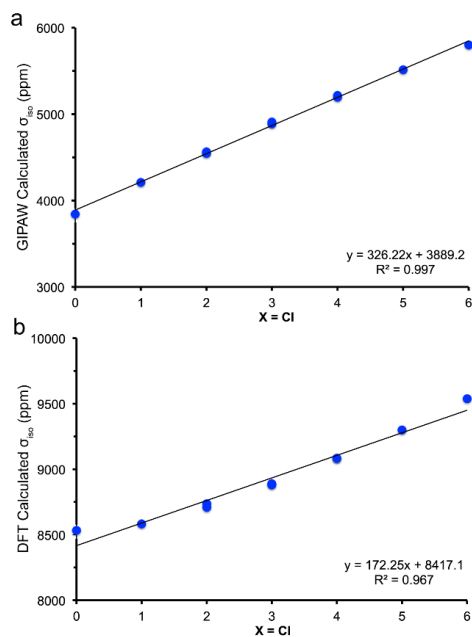


Figure A7. Comparison of DFT calculated isotropic ^{207}Pb shielding parameter (ppm) on Cl/Br substituted $[\text{PbX}_x\text{X}'_{6-x}]^{4-}$ octahedra using a $2 \times 2 \times 2$ supercell (GIPAW) as implemented in CASTEP (a) or on a model anion as implemented in ADF (b).

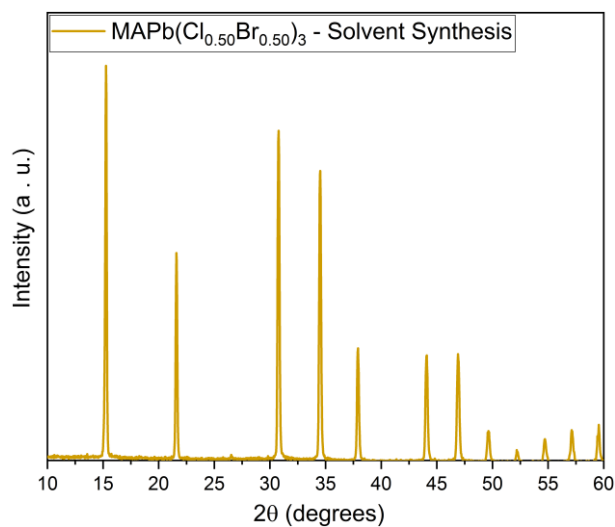


Figure A8. Powder XRD pattern for $\text{MAPb}(\text{Cl}_{0.5}\text{Br}_{0.5})_3$ prepared using the SS method.

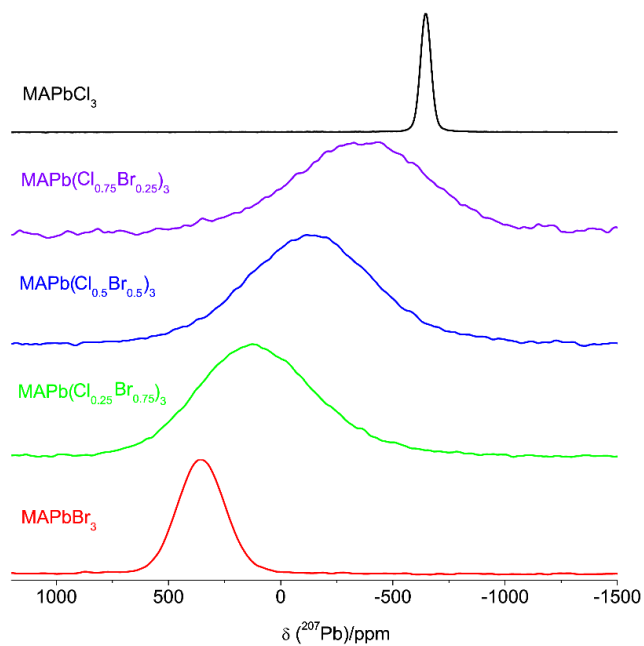
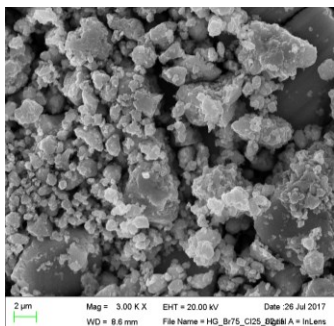
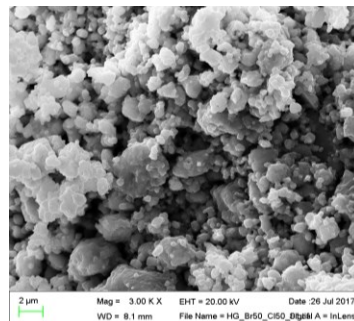


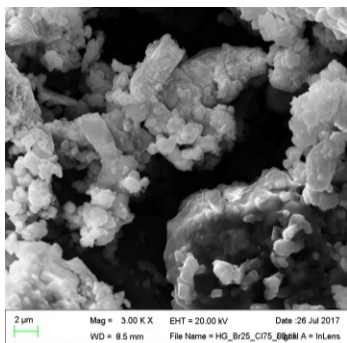
Figure A9. ^{207}Pb NMR spectra for non-spinning $\text{MAPb}(\text{Cl}_x\text{Br}_{1-x})_3$, where $x = 0, 0.25, 0.50, 0.75$ and 1 . MCS-BM method was used to prepare MHPs (purple, blue and green). Samples were ball milled for a period of 1 hr. All spectra were acquired at 7.05 T.



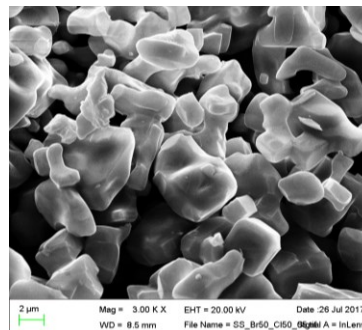
(a) $\text{MAPb}(\text{Cl}_{0.25}\text{Br}_{0.75})_3 - \text{HG}$



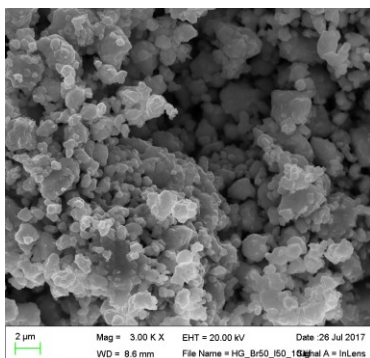
(b) $\text{MAPb}(\text{Cl}_{0.5}\text{Br}_{0.5})_3 - \text{HG}$



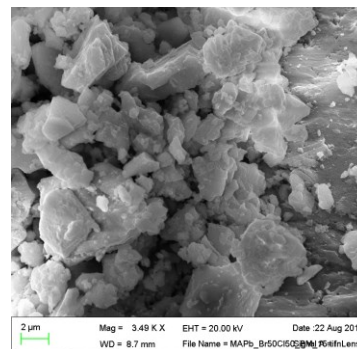
(c) $\text{MAPb}(\text{Cl}_{0.75}\text{Br}_{0.25})_3 - \text{HG}$



(d) $\text{MAPb}(\text{Cl}_{0.5}\text{Br}_{0.5})_3 - \text{SS}$



(e) $\text{MAPb}(\text{Cl}_{0.5}\text{Br}_{0.5})_3 - \text{HG}$



(f) $\text{MAPb}(\text{Cl}_{0.5}\text{Br}_{0.5})_3 - \text{BM}$

Figure A10. FESEM images for the MHP samples prepared by SS, MCS-HG and MCS-BM.

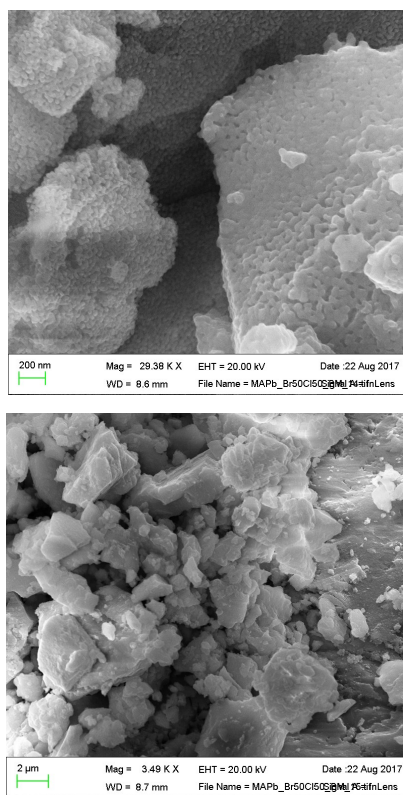


Figure A11. FESEM images for MCS-BM MHP sample $\text{MAPb}(\text{Cl}_{0.5}\text{Br}_{0.5})_3$ high (top, 200 nm) and low (bottom, 2 μm) magnification.

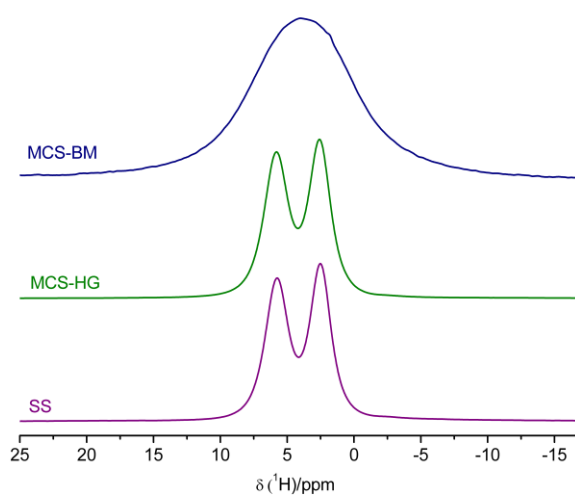


Figure A12. ^1H NMR spectra of $\text{MAPb}(\text{Cl}_{0.5}\text{Br}_{0.5})_3$ samples acquired at 7.05 T with 10 kHz MAS; samples prepared by the indicated techniques.

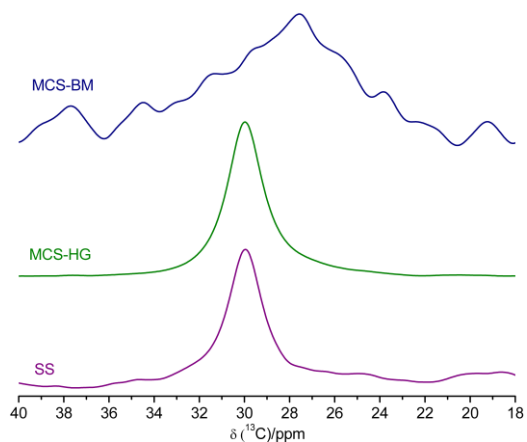


Figure A13. ^{13}C CP NMR spectra of $\text{MAPb}(\text{Cl}_{0.5}\text{Br}_{0.5})_3$ samples, obtained at 7.05 T with 10 kHz MAS. The samples were prepared by the indicated techniques.

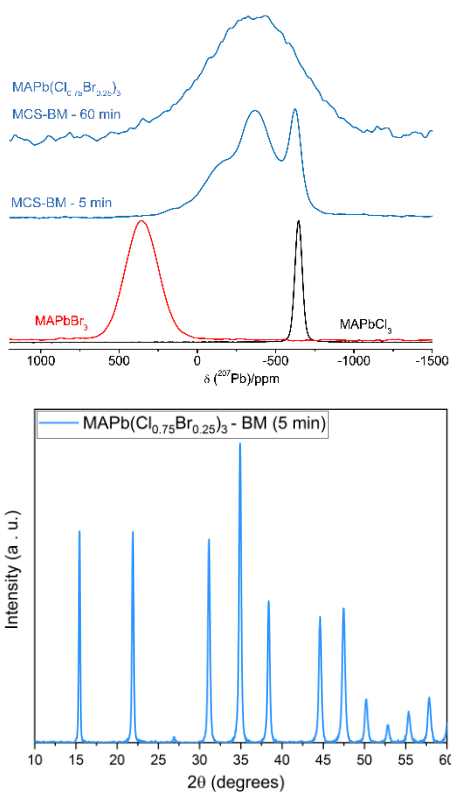


Figure A14. ^{207}Pb NMR spectra of non-spinning $\text{MAPb}(\text{Cl}_{0.75}\text{Br}_{0.25})_3$, prepared by using the MCS-BM method for 5 min and 1 hr (top) and XRD pattern, obtained after using the MCS-BM method for 5 min (bottom).

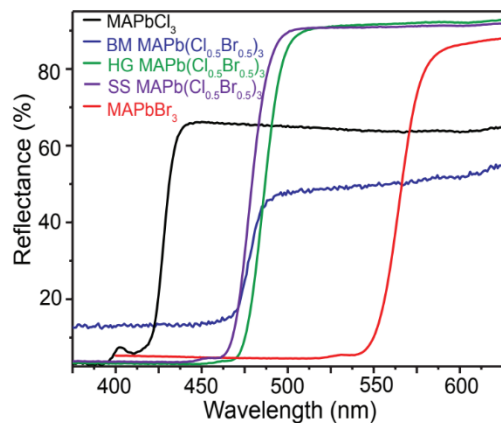


Figure A15. Diffuse reflectance spectra for $\text{MAPb}(\text{Cl}_{0.5}\text{Br}_{0.5})_3$, prepared by BM, HG, and SS, along with those for the parent compounds, MAPbBr_3 and MAPbCl_3 .

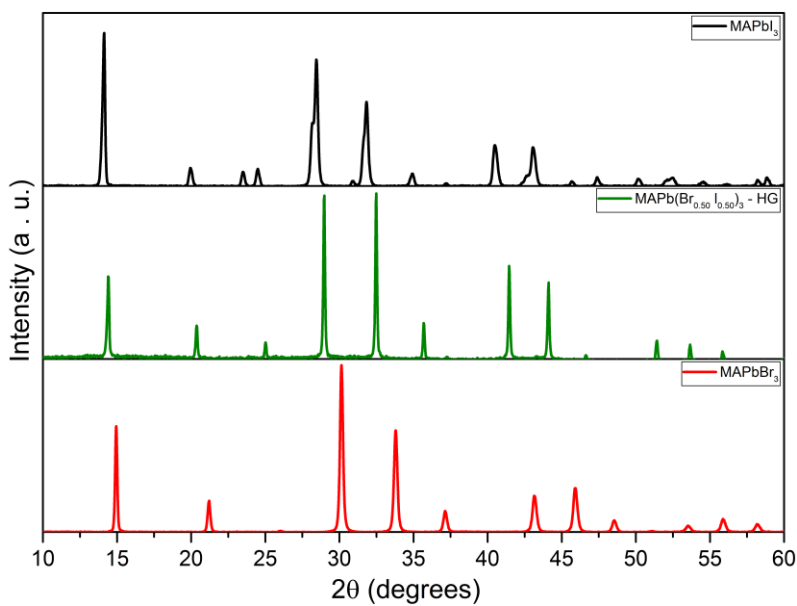


Figure A16. Comparison between XRD patterns of $\text{MAPb}(\text{Br}_{0.5}\text{I}_{0.5})_3$ prepared by MCS-HG (2 hr) and those for the parent compounds, MAPbI_3 (tetragonal) and MAPbBr_3 (cubic).

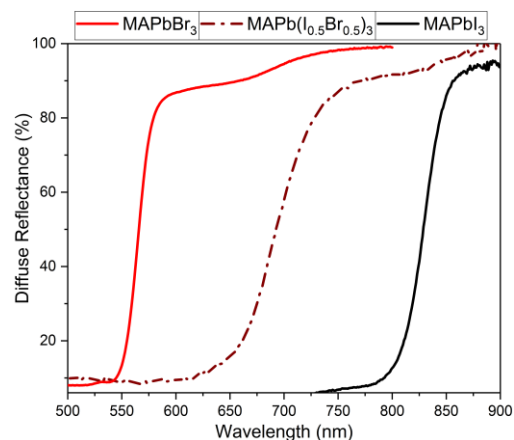


Figure A17. Diffuse reflectance spectra of the $\text{MAPb}(\text{Br}_{0.5}\text{I}_{0.5})_3$ sample prepared by MCS-HG, along with those for the parent compounds, MAPbBr_3 and MAPbI_3 .

References

- (1) Roiland, C.; Trippe-Allard, G.; Jemli, K.; Alonso, B.; Ameline, J.-C.; Gautier, R.; Bataille, T.; Le Polles, L.; Deleporte, E.; Even, J., et al., Multinuclear NMR as a Tool for Studying Local Order and Dynamics in $\text{CH}_3\text{NH}_3\text{PbX}_3$ ($X = \text{Cl}, \text{Br}, \text{I}$) Hybrid Perovskites. *Phys. Chem. Chem. Phys.* 2016, 18 (39), 27133-27142.
- (2) Rosales, B. A.; Men, L.; Cady, S. D.; Hanrahan, M. P.; Rossini, A. J.; Vela, J., Persistent Dopants and Phase Segregation in Organolead Mixed-Halide Perovskites. *Chem. Mater.* 2016, 28 (19), 6848-6859.
- (3) Burger, M. R.; Kramer, J.; Chermette, H.; Koch, K. R. A Comparison of Experimental and DFT Calculations of ^{195}Pt NMR Shielding Trends for $[\text{PtX}_n\text{Y}_{6-n}]^{2-}$ ($X = \text{Cl}, \text{Br}, \text{F}, \text{and I}$) Anions. *Magn. Reson. Chem.* 2010, 48, S38–S47.
- (4) Fowe, E. P.; Belser, P. Daul, C.; Chermette, H. Assessment of Theoretical Prediction of the NMR Shielding Tensor of $^{195}\text{PtCl}_x\text{Br}_{6-x}^{2-}$ Complexes by DFT Calculations: Experimental and Computational Results. *Phys. Chem. Chem. Phys.* 2005, 7, 1732–1738.

Appendix B: Supplementary Data for Chapter 3

Influence of Hidden Halogen Mobility on Local Structure of $\text{CsSn}(\text{Cl}_{1-x}\text{Br}_x)_3$ Mixed-Halide Perovskites by Solid-State NMR

Experimental

Materials

Starting materials were purchased from the following commercial sources and were used without further modification: CsCl (Terochem Laboratories Ltd. 99.7%), CsBr (Sigma, 99.99%), SnCl₂ (Alfa Aesar, >99%), SnBr₂ (Alfa Aesar, 99.2%), SnBr₄ (Sigma, 99%), HBr (Anachemia, 48%), and H₃PO₂ (Sigma, 50 wt.% in H₂O).

High-Temperature Synthesis of $\text{CsSn}(\text{Cl}_{1-x}\text{Br}_x)_3$ ($0 \leq x \leq 1$)

Various members of the solid solution $\text{CsSn}(\text{Cl}_{1-x}\text{Br}_x)_3$ were prepared by reactions at high temperature. CsX and SnX₂ (X = Cl, Br) were combined in stoichiometric ratios on a 0.5-g scale, finely ground using an agate mortar and pestle, pressed into pellets, and loaded into fused-silica tubes which were evacuated under a pressure of 10⁻³ mbar and sealed. The tubes were heated at 1.5 K/min to either 673 or 723 K (depending on composition), held at that temperature for 15 h, and then cooled to room temperature at 5 K/min. The samples were stored in glass vials and further characterized under ambient conditions.

Cubic CsSnCl₃ was obtained as a metastable phase at room temperature as follows: a sample of CsSnCl₃ prepared as described above was heated to 673 K, kept at this temperature for 15 h, cooled to 573 K at 5 K/min, and then quenched in an ice-water bath.

Mechanochemical Synthesis of CsSnBr₃

A mixture of 1.5 mmol each of CsBr and SnBr₂ was ground using an agate mortar and pestle for 10 min. Within an argon-filled glove box, the mixture was transferred to a 50-mL zirconia grinding vessel (containing *ca.* 50 g of zirconia balls with 3–8 mm diameter), which was sealed with parafilm to minimize exposure to air. The sample was ground in a Changsha Deco DECO-PBM-V-0.4L electric planetary ball mill at a rotation frequency of 550 rpm for 0.5 h. The vessel was opened to scratch its inner wall by using a clean spatula and sealed again under an inert atmosphere (Ar glove box). This process was repeated four times for a total of 2.5 h of grinding time.

Solvent Synthesis of CsSnBr₃

A mixture of 1 mmol each of CsBr and SnBr₂ was placed in a 40-mL glass vial to which 4.5 mL of concentrated HBr and 0.5 mL of H₃PO₂ were added. The mixture was heated under a nitrogen atmosphere to 120 °C on a hot plate, with continuous stirring by a magnetic stir bar. A black precipitate formed immediately. After the mixture was heated for 0.5 h, it was cooled over 1 h to room temperature. The precipitate was filtered under reduced pressure, washed with isopropyl alcohol, dried for 0.5 h, and quickly packed into a 4-mm o.d. ZrO₂ rotor for the solid-state NMR experiments.

Solvent Synthesis of Cs₂SnBr₆

A mixture of CsBr (2 mmol) and SnBr₄ (1 mmol) was placed in a 10-mL glass vial to which 5 mL of concentrated HBr was added. The mixture was heated to 120 °C on a hot plate, with continuous stirring by a magnetic stir bar. A white precipitate formed immediately. After the mixture was heated for 1 h, it was cooled over 1 h to room temperature. The precipitate was filtered using a Buchner funnel, washed with 95% ethanol, dried overnight, and stored in a vial under ambient conditions.

Powder X-ray Diffraction

Powder XRD patterns were collected on a Rigaku Ultima IV diffractometer equipped with a Co K α radiation source ($K_{\alpha 1}$, 1.78900 Å; $K_{\alpha 2}$, 1.79283 Å) operated at 38 kV and 38 mA, and a D/Tex Ultra detector with a Fe filter to eliminate K_{β} radiation (1.62083 Å). The samples were placed on zero background plates. Data were collected in

continuous scan mode between 5 and 90° in 2θ with a step size of 0.0200°. Profile fitting was performed using the FullProf suite of software and unit cell parameters were refined.

Energy-dispersive X-ray Spectroscopy and Field Emission Scanning Electron Microscopy

Samples were examined on Zeiss Sigma 300 VP field emission scanning electron microscope equipped with dual silicon drift detectors for energy-dispersive X-ray spectroscopy to determine chemical compositions.

UV-Visible Diffuse Reflectance Spectroscopy

Diffuse reflectance spectra were collected on a Cary 5000 UV-vis-NIR spectrophotometer between 200 and 800 nm and calibrated with a Spectralon (>99%) reflectance standard. The diffuse reflectance spectra were converted to absorption spectra using the Kubelka-Munk function, $\alpha/S = (1-R)^2/2R$, where α is the Kubelka-Munk absorption coefficient, S is the scattering coefficient, and R is the reflectance. Direct bandgaps were extrapolated from the intercepts in Tauc plots of $(\alpha hv)^2$ vs E (eV).

Solid-State Nuclear Magnetic Resonance (NMR) Spectroscopy

I. Cesium-133 NMR Spectroscopy: Solid-state ^{133}Cs NMR measurements were performed at 11.75 T (^1H , 500 MHz) on a Bruker Avance NEO 500 spectrometer, under magic angle spinning (MAS) conditions using a 4 mm H/X MAS Bruker probe with $\omega_0/2\pi(^{133}\text{Cs}) = 65.6$ MHz. All samples were packed into 4 mm o.d. ZrO_2 rotors and NMR data were acquired using a Bloch decay pulse sequence using a short tip angle pulse of 1.38 μs ($\pi/2$ pulse = 5.5 μs , solution $\gamma B_1/2\pi = 45.5$ kHz) with an acquisition time of 100 ms and an optimized recycle delay of 10 to 1800 s. The nuclear spin-lattice relaxation time (T_1) values of ^{133}Cs nuclei for all samples were measured using an inversion recovery pulse sequence. The T_1 values were calculated by fitting the peak intensity values using a three-parameter exponential decay function: $I(t) = I(\infty) + Ae^{-t/T_1}$, where $I(t)$ and $I(\infty)$ are the NMR signal intensities measured at time t and at t infinity,

respectively, and T_1 are A are the spin-lattice relaxation time and pre-exponential constant, respectively. All ^{133}Cs NMR spectra discussed here were referenced by setting a 0.1 M CsNO_3 (aq.) solution at (^{133}Cs) = 0.00 ppm.

II. Tin-119 NMR Spectroscopy: Solid-state ^{119}Sn NMR measurements were performed at 11.75 T (^1H , 500 MHz) on a Bruker Avance NEO 500 spectrometer under both MAS and non-spinning conditions using a 4 mm H/X MAS Bruker probe with $\omega_0/2\pi(^{119}\text{Sn}) = 186.5$ MHz. All samples were packed into 4 mm o.d. ZrO_2 rotors and NMR data were acquired using a $4.0 \mu\text{s} \pi/2$ ($\gamma\text{B}_1/2\pi = 62.5$ kHz) either with a Hahn-echo pulse sequence $((\pi/2)_x - \tau_1 - (\pi)_y - \tau_2 - \text{ACQ}$, where τ represents the interpulse and refocusing delays) or with a Bloch pulse sequence with an acquisition time of 4-5 ms and an optimized recycle delay of 0.01-200 s. Variable temperature (VT) ^{119}Sn NMR spectra were acquired between 230 and 418 K with the same instrument under non-spinning conditions using a Bruker VT unit and calibrated using the ^{207}Pb chemical shifts of MAPbCl_3 .² Dry $\text{N}_2(\text{g})$ was used as the VT gas and gas flow rates were adjusted to reach the target temperatures. The ^{119}Sn T_1 values were measured using an inversion recovery pulse sequence as discussed in the ^{133}Cs NMR experimental section. All ^{119}Sn NMR spectra were referenced by setting the ^{119}Sn signal of a tetracyclohexyl-tin(IV) powder to $\delta(^{119}\text{Sn}) = -97.35$ ppm, a secondary reference with respect to $\text{Sn}(\text{CH}_3)_4$ at $\delta(^{119}\text{Sn}) = 0.00$ ppm.

Table B1. Elemental analysis of $\text{CsSn}(\text{Cl}_{1-x}\text{Br}_x)_3$ materials measured by EDS.

Sample (Nominal composition)	Elemental atomic %				%Cl : %Br
	Cs	Sn	Cl	Br	
CsSnCl_3	19.3	19.4	61.3	-	100 : 0
$\text{CsSn}(\text{Cl}_{0.90}\text{Br}_{0.10})_3$	18.9	19.5	54.6	7.0	89 : 11
$\text{CsSn}(\text{Cl}_{0.67}\text{Br}_{0.33})_3$	18.8	19.4	39.6	22.2	64 : 36
$\text{CsSn}(\text{Cl}_{0.50}\text{Br}_{0.50})_3$	18.8	18.6	29.4	33.2	47 : 53
$\text{CsSn}(\text{Cl}_{0.33}\text{Br}_{0.67})_3$	18.3	19.1	19.0	43.6	30 : 70
$\text{CsSn}(\text{Cl}_{0.10}\text{Br}_{0.90})_3$	19.4	18.7	6.0	55.9	10 : 90
CsSnBr_3	17.3	18.0	-	64.7	0 : 100

Table B2. Unit cell constants (a) and direct bandgap values for CsSn(Cl_{1-x}Br_x)₃ materials.

Sample	Unit cell constant, a (Å)	Direct bandgap (eV)
CsSnCl ₃ (cubic)	5.5894(5)	2.83
CsSn(Cl _{0.90} Br _{0.10}) ₃	5.6108(3)	2.71
CsSn(Cl _{0.67} Br _{0.33}) ₃	5.6642(3)	2.42
CsSn(Cl _{0.50} Br _{0.50}) ₃	5.6991(6)	2.26
CsSn(Cl _{0.33} Br _{0.67}) ₃	5.7353(7)	2.10
CsSn(Cl _{0.10} Br _{0.90}) ₃	5.7830(2)	1.87
CsSnBr ₃	5.8031(3)	1.79

Table B3. Room temperature solid-state ¹³³Cs NMR experimental parameters, chemical shifts, fwhm and spin-lattice relaxation (*T*₁) values for CsSn(Cl_{1-x}Br_x)₃ materials. The ¹³³Cs NMR spectra were acquired at 11.75 T using a Bloch pulse sequence.

Sample	<i>v</i> _{rot} (kHz)	Recycle delay (s)	¹³³ Cs fwhm (Hz) ± 5	δ(¹³³ Cs) (ppm) ± 0.1	<i>T</i> ₁ (¹³³ Cs) (s)
CsSnCl ₃ (cubic)	13.0	300	138	64.7	14.8 ± 0.2
CsSn(Cl _{0.90} Br _{0.10}) ₃		60	92	68.6	9.8 ± 0.2
CsSn(Cl _{0.67} Br _{0.33}) ₃		100	82	73.7	15.3 ± 0.4
CsSn(Cl _{0.50} Br _{0.50}) ₃		60	114	74.7	19.7 ± 0.1
CsSn(Cl _{0.33} Br _{0.67}) ₃		60	149	73.4	25.0 ± 0.1
CsSn(Cl _{0.10} Br _{0.90}) ₃		60	125	67.7	35.3 ± 0.1
CsSnBr ₃		60	70	64.0	34.9 ± 0.1

Table B4. Room temperature solid-state ^{119}Sn NMR experimental parameters, chemical shifts, fwhm and spin-lattice relaxation (T_1) values for $\text{CsSn}(\text{Cl}_{1-x}\text{Br}_x)_3$ materials. The ^{119}Sn NMR spectra were acquired at 11.75 T using a Hahn-echo ($\nu_{\text{rf}} = 62.5$ kHz).

Sample	ν_{rot} (kHz)	Recycle delay (s)	$\delta(^{119}\text{Sn})$ (ppm)	^{119}Sn fwhm (kHz) ± 0.1	$T_1(^{119}\text{Sn})$ (s)
CsSnCl_3 (cubic)	10.0	10	-562 ± 1	1.8	3.5
$\text{CsSn}(\text{Cl}_{0.90}\text{Br}_{0.10})_3$		1	-544 ± 1	1.4	3.4
$\text{CsSn}(\text{Cl}_{0.67}\text{Br}_{0.33})_3$		1	-510 ± 1	1.7	2.4
$\text{CsSn}(\text{Cl}_{0.50}\text{Br}_{0.50})_3$		5	-487 ± 1	2.7	3.0×10^{-1}
$\text{CsSn}(\text{Cl}_{0.33}\text{Br}_{0.67})_3$		1	-458 ± 2	4.3	2.7×10^{-2}
$\text{CsSn}(\text{Cl}_{0.10}\text{Br}_{0.90})_3$		0.01	-365 ± 5	17.0	8.0×10^{-3}
CsSnBr_3		0.20	-289 ± 5	19.0	5.6×10^{-3}

Table B5. Room temperature solid-state ^{119}Sn NMR experimental parameters, chemical shifts, fwhm and spin-lattice relaxation (T_1) for CsSnBr_3 materials prepared by the solvent synthesis (SS), high temperature (HT) and mechanochemical synthesis (MCS) methods. The ^{119}Sn NMR spectra were acquired at 11.75 T using a Hahn-echo ($\nu_{\text{rf}} = 62.5$ kHz).

Sample	ν_{rot} (kHz)	Recycle delay (s)	$\delta(^{119}\text{Sn})$ (ppm)	^{119}Sn fwhm (kHz)	$T_1(^{119}\text{Sn})$ (s)
CsSnBr_3 (SS)	0.0	0.05	-386 ± 2	7.5 ± 0.2	0.025 ± 0.001
CsSnBr_3 (HT)		0.2	-284 ± 5	21.0 ± 0.5	0.007 ± 0.001
CsSnBr_3 (MCS)		0.2	-295 ± 10	34.0 ± 1.0	0.003 ± 0.001

Table B6. Variable-temperature ^{119}Sn NMR parameters for CsSnBr_3 (SS) acquired under non-spinning sample conditions at 11.75 T using a $4.0 \mu\text{s}$ $\pi/2$ Bloch pulse sequence.

T(set) (K)	T(calibrated) (K) ± 2	$\delta_{\text{iso}}(^{119}\text{Sn})^\dagger$ (ppm)	Ω^\dagger (ppm)	κ^\dagger	^{119}Sn <i>fwhm</i> (kHz) ± 0.1	^{119}Sn T_2^* (ms)	^{119}Sn T_1 (ms)
233	229.5	-393	85	-0.1	14.7	0.068	635(200)
253	250.9	-393	75	-0.1	13.6	0.074	390(85)
273	273.6	-390	75	-0.25	10.6	0.094	123(12)
292.4	295.4	-386	35	-1.0	7.2	0.139	25(1)
313	318.7	-371	0	NA	6.5	0.154	14(1)
333	341.5	-364	0	NA	6.1	0.164	8.8(5)
353	366.4	-350	0	NA	5.7	0.175	4.12(15)
373	385.5	-334	0	NA	6.0	0.167	2.16(9)
393	407.6	-319.6	0	NA	5.4	0.185	1.14(5)
403	417.9	-317.7	0	NA	4.5	0.222	0.92(2)

NA – not applicable

\dagger - δ_{iso} , Ω and κ are isotropic chemical shift, span and skew, respectively, where $\delta_{\text{iso}} = \frac{\delta_{11} + \delta_{22} + \delta_{33}}{3}$, $\Omega = (\delta_{11} - \delta_{33})$ and $\kappa = 3\left(\frac{\delta_{22} - \delta_{\text{iso}}}{\Omega}\right)$

Appendix Note B1

The variable temperature ^{119}Sn spin-lattice relaxation time (T_1) is related to the absolute temperature values for CsSnBr_3 (SS) as shown in Table B6. $\log_{10}[T_1/\text{s}]$ linearly depends on $[1000/\text{T(K)}]$ (i.e., an Arrhenius relationship) within the temperature range of 230 to 418 K. The slope of the Arrhenius fit is related to the activation energy as $E_a = (2303 \cdot \text{R}) \cdot (\text{slope})$, where $\text{R} = 8.314 \text{ J}/(\text{mol} \cdot \text{K})$. A slope value of $1.51 \pm 0.06 \text{ K}$ was obtained from the least-squares Arrhenius fit; hence $E_a = 28.9 \pm 1.2 \text{ kJ/mol}$ or $0.30 \pm 0.01 \text{ eV}$

Table B7. Solid-state ^{133}Cs NMR acquisition parameters and experimental conditions used for the CsSnBr_3 areal degradation study (see Figure 9b in the manuscript). The ^{133}Cs NMR spectra were acquired at 11.75 T using a Bloch pulse sequence.

Material	T_1 (s)	ν_{rot} (kHz)	Recycle delay (s)	# of scans	Acquisition time (min)
CsSnBr_3 (degraded)	-	5 kHz	1800	4	120
CsSnBr_3	34.9		60	4	4
Cs_2SnBr_6	170		500	4	33
CsBr	631		300	4	20

Table B8. Solid-state ^{119}Sn NMR acquisition parameters and experimental conditions used for the CsSnBr_3 areal degradation study (see Figure 9c in the manuscript). The ^{119}Sn NMR spectra were acquired at 11.75 T using a Hahn-echo ($\nu_{\text{rf}} = 62.5$ kHz).

Material	T_1 (s)	ν_{rot} (kHz)	Recycle delay (s)	# of scans	Acquisition time (min)	
CsSnBr_3 (degraded)	region-1	-	0	0.2	512	1.7
	region-1	-	10	0.2	512	1.7
	region-2	-	10	100	512	853
	region-3	-	10	100	512	853
	region-4	-	12	0.01	2,000,000	736
CsSnBr_3	0.006	10	0.2	1024	3.4	
Cs_2SnBr_6	12.3	10	100	32	53	
SnO_2	3.1 ^{ref.3}	10	30	32	15	
SnBr_4	1.95 ^{ref.4}	0	3	512	25.6	
SnBr_2	1.12 ^{ref.4}	13	1.5	512	12.8	
SnBr_2 region (trace metal grade) β -Sn region	0.00012 ^{ref.4}	12	0.005	2,000,000	537	

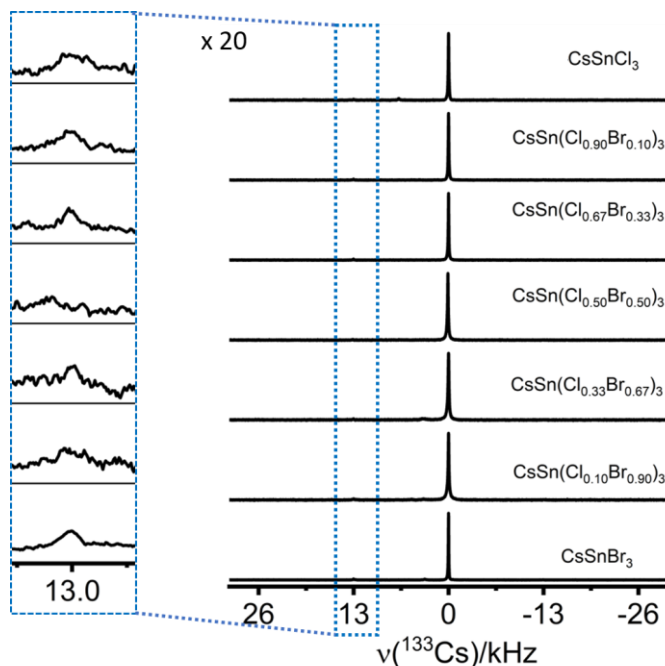


Figure B1. Room temperature solid-state ^{133}Cs NMR spectra of $\text{CsSn}(\text{Cl}_{1-x}\text{Br}_x)_3$ materials at 11.75 T with a magic angle spinning frequency of 13 kHz. Expansion shows the corresponding spinning side band.

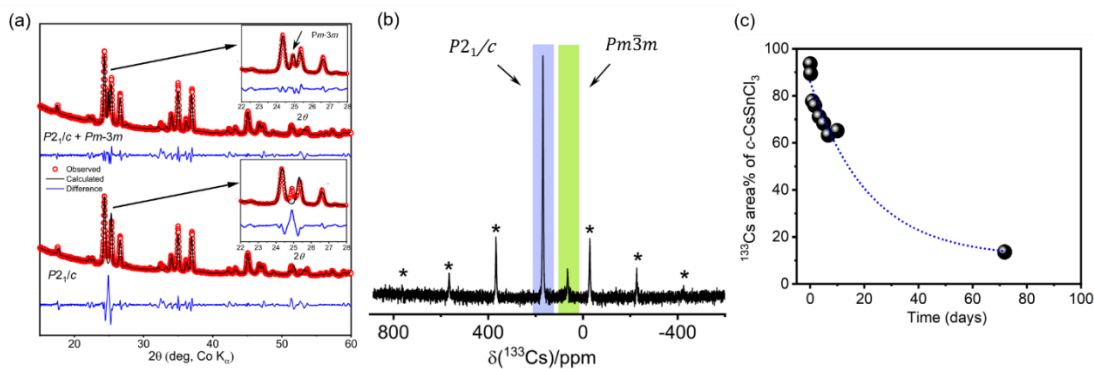


Figure B2. Room temperature PXRD (a) and ^{133}Cs NMR spectra (b) of CsSnCl_3 materials prepared by the high-temperature sealed-tube method followed by slow-cooling (5 K/min). PXRD patterns were collected within 24 h of synthesis and ^{133}Cs NMR spectra were acquired at 11.75 T after six days of synthesis. The asterisks (*) in (b) indicate spinning sidebands for monoclinic CsSnCl_3 . Plot of ^{133}Cs NMR peak area for the cubic CsSnCl_3 phase as a function of time (up to 72 days) showing mono-

exponential like decay kinetics for the cubic to monoclinic phase transition in CsSnCl_3 (c). The data points between 10 to 72 days are missing because of the sudden institutional lockdown (~ 60 days) during the first wave of COVID-19 pandemic in early 2020.

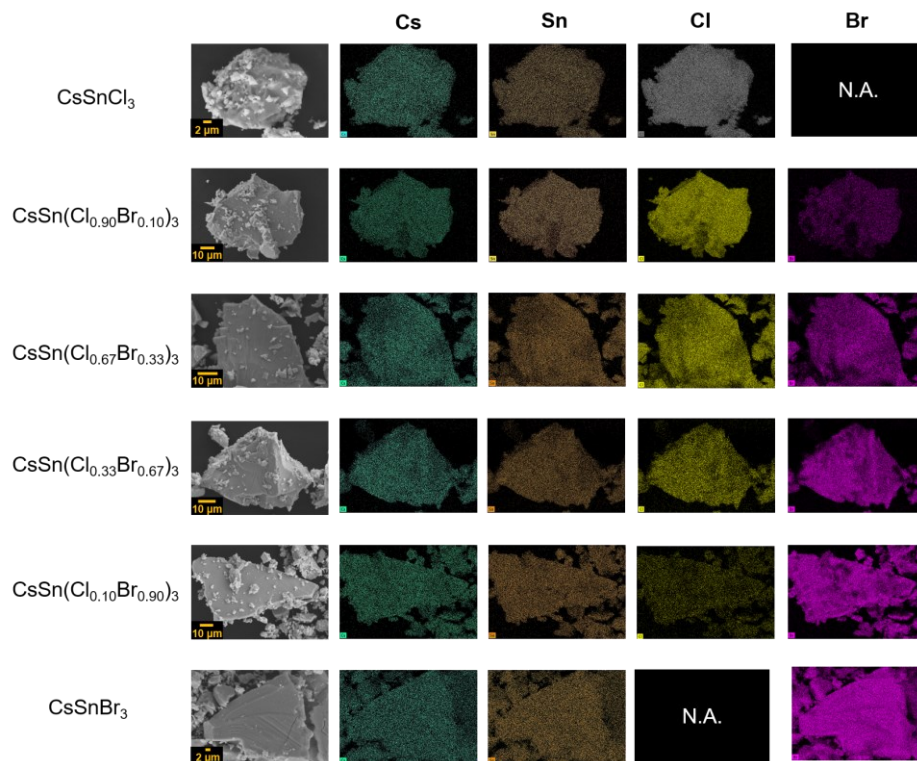


Figure B3. FESEM images and the corresponding EDS elemental mapping for Cs, Sn, Cl and Br for the $\text{CsSn}(\text{Cl}_{1-x}\text{Br}_x)_3$ materials (top to bottom: $x = 0.00, 0.10, 0.33, 0.67$ and 1.00).

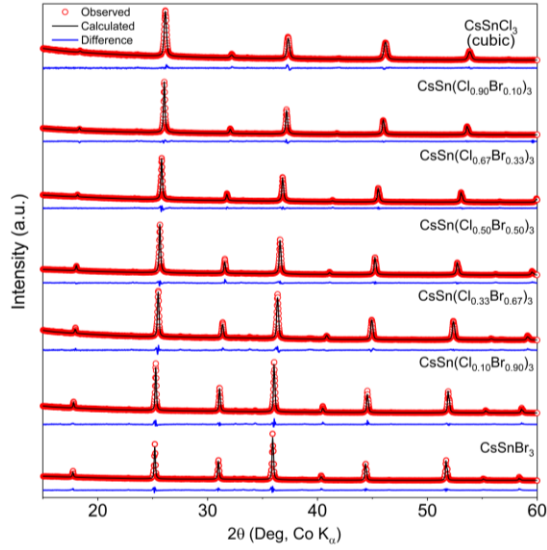


Figure B4. Room temperature experimental and fitted PXRD diagrams for the $\text{CsSn}(\text{Cl}_{1-x}\text{Br}_x)_3$ series. All the diffraction data are fitted assuming a cubic ($\text{Pm}\bar{3}\text{m}$) space group symmetry.

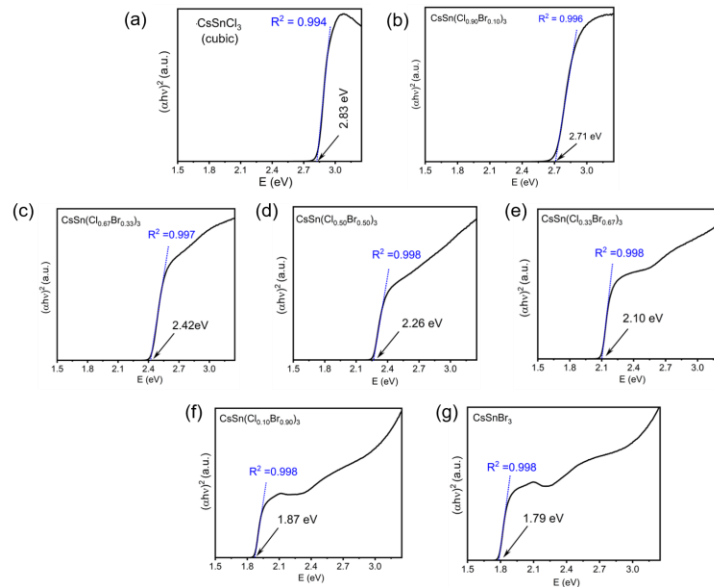


Figure B5. Tauc plots showing direct bandgaps of the cubic phases of $\text{CsSn}(\text{Cl}_{1-x}\text{Br}_x)_3$ materials; c- CsSnCl_3 (a), $\text{CsSn}(\text{Cl}_{0.90}\text{Br}_{0.10})_3$ (b), $\text{CsSn}(\text{Cl}_{0.67}\text{Br}_{0.33})_3$ (c), $\text{CsSn}(\text{Cl}_{0.50}\text{Br}_{0.50})_3$ (d), $\text{CsSn}(\text{Cl}_{0.33}\text{Br}_{0.67})_3$ (e), $\text{CsSn}(\text{Cl}_{0.10}\text{Br}_{0.90})_3$ (f) and CsSnBr_3 (g).

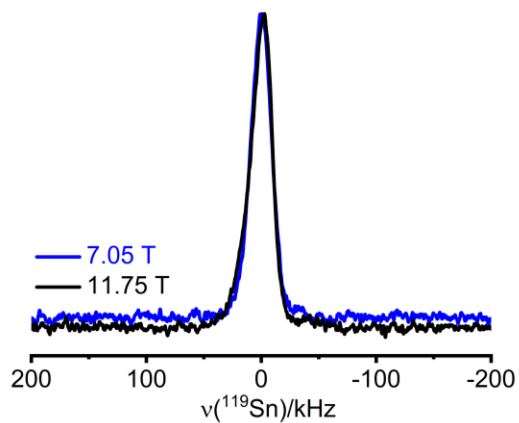


Figure B6. Solid-state ^{119}Sn NMR spectra of CsSnBr_3 at 7.05 and 11.75 T under non-spinning sample conditions. The scales are vertically normalized.

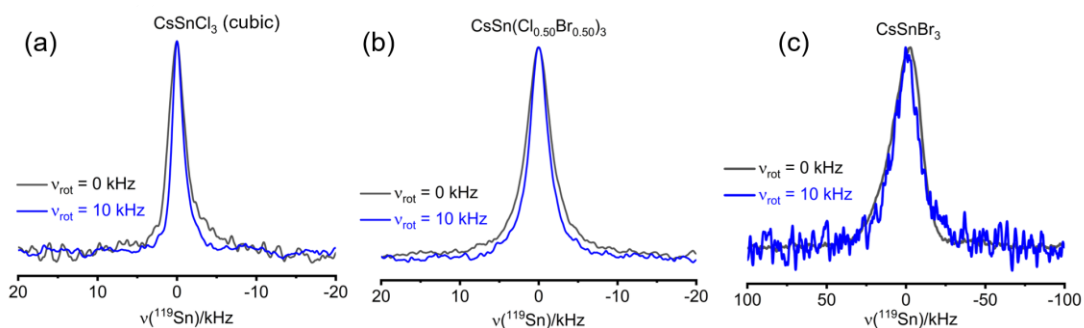


Figure B7. Solid-state ^{119}Sn NMR spectra of c- CsSnCl_3 (a), $\text{CsSn}(\text{Cl}_{0.50}\text{Br}_{0.50})_3$ (b) and CsSnBr_3 (c) at 11.75 T acquired with spinning frequencies of 0 and 10 kHz. The scales are vertically normalized.

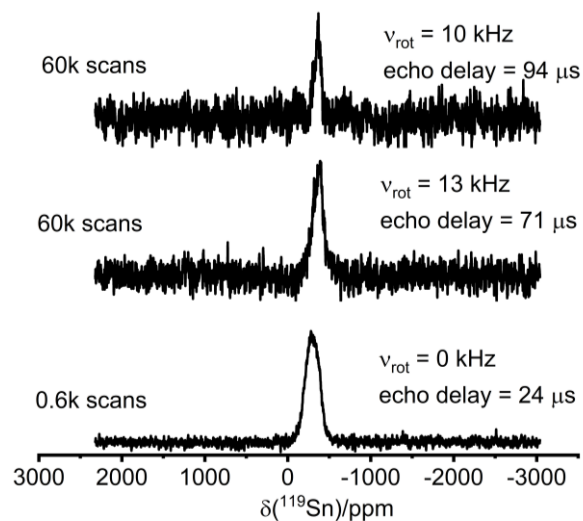


Figure B8. Solid-state ^{119}Sn NMR spectra of $\text{CsSn}(\text{Cl}_{0.10}\text{Br}_{0.90})_3$ at 11.75 T acquired with spinning frequencies between 0 to 13 kHz with the Hahn-echo pulse sequence and with various echo-delays as indicated. The scales are vertically normalized.

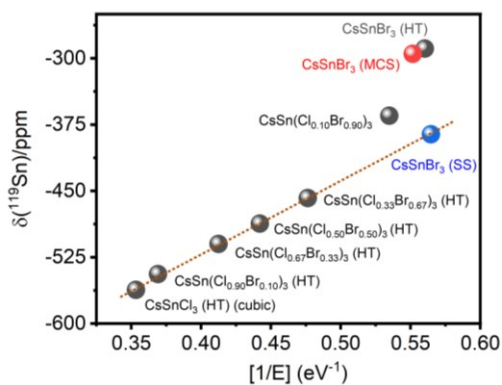


Figure B9. Solid-state ^{119}Sn NMR chemical shifts vs the inverse of direct bandgap values for the $\text{CsSn}(\text{Cl}_{1-x}\text{Br}_x)_3$ series.

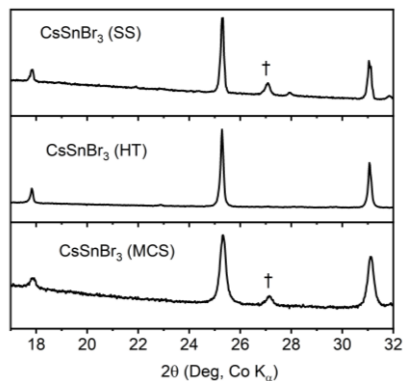


Figure B10. Room temperature PXRD patterns for the CsSnBr_3 parent material synthesized by the solvent synthesis (SS), high temperature (HT) and mechanochemical synthesis (MCS) methods. The dagger (\dagger) indicates signal from Cs_2SnBr_6 .

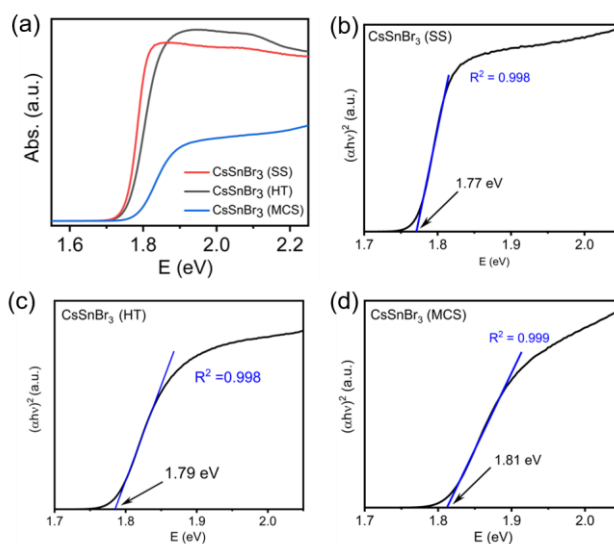


Figure B11. UV-Vis absorption spectra (a) and Tauc plots showing direct bandgaps (b-d) for the CsSnBr_3 parent material synthesized by the solvent synthesis (SS), high temperature (HT) and mechanochemical synthesis (MCS) methods.

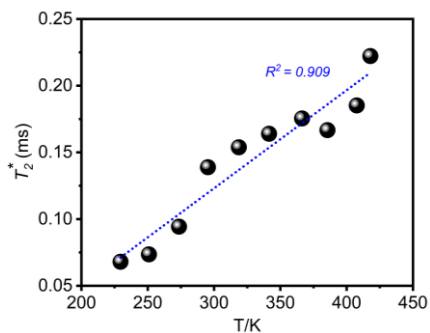


Figure B12. ^{119}Sn T_2^* (i.e., $\frac{1}{\text{fwhm}}$) relaxation time as a function of absolute temperature (230–418 K) for the CsSnBr_3 (SS) material. ^{119}Sn NMR spectra were acquired at 11.75 T under non-spinning sample conditions. The data were fit by a least-squares method with the following equation: $T_2^*/\text{ms} = -0.098(0.023) + 7.36(0.77) \times 10^{-4} \cdot T/\text{K}$.

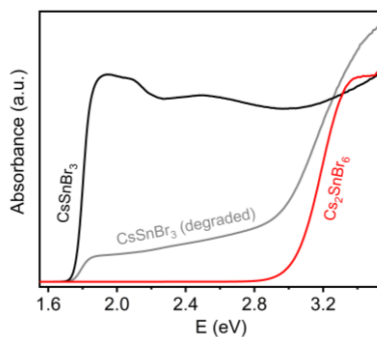


Figure B13. UV-Vis absorption spectra for a CsSnBr_3 sample that was stored under ambient laboratory conditions over 300 days (degraded CsSnBr_3), pristine CsSnBr_3 and Cs_2SnBr_6 .

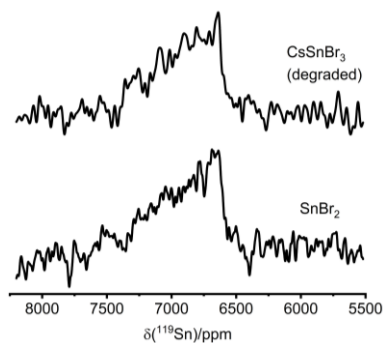


Figure B14. Solid-state ^{119}Sn NMR spectra of the degraded CsSnBr_3 parent and SnBr_2 starting precursor at 11.75 T acquired with spinning frequencies of 12 kHz with 2,000,000 scans each.

References

- (1) Kubelka, P.; Munk, F. Ein Beitrag Zur Optik Der Farbanstriche. *Z.Tech. Phys. (Leipzig)* **1931**, *12*, 593–601.
- (2) Bernard, G. M.; Goyal, A.; Miskolzie, M.; McKay, R.; Wu, Q.; Wasylshen, R. E.; Michaelis, V. K. Methylammonium Lead Chloride: A Sensitive Sample for an Accurate NMR Thermometer. *J. Magn. Reson.* **2017**, *283*, 14–21.
- (3) Cossement, C.; Darville, J.; Gilles, J. -M; Nagy, J. B.; Fernandez, C.; Amoureux, J. -P. Chemical Shift Anisotropy and Indirect Coupling in SnO_2 and SnO . *Magn. Reson. Chem.* **1992**, *30* (3), 263–270.
- (4) Kubicki, D. J.; Prochowicz, D.; Salager, E.; Rakhmatullin, A.; Grey, C. P.; Emsley, L.; Stranks, S. D. Local Structure and Dynamics in Methylammonium, Formamidinium and Cesium Tin(II) Mixed-halide Perovskites from ^{119}Sn Solid-State NMR. *J. Am. Chem. Soc.* **2020**, *142*, 7813–7826.

Appendix C: Supplementary Data for Chapter 4

Cu(II)-Doped Cs₂SbAgCl₆ Double Perovskite: A Lead-Free, Low-Bandgap Material

Experimental

Materials and Methods

All starting precursor materials and solvents were obtained from commercial sources and used without further purification: CsCl (>99%, Acros Organics, NJ, USA), Sb₂O₃ (99%, Sigma Aldrich Co., St. Louis, MO, USA), AgNO₃ (EM Science, NJ, USA), CuCl₂•2H₂O (Aldrich Chemical Company, Inc, USA), HCl (EMD Chemical Inc., Darmstadt, Germany), H₃PO₂ (50 wt. % in H₂O, Sigma-Aldrich Co., St. Louis, MO, USA). All reactions were performed under ambient conditions.

Synthesis of Polycrystalline Cs₂SbAgCl₆

Freshly prepared AgCl was used in this synthesis. AgCl was formed by adding 10 M HCl (in excess) to an aqueous solution of AgNO₃, resulting in the precipitation of a white solid, which was filtered using a Buchner funnel, washed with 95% ethanol and dried under suction filtration. First, 4 mL of 10 M HCl and 1 mL of H₃PO₂ solvent were placed into a vial and heated to 120 °C using a hot plate with gentle stirring using a magnetic stir bar. Then 0.5 mmol of solid Sb₂O₃ (0.146 g) and 1 mmol of freshly prepared AgCl (0.143 g) were added to the hot solvent mixture, followed by the addition of 2 mmol of CsCl (0.337 g); immediately, a pale-yellow precipitate was observed (later confirmed via PXRD and EDX to be Cs₂SbAgCl₆). The mixture was heated for one hour and then left at room temperature for two hours. The polycrystalline solid was filtered using a Buchner funnel and washed with 95% ethanol, followed by overnight drying. We note that a small amount of Cs₃Sb₂Cl₉ can form as an impurity during the synthesis as shown in Figure C15.

Synthesis of Polycrystalline $\text{Cs}_2\text{Sb}_{1-a}\text{Ag}_{1-b}\text{Cu}_{2x}\text{Cl}_6$ ($a+b = 2x$, $x = 0.01, 0.05$, and 0.10)

AgCl was prepared as described above.

For $x = 0.01$: 0.034 g of $\text{CuCl}_2 \cdot 2\text{H}_2\text{O}$ (0.20 mmol) was dissolved in 5 mL of 10 M HCl and a homogeneous solution was obtained. In a separate reaction, 10 mL of 10 M HCl was placed into a vial and heated to 120 °C with gentle stirring using a hot plate equipped with a magnetic stirrer. 1 mmol of white solid Sb_2O_3 powder (0.292 g) and 2 mmol of freshly prepared AgCl (0.287 g) were dissolved in the hot solvent mixture. Following dissolution, 4 mmol of CsCl (0.673 g) and 0.04 mmol (corresponding to 0.0068 g or 1 mL solution) of $\text{CuCl}_2 \cdot 2\text{H}_2\text{O}$, prepared as described above, were added to the solution. A black precipitate was immediately observed. The mixture was heated for one hour and then left at room temperature for two hours. The polycrystalline solid was filtered using a Buchner funnel, washed with 95% ethanol, and followed by overnight drying.

For $x = 0.05, 0.10$: 10 mL of 10 M HCl was placed into a vial with gentle stirring and heated to 120 °C using a hot plate equipped with a magnetic stir bar. 0.95 mmol (0.277 g) or 0.90 mmol (0.262 g) of white solid Sb_2O_3 powder and 1.9 mmol (0.272 g) or 1.8 mmol (0.258 g) of freshly prepared AgCl, for $x = 0.05$ and 0.10, respectively, were dissolved in the hot solvent mixture. Following dissolution, 4 mmol of CsCl (0.673 g) and 0.2 mmol (0.034 g) or 0.4 mmol (0.068g) of $\text{CuCl}_2 \cdot 2\text{H}_2\text{O}$, for $x = 0.05$ and 0.10, respectively, were added to the solution. Immediately following this step, a black precipitate was observed. The mixture was heated for one hour and then allowed to stand at room temperature for two hours. The polycrystalline solid was filtered using a Buchner funnel, washed with 95% ethanol, and allowed to dry overnight.

Diffuse Reflectance (DR) Spectroscopy

A Cary 5000 UV–Vis–NIR spectrophotometer, equipped for the analysis of small-quantity fine powdered samples, was used to obtain DR data (Analytical and Instrumental Laboratory, University of Alberta). Each sample was packed into a black boat (~100 mg/sample) and each measurement was acquired between the wavelengths of 2500 and 200 nm.

The diffuse reflectance spectra were converted to pseudo-absorbance spectra using the following Kubelka-Munk transformation:⁵ $\alpha \sim \frac{(1-R)^2}{2R}$, where R = absolute reflectance and α = pseudo-absorbance. The direct and indirect bandgaps were measured by taking the intercept upon extrapolation of the linear regions of $(\alpha h\nu)^2$ vs $E(\text{eV})$ and $(\alpha h\nu)^{1/2}$ vs $E(\text{eV})$ plots, respectively.

Powder X-Ray Diffraction (PXRD)

Powder X-ray diffraction (PXRD) measurements were collected on an Inel MPD multi-purpose diffractometer (40 kV, 50mA) system (Department of Chemistry, University of Alberta) equipped with a CPS 120 curved position sensitive X-ray detector and Cu K_α radiation source (1.540596 Å). Samples were placed on a plastic sample holder and 2θ data were collected from 0.290° to 113.767° with a step increment of 0.029° .

Energy Dispersion X-Ray (EDX) Measurements

The energy dispersive X-ray (EDX) analysis was performed using a low vacuum JEOL JSM-6010LA InTouchScope (Scanning Electron Microscope Laboratory, University of Alberta), equipped with the latest Bruker Silicon Drift Detector.

Inductively Coupled Plasma-Optical Emission Spectrometric (ICP-OES) Measurements

The inductively coupled plasma-optical emission spectrometric (ICP-OES) analysis was performed using a Argon plasma ICP spectrophotometer Perkin Elmer Optima 2000 OES DV (Laboratorio di Microanalisi, University of Florence) instrument. The samples were dissolved in *aqua regia*.

Thermogravimetric Analysis (TGA)

Thermogravimetric analysis was performed using a Perkin Elmer Pyris 1 instrument (Analytical and Instrumental Laboratory, University of Alberta) with a nitrogen gas flow of 20 mL/min and a heating rate of $5^\circ\text{C}/\text{min}$. The temperature range was 25-800 $^\circ\text{C}$.

Humidity and Thermal Stress Tests

A small amount of freshly prepared $\text{Cs}_2\text{SbAgCl}_6$ ($x = 0.00$) and highest Cu^{2+} -doped ($x = 0.10$) materials were placed in a custom-built humidifying chamber at $55 \pm 5\%$ relative humidity at 295 K (Figure C12). The samples were placed in a fume hood within this chamber in the presence of normal laboratory light (natural and artificial). After one year ($x = 0.00$) or one month ($x = 0.10$), the samples were removed from the humidifying chamber, and further analyses including, PXRD, ^{133}Cs MAS NMR, and DR were collected.

A small amount of freshly prepared $\text{Cs}_2\text{SbAgCl}_6$ ($x = 0.00$) and highest Cu^{2+} doped ($x = 0.10$) materials were placed in an oven at approximately 110 °C for six days, then removed and placed on the bench to cool to ambient temperature. Samples were then analyzed by PXRD, ^{133}Cs MAS NMR spectroscopy and DR experiments to confirm *purity and stability of the samples*.

Electron Paramagnetic Resonance (EPR) Spectroscopy

EPR spectra were acquired at X-band (9.77 GHz) on a Bruker ELEXSYS spectrometer (CERM, University of Florence), equipped with a standard ST4102 cavity. Field modulation was 20 G at 100 kHz and four scans were taken for each sample under ambient conditions. MW power was set to 50 mW; no evidence of saturation was observed.

Solid-State Nuclear Magnetic Resonance (NMR) Spectroscopy

^{121}Sb NMR: Antimony-121 NMR spectra were acquired at 7.05 T (300 MHz, ^1H) and 11.75 T (500 MHz, ^1H) on Bruker Avance 300 and 500 NMR spectrometers, respectively, using a non-selective Bloch pulse (short tip angle) or a selective ($1.3 \mu\text{s}$ $\pi/2$, $\gamma B_1/2\pi = 65$ kHz) Hahn-echo pulse sequence ($(\pi/2)_x - \tau_1 - (\pi)_y - \tau_2 - \text{ACQ}$, where τ_1 and τ_2 represent the inter-pulse and refocusing delays, respectively), 1,000 to 29,000 co-added transients and a recycle delay of 2 s. Samples were packed in 4 mm OD ZrO_2 rotors (80 μL fill volume) and spectra were acquired under non-spinning and magic-angle spinning (MAS) conditions with a spinning frequency between 10 and 12 kHz. Additional ^{121}Sb NMR spectra were acquired at 21.1 T (900 MHz, ^1H) on a Bruker

Avance II 900 NMR spectrometer using a 4 mm H/X MAS Bruker probe and a modified solid-echo pulse sequence $((\pi/2)_x - \tau_1 - (\pi)_y - \tau_2 - \text{ACQ})$,⁶⁻⁸ $\gamma B_1/2\pi = 83$ kHz (1.0 μs $\pi/2$), 1,024 co-added transients and a recycle delay of 2 s. All ^{121}Sb NMR spectra were referenced by setting the peak for 0.5 M KSbF_6 to $\delta = 0.00$ ppm.^{1,2}

^{133}Cs NMR: Cesium-133 NMR spectra of the $\text{Cs}_2\text{SbAgCl}_6$ parent ($x = 0.00$) and of the Cu^{2+} -doped (0.01, 0.05, and 0.10) materials were acquired at 11.75 T (500 MHz ^1H) on a Bruker Avance 500 NMR spectrometer, with a Bloch pulse using a short pulse (1.25 μs , $\gamma B_1/2\pi = 50$ kHz), 64 to 512 co-added transients and a recycle delay between 60 and 500 s. Samples were packed in 4 mm OD ZrO_2 rotors and spectra were collected under MAS conditions ($\omega_r/2\pi = 13$ kHz). Variable temperature NMR spectra were acquired at 238, 291, 323, and 343 K using appropriate relaxation delays (determined using a saturation recovery pulse sequence) to obtain pseudo-quantitative spectra (some paramagnetic quenching is likely due to the presence of Cu^{2+}). The sample and probe temperature were permitted to stabilize for 10-15 minutes prior to each VT data point acquisition. The temperatures were calibrated with ^{207}Pb NMR using MAPbCl_3 .³ Cesium-133 NMR spectra of Cu^{2+} doped $\text{Cs}_2\text{SbAgCl}_6$ materials ($x = 0.01, 0.05,$ and 0.10) were acquired at 21.1 T (900 MHz ^1H) on a Bruker Avance II 900 spectrometer using a 2.5 mm H/X MAS Bruker probe and a solid pulse (1.0 μs $\pi/4$ pulse) with 10 s recycle delays. Samples were packed in 2.5 mm OD ZrO_2 rotors and spectra were collected using a spinning frequency of 30 kHz. ^{133}Cs 2D exchange spectroscopy (EXSY)⁹ spectra were acquired at a spinning frequency of 30 kHz with $\pi/2$ pulses of 2.0 μs , recycle delays of 5 s, 96 to 128 co-added transients and 128 t_1 increments; mixing times ranged from 0.1 ms to 1 sec (Figure C13). All ^{133}Cs NMR spectra were referenced by setting the ^{133}Cs peak of a 0.1 M CsCl solution to $\delta = 0.00$ ppm.

Table C1. Nominal and elemental analyzed results (EDX, ICP-OES and ^{133}Cs NMR) for $\text{Cs}_2\text{SbAgCl}_6$ ($x = 0.00$) and for the Cu^{2+} -doped ($x = 0.01, 0.05, 0.10$) materials.

x^a	Atom% by EDX ^b					Cu Composition				
	Cs	Sb	Ag	Cl	Cu	Nominal (at. ratio %)		ICP-OES ^c (at. ratio %)		^{133}Cs NMR % Cu_{2x}^d (± 0.5)
						Cu/Cs	Cu/Sb	Cu/Cs	Cu/Sb	
0.00	21.64 (0.93)	11.24 (0.63)	9.72 (0.74)	57.40 (0.90)	-	-	-	--	--	-
0.010	21.04 (0.42)	11.07 (0.54)	10.31 (0.14)	56.84 (1.05)	0.74 (0.46)	1.00	2.00	0.55	1.07	0.43
0.050	21.84 (0.74)	11.12 (0.47)	8.78 (0.72)	57.18 (0.78)	1.08 (0.69)	5.00	10.53	1.52	3.48	2.54
0.100	22.12 (0.71)	11.19 (0.60)	6.80 (0.51)	58.33 (1.20)	1.55 (0.94)	10.00	22.22	2.53	6.09	3.94

^a x is the nominal Cu^{2+} composition in $\text{Cs}_2\text{Sb}_{1-a}\text{Ag}_{1-b}\text{Cu}_{2x}\text{Cl}_6$.

^b EDX is energy-dispersive X-ray spectroscopic analysis (in quintuplicate).

^c ICP-OES is inductively coupled plasma-optical emission spectrometric analysis (in triplicate).

^d Cu_{2x} is % Cu^{2+} concentration in the final product of $\text{Cs}_2\text{Sb}_{1-a}\text{Ag}_{1-b}\text{Cu}_{2x}\text{Cl}_6$ from ^{133}Cs NMR.

Note: Uncertainties are provided in the parentheses, as the dopant concentrations are near the detection limits, hence the larger uncertainties. Figure C9 shows a nearly linear relationship between quantitatively measured Cu concentrations and the Cu/Sb atomic ratio by synthetic loading (nominal composition). Due to the low Cu concentrations and associated challenges in elemental analysis of these materials, we refer to all Cu-doped materials via their nominal composition, x .

Table C2. ^{133}Cs and ^{121}Sb NMR relaxation parameters (T_1 and T_2^*) for $\text{Cs}_2\text{SbAgCl}_6$ ($x = 0.00$) and for the $x = 0.10$ Cu^{2+} -doped materials. All ^{133}Cs NMR relaxation parameters (T_1 and T_2^*) were measured at 11.75 T and whereas all ^{121}Sb NMR relaxation parameters (T_2^*) were measured at 7.05 T.

x	^{133}Cs (T_1), sec	^{133}Cs (T_2^*), ms	^{121}Sb (T_2^*), μs
0	51 ± 6	6 ± 1	360 ± 40
0.10	2.7 ± 0.5	1.3 ± 0.1	130 ± 30

Table C3. Calculated contributions from the three ^{133}Cs MAS NMR peaks (Peak-1, Peak-2, and Peak-3) and the fitted line equations.

^{133}Cs NMR Peak	Area % for x ($\pm 1\%$)				Fitted Linear Equation
	0.00	0.01	0.05	0.10	
Peak-1	100	97.4	79.8	67.5	$\delta_{\text{iso}}(^{133}\text{Cs}) / \text{ppm} = -334(32)x + 100(2)$; $R^2 = 0.973$
Peak-2	0	2.5	19.1	29.6	$\delta_{\text{iso}}(^{133}\text{Cs}) / \text{ppm} = 305(34)x + 1(2)$; $R^2 = 0.963$
Peak-3	0	0.2	1.1	2.9	$\delta_{\text{iso}}(^{133}\text{Cs}) / \text{ppm} = 29(3)x + 0(0)$; $R^2 = 0.971$

Table C4. FWHM values for ^{133}Cs MAS NMR spectra (Peak-1 and Peak-2 of Figure C5) for $\text{Cs}_2\text{SbAgCl}_6$ without or with Cu^{2+} doping, acquired at 11.75 T, $T = 291$ K and a spinning frequency of 13 kHz.

Cu^{2+} composition (x)	FWHM (Hz)	
	Peak-1	Peak-2
0.00	200(5)	-
0.01	205(5)	1350(20)
0.05	615(10)	1360(10)
0.10	770(10)	1350(10)

Table C5. FWHM values of ^{133}Cs MAS NMR spectra ($B_0=21.1$ T, $\omega_r/2\pi = 30$ kHz) for $\text{Cs}_2\text{SbAgCl}_6$ (Figure C6).

Cu²⁺ composition (x)	FWHM (Hz)		
	Peak-1	Peak-2	Peak-3
0.01	305(5)	1625(25)	–
0.05	1035(10)	2080(20)	2500(200)
0.10	1410(10)	2310(20)	2700(100)

Table C6. Temperature dependence of chemical shifts and fitted line equations for Peak-1, Peak-2, and Peak-3 of the ^{133}Cs MAS NMR spectra for the Cu^{2+} -doped material ($x = 0.10$); acquired at 11.75 T with a spinning frequency of 13 kHz.

$\delta_{\text{iso}}(^{133}\text{Cs})$	Temperature (T/K)				Fitted Linear Equation
	238	291	323	343	
Peak-1	77	82	84	85	$\delta_{\text{iso}}(^{133}\text{Cs}) / \text{ppm} = -6.3 (1000/T) + 102.9;$ $R^2 = 0.999$
Peak-2	-34	-13	-3	3	$\delta_{\text{iso}}(^{133}\text{Cs}) / \text{ppm} = -30.9 (1000/T) + 89.9;$ $R^2 = 0.999$
Peak-3	-147	-105	-87	-74	$\delta_{\text{iso}}(^{133}\text{Cs}) / \text{ppm} = -60.4 (1000/T) + 95.4;$ $R^2 = 0.998$

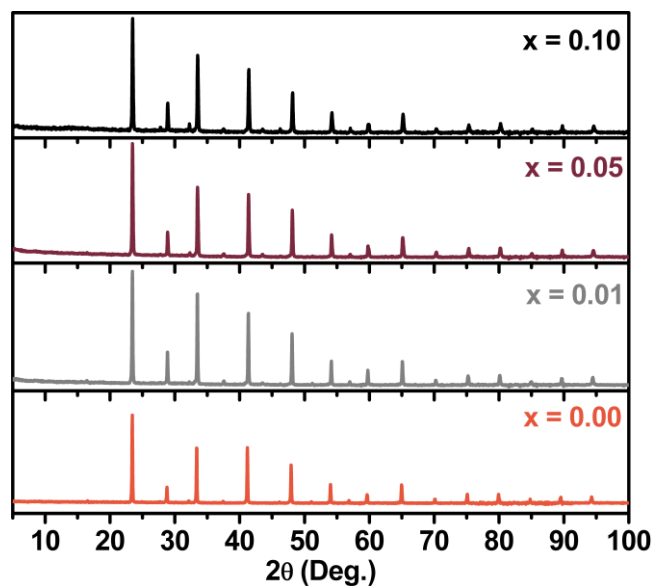


Figure C1. Enlargement of powder XRD patterns for $\text{Cs}_2\text{SbAgCl}_6$ ($x = 0.00$) and for Cu^{2+} -doped $\text{Cs}_2\text{SbAgCl}_6$ materials.

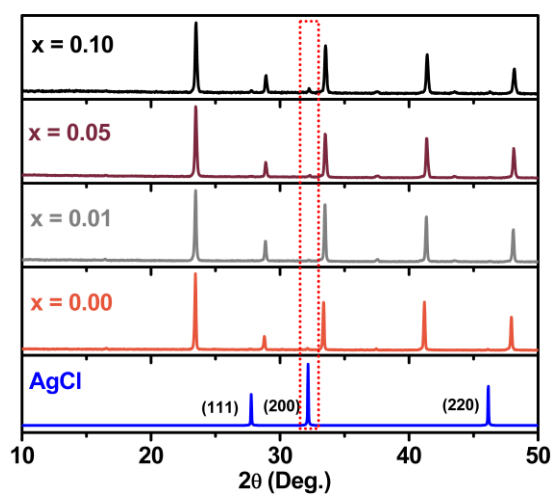


Figure C2. Powder XRD patterns for AgCl , $\text{Cs}_2\text{SbAgCl}_6$ and for the latter with the indicated level of nominal Cu^{2+} doping. The presence of AgCl in the double perovskite materials is indicated, with the relative intensity of the AgCl (200) peak increasing as the Cu^{2+} doping increases (dotted red box). Please note that the PXRD pattern for AgCl is simulated.⁴

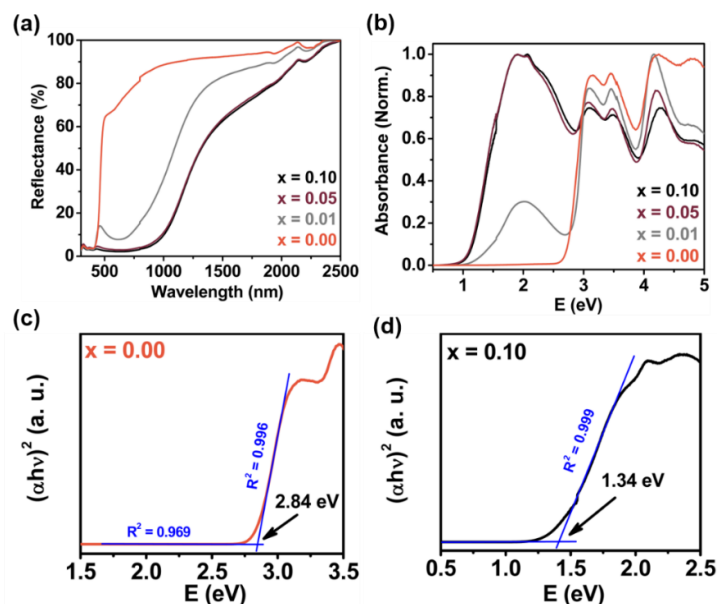


Figure C3. UV-VIS-NIR DR (a), and normalized absorption (b) spectrum for $\text{Cs}_2\text{SbAgCl}_6$ parent (i.e. $x = 0.00$) and all Cu^{2+} -doped ($x = 0.01, 0.05$, and 0.10) materials. The DR spectra is converted to absorbance by using the Kubelka-Munk equation (see Materials and Methods). The Tauc plots, which yield, assuming a direct allowed transition, bandgaps of 2.84 eV for $\text{Cs}_2\text{SbAgCl}_6$ ($x = 0.00$) (c), and 1.34 eV for the maximum Cu^{2+} doped material ($x = 0.10$) (d).

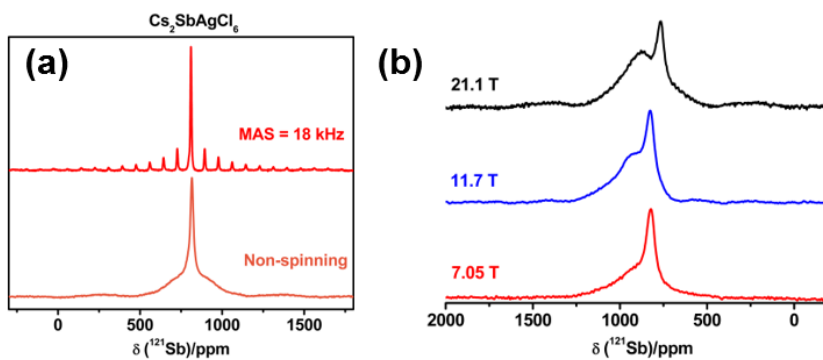


Figure C4. Comparison of ^{121}Sb NMR spectra of $\text{Cs}_2\text{SbAgCl}_6$ parent under non-spinning and magic-angle spinning (18 kHz) conditions at 21.1 T (a). Comparison of ^{121}Sb NMR spectra acquired at 7.05, 11.75, and 21.1 T for non-spinning $\text{Cs}_2\text{SbAgCl}_6$ with Cu^{2+} doping of $x = 0.10$, showing the improved Sb site resolution with increasing

magnetic field strength. Data were acquired with a selective central transition pulse, optimized for the larger C_Q resonance to higher frequency (i.e. for the peak centered at ≈ 900 ppm) (b).

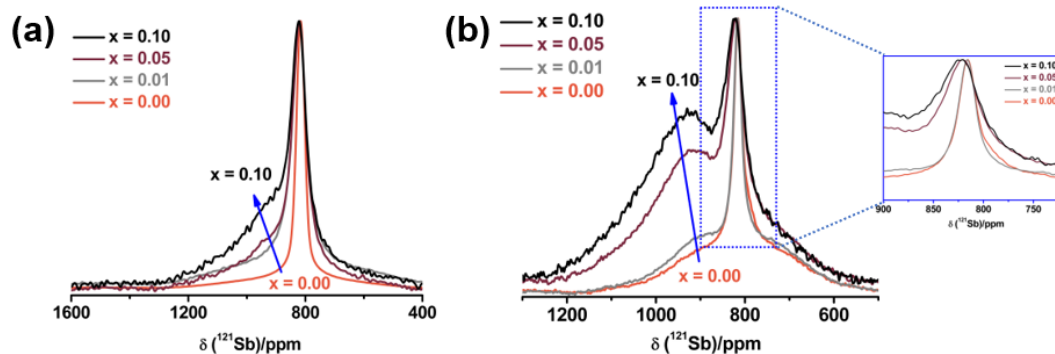


Figure C5. Comparison of ^{121}Sb NMR spectra acquired at 7.05 T (a) and 21.1 T (b) for non-spinning $\text{Cs}_2\text{SbAgCl}_6$ ($x = 0.00$) and for this material with Cu^{2+} doping ($x = 0.01$, 0.05, and 0.10), showing both the intensity of the high-frequency peak ($\delta \sim 900$ ppm) and illustrating that the linewidth of the parent peak (i.e. the low frequency peak) increases with Cu^{2+} doping (insert).

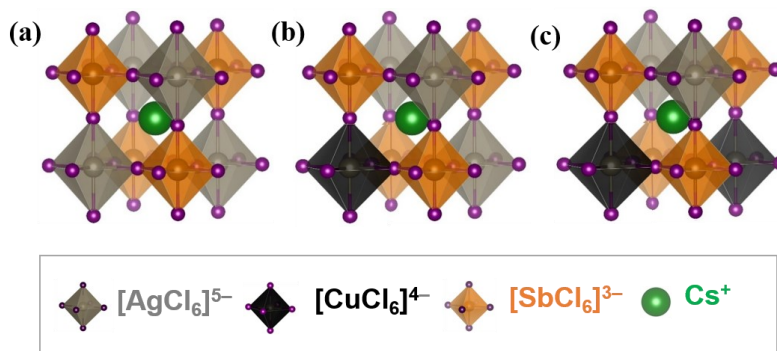


Figure C6. Schematic representation of $\text{Cs}_2\text{SbAgCl}_6$ double perovskites without (a), and with Cu^{2+} doping at one (b) or two (c) sites. This representation assumes that $[\text{CuCl}_6]^{4-}$ will generally only substitute $[\text{AgCl}_6]^{5-}$ sites (see the Chapter 4).

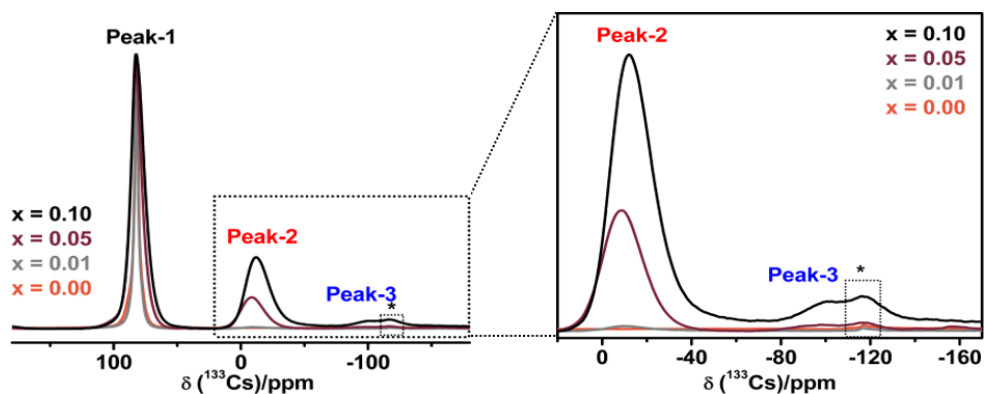


Figure C7. Comparison of ^{133}Cs MAS NMR spectra for $\text{Cs}_2\text{SbAgCl}_6$ without ($x = 0.00$) and with ($x = 0.01, 0.05,$ and 0.10) Cu^{2+} doping, acquired at 11.75 T with a spinning frequency of 13 kHz, showing that the linewidth of Peak-1 increases with Cu^{2+} content (left), and that the relative intensities (with respect to the normalized Peak-1) of Peak-2 and Peak-3 increase with Cu^{2+} doping concentration (right). Spinning sidebands are indicated with an asterisk (*).

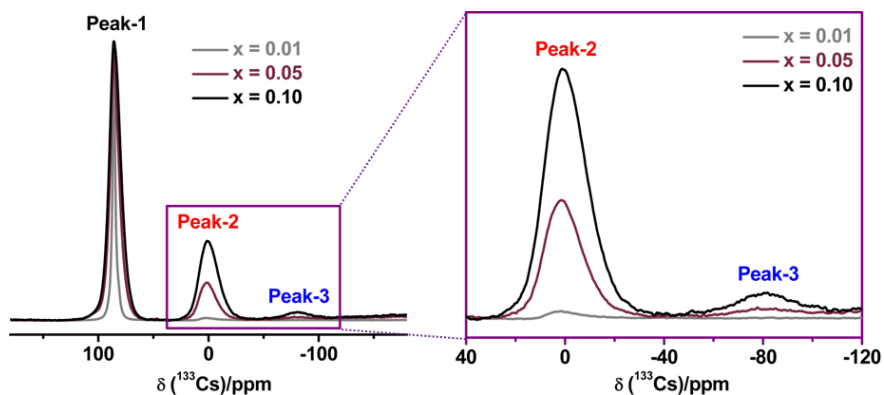


Figure C8. Comparison of ^{133}Cs MAS NMR spectra for $\text{Cs}_2\text{SbAgCl}_6$ with or without Cu^{2+} doping, acquired at 21.1 T with a spinning frequency of 30 kHz, showing that the linewidth of Peak-1 increases with Cu^{2+} content (left), and that the relative intensities (with respect to the normalized Peak-1) of Peak-2 and Peak-3 increase with Cu^{2+} doping content (right).

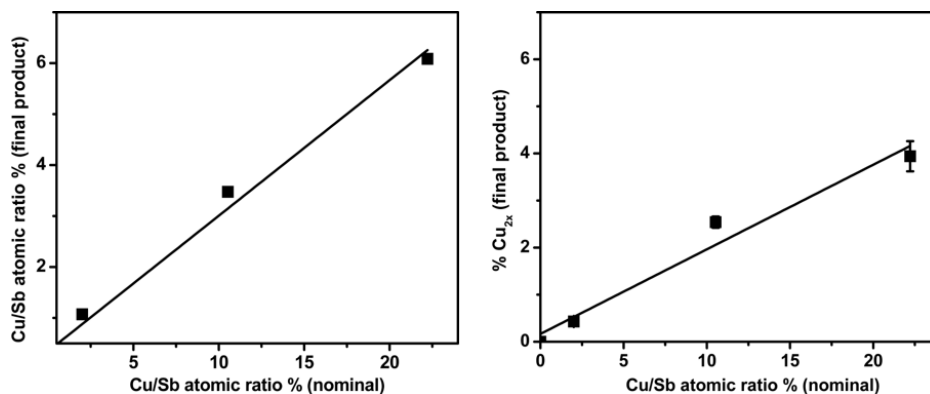


Figure C9. Linear relation of Cu/Sb atomic ratio % before (nominal) and after (final product) the synthesis based on the ICP-OES data (left) and Cu-composition based on ^{133}Cs MAS NMR spectra acquired at 11.75 T against nominal Cu/Sb atomic ratio % (right).

^{133}Cs NMR Analysis

From the crystal structure of $\text{Cs}_2\text{SbAgCl}_6$, the Cs^+ ion resides in the cubooctahedral void, surrounded by a total of eight (four Ag^+ and four Sb^{3+}) octahedral sites (Figure C6a). Similarly, each Ag^+ or Sb^{3+} site is also surrounded by eight Cs^+ ions. Since the peaks labeled Peak-2 in the ^{133}Cs NMR spectra arise from Cu^{2+} substitution in a Ag^+ site, each Cu^{2+} ion is surrounded by eight Cs^+ ions. If we neglect the minor contribution giving rise to Peak-3, then from the ^{133}Cs NMR spectra, the total Cu^{2+} concentration in the final product is given by Eq. C1.

$$(2x) = \frac{1}{8} \times (\text{Area}/\%) \quad (\text{Eq. C1})$$

where Area/% refers to the percent contribution of Peak-2 to the total ^{133}Cs spectrum. For example, when $x = 0.10$, the area for Peak-2 in the ^{133}Cs NMR spectrum is 29.5 % and thus,

$$(2x) = (a+b) = \left(\frac{1}{8} \times 29.5\right) \% = 3.37 \% = 0.037 \quad (\text{Eq. C2})$$

Hence, $x = \left(\frac{1}{2} \times 0.037\right) = 0.0185$.

Please note that the general formula of Cu^{2+} doped material is: $\text{Cs}_2\text{Sb}_{1-a}\text{Ag}_{1-b}\text{Cu}_{2x}\text{Cl}_6$ ($a + b = 2x$) and that the $(2x)$ value represents the fraction of octahedral sites (Sb^{3+} or Ag^+) that are substituted by Cu^{2+} ions.

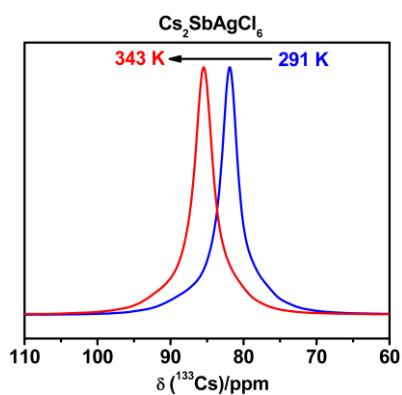


Figure C10. Temperature dependent ^{133}Cs MAS NMR spectra of $\text{Cs}_2\text{SbAgCl}_6$ parent.

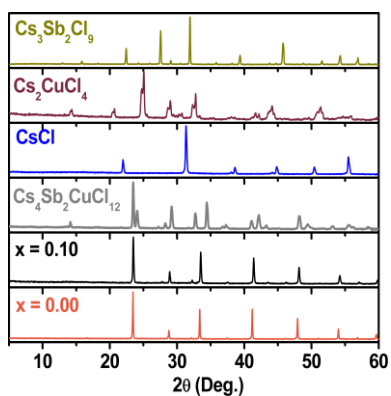
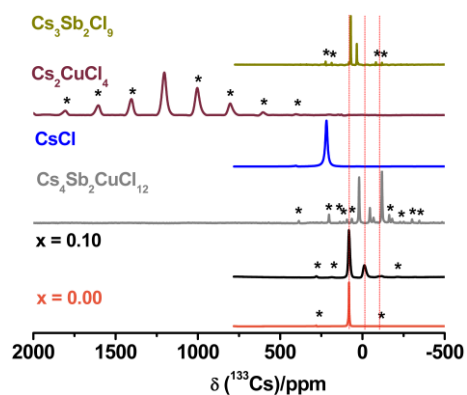


Figure C11. Cesium-133 MAS NMR spectra ($B_0 = 11.75$ T, top) and PXRD patterns (bottom) for $\text{Cs}_2\text{SbAgCl}_6$ ($x = 0.00$ and 0.10), $\text{Cs}_4\text{Sb}_2\text{CuCl}_{12}$, CsCl , Cs_2CuCl_4 and $\text{Cs}_3\text{Sb}_2\text{Cl}_9$. The asterisks (*) indicate spinning sidebands.

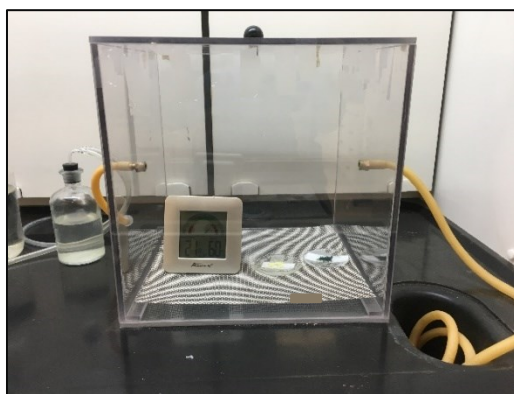


Figure C12. Photograph of the custom-built humidifying chamber.

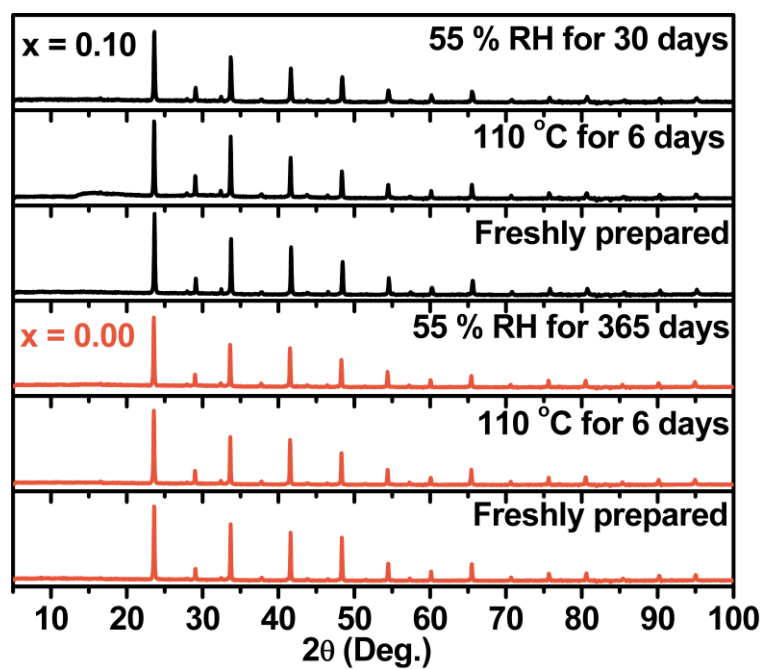


Figure C13. Enlarged version of powder XRD pattern for the stability experiments of $\text{Cs}_2\text{SbAgCl}_6$ parent ($x = 0.00$) and the maximum Cu^{2+} -doped ($x = 0.10$) materials under the indicated conditions.

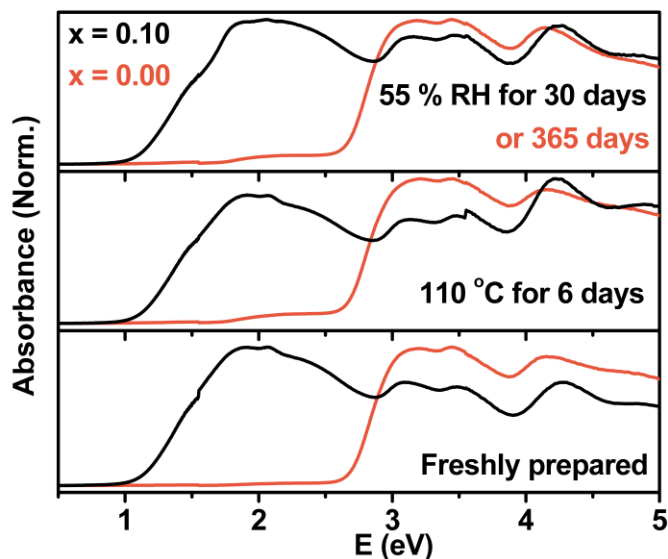


Figure C14. Absorption spectra of $\text{Cs}_2\text{SbAgCl}_6$ parent ($x = 0.00$, red) and the maximum Cu^{2+} -doped ($x = 0.10$, black) materials under the indicated conditions. The absorption spectra were extracted from DR data by using the Kubelka-Munk equation (see Materials and Methods).

Determination of the Pseudocontact Contribution

The pseudocontact contribution to the shift arises because of the interaction of the nuclear spin with the average magnetic moment of the paramagnetic center, which does not average to zero in the case when magnetic susceptibility of the metal center is anisotropic. It can be related to the magnetic susceptibility through the Kurland-McGarvey equation¹⁰ and, for the case of $S=1/2$ spins, it can be directly related to the electron g -matrix from EPR:

$$\delta^{\text{pc}} = \frac{1}{12\pi r^3} \frac{\mu_0 \mu_{\text{B}}^2 S(S+1)}{3kT} (g_{\parallel}^2 - g_{\perp}^2)(3\cos^2\theta - 1)$$

Using $g_{\parallel} = 2.3$ and $g_{\perp} = 2.0$, at about 4.5 \AA the expected PCS value is 1.2 ppm, to which a further contribution amounting to about 20% coming from the temperature independent paramagnetism could be added.¹¹

¹²¹Sb NMR Lineshape Analysis of Cs₂SbAgCl₆

Since ¹²¹Sb has a large quadrupole moment ($Q = -36.0 \text{ fm}^2$) and $I = 5/2$, the lineshape and breadth of the NMR spectra are often dominated by the quadrupolar interaction. However, for the parent Cs₂SbAgCl₆ material, the Sb sites are located at an octahedral position within a cubic space group such that the overall EFG would be expected to be zero. In practice, slight defects or distortions within the lattice may impact the symmetry about some ¹²¹Sb nuclei, such that a quadrupolar interaction is detected despite the octahedral symmetry. Analysis of the spectra acquired under non-spinning and MAS conditions as well as at multiple field strengths assist in determining these interactions. Other anisotropic interactions that may contribute to the linewidth and shape include magnetic shielding anisotropy, and direct (dipolar) and indirect (J-coupling) spin-spin coupling. A small quadrupolar interaction of 1 MHz would lead to a 30 Hz second order broadening contribution at 21.1 T, while the non-spinning linewidth is 3.2 kHz. The linewidth remains nearly constant across three magnetic field strengths ($B_0 = 7.05, 11.75$ and 21.1 T). Since magnetic shielding scales linearly with field and the second order quadrupole broadening is inversely related, these anisotropic interactions are negligible in their contribution (i.e. < 1 ppm). Magic-angle spinning reduces the linewidth by nearly 50% (1.5 kHz) to a FWHM of 1.8 kHz, indicating a contribution from heteronuclear dipole coupling between ¹²¹Sb and ^{35/37}Cl; the remaining MAS linewidth is attributed to indirect spin-spin coupling between ¹²¹Sb (N.A. = 57.2 %) and the six coordinating ^{35/37}Cl anions (³⁵Cl: N.A. = 75.8%, $I = 3/2$ and ³⁷Cl: N.A. = 24.2%, $I = 3/2$). The Gaussian-like ¹²¹Sb peak is attributed to the complex splitting pattern arising from spin-spin coupling of ¹²¹Sb to the two Cl isotopes, further complicated by the quadrupole coupling interaction expected for the Cl isotopes, which is expected to be significant since these nuclei are not in a high-symmetry position. Hence, a complex J-splitting pattern that is unresolved at 7.05 T is observed.¹

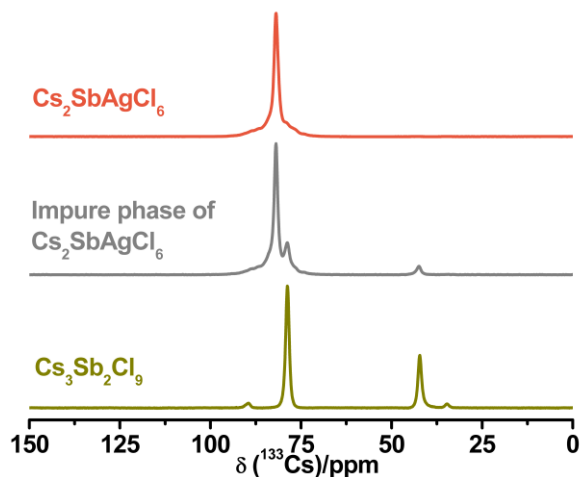


Figure C15. Cesium-133 MAS NMR spectra for $\text{Cs}_2\text{SbAgCl}_6$ and impure $\text{Cs}_2\text{SbAgCl}_6$ double perovskite and $\text{Cs}_3\text{Sb}_2\text{Cl}_9$.

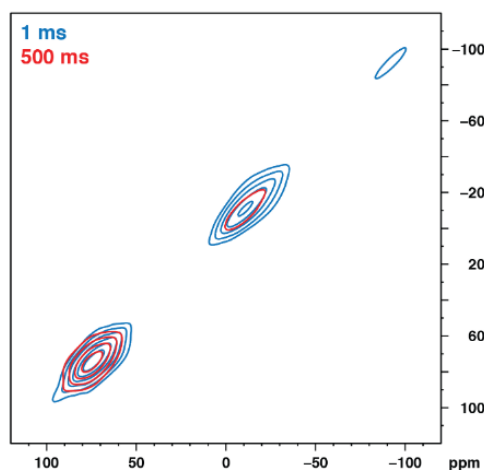


Figure C16. Two-dimensional ^{133}Cs EXSY NMR ($B_o = 21.1$ T; $\omega_r/2\pi = 30$ kHz) contour plots of Cu^{2+} -doped $\text{Cs}_2\text{SbAgCl}_6$ ($x = 0.10$) with 1 ms (blue) and 500 ms (red) mixing times, showing no Cs exchange.

References

- (1) Faucher, A.; Terskikh, V. V.; Wasylishen, R. E. Assessing Distortion of the AF_6 (A= As, Sb) Octahedra in Solid Hexafluorometallates (V) via NMR Spectroscopy. *Can. J. Chem.* **2015**, *93*, 938–944.
- (2) Harris, R. K.; Becker, E. D.; de Menrzes, S. M. C.; Goodfellow, R.; Granger, P.

- Commission on Molecular Structure and Spectroscopy. *Pure Appl. Chem.* **2001**, *73*, 1795–1818.
- (3) Bernard, G. M.; Goyal, A.; Miskolzie, M.; McKay, R.; Wu, Q.; Wasylshen, R. E.; Michaelis, V. K. Methylammonium Lead Chloride: A Sensitive Sample for an Accurate NMR Thermometer. *J. Magn. Reson.* **2017**, *283*, 14–21.
- (4) Hull, S.; Keen, D. A. Pressure-Induced Phase Transitions in AgCl, AgBr, and AgI. *Phys. Rev. B* **1999**, *59*, 750–761.
- (5) Kubelka, P.; Munk, F. Z. Ein Beitrag Zur Optik Der Farbanstriche. *Technol. Phys.* **1931**, *12*, 593–601.
- (6) Mansfield, P. Multiple-Pulse Nuclear Magnetic Resonance Transients in Solids. *Phys. Rev.* **1965**, *137*, A961–A974.
- (7) Bodart, P. R.; Amoureux, J. P.; Dumazy, Y.; Lefort, R. Theoretical and Experimental Study of Quadrupolar Echoes for Half-integer Spins in Static Solid State NMR. *Mol. Phys.* **2000**, *98*, 1545–1551.
- (8) Davis, J. H.; Jeffrey, K. R.; Bloom, M.; Valic, M. I.; Higgs, T. P. Quadrupolar Echo Deuteron Magnetic Resonance Spectroscopy in Ordered Hydrocarbon Chains. *Chem. Phys. Lett.* **1976**, *42*, 390–394.
- (9) Jeener, J.; Meier, B. H.; Bachmann, P.; Ernst, R. R. Investigation of Exchange Processes by Two-dimensional NMR Spectroscopy. *J. Chem. Phys.* **1979**, *71*, 4546–4553.
- (10) Kurland, R. J.; McGarvey, B. R. Isotropic NMR Shifts in Transition Metal Complexes: The Calculation of the Fermi Contact and Pseudocontact Terms. *J. Magn. Reson.* **1970**, *2*, 286–301.
- (11) Walder, B. J.; Patterson, A. M.; Baltisberger, J. H.; Grandinetti, P. J. Hydrogen Motional Disorder in Crystalline Iron Group Chloride Dihydrates. *J. Chem. Phys.* **2018**, *149*, 084503.

Appendix D: Supplementary Data for Chapter 5

Tailorable Indirect to Direct Bandgap Double Perovskites with Bright White-Light Emission: Decoding Chemical Structure Using Solid-State NMR

Experimental

Materials and Methods

All starting materials and solvents were purchased from various commercial sources and used without further purification: CsCl (Tecochem Laboratories Ltd., AB, Canada), BiCl₃ (MilliporeSigma, MO, USA), InCl₃ (Alfa Inorganics, Inc., MA, USA), AgNO₃ (EM Science, Darmstadt, Germany), HCl (Caledon Laboratory Chemicals, ON, Canada). All materials were synthesized and characterized under ambient atmosphere and temperature.

Synthesis of Polycrystalline Cs₂Bi_{1-x}In_xAgCl₆ (0 ≤ x ≤ 1) HDPs

AgCl salt was freshly synthesized by the addition of an excess amount of concentrated HCl to an aqueous solution of AgNO₃, resulting in a solid white precipitate. This white solid was filtered with a Buchner funnel, washed with 95% ethanol, and then dried under vacuum filtration. Afterwards, 1 mmol of freshly prepared AgCl in conc. HCl (at *ca.* 120 °C and constant stirring), (1-x) mmol of BiCl₃ and x mmol of InCl₃ were added to the hot conc. HCl solvent within the vial, followed by an addition of 2 mmol of CsCl powder. White (when x = 1.0) to yellow (when x = 0.0) precipitates were observed immediately. The mixtures were heated for an hour with medium stirring and then allowed to stand at room temperature for two more hours. The precipitates were then filtered using a Buchner funnel and washed with 95% washing ethanol. These solid samples were stored in vials under ambient conditions and used for further characterization.

Powder X-ray Diffraction (PXRD)

Powder X-ray diffraction measurements for the polycrystalline solid samples were collected on an Inel MPD multi-purpose diffractometer (40 kV, 50 mA) system equipped with a CPS 120 curved position sensitive X-ray detector and a 1.540596 Å Cu K α radiation source. All samples were placed on a plastic sample holder and 2 θ data from $\sim 0^\circ$ to 113 $^\circ$ were collected. The cell constants were determined from the profile fitting of the PXRD patterns using the FullProf Suite software.

Energy-dispersive X-ray spectroscopy (EDS) and Field Emissive Scanning Electron Microscopy (FESEM)

The FESEM measurements were performed using a Zeiss Sigma 300 VP equipped with dual silicon drift detectors for EDS measurements.

Inductively Coupled Plasma Optical Emission Spectroscopy (ICP-OES)

A Thermo iCAP 6000 series ICP-OES spectrometer was used for Bi and In concentration measurements. The samples were dissolved in *aqua regia* and the resultant solution was further diluted with deionized water.

Thermogravimetric Analysis (TGA)

TGA analyses were performed on a Perkin Elmer Pyris 1 Thermogravimetric Analyzer. The samples were heated under an N $_2$ atmosphere at a heating rate of 5–10 $^\circ\text{C}/\text{min}$ from 25–800 $^\circ\text{C}$.

UV-Vis Diffuse Reflectance (DR) Spectroscopy

All the UV-Vis diffuse reflectance spectra for the polycrystalline Cs $_2$ Bi $_{1-x}$ In $_x$ AgCl $_6$ double perovskite samples were collected using a Cary 5000 UV–Vis–NIR spectrophotometer. For each sample, a small amount (50 to 100 mg) of powder was packed into a black boat and measurements were obtained at wavelengths between 200 and 800 nm. The instrument was calibrated with a Spectralon (>99%) reflectance standard.

All the DR spectra were converted to pseudo-absorbance spectra using the Kubelka-Munk¹ transformation as follows: $\alpha \sim (1-R)^2/(2R)$, where, R and α are the absolute reflectance and pseudo-absorbance, respectively. The indirect and direct bandgaps were experimentally determined from the intercept values upon extrapolation of the linear regions of $(\alpha h\nu)^{1/2}$ vs E(eV) and $(\alpha h\nu)^2$ vs E(eV) plots, respectively.

Steady-State and Time-Resolved Photoluminescent (PL) Spectroscopy and PLQY

Photoluminescence spectroscopy was performed using a 365+351 nm Ar ion laser source. A 400-nm longpass filter was used to block the scattered laser light and the spectra were measured with an intensity-calibrated Ocean Optics USB2000 spectrometer. Time-resolved PL measurements were performed using a pulsed laser excitation of 365+351 nm Ar ion laser interfaced to an acousto-optic modulator (~10 ns response time) and a Hamamatsu H7422 PMT.

The PLQY was measured using a Photon Technology International (PTI) MP1 Fluorescence System with a 75 W Xenon arc lamp as an excitation source and equipped with an integrating sphere. Solid BaSO₄ was used as a reference sample. Equivalent amounts of sample and reference solids were taken in melting point capillary tubes which were placed in the integrating sphere for further measurements. Samples and the reference were excited at $\lambda_{\text{max}} = 370$ or 380 nm and emission spectra were collected between 410 to 900 nm, respectively.

Solid-State Nuclear Magnetic Resonance (NMR) Spectroscopy

(i) Cesium-133 NMR spectroscopy: (a) Solid-state ¹³³Cs NMR spectra were acquired at 21.14 T (900 MHz, ¹H) on a Bruker Avance II 900 spectrometer under magic angle spinning (MAS) conditions using a 2.5 mm H/X MAS Bruker probe with $\gamma B_0/2\pi(^{133}\text{Cs}) = 118.0$ MHz and the sample spinning at a spinning frequency of 30 kHz. All samples were packed into 2.5 mm o.d. ZrO₂ rotors. A Bloch decay pulse sequence was used with a 0.50 μs pulse width (~20° tip angle, $\gamma B_1/2\pi$ (solid) = 111 kHz), an acquisition time of 20 ms, an optimized recycle delay of 90 s (see Figure D18, Table D6) and 32 co-added transients.

(b) Solid-state ^{133}Cs NMR measurements were performed at 11.75 T (500 MHz, ^1H) on a Bruker Avance 500 spectrometer under MAS conditions using a 4 mm H/X Bruker MAS probe with $\gamma B_0/2\pi(^{133}\text{Cs}) = 65.6$ MHz and a MAS frequency of 13 kHz. All samples were packed into 4 mm o.d. ZrO_2 rotors. Data were acquired using a Bloch decay pulse ($\pi/2$ pulse of 1.25 μs , $\gamma B_1/2\pi$ (solution) = 50.0 kHz), an acquisition time of 50-100 ms, a recycle delay of 300-5000 s and 1-8 co-added transients.

All ^{133}Cs NMR spectra discussed here were referenced by setting the ^{133}Cs NMR peak of a 0.1 M CsCl aqueous solution to $\delta = 0.0$ ppm.

(ii) Bismuth-209 NMR spectroscopy: (a) Solid-state ^{209}Bi NMR spectra were acquired at 21.14 T (900 MHz, ^1H) on the Bruker Avance II 900 spectrometer. Non-spinning ^{209}Bi NMR spectra were collected using a 4 mm H/X MAS Bruker probe with $\gamma B_0/2\pi(^{209}\text{Bi}) = 145$ MHz. Samples were packed in 4 mm thick-walled Bruker o.d. ZrO_2 rotors and a modified quadrupolar-echo pulse sequence^{2,3} ($(\pi/2)_x - \tau_1 - (\pi/2)_y - \tau_2 - \text{ACQ}$), where τ_1 and τ_2 represent the inter-pulse and refocusing delays, respectively) was used to achieve broader excitation width and minimize line distortions at higher magnetic field strengths with a solid 1.0 μs $\pi/2$ pulses ($\gamma B_1/2\pi$ (solution) = 50 kHz). An echo delay of 20 μs was used for all the measurements. A recycle delay of 0.5 s and 16,000 to 80,000 co-added transients were used for each non-spinning ^{209}Bi NMR measurement.

Magic-angle spinning ^{209}Bi NMR spectra were collected using a 2.5 mm H/X MAS Bruker probe with $\gamma B_0/2\pi(^{209}\text{Bi}) = 145$ MHz with magic-angle spinning frequency of 30 kHz. The spectra were acquired using either a Bloch decay pulse of 0.2 μs (short tip angle $\sim 20^\circ$ solid) or a modified rotor-synchronized quadrupolar-echo pulse sequence^{2,3} ($(\pi/2)_x - \tau_1 - (\pi/2)_y - \tau_2 - \text{ACQ}$), where τ_1 and τ_2 represent the inter-pulse and refocusing delays, with a 0.5 μs $\pi/2$ pulses ($\gamma B_1/2\pi$ (solution) = 100 kHz). An echo delay of 33 μs was used for rotor-synchronized quadrupolar-echo experiments. A recycle delay of 0.5 s and 1,000-48,000 co-added transients were used for each ^{209}Bi MAS NMR measurement.

(b) An additional ^{209}Bi NMR measurement for $\text{Cs}_2\text{BiAgCl}_6$ parent material were performed at 7.05 T (300 MHz, ^1H) and 11.75 T (500 MHz, ^1H) on a Bruker Avance 300 and 500 spectrometers with $\gamma B_0/2\pi(^{209}\text{Bi}) = 48.5$ and 80.7 MHz,

respectively, using a 4 mm H/X Bruker MAS probe. Samples were packed in 4 mm o.d. ZrO₂ rotors and magic-angle spinning (MAS = 10 kHz) spectra were acquired using a Bloch decay pulse of 1 μs (solid $\pi/2$; $\gamma B_1/2\pi$ (solution) = 50 kHz) and non-spinning spectra were acquired using a Hahn-echo pulse sequence ($(\pi/2)_x - \tau_1 - (\pi)_y - \tau_2 - \text{ACQ}$), where τ_1 and τ_2 represent the inter-pulse and refocusing delays), with a 1.0 μs $\pi/2$ pulses ($\gamma B_1/2\pi = 50$ kHz). An echo delay of 40 μs and recycle delay of 0.2-1.0 s were used.

All ²⁰⁹Bi NMR spectra discussed above were referenced using saturated Bi(NO₃)₃ in a concentrated HNO₃ solution to set the ²⁰⁹Bi peak at $\delta = 0.0$ ppm.

(iii) Indium-115 NMR spectroscopy: Solid-state ¹¹⁵In NMR spectra were acquired at 21.14 T (900 MHz, ¹H) on the Bruker Avance II 900 spectrometer with the 4 mm H/X MAS Bruker probe with $\gamma B_0/2\pi(^{115}\text{In}) = 197.1$ MHz, using either a Bloch decay pulse of 0.2 μs (short tip angle $\sim 20^\circ$ solid) or a modified quadrupolar-echo pulse sequence^{2,3} ($(\pi/2)_x - \tau_1 - (\pi/2)_y - \tau_2 - \text{ACQ}$), where τ_1 and τ_2 represent the inter-pulse and refocusing delays), with a solid 1.0 μs $\pi/2$ pulses ($\gamma B_1/2\pi$ (solution) = 50 kHz). ¹¹⁵In MAS NMR spectra were acquired using the Bloch decay pulse and a spinning frequency of 18 kHz. Non-spinning ¹¹⁵In NMR data were acquired using the quadrupolar-echo pulse sequence with an echo delay of 20 μs and 4,000-40,000 co-added transients. A recycle delay of 1 s was used for all the measurements.

An additional ¹¹⁵In NMR measurement for Cs₂InAgCl₆ parent material were performed at 11.75 T (500 MHz, ¹H) on a Bruker Avance 500 spectrometers with $\gamma B_0/2\pi(^{115}\text{In}) = 109.6$ MHz, using a 4 mm H/X Bruker MAS probe. Samples were packed in 4 mm o.d. ZrO₂ rotors and magic-angle spinning (MAS = 10 kHz) spectra were acquired using a Bloch decay pulse of 0.7 μs (solid $\pi/2$; $\gamma B_1/2\pi$ (solution) = 71.4 kHz) and non-spinning spectra were acquired using a solid-echo pulse sequence ($(\pi/2)_x - \tau_1 - (\pi/2)_y - \tau_2 - \text{ACQ}$), here τ_1 and τ_2 represent the inter-pulse and refocusing delays), with a 0.7 μs solid $\pi/2$ pulses ($\gamma B_1/2\pi = 71.4$ kHz). An echo delay of 40 μs and recycle delay of 2.0 s were used.

All ¹¹⁵In NMR spectra were referenced using 0.1 M In(NO₃)₃ in 0.5 M HNO₃ to set the ¹¹⁵In peak at $\delta = 0.0$ ppm.

Quantum Chemical Calculations

(i) Electronic Band Structure Calculations: Five structural models of the $\text{Cs}_2\text{Bi}_{1-x}\text{In}_x\text{AgCl}_6$ compounds were used for calculations, with $x = 0, 0.25, 0.5, 0.75,$ and 1. Structure optimization, total energy calculations, band dispersion, density of states, and electron localization function calculations⁴⁻⁶ were performed with the Vienna Ab Initio Simulation Package (VASP) within the density functional theory framework.^{7,8} The electronic wave functions were defined with the plane-wave basis set and projector-augmented wave potentials.⁹ The structural optimization electronic convergence criteria were set to 1×10^{-8} eV, and the ionic optimization was set to 1×10^{-2} eV/Å. A 500 eV plane wave cutoff energy was used and the integration of the first Brillouin zone was carried out using a Monkhorst–Pack k-point grid of $8 \times 8 \times 8$. The HSE06 functional was implemented to estimate the bandgap (corrected for the significant underestimation of the Perdew-Bruke-Ernzerhof (PBE) bandgap), which resulted in $E_g = 2.52$ eV and 3.51 eV for $\text{Cs}_2\text{BiAgCl}_6$ and $\text{Cs}_2\text{InAgCl}_6$, respectively, which is in a good agreement with the experimental values (2.70 eV and 3.67 eV, respectively). The calculated bandgap values were obtained by implementing a mixture of PBE : Hartree–Fock (75:25). To analyse the valence electron charge redistribution, a Bader charge analysis was employed.¹⁰

(ii) DFT: A series of gauge-including projector-augmented wave (GIPAW) DFT calculations were performed to assess the impact of B'(III)-site substitutions on the ^{209}Bi and ^{115}In electric field gradients (EFG), implemented within version 4.4 of the CASTEP software.¹¹ Using a primitive symmetry supercell the computed EFGs were obtained on a series of model structures by varying the Bi/In substitutions. All calculations used the PBE functional in the GGA for the exchange- correlation energy^{12,13} and ultrasoft pseudopotentials¹⁴ on all-atom geometry-optimized primitive clusters. Calculations were performed with a coarse accuracy basis set and a maximum plane-wave energy of 244.90 eV using an HP xw4400 workstation with a single Intel Dual-Core 2.67 GHz processor and 8 GB RAM. The computed EFGs were converted to quadrupole coupling constants using 0.81 and 0.516 barn for the ^{115}In and ^{209}Bi quadrupolar moments.¹⁵ The DFT calculations were performed on the most symmetric substitutions that could be accommodated with current hardware that is restricted in

handling large unit cell volumes. Therefore, the presented calculations are considered “best-case” symmetric scenarios. The non-symmetric Bi/In substitutions within the 12 possible environments could increase the experimental quadrupolar coupling constants beyond these values. Considering the potential for sizable quadrupole couplings and populations there is the potential for invisible Bi (or In) environments.

Table D1. Elemental analysis of $\text{Cs}_2\text{Bi}_{1-x}\text{In}_x\text{AgCl}_6$ mixed-cationic double perovskites measured by EDS and ICP-OES.

Sample (Nominal composition)	Atom% by EDS ^a					Atomic ratio of In : Bi		
	Cs	Bi	In	Ag	Cl	Nominal	EDS	ICP-OES
$\text{Cs}_2\text{InAgCl}_6$	18.83 (1.15)	-	9.96 (0.89)	9.56 (0.72)	61.65 (1.85)	1.00: 0.00	1.00: 0.00	-
$\text{Cs}_2\text{Bi}_{0.01}\text{In}_{0.99}\text{AgCl}_6$	19.46 (0.80)	0.00 (0.00)	10.08 (0.34)	9.05 (0.52)	61.40 (1.09)	0.99: 0.01	1.00: 0.00	0.981:0.019
$\text{Cs}_2\text{Bi}_{0.05}\text{In}_{0.95}\text{AgCl}_6$	19.20 (0.46)	0.05 (0.04)	9.28 (0.15)	9.71 (0.32)	61.76 (0.82)	0.95: 0.05	0.99: 0.01	0.915:0.085
$\text{Cs}_2\text{Bi}_{0.25}\text{In}_{0.75}\text{AgCl}_6$	18.82 (0.56)	1.65 (0.17)	7.74 (0.29)	9.46 (0.46)	62.33 (1.20)	0.75: 0.25	0.82: 0.18	0.78:0.22
$\text{Cs}_2\text{Bi}_{0.35}\text{In}_{0.65}\text{AgCl}_6$	19.28 (0.36)	2.58 (0.41)	6.65 (0.50)	9.11 (0.69)	62.38 (1.02)	0.65: 0.35	0.72: 0.28	0.65 :0.35
$\text{Cs}_2\text{Bi}_{0.50}\text{In}_{0.50}\text{AgCl}_6$	19.98 (0.70)	4.65 (0.45)	4.85 (0.28)	10.48 (1.04)	60.04 (1.90)	0.50: 0.50	0.51:0.49	0.50: 0.50
$\text{Cs}_2\text{Bi}_{0.75}\text{In}_{0.25}\text{AgCl}_6$	19.68 (0.44)	7.06 (0.37)	2.18 (0.29)	10.07 (0.93)	61.00 (0.78)	0.25: 0.75	0.24:0.76	0.28: 0.72
$\text{Cs}_2\text{Bi}_{0.95}\text{In}_{0.05}\text{AgCl}_6$	19.98 (1.21)	8.87 (0.52)	0.33 (0.09)	9.32 (0.54)	61.50 (1.18)	0.05:0.95	0.04:0.96	0.076:0.924
$\text{Cs}_2\text{BiAgCl}_6$	20.37 (1.75)	10.22 (0.40)	-	9.37 (0.64)	60.03 (1.57)	0.00: 1.00	0.00:0.00	-

^aStandard deviation of EDS measurements based on 5-point measurements.

Table D2. Chemical formula of $\text{Cs}_2\text{Bi}_{1-x}\text{In}_x\text{AgCl}_6$ pre- and post-synthesis as determined by EDS and ICP-OES elemental analysis.

Nominal compositions	Chemical composition of the products	
	EDS	ICP-OES
$\text{Cs}_2\text{InAgCl}_6$	$\text{Cs}_2\text{InAgCl}_6$	$\text{Cs}_2\text{InAgCl}_6$
$\text{Cs}_2\text{Bi}_{0.01}\text{In}_{0.99}\text{AgCl}_6$	$\text{Cs}_2\text{Bi}_{0.00}\text{In}_{1.00}\text{AgCl}_6$	$\text{Cs}_2\text{Bi}_{0.019}\text{In}_{0.981}\text{AgCl}_6$
$\text{Cs}_2\text{Bi}_{0.05}\text{In}_{0.95}\text{AgCl}_6$	$\text{Cs}_2\text{Bi}_{0.02}\text{In}_{0.98}\text{AgCl}_6$	$\text{Cs}_2\text{Bi}_{0.085}\text{In}_{0.915}\text{AgCl}_6$
$\text{Cs}_2\text{Bi}_{0.25}\text{In}_{0.75}\text{AgCl}_6$	$\text{Cs}_2\text{Bi}_{0.18}\text{In}_{0.82}\text{AgCl}_6$	$\text{Cs}_2\text{Bi}_{0.22}\text{In}_{0.78}\text{AgCl}_6$
$\text{Cs}_2\text{Bi}_{0.35}\text{In}_{0.65}\text{AgCl}_6$	$\text{Cs}_2\text{Bi}_{0.28}\text{In}_{0.72}\text{AgCl}_6$	$\text{Cs}_2\text{Bi}_{0.35}\text{In}_{0.65}\text{AgCl}_6$
$\text{Cs}_2\text{Bi}_{0.50}\text{In}_{0.50}\text{AgCl}_6$	$\text{Cs}_2\text{Bi}_{0.49}\text{In}_{0.51}\text{AgCl}_6$	$\text{Cs}_2\text{Bi}_{0.50}\text{In}_{0.50}\text{AgCl}_6$
$\text{Cs}_2\text{Bi}_{0.75}\text{In}_{0.25}\text{AgCl}_6$	$\text{Cs}_2\text{Bi}_{0.76}\text{In}_{0.24}\text{AgCl}_6$	$\text{Cs}_2\text{Bi}_{0.72}\text{In}_{0.28}\text{AgCl}_6$
$\text{Cs}_2\text{Bi}_{0.95}\text{In}_{0.05}\text{AgCl}_6$	$\text{Cs}_2\text{Bi}_{0.96}\text{In}_{0.04}\text{AgCl}_6$	$\text{Cs}_2\text{Bi}_{0.924}\text{In}_{0.076}\text{AgCl}_6$
$\text{Cs}_2\text{BiAgCl}_6$	$\text{Cs}_2\text{BiAgCl}_6$	$\text{Cs}_2\text{BiAgCl}_6$

Table D3. Bader charges for the $\text{Cs}_2\text{Bi}_{1-x}\text{In}_x\text{AgCl}_6$ series.

In_x	Cs	Bi	In	Ag	Cl
0	+0.8794	+1.6453	N/A	+0.6136	-0.6696
0.25	+0.8838	+1.5053	+1.2798	+0.6034	-0.6367
0.5	+0.8848	+1.4463	+1.2753	+0.5878	-0.6197
0.75	+0.8835	+1.4746	+1.3183	+0.5703	-0.6158
1.0	+0.8815	N/A	+1.8006	+0.5559	-0.6075

Table D4. Mono-, bi-, and stretched exponential fitting parameters of PL decay for $\text{Cs}_2\text{Bi}_{0.085}\text{In}_{0.915}\text{AgCl}_6$ and $\text{Cs}_2\text{Bi}_{0.22}\text{In}_{0.78}\text{AgCl}_6$ HDPs upon laser excitation of $\lambda_{\text{ex}} = 364$ nm and $\lambda_{\text{em}} = 625$ nm.

Sample	Fitting Model	Model Equations ^a	Fitted Parameters	Reduced χ^2
Cs ₂ Bi _{0.085} In _{0.915} AgCl ₆	Monoexp.	$I = a_1 e^{-t/\tau}$	$\tau = 662 \pm 2$ ns	$8.0 \cdot 10^{-5}$
	Biexp.	$I = a_1 e^{-t/\tau_1} + a_2 e^{-t/\tau_2}$	$\tau_1 = 279 \pm 3$ ns ($a_1 = 36\%$) $\tau_2 = 865 \pm 4$ ns ($a_2 = 64\%$)	$7.2 \cdot 10^{-6}$
	Stretched exp.	$I = a_1 e^{-(t/\tau_{SE})^\beta}$	$\tau_{SE} = 571 \pm 1$ ns $\beta = 0.82$	$7.6 \cdot 10^{-6}$
Cs ₂ Bi _{0.22} In _{0.78} AgCl ₆	Monoexp.	$I = a_1 e^{-t/\tau}$	$\tau = 925 \pm 1$ ns	$2.4 \cdot 10^{-5}$
	Biexp.	$I = a_1 e^{-t/\tau_1} + a_2 e^{-t/\tau_2}$	$\tau_1 = 403 \pm 14$ ns ($a_1 = 17\%$) $\tau_2 = 1022 \pm 5$ ns ($a_2 = 83\%$)	$9.8 \cdot 10^{-6}$
	Stretched exp	$I = a_1 e^{-(t/\tau_{SE})^\beta}$	$\tau_{SE} = 883 \pm 1$ ns $\beta = 0.93$	$9.6 \cdot 10^{-6}$

^aIn equations: I = time-dependent luminescence intensity, a = amplitude, t = time, τ = time constant, β = stretching parameter ($0 < \beta < 1$).

Table D5. Biexponential fitting of wavelength dependent PL decay for Cs₂Bi_{0.085}In_{0.915}AgCl₆ and Cs₂Bi_{0.22}In_{0.78}AgCl₆ HDPs upon laser excitation of $\lambda_{ex} = 364$ nm.

Sample	λ_{em}	PL lifetime (τ) and their contribution (a)		Average lifetime, ^a τ_{avg}/ns
		τ_1/ns (a ₁)	τ_2/ns (a ₂)	
Cs ₂ Bi _{0.085} In _{0.915} AgCl ₆	550	250 ± 3	834 ± 3	746
	nm	(37%)	(63%)	

	625 nm	279 ± 3 (36%)	865 ± 4 (64%)	774
	700 nm	288 ± 4 (35%)	877 ± 4 (65%)	790
Cs ₂ Bi _{0.22} In _{0.78} AgCl ₆	550 nm	405 ± 13 (19%)	1027 ± 5 (81%)	976
	625 nm	403 ± 14 (17%)	1022 ± 5 (83%)	978
	700 nm	464 ± 17 (19%)	1058 ± 7 (81%)	1003

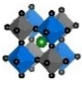
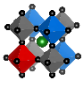
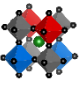
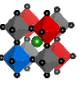
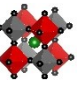
^a Intensity average lifetime (τ_{avg}) = $\frac{(a_1\tau_1^2 + a_2\tau_2^2)}{(a_1\tau_1 + a_2\tau_2)}$

Table D6. Spin-lattice relaxation time (T_1) values.

(a) ¹¹⁵In and ²⁰⁹Bi T_1 values at 7.05 T under non-spinning sample conditions.

Sample	$T_1(^{115}\text{In})/\text{s}$	$T_1(^{209}\text{Bi})/\text{s}$
Cs ₂ InAgCl ₆	0.0380 ± 0.0003	NA
Cs ₂ BiAgCl ₆	NA	0.0250 ± 0.0004

(b) ^{133}Cs T_1 values at 11.75 T under magic-angle spinning ($\nu_{\text{rot}} = 13$ kHz) sample condition.

Sample	$T_1(^{133}\text{Cs})/\text{s}$				
	Cuboctahedron sites				
	Site 1 	Site 2 	Site 3 	Site 4 	Site 5 
$\text{Cs}_2\text{BiAgCl}_6$	157 ± 23	-	-	-	-
$\text{Cs}_2\text{Bi}_{0.924}\text{In}_{0.076}\text{AgCl}_6$	235 ± 20	271 ± 26	-	-	-
$\text{Cs}_2\text{Bi}_{0.50}\text{In}_{0.50}\text{AgCl}_6$	-	-	548 ± 26	-	-
$\text{Cs}_2\text{Bi}_{0.085}\text{In}_{0.915}\text{AgCl}_6$	-	-	-	914 ± 38	920 ± 15
$\text{Cs}_2\text{InAgCl}_6$	-	-	-		931 ± 5

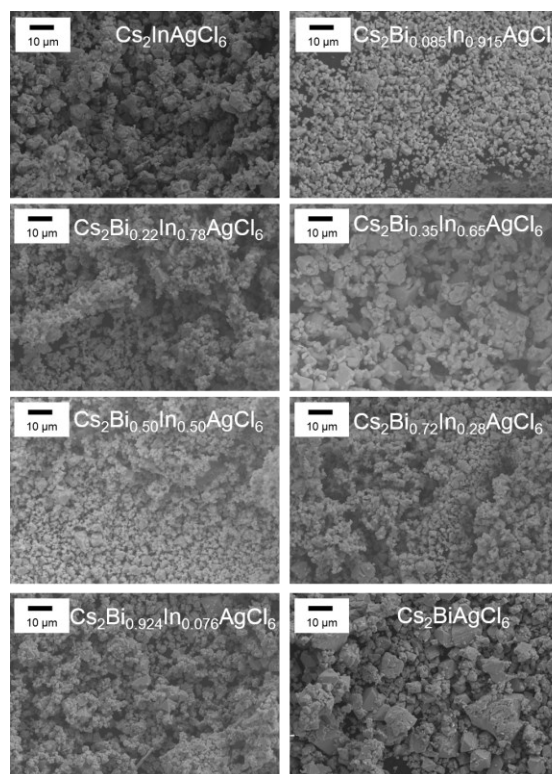


Figure D1. FESEM images of the $\text{Cs}_2\text{Bi}_{1-x}\text{In}_x\text{AgCl}_6$ series.

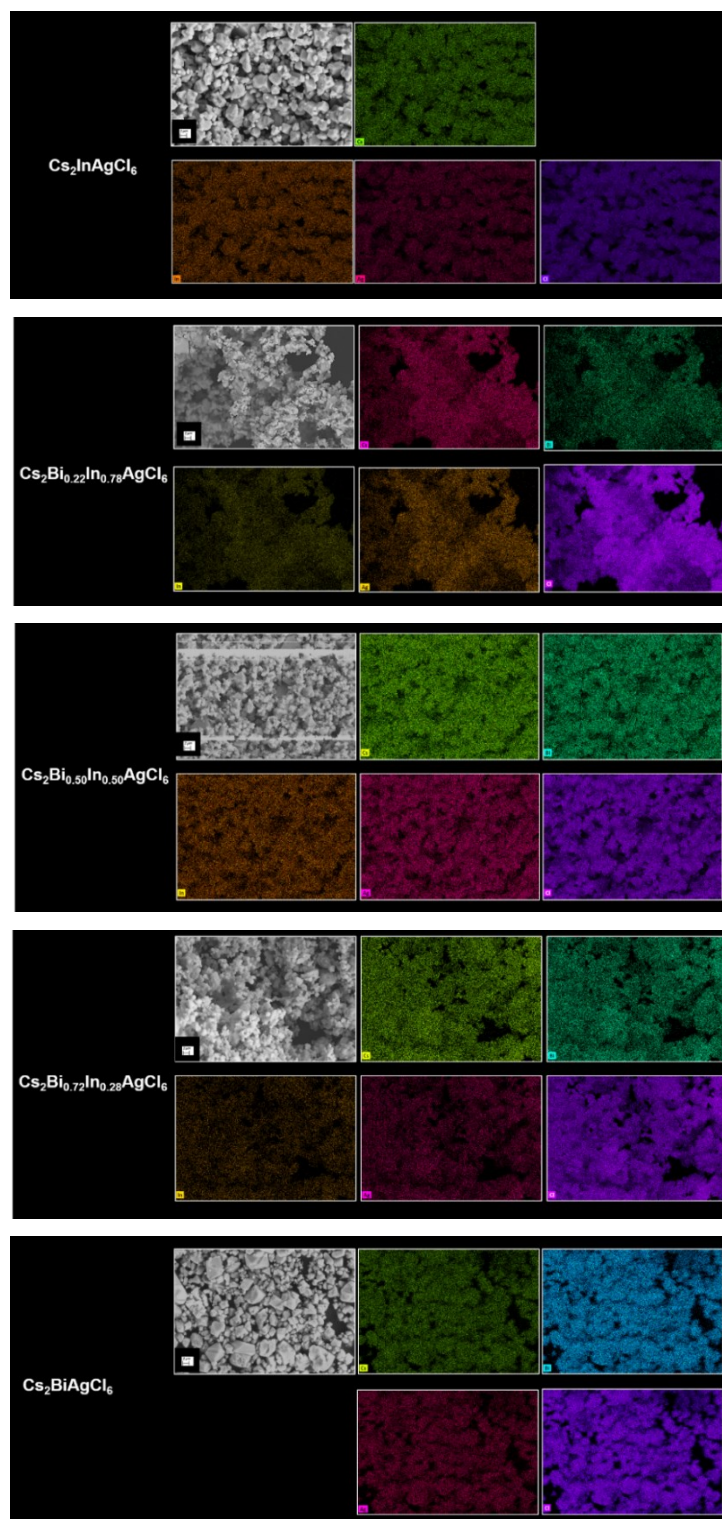


Figure D2. EDS elemental mapping of Cs, Bi, In, Ag, and Cl for $\text{Cs}_2\text{Bi}_{1-x}\text{In}_x\text{AgCl}_6$ (top to bottom sequence, $x = 1.00, 0.78, 0.50, 0.22,$ and 0.00).

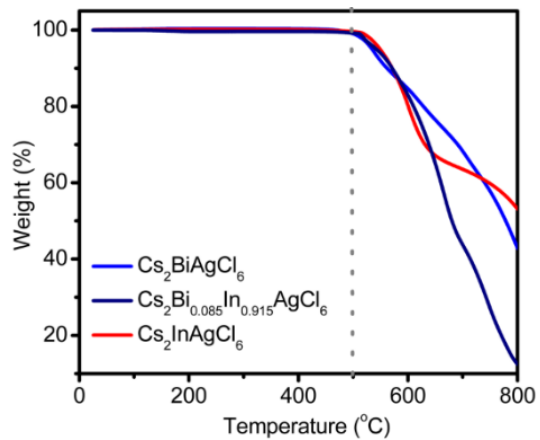


Figure D3. Thermogravimetric analyses (TGA) for $\text{Cs}_2\text{BiAgCl}_6$, $\text{Cs}_2\text{InAgCl}_6$, and $\text{Cs}_2\text{Bi}_{0.085}\text{In}_{0.915}\text{AgCl}_6$.

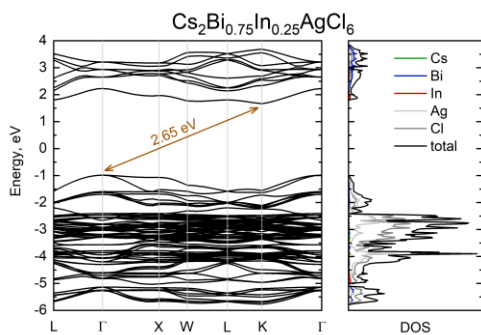


Figure D4. HSE06 DFT band structure and density of states for $\text{Cs}_2\text{Bi}_{0.75}\text{In}_{0.25}\text{AgCl}_6$.

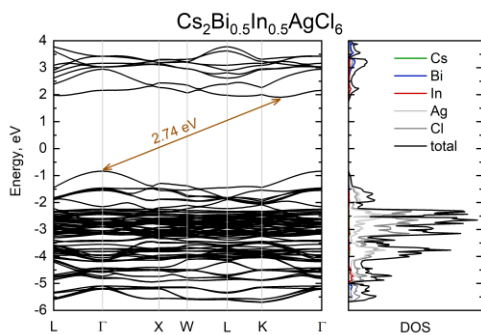


Figure D5. HSE06 DFT band structure and density of states for $\text{Cs}_2\text{Bi}_{1-x}\text{In}_x\text{AgCl}_6$.

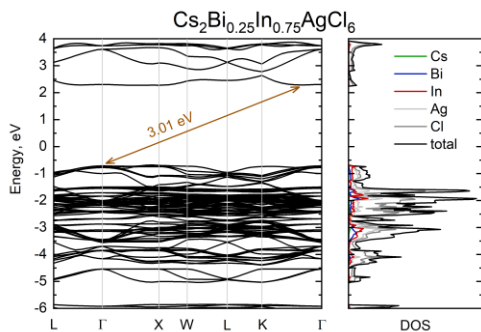


Figure D6. HSE06 DFT band structure and density of states for $\text{Cs}_2\text{Bi}_{1-x}\text{In}_x\text{AgCl}_6$.

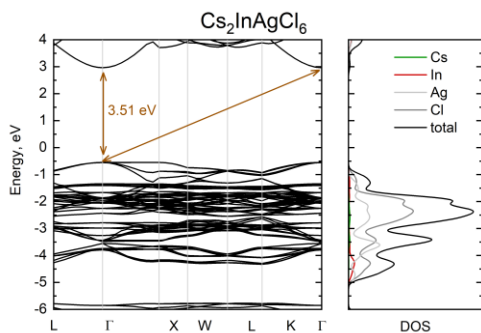


Figure D7. HSE06 DFT band structure and density of states for $\text{Cs}_2\text{InAgCl}_6$.

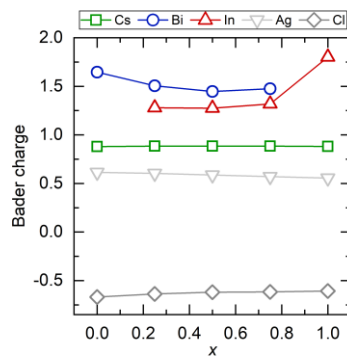


Figure D8. Average Bader charge change in the $\text{Cs}_2\text{Bi}_{1-x}\text{In}_x\text{AgCl}_6$ compound series.

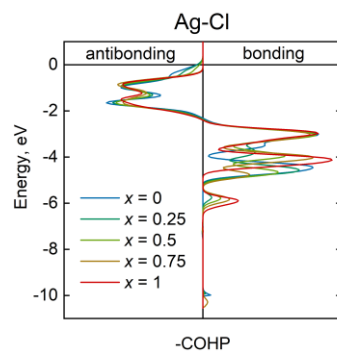


Figure D9. Crystal Orbital Overlap Population (COOP) analysis of the Ag-Cl interactions.

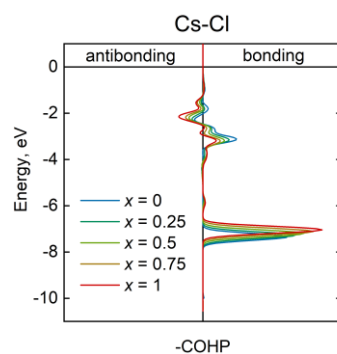


Figure D10. COOP analysis of the Cs-Cl interactions.

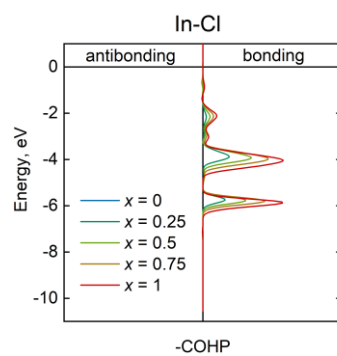


Figure D11. COOP analysis of the In-Cl interactions.

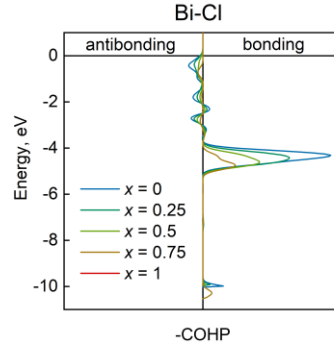


Figure D12. COOP analysis of the Bi-Cl interactions.

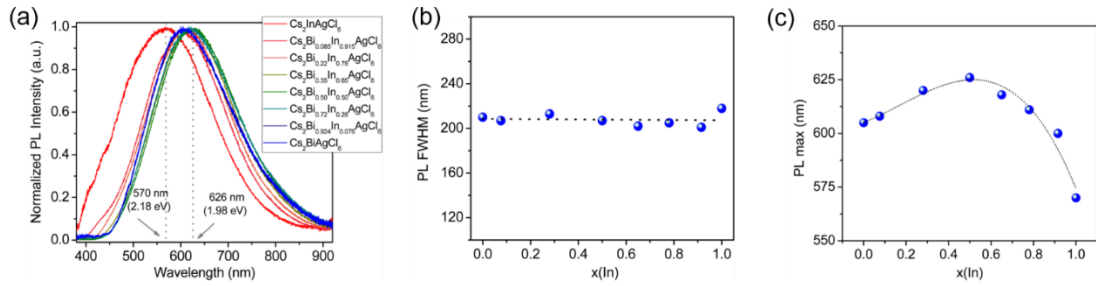


Figure D13. Normalized steady-state PL spectra (a), change in PL FWHM (b), and PL maxima (c) vs indium composition, $x(\text{In})$, in $\text{Cs}_2\text{Bi}_{1-x}\text{In}_x\text{AgCl}_6$ ($0 \leq x \leq 1$) HDPs.

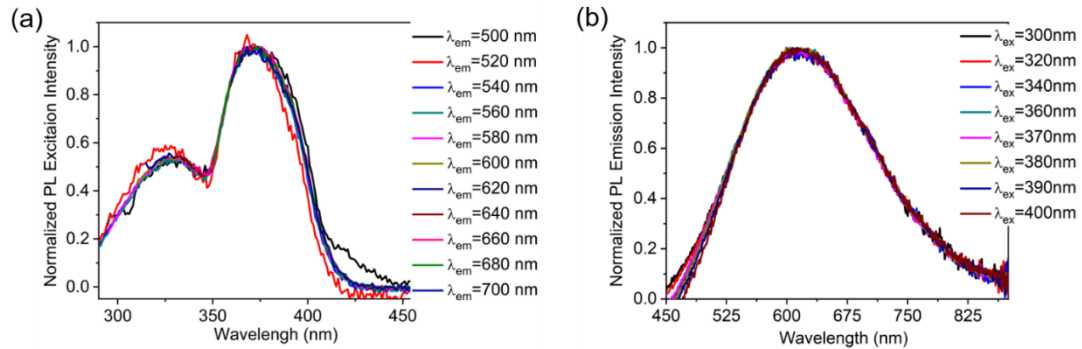


Figure D14. Normalized PL excitation spectra at variable emission wavelengths from 500-700 nm (a), and normalized PL emission spectra with variable excitation wavelengths from 300-400 nm (b) for $\text{Cs}_2\text{Bi}_{0.085}\text{In}_{0.915}\text{AgCl}_6$ HDPs.

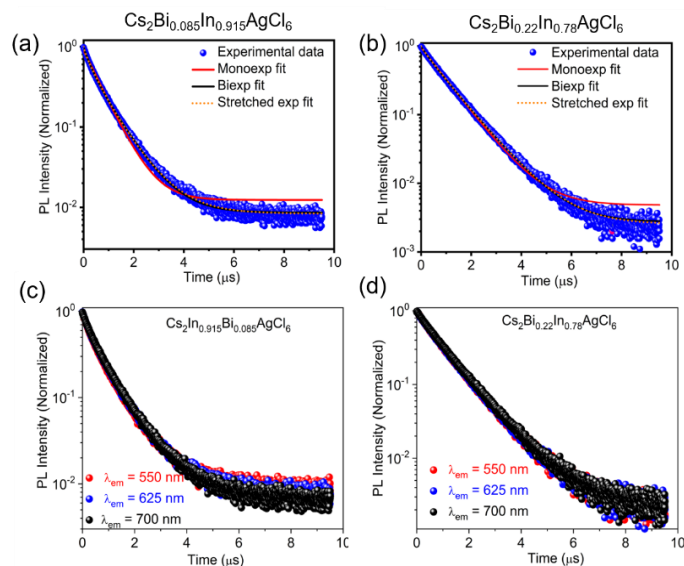


Figure D15. Experimental PL decay with $\lambda_{em} = 625$ nm and its monoexponential, biexponential, and stretched-exponential decay fit for $\text{Cs}_2\text{Bi}_{0.085}\text{In}_{0.915}\text{AgCl}_6$ (a) and $\text{Cs}_2\text{Bi}_{0.22}\text{In}_{0.78}\text{AgCl}_6$ (b) HDPs. Wavelength dependent PL decay plots for $\text{Cs}_2\text{Bi}_{0.085}\text{In}_{0.915}\text{AgCl}_6$ (c) and $\text{Cs}_2\text{Bi}_{0.22}\text{In}_{0.78}\text{AgCl}_6$ (d) HDPs. Samples were excited using laser excitation at 364 nm.

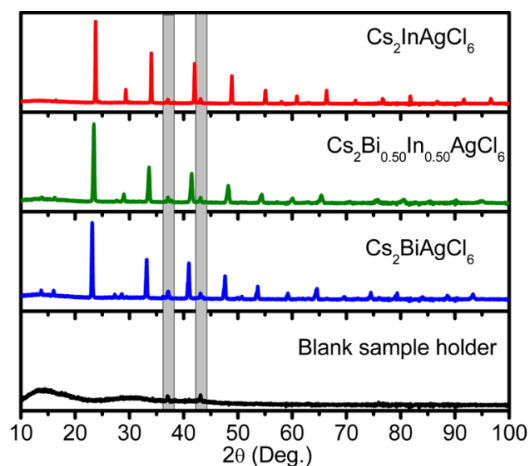


Figure D16. Two background signals (grey highlighted region) appeared in all PXRD patterns at $2\theta \sim 37^\circ$ and $\sim 43^\circ$ for all $\text{Cs}_2\text{Bi}_{1-x}\text{In}_x\text{AgCl}_6$ HDPs. Here, we are showing PXRD of three representative materials ($x = 0.00, 0.50,$ and 1.00) along with the PXRD signals from a blank sample holder.

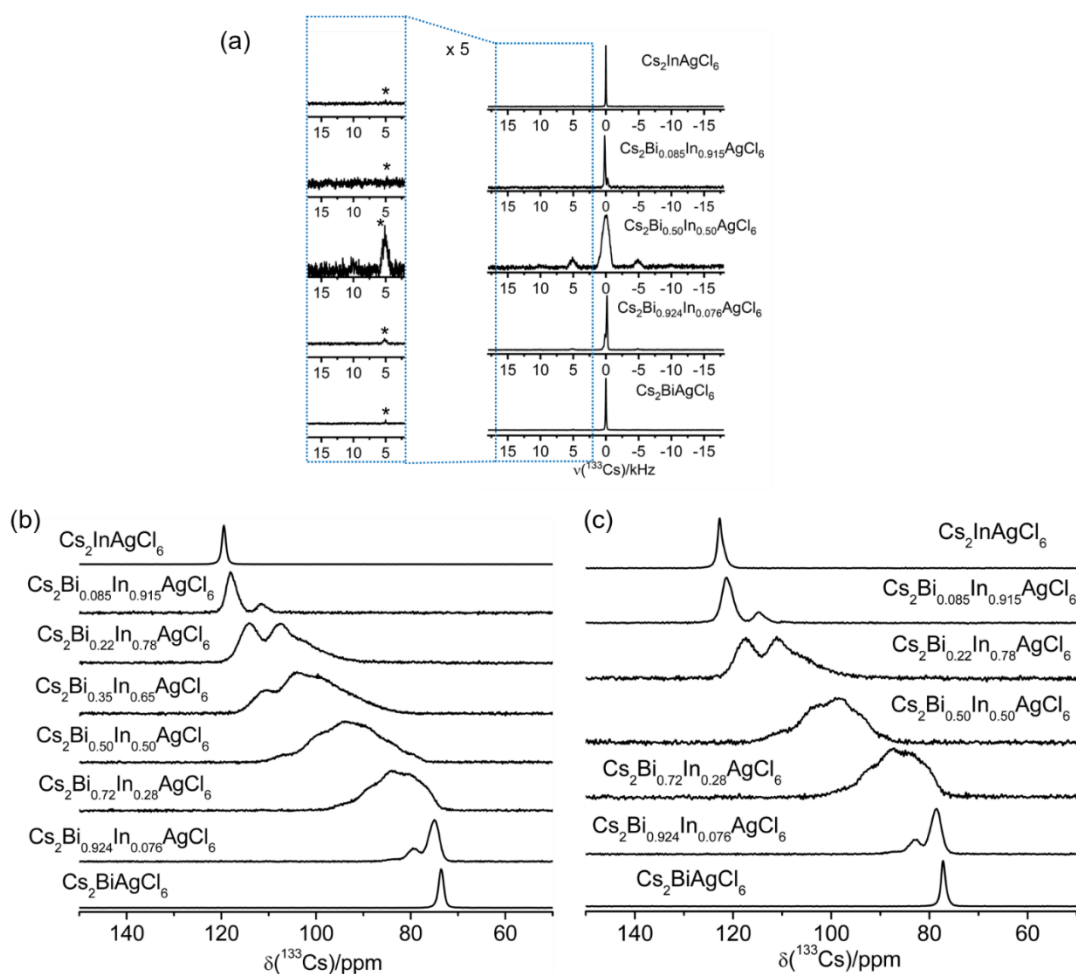


Figure D17. Solid-state ^{133}Cs NMR spectra for $\text{Cs}_2\text{Bi}_x\text{In}_{1-x}\text{AgCl}_6$ samples at 11.75 T (a, b) and 21.14 T (c). The spectra are acquired under magic-angle spinning sample conditions with MAS frequencies of 5 kHz (a), 13 kHz (b) and 30 kHz (c). Spectra are scaled to the same vertical intensity. Please note that the different ^{133}Cs chemical shifts at 11.75 and 21.14 T with magic-angle spinning frequencies of 13 and 30 kHz, respectively, are due to the temperature effect upon magic-angle spinning.¹⁶ The ^{133}Cs NMR peak is shifted towards higher frequencies as the sample temperature is $\sim 12^\circ\text{C}$ warmer during the measurement (assuming identical ambient conditions, a 4 mm rotor at 13 kHz will add $\sim 24^\circ\text{C}$ vs. $\sim 36^\circ\text{C}$ for a 2.5 mm rotor at 30 kHz, due to frictional heating).¹⁷

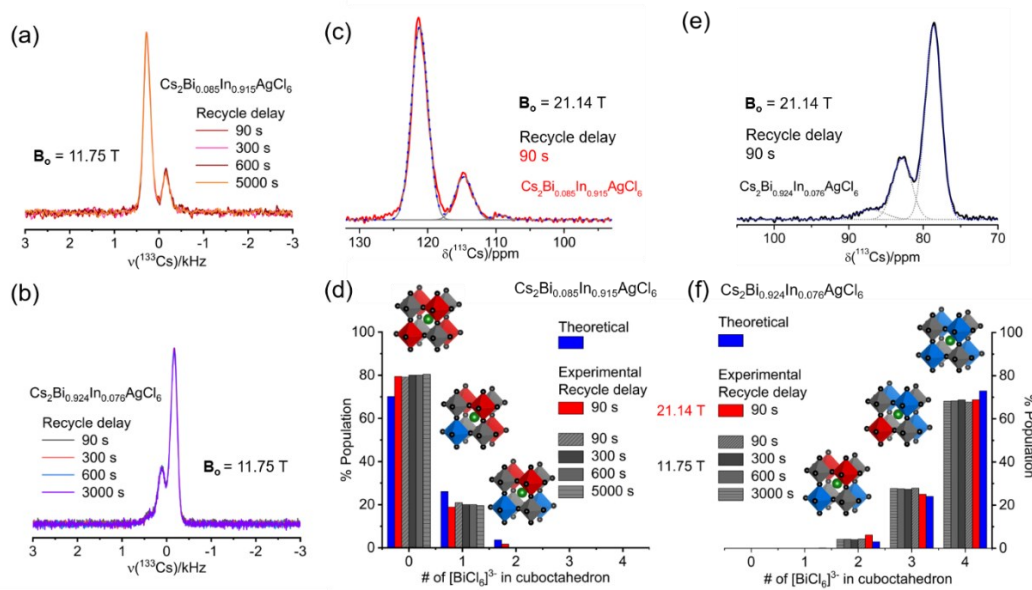


Figure D18. Normalized solid-state ^{133}Cs NMR spectra that are showing spectral overlap of multiple cuboctahedral environments for $\text{Cs}_2\text{Bi}_{0.085}\text{In}_{0.915}\text{AgCl}_6$ (a) and $\text{Cs}_2\text{Bi}_{0.924}\text{In}_{0.076}\text{AgCl}_6$ (b). The spectra were acquired at 11.75 T with a spinning frequency of 13 kHz and with various recycle delay values as indicated. Gaussian fits of solid-state ^{133}Cs NMR spectra for $\text{Cs}_2\text{Bi}_{0.085}\text{In}_{0.915}\text{AgCl}_6$ (c) and $\text{Cs}_2\text{Bi}_{0.924}\text{In}_{0.076}\text{AgCl}_6$ (e), acquired at 21.14 T with spinning frequencies of 30 kHz and recycle delay of 90 s. The bar diagrams show the binomial distributions of different ^{133}Cs cuboctahedral sites using Gaussian fits with various recycle delays for $\text{Cs}_2\text{Bi}_{0.085}\text{In}_{0.915}\text{AgCl}_6$ (d) and for $\text{Cs}_2\text{Bi}_{0.924}\text{In}_{0.076}\text{AgCl}_6$ (f) as indicated.

Appendix Note D1

The formula of the binomial distribution is as follows: $P(x) = \frac{n!}{x!(n-x)!} p^x (1-p)^{n-x}$,

where, n and p are the number of trials and the probability of a given trial, respectively.

Here, $n = 4$, the fraction of bismuth present in B'(III) site is given by $p = 0.085$ and 0.924 for $\text{Cs}_2\text{Bi}_{0.085}\text{In}_{0.915}\text{AgCl}_6$ and $\text{Cs}_2\text{Bi}_{0.924}\text{In}_{0.076}\text{AgCl}_6$, respectively, the number of $[\text{BiCl}_6]^{4-}$ sites in the cuboctahedron are $x = 0, 1, 2, 3, 4$.

When, $p = 0.085$, then the probability $P(0) = 70.1\%$, $P(1) = 26.1\%$, $P(2) = 3.6\%$, $P(3) = 0.2\%$ and $P(4) = 0.0\%$.

And when $p = 0.924$, then $P(0) = 0.0\%$, $P(1) = 0.2\%$, $P(2) = 2.9\%$, $P(3) = 24.0\%$ and $P(4) = 72.9\%$.

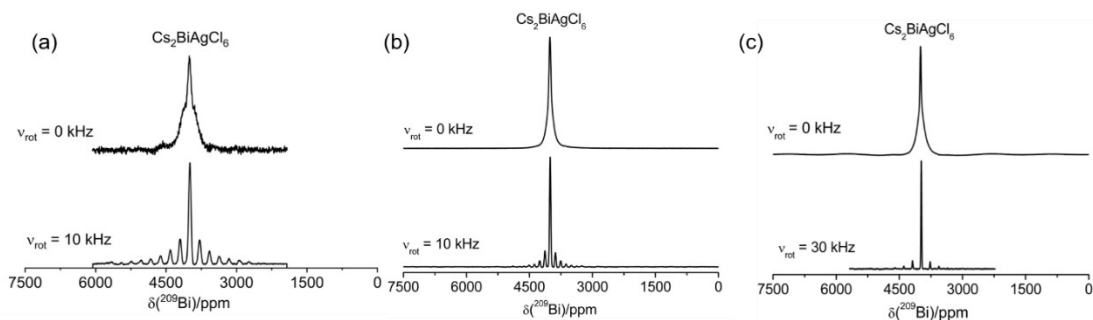


Figure D19. Solid-state ^{209}Bi NMR of $\text{Cs}_2\text{BiAgCl}_6$ at 7.05 T (a), 11.75 T (b), and 21.14 T (c). The sample was acquired under non-spinning and magic-angle spinning (10 kHz at 7.05 T and 11.75 T, and 30 kHz at 21.14 T) conditions.

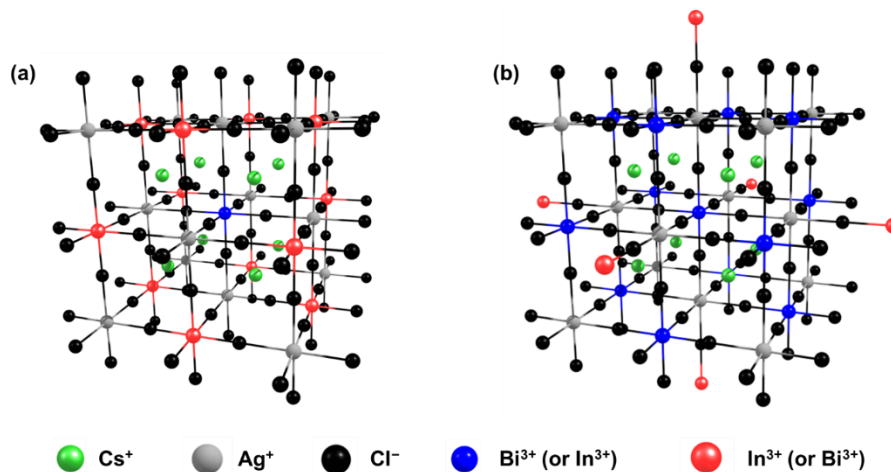


Figure D20. Crystal structures of the mixed In-Bi HDPs, illustrating the 12 possible substitution sites in the first B'(III) coordination sphere (a) and the 6 possible substitution sites in the second B'(III) coordination sphere (b); the substitution atom is shown in red.

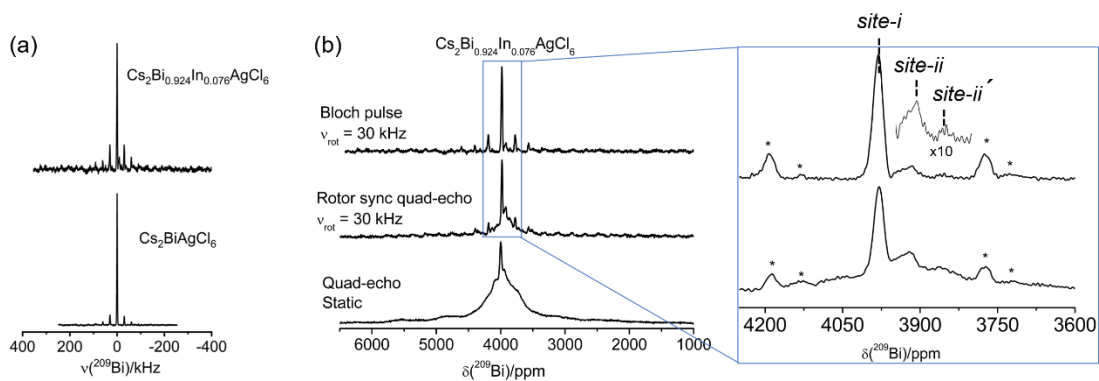


Figure D21. Solid-state ^{209}Bi NMR spectra of $\text{Cs}_2\text{BiAgCl}_6$ and In^{3+} -doped $\text{Cs}_2\text{Bi}_{0.924}\text{In}_{0.076}\text{AgCl}_6$ acquired with a magic angle spinning frequency of 30 kHz at 21.14 T (a). Solid-state ^{209}Bi NMR spectra of $\text{Cs}_2\text{Bi}_{0.924}\text{In}_{0.076}\text{AgCl}_6$ acquired under non-spinning and magic-angle spinning (30 kHz) conditions at 21.14 T (b). The ^{209}Bi NMR sites in (b) correspond to distinguishable Bi sites with different medium-range structural environments. The asterisks (*) in (b) indicate spinning sidebands.

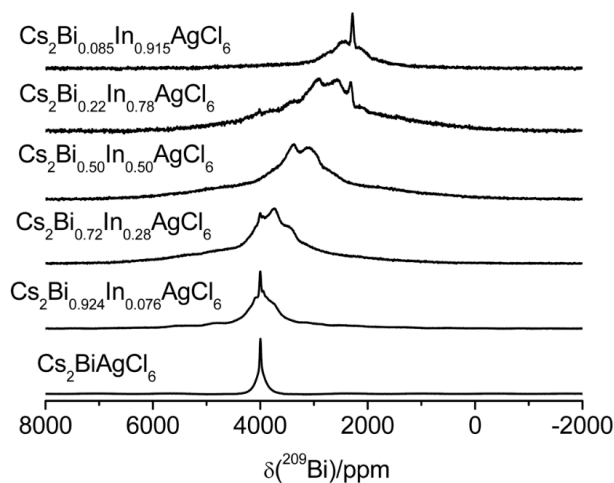


Figure D22. Solid-state ^{209}Bi NMR spectra for $\text{Cs}_2\text{Bi}_{1-x}\text{In}_x\text{AgCl}_6$ acquired under non-spinning conditions at 21.14 T. Spectra scaled to the same vertical intensity.

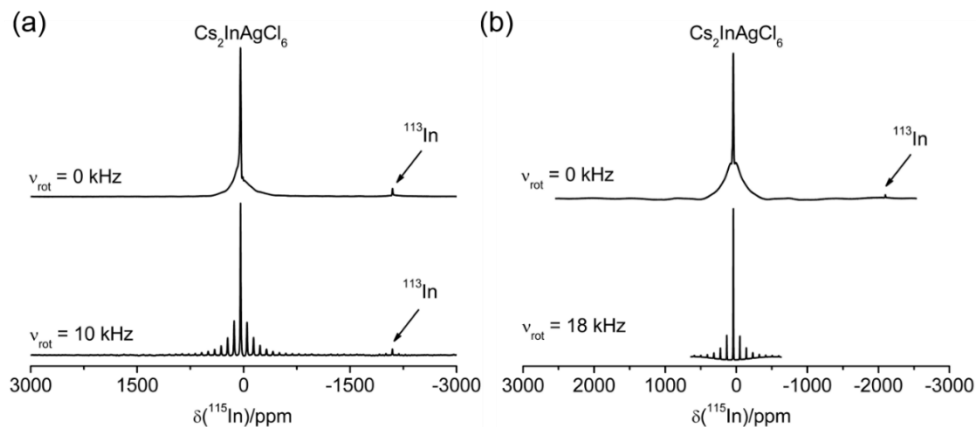


Figure D23. Solid-state ^{115}In NMR spectra of $\text{Cs}_2\text{InAgCl}_6$ at 11.75 T (a) and 21.14 T (b). The sample was acquired under non-spinning or magic angle spinning conditions as indicated. Note: Spectral width was reduced for acquisition of the MAS NMR spectrum in pane b (bottom).

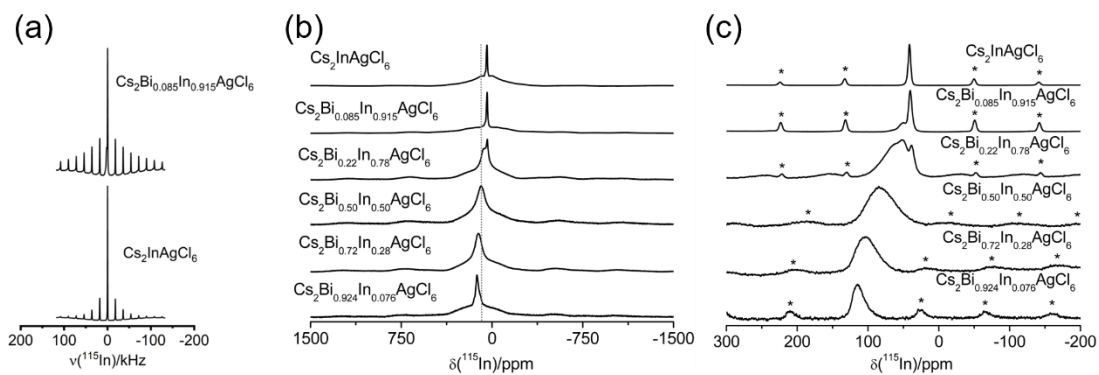


Figure D24. Solid-state ^{115}In NMR spectra of $\text{Cs}_2\text{InAgCl}_6$ and $\text{Cs}_2\text{Bi}_{0.085}\text{In}_{0.915}\text{AgCl}_6$ acquired with a spinning frequency of 18 kHz at 21.14 T (a). Solid-state ^{115}In NMR spectra of non-spinning (b) and of magic angle spinning (18 kHz, c) samples of $\text{Cs}_2\text{Bi}_{1-x}\text{In}_x\text{AgCl}_6$ acquired at 21.14 T. The asterisks (*) in (c) indicate spinning sidebands. Spectra scaled to the same vertical intensity.

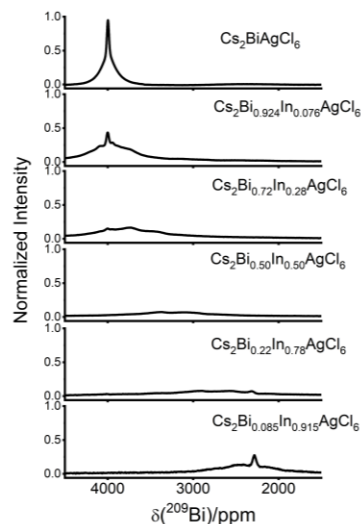


Figure D25. Normalized intensities of ^{209}Bi NMR spectra for non-spinning $\text{Cs}_2\text{Bi}_{1-x}\text{In}_x\text{AgCl}_6$ samples. The normalization signifies that the intensity is vertically scaled to the same amount of Bi in the sample for a given number of scans.

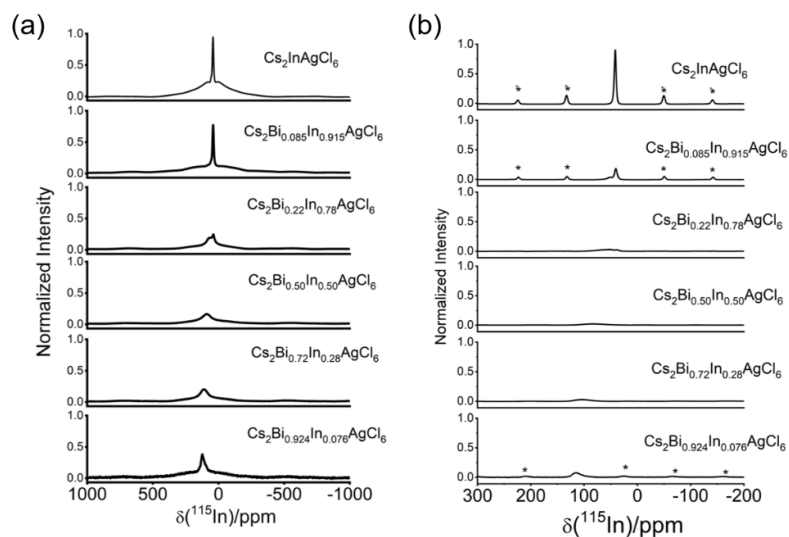


Figure D26. Normalized intensities of the ^{115}In NMR spectra for non-spinning (a) and 18 kHz magic-angle spinning (b) $\text{Cs}_2\text{Bi}_{1-x}\text{In}_x\text{AgCl}_6$ samples as indicated. The asterisks (*) in (b) indicate spinning sidebands. The normalization signifies that the intensity is vertically scaled to the same amount of In in the sample for a given number of scans.

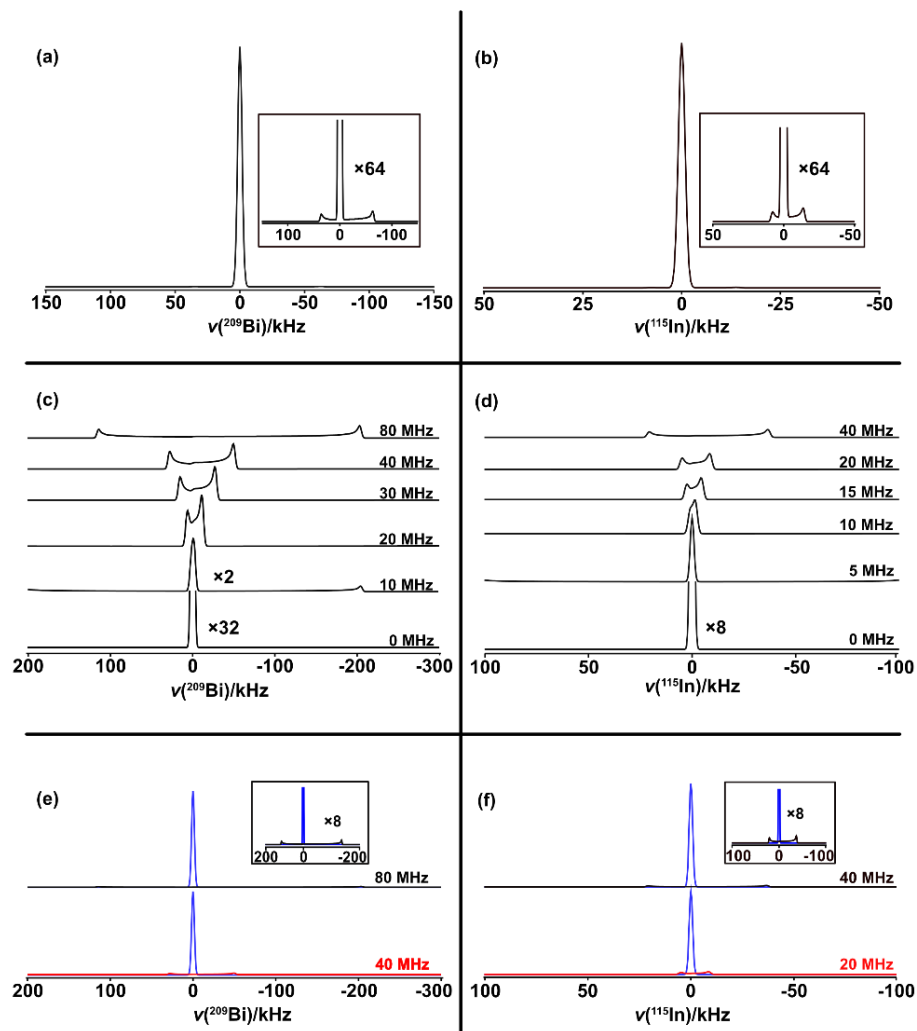


Figure D27. Simulated ^{209}Bi (a) and ^{115}In (b) NMR spectra expected for spectra acquired at 21.14 T assuming a two sites model, with $C_Q = 0$ and 45 MHz (^{209}Bi) or 0 and 25 MHz (^{115}In); both spectra were simulated assuming 90 % of the sites were those with no quadrupolar interaction. In (c) and (d), ^{209}Bi and ^{115}In NMR spectra, simulated with the indicated C_Q at 21.14 T, illustrate the relative impact of C_Q on the intensity of that peak, assuming an equal probability for a given NMR site. The peak at -200 kHz and $C_Q = 10$ MHz in (c) is due to the signal expected for the $3/2 - 1/2$ transition. In (e) and (f), Spectra with the indicated quadrupolar coupling, shown in red and black, are overlain with those for the nucleus with $C_Q = 0$, shown in blue; the simulations assumed equal probabilities for the two sites in the spectra shown in (e) and (f).

References

- (1) Kubelka, P.; Munk, F. Ein Beitrag Zur Optik Der Farbanstriche. *Z.Tech. Phys. (Leipzig)* **1931**, *12*, 593–601.
- (2) J. H. Davis; K. R. Jeffrey; M. Bloom; M. I. Valic; T. P. Higgs. Quadrupolar Echo Deuteron Magnetic Resonance Spectroscopy in Ordered Hydrocarbon Chains. *Chem. Phys. Lett.* **1976**, *42*, 390–394.
- (3) Bodart, P. R.; Amoureux, J.-P.; Dumazy, Y.; Lefort, R. Theoretical and Experimental Study of Quadrupolar Echoes for Half-Integer Spins in Static Solid-State NMR. *Mol. Phys.* **2000**, *98*, 1545–1551.
- (4) Kohout, M.; Wagner, F. R.; Grin, Y. Electron Localization Function for Transition-Metal Compounds. *Theor. Chem. Acc.* **2002**, *108*, 150–156.
- (5) Grin, Y.; Savin, A.; Silvi, B. The ELF Perspective of Chemical Bonding. In *Wiley-VCH Verlag GmbH & Co. KGaA: Weinheim, Germany*; 2014; 345–382.
- (6) Kohout, M.; Savin, A. Influence of Core-Valence Separation of Electron Localization Function. *J. Comput. Chem.* **1997**, *18*, 1431–1439.
- (7) Rezende, M. V. d. S. .; Araujo, R. M. .; Valerio, M. E. G. .; Jackson, R. A. Intrinsic Defects in Strontium Aluminates Studied via Computer Simulation Technique. *J. Phys. Conf. Ser.* **2010**, *249*, 012042.
- (8) Kresse, G.; Joubert, D. From Ultrasoft Pseudopotentials to the Projector Augmented-Wave Method. *Phys. Rev. B Condens. Matter Mater. Phys.* **1999**, *59*, 1758–1775.
- (9) Kresse, G.; Furthmuller, J. Efficient Iterative Schemes for Ab Initio Total-Energy Calculations Using a Plane-Wave Basis Set. *Phys. Rev. B Condens. Matter Mater. Phys.* **1996**, *54*, 11169–11186.
- (10) Tang, W.; Sanville, E.; Henkelman, G. A Grid-Based Bader Analysis Algorithm without Lattice Bias. *J. Phys. Condens. Matter* **2009**, *21*, 084204.
- (11) Clark, S. J.; Segall, M. D.; Pickard, C. J.; Hasnip, P. J.; Probert, M. I. J.; Refson, K.; Payne, M. C. First Principles Methods Using CASTEP. *Z. Krist. - Cryst. Mater* **2005**, *220*, 567–570.
- (12) Perdew, J. P.; Burke, K.; Ernzerhof, M. Generalized Gradient Approximation Made Simple. *Phys. Rev. Lett.* **1996**, *77*, 3865–3868.

- (13) Perdew, J. P.; Burke, K.; Ernzerhof, M. Perdew, Burke, and Ernzerhof Reply. *Phys. Rev. Lett.* **1998**, *80*, 891.
- (14) Yates, J. R.; Pickard, C. J.; Mauri, F. Calculation of NMR Chemical Shifts for Extended Systems Using Ultrasoft Pseudopotentials. *Phys. Rev. B* **2007**, *76*, 024401.
- (15) Harris, R. K.; Becker, E. D. NMR Nomenclature: Nuclear Spin Properties and Conventions for Chemical Shifts—IUPAC Recommendations. *J. Magn. Reson.* **2002**, *156*, 323–326.
- (16) Karmakar, A.; Dodd, M. S.; Agnihotri, S.; Ravera, E.; Michaelis, V. K. Cu(II)-Doped Cs₂SbAgCl₆ Double Perovskite: A Lead-Free, Low-Bandgap Material. *Chem. Mater.* **2018**, *30*, 8280–8290. h
- (17) Bernard, G. M.; Goyal, A.; Miskolzie, M.; McKay, R.; Wu, Q.; Wasylshen, R. E.; Michaelis, V. K. Methylammonium Lead Chloride: A Sensitive Sample for an Accurate NMR Thermometer. *J. Magn. Reson.* **2017**, *283*, 14–21.

Appendix E: Supplementary Data for Chapter 6

Uncovering Halogen Mixing and Octahedral Dynamics in Cs_2SnX_6 by Multinuclear Magnetic Resonance Spectroscopy

Table E1. Naturally occurring NMR-active isotopes in Cs_2SnX_6 .¹

Element	Isotope(s)	Nuclear spin (I)	Natural abundance (%)	Magnetogyric ratio ($\gamma/10^7 \text{ rad s}^{-1} \text{ T}^{-1}$)	Frequency ratio ($\Xi/\%$)	Quadrupolar moment (Q/fm^2)
Cs	^{133}Cs	7/2	100	3.5332539	13.116142	-0.343
Sn	^{115}Sn	1/2	0.34	-8.8013	32.718749	N.A.
	^{117}Sn	1/2	7.68	-9.58879	35.632259	N.A.
	^{119}Sn	1/2	8.59	-10.0317	37.290632	N.A.
Cl	^{35}Cl	3/2	75.78	2.624198	9.797909	-8.165
	^{37}Cl	3/2	24.22	2.184368	8.155725	-6.435
Br	^{79}Br	3/2	50.69	6.725616	25.053980	31.3
	^{81}Br	3/2	49.31	7.249776	27.006518	26.2
I	^{127}I	5/2	100	5.389573	20.007486	-71.0

Table E2. Elemental composition analysis by EDS.

Samples	Synthesis route	Atom%					Halogen atomic ratio
		Cs	Sn	Cl	Br	I	
Cs ₂ SnCl ₆	Solvent-assisted	21.7	11.0	67.3	-	-	100% Cl
Cs ₂ SnBr ₆		20.5	10.2	-	69.3	-	100% Br
Cs ₂ SnI ₆		20.0	12.5	-	-	67.5	100% I
Cs ₂ SnI ₆	Hand-grinding	18.5	12.6	-	-	68.9	100% I
Cs ₂ SnCl ₃ Br ₃	ball-milling	21.2	10.9	31.7	36.2	-	47% Cl : 53% Br
Cs ₂ SnBr ₆		21.1	10.5	-	68.3	-	100% Br
Cs ₂ SnBr _{4.5} I _{1.5}		23.8	9.8	-	53.7	12.7	81% Br : 19% I
Cs ₂ SnBr ₃ I ₃		26.2	11.3	-	34.8	27.7	56% Br : 44% I
Cs ₂ SnBr _{1.5} I _{4.5}		24.3	11.2	-	15.7	48.8	24% Br : 76% I
Cs ₂ SnI ₆		20.2	11.8	-	-	68.0	100% I

Table E3. Paramagnetic, diamagnetic and spin-orbit components of the total isotropic shielding tensors for the tin(IV) atoms of Cs₂SnX₆ (X = Cl, Br, I) at the ZORA/PBE0/TZ2P level of theory, including spin-orbit effects, without the FXC option. At experimental geometries (at optimized geometries in parentheses).

Shielding tensor	Cs ₂ SnCl ₆ (ppm)	Cs ₂ SnBr ₆ (ppm)	Cs ₂ SnI ₆ (ppm)
Paramagnetic	-2192.958 (-2197.985)	-2286.456 (-2283.346)	-2257.522 (-2292.756)
Diamagnetic	5109.444 (5109.790)	5105.075 (5104.772)	5108.829 (5108.431)
Spin-orbit	890.972 (872.728)	2095.717 (2492.755)	5395.917 (5571.179)
Total	3807.458 (3784.533)	4914.336 (5314.181)	8247.225 (8386.854)
Total (with FXC)	3853.663 (3828.557)	4991.516 (5407.830)	8159.092 (8219.273)

Table E4. ¹¹⁹Sn NMR parameters for the solvent synthesized Cs₂SnI₆ sample obtained at various temperatures at 11.75 T under non-spinning sample conditions.

Calibrated temperature (K)	¹¹⁹ Sn chemical shift (ppm) ± 2	¹¹⁹ Sn fwhm (kHz) ± 1	¹¹⁹ Sn T ₁ (s)
207.5	-4522	17.0	4.63 ± 1.26
212.2	-4524	17.0	2.48 ± 0.41
252.5	-4530	18.5	0.818 ± 0.130
294.1	-4535	18.4	0.577 ± 0.106
328.6	-4542	18.2	0.264 ± 0.098
355.2	-4545	18.7	0.192 ± 0.034
379.9	-4547	18.0	0.117 ± 0.021

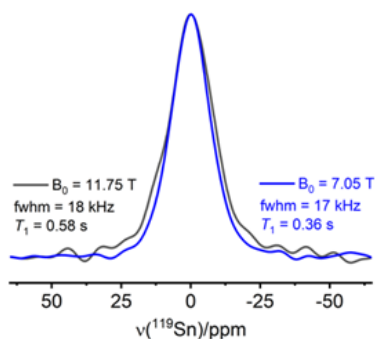
Appendix Note E1

The following relaxation mechanisms are possible contributors to ^{119}Sn spin-lattice relaxation in Cs_2SnI_6 : chemical-shift-anisotropy, scalar relaxation, spin-phonon Raman scattering processes, magic-angle-spinning induced heteronuclear polarization changes, and dipole-dipole interactions. Below, these are considered separately to determine which mechanism dominates for Cs_2SnI_6 .

(1) The equation below describes the chemical-shift-anisotropy (CSA) contribution to T_1 .^{2,3} If this mechanism dominates, then the T_1 values should be strongly dependent on the magnetic-field strength, with the nuclear spin-lattice relaxation time following an inverse proportional relationship with the square of magnetic field strength. The ^{119}Sn NMR spectra for Cs_2SnI_6 have similar FWHM, show no evidence of CSA and the measured ^{119}Sn T_1 change is small when going from 7.05 ($T_1 = 0.36$ s) to 11.75 T ($T_1 = 0.58$ s). Hence, the CSA mechanism cannot account for this observation.

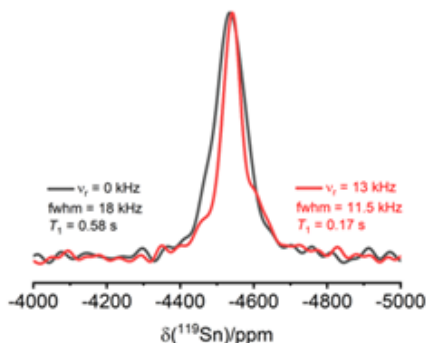
$$\frac{1}{T_1^{CSA}} = \frac{2}{15} \gamma^2 B_0^2 (\Delta\delta)^2 \left(\frac{1}{1 + \omega^2 \tau_c^2} \right) \tau_c$$

where $\Delta\delta =$ the anisotropy of the magnetic shielding.



(2) The physical origins of the scalar relaxation process for both the first (chemical exchange) and second (fast quadrupolar relaxation ^{127}I) kinds can be evaluated from the temperature dependence of the transverse relaxation times.³ Across a temperature range of *ca.* 170 K, we observed little to no change in the T_2^* values based on an assessment of the FWHM (Table E4 and Figure E8a). In addition, the FWHM for the ^{119}Sn NMR resonance does not change with magnetic field strength and

therefore we can assume T_2^* is approximately T_2 .⁴ From these two observations, scalar relaxation may be neglected as the dominant relaxation process in this instance.



(3) The spin-phonon Raman scattering⁵ mechanism is independent of the applied magnetic field strength and inversely proportional to the square of absolute temperature. The ^{119}Sn relaxation rate ($R = 1/T_1$) as a function of the square of the absolute temperature ($T(\text{K})^2$) is shown in Figure E8d. The data does not appear to follow a statistical rigid linear relationship ($R^2 > 0.9$) suggesting this is not the primary relaxation mechanism responsible for ^{119}Sn relaxation in Cs_2SnI_6 studied here. However, due to limitations in temperature range of our hardware and the sizeable ^{127}I quadrupolar coupling constant for Cs_2SnI_6 computed by DFT ($C_Q(^{127}\text{I}) = \sim 1.1$ GHz), we cannot completely discount contributions from this mechanism.

(4) Magic-angle-spinning induced heteronuclear polarization change⁶ can arise when there is crossing between energy levels for $I = 1/2$ (e.g., ^{207}Pb , ^{199}Hg , ^{119}Sn) spins and adjacent quadrupolar spin nuclei ($I > 1/2$) (e.g., $^{79/81}\text{Br}$, ^{127}I in this work), but requires that these be close in nuclear Larmor frequencies (ν_L). If this is the case, the T_1 value will change significantly when the sample is spun. For example, for PbI_2 ($B_0 = 11.75$ T; $\nu_L(^{127}\text{I}) = 100$ MHz vs. $\nu_L(^{207}\text{Pb}) = 104$ MHz), a nuclear T_1 of 1.5 s (non-spinning conditions) is observed, but under slow magic angle spinning T_1 decreases by two orders of magnitude ($T_1 = 0.013$ s).⁶ For Cs_2SnI_6 , minor changes (attributed to the effects of frictional heating) in ^{119}Sn T_1 is observed between non-spinning (0.6 s) and MAS (0.2 s) conditions at $B_0 = 11.75$ T, respectively. The insignificant MAS-induced polarization change may be attributed to the much greater difference in Larmor frequencies for this spin pair ($\nu_L(^{127}\text{I}) = 100$ MHz vs. $\nu_L(^{119}\text{Sn}) = 186$ MHz). Therefore, this relaxation mechanism can be ignored.

(5) The heteronuclear dipole-dipole coupling for a $^{119}\text{Sn}-^{127}\text{I}$ spin pair in Cs_2SnI_6 is ~ 370 Hz, but considering the six neighboring I, significant broadening due to this interaction is expected. This is confirmed by the fact that a sizable decrease in FWHM, from 18 to 11.5 kHz, is observed when comparing MAS ($v_r = 13$ kHz) and non-spinning NMR spectra. This decrease in linewidth is attributed to magic-angle spinning attenuating the Sn-I heteronuclear dipole interaction. The change in nuclear T_1 between MAS and non-spinning is attributed mainly to frictional heating (~ 30 K of sample heating).³

Using the Bloembergen, Purcell and Pound (BPP) model, the nuclear spin lattice relaxation rate for a dipole-dipole interaction^{2,3} (between nuclear spin I and S , where $I = 1/2$ and $S = 5/2$) can be written as:

$$\frac{1}{T_1^{DD}} = \frac{2}{15} \gamma_{\text{Sn}}^2 \gamma_I^2 \left(\frac{\mu_0}{4\pi} \right)^2 \left(\frac{h}{2\pi} \right)^2 S(S+1) \sum_{\text{Sn-I}} r_{\text{Sn-I}}^{-6} \left(\frac{1}{1 + (\omega_{\text{Sn}} - \omega_I)^2 \tau_c^2} + \frac{3}{1 + \omega_I^2 \tau_c^2} + \frac{6}{1 + (\omega_{\text{Sn}} + \omega_I)^2 \tau_c^2} \right) \tau_c$$

here, $\gamma_{\text{Sn}-119} = -10.01926 \times 10^7 \text{ rad} \cdot \text{T}^{-1} \cdot \text{s}^{-1}$

$\gamma_{I-127} = 5.37937 \times 10^7 \text{ rad} \cdot \text{T}^{-1} \cdot \text{s}^{-1}$

$\left(\frac{\mu_0}{4\pi} \right) = 10^{-7} \text{ N} \cdot \text{A}^{-2}$

$h = 6.626 \times 10^{-34} \text{ J} \cdot \text{s}$

$S(^{127}\text{I}) = 5/2$

$r_{\text{Sn-I}} = 2.909 \times 10^{-10} \text{ m}$

At 11.75 T, $\omega_{\text{Sn}} = 185.71 \times 10^6 \text{ s}^{-1}$ and $\omega_I = 100.01 \times 10^6 \text{ s}^{-1}$

Note that a total six ^{127}I nuclei are attached to each ^{119}Sn nucleus. Hence, $\sum_{\text{Sn-I}} r_{\text{Sn-I}}^{-6} = 6 \times r_{\text{Sn-I}}^{-6}$

If we assume the correlation time, $\tau_c = 0.5 \text{ ns} = 5 \times 10^{-10} \text{ s}$, then $T_1^{DD} = 5.42 \text{ s}$; $\tau_c = 1 \text{ ns} = 10^{-9} \text{ s}$, then $T_1^{DD} = 2.81 \text{ s}$; while if $\tau_c = 10 \text{ ns} = 10^{-8} \text{ s}$, then $T_1^{DD} = 0.98 \text{ s}$

The experimentally measured ^{119}Sn T_1 values range from 4.6 to 0.1 seconds over a temperature range of 208 to 380 K. Considering previous X-ray pair distribution function analyses that indicated rotational disorder for the isolated SnI_6 octahedral

units,^{7,8} changes in temperature can modulate the anharmonic lattice dynamics of SnI₆ octahedra whereby higher temperatures increase the dynamics, reducing the ¹¹⁹Sn nuclear spin-lattice relaxation time.

Considering the five possible mechanisms listed above, if the dipole-dipole coupling is the primary relaxation mechanism, the associated activation energy would be attributed to the anharmonic lattice dynamics.

Appendix Note E2

Between the temperature range of 208 to 380 K, the data of $\ln(T_1/s)$ vary linearly with $[1000/T(K)]$ following an Arrhenius relationship [equation: $\ln(T_1/s) = (1.49769 \pm 0.10503) \times \frac{1000}{T(K)} - (5.92217 \pm 0.39057)$], as shown in Figure 6.4b in the Chapter 6. The slope of the Arrhenius plot is related to the activation energy as $E_a = \text{slope} \times 1000R$, where $R = 8.314 \text{ J}/(\text{mol} \cdot \text{K})$. Therefore, $E_a = 1.49769 \times 1000 \times 8.314 \text{ J/mol} = 12.45 \pm 0.87 \text{ kJ/mol}$ or $0.129 \pm 0.009 \text{ eV}$.

Appendix Note E3

The binomial population can be calculated as: $P(k) = \frac{a!}{k!(a-k)!} p^k \cdot (1-p)^{a-k}$, where $a =$ number of trials and $p =$ probability of the given trial. For example:

(i) CsBr_mI_{12-m} in Cs₂SnBr_xI_{6-x}: $a = 12$; $k = m = 0, 1, 2, 3, \dots, 10, 11, 12$; $p =$ interhalogen mole fraction = 0, 0.25, 0.50, 0.75, 1.

(ii) SnBr_nI_{6-n} in Cs₂SnBr_xI_{6-x}: $a = 6$; $k = n = 0, 1, 2, 3, 4, 5, 6$; $p =$ interhalogen mole fraction = 0, 0.25, 0.50, 0.75, 1.

Table E5. Starting materials and their weights used for the ball-mill preparation of the $\text{Cs}_2\text{SnCl}_x\text{Br}_{6-x}$ and $\text{Cs}_2\text{SnBr}_x\text{I}_{6-x}$ samples.

Targeted samples	Starting materials and weights	Ball-milling time (h)
$\text{Cs}_2\text{SnCl}_3\text{Br}_3$	Cs_2SnCl_6 (179 mg) + Cs_2SnBr_6 (259 mg)	3.0
Cs_2SnBr_6	CsBr (425 mg) + SnBr_4 (505 mg) ^a	1.5
$\text{Cs}_2\text{SnBr}_{4.5}\text{I}_{1.5}$	Cs_2SnBr_6 (388 mg) + CsI (78 mg) + SnI_4 (94 mg)	3.0
$\text{Cs}_2\text{SnBr}_3\text{I}_3$	Cs_2SnBr_6 (259 mg) + CsI (155 mg) + SnI_4 (188 mg)	3.0
$\text{Cs}_2\text{SnBr}_{1.5}\text{I}_{4.5}$	Cs_2SnBr_6 (129 mg) + CsI (234 mg) + SnI_4 (281 mg)	3.0
Cs_2SnI_6	CsI (261 mg) + SnI_4 (314 mg)	1.5

^amolar ratio of $\text{CsBr}/\text{SnBr}_4$ is 2/1.15 to obtain a pure phase product as confirmed by powder XRD (see Figure E8).

Table E6. Unit cell parameters and direct bandgap values for the ball-milled samples.

Samples	Cell parameter (a/Å)	Bandgap (eV)
$\text{Cs}_2\text{SnCl}_3\text{Br}_3$	10.6334(3)	3.53
Cs_2SnBr_6	10.8306(3)	3.30
$\text{Cs}_2\text{SnBr}_{4.5}\text{I}_{1.5}$	11.0835(9)	2.25
$\text{Cs}_2\text{SnBr}_3\text{I}_3$	11.3218(11)	1.80
$\text{Cs}_2\text{SnBr}_{1.5}\text{I}_{4.5}$	11.5029(9)	1.67
Cs_2SnI_6	11.6441(4)	1.56

Table E7. Calculated population distributions (binomial) for the $\text{CsCl}_m\text{Br}_{12-m}$ and $\text{CsBr}_m\text{I}_{12-m}$ environments in $\text{Cs}_2\text{SnCl}_x\text{Br}_{6-x}$ and $\text{Cs}_2\text{SnBr}_x\text{I}_{6-x}$ ($0 \leq x \leq 6$).

<i>m</i> in $\text{CsCl}_m\text{Br}_{12-m}$ <i>m</i>	$\text{CsCl}_m\text{Br}_{12-m}$ <i>m</i>	Calculated populations (%)				
		Cs_2SnCl_6	$\text{Cs}_2\text{SnCl}_3\text{Br}_3$	Cs_2SnBr_6		
0	CsBr_{12}	-	0.02	100		
1	$\text{CsCl}_1\text{Br}_{11}$	-	0.29	-		
2	$\text{CsCl}_2\text{Br}_{10}$	-	1.61	-		
3	CsCl_3Br_9	-	5.37	-		
4	CsCl_4Br_8	-	12.09	-		
5	CsCl_5Br_7	-	19.34	-		
6	CsCl_6Br_6	-	22.56	-		
7	CsCl_7Br_5	-	19.34	-		
8	CsCl_8Br_4	-	12.09	-		
9	CsCl_9Br_3	-	5.37	-		
10	$\text{CsCl}_{10}\text{Br}_2$	-	1.61	-		
11	$\text{CsCl}_{11}\text{Br}_1$	-	0.29	-		
12	CsCl_{12}	100	0.02	-		
<i>m</i> in $\text{CsBr}_m\text{I}_{12-m}$ $\text{CsBr}_m\text{I}_{12-m}$	$\text{CsBr}_m\text{I}_{12-m}$	Calculated populations (%)				
		Cs_2SnBr_6	$\text{Cs}_2\text{SnBr}_{4.5}\text{I}_1$	$\text{Cs}_2\text{SnBr}_3\text{I}$	$\text{Cs}_2\text{SnBr}_{1.5}\text{I}_4$	Cs_2SnI_6
		6	5	3	5	
0	CsI_{12}	-	0.00	0.02	3.17	100
1	$\text{CsBr}_1\text{I}_{11}$	-	0.00	0.29	12.67	-
2	$\text{CsBr}_2\text{I}_{10}$	-	0.00	1.61	23.23	-
3	CsBr_3I_9	-	0.04	5.37	25.81	-
4	CsBr_4I_8	-	0.23	12.09	19.36	-
5	CsBr_5I_7	-	1.15	19.34	10.32	-
6	CsBr_6I_6	-	4.02	22.56	4.02	-
7	CsBr_7I_5	-	10.32	19.34	1.15	-
8	CsBr_8I_4	-	19.36	12.09	0.23	-
9	CsBr_9I_3	-	25.81	5.37	0.04	-
10	$\text{CsBr}_{10}\text{I}_2$	-	23.23	1.61	0.00	-
11	$\text{CsBr}_{11}\text{I}_1$	-	12.67	0.29	0.00	-
12	CsBr_{12}	100	3.17	0.02	0.00	-

Table E8. Lorentzian profile fitted ^{133}Cs MAS NMR spectra and ^{133}Cs T_{1s} for $\text{CsBr}_m\text{I}_{12-m}$ environments in $\text{Cs}_2\text{SnBr}_{1.5}\text{I}_{4.5}$.

$\text{CsBr}_m\text{I}_{12-m}$	Calculated binomial population (%)	Experimental (fitted ^{133}Cs NMR spectra)			^{133}Cs T_1 (s)
		Area% (± 3)	δ_{iso} (ppm)	fwhm (Hz)	
CsI_{12}	3.17	9.3	-38.4	499	39.9 ± 4.5
$\text{CsBr}_1\text{I}_{11}$	12.67	18.1	-19.0	420	33.0 ± 3.5
$\text{CsBr}_2\text{I}_{10}$	23.23	22.9	-1.5	529	27.9 ± 3.0
CsBr_3I_9	25.81	23.0	14.9	757	23.7 ± 2.7
CsBr_4I_8	19.36	19.0	30.7	1125	19.8 ± 2.3
CsBr_5I_7	10.32	7.7	47.5	1195	14.2 ± 2.0

Table E9. Solid-state ^{133}Cs and ^{119}Sn NMR experimental parameters.

Table E9a. Solid-state ^{133}Cs MAS NMR experimental parameters as discussed in Figure 6.2a in the main text. The ^{133}Cs NMR spectra were acquired at 11.75 T using a 1.38 μs (5.5 μs $\pi/2$) Bloch pulse sequence.

Samples	ν_{rot} (kHz)	Recycle delay (s)	# of scans	Acquisition time (min)
Cs_2SnCl_6	5.0	1200	4	80.0
Cs_2SnBr_6		500	4	33.3
Cs_2SnI_6		300	4	20.0

Table E9b. Solid-state ^{119}Sn MAS NMR experimental parameters as discussed in Figure 6.2b in the main text. The ^{119}Sn NMR spectra were acquired at 11.75 T with 13 kHz MAS using a 4.0 μs $\pi/2$ Hahn-echo pulse sequence.

Samples	ν_{rot} (kHz)	Echo delay (μs)	Recycle delay (s)	# of scans	Acquisition time (min)
Cs ₂ SnCl ₆	10.0	70.9	200	32	107
Cs ₂ SnBr ₆			15	512	128
Cs ₂ SnI ₆			1	1024	17

Table E9c. Solid-state ¹³³Cs MAS NMR experimental parameters as discussed in Figure 6.6a in the main text. The ¹³³Cs NMR spectra were acquired at 11.75 T using a 1.38 μs (5.5 μs $\pi/2$) Bloch pulse sequence.

Samples	ν_{rot} (kHz)	Recycle delay (s)	# of scans	Acquisition time (min)
Cs ₂ SnCl ₆	13.0	1900	4	128
Cs ₂ SnCl ₃ Br ₃		1900	30	950
Cs ₂ SnBr ₆		850	4	57
Cs ₂ SnBr _{4.5} I _{1.5}		600	8	80
Cs ₂ SnBr ₃ I ₃		850	8	113
Cs ₂ SnBr _{1.5} I _{4.5}		850	16	227
Cs ₂ SnI ₆		450	4	30

Table E9d. Solid-state ^{119}Sn NMR experimental parameters as discussed in Figure 6.7 in the main text. The ^{119}Sn NMR spectra were acquired at 7.05 T using either $4.0\ \mu\text{s}$ (62.5 kHz) or $1.7\ \mu\text{s}$ (147.1 kHz) $\pi/2$ pulse in a Hahn-echo pulse sequence.

Samples	v_{rot} (kHz)	v_{rf} (kHz)	Echo delay (μs)	Recycle delay (s)	# of scans	Acquisition time (min)
Cs_2SnCl_6	0.0	62.5	24.0	200	64	213
$\text{Cs}_2\text{SnCl}_3\text{Br}_3$		147.1	27.0	210	768	2688
Cs_2SnBr_6		62.5	24.0	15	256	64
$\text{Cs}_2\text{SnBr}_{4.5}\text{I}_1$.5		147.1	27.5	15	5120×2 offsets	1280 / offset
$\text{Cs}_2\text{SnBr}_3\text{I}_3$		147.1	27.5	15	5120×3 offsets	1280 / offset
$\text{Cs}_2\text{SnBr}_{1.5}\text{I}_4$.5		147.1	27.5	15	6144×2 offsets	1536 / offset
Cs_2SnI_6		62.5	24.0	0.2	15360	54

Table E9e. Solid-state ^{133}Cs MAS NMR experimental parameters as discussed in Figure 6.9a in the main text. The ^{133}Cs NMR spectra were acquired at 11.75 T using a $1.38\ \mu\text{s}$ ($5.5\ \mu\text{s}\ \pi/2$) Bloch pulse sequence.

Samples	v_{rot} (kHz)	Recycle delay (s)	# of scans	Acquisition time (min)
BM- Cs_2SnI_6	5.0	120	4	8
HG- Cs_2SnI_6		120	16	32
SS- Cs_2SnI_6		120	16	32

Table E9f. Solid-state ^{119}Sn NMR experimental parameters as discussed in Figure 6.9b in the main text. The ^{119}Sn NMR spectra were acquired at 7.05 T using a $4.0\ \mu\text{s}\ \pi/2$ Hahn-echo pulse sequence.

Samples	ν_{rot} (kHz)	Echo delay (μs)	Recycle delay (s)	# of scans	Acquisition time (min)
BM- Cs_2SnI_6	0.0	24.0	0.05	10240	9
HG- Cs_2SnI_6			0.2	10240	34
SS- Cs_2SnI_6			1.5	20480	512

Table E10. DFT computed NMR shielding parameters for structurally optimized $\text{SnCl}_n\text{Br}_{6-n}$ and $\text{SnBr}_n\text{I}_{6-n}$ ($n = 0-6$) octahedral species determined using PBE0/TZ2P, incorporating relativistic effects with ZORA and spin-orbit coupling. Optimized structures are available in Table E11.

Octahedral species	Isotropic magnetic shielding, σ_{iso} (ppm)	Isotropic chemical shift, δ_{iso} (ppm) ^a	Span, Ω (ppm)	Skew, κ
SnCl_6	3828.6	-813.3	0.0	1.0
SnCl_5Br	4040.6	-1025.9	375.2	1.0
cis- SnCl_4Br_2	4282.0	-1268.1	451.5	-0.95
trans- SnCl_4Br_2	4247.5	-1233.5	748.7	1.0
fac- SnCl_3Br_3	4550.7	-1537.6	20.6	-1.0
mer- SnCl_3Br_3	4517.2	-1504.0	895.8	-0.17
cis- SnCl_2Br_4	4812.0	-1799.7	458.6	0.93
trans- SnCl_2Br_4	4780.4	-1768.0	1058.3	-1.0
SnClBr_5	5098.6	-2087.1	537.1	-1.0

SnBr ₆	5407.8	-2397.3	0.0	0.05
SnBr ₅ I	5927.2	-2918.3	1294.0	1.0
cis-SnBr ₄ I ₂	6461.9	-3454.6	1763.9	-0.97
trans-SnBr ₄ I ₂	6426.5	-3419.1	2616.8	1.0
fac-SnBr ₃ I ₃	6971.1	-3965.3	48.8	-1.0
mer-SnBr ₃ I ₃	6965.1	-3959.4	3579.8	-0.26
cis-SnBr ₂ I ₄	7440.4	-4436.0	1839.3	0.96
trans-SnI ₄ Br ₂	7461.3	-4457.0	4702.2	-1.0
SnBrI ₅	7867.2	-4864.1	2426.9	-1.0
SnI ₆	8219.3	-5217.3	0.2	0.01

^a Referenced with SnMe₄ ($\sigma_{\text{iso}} = 3017.74$ ppm) at the same level of theory.

$$\delta_{\text{iso}} = \frac{\sigma_{\text{iso}}(\text{reference,ppm}) - \sigma_{\text{iso}}(\text{sample,ppm})}{1 - \{\sigma_{\text{iso}}(\text{reference,ppm}) \times 10^{-6}\}}$$

Table E11. Optimized Cartesian coordinates of SnCl_nBr_{6-n} and SnBr_nI_{6-n} ($n = 0-6$) octahedral species described in Table E10. Units are Å.

SnBr ₆				SnCl ₆			
Atom	X	Y	Z	Atom	X	Y	Z
Sn	-0.000003	-0.000003	-0.000003	Sn	-0.000001	-0.000001	-0.000001
Br	2.639876	0.000003	0.000003	Cl	2.469410	0.000001	0.000001
Br	0.000003	2.639881	0.000003	Cl	0.000001	2.469411	0.000001
Br	0.000003	0.000003	2.639886	Cl	0.000001	0.000001	2.469412
Br	-2.639887	0.000003	0.000003	Cl	-2.469413	0.000001	0.000001
Br	0.000003	-2.639892	0.000003	Cl	0.000001	-2.469414	0.000001
Br	0.000003	0.000003	-2.639897	Cl	0.000001	0.000001	-2.469415
SnI ₆				SnClBr ₅			
Atom	X	Y	Z	Atom	X	Y	Z
Sn	-0.000004	-0.000004	-0.000005	Sn	-0.000003	-0.000003	-0.018109
I	2.893406	0.000005	0.000005	Br	2.641710	0.000004	-0.013676

I	0.000005	2.893414	0.000005		Br	0.000004	2.641715	-0.013664
I	0.000005	0.000005	2.893421		Br	0.000004	0.000002	2.626767
I	-2.893422	0.000005	0.000005		Br	-2.641721	0.000004	-0.013674
I	0.000005	-2.893429	0.000005		Br	0.000004	-2.641726	-0.013666
I	0.000005	0.000005	-2.893437		Cl	0.000003	0.000004	-2.475419
SnCl₃Br					SnBrI₅			
Atom	X	Y	Z		Atom	X	Y	Z
Sn	-0.000001	-0.000001	0.022119		Sn	-0.000004	-0.000004	-0.001161
Cl	2.466313	-0.000002	0.012272		I	2.894896	0.000008	0.004809
Cl	0.000003	2.466314	0.012272		I	0.000007	2.894905	0.004829
Cl	0.000000	0.000002	2.486203		I	0.000002	0.000001	2.901733
Cl	-2.466315	-0.000002	0.012274		I	-2.894912	0.000008	0.004811
Cl	0.000003	-2.466317	0.012271		I	0.000007	-2.894921	0.004831
Br	-0.000003	0.000005	-2.635972		Br	0.000005	0.000004	-2.626872
SnBr₅I					cis-SnCl₄Br₂			
Atom	X	Y	Z		Atom	X	Y	Z
Sn	-0.000004	-0.000004	0.008609		Sn	-0.000001	0.020988	0.020987
Br	2.636476	0.000003	-0.007286		Cl	2.464143	0.011742	0.011732
Br	0.000003	2.636481	-0.007288		Cl	-0.000002	2.482497	0.012951
Br	0.000004	0.000003	2.638473		Cl	0.000004	0.012945	2.482498
Br	-2.636488	0.000003	-0.007281		Cl	-2.464145	0.011735	0.011738
Br	0.000003	-2.636493	-0.007286		Br	0.000004	-2.632555	0.014093
I	0.000005	0.000007	-2.910922		Br	-0.000002	0.014087	-2.632560
trans-SnCl₄Br₂					fac-SnCl₃Br₃			
Atom	X	Y	Z		Atom	X	Y	Z
Sn	-0.000000	-0.000000	0.000000		Sn	0.019967	-0.019970	-0.019969
Cl	2.463699	0.000002	0.000000		Cl	2.479708	-0.012417	-0.012410
Cl	0.000002	2.463700	-0.000000		Br	0.013551	2.630149	-0.013546
Br	-0.000001	-0.000001	2.650822		Br	0.013540	-0.013549	2.630154
Cl	-2.463700	0.000002	0.000000		Br	-2.630159	-0.013529	-0.013529
Cl	0.000002	-2.463701	-0.000000		Cl	0.012417	-2.479710	-0.012428
Br	-0.000001	-0.000001	-2.650822		Cl	0.012417	-0.012414	-2.479711

mer-SnCl₃Br₃					cis-SnCl₂Br₄			
Atom	X	Y	Z		Atom	X	Y	Z
Sn	-0.000001	-0.000000	-0.019922		Sn	-0.000003	-0.018998	-0.018998

Cl	-0.000005	2.462300	-0.011247		Br	2.644252	-0.014176	-0.014179
Br	2.647077	0.000000	-0.014742		Br	0.000001	2.628099	-0.013039
Br	0.000009	0.000000	2.629670		Br	0.000006	-0.013034	2.628104
Br	-2.647083	-0.000000	-0.014744		Br	-2.644263	-0.014181	-0.014173
Cl	-0.000005	-2.462300	-0.011247		Cl	0.000006	-2.477216	-0.011938
Cl	0.000008	-0.000000	-2.479209		Cl	0.000001	-0.011933	-2.477217
trans-SnCl₂Br₄					cis-SnBr₄I₂			
Atom	X	Y	Z		Atom	X	Y	Z
Sn	-0.000002	-0.000002	0.000000		Sn	-0.000004	0.006369	0.006370
Br	2.643734	0.000009	-0.000000		Br	2.634721	-0.008371	-0.008373
Br	0.000009	2.643739	0.000000		Br	0.000003	2.633869	-0.006290
Cl	-0.000005	-0.000005	2.461125		Br	0.000003	-0.006290	2.633877
Br	-2.643740	0.000009	-0.000000		Br	-2.634734	-0.008370	-0.008368
Br	0.000009	-2.643745	0.000000		I	0.000007	-2.906641	-0.003545
Cl	-0.000005	-0.000005	-2.461125		I	0.000005	-0.003545	-2.906651
trans-SnBr₄I₂					fac-SnBr₃I₃			
Atom	X	Y	Z		Atom	X	Y	Z
Sn	-0.000002	-0.000002	-0.000000		Sn	0.004533	-0.004539	-0.004541
Br	2.633990	0.000008	0.000000		Br	2.630937	0.007380	0.007376
Br	0.000008	2.633995	0.000000		I	-0.004723	2.904260	0.004719
I	-0.000005	-0.000005	2.904931		I	-0.004738	0.004719	2.904268
Br	-2.633995	0.000008	-0.000000		I	-2.904277	0.004752	0.004755
Br	0.000008	-2.634000	-0.000000		Br	-0.007351	-2.630945	0.007355
I	-0.000005	-0.000005	-2.904931		Br	-0.007361	0.007353	-2.630953
mer-SnBr₃I₃					cis-SnBr₂I₄			
Atom	X	Y	Z		Atom	X	Y	Z
Sn	-0.000002	-0.000000	-0.004261		Sn	-0.000004	-0.002737	-0.002738
I	2.900318	0.000000	0.002595		I	2.897433	0.003773	0.003770
Br	-0.000007	2.633482	0.009317		I	0.000003	2.902460	0.005789
I	0.000014	0.000000	2.903430		I	0.000004	0.005786	2.902467
I	-2.900328	0.000000	0.002592		I	-2.897450	0.003774	0.003773
Br	-0.000007	-2.633482	0.009316		Br	0.000007	-2.628388	0.008315
Br	0.000012	0.000000	-2.630009		Br	0.000006	0.008312	-2.628396
trans-SnBr₂I₄								
Atom	X	Y	Z					
Sn	-0.000003	-0.000003	-0.000000					

I	2.896449	0.000014	0.000000
I	0.000014	2.896458	-0.000000
Br	-0.000007	-0.000008	2.633178
I	-2.896459	0.000014	0.000000
I	0.000014	-2.896469	-0.000000
Br	-0.000007	-0.000007	-2.633178

Table E12. Calculated population distribution (binomial) for $\text{SnCl}_n\text{Br}_{6-n}$ and $\text{SnBr}_n\text{I}_{6-n}$ environments in $\text{Cs}_2\text{SnCl}_x\text{Br}_{6-x}$ and $\text{Cs}_2\text{SnBr}_x\text{I}_{6-x}$ ($0 \leq x \leq 6$).

$\text{Cs}_2\text{SnCl}_x\text{Br}_{6-x}$	Calculated population of $\text{SnCl}_n\text{Br}_{6-n}$ (%)						
	SnCl_6	SnCl_5Br	SnCl_4Br_2 (cis + trans)	SnCl_3Br_3 (fac + mer)	SnCl_2Br_4 (cis + trans)	SnClBr_5	SnBr_6
Cs_2SnCl_6	100	-	-	-	-	-	-
$\text{Cs}_2\text{SnCl}_3\text{Br}_3$	1.56	9.38	23.44	31.25	23.44	9.38	1.56
Cs_2SnBr_6	-	-	-	-	-	-	100
$\text{Cs}_2\text{SnBr}_x\text{I}_{6-x}$	Calculated population of $\text{SnBr}_n\text{I}_{6-n}$ (%)						
	SnBr_6	SnBr_5I	SnBr_4I_2 (cis + trans)	SnBr_3I_3 (fac + mer)	SnBr_2I_4 (cis + trans)	SnBrI_5	SnI_6
Cs_2SnBr_6	100	-	-	-	-	-	-
$\text{Cs}_2\text{SnBr}_{4.5}\text{I}_{1.5}$	17.80	35.60	29.66	13.18	3.30	0.44	0.02
$\text{Cs}_2\text{SnBr}_3\text{I}_3$	1.56	9.38	23.44	31.25	23.44	9.38	1.56
$\text{Cs}_2\text{SnBr}_{1.5}\text{I}_{4.5}$	0.02	0.44	3.30	13.18	29.66	35.60	17.80
Cs_2SnI_6	-	-	-	-	-	-	100

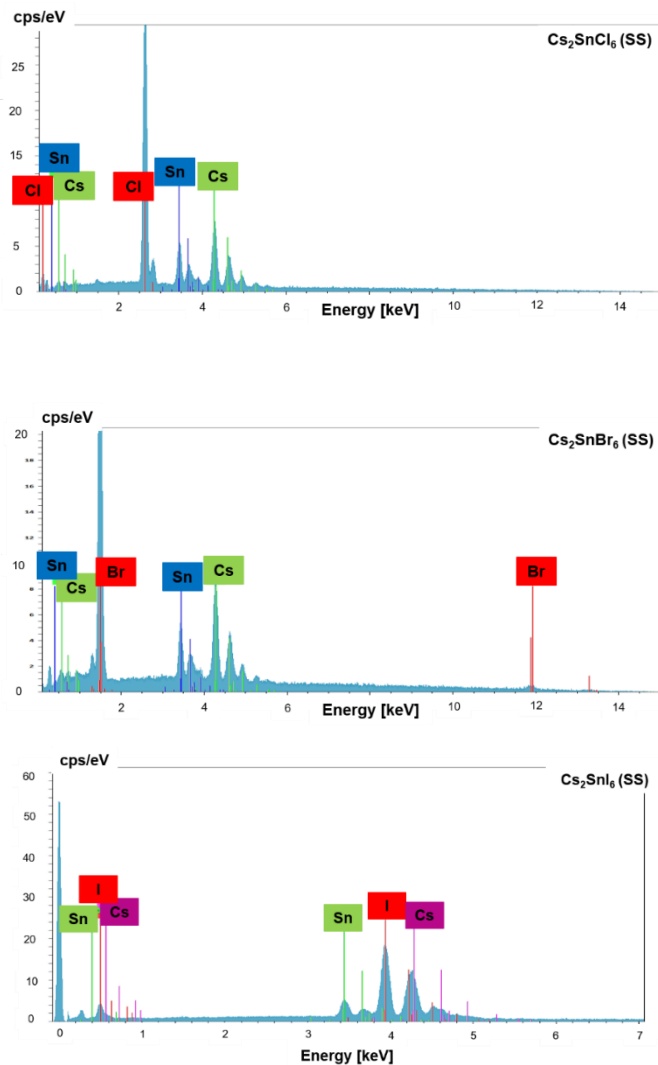


Figure E1. Elemental analysis via energy dispersive X-ray spectroscopy for the solvent synthesized Cs_2SnX_6 ($\text{X} = \text{Cl}, \text{Br}, \text{I}$) parents as indicated.

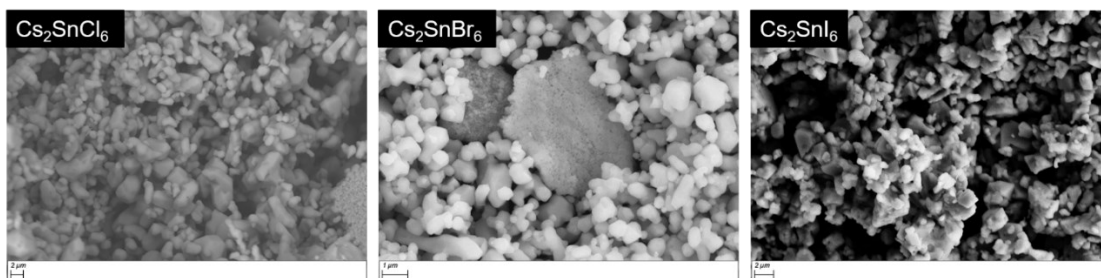


Figure E2. FESEM images for the solvent synthesized Cs_2SnX_6 ($\text{X} = \text{Cl}, \text{Br}, \text{I}$) parents.

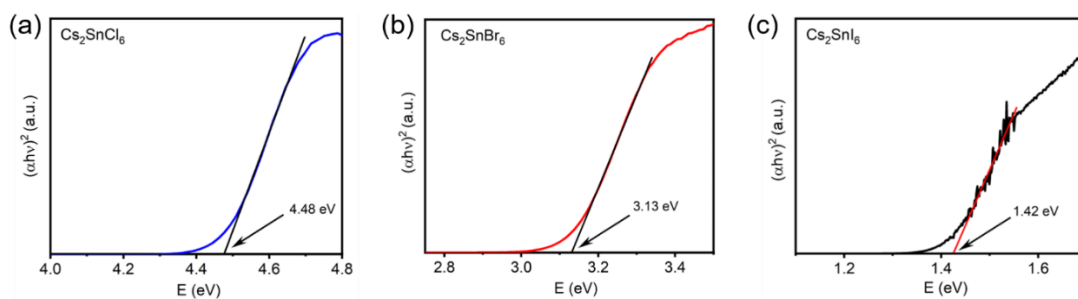


Figure E3. Tauc plots showing direct bandgaps of the solvent synthesized Cs_2SnX_6 ($X = \text{Cl, Br, I}$) parents.

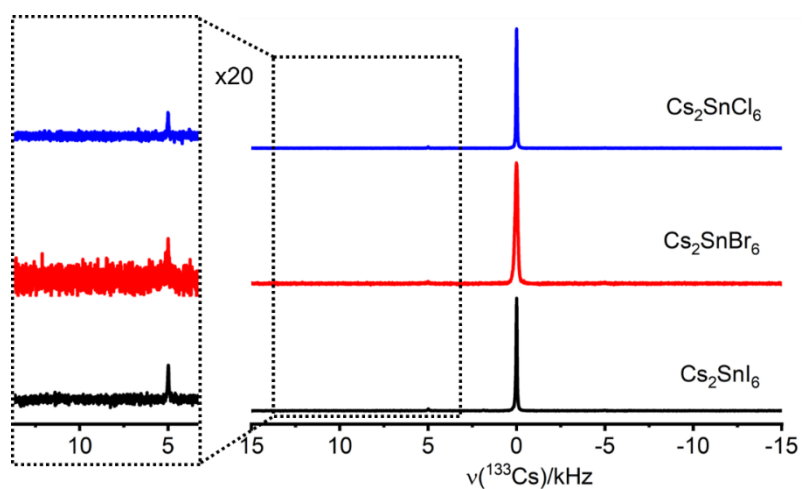


Figure E4. Solid-state ^{133}Cs NMR spectra (frequency scale) of the solvent synthesized Cs_2SnX_6 ($X = \text{Cl, Br, I}$) parents at 11.75 T and $\nu_r = 5$ kHz. The expansion shows the corresponding spinning side band.

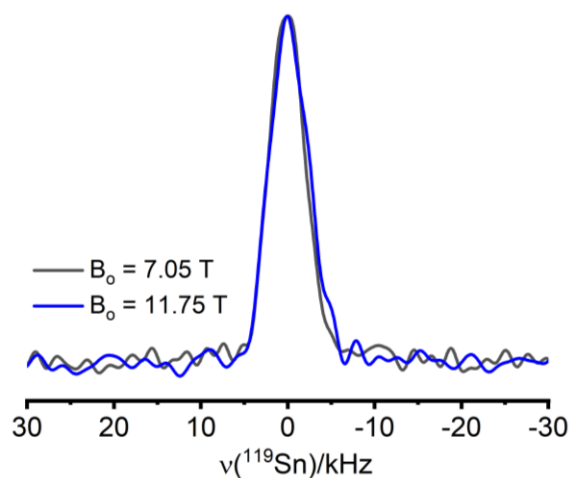


Figure E5. Solid-state ^{119}Sn NMR spectra (frequency scale) of solvent synthesized Cs_2SnBr_6 at 7.05 and 11.75 T under MAS ($\nu_r = 10$ kHz) conditions. The scales are vertically normalized.

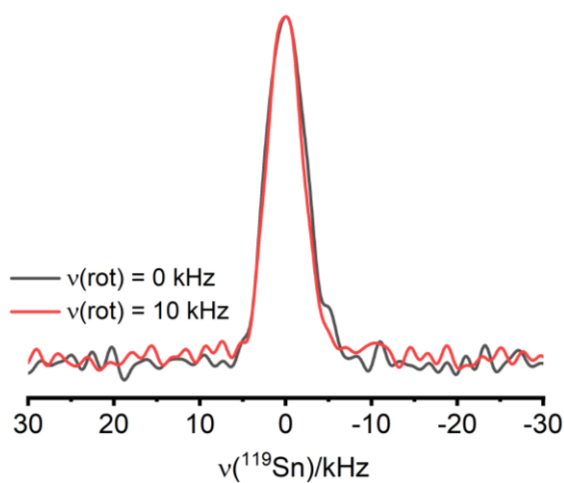


Figure E6. Solid-state ^{119}Sn NMR spectra (frequency scale) of solvent synthesized Cs_2SnBr_6 at 7.05 T under non-spinning and MAS ($\nu_r = 10$ kHz) conditions. The scales are vertically normalized.

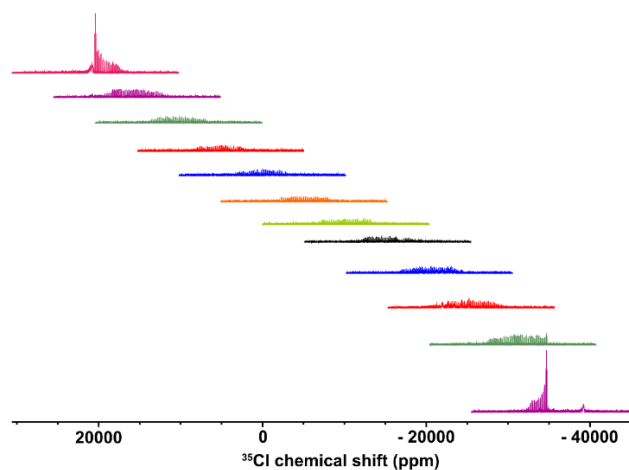


Figure E7. Solid-state ^{35}Cl NMR subspectra with different frequency offsets (250 kHz step size), each acquired at 11.75 T using the WURST-CPMG pulse sequence. Each spectrum was acquired using the following parameters: recycle delay = 1 s, number of scans = 512, number of echos = 50, spikelet spacing = 5 kHz.

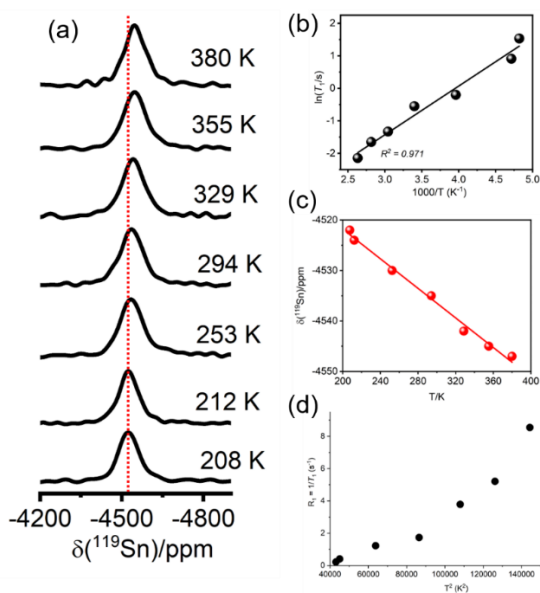


Figure E8. Temperature-dependent ^{119}Sn NMR data ($\nu_r = 0$ kHz, $B_0 = 11.75$ T) for the solvent-synthesized Cs_2SnI_6 sample. (a) ^{119}Sn NMR spectra, (b) Arrhenius plot, plots of (c) ^{119}Sn chemical shift against temperature and (d) inverse of ^{119}Sn T_1 against square of temperature.

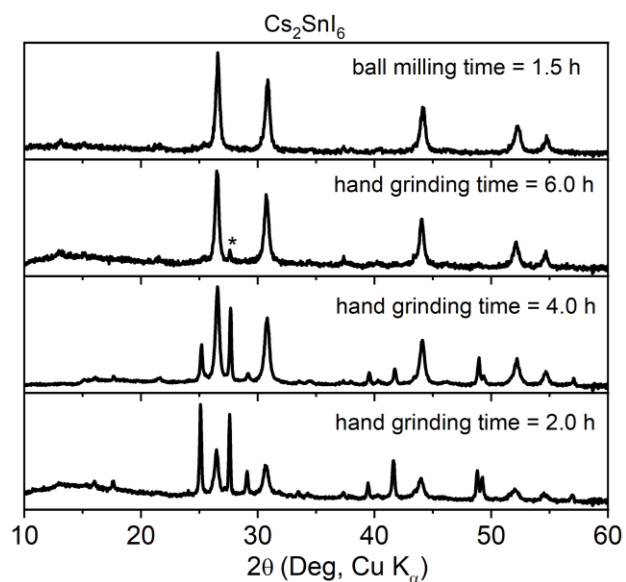


Figure E9. Powder XRD patterns of ball-mill and hand-grind synthesized Cs_2SnI_6 materials at different grinding times as indicated. The asterisk (*) indicates unreacted CsI present in the final hand-ground product.

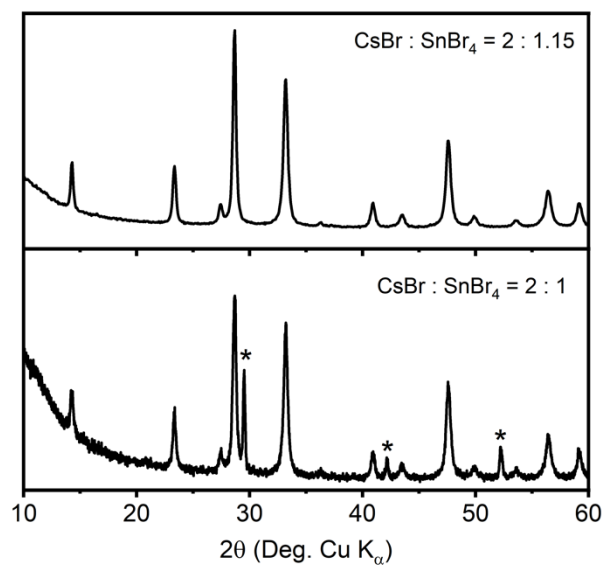


Figure E10. Powder XRD patterns for ball mill synthesized Cs_2SnBr_6 materials with different CsBr and SnBr_4 molar ratios. The ball milling times are 1.5 and 3.0 h for top and bottom traces, respectively. The asterisks (*) indicate excess CsBr present in the final product.

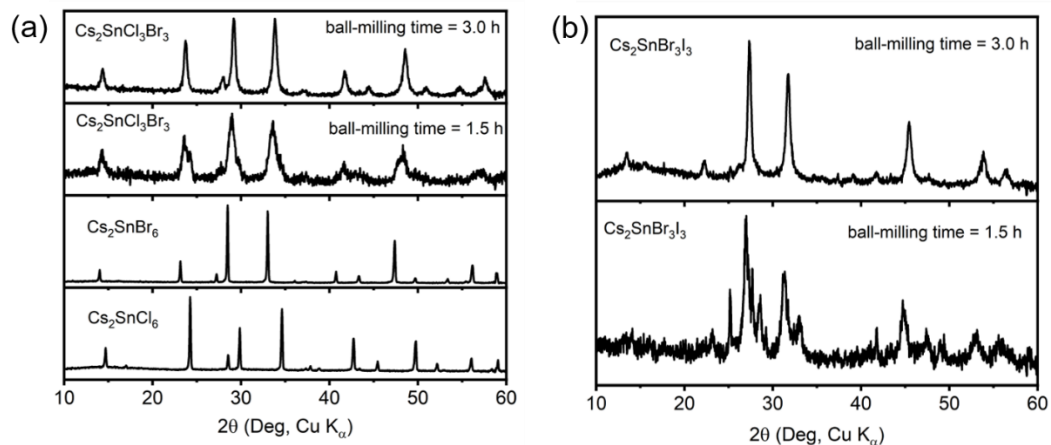


Figure E11. Powder XRD patterns of the (a) $\text{Cs}_2\text{SnCl}_3\text{Br}_3$ and (b) $\text{Cs}_2\text{SnBr}_3\text{I}_3$ materials after 1.5 and 3.0 h of ball milling.

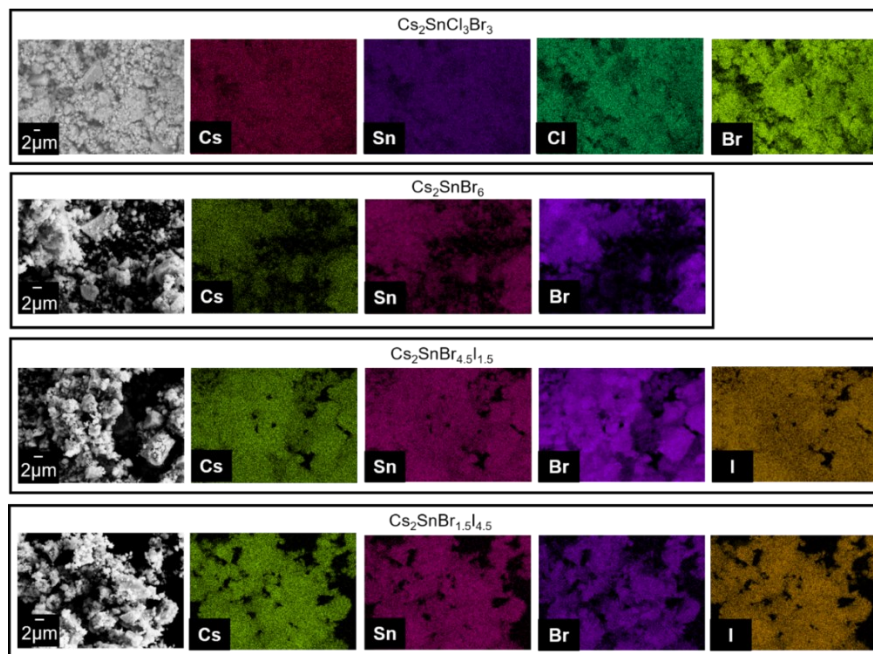
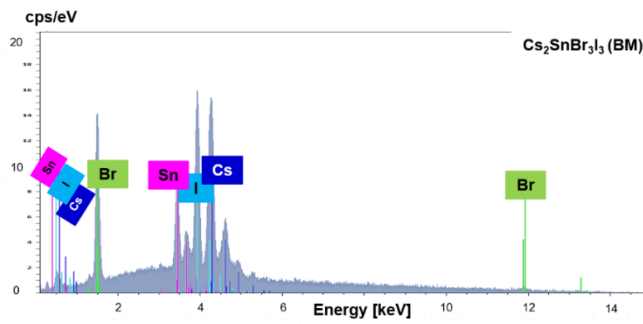
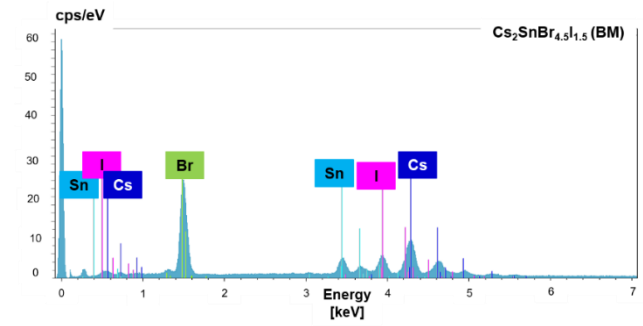
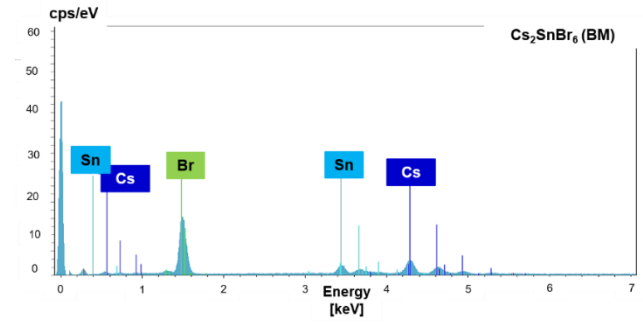
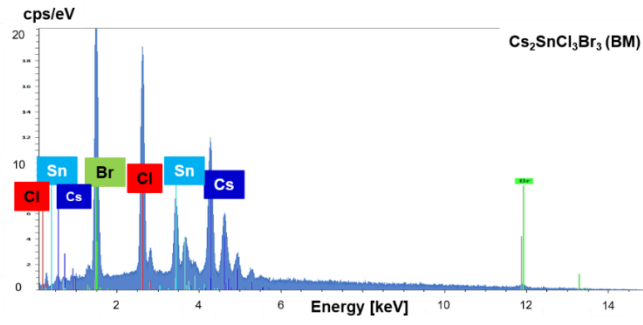


Figure E12. FESEM images and the corresponding EDS elemental mapping for Cs, Sn, Cl, Br and I for the ball-milled $\text{Cs}_2\text{SnCl}_3\text{Br}_3$, Cs_2SnBr_6 , $\text{Cs}_2\text{SnBr}_{4.5}\text{I}_{1.5}$ and $\text{Cs}_2\text{SnBr}_{1.5}\text{I}_{4.5}$ samples as indicated.



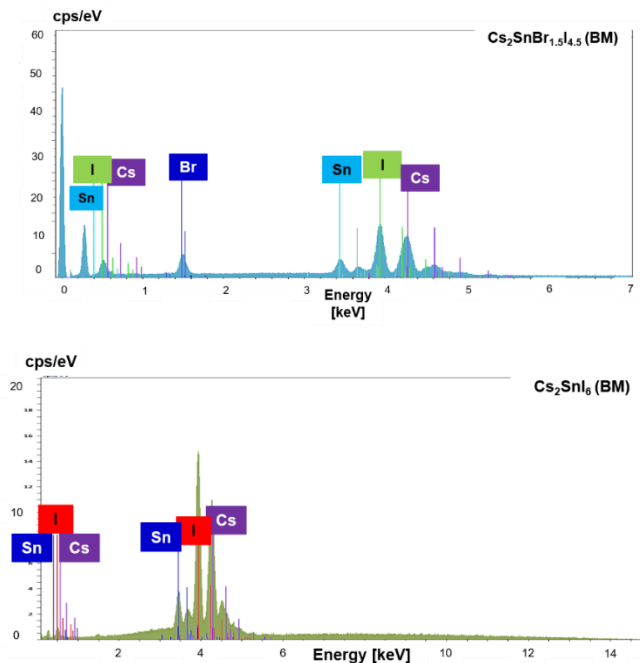


Figure E13. Elemental analysis via energy dispersive X-ray spectroscopy for the ball-milled $\text{Cs}_2\text{SnCl}_x\text{Br}_{6-x}$ ($x = 3$) and $\text{Cs}_2\text{SnBr}_x\text{I}_{6-x}$ ($x = 0, 1.5, 3, 4.5, 6$) samples, as indicated.

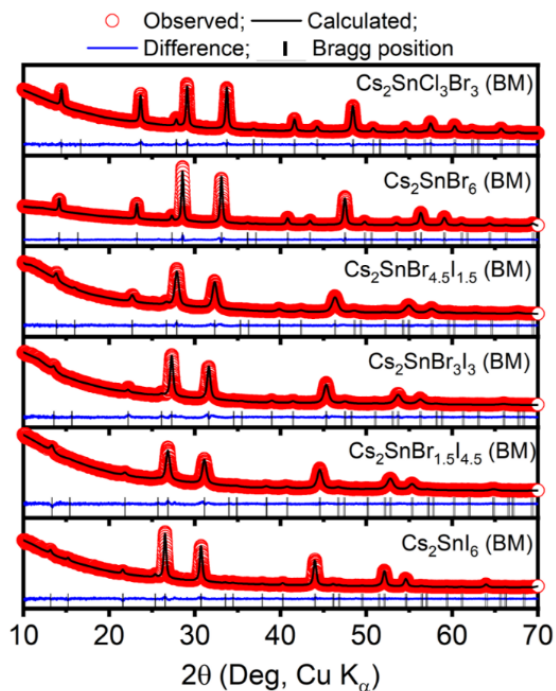


Figure E14. Experimental and fitted powder XRD diagrams for the ball-milled $\text{Cs}_2\text{SnCl}_x\text{Br}_{6-x}$ ($x = 3$) and $\text{Cs}_2\text{SnBr}_x\text{I}_{6-x}$ ($x = 0, 1.5, 3, 4.5, 6$) samples. All the diffraction data are fitted assuming a cubic ($Fm\bar{3}m$) space group symmetry.

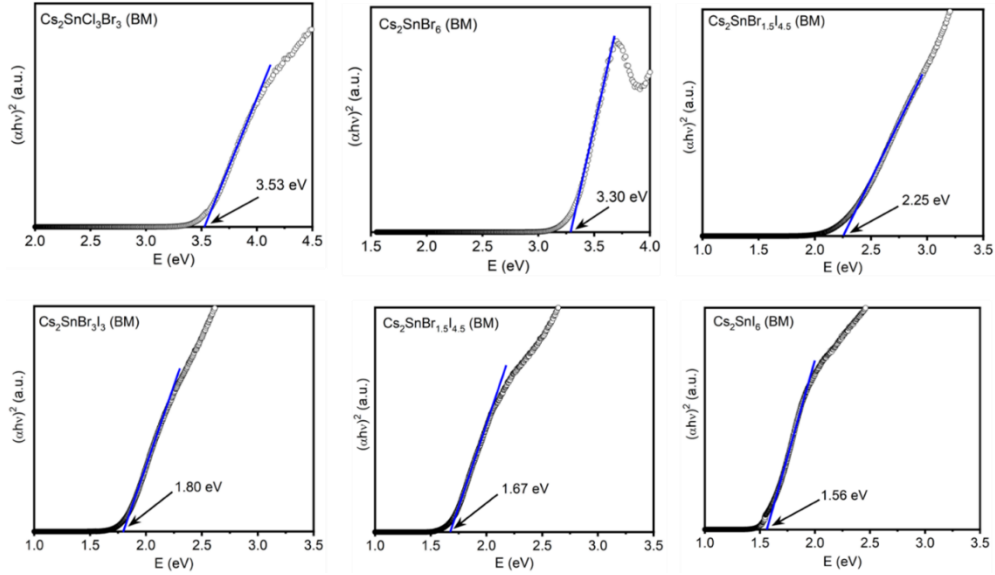


Figure E15. Tauc plots showing direct bandgaps of ball-milled $\text{Cs}_2\text{SnCl}_x\text{Br}_{6-x}$ ($x = 3$) and $\text{Cs}_2\text{SnBr}_x\text{I}_{6-x}$ ($x = 0, 1.5, 3, 4.5, 6$) samples.

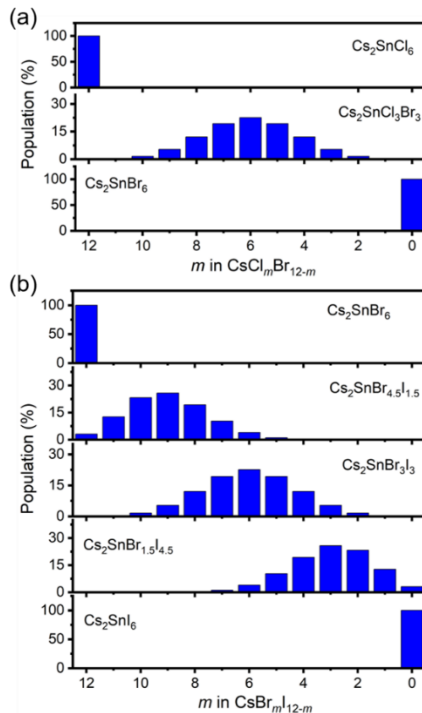


Figure E16. Calculated population distributions (binomial) of local cubooctahedral environments: (a) $\text{CsCl}_m\text{Br}_{12-m}$ in $\text{Cs}_2\text{SnCl}_x\text{Br}_{6-x}$ ($x = 0, 3, 6$) and (b) $\text{CsBr}_m\text{I}_{12-m}$ in $\text{Cs}_2\text{SnBr}_x\text{I}_{6-x}$ ($x = 0, 1.5, 3, 4.5, 6$).

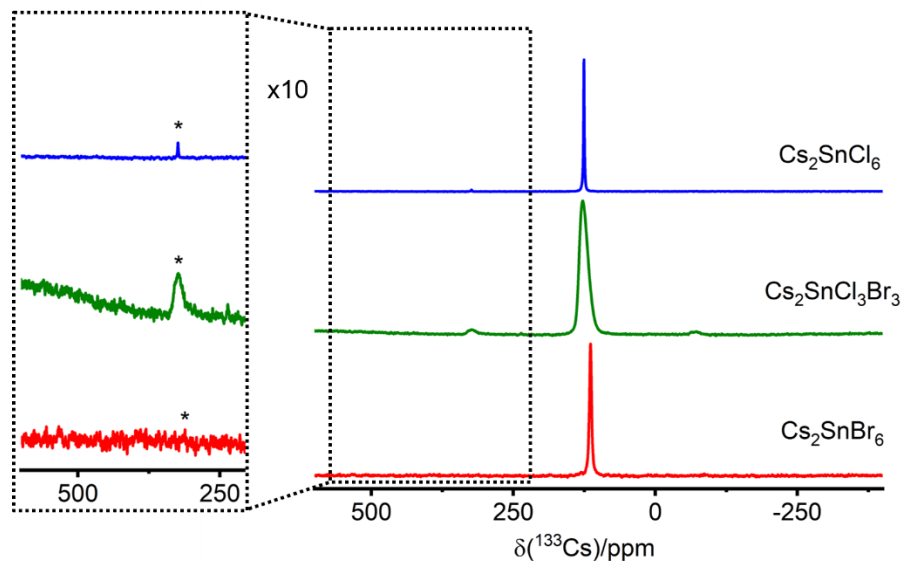


Figure E17. Solid-state ^{133}Cs MAS NMR spectra of Cs_2SnCl_6 , $\text{Cs}_2\text{SnCl}_3\text{Br}_3$ and Cs_2SnBr_6 acquired at 11.75 T with a MAS frequency of 13 kHz. The expansion shows the corresponding spinning side band.

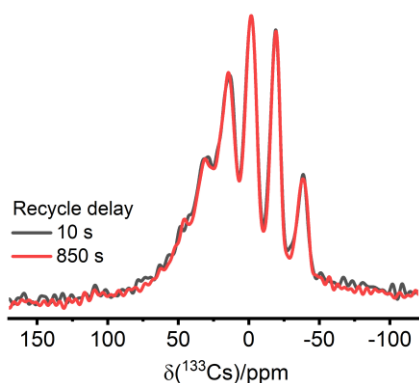


Figure E18. Normalized ^{133}Cs NMR spectra ($B_0 = 11.75$ T, $\nu_{\text{rot}} = 13$ kHz) exhibiting spectral overlap of multiple resonances with recycle delays of 10 and 850 s for

$\text{Cs}_2\text{SnBr}_{1.5}\text{I}_{4.5}$. The ^{133}Cs NMR spectra were acquired using a Bloch pulse sequence with a short tip angle ($\sim 20^\circ$).

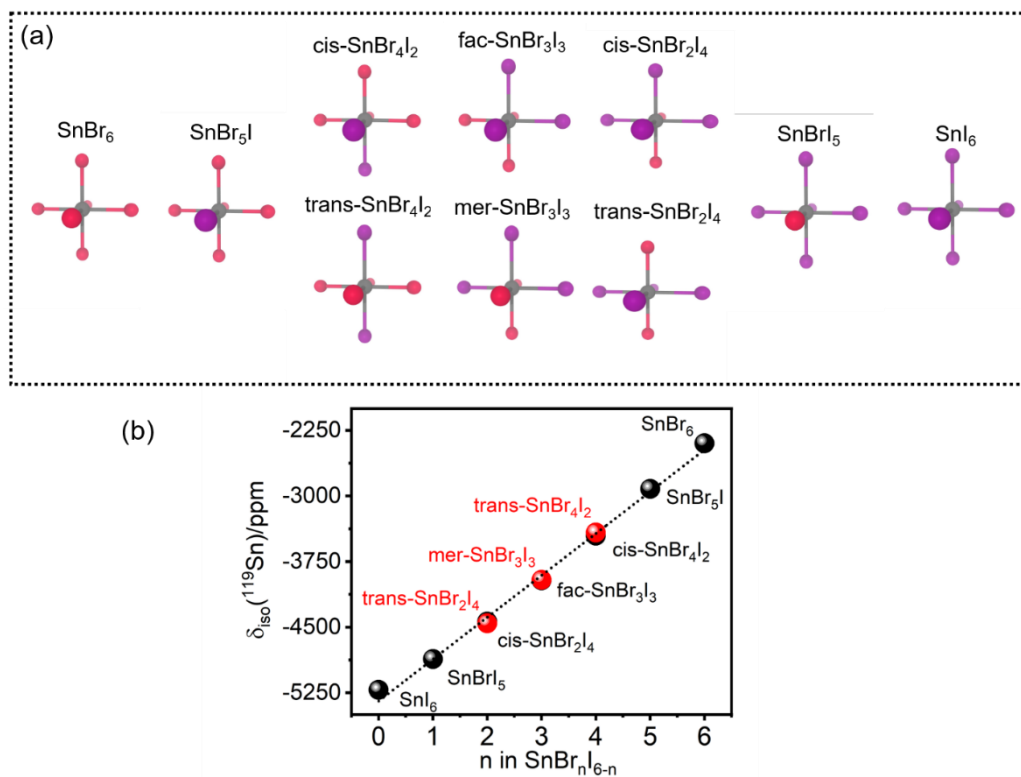


Figure E19. DFT computed results for $\text{SnBr}_n\text{I}_{6-n}$ ($n = 0-6$) environments: (a) optimized geometries and (b) ^{119}Sn isotropic chemical shift as a function of the number of attached Br atoms in $\text{SnBr}_n\text{I}_{6-n}$.

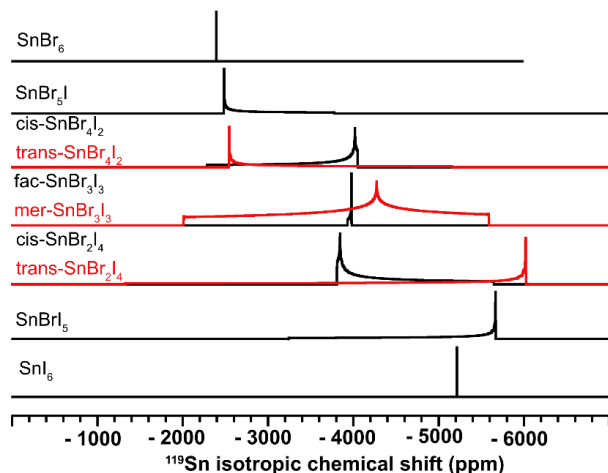


Figure E20. Simulated ^{119}Sn NMR spectra for $\text{SnBr}_n\text{I}_{6-n}$ ($n = 0-6$) environments. The principal tensor components were obtained from the DFT computations.

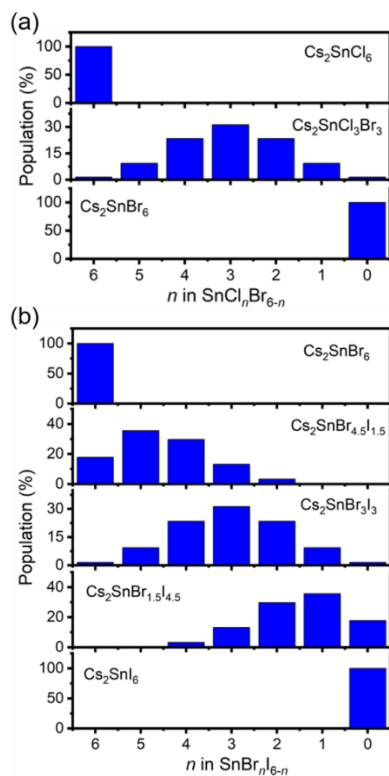


Figure E21. Calculated population distributions (binomial) for local octahedral environments: (a) $\text{SnCl}_n\text{Br}_{6-n}$ in $\text{Cs}_2\text{SnCl}_x\text{Br}_{6-x}$ ($x = 0, 3, 6$) and (b) $\text{SnBr}_n\text{I}_{6-n}$ in $\text{Cs}_2\text{SnBr}_x\text{I}_{6-x}$ ($x = 0, 1.5, 3, 4.5, 6$).

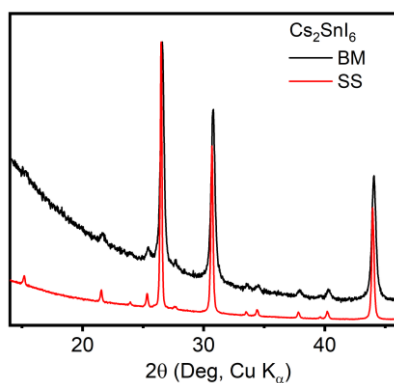


Figure E22. Powder XRD patterns for Cs_2SnI_6 samples prepared by the ball-milling (BM) and solvent-synthesis (SS) routes.

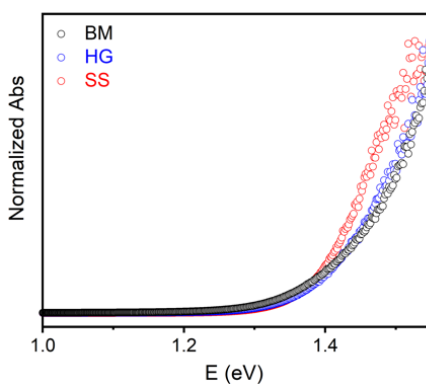


Figure E23. Normalized optical absorption spectra for Cs_2SnI_6 samples prepared by the ball-milling (BM), Hand grinding (HG), and solvent-synthesis (SS) routes.

References

- (1) Harris, R. K.; Becker, E. D. NMR Nomenclature: Nuclear Spin Properties and Conventions for Chemical Shifts—IUPAC Recommendations. *J. Magn. Reson.* **2002**, *156*, 323–326.
- (2) Moudrakovski, I. L. *Local Dynamics in Hybrid Perovskites by Solid-State NMR*, 1st ed.; Elsevier Ltd., 2021; Vol. 102. <https://doi.org/10.1016/bs.arnmr.2020.10.004>.
- (3) Abragam, A. *The Principles of Nuclear Magnetism*, Oxford University Press; Oxford university press, 1961.

- (4) Kubicki, D. J.; Prochowicz, D.; Salager, E.; Rakhmatullin, A.; Grey, C. P.; Emsley, L.; Stranks, S. D. Local Structure and Dynamics in Methylammonium, Formamidinium and Cesium Tin(II) Mixed-halide Perovskites from ^{119}Sn Solid-state NMR. *J. Am. Chem. Soc.* **2020**, *142*, 7813–7826.
- (5) Grutzner, J. B.; Stewart, K. W.; Wasylishen, R. E.; Lumsden, M. D.; Dybowski, C.; Beckmann, P. A. A New Mechanism for Spin-Lattice Relaxation of Heavy Nuclei in the Solid State: ^{207}Pb Relaxation in Lead Nitrate. *J. Am. Chem. Soc.* **2001**, *123*, 7094–7100.
- (6) Shmyreva, A. A.; Safdari, M.; Furó, I.; Dvinskikh, S. V. NMR Longitudinal Relaxation Enhancement in Metal Halides by Heteronuclear Polarization Exchange during Magic-Angle Spinning. *J. Chem. Phys.* **2016**, *144*, 224201.
- (7) Maughan, A. E.; Ganose, A. M.; Candia, A. M.; Granger, J. T.; Scanlon, D. O.; Neilson, J. R. Anharmonicity and Octahedral Tilting in Hybrid Vacancy-Ordered Double Perovskites. *Chem. Mater.* **2018**, *30*, 472–483.
- (8) Maughan, A. E.; Paecklar, A. A.; Neilson, J. R. Bond Valences and Anharmonicity in Vacancy-Ordered Double Perovskite Halides. *J. Mater. Chem. C* **2018**, *6*, 12095–12104.